Modern Aspects of Electrochemistry 60

Stojan Djokić *Editor*

Biomedical and Pharmaceutical Applications of Electrochemistry

Springer

MODERN ASPECTS OF ELECTROCHEMISTRY

No. 58

Series Editors:
Ralph E. White
Department of Chemical Engineering
University of South Carolina
Columbia, SC 29208

Constantinos G. Vayenas
Department of Chemical Engineering
University of Patras
Patras 265 00
Greece

More information about this series at
http://www.springer.com/series/6251

Previously from Modern Aspects of Electrochemistry

Modern Aspects of Electrochemistry No. 56

Applications of Electrochemistry in Medicine

Edited by Mordechay Schlesinger, Professor Emeritus, Department of Physics, University of Windsor, Canada.

Topics in Number 56 include:

- Electrochemistry in the design and development of medical technologies and devices
- Medical devices at the interface of biology and electrochemistry
- Sensing by screen printed electrodes for medical diagnosis
- Electrochemical glucose sensors
- Electrochemistry of adhesion and spreading of lipid vesicles on electrodes
- Bio-Electrochemistry and chalcogens
- Nanoplasmonics in medicine
- Extravascular hemoglobin: aging contusions
- Modeling tumor growth and response to radiation

Modern Aspects of Electrochemistry No. 57

Electrodeposition and Surface Finishing

Edited by Stojan S. Djokić, Professor of Chemical & Materials Engineering at the University of Alberta

Topics in Number 57 include:

- Electrodeposition and the characterization of alloys and composite materials
- Mechanistic aspects of lead electrodeposition
- Electrophoretic deposition of ceramic materials onto metal surfaces
- Metal oxides for energy conversion and storage
- Electrochemical aspects of chemical mechanical polishing
- Surface treatments prior to metallization of semiconductors, ceramics, and polymers
- Anodization of aluminum

Stojan Djokić
Editor

Biomedical and Pharmaceutical Applications of Electrochemistry

Editor
Stojan Djokić
Elchem Consulting Ltd.
Edmonton, AB, Canada

ISSN 0076-9924 ISSN 2197-7941 (electronic)
Modern Aspects of Electrochemistry
ISBN 978-3-319-31847-9 ISBN 978-3-319-31849-3 (eBook)
DOI 10.1007/978-3-319-31849-3

Library of Congress Control Number: 2016943423

Printed on acid-free paper

This Springer imprint is published by Springer Nature
The registered company is Springer International Publishing AG Switzerland

Preface

Research in electrochemical science and technology has brought tremendous achievements. Beyond the traditional applications in the electronics, energy devices, aerospace, and automotive areas, developments in electrochemistry are very important for practical biomedical applications. In particular, developments related to medical devices, implants, sensors, antimicrobially active material/materials, drug delivery systems etc., have significantly advanced in the past few decades.

The aim of this issue of Modern Aspects of Electrochemistry is to review the electrochemical aspects of the latest developments of various materials and/or methods used in biomedical and pharmaceutical applications. I must express my great thanks to Dr. Kenneth Howell of Springer for his continuous encouragement in collecting and editing these very valuable contributions from distinguished scientists in the field of electrochemical science and technology around the globe.

Ingrid Milošev in Chap. 1 analyses recent developments in antimicrobial coatings on titanium and titanium alloys. Titanium and titanium alloys are important biomedical materials since they exhibit excellent biocompatibility and very good mechanical properties. However, adhesion of bacteria and their colonization on titanium-based materials cause inflammatory process leading to the destruction of both soft and hard tissue around the implant. These problems require preventive measures in order to avoid or at least to reduce implant-related infection. For this purpose antimicrobial coatings are applied on the surface of titanium-based

implants. Several approaches have been proposed for this target and they are reviewed in this chapter. Of course, the electrochemical aspects are thoroughly discussed.

In Chap. 2, by Avramov-Ivić, Petrović, and Mijin, recent advances in electrochemical analysis of pharmaceuticals are discussed in detail. The application of the most commonly used voltammetric techniques combined with different chromatographic, spectrophotometric, and spectroscopic techniques in the analysis of the pharmaceuticals is reviewed. Pharmaceutically active compounds under consideration belong to chemotherapeutic agents (antibiotics), drugs affecting neurotransmission and enzymes as catalytic receptors, drugs affecting the cardiovascular system, drugs affecting the immune systems, and some other drugs. The new electroanalytical methods for qualitative and quantitative determination of standard substances are discussed in cases such as five macrolide antibiotics, amphetamines, carbamazepine, donepezil, amlodipine, nifedipine, clopidogrel, tamiflu, and oxaprozin. Some drugs are analyzed in human biological samples.

Chapter 3 by Ceré, Gomez Sanchez, and Ballarre describes anodization and sol gel coatings as surface modification to promote osseointegration in metallic prostheses. Orthopedic devices for permanent implants require short-term fixation and fast bone attachment and healing. Also they are required to have excellent mechanical properties in load bearing sites and to be corrosion resistant. This chapter reviews the surface modifications produced on orthopedic and dentistry metallic materials by anodization and by hybrid coatings by sol gel technique from an electrochemical point of view. Both of these processes promote corrosion resistance in physiological fluids and bioactivity.

In Chap. 4 by Mišković-Stanković novel nanostructured materials synthesized according to original electrochemical procedures are described and discussed. A constant increase in the number of microorganisms resistant to existing antibiotics has stimulated a revival in the clinical use of silver. Various products containing silver ions have been developed and utilized for treatments of infections in burns, open wounds, and chronic ulcers. Hydrogels are useful as wound dressings or soft tissue implants. Silver nanoparticles embedded in hydrogel matrices are attractive

for biomedical applications due to the possibility for the controlled release of Ag(I) ions resulting in antimicrobial activity. These gels are hydrophilic, biocompatible, biodegradable, easily processed into different shapes, and approved for medical use. Two electrochemical methods for material fabrication are described: (1) electrochemical synthesis of silver nanoparticles in the polymer solution under galvanostatic conditions, followed by electrostatic extrusion or freezing-thawing, and (2) electrochemical reduction of Ag^+ ions into silver nanoparticles inside the polymer hydrogel, with the variation of applied voltage and implementation time. The nanocomposites produced by the suggested electrochemical methods are suitable for wound dressings, soft tissue implants, drug delivery devices, and carriers for cell cultivation. Silver alginates, silver-poly (*N*-vinyl-2-pyrrolidone), and silver-polyvinyl alcohol are examples of such materials discussed here. According to cytotoxicity, antimicrobial, in vitro bioactivity, and bioreactor tests, electrochemically produced materials for soft tissue implants are very promising candidates for future biomedical applications.

Chapter 5 by Mišković-Stanković describes biomaterials for hard tissue implants. The development of synthetic materials with acceptable mechanical properties and excellent biocompatibility is required for hard tissue implants. Hydroxyapatite (HAP) is very brittle, and for this reason, great attention has been focused on the development of composite coatings. Natural biodegradable polymer lignin (Lig) is considered a promising alternative for a new biocomposite coating. Application of graphene as a filler minimizes the brittleness of HAP and improves the mechanical properties of biocomposite coatings. However, bacterial infection of bone implants has resulted from rejection. This chapter explores the novel nanostructured biomaterials suitable for medical applications as hard tissue implants (hips, knees, ankle, shoulder, elbow joints), drug delivery devices, and dental restorations, implants, and orthodontics, synthesized according to electrochemical procedures. Lignin and graphene-based nanocomposite coatings doped with silver and deposited on titanium substrate using electrophoretic deposition method are explored in this chapter. Electrophoretic deposition produces thin films of controlled thickness and surface

morphology, by changing the electrochemical conditions. Coatings for hard tissue implants produced via electrochemical deposition are excellent candidates for future biomedical applications.

This new volume of Modern Aspects of Electrochemistry brings to scientists, engineers, and students new concepts and summarized results related to the application of electrochemical processes in the pharmaceutical and biomedical fields. I believe that the results presented in this issue of Modern Aspects of Electrochemistry will have significant influence for future practical applications.

Edmonton, AB, Canada Stojan S. Djokić

Contents

Contributors

Josefina Ballarre Electrochemistry and Corrosion Division, INTEMA (CONICET-University of Mar del Plata), Mar del Plata, Argentina

Silvia Cere Electrochemistry and Corrosion Division, INTEMA (CONICET-University of Mar del Plata), Mar del Plata, Argentina

Milka L. Avramov Ivić ICTM-Institute of Electrochemistry, University of Belgrade, Belgrade, Serbia

Dušan Ž. Mijin Faculty of Technology and Metallurgy, University of Belgrade, Belgrade, Serbia

Ingrid Milošev Jožef Stefan Institute, Ljubljana, Slovenia

Valdoltra Orthopedic Hospital, Ankaran, Slovenia

Vesna B. Mišković-Stanković Faculty of Technology and Metallurgy, University of Belgrade, Belgrade, Serbia

Slobodan D. Petrović Faculty of Technology and Metallurgy, University of Belgrade, Belgrade, Serbia

Andrea Gomez Sanchez Electrochemistry and Corrosion Division, INTEMA (CONICET-University of Mar del Plata), Mar del Plata, Argentina

Chapter 1
Surface Treatments of Titanium with Antibacterial Agents for Implant Applications

Ingrid Milošev

1.1 Introduction

It was only in the twentieth century that technology enabled the isolation of metallic titanium from its minerals [1]. Thus, industrial production of titanium began relatively late, in 1946. Due to its low density and high corrosion resistance, titanium became indispensable in the aerospace industry. The use of titanium in biomedical applications dates from 1965. Commercially pure titanium and its alloy Ti–6Al–4V are the most commonly used titanium-based biomaterials, especially in orthopedics. Millions of patients are treated with various joint replacements, many patients also with other types of prostheses, such as tumor prostheses, small joint prostheses, fracture-treatment devices, etc.

Titanium and its alloys do not provoke allergic reactions and are considered to be biocompatible. None of these materials is ferromagnetic. Commercially pure titanium does not yield sufficient hardness for load-bearing applications and is therefore mainly used in dental surgery, and in orthopedic surgery for the manufacture of acetabular shells, and in the form of coatings for joint replacements. The titanium alloys Ti–6Al–4V and Ti–6Al–7Nb

I. Milošev (✉)
Jožef Stefan Institute, Jamova c. 39, 1000 Ljubljana, Slovenia

Valdoltra Orthopedic Hospital, Jadranska c. 31, 6280 Ankaran, Slovenia
e-mail: ingrid.milosev@ijs.si

S. Djokić (ed.), *Biomedical and Pharmaceutical Applications of Electrochemistry*, Modern Aspects of Electrochemistry 60,
DOI 10.1007/978-3-319-31849-3_1

exhibit an α+β structure and higher compression strength compared to titanium, consequently their range of applications in orthopedics is broader. Titanium(IV) oxide, TiO_2, passive film forms spontaneously at the alloy surface and due its high stability protects the underlying alloy against dissolution. A specific property of these materials is their osseointegration ability, which is based on the formation of bone cells and mineralized bone matrix on the titanium surface. The effect of osseointegration can be increased by increasing surface roughness and consequently surface area. This can be achieved by means of various processes encouraging bone in-growth and providing enhanced fixation, such as surface roughening, a porous coating, using wire as fiber-metal coatings, employing a beaded surface or plasma-sprayed surface, etc. In addition to osseointegration, another property of material surface, i.e., the ability to resist of bacteria attack, is important. Implant-related infection is a serious complication which requires a long-term antibiotic treatment and, very often, implant removal. This is related to personal suffering for the patient and also high medical costs. Despite relatively low incidence (0.2–2 %) of infections of orthopedic joint replacements, this poses a serious problem due to the growing number of implanted prosthetic devices worldwide [2]. The use of prophylactic systemic antibiotics has been shown to dramatically reduce the incidence of implant-related infection. Further, the local delivery of antibiotics in bone cement is already a part of routine practice. There are studies directed toward the possibility to apply antibiotics directly or incorporated in the coatings [3] which obviously has potential advantages due to local delivery but is probably difficult to achieve the optimum between sufficiently long delivery period and development of antibiotic resistance [4]. Bacterial colonization and biofilm formation on the implant may lead to acute and chronic infection of the underlying bone and the adjacent tissue. Free-floating planktonic bacteria located in fluids and tissues are normally accessible to appropriate systemic antibiotics [4]. However, bacteria adherent to implants are often largely embedded in so-called biofilm, i.e., bacteria embedded in a extracellular matrix or “slime,” and the surface is then hidden from the most host’s immune system and resistant to antibiotics. As prolonged use of antibiotics may lead to drug resistance and even compro-

mise osseointegration and immune system, alternative strategies are being explored in the last decade, as reviewed in several recent reviews discussing various approaches either more systematically, or one approach in more detail [4–7]. In the present review, a systemic approach is taken to present two different strategies—so called passive (aiming to repel the bacteria attack) and active (aiming to sustain or combat the bacteria attack) coatings, as proposed by Goodman et al., bringing also more fundamental knowledge on each approach [4]. A special emphasis is given to the coatings or composite deposited on titanium. Finally, advantages and drawbacks are commented in the concluding remarks.

1.2 Passive Coatings: Antiadhesion and Bacteria Repellent Coatings

1.2.1 Cellular and Bacteria Adhesion via Surface Nanostructuring or Substrate Composition

Nanotechnology offers new possibilities in the field of substrate–cell and substrate–bacteria interactions [8]. Cell–substrate interactions are mediated by the proteins adsorbed from biological fluids on the substrate. Nanoscale surface pattern can thus affect the adhesion of cells which is mediated by integrin receptors which cluster together and recruit cytoplasmic proteins to form a local contact. Surface pattering at the nanoscale can be performed using numerous techniques from photolithography, nanoimprint lithography, anodic oxidation, electron beam lithography, electrospinning, chemical pattering, etc.

Increased surface area, nanoroughness, and a higher number of particle boundaries led to greater surface energy or wettability of nanostructured Ti compared to conventional [8]. Such surface is more prone to adsorption of proteins and glycoproteins (e.g., vibronectin, fibronectin) which promote bone cell attachment. Further, biphasic electrical stimulation enhanced osteoblast functions on nanotubular titanium [9].

Nanorough regions of titanium oxide surfaces with sharp edges and spikes could promote the adhesion of osteoblast and lead to

strong binding affinity on its surface [10]. Osteoblasts cultured on nanotube surfaces show higher adhesion, proliferation, alkaline phosphatase activity (ALP), and bone matrix deposition. A diameter size of 15–20 nm is optimal for increased cell adhesion and proliferation. Integrin clustering in the cell membrane leads to a focal adhesion complex with a size of about 10 nm in diameter, thus being a perfect fit for nanotubes with diameter of about 15 nm [10].

The fate of the biomaterial was pictured as a race between microbial adhesion and biofilm growth in the concept "race for the surface" [11]. The equilibrium between osteoblast formation and bacteria attachment should be reached when designing new approaches to surface modification. The interactions of cells and bacteria with surfaces structured at the nanometer scale are recently reviewed by Anselme et al. [12]. In addition to different structure and functions, osteoblasts and bacteria differ also in their size and shape [13]. Osteoblasts are typically several microns in diameter and change their shape due to relatively flexible cell membrane (Fig. 1.1a). They bind to external surface by means of submicron sized focal contacts and focal adhesion. *Staphylococci*, on the other hand, are much smaller, approximately 1 μm in diameter and have a rigid, cross-linked wall (Fig. 1.1b); the binding to external surface occurs by both specific and nonspecific mechanisms. Due to these differences, surface topography affects the local response of osteoblasts and bacteria. Traditionally, titanium surface was roughened to allow easier osseointegration; however, it has been reported the response to different types of cells largely

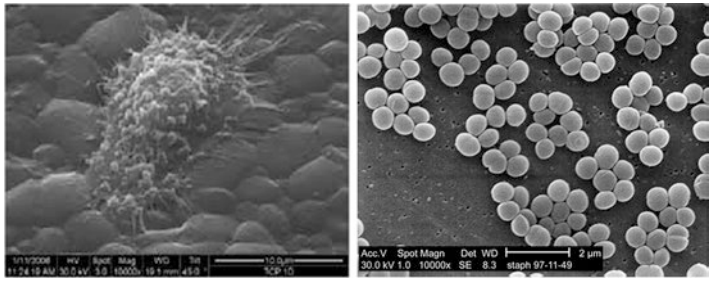

Fig. 1.1 Examples of osteoblast (*left*) and bacterial cells *Staphylococcus aureus (right)*

differ. Therefore, what is beneficial for osteoblasts may be disadvantage due to easier bacteria attachment. Wu et al. performed a systematic study aiming to investigate the response of titanium alloy (Ti–6Al–4V) surface of varying surface roughness to attachment of *S. epidermidis* and osteoblasts [13]. Four types of surfaces were tested differing in mean roughness (R_a): polished (R_a 0.006 μm), satin (R_a 0.83 μm), grit blasted (R_a 11 μm), and plasma sprayed (R_a 33 μm). In addition to the roughness, which describes the topographic fluctuations in vertical direction, lateral periodicity should be considered, i.e., two types of roughness are differed—on the microscopic and micrometer length scale. For example, although plasma-sprayed samples had the largest vertical fluctuations, they were smooth at the micrometer length. *S. epidermidis* colonization was the largest on surfaces that contain roughness at microscopic length scale, i.e., satin and grit-blasted surfaces. Bacteria favored micrometer-sized concave features such as surface valleys, depressions, pits, and edges (Fig. 1.2) [13].

In contrast, osteoblasts responded most favorably to surfaces that are smooth at microscopic length scale and rough at the macroscopic length scale, i.e., polished and plasma sprayed samples, which are comparable in size to that of osteoblast cells (tens of micrometer). This is reflected in significantly larger ALP activity and calcium content [13]. This result implies that traditionally used rough surface that allows easy osseointegration can be further optimized also to reduce bacteria colonization.

The relationship between the nanostructure of titanium surface and bacterial attachment was investigated in order to reveal whether the nanotopography can be tailored to reduce bacteria adhesion [14]. Among conventional, nanorough (electron-beam evaporized), nanotextured (anodized in 0.5 % HF), and nanotubular (anodized in 1.5 % HF) titanium surfaces, nanorough surface was the most effective for inhibiting of bacterial adhesion regardless of the bacteria type (*S. aureus*, *S. epidermidis*, and *P. aeruginosa*) (Fig. 1.3) [14]. Interestingly, although increased surface energy and fibronectin adsorption increased from nanorough to nanotubular surface, nanorough surface exhibited the least bacterial adhesion, presumably due to the effect of surface chemistry. Namely, nanotextured and nanotubular surface contained fluorine, which increases bacterial adhesion. Another important difference

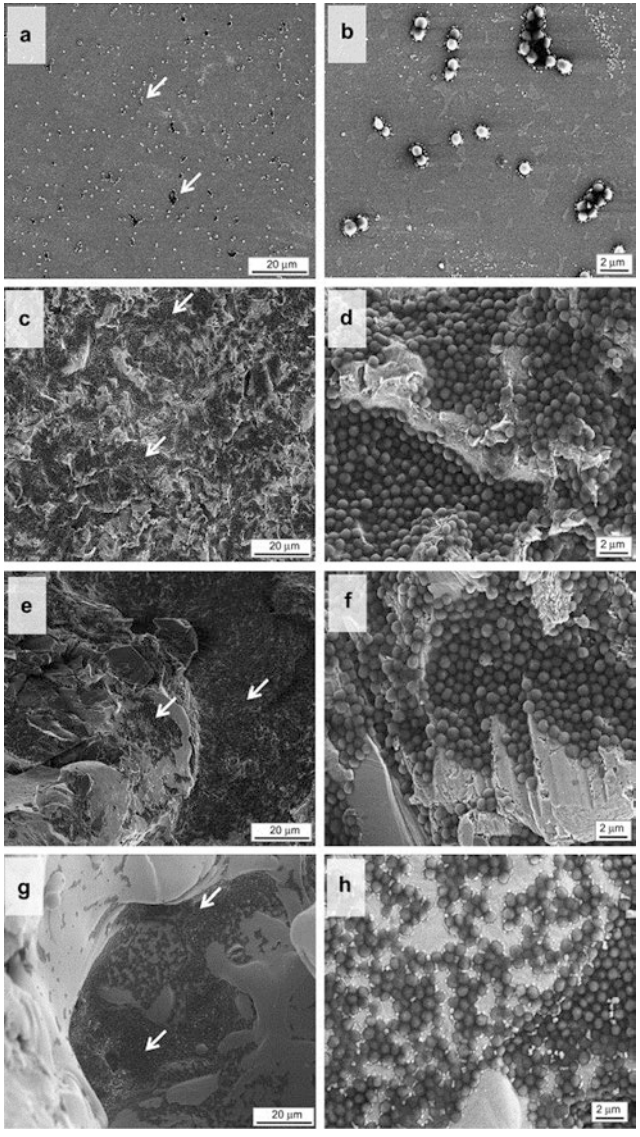

Fig. 1.2 SEM micrographs of *S. epidermidis* colonization (24 h) on (**a**, **b**) polished Ti; (**c**, **d**) satin Ti; (**e**, **f**) grit-blasted Ti; (**g**, **h**) plasma-sprayed Ti. Arrows indicate positions of bacteria on the lower magnification images. (*Reprinted from the publication by Wu Y, Zitelli J P, TenHuisen K S, Yu X, Libera M R* (*2011*) *Differential response of Staphylococci and osteoblasts to varying titanium surface roughness. Biomaterials 32*:*951–960, with permission from Elsevier*)

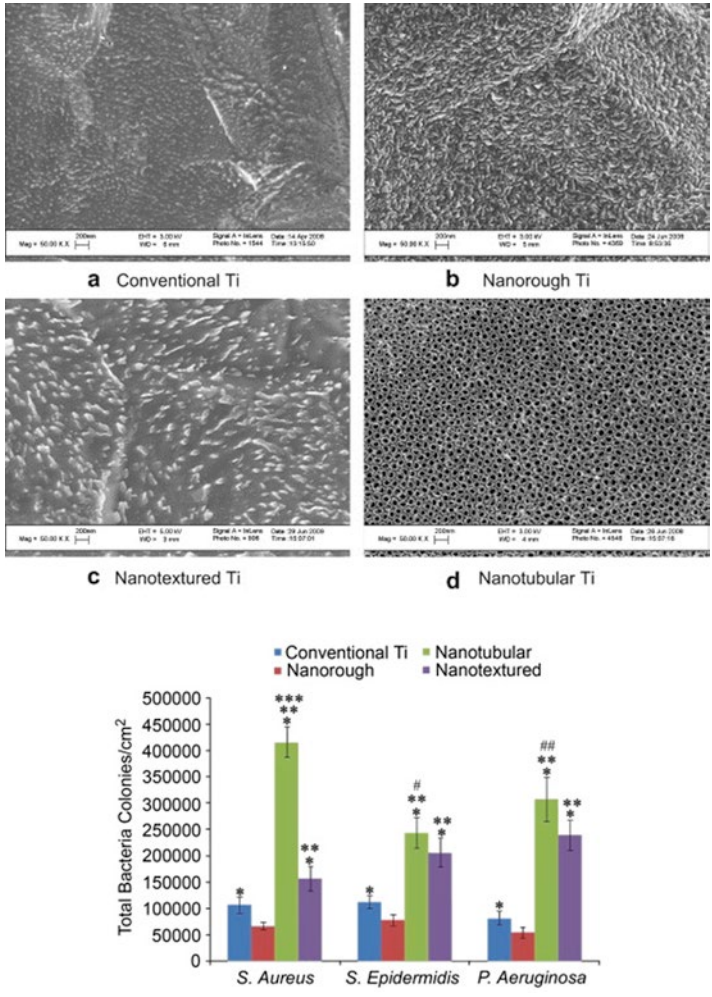

Fig. 1.3 (*Upper panel*) SEM micrographs of Ti before and after electron beam evaporation and anodization: (**a**) conventional Ti as purchased from the vendor; (**b**) nanorough Ti after electron beam evaporation; (**c**) nanotextured Ti after anodization for 1 min in 0.5 % HF at 20 V; (**d**) nanotubular Ti after anodization for 10 min in 1.5%HF at 20 V. Scale bars = 200 nm. (*Lower panel*) Decreased *S aureus*, *S. epidermidis*, and *P. aeruginosa* colonies on nanorough and conventional Ti compared to nanotubular and nanotextured Ti after 1 h. (*Reprinted from the publication by Puckett S D, Taylor E, Raimondo T, Webster T J (2010) The relationship between the nanostructure of titanium surfaces and bacterial attachment. Biomaterials 31:706–713, with permission from Elsevier*)

between these nanostructured surfaces is the crystallinity; nanotextured and nanotubular surfaces contain amorphous TiO_2, which promote bacteria attachment. On the other hand, conventional Ti surface contained rutile TiO_2 and nanorough surface anatase TiO_2. Therefore, especially anatase TiO_2 is effective in reducing bacteria adhesion.

Even UV irradiation can lead to increase in wettability of the surface which inhibits bacterial adhesion [4, 15]. Further, the size of the nanotubes also affects the bacteria attachment, as was shown for nanotubes grown on Ti50Zr alloy [16]. Smaller diameter nanotubes (20–30 nm) showed the best antibacterial performance compared to the bigger diameter of 50–70 nm, due to the smaller active area for bacteria colonization of such nanotubes [16].

Nanoscale roughness of hydroxyapatite (HAP) produced by electrophoretic deposition on titanium showed significantly decreased bacteria density compared to plasma-spray deposited HAP (Fig. 1.4) [17]. This was explained by the increased surface wettability and greater surface area leading to increased adsorption of hydrophilic proteins to promote osteoblast density.

In several studies no effect on surface roughness on the adhesion of bacteria was observed [18]. These significant variations in results can be explained by difficulty to assure that surface topography does not change the surface chemistry, i.e., large variations in experimental conditions are difficult to compare.

Beta-type Ti alloys with body-centered cubic system exhibit excellent mechanical properties and are interesting for numerous orthopedic and dental applications. To improve their cytocompatibility properties, the surface can be optimized not only by nanotexturing but also by changing the chemical composition of the substrate [10]. For example, the addition of Zr [19] or Sn [20] can increase antibacterial properties on titanium alloy. Nanotubes and nanofeatures on Ti–35Nb and Ti–35Nb–4Sn alloys were created by anodization; regardless of the crystalline type (anatase/rutile/mixture), the addition of Sn strongly decreased the adhesion of *S. aureus* [20]. This was ascribed to the formation of SnO_2 in the titanium oxide layer structure. Also, the addition of Sn changed the wettability which may affect the surface properties.

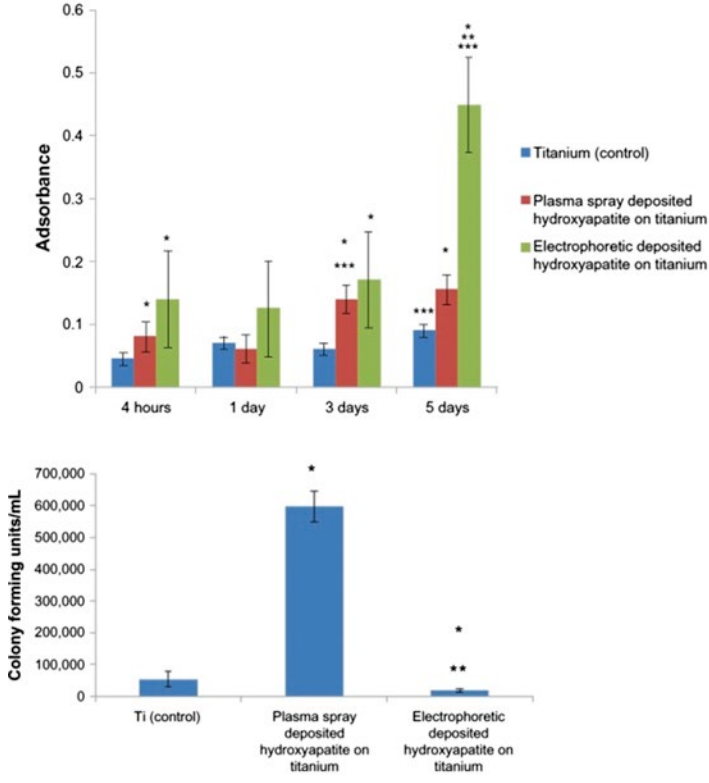

Fig. 1.4 (*Upper panel*) Increased osteoblast density and (*Lower panel*) significantly decreased bacteria density on nanostructured electrophoretic-deposited HAP on titanium compared to Ti control and plasma-spray deposited HAP on Ti. (*Reprinted from the publication by Mathew D, Bhardwaj G, Wang Qm Sun L, Ercan B, Geetha M, Webster T J (2014) Decreased Staphylococcus aureus and increased osteoblast density on nanostructured electrophoretic-deposited hydroxyapatite on titanium without the use of pharmaceutical. Int J Nanomed 9:1775–1781, with permission from DOVE Medical Press*)

1.2.2 Bacterial Adhesion via Surface Chemistry

Ideally, implant should inhibit nonspecific protein adsorption, bacterial adhesion, and at the same time, depending on the final application, be selective toward cellular adhesion and spreading for all or only selected cell types. Bacterial behavior varies especially as

a function of material hydrophobicity and electrostatic charge. In general, low-adhesion surfaces are hydrophilic and highly hydrated; antifouling surface can also be superhydrophobic. The adhesion of bacteria to surfaces is decreased due to the formation of an interfacial layer to prevent direct contact of surface and proteins [21]. Most typical antiadhesive surfaces are polymers like poly(ethylene oxide) (PEO) and polymetacrylic acid (PMA), which are both hydrophilic, and poly(ethylene)glycol (PEG) which is protein resistant [4].

The exact nature of the surface required to combat bacteria adhesion is dependent on the type of media. Upon implantation, a protein film rapidly forms on the biomaterial surface and affects the adhesion of bacteria. This protein film can be considered as the real interface with bacteria. Namely, proteins are a major factor in the process of bacteria attachment and biofilm formation. Many bacteria bind to extracellular cell adhesion properties including fibronectin and fibrinogen. In protein-free or low protein solution the inert, noncharged antiadhesive surfaces, e.g., polymer brush coatings, self-assembled monolayers, hydrogel coatings, may be sufficient to combat the bacterial attack. Polymer brushes are polymers applied to the surface in a high density; the higher the surface density of polymer chains, the better the antiadhesive properties. Also the chain length of polymers is of importance; longer chains are more effective in prevention of bacterial adhesion. As they are hydrophilic, water is attracted into the brush polymer layer via hydrogen bonding. A repellent layer is formed close to the surface. Proteins and bacteria encountering the brush surface will be repelled by steric hindrance due to bound water in the brush and the elasticity of the polymer chain [22]. Macromolecular polymer chains are in sufficient proximity to the surface so that the unperturbed solution dimensions (in a good solvent) of the chains are altered. Common applications of polymer brushes include interactions of the polymer brushes with liquids, solids, particles, proteins, cells, etc.

There are many ways in which polymers are attached at the surface; they vary from linear to branched, and from homo- to block-polymers. They are usually kept to the surface by noncovalent interactions, but also via direct covalent coupling to the

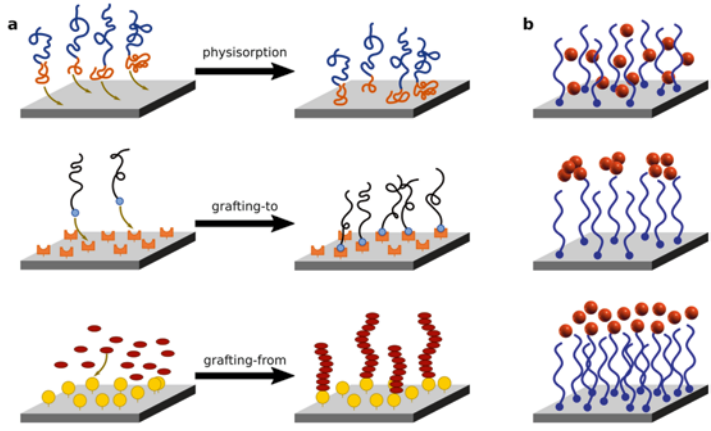

Fig. 1.5 Schematic presentation of (**a**) physisorption, grafting-to and grafting-from principles, and (**b**) functioning of polymer brush as a function of grafting density

reactive groups at the surface, e.g., binding of polymer brush to amine group. Much of the early work on polymer brushes focused on systems formed by physisorption (Fig. 1.5); that is, the selective adsorption of one block of a diblock copolymer to a surface. The covalent binding of polymer chains at the interface has attracted interest because of the enhanced stability of the tethered polymer layers. Covalently attached (chemisorbed) polymer chains can be synthesized by either the "grafting onto" or "grafting from" method (Fig. 1.5). "Grafting-to" involves the chemical reaction of preformed, functionalized polymers with reactive sites to couple with reactive sites on the substrate (Fig. 1.5a). "Grafting-from" approach involves in situ polymerization of an initiator functionalized surface with monomer. A variety of linkers can be used [22].

At low grafting densities molecules or particles can mix with grafted polymer chains, penetrate the brush, and interact with the underlying substrate (Fig. 1.5b). In this case, van der Waals interactions may strongly dominate. As the grafting density increases, repulsive forces may dominate (e.g., colloidal stabilization, resistance to protein adsorption) and big aggregates are expelled toward the brush–air interface (Fig. 1.5b). At a very high grafting density

the particles will be expelled from the brush (Fig. 1.5b). This example introduces nicely the concept of an optimum grafting density. In addition to polymers, other compounds were considered as antiadhesive agents. Natural products or plant-derived extracts, i.e., polyvalent, high-molecular carbohydrates and tannin-like plant-derived compounds, especially polysaccharides (e.g., pectin, arabinogalactan, fucans, heparins, xyloglucan) were considered [23]. Zeolites are crystalline aluminosilicates with regular micropores which have important applications in catalysis and ion exchange. Superhydrophilic nature of zeolite coating on Ti–6Al–4V alloys provided antiadhesive properties and show good cytotoxic assay [24].

In protein-rich media, however, further actions are needed and the adsorption of proteins can be reduced by electrostatic interactions, which slow down the rate of adsorption by creating high potential barrier for interactions. Polyanionic functionalized surfaces can exert an electrostatic repulsion effect on similarly charged bacterial cells. Generally, Gram-negative bacteria have a polyanionic glycocalix.[1] Gram-positive bacteria generally have a polycationic glycocalix. Comb-like polyelectrolyte like poly(L-lysine)-grafted-poly(ethylene glycol) (PLL-*g*-PEG) was often used. PEG can be combined by polypyrrole (PPy) which is a conductive polymer and its incorporation in PEG enhances the ion mobility in the coating in electrolyte solution [25]. Composite PPy-PEG coating on TiAlZr alloy exhibited more dense structure, was electrochemically more stable, and more effective as antibacterial coating regarding *E. coli*. This was explained by small roughness and significant hydrophilic character [25]. Similar coatings, containing ethylene glycol and polyethylene glycols with different average molecular weight, were prepared on TiO_2 nanotubes [26].

As some of polymer coatings may impair local osteoblast function, the use of additional bioactive molecules is required to restore the impaired cell function. Several surface modifications have been employed to prevent nonspecific protein adsorption from biological environment upon implantation and to prevent adhesion of bacteria.

[1] Glycocalix—the glycoprotein–polysaccharide covering that surrounds many cells.

These include, for example, integrin-active peptide such as RGD (Arg-Gly-Asp), bone-morphogenetic protein (BMP-2), silk sericin protein, etc., as discussed in recent reviews [5, 18, 21]. PLL-*g*-PEG has been shown to adsorb from aqueous solution onto negatively charged metal oxide surfaces, reducing protein adsorption significantly but also that of fibroblast, osteoblast, and epithelial cell adhesion. Further, PLL-*g*-PEG largely inhibits protein adsorption and the adherence of *S. aureus* to coated titanium; however, a coating functionalized with an RGD-type peptide (PLL-*g*-PEG/PEG-RGD) restores fibroblast and osteoblast attachment, while inhibiting the adherence of *S. aureus* [27]. Therefore, coating surfaces with PLL-*g*-PEG/PEG-RGD allow cells such as fibroblasts and osteoblasts to attach but not bacteria, resulting in a selective biointeractive pattern that may be useful on medical implants. A thick confluent layer of *S. aureus* and *S. epidermidis* can be seen on the Ti surface, while *Strep. mutans* and *P. aeruginosa* have adhered less (Fig. 1.6) [28].

PEG coatings on Ti biofunctionalized with anti-CD34 antibody stimulated adhesion of endothelial progenitor cells, while showing antifouling properties [29]. Polymer brush obtained by the immobilization of trichlorosilane coupling agent and methacrylic acid sodium salt on the titanium surface was enriched by the attachment of silk sericin [30]. Sericin and fibroin are silk macromoleculer proteins showing excellent mechanical properties and are water soluble glycoproteins. Such covalently immobilized brush, Ti-*g*-P(MAA)-Silk, significantly reduced the adhesion of two bacterial strains (*S. aureus* and *S. epidermidis*) on titanium (Fig. 1.7) [30]. The silk sericin-immobilized surfaces, at the same time, promoted osteoblast cells' adhesion, proliferation, and alkaline phosphatase activity [30].

1.3 Active Coatings: Peptides, Polysaccharides, and Inorganic Agents

In contrast to passive coatings, whose antimicrobial effect is based on the antiadhesive and repellant ability, active coatings are based on the intrinsically antimicrobial materials which can

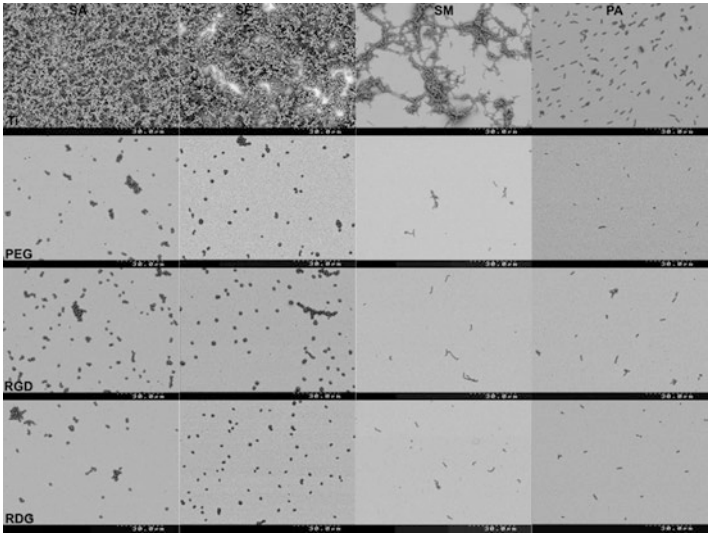

Fig. 1.6 SEM images of *S. aureus* (SA, first column), *S. epidermidis* (SE, second column), *Strep. mutans* (SM, third column), and *P. aeruginosa* (PA, fourth column) on the different surfaces after 4 h of culturing. Each row of images signifies a surface chemistry, going down from Ti, PEG, RGD, and R*D*G. A thick cofluent layer of *S. aureus* and *S. epidermidis* can be seen on the Ti surface, while *Strep. mutans* and *P. aeruginosa* have adhered less. Bacterial adhesion of all four types was significantly reduced on the PEG-, RDG-, and R*D*G-coated titanium surfaces in comparison with uncoated Ti. (*Reprinted from the publication by Maddikeri R R, Tosatti S, Schuler M, Chessari S, Textor M, Richards R G, Harris L G* (*2008*) *Reduced medical infection related bacterial strains adhesion on bioactive RGD modified titanium surfaces*: *A first step toward cell selective surfaces J Biomed Mater Res 84A*:*425–43*, *with permission from John Wiley and Sons*)

be used either in the form of bulk coatings, e.g., silver, chitosan, or hyaluronic acid, or incorporated in some other coatings and then released, e.g., silver, zinc oxide, antimicrobial peptides. Among inorganic materials, mainly silver will be discussed; however, other materials also exhibit antimicrobial activity like zinc oxide, copper, tin, etc. Regardless of whether present as bulk or in incorporated form, the antimicrobial effect is based on the action produced by released compounds which can proceed

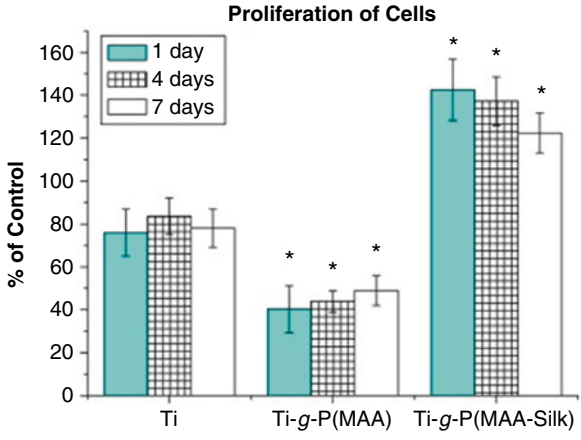

Fig. 1.7 Comparison of osteoblast proliferation with 5000 cells/cm^2 seeded on surfaces of pristine and functionalized Ti substrates after 1, 4, and 7 days. The number of cells per cm^2 was expressed as percentage of the number obtained in the control experiment using polystyrene cell culture surface. (*Reprinted from the publication by Zhang F, Zhang Z, Zhu X, Kang E-T, Neoh K-G (2008) Silk-functionalized titanium surfaces for enhancing osteoblast functions and reducing bacterial adhesion. Biomaterialss 29: 47515–4759, with permission from Elsevier*)

through different mechanisms as will be discussed later. In order to fulfill several requirements posed upon a biomaterial, it is often of interest to combine several properties within one material, for example, to add antimicrobial activity to the coatings capable of osseointegration, coatings able to resist dissolution, or to increase the biocompatibility of antimicrobial coating, etc.

1.3.1 Antimicrobial Peptides

1.3.1.1 General Characteristics of Antimicrobial Peptides

In order to avoid antibiotics and introduce the antimicrobial agents without the leaching effect, numerous studies were directed toward antimicrobial peptides (AMPs) [31–33]. Although their potency

against bacteria may be lower than that of conventional low molecular weight antibiotic compounds, they have several advantages including fast killing rate, broad range of activity, low toxicity, and minimal development of resistance. AMPs are oligopeptides with varying number of amino acids. They were discovered by Dubos in 1939 when it was demonstrated that extract of an antimicrobial agent from a soil *Bacillus* strain can protect mice from pneumococci infection. AMPs are a part of the first line of the innate immune system of all multicellular organisms. They act similar as antibiotics but it seems that they have the additional ability to affect the inflammatory response of the host immune systems. AMPs exhibit several important properties including bactericidal, fungicidal, viricidal, and tumoricidal properties [33]. As these properties are attractive for designing new drugs, numerous studies were devoted to searching for new AMP compounds. The family of AMPs is large and so far, more than 750 natural AMPs were isolated from different plants, animals, bacteria, fungi, and viruses [32]. Although AMPs are effective toward both Gram-positive and Gram-negative bacteria, several properties of natural AMPs such as possible specific bacterial resistance and so-called enhancement effect (promotion to uptake of conventional antibiotics across the outer membrane) were driven to the rationally engineered synthetic AMPs. In addition to natural AMPs, synthetic AMPs are also interesting and up to date more than 5000 AMPs were synthesized.

AMPs may be soluble or tethered, i.e., covalently attached to the surface. Immobilization of peptide indeed results in the limitation of peptide mobility and thus their ability to translocate across the membrane [34]. In general, a two-step approach is used to treat the surface for attachment of antimicrobial agents: (1) provide the functional groups amenable to attachment chemistry, and (2) tethering of active antimicrobial compound by reaction involving these functional groups [31]. An intermediate step may be occasionally necessary, i.e., the use of “linkers” or “spacers” between the antimicrobial agent and the surface. The first step is usually carried out by plasma treatments, plasma deposition, radiation, or wet chemistry which produces reactive sites or introduces new functionality of the surface. The second step of tethering can be performed using a number of methods: covalent attachment, e.g.,

using alkoxysilane, bioconjugation (tailored matching of reagents with appropriate functional groups resulting in a covalent bond, e.g., primary amines, thiols, aldehydes, hydroxyl groups, and carboxylic acids), and antimicrobial attachment using graft polymerization ("grafting from" or "grafting onto"). A variety of linkers can be used [31].

Although the AMPs family comprises chemically and structurally very heterogeneous compounds, there are several characteristics that are common: (1) small size, usually 10–25 amino acids, with molecular weights between 1 and 5 kDa; (2) highly cationic character; and (3) tendency to adopt amphipathic structure, i.e., structure containing separate hydrophilic and hydrophobic domains. There are several types of AMPs: anionic, anionic and cationic, and cationic; the latter being the most important for antibacterial activity. Due to cationic character with net positive charge, AMPs have a tendency to be electrostatically attracted to the negatively charged microbial cell membrane. Cationic peptides are rich in proline, arginine, phenylalanine, glycine, and tryptophane. Based on their structure they can be divided into four types: β-sheet, α-helix, extended, and loop [33]. The former two are more common, the α-helix being the most studied AMP to date (e.g., magainin, protegrin, indolicin). In α-helix the angle between two consecutive amino acids in the sequence is 100°, the distance between two adjacent acids being 0.15 nm.

1.3.1.2 Mechanism of Antibacterial Activity of Antimicrobial Peptides

Bacterial membranes have the outermost leaflet of the bilayer heavily occupied by lipids with negatively charged phospholipids groups. In contrast, the outer leaflet of the membranes of plants and animals is composed of lipids with no net charge (i.e., negative charge is facing inward, not outward). AMPs target the lipopolysaccharide layer of cell membrane (unlike antibiotics which target specific cellular activities) [33].

The contact of bacteria with active tethered peptides leads to dramatic change in morphology. Surfaces in contact with bacteria

P. aeruginosa were characterized by dense distribution of small protuberant structures in contrast to control surfaces which had smooth appearance (Fig. 1.8) [34]. These observations indicated that the tethered peptides can destabilize the bacterial wall.

Although the exact mechanism of AMB action on bacteria wall is still under discussion, there are two general steps: positively charged peptide is electrostatically attracted to negatively charged phospholipids groups of the bacterial membrane. Upon binding, the AMP adopts amphipathic structure which is believed to lead to a lethal increase in the permeability of cell membrane [32]. Three models were proposed to explain the actions of AMPs (Fig. 1.9) [32, 33, 35]: (1) Barrel-Stave model where AMP molecules insert themselves into the membrane perpendicularly, (2) carpet model where small areas of the membrane are coated with AMP molecules with hydrophobic sites facing inward leaving pores behind the membrane, and (3) toroidal pore model where AMPs insert perpendicularly but are always in contact with phospholipid head groups of the membrane. Another important feature is their rapid killing effect, e.g., some kill in seconds after the initial contact with the cell membrane. In addition to membrane-active AMPs, there are some AMPs which can cause killing of bacteria cells without causing membrane permeabilization. For example, indolicin was shown to bind to DNA with a preferred sequence; others can inhibit DNA and protein synthesis [33].

Several physicochemical properties of the AMPs affect their activity and target spectrum. Recently, more than 1000 peptides were analyzed using artificial network models that can predict and rank the relative activities of AMPs [36]. The best peptides identified through screening were found to have activities comparable or superior to those of four conventional antibiotics. The activity of tethered peptides is dependent on the extent and positioning of positive charges and hydrophobic residues [34]. When designing new AMPs, length of the compound is important, as there is a minimum length to form amphipathic structure at the surface. The length may also affect its toxicity. Net charge of the AMPs may vary from positive to negative; by varying the charge its antimicrobial activity can be altered. Cationic residues located

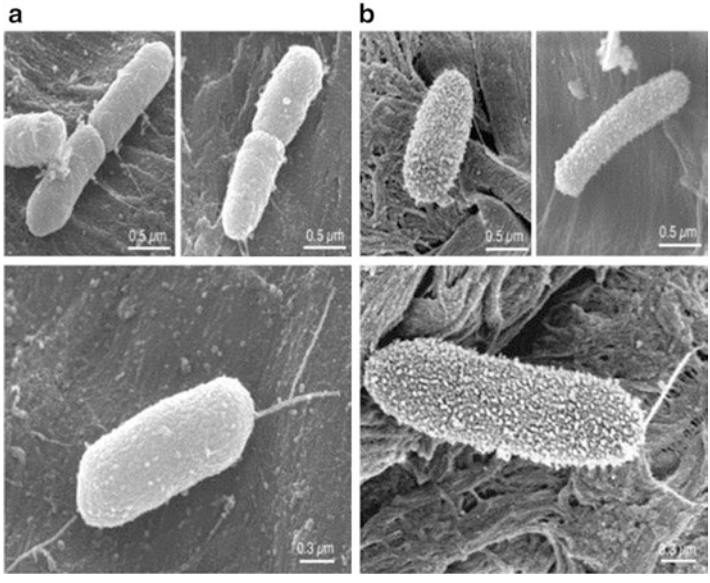

Fig. 1.8 Bacterial membrane damage induced by tethered peptides: SEM of *P. aeruginosa* cells that were in contact with (**a**) membrane without peptide (*bottom large picture* and *small picture* to the *right*), an inactive peptide (*small picture* to the *left*), and (**b**) membrane with the active tethered peptide Tet009 (*bottom large picture* and *small picture* to the *left right*) and the active tethered peptide Tet052 (*small picture* to the *left*). The bacteria were incubated in contact with membranes for 4 h at 37 °C before fixation and preparation for SEM. (*Reprinted from the publication by Hilpert K, Elliot M, Jenssen H, Kindrachuk J, Fjell C D, Körner J, Winkler D F H, Weaver L L, Henklein P, Ulrich A S, Chiang S H Y, Farmer S W, Pante N, Volkmer R, Hancock R E W (2009) Screening and characterization of surface-tethered cationic peptides for antimicrobial activity. Chem Biol 16:58–69, with permission from Elsevier*)

proximal to the linker site correlated with increased antimicrobial activity [34]. Hydrophobicity is very important: the positioning of hydrophobic residues close to the N terminus was critical for the activity [34]. Decreasing hydrophobicity can reduce antimicrobial activity [33]. Amphipathicity is important for sectioning of membrane into hydrophilic and hydrophobic parts. Finally, AMPs should be soluble in aqueous media as aggregated molecules cannot interact with the cell membrane. Modification of AMP may be

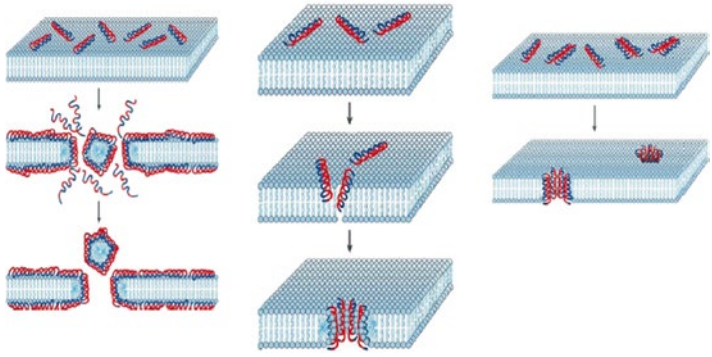

Fig. 1.9 Models of the mechanism of action of membrane-active antimicrobial peptides (AMPs): (*left*) carte model, (*middle*) toroidal pore model; (*right*) Barrel-Stave model. (*Reprinted from the publication by Costa F, Carvalho I F, Montelaro R C, Gomes P, Martins A C L (2011) Covalent immobilization of antimicrobial peptides (AMPs) onto biomaterials surfaces. Acta Biomater 7:1431–1440, with permission from Elsevier*)

used to improve their function. These modifications commonly comprise phosphorylation, addition of D-amino acids, methylation, amidation, glycosylation, etc. [33].

1.3.1.3 Examples of Coatings Containing Antimicrobial Peptides on Titanium

Several recent examples will be given on AMPs attached to titanium substrate by different methods. Covalently grafted hydrophilic polymer brushes on titanium were conjugated with different AMPs achieving surface concentration as high as 5.9 μg/cm^2 [37]. The polymer brush was primary amine functionalized copolymer containing *N*,*N*-dimethylacrylamide and amino propyl methacrylamide hydrochloride prepared by radical polymerization. This layer was then immobilized using AMPs containing different sequences of amino acids (Tet-20, Tet-213, Tet-21, Tet-26, HH2, 1010cys, and MXXX226). All investigated AMPs showed excellent antimicrobial activity toward *P. aeruginosa*, the highest inhibition was noticed for Tet-26, followed by

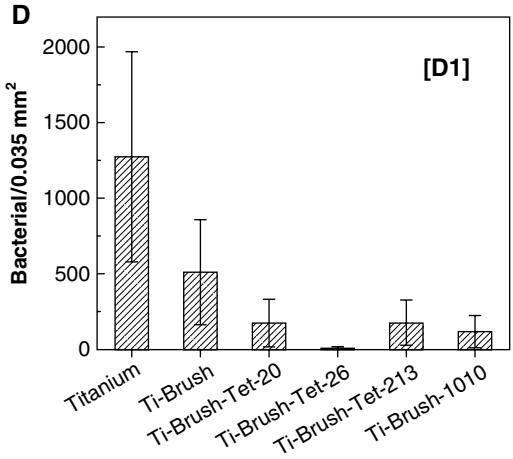

Fig. 1.10 Antimicrobial activity of surface immobilized peptides: comparison of biofilm formation on copolymer brushes and AMPs conjugated (Tet-20, Tet-26, Tet-213, 1010) copolymer brushes on Ti surface (*Reprinted from the publication by Gao G, Lange D, Hilpert K, Kindrachuk J, Zou Y, Cheng J T J, Kazemzadeh-Narbat M, Yu K, Wang R, Straus S K, Brooks D E, Chew B H, Hancock R E W, Kizhakkedathu J N (2011) The biocompatibility and biofilm resistance of implant coatings based on hydrophilic polymer brushes conjugated with antimicrobial peptides. Biomaterials 32:3899–390910, with permission from Elsevier*)

Tet-20 (Fig. 1.10a) [37]. The effect was attributed to the combined effect of polymer structure—the presence of AMPs and hydrophobic/hydrophilic character of the coating. A direct correlation was found between the adhesive force and water contact angle at the surface, with surfaces that yielded high adhesive forces also had the highest water contact angle. This suggests that hydrophobic interaction plays a major role in the ability of bacteria to form biofilms between AMPs and the surface. Further, the change in conformation of soluble AMPs upon interaction with bacterial membrane and its subsequent incorporation is one of the mechanisms for their antimicrobial activity. The percentage of α-helix conformation of soluble Tet-20 changed from 25 % in PBS to 92 % in the presence of lipid membrane. In contrast, the copolymer brush conjugated Tet-20 changed

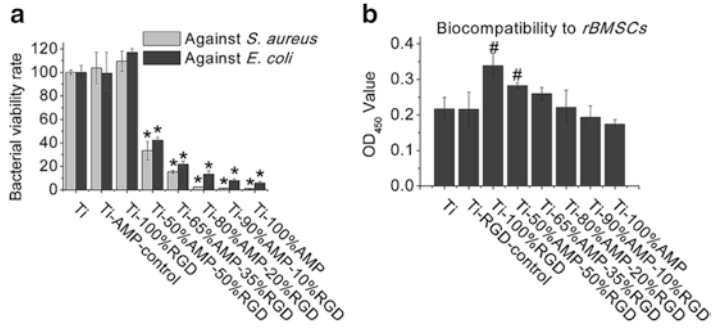

Fig. 1.11 The antimicrobial activity ($n=3$) and biocompatibility ($n=3$) of the indicated samples of combinations of RGD and AMP. (*Reprinted from the publication by Lin W, Junjian C, Chengzhi C, Lin S, Sa L, Li R, Yingjun W (2015) Multi-biofunctionalization of a titanium surface with a mixture of peptides to achieve excellent antimicrobial activity and biocompatibility. J Mater Chem B 3:30–3311, with permission from Royal Society of Chemistry*)

conformation to a substantially lesser degree indicating that tethered peptides behave quite differently from soluble peptides, presumably due to sterical restriction by covalent conjugation to the polymer brush. It was suggested that the disturbance of electrostatics induced by the presence of tethered peptides may trigger an autolytic and/or cell death mechanism. No toxicity toward human cells was observed [37].

Aiming to combine antimicrobial activity with improved biocompatibility a mixture of AMPs was used: RGD and HHC-36 AMP (Fig. 1.11) [38]. The AMPs were biofunctionalized on titanium surface with a silane coupling agent. Both AMPs have comparative advantages: HHC-36 exhibits improved antibacterial activity and lower immunogenicity, while RGD could specifically combine with 11 species of integrin. The antibacterial activity increased with the ratio between the two peptides: Ti-50%HHC36-50%RGD could kill about 77 % of *S. aureus* and 58 % of *E. coli*. Ti-80%HHC36-20%RGD could kill about 98 % of *S. aureus* and 87 % of *E. coli* and Ti-90%HHC36-10%RGD could kill about 99 % of *S. aureus* and *E. coli*. However, biocompatibility was also dependent on the HHC36-RGD ratio: with the decrease of HHC-36 and the increase of RGD, the biocompatibility of the samples increased.

Therefore, the optimum ratio of Ti-80%HHC36-20%RGD was determined due to similar biocompatibility to titanium and excellent antimicrobial activity [38].

Electrostatic interactions of AMP with the negatively charged titanium oxide layer are dependent on pH [39]. Tet-124 AMP and Tet-124 modified at the C- and N-terminus with the sequence glycine-3,4-dihydroxyphenylalanine-glycine (G-DOPA-G) was prepared by solid phase synthesis and attached to substrate by immersion. At a low pH (4.75), Tet-124 and Tet-124-G-DOPA-G form rigid layers resulting from electrostatic interaction of the positively charged lysine and arginine residues in the peptide sequence with negatively charged Ti oxide layer. At a pH level of 6.9, Tet-124 showed a lower mass adsorption at the surface than Tet-124-G-DOPA-G which was attributed to the interaction of catechol due to the formation of complexes with Ti oxide substrate [39].

The minimal inhibitor concentration of HHC-36 is as low as 1.4–2.9 μM against *Methicillin-resistant S. aureus* and 0.7–5.7 μM against multidrug resistant *P. aeruginosa* [36]. It is of interest to combine this excellent property with other ability of the coating, i.e., with osseointegration. A thin layer (~7 μm) of calcium phosphate (CaP) coating was processed by electrolytic deposition onto the surface of titanium, as the drug carrier [40]. Then, a broad spectrum AMP Tet-213 (also noted as C-terminally modified HHC-36) was loaded into CaP coatings. Up to 9 μg/cm^2 could be loaded using a simple soaking technique. The CaP-Tet-213 had antimicrobial activity against both Gram-positive (*S. aureus*) and Gram-negative (*P. aeruginosa*) bacteria with 10^6 fold reductions of both bacterial strains within 30 min as assessed my measuring colony forming units. This was more efficient compared to commercially developed AMPs, i.e., MX226 and hLF1-11 or Tobramycin antibiotic. In terms of biocompatibility, no cytotoxicity was observed on osteoblast-like cells [40]. Therefore, the local delivery of AMP through implant surfaces could be a potential solution for early stage peri-implant infection.

Potential drawback of AMPs is the initial burst within first few hours after exposure to bacteria. Release kinetics can be followed using UV–Vis spectroscopy by recording absorption peak characteristic for tryptophane (one of the amino acid in HHC-36). In order to more closely control the initial burst of HHC-36, phospholipid

(POPC, palmitoyl-oleoyl phosphatidyl-choline) film was topped on titania nanotubes and CaP coatings impregnated with AMP [41]. POPC is found in eukaryotic cell membranes and offers the least support for bacteria growth reduction (81 % reduction) and the most suitable platform for bone cell attachment. Compared to a burst release within first few hours after incubation when attached to CaP or TiO_2 NP only, the attachment of HHC-36 to POPC led to a slow and steady release during 100 h.

1.3.2 Natural Polysaccharide-Based Polymers

1.3.2.1 Chitosan

General Characteristics of Chitosan

Chitosan (CH), discovered by Rouget in 1858, is a linear polycationic heterosaccharide consisting of more than 5000 glucosamine units. It is obtained from chitin [42–45]. Chitin is inexpensive compound of animal origin; it forms the basis of the main constituent of the outer skeleton of insects and crustaceans like shrimp, crabs, and lobster. Chitin is chemically similar to cellulose, having one hydroxyl group on each monomer substituted with an acetylamine group (Fig. 1.12). In its crude form, chitin has low reactivity and solubility. Chitosan is obtained by deacetylation of chitin, usually through alkaline hydrolysis at 120 °C by one of the N-acetyl groups which are bonded to amine radical in the C2 position on the glucan ring. Since the process of N-deacetylation is almost never complete, chitosan is referred as partially N-deacetylated derivative of chitin. Chitosan is commercially available with >85 % deacetylated units, i.e., degree of deacetylation (DA) <15 %. Another parameter important for the properties of CH is the molecular weight (MW) which is usually classified as low (<50 kDA), medium (50–150 kDa), and high (>150 kDa). Upon dissolution of CH, a viscous solution is formed. The viscosity of commercial CH is from 10 to 1000 mPa s. Therefore, chitosan is a collective name for a group of partially and fully deacetylated chitin [45].

CH is weak base and is insoluble in water, in alkaline medium, and even in organic solvents. Below its pKa (~6.3), it is soluble in dilute aqueous solution of inorganic acid such as hydrochloride acid and organic acids (acetic, formic, succinic, lactic, and malic acid). The solubility in acidic medium is attributed to the conversion of amine groups ($–NH_2$) into soluble protonated cationic amine groups ($–NH_3^+$).

Chitosan is inactive in neutral media because of the presence of uncharged amino groups and the poor solubility. It possesses three functional groups: an amino group of each deacetylated unit, and primary and secondary hydroxyl groups of each repeat unit (Fig. 1.12). These groups can be used for further derivatization to modify its physicochemical properties, i.e., solubility at neutral pH range. Derivatization can be, for example, performed by the quaternization of the nitrogen atoms of the amino groups, e.g., extensive methylation of chitosan in suspension of dimethylsulfate, sodium hydroxide, and sodium chloride resulting in *N*,*N*,*N*-trimethylchitosan [44]. In addition to quaternary salts of CH, other aqueous soluble derivatives such as hydroxypropyl and carboxymethyl chitosan exist. Derivatives of, e.g., *N*-propyl-*N*,*N*-dimethyl chitosan against *E. coli* were 20 times higher than that of CH [44]. Hydroxypropyl derivative drafted with maleic acid shows high antibacterial activity. In the case of alkyl-substituted derivatives, better performance was attributed to the contribution of hydrophobic portions of the derivatives.

Due to its favorable properties including biodegradability, biocompatibility, antiviral and antimicrobial properties, chelating ability and nontoxicity, chitosan is used in numerous applications.

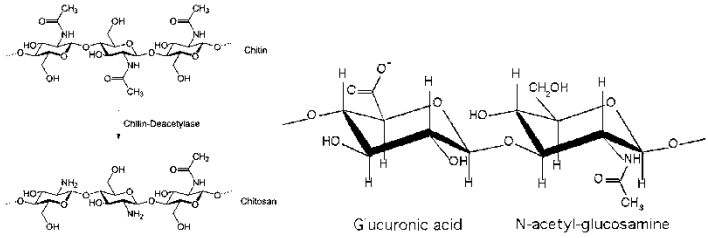

Fig. 1.12 Structural formula of (*left*) chitosan and (*right*) hyaluronic acid

In food industry, chitosan is used as food preservative against common foodborne pathogen like *E. coli*, *Listeria monocytogenes*, etc. It is applied as food additive or preservative, or as a packaging material, both to retard microorganism growth in food and to improve the quality and shelf life of food [45]. Edible antimicrobial films are prepared from chitosan and other edible food ingredients, e.g., essential oils, nisin, starch, etc. In textile industry, CH has found numerous applications for cotton fabric to prevent or retard the growth of bacteria, also for sportswear made of man-made fibers to impart for antiodor and biostatic properties. In medicine, CH is commercially available in various wound dressing or hemostatic products [45]. CH provides antimicrobial effect on four forms: fiber, membrane, sponge, and hydrogel. Another important use of CH is in plant industry as a biocontrol tool against plant pathogen. CH offers perspective use in dentistry as plaque-reducing agent as well as in vitro antibacterial agent against several oral pathogens (*S. mutans*, *Porphyromonas gingivalis*), as well as in orthopedics to reduce infection related to orthopedic implants [43].

Mechanism of Antibacterial Activity of Chitosan

Chitosan is active against virus, fungi, yeast, and bacteria; it is more effective against Gram-positive than Gram-negative bacteria [46]. It seems that the activity is dependent on the molecular weight of CH, with lower chitosan MW having a greater effect on reducing the microorganism growth and multiplication [44]. It was also reported that it is not possible to pinpoint the relationship between MW and activity; however, it seems that MW of 10 kDA is required for minimal activity [43]. Chitosans with higher DA are more effective than those with a low DA. Activity is higher at lower pH. The addition of metal ions reduces the antibacterial effect, probably due to complex formation between CH and metal ions. The choice of solvent (inorganic or organic acid) does not seem to affect the activity.

Generally, it is assumed that site of antibacterial action is the bacterial cell surface. Polycationic nature of CH, with the positively charged $-NH_3^+$ group of glucosamine, interacts with negatively charged surface components of fungi and bacteria and causes the

cell damage. Hydrolysis of peptidoglycans in the bacteria wall leads to leakage of intracellular substances, and, ultimately, impairment of vital bacterial activities and cell death. The nature of surface components involved in this electrostatic interaction is not defined in detail. Rafaat et al. suggested that electrostatic interaction occurs with the negatively charged teichoic acid, which is found in the peptidoglycan layer of only Gram-positive bacteria and are essential polyanionic polymers that contribute to the negative charge of the surface wall [43]. This mechanism is consistent with much lower activity of the CH against Gram-negative bacteria. In the latter, the outer membrane contains lipopolysaccharide, which provides the bacterium with a hydrophilic surface and contains anionic group (phosphate, carbonate), which contributes to the stability through electrostatic interaction with divalent cations. The second mechanism assumes that CH is able to pass through the bacteria cell wall and reach the plasma membrane, which was argued due to the large molecular size of CH to be taken up by the cell [43]. Third mechanism is based on the chelating activity of CH which contributes to selective binding to essential trace metal and thus inhibits the production of toxins and microbial growth. Kong et al. pointed out that at environmental pH below the pK_a of CH and its derivatives, electrostatic interaction between the polycationic structure and the predominantly polyanionic components of the microorganism's surface plays a primary role in antibacterial activity [45]. When environmental pH is above p*K*a, hydrophobic and chelating effects are responsible for antibacterial effects. These two latter mechanisms are not pH dependent but at lower pH they are overwhelmed by predominant electrostatic effects.

1.3.2.2 Hyaluronic Acid

General Characteristics of Hyaluronic Acid

Hyluronic acid (HA), a natural polydisaccharide, is periodic structure of disaccharide N-acetylglucozamine and D-glucuronic acid (Fig. 1.12) [47]. It is commonly found in connective, epithelial, and neural tissues and is one of the main components of extracellular matrix and cartilage. It affects the cell proliferation and

migration and physical properties of synovial fluid since it is responsible for resistance to compressive stress. HA is the main component of skin, is involved in skin healing, and is commonly found in skin care products; it is used in the treatment of pain with knee osteoarthrosis [48]. HA gains popularity also as scaffold in tissue engineering.

At physiological pH and ionic strength HA can be described as stiffened random coil. Rigidity is related to the intramolecular hydrogen bonds between glycoside groups and electrostatic repulsion between carboxylic groups [49].

Mechanism of Antibacterial Activity of Hyaluronic Acid

Bacteriostatic effects of common biomaterials used in orthopedic surgery—collagen type I, hyaluronic acid, hydroxyapatite, and polylactic polyglycolic acid (PLGA)—were tested against four common pathogens in orthopedics: *S. aureus*, *S. epidermidis*, β-hemolytic *Streptococcus*, and *P. aeruginosa* [50]. HA demonstrated the largest bacteriostatic effect on these pathogens by inhibiting bacteria growth by an average of 76.8 %. HAP and collagen inhibited growth on average 49.7 and 37.5 %, while PLGA exhibited small inhibition of only 9.8 %. It was noted that bacteriostatic effect of HA may be due to the saturation of bacterial hyaluronate lyase by the excess HA. Hyaluronate lyase is an enzyme that catalyses the chemical reaction of cleavage of HA chain. Saturation then prevents bacteria from maintaining elevated levels of tissue permeability. It was also noted that different strains belonging to the same bacterial species are differently affected by HA [51]. Titanium coating with sodium hyaluronate significantly decreased the density of *S. aureus* adhering to the surface [52].

1.3.2.3 Examples of Coatings Containing Natural Polysaccharides on Titanium

Layer-by-layer adsorption has been recognized as a versatile yet simple technique for the functionalization of a variety of surfaces. It involves alternate adsorption of polyanions and polycations via

electrostatic interaction on a charged surface. Alternating successive immersion of the charged surfaces in oppositely charged polyelectrolyte solution results in a coherent coating, typically ranging from tens to hundreds of nanometers [53]. Chua et al. deposited polyelectrolyte multilayers on titanium based on alternating hyaluronic acid and chitosan layers [54]. Thus, functionalized surface was more hydrophilic and smoother compared to pristine titanium and caused up to an order of magnitude decrease in adhesion of *S. aureus*. Upon cross-linking of these layers upon which activated carboxylic sites of HA react with amine group from CH, the structural stability of the coating was increased and retains its antibacterial properties even after 2-day immersion in phosphate buffer saline. The HA/CH functionalized surface was not cytotoxic but decreased osteoblast adhesion was noticed on both cross-linked and non-cross-linked coatings when using rinsing after incubation with osteoblasts. This step has provoked the removal of the nonadhered cells. It was suggested that HA may be responsible for smaller osteoblast attachment, as CH is known to support this process [55]. To overcome this property and promote the osteoblast functions, RGD peptide was incorporated in this coating [56]. RGD immobilization was performed on cross-linked HA/CH polyelectrolyte multilayers (Fig. 1.13) with CH as the outermost layer which showed the best antibacterial performance. The immobilized peptide had a profound beneficial influence of osteoblast adhesion and proliferation without affecting the antibacterial activity of the coating [56].

Complexes of HA and CH were combined with silver phosphate Ag_3PO_4 nanoparticles (NPs) or silver ions ($AgNO_3$) in order to increase their effect on *S. aureus* [57]. The complexes of polymer with silver NPs had higher antibacterial effect than individual polymer complexes which did not inhibit bacterial growth at the applied concentration. The greatest inhibitory effect had the combination of 9.7 mM CH and 300 μM Ag(I) ions or 300 μM silver phosphate NPs. Combination of HA with silver had significantly smaller effect [57]. These complexes may have potential to use in vascular graft application. Layer-by-layer technique was also used to prepare self-assembly of CH/alginate multilayers on titanium [58]. Multilayers were functionalized with minocycline, a broad-

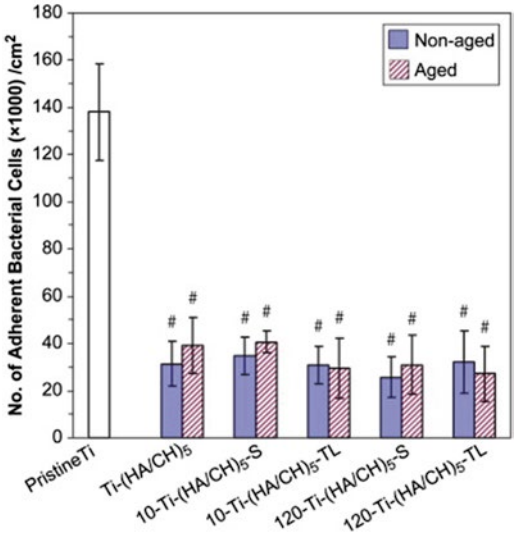

Fig. 1.13 Number of adherent *S. aureus* cells/cm^2 on the Ti substrates coated with various chitosan (CH) and hyaluronan (HA) coatings with AMP RGD (denoted -S and -TL) after exposure to bacterial suspension (10^6 cell/mL) in PBS for 4 h. (*Reprinted from the publication by Chua P-H, Neoh K-G, Kang E-T, Wang W (2007) Surface functionalization of titanium with hyaluronic acid/chitosan polyelectrolyte multilayers and RGD for promoting osteoblast functions and inhibiting bacterial adhesion. Biomaterials 29:1412–1421, with permission from Elsevier*)

spectrum antibiotic synthesized from natural tetracyclines, in the outermost layer. Monolayer coating loaded with antibiotics cannot provide long-term antibacterial effect. In contrast, multilayer antibiotics-loaded coating on titanium was effective even after 14 days against colonization of *S. aureus*, i.e., during the most important period of wound healing or formation of biological seal [58]. This is beneficial as overlong release time at lower concentration may provoke adverse effect of development of the antibiotic-resistant bacteria. Hydrophilic surface of coating compared to pristine titanium also contributed to the reduced bacteria attachment.

Chitosan nanocomposite coatings were prepared on silanized titanium substrate using spreading technique [59]. Coatings

contained CH and polyvinyl alcohol (PVA)-capped Ag NPs obtained by a green method of microwave irradiation of aqueous solution of PVA and $AgNO_3$. PVA served as a capping agent. This nanocomposite exhibited increased mechanical stability and bactericidal activity against *E. coli* and *S. aureus*. Fourier transform infrared spectra indicated the involvement of primary amino and amide groups of CH with metal particles. The amine ($–NH_2$) groups can electrostatically interact and coordinate with Ag^+ adsorbed over the surface of NPs, avoiding agglomeration of reduced Ag. Very smooth surface of the coatings and sustainable long release of Ag^+ ions conferred to the coating an antibacterial activity.

Layered acrylic particles containing epoxy functional groups were prepared via a seeded emulsion polymerization in the presence of CTAB (cetyltrimethylammonium bromide) as a cationic surfactant [60]. When adding chitosan, an efficient dispersion in polyacrylic matrix was achieved which acted against *S. aureus* and *E. coli*, especially when containing 40 wt% of positively charged CH. The complexes were nontoxic and have potential to be used as a new generation of antibacterial and nontoxic coatings.

HA was used to fabricate multilayer films with PDDA (poly(dimethyldiallylammonium chloride)) through electrostatic interaction between positively charged PDDA and negatively charged HA [61]. In multilayer HA/PDDA, Ag NPs were embedded by binding Ag^+ to negatively charged carboxylic group of HA [62]. HA acted as a stabilizing as well as reducing agent and reduced Ag^+ to Ag NPs under UV irradiation. After exposure to HA/PDDA with Ag nanoarrays, the most of *E. coli* cells were dead. In contrast, HA/PDDA surface without embedded Ag particles was stimulating for bacteria growth. The antibacterial activity of Ag NPs reduced using HA or DAPHP (diaminopyridinylated heparin) as capping and reducing agents was reported [63]. Potent antimicrobial activity was obtained when tested against *S. aureus*, and modest against *E. coli*. Ag–HA showed greater antimicrobial activity than silver-DAPHP. In contrast, neither HA or DAPHP showed activity against *S. aureus* or *E. coli*.

1.3.3 Inorganic Bioactive Agents

Several metals exhibit antimicrobial properties: silver, copper, zinc, tin, platinum, etc. This section is largely devoted to silver itself, i.e., not used in the form of coating or incorporated in other coating. First, the mechanism of antibacterial activity of silver ions and nanoparticles will be presented, followed by the presentation of different factors which affect the activity (size, shape, concentration, method of preparation), as well as issues related to cytotoxicity of silver. This part will be the basis for the use of silver incorporated in hydroxyapatite (HAP) or TiO_2 coatings which then serves as additional functional ability, i.e., antimicrobial property of these coatings.

1.3.3.1 Silver

General Characteristics of Silver

Silver has been used as disinfectant since ancient times. In the nineteenth and twentieth century, it has been applied as sulfadiazine for treatments of burns and wounds and as $AgNO_3$ solution as disinfectant. After the introduction of antibiotics the use of silver rapidly declined. The boom in the renewed interest in silver is related to the introduction of nanotechnology and new possibilities for bioapplications, especially those related to dental and orthopedic applications. Due to the natural antimicrobial property of silver it may be presumably used instead or combined with antibiotics. In contrast to the latter, it seems that the resistance to Ag cannot be developed and in that sense Ag is advantageous to antibiotics, toward which humans develop the resistance. Since metal attacks a broad range of targets (unlikely antibiotics which are narrow target) the organisms would have to develop a host of mutations simultaneously to protect themselves [64]. Drawback of use of silver can be argyria, gray-blue discoloration of the skin related to excessive exposure to silver noticed in some workers professionally exposed to silver compounds. However, the levels of Ag used as antimicrobial agents are relatively low, i.e., below the threshold for argyria.

Mechanism of Inhibition by Silver Ions and Silver Nanoparticles

The mechanism of antibacterial activity of silver is complicated and proceeds at several levels. Ag NPs show substantially different physicochemical properties from those of bulk silver. Primarily, their large surface area provides better contact with microorganisms. This results in different toxicity mechanism. Ag NPs also produce Ag^+ ions, so in that sense they act in the same manner as when Ag^+ ions are used only. Silver has a high affinity to interact with thiol group from L-cysteine. As thiol group is responsible for enzymes activation, this leads to deposition of proteins inside the cell. Ag^+ treated cells showed increased propidium iodide (PI)[2] fluorescence relative to untreated cells, indicating destabilization of the cellular envelope and increased membrane permeability [65].

Silver reacts also with phosphorus-containing compounds like DNA. Silver ions penetrate the bacterial cell wall and enter into cells (Fig. 1.14) [65]. Feng et al. detected an electron light region on the center of the cell which contains DNA indicating that DNA is turned into condensed form and thus lost its ability to replicate [66, 67]. These processes lead to damage and even cell death. Silver ions are more active under aerobic conditions, i.e., antibacterial activity is related to the presence of oxygen [68]. Namely, silver ions mediate reactive oxygen species (ROS) generation, mainly superoxide radical ($O_2^{\bullet-}$). At least half of the log scale antibacterial activity of silver ions can be attributed to ROS-mediated activity.

When considering differences in mechanism of silver ions and NPs, Ag NPs also produce Ag^+ ions, so they act in the same manner as when ions are used only [69]. Additionally, NPs get attached to the cell membrane, penetrate inside the cell, damage the membrane, and lead to disruption of the ion flux system [70]. The oxidative damage as well as structural damage of the membrane is smaller when using Ag^+ ions compared to Ag NPs, i.e., NPs cause more damage than Ag^+ [69]. In that sense the ability of Ag^+ ions is inferior to antibacterial ability of Ag NPs. However, Ag NPs do not result in

[2] PI is a membrane-impermeable fluorescent dye that is used to detect permeation of the cell membrane.

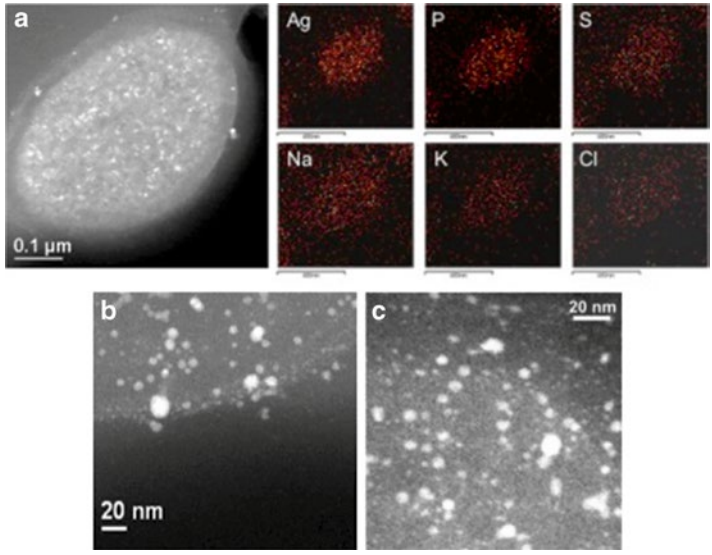

Fig. 1.14 (**a**) *Left*: a considerable presence of silver nanoparticles is found in membrane and the inside of an *E. coli* sample. *Right*: Elemental mapping showing well distributed silver through the sample. (**b**) A close-up of the interior and (**c**) membrane of an *E. coli* treated sample. (*Reprinted from the publication by Morones J R, Elechiguerra J L, Camacho A, Holt K, Kouri J B, Ramírez J T, Yacaman M J (2005) The bactericidal effect of silver nanoparticles. Nanotechnology 16:2346–2353, with permission from IOP Science*)

DNA damage [69]. Ag NPs and ions act differently to different organisms [71]. The NPs show the highest inhibition to autotrophic nitrifying organisms, whereas Ag^+ ions are most toxic to heterotrophic growth (Fig. 1.15) [71]. Silver NPs strongly inhibited microbial growth. At 1 mg/L Ag, the inhibitions on nitrifying bacterial growth by Ag NPs and Ag^+ ions were 86 ± 3 % and 42 ± 7 %, respectively. At 4.2 µM Ag, the inhibitions on the growth of *E. coli* by Ag NPs and Ag^+ ions were 55 ± 8 % and 100 %, respectively [71].

Silver can be used in combination to conventional antibiotics. Gram-negative bacteria have a protective outer membrane that prevents entry of a variety of larger antibiotics, such as glycopeptide vancomycin [72]. The combination of low doses of Ag^+ ions and vancomycin resulted in significantly greater bacterial cell death rela-

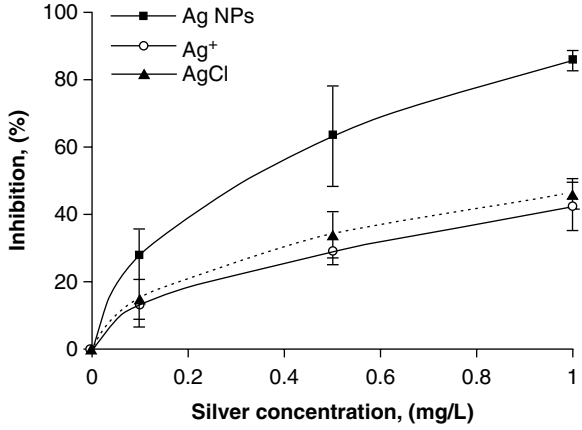

Fig. 1.15 Nitrification inhibition as a function of the concentrations of silver in the form of Ag NPs, Ag^+ ions, and AgCl colloids. (*Reprinted from the publication by Choi O, Deng K K, Kim N-J, Ross Jr L, Surampalli R Y, Hu Z (2008) The inhibitory effects of silver nanoparticles, silver ions, and silver chloride colloids on microbial growth. Water Res 42:3066–3074, with permission from Elsevier*)

tive to treatments with Ag^+ ions or vancomycin alone. This synergistic effect can be used to increase the effectiveness of vancomycin against Gram-negative bacteria by Ag^+-induced outer membrane permeability. Greater bactericidal activities were also obtained in combination with other antibiotics, i.e., gentamicin, ampicillin, and ofloxacin.

Size and Shape of Silver Nanoparticles

The toxic activity of NPs is strongly dependent on their size. Morones et al. showed that only NPs with diameter between 1 and 10 nm present direct interaction with bacteria [65]. The advantages of nanoparticles are, in addition to high specific surface area and high dispersion of the active component, the presence of specific energetic surface sites [73]. In the literature different mean sizes of NPs were used but all in the active size region: 12 [70, 74], 11.23 [75], 13.4 [76], 14 [71], 10–15 [77], 5 and 24 [78], and 39 nm [64]. Shameli et al. produced Ag NPs of different sizes in

the range from 10.60 to 25.31 nm using sugar as reducing agent and polyethylene glycol as a complexation agent [75]. The size affected the antibacterial activity to *S. aureus* and *Salmonella typhimurium* showing higher activity at smaller size.

Shape of the particles also affects their toxic effect. Zeng et al. controlled the particle shape using different capping agents keeping other conditions identical (seed, precursor concentration, temperature, reducing agent) [79]. When using citrate, octahedrons were obtained; in contrast, capping using poly(vinyl pyrrolidine) resulted in the formation of nanocubes and nanobars. Pal et al. studied specifically the effect of shape on the antibacterial effect of NPs [64]. Three particle shapes were produced: truncated, triangular, and elongated rod shaped were obtained by a solution-phase method from $AgNO_3$, ascorbic acid, CTAB, Ag seeds, and NaOH. Spherical particles were deposited by reducing aqueous $AgNO_3$ with sodium citrate at near-boiling temperature. Among three particle shapes the triangular particles showed the strongest biocidal activity, i.e., a complete inhibition of bacterial growth at the microgram range. At 10^7 colony forming units (CFU)/mL *E. coli*, spherical particles reduced growth (50–100 %) at concentrations >12.5 μg, while rod-shaped particles and Ag^+ showed inferior performance. The effect of shape on the antibacterial activity was explained in terms of different percentage of active facets present in Ag NPs. Ag reactivity is favored by high-atom density facets like (111) [65, 73]. Top basal plane in truncated triangular particles is (111), while spherical and rods have predominantly (100) and small percentage of (111) facets [64]. Morones et al. showed that ~98 % of particles have octahedral and multiple-twinned icosahedral and decahedral in shape; these exhibit the highest activity [65].

In order to understand the mechanism of nanosilver toxicity, nanosized Ag spheres (10, 20, and 40 nm), plates (32 nm), and wires (65 nm × 20 μm) were investigated in a fish gill epithelial cell line and in zebrafish embryos [80]. Ag nanoplates, whose shape varied from circular to triangular but always exhibiting edges, were considerably more toxic than other particle shapes (Fig. 1.16) [80]. Ag nanoplates induced significant cell death even at the lowest dose, while the nanospheres induced cytotoxicity at the highest dose and Ag nanowires did not. At the same time the

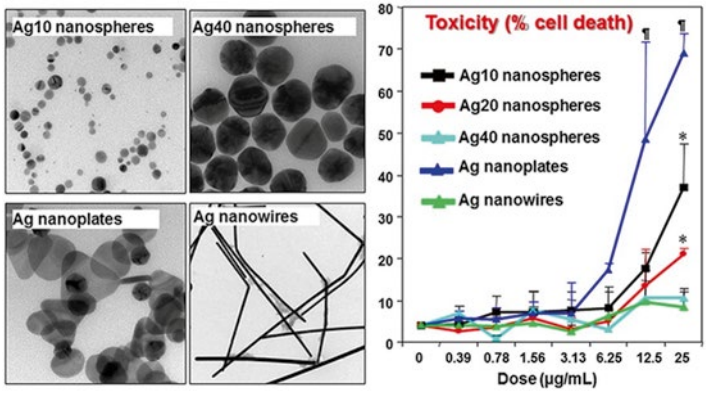

Fig. 1.16 TEM images of Ag nanospheres, nanoplates, and nanotubes and the related toxicity (*Reprinted from the publication by George S, Lin S, Ji Z, Thomas C R, Li L, Mecklenburg M, Meng H, Wang X, Zhang H, Xia T, Hohman J N, Lin S, Zink J I, Weiss P S, Nel A E (2012) Surface defects on plate-shaped silver nanoparticles contribute to its hazard potential in a fish gill cell line and zebrafish embryos. ACS Nano 6:3745–3759, with permission from Americal Chemical Society*)

Ag nanoplates triggered the highest superoxide production but the smallest release of Ag^+ ions into solution. Toxicity mechanism induced by nanoplates differed from that of nanospheres as it was not related to bioavailability and uptake. This was ascribed to a high level of crystal defects (stacking faults and point defects) on the nanoplate surfaces. In contrast, nanospheres showed multiple crystal domains, including the presence of twin planes that form at the boundaries between crystal domains. Examination of nanoplates by transmission electron microscopy (TEM) demonstrated that alternating {111} and {200} stacking planes create material defects that are enriched for dangling bonds, which could confer higher electrocatalytic activity due to local increase in electron density [80]. Therefore, the expression of crystal defects should be considered as another important mechanism for Ag nanoparticle toxicity, in addition to Ag^+ ion release.

The particles differed not only in shape but also in size: triangular particles with 40 nm average edge length, rod-shape particles with 133 nm × 16 nm average dimension, and spherical

particles with 39 nm diameter [64]. These particles showed distinctively different UV spectra due to the surface plasmon resonance shift to a longer wavelength with increase in particle size [67]. Nanoparticles have a surface plasmon resonance absorption in the UV–visible region [81]. The surface plasmon band arises from the coherent existence of free electrons in the conduction band due to the small particles size. As the change in absorbance is a measure of the particle size, shape, and chemical environment, the band shift reflects the change in particle size and shape. Spherical particles showed UV peak at 420 nm, while for rod-shape particles four peaks (384, 420, 485, and shoulder at 373 nm) were observed [64]. Triangular particles gave peak at 418 and 514 nm. George et al. also observed different UV spectra depending on the particle shape: spherical particles showed a single plasmonic resonance peak at 390–410 nm, nanoplates showed peaks at 330, 410, and 430 nm, confirming their anisotropy [80]. In the majority of literature studies, the spherical particles were used which show UV peaks between 391 and 437 nm [70, 71, 74–76, 78].

Concentration of Bacteria and Concentration of Silver

Inhibition of bacterial growth depends also on the concentration of bacteria, as well as concentration of silver [64, 70]. At 10^5 CFU/mL *E.* coli, the efficiency of biocidal action was lower compared to 10^7 CFU/mL indicating that at given concentration of silver, inhibition of bacterial growth depends on the initial number of cells [64].

At a given concentration of bacteria cell, the inhibition depends on the concentration of silver [68–71, 76, 82]. Sondi and Salopek-Sondi investigated the effect of concentration of Ag NPs in the range between 10 and 100 μg/mL against *E. coli* and found out that at concentration >50–60 μg/mL caused a 100 % inhibition of growth [70]. A concentration-dependent increase in growth inhibition against *E. coli* was observed for silver NPs also in the range between 0 and 1 mg/L [69]. Similar effect was observed for *S. aureus*: at 20 μg/mL Ag NPs no growth was observed over 7 days (thus determined minimum

bactericidal concentration), while at 50 μg/mL the cell DNA was condensed to a tension state indicating that it could have lost its replicating ability [82]. Using bacterial reporter strains specifically responding to superoxide radicals Park et al. presented the evidence that the generation of oxidative stress induction is dependent on Ag^+ concentration [68]. The highest level of induction was observed at 0.3–0.5 mg/L Ag^+, and the induction decreased at higher concentrations.

The concentration-dependent inhibition of silver differs for different types of bacteria [76]. When tested against Gram-negative *E. coli*, Ag NPs effectively inhibited bacterial growth; inhibition was progressively stronger with increasing Ag NPs concentration from 0.4 to 33 nM [76]. In contrast, the inhibitory effect was mild against Gram-positive *S. aureus*. The reason for this behavior lies in the difference in membrane structure between Gram-positive and Gram-negative bacteria. Gram-positive bacteria have a thick, multilayer peptidoglycan layer, and Gram-negative bacteria have a thin peptidoglycan layer but also an outer membrane layer composed mainly of lipopolysaccharides. Compared with Gram-positive bacteria, Gram-negative bacteria are more resistant against antibiotics because of their impenetrable outer cell wall. Review of bacteria strains against which silver NPs and ions were tested is given in Table 1.1.

Methods of Preparation of Silver Nanoparticles

Sharma et al. have recently reviewed the preparation of Ag NPs by green synthesis approaches opposed to traditional methods involving chemical agents which may be associated with environmental toxicity [81]. The simplest way of producing the Ag NPs is the chemical reduction of silver salt, usually $AgNO_3$, accompanied by the use of a reducing agent, e.g., ascorbic acid [70], sodium borohydrate ($NaBH_4$) [74, 76], $NaBH_4$, and polyvinylalcohol as capping agent to control the growth [71], citric acid [79], and sodium citrate [64]. The reduction of silver ions in aqueous solution generally yields colloidal silver with particle size of several nanometers [81].

Table 1.1 Summary of bacterial strains against which Ag NPs and Ag^+ ions were tested

Reference	Bacteria	Type
Pal et al. [64]	*Escherichia coli*	Gram-negative
Sondi and Salopek-Sondi [70]	*Escherichia coli*	Gram-negative
Choi et al. [71]	*Escherichia coli*	Gram-negative
Park et al. [68]	*Escherichia coli*	Gram-negative
Morones-Ramirez et al. [72]	*Escherichia coli*	Gram-negative
Guin et al. [77]	*Escherichia coli*	Gram-negative
Li et al. [82]	*Staphylococcus aureus*	Gram-positive
Kim et al. [76]	*Escherichia coli*	Gram-negative
	Staphylococcus aureus	Gram-positive
Li et al. [83]	*Escherichia coli*	Gram-negative
	Staphylococcus aureus	Gram-positive
Morones et al. [65]	*Pseudomonas aeruginosa*	Gram-negative
	Vibrio cholerae	Gram-negative
	Escherichia coli	Gram-negative
	Scrub typhus	Gram-negative
Shameli et al. [75]	*Staphylococcus aureus*	Gram-positive
	Salmonela typhimurium	Gram-negative
Feng et al. [66]	*Staphylococcus aureus*	Gram-positive
Aguilar Mendez et al. [78]	*Colletotrichum gloeosporioides*	Phytopathogen

Initial formation of silver atoms is followed by agglomeration into oligomeric clusters and eventually colloidal nanoparticles. The color of colloidal dispersion varies depending on the stage of aggregation from yellow (the particles are smaller and absorb in the 380–400 nm) to dark yellow, violet and eventually grayish, after which the colloids break down and particles settle out [74].

The choice of reducing agent affects the size distribution which is narrow in the case of $NaBH_4$ and broader when citrate was used. It should be noted that $NaBH_4$ is toxic.

For green synthesis three main steps should be environmentally benign: choice of solvent medium, choice of reducing agents, and substances to assure NP stability. The following methods can be summarized [81]:

- Polysaccharide method uses water and polysaccharide as a capping agent, e.g., starch, glucose; the latter can also serve as a reducing agent.
- Tollens method involves Tollens reagent and an aldehyde

$$\mathrm{Ag(NH_3)_2^+(aq) + RCHO(aq) \rightarrow Ag(s) + RCOOH(aq)}$$

  In a modified Tollens procedure, Ag^+ ions are reduced by saccharides in the presence of ammonia.
- Irradiation method does not require the use of reducing agent. These methods involve laser, microwave irradiation, or radiolysis of aqueous solution of silver salt.
- Biological method involves the reduction of Ag^+ ions by combination of molecules found in enzymes, proteins, amino acids, vitamins, etc.
- Polyoxometalates method uses polyoxymethalate as a reducing agent and stabilizing agent.
- Electrochemical synthesis performs by electroreduction of anodically dissolved silver ions in acetonitrile containing tetrabutylammonium salts.

Cytotoxicity of Silver

Silver has not been identified as a trace metal, and thus seems to be nonessentials to humans [84]. As such, exposure to silver is unwanted. Orally administered silver has been described to be absorbed in the range of 0.4–18 % in mammals with a human value of 18 %. Humans can come into contact with silver via brazing or soldering, coins, tableware, jewelry, dental fillings,

dietary supplements, and different products that contain silver, i.e., wound dressings, textile products, bone cement, etc. When administrated, it can become deposited in a wide range of organs; the most well described depositional effect in the blue-gray discoloration of the skin called argyria. For the general population, the human use of silver has been described to be 0.4–27 μm/day [84], which corresponds to 0.007–0.5 μg/kg of body weight/day. Toxicity of silver is dose dependent. The dose level of 0.25 mg/kg of body weight/day was reported as "no-observed adverse effect-level" and tolerable daily intake of 2.5 μg/kg of body weight/day [84]. Median lethal dose LD_{50} is the drug dose at which 50 % of the treated mice survive. For Ag^+, LD_{50} was reported between 120 and 240 μM, i.e., low levels are not cytotoxic [72].

Wang et al. emphasized that substantial progress has been made in understanding the acute silver toxicity; however, the consequences of chronic low doses (i.e., sublethal doses) of silver have not been sufficiently considered [85]. Ag NPs and ions can be involved in both lethal and sublethal doses. The direct indication of lethal cytotoxicity of nanosilver is cell death through increased ROS generation, oxidative stress, and enhanced permeability of mitochondrial membrane leading to overt toxic effects. Under sublethal doses, nanosilver can interfere with biomolecules in a more subtle manner with minimal ROS production and little impact on cell viability but it can disturb the function of crucial proteins and induce changes in gene and protein expression levels.

1.3.3.2 Silver Coatings on Titanium

Silver can be used in various forms: as bulk coating which then releases Ag^+ ions or as Ag nanoparticles incorporated in other coating. Silver is also used in a colloidal form.

Silver-based bulk coatings have been used on various medical device including catheters; also for treatments of infection of orthopedic prostheses for treatments of osteoarthrosis and tumors [86, 87]. Prostheses with silver-based coatings are commercially available and are used in clinical practice to treat implant infec-

tion. The longest on the market are the prostheses by the company Waldemar Link (Hamburg, Germany) currently marketed as PorAg™. An approximately 1 μm thick surface modification consists of a silver bottom layer and an open porous 100 nm thick top layer consisting of Ti/Ag nitride (TiAgN). Other combinations are also under study. Approximately 2 μm thick Ti/Ag coatings (0.7–9 % Ag) were deposited on Ti by physical vapor deposition (PVD) and tested against *S. epidermidis* and *K. pneumonia* [88]. The adhesion of bacteria was significantly reduced without compromising biocompatibility properties on epithelial and osteoblast cells. Ag/plasma polymer coating of the stem (Bio-Gate AG, Bremen, Germany) was also performed and tested in a canine model [89]. Elemental silver particles were sputtered onto the surface of the stem in PVD process and covered by a plasma polymer layer using a subsequent chemical vapor deposition (CVD) process with hexamethyldisiloxane as precursor. Four of nine PVD-silver-coated titanium stems underwent stable osseous integration after implantation in a canine model [89].

1.3.3.3 Hydroxyapatite and Silver

General Characteristics of Hydroxyapatite

Titanium alloys are grouped into bioinert materials as well as ceramics like alumina, zirconia, etc., and their biocompatibility is inferior to that of calcium phosphate (CaP) or hydroxyapatite (HAP), which are grouped into bioactive materials [90]. Therefore, bioactive surface treatment (bioactive surface modification) is, in general, applied to titanium alloys for biomedical applications in order to improve their biocompatibility further. In that case, phosphate calcium-type ceramics such as CaP, HAP, and tricalcium phosphate TCP (α- or β-$Ca_3(PO_4)_2$) are mainly coated on the surface of titanium alloy. In general, formation of hydroxyapatite is finally targeted.

Hydroxyapatite belongs to a family of calcium orthophosphates present in bones and teeth, comprising approximately 40–75 % of mineral phase, the rest being water (10 %) and collagen. The bone mineral is of an idealized formula $Ca_{10}(PO_4)_6(OH)_2$ but is associated

with minor groups and elements, e.g., CO_3^{2-}, HPO_4^{2-}, Na^+, Mg^{2+} and trace elements, e.g., Sr^{2+}, K^+, Cl^-, and F^- [91]. Some of these play a vital role in the biochemical reactions associated with bone metabolism. A significant variation in concentration of CO_3^{2-}, Na^+, Mg^{2+}, K^+, and Cl^- was observed in human bone specimens; concentrations of CO_3^{2-} and Na^+ increase with age, whereas concentrations of Mg^{2+}, K^+, and Cl^- decrease with age [91]. The use of calcium orthophosphates in orthopedics and dental medicine is based on their similarity with bone and enamel. Biphasic calcium phosphates (BCP) (HAP+α-TCP or HAP+β-TCP) are bioresorbable materials. The β-TCP and α-TCP are obtained by sintering at temperatures above 800 and 1125 °C, respectively.

The bioactive surface treatment processes are, in general, divided into dry process and wet process [90]. Dry processes are divided into direct HAP forming methods such as plasma spray method, ion plating, radiofrequency magnetron sputtering, pulse laser deposition, ion beam dynamic mixing, etc., where HAP are formed directly on titanium alloy surface. Indirect HAP forming methods include, for example, calcium ion implantation where calcium ions are implanted into biomedical titanium alloys, and calcium ion mixing method where Ca is sputtered on the surface of biomedical titanium alloys followed by Ar ion implantation, etc. Wet processes are also divided into direct HAP forming methods such as, for example, electrochemical treatment, electrophoretic deposition, sol–gel methods, and indirect HAP forming methods such as, for example, alkali treatment where titanium alloy is immersed into NaOH solution and heated followed by immersing the alloy into living body liquid [90].

Methods of Preparation of Hydroxyapatite Containing Silver and Related Morphology

The main idea behind incorporation of silver into the structure of HAP coating is to combine the osseointegration ability of HAP with antibacterial ability of Ag in order to increase the functionality of the coating. As there are numerous methods for HAP preparation, several possible routes for Ag incorporation have been explored. The methods are regarded according to the same

strategies as for pure HAP, i.e., dry and wet direct and indirect methods (Table 1.2).

Needle-like morphology typical for HAP was usually observed [92–95], with nanocrystals comparable to that of bone apatite (Fig. 1.17) [92]. Silver particles were evenly dispersed within the layer structure which was dependent on the method of preparation. Porous structure with typical needle-like HAP could facilitate cell adhesion (Fig. 1.18) [94]. The EDS analysis revealed the presence of titanium, phosphorus, calcium, and silver (Fig. 1.18) [94]. A layered structure with mostly amorphous layer on top and mostly crystalline layer toward to top coating interface was obtained by IBAD method [96]. Ag particles sized 10–50 nm were evenly distributed throughout the coating thickness. By rf magnetron sputtering nanopatterned Ag layer was obtained which imparted for hydrophobicity [97]. When using microarc oxidation the morphology was dependent on the voltage and Ag content [98]. At low voltages a porous microstructure was observed with spherical pores well separated and homogeneously distributed. The pore size increased with voltage. Above 380 V the surface became irregular and rough, instead of pores numerous flakes appeared [98]. Similarly, when using electrochemical deposition needle-like crystals were obtained after oxidation at −1.3 V; no Ag particles were observed [99]. At −2.0 V the porous network of needle-like crystals with white spots of Ag particles sparsely dispersed. Particles became more distinct after oxidation at −3.5 and −4.0 V. Uniform sol–gel Ag–HAP composite coating composed of spherular HA crystals with an average diameter of several micrometer and white spot-like Ag particles were formed [102–104].

Microstructure and Phase Composition of Hydroxyapatite Containing Silver

X-ray diffraction (XRD) is commonly used to investigate the phase composition and microstructure of the deposited coatings. When considering dry coatings, typical peaks related to crystalline HAP were detected; in some studies Ag peaks were observed [92, 104,

Table 1.2 Methods used for the preparation of silver–hydroxyapatite composites or coatings on titanium-based substrates divided according to the type of preparation method

Method/substrate	Heat treatment	Ag conc. range	Optimal Ag conc.	Bacteria strain	Reference
Dry methods					
Ion beam-assisted deposition (IBAD)/Ti6Al4V	500 °C/2 h	5–100 ppm $AgNO_3$ $(Ag,Ca)_{10}(PO_4)_6(OH)_2$	20 ppm		Feng et al. [103]
IBAD/Ti	450–550 °C	1; 3; 6.5 wt%			Bai et al. [96]
Magnetron cosputtering/Ti	550 °C/4 h	2.05 ± 0.55 wt%		*S. aureus*	Chen et al. [104]
				S. epidermidis	
Radiofrequency magnetron sputtering/Ti	1100 °C/2 h	0.13–0.36 wt%			Grubova et al. [97]
Vacuum plasma spraying/Ti		1–5 wt%	<5 wt%	*S. aureus*	Chen et al. [105]
				E. coli	
				P. aeruginosa	
Microarc oxidation/Ti		0.00003–0.004 mol/L		*S. aureus*	Song et al. [98]
				E. coli	
Plasma-based ion implantation and sputtering/Ti	1000 °C/4 h	0.5; 1.5 wt%		*S. epidermidis*	Trujilo et al. [106]
				P. aeruginosa	

Microwave irradiation	900 °C/4 h	0.05–0.6. wt%	0.05	*E. coli* *S. aureus*	Rameshbabu et al. [92]
Wet methods					
Wet chemical method	1200 °C/2 h	$Ca_{10-x}Ag_x(PO_4)_6(OH)_2$ $0 \leq x \leq 0.5$	$x < 0.3$	*E. coli*	Singh et al. [107]
Electrochemical deposition/Ti	700–900 °C/2 h	6.7; 14.8 wt%	6.7 wt%	*E. coli* *S. albus*	Lu et al. [99]
Electrochemical deposition/ nanotubes TiO_2	0.1 M NaOH, 37 °C/2 h	2.03 wt%		*E. coli*	Yan et al. [94]
Sol–gel/Ti	650 °C/3 h	1; 1.5 wt%	1 wt%	*S. epidermidis* *S. aureus*	Chen et al. [108]
Sol–gel/Ti	400–700 °C/10 min	0.16 wt%		*E. coli* *S. aureus*	Mo et al. [100]
Sol–gel	800 °C	5; 10; 20 wt%		*S. aureus*	Sygnatowicz et al. [101]
Sol–gel/porous Ti	300 °C/15 min	0.8; 1.6 wt%	0.8 wt%	*Escherichia coli* *S. albus*	Qu et al. [102]
Sol–gel	250–650 °C/30 min	200–2000 ppm		*S. mutans*	Chung et al. [109]

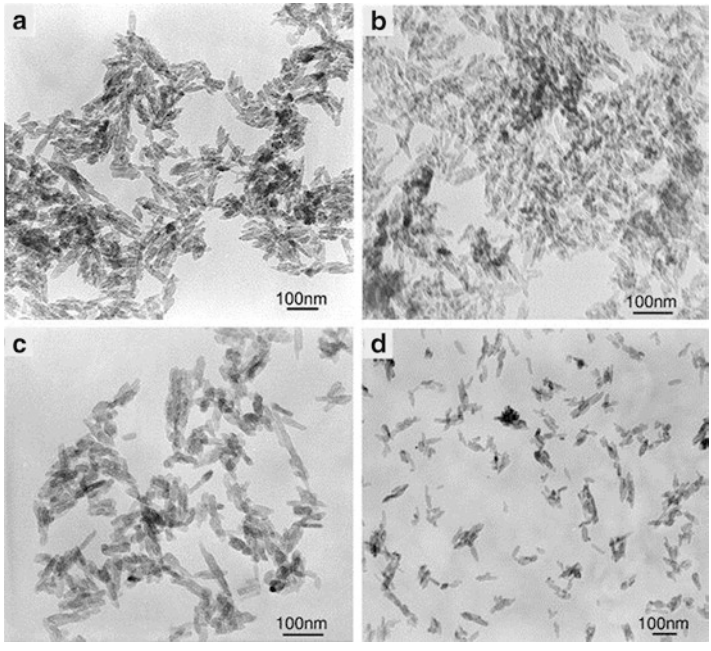

Fig. 1.17 TEM morphology of the HA (**a**), 0.5AgHA, (**b**), 2AhHA (**c**), and 5AgHA (**d**) samples. (*Reprinted from the publication by Rameshbabu N, Sampath Kumar T S S, Prabhakar T G, Sastry V S, Murty K V G K, Rao K P (2007) Antibacterial nanosized silver substituted hydroxyapatite: Synthesis and characterization. J Biomed Mater Res A 80A:581–591, with permission from John Wiley and Sons*)

105], in other it was not [97, 98]. When Ag-related peaks were detected, they were ascribed to the incorporation of Ag into HAP lattice structure. Chung et al. observed Ag peak only at 2000 ppm [109]. Chen et al. reported [105] that in addition to HAP and Ag peaks, peaks related to β-TCP and CaO were detected indicating that HAP was decomposed during plasma spraying. The intensity of Ag peaks increased with Ag content in the HAP. In Ag–HAP synthesized by microwave processing cell parameters increased with increasing Ag content indicating the effect of Ag ions on the crystallinity of HAP lattice [92]. The substitution of Ag^{+} ion (size 1.28 Å) takes place for Ca^{2+} ion size (0.99 Å) preferentially in Ca(1) site of HAP and this leads to an increase in lattice parameters

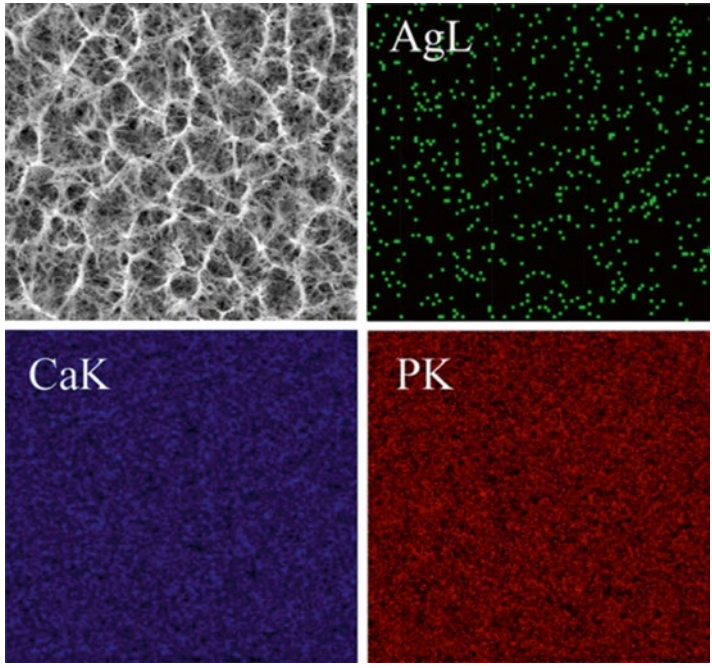

Fig. 1.18 Scanning electron microscopy (SEM) image and elemental energy dispersion X-ray spectroscopy (EDS) mapping of Ag–HAP coating synthesized via electrochemical deposition on anodized titanium nanotubes. (*Reprinted from the publication by Yan Y, Zhang X, Huang Y, Ding Q, Pang X (2014) Antibacterial and bioactivity of silver substituted hydroxyapatite/TiO2 nanotube composite coatings on titanium. Appl Surf Sci 314:348–357, with permission from Elsevier*)

linearly with the amount of Ag added. After heat treatment crystallinity improved and the presence of TPC was noticed for $x_{Ag}>0.5$. The presence of TCP is beneficial in terms of biocompatibility as it provokes more favorable cell proliferation [90].

In some studies, Ag-related peaks were not observed and explained by the substitution of Ca^{2+} by Ag^{+} which does not lead to apparent varieties of crystalline structure and significant differences in lattice parameters [97]. When Ag could not be detected by XRD patterns, complementary methods were also used, e.g., energy dispersive X-ray spectroscopy (EDS) [98, 106] or Raman spectroscopy [106].

When considering wet coatings, similar situation is encountered. In all the coatings, typical XRD peaks related to HAP were detected [94, 95, 99–102, 107–109]. The XRD peaks related to Ag were detected in the coatings obtained by electrochemical deposition [95, 99] and sol–gel methods [101, 102]. In other coatings prepared by wet methods, silver was not detected by XRD indicating that the presence of Ag was either too small or did not affect the structure of HAP [94, 100, 107, 108]. Sygnatowicz et al. concluded that Ag is present primarily in Ag metal form and it is not dissolved in HAP or in phosphate phase [101].

Cytotoxicity and Optimum Silver Concentration in Hydroxyapatite Containing Silver

Ranges of silver concentrations used in different methods are listed in Table 1.2. When using silver it is important to determine the optimum concentration in sense that it minimizes bacterial risk without compromising biocompatibility of the coating. This usually includes the evaluation of cytotoxicity through cell proliferation[3] and osteoblast cell attachment.[4] No cytotoxicity was

[3] There are several possibilities to evaluate *cell viability and proliferation*:

- MTT reagent [3-(4,5-dimethylthiazol-2-yl)-2,5-diphenyl tetrazolim bromide] is usually used to detect cell viability or proliferation of cells in contact with the material surface. MTT reagent reacts directly with mitochondrial to form formazan crystals on metabolically active cells.
- Alamar blue® assay is designed to measure quantitatively the proliferation of various human and animal cell lines, bacteria, and fungi. It incorporates a fluorometric/colorimetric growth indicator based on detection of metabolic activity. Specifically, the system incorporates an oxidation–reduction indicator that both fluoresces and changes color in response to chemical reduction of growth medium resulting from cell growth.
- Double-stranded DNA (dsDNA) test using an ultrasensitive fluorescent nucleic acid stain for quantitating dsDNA in solution. Detecting and quantitating small amounts of DNA is extremely important in a wide variety of biological applications.
- Lactate dehydrogenase (LDH) activity, which is a marker for tissue damage.

[4] The *activity and attachment of osteoblast cells* can be evaluated by:

- Cell adhesion analyzed under electron microscope after culturing with osteoblast cell line.

noticed using MTT assay for Ag–HAP coatings containing less than 5 wt% Ag produced by vacuum plasma spraying on titanium [105]. No significant change in cell morphology occurred after culturing with murine fibroblast cell line L929. Similarly, Lu et al. observed no significant change in morphology when culturing osteoblast cells from rats at the surface of electrochemically deposited Ag–HAP coatings on titanium [99]. Pure HAP coating showed the highest ALP activity compared to Ag-containing coatings but the activity of Ag–HAP coatings continued to increase even after 7 days. Feng et al. observed no significant morphological changes of murine macrophages and osteoblast cell line after 48 h exposure of Ag–HAP coating formed by IBAD on Ti–6Al–4V substrate [103].

In contrast, Sing et al. noticed a significantly affected cell viability for $Ca_{10-}xAgx(PO_4)_6(OH)_2$ coatings with $x>0.3$ (3 % Ag) [107]. After 7 days culturing, the MTT assay results were significantly decreased compared to pure HAP, irrespective of their initial cell adhesion. Rameshbabu et al. investigated cell adhesion test using human osteoblast cell line [92]. Osteoblast cell attachment in varying density was noticed on HAP coatings containing 0.5, 1, and 1.5 wt% Ag indicating that all the surfaces support cell growth. However, osteoblast function was significantly greater on coating containing 0.5 wt% Ag with osteoblasts well spread and adhered. At higher Ag contents osteoblasts were attached but could not spread [92]. Chen et al. evaluated cell proliferation by measuring the production of dsDNA on Ag-modified sol–gel coatings on titanium [108]. After 15 days no significant difference compared to pure HAP was observed. However, by the 12th day, a significantly less ALP specific activity was observed in Ag–HAP coating containing 1.5 wt% Ag but not on that containing 1 wt%. Similar results were reported for Ag–HAP sol–gel coatings on porous titanium [102]. After 7 days osteoblast cells from rats showed a good adhering and spreading with abundant cell filopods forming bridges between the pores of the composite coatings. Proliferation and

– Osteoblast activity measured by alkaline phosphatase (ALP) activity. ALP is a hydrolase enzyme responsible for removing phosphate groups from many types of molecules, including nucleotides, proteins, and alkaloids. Also, ALP increases if there is active bone formation occurring, as ALP is a by-product of osteoblast activity.

differentiation activity tests on osteoblast show that Ag–HAP containing 0.8 wt% Ag is optimal composite because at higher Ag contents significantly less osteoblast proliferation rates and ALP activity were obtained. Similar results were obtained by Feng et al. [103]. At concentration of silver ions ≤20 ppm $AgNO_3$ no significant morphological change on Ag–HAP coatings was observed. On the specimens treated with 100 ppm $AgNO_3$ the cells were seriously damaged; they did not have any pseudopodium and lost their round form [103].

The presented results show that there exists a threshold concentration above which the presence of Ag affects the biocompatibility of the coating. Therefore, an optimum Ag concentration should be determined, always combining several methods for biocompatibility determination as the experimental results show that the cytotoxic effects are complex and multifactorial.

Silver Release Rate from Hydroxyapatite

Rate of silver release from the coating should be optimized in a way to assure the antibacterial effect in a prolonged period of time and yet not to cumulatively overcome the threshold for silver toxicity. The results are difficult to compare as a variety of conditions were used differing in medium, time of exposure, Ag content in the coating, etc. The release of silver from HAP coatings has been measured by inductively coupled plasma mass spectroscopy (ICP-MS) [94, 107] or photometrically [96]. The release of silver increased with time but the magnitude of loss depended on the silver content. After 3 days the dissolution of silver in acetate buffer (pH = 4.2) reached up to 0.006 ppm depending on the Ag content, respectively, in the $Ca_{10-x}Ag_x(PO_4)_6(OH)_2$ coating [107]. Yan et al. reported that in phosphate saline buffer the initial Ag release was fast during first 7 days of immersion of coatings formed electrochemically on TiO_2 nanotubes [94]. After that it reached a plateau indicating a long-term sustainable release. The release at the first day was 0.2 ppm, at the 14th day 1.52 ppm [94]. Bai et al. measured photometrically the release of silver from Ag–HAP coatings on titanium immersed in ultra pure water [96]. The release was high in the first 4 h and then

gradually decreased over a period of 7 days. The magnitude of release increased with increasing Ag content (increasing from 0.8 ppm for 1 wt% to 1.7 ppm for 6.5 wt% Ag at the seventh day of immersion). It was reported that the Ag content should be at least 0.1 ppm to assure a bactericidal effect but lower than 1.6 ppm to avoid cytotoxicity of somatic cells [94].

Effect of Hydroxyapatite Containing Silver on Bacteria

The effect on different Ag–HAP coatings on bacteria is summarized in Table 1.3. Although all coatings showed antibacterial effect the experimental conditions are very different and do not allow direct comparison between coatings prepared by different methods (given in Table 1.2). The effect of differently Ag-doped HAP on bacteria is exampled in Fig. 1.19 [106].

1.3.3.4 Hydroxyapatite and Other Inorganic Agents

Zinc oxide (ZnO) also possesses antimicrobial properties. $Zn(NO_3)_2$ was incorporated into HAP structure produced by sol–gel process from $Ca(NO_3)_2$ and triethyl phosphate and tested against *S. mutans* [109]. Zn-doped HAP powders doped at 2000 ppm Zn exhibited inhibition zone, similar to Ag-doped HAP. Nanoparticles of HAP (nHAP) were doped with Zn using wet chemical method and the ion exchange method [110]. The nHAP-Zn was found to be nontoxic to osteoprogenitor cells and at the same time showed antibacterial activity toward Gram-positive and Gram-negative bacterial strains.

Complexes of calcium phosphate and platinum also exhibit antibacterial and antitumor activities [98]. HAP was produced by microarc oxidation at 250–450 V in an electrolytic solution containing β-glycero-phosphate disodium salt, calcium acetate, and hexachloroplatinic acid, H_2PtCl_6. No peaks of Pt were detected in XRD and EDS spectra of HAP coatings indicating low incorporation. As Ag-doped HAP, Pt-doped HAP showed no cytotoxicity at low concentrations. In contrast to Ag, however, Pt-doped HAP

Table 1.3 Results on antibacterial activity on tested bacteria strains on various hydroxyapatite coatings containing silver on titanium obtained by different preparation methods (Table 1.2)

Reference	Bacteria strain	Effect
Dry methods		
Bai et al. [96]	*S. aureus*	Significant reduction in bacteria total colony forming units after incubation at 35–36 °C for 3 h
Chen et al. [104]	*S. aureus*	Significant reduction in bacteria total colony forming units (>3 times reduction) after incubation at 37 °C for 3 h
	S. epidermidis	
Chen et al. [105]	*S. aureus*	Significant reduction in bacteria total colony forming units (antibacterial ratio between 97 and 100 %) after incubation at 37 °C for 24 h at 1×10^6 CFU/mL
	E. coli	
	P. aeruginosa	
Song et al. [98]	*S. aureus*	Antibacterial efficacy >99.8 % after incubation at 35 °C for 24 h at 1.3–1.6×10^5 cells/mL
	E. coli	
Trujilo et al. [106]	*S. epidermidis*	Significantly higher increase in % of dead bacteria for *S. epider.*; lower number for *P. auger.* after incubation at 37 °C for 48 h at 5×10^4 cells/mL
	P. aeruginosa	
Rameshbabu et al. [92]	*E. coli*	Complete inhibition even after 48 h after incubation at 37 °C for 48 h at 1×10^5 cells/mL
	S. aureus	

Wet methods		
Singh et al. [107]	*E. coli*	Significantly smaller mean optical density/cm^2 after incubation at 37 °C for 4 h at 1×10^7 CFU/mL
Lu et al. [99]	*E. coli*	Bactericidal ratio between 97.4 and 100 % for *E. coli* and between 96.4 and 99.6 % for *S. albus* after incubation at 36 °C for 12 h at 1×10^8 CFU/mL
	S. albus	
Yan et al. [94]	*E. coli*	Antibacterial efficacy of 97.5 % after incubation at 37 °C for 24 h at 1×10^5 CFU/mL
Chen et al. [108]	*S. epidermidis*	Significant reduction (>5 times reduction) in bacteria total colony forming units after incubation at 37 °C for 3 h
	S. aureus	
Mo et al. [100]	*E. coli*	Antibacterial efficacy of 98 % for *S. aureus* and >99 % for *E. coli* after incubation at 37 °C for 24 h at 1×10^6 cells/mL
	S. aureus	
Sygnatowicz et al. [101]	*S. aureus*	Similar bacterial colony counts but reduced size after incubation at 35 °C for 24 h
Qu et al. [102]	*E. coli*	Bactericidal ratio of >95 % for *E. coli* and *S. albus* after incubation at 36 °C for 12 h at 1×10^6 cells/mL
	S. albus	
Chung et al. [109]	*S. mutans*	Inhibition zone after incubation at 37 °C for 48 h at 5×10^5 cells/mL

CFU colony forming units

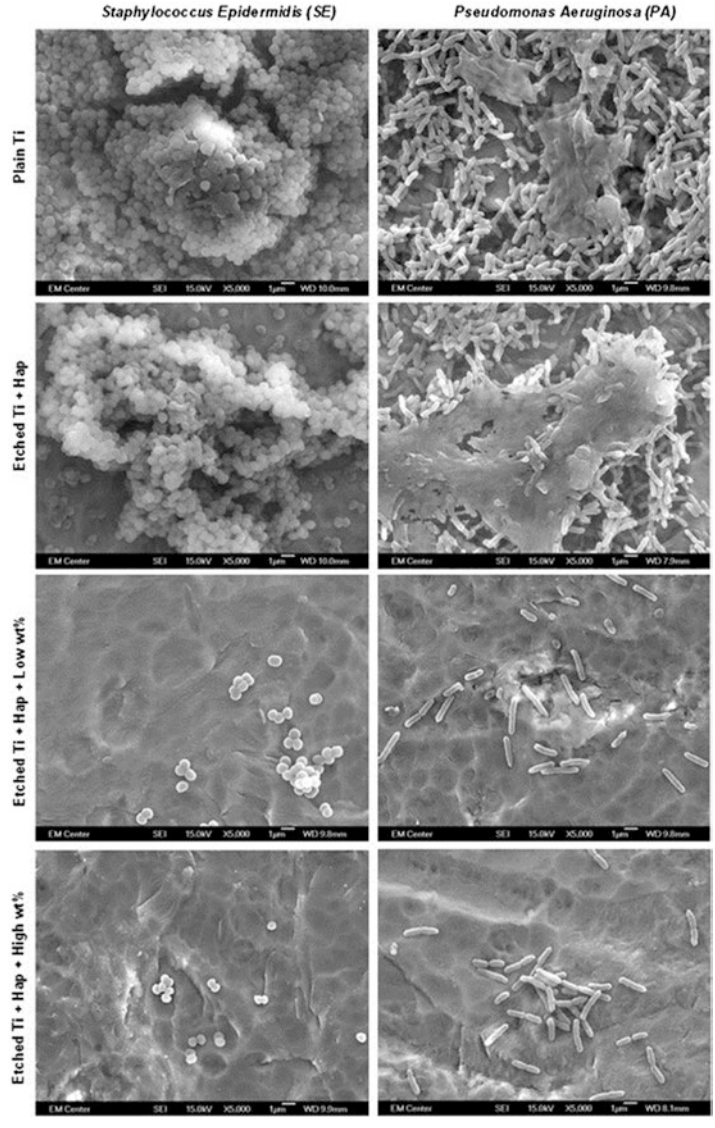

Fig. 1.19 SEM images of *S. epidermidis* (SE) and *P. aeruginos*a (PA) bacteria on plain titanium and hydroxyapatite, etched titanium and hydroxyapatite doped with a low and high weight percentage of silver. (*Reprinted from the publication by Trujillo N A, Oldinski R A, Ma H, Bryers J D, Williams J D, Popat K C (2012) Antibacterial effects of silver-doped hydroxyapatite thin films sputter deposited on titanium. Mater Sci Eng 32:2135–2144, with permission from Elsevier*)

showed antibacterial activity similar to that of TiO_2, and almost five times less effective than that of Ag-doped HAP [98].

1.3.3.5 Titanium Oxide and Silver

General Characteristics of TiO_2 and Its Photocatalytic Effect

Due to photo-induced hydrophilic and photocatalytic activity is TiO_2 widely researched in the field of air and water remediation, self-cleaning and self-sterilizing surfaces and electrolysis of water to generate hydrogen. These reactions are photocatalyzed by the presence of adsorbed radicals on the TiO_2 surface [111, 112]. When TiO_2 is exposed to radiation exceeding its band gap (290–360 nm) electron–hole pairs are formed when an electron is elevated from valence band to the conducting band, leaving behind an electron–hole pair (Fig. 1.20):

$$TiO_2 + h\nu \rightarrow e^-_{CB} + h^+_{VB}$$

$$e^- + O_2 \rightarrow O_2^{\bullet -}$$

$$O_2^{\bullet -} + H^+ \rightarrow HOO\bullet$$

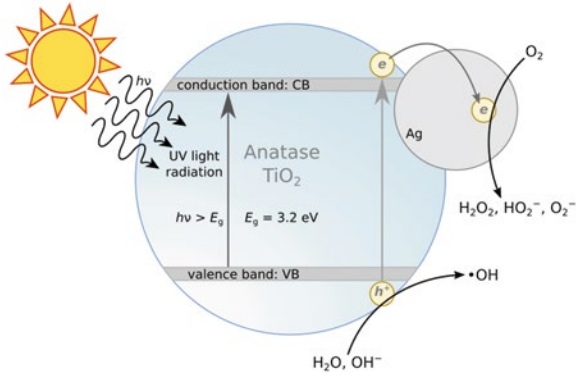

Fig. 1.20 Mechanism of photocatalytic activity of TiO_2 and Ag-doped TiO_2

$$\mathrm{HOO}\bullet + \mathrm{H}^{+} \rightarrow \mathrm{H_2O_2}$$

$$\mathrm{H_2O_2} + e^{-} \rightarrow \left(\bullet\mathrm{OH}\right)_{\mathrm{ad}} + \mathrm{OH}^{-}$$

$$\mathrm{H_2O} + h^{+} \rightarrow \left(\bullet\mathrm{OH}\right)_{\mathrm{ad}} + \mathrm{H}^{+}$$

$$\mathrm{OH}^{-} + h^{+} \rightarrow \left(\bullet\mathrm{OH}\right)_{\mathrm{ad}}$$

where e^{-}_{CB} and h^{+}_{VB} are electron and hole pair. Molecular oxygen can act as electron scavenger leading to the formation of superoxide radicals $\mathrm{O_2}$. The latter attach to intermediate product in the oxidation reaction, forming peroxide or changing to hydrogen peroxide and water. This represents the initiation phase of a free-radical chain promoted by water leading to the formation of hydroxyl radicals (·OH). The latter can be also generated via direct oxidation of water and adsorbed hydroxide ion. Hydroxyl radicals were detected at the surface of $\mathrm{TiO_2}$ irradiated by UV.

The slow recombination of carriers $\mathrm{TiO_2}$ is the basis of its strong photocatalytic activity. One of the notable features of $\mathrm{TiO_2}$ is the strong oxidation power of positive holes. In the presence of water, hydroxyl radicals (·OH) with strong oxidative decomposing power are formed when reacting with organic matter. If oxygen is present, the intermediate radical in the organic compound and oxygen molecules can undergo chain reaction, consume oxygen, and eventually organic matter decompose to $\mathrm{CO_2}$ and water [113]:

$$\left(\bullet\mathrm{OH}\right)_{\mathrm{ad}} + \mathrm{RH} \rightarrow \mathrm{R}\bullet + \mathrm{H_2O}$$

$$\mathrm{R}\bullet + \left(\bullet\mathrm{OH}\right)_{\mathrm{ad}} \rightarrow \left(\mathrm{ROH}\right)_{\mathrm{ad}}$$

$$\left(\mathrm{ROH}\right)_{\mathrm{ad}} + \left(\bullet\mathrm{OH}\right)_{\mathrm{ad}} \rightarrow \mathrm{RO}\bullet + \mathrm{H_2O}$$

This discovery has led to widespread use of $\mathrm{TiO_2}$ as a coating for glass, making this self-cleaning, and of special benefit for side mirrors on automobiles [111]. Namely, water enhances self-cleaning as it penetrates between the organic stain and superhydrophilic $\mathrm{TiO_2}$ surface.

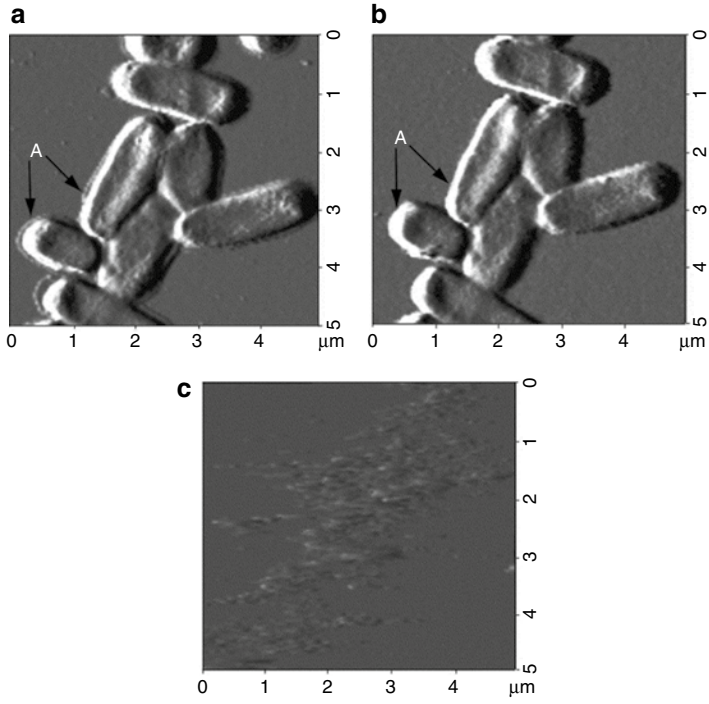

Fig. 1.21 AFM images of *E. coli* on the TiO_2 film: (**a**) no illumination, (**b**) illumination for 1 day, (**c**) illumination for 6 days. Light intensity was 1 mW/cm^2. (*Reprinted from the publication by Sunada K, Watanabe T, Hashimoto K (2003) Studies on photokilling of bacteria on TiO2 thin film. J Photochem Photobiol Chem 156:227–233, with permission from Elsevier*)

Mechanism of Antibacterial Activity of TiO_2

Antibacterial activity of TiO_2 is photoactivated, i.e., it requires UV light for activation [111–116]. Photo-killing of bacteria by photocatalytic action of illuminated TiO_2 proceeds in three stages: disordering of outer membrane of bacteria cell by reactive species (·OH, H_2O_2, O_2), disordering of the inner membrane (cytoplasmic) and killing the cell, and decomposition of the dead cell (Fig. 1.21) [116]. The effect can be enhanced by combination of TiO_2 and silver, another natural antimicrobial agent, or copper. Photoactivated TiO_2 is effective toward other Gram-negative bacteria *S.*

marcescens, etc., and also Gram-positive bacteria like MRSA, *Enterococcus* spp., *Pseudomonas augerinosa*, etc. [115]. The effect is generally smaller in the latter group due to the outer membrane barrier.

Both anatase and rutile express the same chemical formula (TiO_2); their crystal structure differs. Both exhibit tetragonal crystal structure but with different lattice parameters and densities. Both anatase, space group I4/amd, and rutile, space group $P4_2/mnm$, consist of TiO_6 octaedra, sharing four edges in anatase and two in rutile. The band gap value in rutile is 3.0 eV, in anatase 3.2 eV; they both absorb only UV light. However, the rutile type can absorb the rays that are slightly closer to the visible light rays. Despite that, anatase shows greater photocatalytic activity; this is due to the difference in energy structure. In anatase, the conduction band is closer to negative position than in the rutile; therefore, the reducing power is stronger and anatase exhibits overall higher photocatalytic activity than rutile [117].

Mechanism of Antibacterial Activity of TiO_2 Containing Silver

The effect can be enhanced by combination of TiO_2 and silver, zinc oxide, or copper. Higher photoinduced activity may be ascribed to the fact that silver (particles) on TiO_2 surface can facilitate the charge separation by attracting photoelectrons, thus more holes are available for the oxidation of organics (Fig. 1.20) [118]:

$$Ag + e^- \rightarrow Ag^{\bullet -}$$

$$H_2O + h^+ \rightarrow H^+ + \bullet OH$$

$$\bullet OH + MO \rightarrow CO_2 + H_2O$$

where MO is organic matter. Silver may act also as electron–hole recombination center rather than an electron trapper:

$$Ag + e^- \rightarrow Ag^{\bullet -}$$

$$Ag^{\bullet -} + h^{+} \rightarrow Ag$$

By incorporating silver, the intrinsic antibacterial ability can be added to the TiO_2, thus providing an antibacterial effect even without light. The Ag loading has an important effect on photocatalytic activity of TiO_2 [119]. Too much Ag may result in photohole trapping effect and the photocatalytic activity declined, e.g., excess Ag inhibits effective electron–hole separation or blocks the active sites of TiO_2 [120].

It was suggested that Cu^{2+} also enhances production of ROS via a Fenton type reaction [121]:

$$Cu^{2+} + e^{-} \rightarrow Cu^{+}$$

$$H_2O_2 + Cu^{+} \rightarrow HO^{-} + \bullet OH + Cu^{2+}$$

Methods of Preparation of TiO_2 Containing Silver and Related Morphology

TiO_2 can be prepared using a variety of methods which can be basically divided into chemical and physical processes. Chemical processes comprise wet chemical routes like sol–gel and hydrothermal methods, electrochemical processes like anodization and electrophoretic deposition, and chemical vapor deposition [113]. Physical processes include plasma spraying, physical vapor deposition, ion implantation, magnetron sputtering, etc.

The methods used for the preparation of Ag–TiO_2 composites can be divided in the same manner. Among chemical methods mainly Ag–TiO_2 nanocomposites or layer structure of nanoparticles TiO_2 surrounded by Ag nanoparticles was produced. Hydrolysis produced TiO_2 nanorods capped with oleic acid and surrounded by 8–35 nm sized Ag particles [122]. Li et al. produced Ag–TiO_2 composites of nanotubes (diameter 10 nm × several hundreds nm length) and Ag particles adsorbed onto both outer and inner surface of nanotubes. At lower Ag concentration Ag particles less than 5 nm are formed and dispersed on nanotube surface, while at higher concentration diameter increased to 40 nm and major part of particles was covered by Ag [118]. Surface templating method produced homogeneous mesopo-

Table 1.4 Methods used for the preparation of silver–TiO_2 composites/layers using chemical and physical methods

Method/substrate	Shape/structure/morphology	Ag concentration range	Reference
Chemical methods			
Hydrolysis Ti tetraisopropoxide and $AgNO_3$	TiO_2 anatase nanorods stabilized by Ag nanoparticles	10^{-6} to 10^{-3} M	Cozzoli et al. [122]
Layer-by-layer adsorption in PDDA and immersion in $AgNO_3$	Ti phosphate ultrathin film with incorporated Ag NPs	10 mM	Wang et al. [127]
Hydrothermal method and immersion in $AgNO_3$	TiO_2 anatase nanotubes decorated by Ag NPs		Li et al. [118]
Surfactant-templating method and immersion in $AgNO_3$	Mesoporous anatase TiO_2 with Ag in pores	5 mg/mL	Liu et al. [123]
Surfactant-templating method and immersion in $AgNO_3$	Ag–TiO_2 anatase thin film on silicon wafer		Yu et al. [124]
Sol–gel from tetrabutyl titanate, diethanolamine and $AgNO_3$	Ag-modified nanostructured anatase TiO_2 thin films	0.1; 0.3; 0.5; 0.9 %	Zheng et al. [119]
Sol–gel from tetrabutyl orthotitanate, diethanolamine and $AgNO_3$	Ag-containing TiO_2 film on NiTi	9.1 at.%	Fu et al. [129]
Sol–gel from Ti tetraisopropoxide and $AgNO_3$	anatase TiO_2 nanopowder with spherical Ag particles	5 wt%	Amin et al. [125]
Sol–gel from Ti isopropoxide, $CaCl_2$ and $AgNO_3$	Ag-decorated monodispersed TiO_2 aggregates (350 nm diameter)	5, 10, 25, 50 mg	Han et al. [120]

Sol–gel from Ti tetrachloride, HCl, $NH_3 + AgNO_3$	Ag–TiO_2 anatase thin film (1.2 μm) on glass		Zhao et al. [128]
Sol–gel from tetramethoxysilane, $AgNO_3$ and PVPD	Ag NPs loaded into porous hybrid network	10 mM	Guo et al. [126]
Sol–gel from Ti tetrabutoxide and $AgNO_3$	Ag-doped NPs (5–10 nm diameter)	3; 7 %	Gupta et al. [139]
Anodization of Ti in NH_4F and immersion in $AgNO_3$	TiO_2 anatase nanotubes with adhered incorporated Ag NPs	0.5; 1; 1.5; 2 M	Zhao et al. [131]
Anodization of Ti in NH_4F and electron-beam evaporated Ag layer on nanotubes	TiO_2 amorphous nanotubes with adhered incorporated Ag NPs		Lan et al. [130]
Anodization of Ti in HF and immersion in $AgNO_3$	Ag NPs loaded nanoporous TiO_2 on Ti substrates	0.05 M	Kamaraj et al. [132]
Anodization of Ti in HF, *Hydrothermal method* in NaOH and immersion in ZnO NPs	ZnO NPs embedded into TiO_2 nanoleafs and nanotubes	ZnO: 375 μM–1.5 mM	Elizabeth et al. [140]
Anodization of Ti in NH_4F and immersion in $Zn(NO_3)_2$	ZnO NPs embedded into TiO_2 nanotubes	ZnO: 0.005 M–0.075 M	Liu et al. [141]
Anodization of Ti in NH_4F and hydrothermally treated in Zn acetate	ZnO NPs embedded into TiO_2 nanotubes	Zn acetate: 0.1 M for 1–3 h	Huo et al. [142]

(continued)

Table 1.4 (continued)

Method/substrate	Shape/structure/morphology	Ag concentration range	Reference
Physical methods			
CVD from Ti chloride, ethyl acetate, and $AgNO_3$	Multilayer nanostructured composite Ag/TiO_2 or TiO_2/Ag		Brook et al. [133]
CVD from Ti isopropoxide and $AgNO_3$	Nanostructured Ag–TiO_2 and CuO–TiO_2 layers composite Ag/TiO_2 or TiO_2/Ag on glass substrate		Foster et al. [121]
Rf magnetron sputtering from Ag-doped Ti target	800–1000 nm thick layer with nanosized Ag–TiO_2 grains on stainless steel	1–4 wt%	Jamuna-Thevi et al. [143]
Electrophoretic deposition from Ag and TiO_2 particle suspension	Ag nanoparticles grown directly on TiO_2 nanoparticles	2 and 20 wt%	Santillan et al. [134]
Plasma spray from Ag and TiO_2 nanopowders	Ag–TiO_2 layers on titanium	0.8 wt%	Li et al. [135]
Plasma spray from Ag and TiO_2 nanopowders	Ag–TiO_2 layers on stainless steel	1–10000 ppm	Gao et al. [136]
Ion implantation and microarc oxidation (MAO) TiO_2 followed by Ag ion implantation	Ag–TiO_2 layers on titanium alloy	0.5; 0.8; 1; 1.2 and 1.3 wt%	Zhang et al. [137]
Plasma immersion ion implantation and rf magnetron sputtering	Ag–TiN layers	1 at.%	Xu et al. [138]

rous TiO_2 layer 200 nm of thickness with Ag particles sized 30 nm [123], or granular 20 nm TiO_2 layers with well dispersed or aggregated Ag particles depending on their concentration [124]. In the majority of studies sol–gel routes were used producing various shapes and dimensions of TiO_2 structure decorated with Ag particles (Table 1.4): nanostructured thin films consisting of 20–30 nm TiO_2 particles "wrapped" by Ag [119], spherical 12–16 nm sized Ag particles deposited in the TiO_2 matrix (crystallite size between 2 and 20 nm) [120, 125], 50 nm sized Ag particles adhered and "wrapped" in sol matrix [126], or thin TiO_2 films with incorporated Ag particles

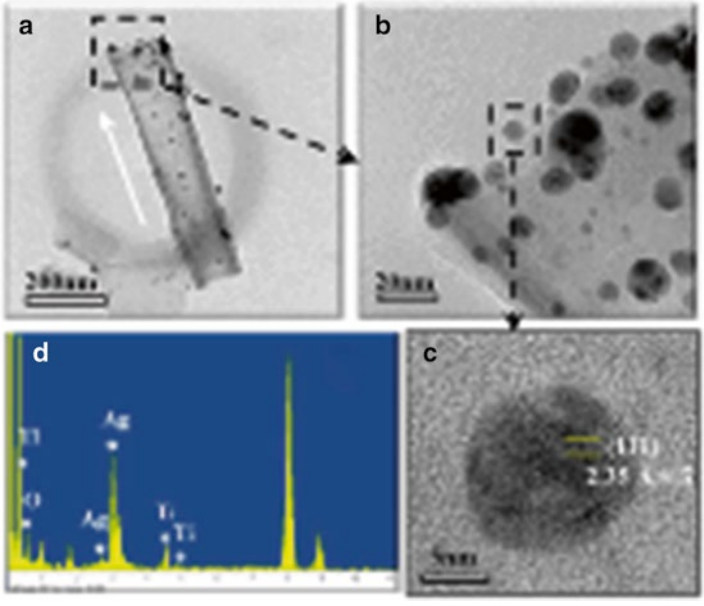

Fig. 1.22 TEM analysis of an Ag-decorated TiO_2 nanotube. (**a**) TEM image taken from an Ag-decorated TiO_2 nanotube with the diameter of 100 nm. (**b**, **c**) High magnification views of the selected regions, and (**d**) the corresponding EDS spectrum. The *white arrow* in (**a**) indicates the growth direction of the TiO_2 nanotube. (*Reprinted from the publication by Lan M Y, Liu C P, Huang H H, Lee S W (2013) Both enhanced biocompatibility and antibacterial activity in Ag-decorated TiO2 nanotubes. PLOS ONE 8:e75364, with permission from PLOS ONE*)

[127], or deposited at the surface [128, 129]. Anodization in fluoride-containing electrolyte at high voltage results in the formation of TiO_2 nanotubes of various diameters: 25–100 nm [130], 30 nm [131], and 65 nm [132]. Following nanotube formation, Ag particles were deposited either by immersion in $AgNO_3$ and UV irradiation [131, 132] or electrodeposition (Fig. 1.22) [130].

Physical methods produced compact, composite, uni-, or multilayers. Flame-assisted chemical vapor deposition can produce layers starting from aqueous solution of inorganic salt with an aerosol to produce NPs. It proceeds at atmospheric pressure. Nanostructured film rather than a continuous layer was produced from titanium precursors and silver salt [121, 133]. Electrophoretic deposition has an advantage of using complex shape components as substrates and creating coating directly from a stable colloidal suspension by application of electric field. Santillán et al. prepared nanocomposites from Ag nanoparticles (4 nm) and TiO_2 (23 nm) in a water–ethanol suspension [134]. Ag particles were deposited by nucleophilic reaction on TiO_2 particles. Plasma spray method produced Ag–TiO_2 layers on titanium substrate containing flat and smooth splats and spheroidal and partially melted fine particles [135]. Ag particles sized 30 nm were distributed homogeneously in the coating. Ag–TiO_2 coatings containing different silver content with particles fully or partially melted within the TiO_2 structure [136]. The combination of various methods was also used, e.g., porously structured TiO_2 was produced by microarc oxidation and followed by Ag implantation [137]. Ag nanoparticles were distributed homogeneously on the surface and inside the pores. Plasma immersion ion implanted silver was deposited onto magnetron sputtered TiN film to produce an outermost layer of TiO_2 and Ag [138].

Microstructure and Composition of TiO_2 Containing Silver

XRD is commonly used to study the microstructure of Ag–TiO_2 layers. In majority of layers prepared by chemical methods which are followed by sintering at high temperatures (Table 1.4), XRD patterns show only anatase peak [119, 120, 123–125, 129]. Crystallite size differed from 10 nm [123] to 28 nm [119]. No Ag XRD peaks

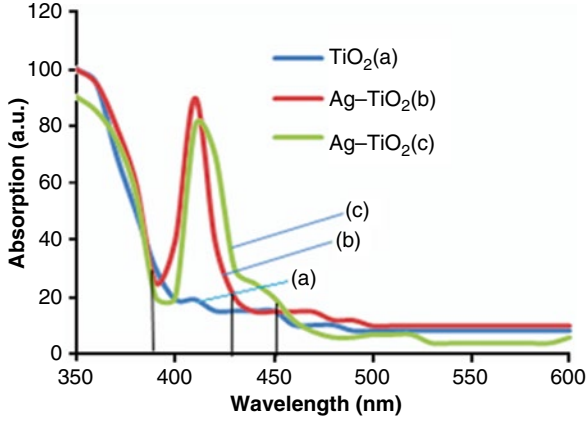

Fig. 1.23 UV–vis absorption spectra of the annealed (**a**) TiO_2 and (**b**) 3 % and (**c**) 7 % Ag-doped TiO_2 nanoparticles. (*Reprinted from the publication by Gupta K, Singh R P, Pandey A, Pandey A (2013) Photocatalytic antibacterial performance of TiO2 and Ag-doped TiO2 against S. aureus, P. aeruginosa and E. coli. Beilstein J Nanotechnol 4:345–351, with permission from Beilstein Journal of Nanotechnology*)

were detected implying that the presence of Ag did not affect the crystallite size. Han et al. reported, however, that the increasing content of Ag induces the decrease in crystallite size from 20 to 10.8 nm [120] although no specific Ag peak was observed. It was noticed that Ag^+ ions cannot be introduced into TiO_2 lattice because of the difference in size, i.e., Ag^+ (126 pm) is much larger than Ti^{4+} (68 pm). Although Ag cannot be detected in Ag–TiO_2 composites/layers by XRD, it can be clearly identified by other methods, i.e., UV–vis and X-ray photoelectron spectroscopy (XPS). Silver increases absorbance in the range between 200 and 800 nm and shift the absorbance of TiO_2 into visible region (Fig. 1.23) [139]. Ag^+ shows the absorption peak at 270 nm which can be used to monitor the adsorption dynamics after reduction [127]. Reduced Ag NPs show peak at 432 nm [127], 490 nm [123], 435 and 450 nm [139], and 350–550 nm [132, 144]. XPS method was also often used to confirm the presence of metallic Ag NPs [123, 124, 127, 129–131, 135] by the appearance of Ag $3d_{5/2}$ peak centered in the range between 386.0 and 368.5 eV. In Ag–TiO_2 layers formed by anodization the peaks related

to Ag were observed in addition to those of anatase TiO_2 indicating the loading in TiO_2 layer [131, 132].

Typical anatase peak was observed in the case of Ag-doped TiO_2 obtained by sol–gel, while in the case of pure annealed TiO_2 both phases, anatase and rutile, were present [139]. Crystal size decreased with Ag doping.

When physical methods were used to prepare the TiO_2 layers the presence of not only anatase but also rutile phase was detected [133, 135, 137], as well as the presence of peak related to silver [133, 135]. The mixture of rutile and anatase was obtained when TiO_2 layer was grown on top of Ag layer formed by chemical vapor deposition when prepared using $TiCl_4$ and ethyl acetate [133]. Gao et al. observed Ag peak only at high Ag loading [136].

Cytotoxicity and Optimum Silver Concentration of TiO_2 Containing Silver

The biological activity of Ag-doped TiO_2 amorphous nanotubes was dependent on tube diameter tested (25, 50, and 100 nm) [130]. The smallest diameter of nanotubes the most promoted adhesion and proliferation of human fibroblasts. This was attributed to the highly irregular topography at the nanoscale. No adverse effect of Ag–TiO_2 produced by rf magnetron sputtering was observed on mouse fibroblasts using MTT assay [143] or MG-63 osteoblasts using Alamar-blue test for Ag–TiO_2 plasma-sprayed layer on titanium [135]. However, for TiO_2 nanotubes with adhered incorporated Ag nanoparticles formed by anodization some cytotoxicity was observed at higher Ag contents [131], as the addition of Ag drastically reduced the ALP activity and intracellular total protein. Further, the level of lactate dehydrogenase (LDH) activity, which is a marker for tissue damage, was increased at the highest Ag content [131].

Silver Release Rate from TiO_2

The release of Ag from Ag–TiO_2 composites or layers was measured in different media, i.e., 0.05 M HNO_3 [123], phosphate saline buffer [130, 131, 143], and deionized water [135, 136] using stripping

voltammetry [123], ICP-MS [130, 131, 143], ICP-optical emission spectroscopy [135], and atomic absorption spectrophotometry [136]. Generally, initial burst of Ag release was observed which then leveled off with time but was still detectable after 30 days. The final values of Ag release at the end of the test largely differed, e.g., 1.6×10^{-8} mol at the 20th day [123], 550 ppb at the 14th day, between 0.1 and 0.2 ppb at the 14th day [131], 0.18 μg/mL cm^2 at the 30th day [135], and between 0.5 and 3.5 μg/L cm^2 at the 30th day [136]. Silver release increased with increasing Ag content [131, 136, 143]. No effect on the TiO_2 nanotube diameter (25 or 100 nm) on silver release was observed [130].

Effect of Bacteria on TiO_2 Containing Silver

The effect on different Ag–TiO_2 coatings on bacteria is summarized in Table 1.5. The antibacterial effect was mainly investigated against *E. coli* [123–125, 127, 133, 135, 136] and *S. aureus* [126, 130, 137, 139], and only rarely against other bacteria strains [132, 136, 139]. The experimental conditions largely differed including type and concentration of bacteria and time of exposure, the most important parameter being UV irradiation. The purpose of UV irradiation is the activation of TiO_2 which shows antibacterial activity only when irradiation by UV light, as explained in section 1.3.3.5.2. The addition of silver shifts the absorption to visible region and therefore should avoid the need for UV activation. Consequently, in some studies the prepared composites/coatings were not UV activated [126–128, 130, 132, 139]; despite that good antibacterial activity was achieved (Table 1.5). For example, nanoporous TiO_2 layer loaded with Ag nanoparticles showed high antimicrobial activity even against Gram-positive bacteria in the visible light [132]. However, UV activation additionally increased the antibacterial effect on Ag-doped TiO_2. Although the mesoporous Ag–TiO_2 composite film exhibited high antibacterial activity even in the dark (9.2% and 55.2% for *E. coli* and *silver-resistant E. coli*, respectively), UV irradiated films show 0% survival for both bacteria strains (Fig. 1.24) [123]. UV lamp of intensity 5 mW/cm^2 LED source for 5 min was used [123]. Similar, Ag–TiO_2 composite films formed by sol–gel synthesis containing the highest Ag content showed the highest antibacterial activity against *E. coli* under UV irradiation (~99%) and in the dark (~82%) [124].

Table 1.5 Results on antibacterial activity on tested bacteria strains on various TiO_2 composites/coatings containing silver obtained by different preparation methods (Table 1.4)

Reference	Bacterial strain	Effect
Chemical methods		
Wang et al. [127]	*E. coli*, 10^4–10^5 CFU/mL, 37 °C, 18 h	Antibacterial rate 99.9 %
Guo et al. [126]	*S. aureus*, 10^8 CFU/mL; 37 °C, 24 h	99.3 % Reduction in bacterial count
Zhao et al. [131]	*S. aureus*,10^5 CFU/mL; 37 °C, 24 h	Antibacterial effectiveness between 30 and 60 % after 4 days
Lan et al. [130]	*S. aureus*, 10^9 CFU/mL; 37 °C, 4 h	Antibacterial effectiveness between 30 and 60 % after 4 days
Kamaraj et al. [132]	*Pseudomonas sp.* and *Bacillus* sp. 10^7–10^8 CFU/mL; 35 °C, 48 h	Total viable count was 1 order of magnitude lower for Ag–TiO_2 than TiO_2
Liu et al. [123]	Normal and Ag-resistant *E. coli*, 10^6 CFU/mL; 37 °C, 20 min	% Survival ratio 0 % for UV irradiated and 9.2 % in dark (Ag-resistant)
Yu et al. [124]	*E. coli*, 10^5–10^6 CFU/mL; UV activation or dark	Between 76.7 and 99.7 % after UV irradiation
Amin et al. [125]	*E. coli*, 10^7–10^9 CFU/mL, 37 °C, 24 h; UV activation	95 % and 45 % inactivation depending on calcination T
Physical methods		
Li et al. [135]	*E. coli*, 10^6 CFU/mL, 37 °C, 24 h	100 % bacteria kill after 24 h; 0 % viability at 7 % Ag at 40 mg/30 mL for *P. aeruginosa*, at and 60 mg/30 mL for *S. aureus* and *E. coli*; at 3 % Ag all bacteria killed at 80 mg/30 mL culture

Gao et al. [136]	*E. coli* and *P. aeruginosa*, 10^8 CFU/mL, 37 °C, 48 h	Bactericidal rate 94.8 % and 95.6 % at 10 ppm, and 10 % at >10 ppm
Zhang et al. [137]	*S. aureus*, 5.6×10^6 CFU/mL, 37 °C, 24 h	Antibacterial rate 100 % at 1.3 wt% Ag
Brook et al. [133]	*E. coli*, 2×10^8 CFU/ml, 37 °C, 24 h; UV activation	100 % bacteria kill after 240 min for TiO_2, after 40 min for Ag and after 60 min for Ag–TiO_2
Foster et al. [121]	*E. coli* and *P. aeruginosa*, 2×10^8 CFU/mL, 37 °C, 48 h	UVA activation; Ag–TiO_2 higher activity in the dark but the Cu–TiO_2 were more active when illuminated with UVA

CFU colony forming units

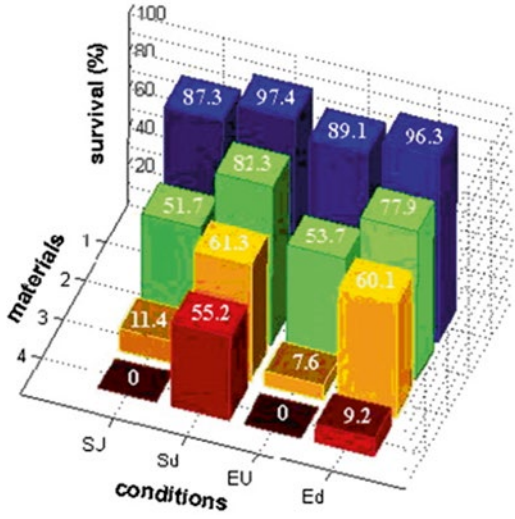

Fig. 1.24 Percentage of survival of *E. coli* (E_U, E_d) and silver-resistant *E. coli* (S_U, S_d) on the glass (1), commercial TiO_2 spin film (2), mesoporous TiO_2 (3), and Ag/TiO_2 composite film (4) under the conditions of dark (E_d, S_d) for 20 min and UV light (E_U, S_U) for 5 min. (*Reprinted from the publication by Liu Y, Wang X, Yang F, Yang X (2008) Excellent antimicrobial properties of mesoporous anatase TiO2 and Ag/TiO2 composite films. Microporous Mesoporous Mater 114:431–439 with permission from Elsevier*)

An UVA 0.6 mW/cm^2 lamp was used emitting in 350–400 nm with a peak at 365 nm. Foster et al. showed that the killing of *E. coli* using Cu–TiO_2 composite was dependent on the UV light intensity, with larger intensity having a stronger effect [121].

In addition to the UV activation, the antibacterial activity was shown to be dependent on the temperature of calcination of Ag–TiO_2 composite obtained by sol–gel method. While in the absence of UV irradiation the bacterial growth was inhibited by 70 % when calcinated at 300 °C, no activation was observed after calcination at 500 °C. Comparable effect under UV irradiation was 95 % and 45 %, respectively. Therefore, Ag–TiO_2 composite calcinated at 300 °C can be used even without UV irradiation (UVC irradiation at 270 nm wavelength was used) [125].

1.3.3.6 Titanium Oxide and Other Inorganic Agents

As for Ag nanoparticles some toxicity was observed (Sect. 1.3.3.1.6.), ZnO may be more preferential candidate. The addition of ZnO NPs can exert much stronger activity through multiple mechanisms such as membrane damage, generation of ROS, and the release of Zn^{2+} [140, 145]. Additionally, Zn^{2+} can enhance bone formation; however, the toxicity may vary so an optimum concentration should be selected. The bacterial adhesion was less on nanoleafs (NLs) than on nanotubes (NTs) [140]. In the presence of ZnO the bacterial adhesion was reduced on NTs, while no significant difference is observed for NLs with and without ZnO NPs. At lower concentration of ZnO (375 μM), NT nanomorphology was far more effective than NL (Fig. 1.25). Furthermore, more mammalian cell adhesion was observed. These results point out the role of nanotopography in controlling cellular fate. In terms of cytotoxicity, it was observed for ZnO > 750 μM with higher percentage of apoptotic or dead human adipose-derived MSC and human osteosarcoma MG63 cell lines [140]. However, preferential ZnO cytotoxicity toward different types of cells was observed (e.g., dermal fibroblast and lymphocytic cells). ZnO acts on bacteria through membrane damage and Zn^{2+} release; the latter was peaked 24 h after immersion but continued up to 7 days [140].

ZnO-decorated TiO_2 nanotubes were explored for dental application where the formation of dental plaque containing *S. mutans* and *P. gingivalis* induce periodontitis and peri-implantitis [141]. ZnO nanoparticles embedded into TiO_2 nanotubes inhibited the expression of *S. mutans* bacterial adhesion genes which are necessary for the adherence of bacteria (Fig. 1.26) [141]. At the same time they did not inhibit mesenchymal stem cell growth up to 7 days. Slow release of Zn^{2+} in PBS increased steadily during the first 9 days; release was dependent on the concentration of ZnO. Huo et al. observed a decrease in Zn^{2+} concentration during 9 days in PBS [142]. Antibacterial activity against *S. aureus* was observed, and at the same time, the ZnO-decorated NTs significantly enhanced osteogenic differentiation due to their optimal nanostructure thus inducing better osseointegration. No cytotoxicity was observed.

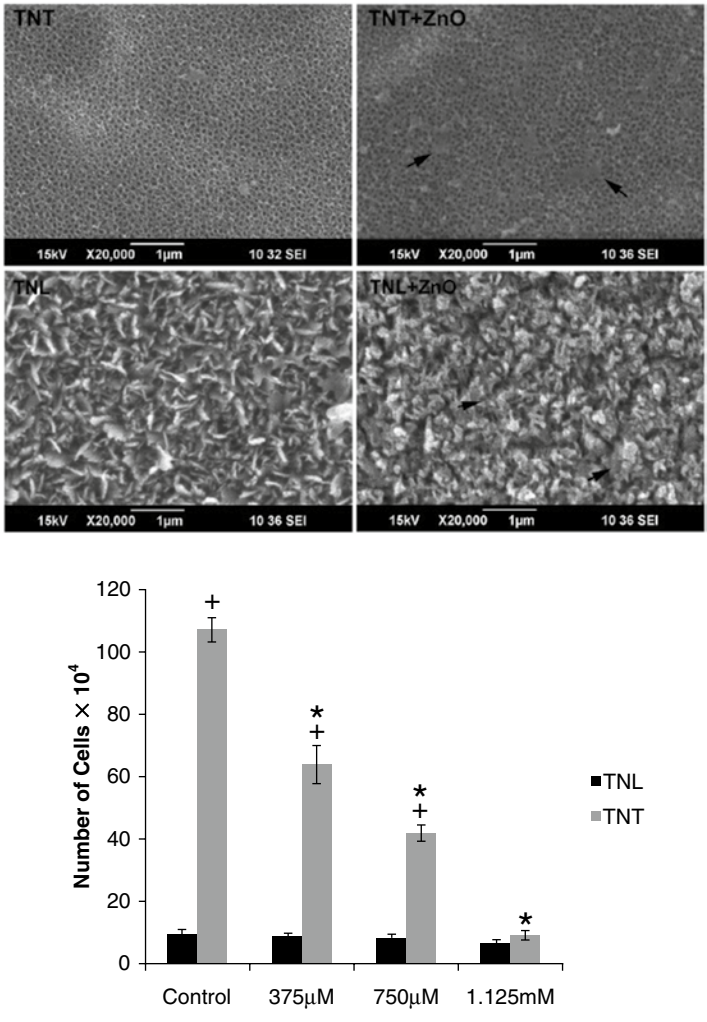

Fig. 1.25 (*Upper panel*) SEM images of titanium nanotubes (TNT) and nanoleafs (TNL) plates with and without ZnO nanoparticles. The inner and outer tube diameter of TNT were 70 ± 5 nm and 100 ± 5 nm, respectively. A homogeneous distribution of ZnO nanoparticles with small aggregation in few areas was observed. (*Lower panel*) The colony count of *S. aureus* adhered onto TNT and TNL Ti plates with and without ZnO—24 h. The colony count was significantly higher on TNT than TNL(+). Additionally, the colony count was significantly higher on TNT Ti slates without ZnO than plates with ZnO. (*Reprinted from the publication by Elizabeth E, Baranwal G, Krishnan A G, Menon D, Nair M* (*2014*) *ZnO nanoparticle incorporated nanostructured metallic titanium for increased mesenchymal stem cell response and antibacterial activity. Nanotechnology 25:115101* (*12 pp*)*, with permission from IOP Science*)

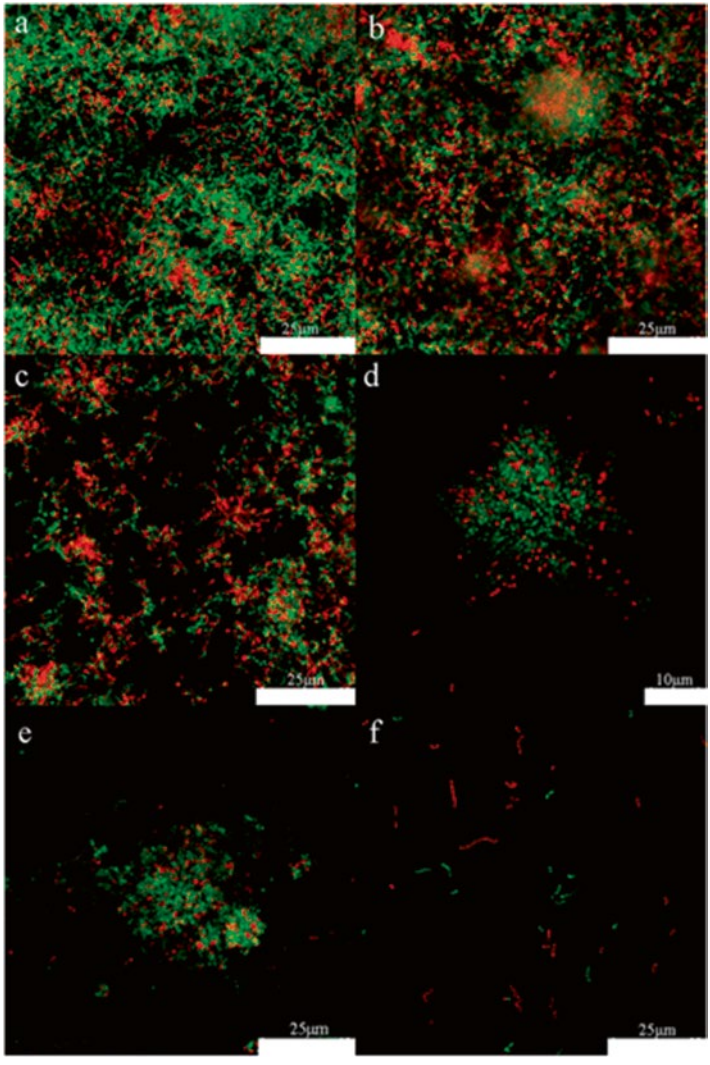

Fig. 1.26 Fluorescence images showing the viability of the *S. mutans* on samples: (**a**) Ti, (**b**) TNT, (**c**) TNT-Zn0.005, (**d**) TNT-Zn0.015, (**e**) TNT-Zn0.030, and (**f**) TNT-Zn0.075. The live bacteria appear *green* while the dead ones appear *orange*. (*Reprinted from the publication by Liu W, Su P, Chen S, Wang N, Ma Y, Liu Y, Wang J, Zhang Z, Li H, Webster T J (2014) Synthesis of TiO2 nanotubes with ZnO nanoparticles to achieve antibacterial properties and stem cell compatibility. Nanoscale 6:9050–9062, with permission from Royal Society of Chemistry*)

1.4 Conclusions

The success of orthopedic reconstruction surgery including prosthetic implants is largely based on the proper selection of materials which have to fulfill many requirements, the most important being biocompatibility, stability, wear and chemical stability, and osseointegration ability. The latter is mainly responsible for the long-term, safe functioning of metal implant. Titanium alloy-based implants are well known for their osseointegration capability based on the formation of bone cells and mineralized bone matrix. Gaining another important ability of the material, i.e., resistance to bacterial adhesion, would enormously contribute to the well-being of numerous patients subjected to implant-related infection. Implant-related infection represents one of the most serious complications of the orthopedic reconstruction surgery. It is in great interest primarily for the patients, but also for medical community and national health fund to keep the infection incidence low. This could be achieved either by improvement of prophylaxis as well as by the use of the materials able to prevent or slow down the development of infection. Keeping in mind the "race for the surface" concept as a race between osteoblast formation and bacteria attachment, new materials should be designed to enable the former process to prevail.

Currently, the coatings based on metal ions (Ag) are used in clinical practice. At the same time there are numerous studies going on in the academic community which are still away from the preclinical or clinical experimental phase. Nevertheless, the potential of these studies is enormous and will eventually have the important impact also on the clinical guidelines. Different strategies were presented herein and each may have potential advantages and drawbacks. The chemical stability of passive coatings may not be acceptable and their long-term efficacy is difficult to achieve [4]. Antimicrobial peptides are relatively chemically complicated to produce; they may exhibit reduced activity in the form of coating compared to soluble form. Further, AMPs exhibit some potential toxicity. Silver as inorganic agent exhibits toxicity at higher doses and this should be taken into account, especially in the form of sublethal doses.

Therefore, other inorganic agents such as zinc oxide have large potential to be used further.

Conditions for antibacterial assay are often nonstandardized and consequently, results are difficult to compare among each other. This is valid also for the release rate. Therefore, the conditions for studying cytotoxicity and release kinetics should be standardized. Further, it should be taken care that the agents used to prevent or combat infection do not interfere with other property of the material, i.e., not only biocompatibility but also osseointegration, hemocompatibility, etc.

Acknowledgments I would like to thank my colleague Prof. Andrej Cör, MD, PhD, of the Valdoltra Orthopaedic Hospital for critical reading of the manuscript and valuable discussions. A special thanks to my coworkers and students at the Jožef Stefan institute: B. Kapun, U. Tiringer, D. Gustinčič, and G. Šekularac for their technical help and support. Financial support by the Slovenian Research Agency is kindly acknowledged (grant No. P2-0393).

References

1. Milošev I (2011) Metallic materials for biomedical applications: laboratory and clinical studies. Pure Appl Chem 83:309–324
2. Namba RS, Inacio MC, Paxton EW (2012) Risk factors associated with surgical site infection in 30,491 primary total hip replacements. J Bone Joint Surg 94:1330–1338
3. Schmidmaier G, Lucke M, Wildemann B, Haas NP, Raschke M (2006) Prophylaxis and treatment of implant-related infections by antibiotics-coated implants: a review. Injury 37:S105–S112
4. Goodman SB, Yao Z, Keeney M, Yang F (2013) The future of biologic coatings for orthopaedic implants. Biomaterials 34:3174–3183
5. Campoccia D, Montanaro L, Arciola CR (2013) A review of the biomaterials technologies for infection-resistant surfaces. Biomaterials 34:8533–8554
6. Knetsch MLW, Koole LH (2011) New strategies in the development of antimicrobial coatings: the example of increasing usage of silver and silver nanoparticles. Polymers 3:340–366
7. Zhao L, Chu PK, Zhang Y, Wu Z (2009) Antibacterial coatings on titanium implants. J Biomed Mater Res 91B:470–480
8. Durmus NG, Webster TJ (2012) Nanostructured titanium: the ideal material for improving orthopedic implant efficacy. Nanomedicine 7:791–793

9. Ercan B, Webster TJ (2010) The effect of biphasic electrical stimulation on osteoblast function at anodized nanotubular titanium surfaces. Biomaterials 31:3684–3693
10. Kulkarni M, Mazare A, Gongadze E, Pertukova Š, Kralj-Iglič V, Milošev I, Schmuki P, Iglič A, Mozetič M (2015) Titanium nanostructures for biomedical applications. Nanotechnology 26:062002 (18p)
11. Gristina AG (1987) Biomaterial-centered infection: microbial adhesion versus tissue integration. Science 237:1588–1595
12. Anselme K, Davidson P, Popa AM, Giazzon M, Liley M, Ploux L (2010) The interaction of cells and bacteria with surfaces structured at the nanometre scale. Acta Biomater 6:3824–3846
13. Wu Y, Zitelli JP, TenHuisen KS, Yu X, Libera MR (2011) Differential response of Staphylococci and osteoblasts to varying titanium surface roughness. Biomaterials 32:951–960
14. Puckett SD, Taylor E, Raimondo T, Webster TJ (2010) The relationship between the nanostructure of titanium surfaces and bacterial attachment. Biomaterials 31:706–713
15. Gallardo-Moreno AM, Pacha-Olivenza MA, Saldana L, Perez-Giraldo C, Bruque JM, Vilaboa N, González-Martín ML (2009) In vitro biocompatibility and bacterial adhesion of physico-chemically modified Ti6Al4V surface by means of UV irradiation. Acta Biomater 5:181–192
16. Grigorescu S, Ungureanu C, Kirchgeorg R, Schmuki P, Demetrescu I (2012) Various sized nanotubes on TiZr for antibacterial surfaces. Appl Surf Sci 270:190–196
17. Mathew D, Bhardwaj G, Wang Q, Sun L, Ercan B, Geetha M, Webster TJ (2014) Decreased *Staphylococcus aureus* and increased osteoblast density on nanostructured electrophoretic-deposited hydroxyapatite on titanium without the use of pharmaceutical. Int J Nanomed 9:1775–1781
18. Neoh KG, Hu X, Zheng D, Kang ET (2012) Balancing osteoblast functions and bacterial adhesion on functionalized titanium surfaces. Biomaterials 33:2813–2822
19. Gowri S, Gandhi R Rajiv, Snethil S, Sundrarajan M (2015) Effect of calcination temperature of *Nyctanthes* plant mediated zirconia nanoparticles; optical and antibacterial activity for optimized zirconia. J Bionanosci 9:181–189
20. Verissimo NC, Gailich BM, Oliveira HG, Caram R, Webster TJ (2015) Reducing *Staphylococcus aureus* growth on Ti alloy nanostructured surfaces through the addition of Sn. J Biomed Mater Res A 103A:3757–3763
21. Guo L, Yuan W, Lu Z, Li CM (2013) Polymer/nanosilver composite coatings for antibacterial applications. Colloid Surf A 439:69–83
22. Leckband D, Sheth S, Halperin A (1999) Grafted poly (ethylene oxide) brushes as nonfouling surface coatings. J Biomater Sci 10:1125–1147
23. Wittschier N, Lengsfeld C, Vorthems S, Stratmann U, Ernst JF, Verspohl EJ, Hensel A (2007) Large molecules as anti-adhesive compounds against pathogens. J Pharm Pharmacol 59:777–786

24. Wang J, Wang Z, Guo S, Zhang J, Song Y, Dong X, Wang, Jihong Yu X (2011) Antibacterial and anti-adhesive zeolite coatings on titanium alloy surface. Microporous Mesoporous Mater 146:216–222
25. Ungureanu C, Pirvu C, Mindroiu M, Demetrescu I (2012) Antibacterial polymeric coating based on polypyrrole and polyethylene glycol on a new alloy TiAlZr. Prog Org Coat 75:349–355
26. Dumitriu C, Popescu M, Ungureanu C, Pirvu C (2015) Antibacterial efficiencies of TiO_2 nanostructured layers prepared in organic viscous electrolytes. Appl Surf Sci 341:157–165
27. Harris LG, Tosatti S, Wieland M, Textor M, Richards RG (2004) *Staphylococcus aureus* adhesion to titanium oxide surfaces coated with non-functionalized and peptide-functionalized poly(l-lysine)-grafted-poly(ethylene glycol) copolymers. Biomaterials 25:4135–4148
28. Maddikeri RR, Tosatti S, Schuler M, Chessari S, Textor M, Richards RG, Harris LG (2008) Reduced medical infection related bacterial strains adhesion on bioactive RGD modified titanium surfaces: A first step toward cell selective surfaces. J Biomed Mater Res 84A:425–435
29. Chen J, Cao J, Wang J, Maitz FM, Guo L, Zhao Y, Li Q, Xiong K, Huang N (2012) Biofunctionalization of titanium with PEG and anti-CD34 for hemocompatibility and stimulated endothelialization. J Colloid Interface Sci 368:636–647
30. Zhang F, Zhang Z, Zhu X, Kang E-T, Neoh K-G (2008) Silk-functionalized titanium surfaces for enhancing osteoblast functions and reducing bacterial adhesion. Biomaterials 29:47515–47519
31. Kugel A, Stafslien S, Chisholm BJ (2011) Antimicrobial coatings produced by "tethering" biocides to the coating matrix: A comprehensive review. Prog Org Coat 72:222–252
32. Costa F, Carvalho IF, Montelaro RC, Gomes P, Martins ACL (2011) Covalent immobilization of antimicrobial peptides (AMPs) onto biomaterials surfaces. Acta Biomater 7:1431–1440
33. Bahar AA, Ren D (2013) Antimicrobial peptides. Pharmaceuticals 6:1543–1575
34. Hilpert K, Elliot M, Jenssen H, Kindrachuk J, Fjell CD, Körner J, Winkler DFH, Weaver LL, Henklein P, Ulrich AS, Chiang SHY, Farmer SW, Pante N, Volkmer R, Hancock REW (2009) Screening and characterization of surface-tethered cationic peptides for antimicrobial activity. Chem Biol 16:58–69
35. Brogden KA (2005) Antimicrobial peptides: pore formers or metabolic inhibitors in bacteria? Nat Rev Microbiol 3:238–250
36. Fjell CD, Jenssen H, Hilper K, Cheung WA, Panté N, Hancock REW, Cherkasov A (2009) Identification of novel antimicrobial peptides by chemoinformatics and machine learning. J Med Chem 52:2006–2015
37. Gao G, Lange D, Hilpert K, Kindrachuk J, Zou Y, Cheng JTJ, Kazemzadeh-Narbat M, Yu K, Wang R, Straus SK, Brooks DE, Chew BH, Hancock REW, Kizhakkedathu JN (2011) The biocompatibility and biofilm resis-

tance of implant coatings based on hydrophilic polymer brushes conjugated with antimicrobial peptides. Biomaterials 32:3899–3909
38. Lin W, Junjian C, Chengzhi C, Lin S, Sa L, Li R, Yingjun W (2015) Multi-biofunctionalization of a titanium surface with a mixture of peptides to achieve excellent antimicrobial activity and biocompatibility. J Mater Chem B 3:30–33
39. Corrales Ureña YR, Wittig L, Vieira Nascimento M, Luiz Faccioni J, Filho PNL, Rischka K (2015) Influences of the pH on the adsorption properties of an antimicrobial peptide on titanium surfaces. Appl Adhes Sci 3:7
40. Kazemzadeh-Narbat M, Kindrachuk Juan K, Jenssen H, Hancock REW, Wang R (2010) Antimicrobial peptides on calcium phosphate-coated titanium for the prevention of implant-associated infections. Biomaterials 21:9519–9526
41. Kazemzadeh-Narbat M, Lai BFL, Ding C, Kizhakkedathu JN, Jancock REW, Wang R (2013) Multilayered coating on titanium for controlled release of antimicrobial peptides for the prevention of implant-associated infections. Biomaterials 34:5969–5977
42. Rabea EI, Badawy ME, Stevens CV, Smagghe G, Steurbaut W (2003) Chitosan as antimicrobial agent: applications and mode of action. Biomacromolecules 4:1457–1465
43. Raafat D, Sahl HG (2009) Chitosan and its antimicrobial potential—a critical literature survey. Microb Biotechnol 2:186–201
44. Goy RC, de Britto D, Assis OBG (2009) A review of the antimicrobial activity of chitosan. Polímeros 19:241–247
45. Kong M, Chen XG, Xing K, Park HJ (2010) Antimicrobial properties of chitosan and mode of action: A state of the art review. Int J Food Microbiol 144:51–63
46. Muzzarelli RAA, Muzzarelli C (2005) Chitosan chemistry: relevance to the biomedical sciences. Adv Polym Sci 186:151–209
47. Day AJ, Sheehan JK (2001) Hyaluronan: polysaccharide chaos to protein organisation. Curr Opin Chem Biol 11:617–622
48. Barbucci R, Lamponi S, Borzacchiello A, Ambrosio L, Fini M, Torricelli P, Giardino R (2002) Hyaluronic acid hydrogel in the treatment of osteoarthritis. Biomaterials 23:4503–4513
49. Gribbon P, Heng BC, Hardingham TE (2000) The analysis of intermolecular interactions in concentrated hyaluronan solutions suggest no evidence for chain-chain association. Biochem J 350:329–335
50. Carlson GA, Dragoo JL, Samimi B, Bruckner DA, Bernard GW, Hedrick M, Benhaim P (2004) Bacteriostatic properties of biomatrices against common orthopaedic pathogens. Biochem Biophys Res Commun 321:472–478
51. Ardizzoni A, Neglia RG, Baschieri MC, Cermelli C, Caratozzolo M, Righi E, Palmieri B, Blasi E (2011) Influence of hyaluronic acid on bacterial and fungal species, including clinically relevant opportunistic pathogens. J Mater Sci Mater Med 22:2329–2338

52. Harris LG, Richards RG (2004) *Staphylococcus aureus* adhesion to different treated titanium surfaces. J Mater Sci Mater Med 15:311–314
53. Croll TI, O'Connor AJ, Stevens GW, Cooper-White JJ (2006) A blank slate? Layer-by-layer deposition of hyaluronic acid and chitosan onto various surfaces. Biomacromolecules 7:1610–1622
54. Chua PH, Neoh KG, Shi Z, Kang ET (2008) Structural stability and bioapplicability assessment of hyaluronic acid–chitosan polyelectrolyte multilayers on titanium substrates. J Biomed Mater Res 87A:1061–1074
55. Cassinelli C, Morra M, Pavesio A, Renier D (2000) Evaluation of interfacial properties of hylarunonan coated poly(methylmethacrylate) intraocular lenses. J Biomater Sci Polym Ed 11:961–977
56. Chua P-H, Neoh K-G, Kang E-T, Wang W (2007) Surface functionalization of titanium with hyaluronic acid/chitosan polyelectrolyte multilayers and RGD for promoting osteoblast functions and inhibiting bacterial adhesion. Biomaterials 29:1412–1421
57. Chudobova D, Nejdl L, Gumulec J, Krystofova O, Rodrigo MAM, Kynicky J, Ruttkay-Nedecky B, Kopel P, Babula P, Adam V, Kizek R (2013) Complexes of silver(I) ions and silver phosphate nanoparticles with hyaluronic acid and/or chitosan as promising antimicrobial agents for vascular grafts. Int J Mol Sci 14:13592–13614
58. Lv H, Chen Z, Yang X, Cen L, Zhang X, Gao P (2014) Layer-by-layer self-assembly of minocycline-loaded chitosan/alginate multilayer on titanium substrates to inhibit biofilm formation. J Dent 42:1464–1472
59. Mishra SK, Ferreira JMF, Kannan S (2015) Mechanically stable antimicrobial chitosan–PVA–silver nanocomposite coatings deposited on titanium implants. Carbohydr Polym 121:37–48
60. Torabi S, Mahdavian AR, Sanei M, Abdollahi A (2016) Chitosan and functionalized acrylic nanoparticles as the precursor of new generation of bio-based antibacterial films. Mater Sci Eng C 59:1–9
61. Cui X, Li CM, Bao H, Zheng X, Lu Z (2008) In situ fabrication of silver nanoarrays in hyaluronan/PDDA layer-by-layer assembled structure. J Colloid Interface Sci 327:459–465
62. Abdel-Mohsen AM, Hrdina R, Burgert L, Krylova G, Abdel-Rahman RM, Krejcova A, Steinhart M, Benes L (2012) Green synthesis of hyaluronan fibers with silver nanoparticles. Carbohydr Polym 89:411–422
63. Kemp MM, Kumar A, Clement D, Ajayan P, Mousa S, Linhardt RJ (2009) Hyaluronan- and heparin-reduced silver nanoparticles with antimicrobial properties. Nanomedicine 4:421–429
64. Pal S, Tak YK, Song JM (2007) Does the antibacterial activity of silver nanoparticles depend on the shape of the nanoparticle? A study of the Gram-negative bacterium *Escherichia coli*. App Environ Microbiol 73:1712–1720

65. Morones JR, Elechiguerra JL, Camacho A, Holt K, Kouri JB, Ramírez JT, Yacaman MJ (2005) The bactericidal effect of silver nanoparticles. Nanotechnology 16:2346–2353
66. Feng QL, Wu J, Chen GQ, Cui FZ, Kim TN, Kim JO (2000) A mechanistic study of the antibacterial effect of silver ions on *Escherichia coli* and *Staphylococcus aureus*. J Biomed Mater Res 52:662–668
67. Rai M, Yadav A, Gade A (2009) Silver nanoparticles as a new generation of antimicrobials. Biotechnol Adv 27:76–83
68. Park H-J, Kim Y, Kim J, Lee J-H, Hahn J-A, Guc MB, Yoona J (2009) Silver-ion-mediated reactive oxygen species generation affecting bactericidal activity. Water Res 43:1027–1032
69. Hwang ET, Lee JH, Chae YJ, Kim YS, Kim BC, Sang B-I, Gu MB (2008) Analysis of the toxic mode of action of silver nanoparticles using stress-specific bioluminescent bacteria. Small 4:746–750
70. Sondi I, Salopek-Sondi B (2003) Silver nanoparticles as antimicrobial agent: a case study on *E. coli* as a model for Gram-negative bacteria. J Colloid Interface Sci 275:177–182
71. Choi O, Deng KK, Kim N-J, Ross L Jr, Surampalli RY, Hu Z (2008) The inhibitory effects of silver nanoparticles, silver ions, and silver chloride colloids on microbial growth. Water Res 42:3066–3074
72. Morones-Ramirez RJ, Winkler JA, Spina CS, Collins JJ (2013) Silver enhances antibiotic activity against Gram-negative bacteria. Sci Transl Med 5:190 (11p)
73. Raimondi F, Scherer GG, Kötz R, Wokaun A (2005) Nanoparticles in energy technology: examples from electrochemistry and catalysis. Angew Chem Int Ed 44:2190–2209
74. Solomon SD, Bahadory M, Jeyarajasingam AV, Rutkowsky SA, Boritz C (2007) Synthesis and study of silver nanoparticles. J Chem Educ 84:322–325
75. Shameli K, Ahmad MB, Jazayeri SD, Shabanzadeh P, Sangpour P, Jahangirian H, Gharayebi Y (2012) Investigation of antibacterial properties silver nanoparticles prepared via green method. Chem Cent J 6:73 (10p)
76. Kim JS, Kuk E, Yu KN et al (2007) Antimicrobial effects of silver nanoparticles. Nanomedicine 3:95–101
77. Guin D, Manorama SV, Latha JNL, Singh S (2007) Photoreduction of silver on bare and colloidal TiO2 nanoparticles/nanotubes: synthesis, characterization, and tested for antibacterial outcome. J Phys Chem 111:13393–13397
78. Aguilar-Méndez MA, Martín-Martínez ES, Ortega-Arroyo L, Cobián-Portillo G, Sánchez-Espíndola E (2011) Synthesis and characterization of silver nanoparticles: effect on phytopathogen *Colletotrichum gloesporioides*. J Nanopart Res 13:2525–2532
79. Zeng J, Zheng Y, Rycenga M, Tao J, Li Z-Y, Zhang Q, Zhu Y, Xia Y (2010) Controlling the shapes of silver nanocrystals with different capping agents. J Am Chem Soc 132:8552–8553

80. George S, Lin S, Ji Z, Thomas CR, Li L, Mecklenburg M, Meng H, Wang X, Zhang H, Xia T, Hohman JN, Lin S, Zink JI, Weiss PS, Nel AE (2012) Surface defects on plate-shaped silver nanoparticles contribute to its hazard potential in a fish gill cell line and zebrafish embryos. ACS Nano 6:3745–3759
81. Sharma VK, Yngard RA, Lin Y (2009) Silver nanoparticles: green synthesis and their antimicrobial activities. Adv Colloid Interface Sci 145:83–96
82. Li W-R, Xie X-B, Shi Q-S, Duan S-S, Ouyang Y-S, Chen Y-B (2011) Antibacterial effect of silver nanoparticles on Staphylococcus aureus. Biometals 24:135–141
83. Li Y, Leung P, Yao L, Song QW, Newton E (2005) Antimicrobial effect of surgical masks coated with nanoparticles. J Hosp Infect 62:58–63
84. Hadrup N, Lam HR (2014) Oral toxicity of silver ions, silver nanoparticles and colloidal silver—a review. Regul Toxicol Pharmacol 68:1–7
85. Wang Z, Xia T, Liu S (2015) Mechanisms of nanosilver-induced toxicological effects: more attention should be paid to its sublethal effects. Nanoscale 7:7470–7481
86. Schierholz JM, Lucas LJ, Rump A, Pulverer G (1998) Efficacy of silver-coated medical devices. J Hosp Infect 40:257–262
87. Gosheger G, Herdes J, Ahrens H, Streitburger A, Buerger H, Erren M, Gunsel A, Kemper FH, Winkelmann W, von Eiff C (2004) Silver-coated megaendoprostheses in a rabbit model—an analysis of the infection rate and toxicological side effects. Biomaterials 25:5547–5556
88. Ewald A, Glückermann SK, Thull R, Gbureck U (2006) Antibacterial titanium/silver PVD coatings on titanium. Biomed Eng Online 5:22 (10p)
89. Hauschild G, Hardes J, Gosheger G, Stoeppeler S, Ahrens H, Blaske F, Wehe C, Karst U, Höll S (2015) Evaluation of osseous integration of PVD-silver-coated hip prostheses in a canine model. Biomed Res Int 2015:292406 (10p)
90. Niinomi M (2003) Recent research and development in titanium alloys for biomedical applications and healthcare goods. Sci Technol Adv Mater 4:445–454
91. Šupová M (2015) Substituted hydroxyapatites for biomedical applications: A review. Ceram Int 41:9203–9231
92. Rameshbabu N, Sampath Kumar TSS, Prabhakar TG, Sastry VS, Murty KVGK, Rao KP (2007) Antibacterial nanosized silver substituted hydroxyapatite: Synthesis and characterization. J Biomed Mater Res A 80A:581–591
93. Arumugam SK, Sastry TP, Sreedhar B, Mandal AB (2006) One step synthesis of silver nanorods by autoreduction of aqueous silver ions with hydroxyapatite: an inorganic–inorganic hybrid nanocomposite. J Biomed Mater Res A 80:391–398
94. Yan Y, Zhang X, Huang Y, Ding Q, Pang X (2014) Antibacterial and bioactivity of silver substituted hydroxyapatite/TiO_2 nanotube composite coatings on titanium. Appl Surf Sci 314:348–357

95. Pang X, Zhitomirsky I (2008) Electrodeposition of hydroxyapatite–silver–chitosan nanocomposite coatings. Surf Coat Technol 202:3815–3821
96. Bai X, Sandukas S, Appleford M, Ong LJ, Rabiei A (2011) Antibacterial effect and cytotoxicity of Ag-doped functionally graded hydroxyapatite coatings. J Biomed Mater Res B Appl Biomater 100B:553–561
97. Grubova YI, Surmeneva MA, Ivanova AA, Kravchuk K, Prymak O, Epple M, Buck V, Surmenev RA (2015) The effect of patterned titanium substrates on the properties of silver-doped hydroxyapatite coatings. Surf Coat Technol 276:595–601
98. Song WH, Ryu HS, Hong SH (2008) Antibacterial properties of Ag (or Pt)-containing calcium phosphate coatings formed by micro-arc oxidation. J Biomed Mater Res A 88A:246–254
99. Lu X, Zhang B, Wang Y, Zhou X, Weng J, Qu S, Feng B, Watari F, Ding Y, Leng Y (2011) Nano-Ag-loaded hydroxyapatite coatings on titanium surfaces by electrochemical deposition. J R Soc Interface 8:529–539
100. Mo A, Liao J, Xu W, Xian S, Li Y, Bai S (2008) Preparation and antibacterial effect of silver–hydroxyapatite/titania nanocomposite thin film on titanium. Appl Surf Sci 255:435–438
101. Sygnatowicz M, Keyshar K, Tiwari A (2010) Antimicrobial properties of silver-doped hydroxyapatite nano-powders and thin films. Biol Biomed Mater 62:65–70
102. Qu J, Lu X, Li D, Ding Y, Leng Y, Weng J, Qu S, Feng B, Watari F (2011) Silver/hydroxyapatite composite coatings on porous titanium surfaces by sol-gel method. J Biomed Mater Res Part B Appl Biomater 97B:40–48
103. Feng QL, Cui FZ, Kim TN, Kim JW (1999) Ag-substituted hydroxyapatite coatings with both antimicrobial effects and biocompatibility. J Mater Sci Lett 18:559–561
104. Chen W, Liu Y, Courtney HS, Bettenga M, Agrawal CM, Bumgardner JD, Ong JL (2006) In vitro anti-bacterial and biological properties of magnetron co-sputtered silver-containing hydroxyapatite coating. Biomaterials 27:5512–5517
105. Chen Y, Zheng X, Xie Y, Ding C, Ruan H, Fan C (2008) Anti-bacterial and cytotoxic properties of plasma sprayed silver-containing HA coatings. J Mater Sci Mater Med 19:3603–3609
106. Trujillo NA, Oldinski RA, Ma H, Bryers JD, Williams JD, Popat KC (2012) Antibacterial effects of silver-doped hydroxyapatite thin films sputter deposited on titanium. Mater Sci Eng 32:2135–2144
107. Singh B, Kumar Dubey A, Kumar S, Saha N, Basu B, Gupta R (2011) In vitro biocompatibility and antimicrobial activity of wet chemically prepared Ca_{10}–x$Ag_x(PO_4)_6(OH)_2 (0.0 \le x \le 0.5)$ hydroxyapatites. Mater Sci Eng 31C:1320–1329
108. Chen W, Oh S, Ong AP, Oh N, Liu Y, Courtney HS, Appleford M, Ong JL (2007) Antibacterial and osteogenic properties of silver-containing hydroxyapatite coatings produced using a sol gel process. J Biomed Mater Res 82A:899–906

109. Chung R-J, Hsieh M-F, Huang K-C, Perng L-H, Chou F-I, Chin T-S (2005) Anti-microbial hydroxyapatite particles synthesized by a sol–gel route. J Sol-Gel Sci Technol 33:229–239
110. Swetha M, Sahithi K, Moorthi A, Saranya N, Saravanan S, Ramasamy K, Srinivasan N, Selvamurugan N (2012) Synthesis, characterization, and antimicrobial activity of nano-hydroxyapatite-zinc for bone tissue engineering applications. J Nanosci Nanotechnol 12:167–172
111. Fujishima A, Zhang X, Tryk DA (2008) TiO_2 photocatalysis and related surface phenomena. Surf Sci Rep 63:515–582
112. Hanaor DAH, Sorrell CC (2011) Review of the anatase to rutile phase transformation. J Mater Sci 46:855–874
113. Visai L, Nardo LD, Punta C, Melone L, Cigada A, Imbriani M, Arciola CR (2011) Titanium oxide antibacterial surfaces in biomedical devices. Int J Artif Organs 34:929–946
114. Bonetta S, Bonetta S, Motta F, Strini A, Carraro E (2013) Photocatalytic bacterial inactivation by TiO_2-coated surfaces. AMB Express 3:1–8
115. Nakano R, Hara M, Ishiguro H, Yao Y, Ochiai T, Nakata K, Murakami T, Kajioka J, Sunada K, Hashimoto K, Fujishima A, Kubota Y (2013) Broad spectrum microbicidal activity of photocatalysis by TiO_2. Catalysts 3:310–323
116. Sunada K, Watanabe T, Hashimoto K (2003) Studies on photokilling of bacteria on TiO_2 thin film. J Photochem Photobiol Chem 156:227–233
117. Jin C, Tang Y, Yang FG, Li XL, Xu S, Fan XY, Huang YY, Yang YJ (2011) Cellular toxicity of TiO_2 nanoparticles in anatase and rutile crystal phase. Biol Trace Elem Res 141:3–15
118. Li H, Duan X, Liu G, Liu X (2008) Photochemical synthesis and characterization of Ag/TiO_2 nanotube composites. J Mater Sci 43:1669–1676
119. Zheng J, Yu H, Li X, Zhang S (2008) Enhanced photocatalytic activity of TiO_2 nano-structured thin film with a silver hierarchical configuration. Appl Surf Sci 254:1630–1635
120. Han C, Likodimos V, Khan JA, Nadagouda MN, Andersen J, Falaras P, Rosales-Lombardi P, Dionysiou DD (2014) UV–visible light-activated Ag-decorated, monodisperse TiO_2 aggregates for treatment of the pharmaceutical oxytetracycline. Environ Sci Pollut Res 21:11781–11793
121. Foster HA, Sheel DW, Sheel P, Evans P, Varghese S, Rutschke N, Yates HM (2010) Antimicrobial activity of titania/silver and titania/copper films prepared by CVD. J Photochem Photobiol Chem 216:283–289
122. Cozzoli PD, Comparelli R, Fanizza E, Curri ML, Agostiano A, Laub D (2004) Photocatalytic synthesis of silver nanoparticles stabilized by TiO2 nanorods: a semiconductor/metal nanocomposite in homogeneous nonpolar solution. J Am Chem Soc 126:3868–3879
123. Liu Y, Wang X, Yang F, Yang X (2008) Excellent antimicrobial properties of mesoporous anatase TiO_2 and Ag/TiO_2 composite films. Microporous Mesoporous Mater 114:431–439

124. Yu B, Leung KM, Guo Q, Lau WM, Yang J (2011) Synthesis of Ag–TiO_2 composite nano thin film for antimicrobial application. Nanotechnology 22:1–9
125. Amin SA, Pazouki M, Hosseinnia A (2009) Synthesis of TiO_2–Ag nanocomposite with sol–gel method and investigation of its antibacterial activity against E. coli. Powder Technol 196:241–245
126. Guo L, Feng W, Liu X et al (2015) Sol–gel synthesis of antibacterial hybrid coatings on titanium. Mater Lett 160:448–451
127. Wang Q, Yu H, Zhong L, Liu J, Sun J, Shen J (2006) Incorporation of silver ions into ultrathin titanium phosphate films: in situ reduction to prepare silver nanoparticles and their antibacterial activity. Chem Mater 18:1988–1994
128. Zhao B, Chen YW (2011) Ag/TiO_2 sol prepared by a sol–gel method and its photocatalytic activity. J Phys Chem Solids 72:1312–1318
129. Fu T, Shen Y, Alajmi Z, Wang Y, Yang S, Li G (2014) Sol–gel derived Ag-containing TiO_2 films on surface roughened biomedical NiTi alloy. Ceram Int 40:12423–12429
130. Lan MY, Liu CP, Huang HH, Lee SW (2013) Both enhanced biocompatibility and antibacterial activity in Ag-decorated TiO_2 nanotubes. PLoS ONE 8, e75364 (8p)
131. Zhao L, Wang H, Huo K, Cui L, Zhang W, Ni H, Zhang Y, Wu Z, Chuet PK (2011) Antibacterial nano-structured titania coating incorporated with silver nanoparticles. Biomaterials 32:5706–5716
132. Kamaraj K, George RP, Anandkumar B, Parvathavarthini N, Kamachi U, Mudali K (2015) A silver nanoparticle loaded TiO_2 nanoporous layer for visible light induced antimicrobial applications. Bioelectrochemistry 106(pt B):290–297
133. Brook LA, Evans P, Foster HA, Pemble ME, Steele A, Sheel DW, Yates HM (2007) Highly bioactive silver and silver/titania composite films grown by chemical vapour deposition. J Photochem Photobiol Chem 187:53–63
134. Santillán MJ, Quaranta NE, Boccaccini AR (2010) Titania and titania–silver nanocomposite coatings grown by electrophoretic deposition from aqueous suspensions. Surf Coat Technol 205:2562–2571
135. Li B, Liu X, Meng F, Chang J, Ding C (2009) Preparation and antibacterial properties of plasma sprayed nano-titania/silver coatings. Mater Chem Phys 118:99–104
136. Gao J, Zhao C, Zhou J, Li C, Shao Y, Shi C, Zhu Y (2015) Plasma sprayed rutile titania-nanosilver antibacterial coatings. Appl Surf Sci 355:593–601
137. Zhang P, Zhang Z, Li W (2013) Antibacterial TiO_2 coating incorporating silver nanoparticles by microarc oxidation and ion implantation. J Nanomater 2013:1–8
138. Xu R, Yang X, Jiang J, Li P, Zhang X, Wu G, Chu PK (2015) Effects of silver plasma immersion ion implantation on the surface characteristics

and cytocompatibility of titanium nitride films. Surf Coat Technol 279:166–170
139. Gupta K, Singh RP, Pandey A, Pandey A (2013) Photocatalytic antibacterial performance of TiO_2 and Ag-doped TiO_2 against *S. aureus*, *P. aeruginosa* and *E. coli*. Beilstein J Nanotechnol 4:345–351
140. Elizabeth E, Baranwal G, Krishnan AG, Menon D, Nair M (2014) ZnO nanoparticle incorporated nanostructured metallic titanium for increased mesenchymal stem cell response and antibacterial activity. Nanotechnology 25:115101 (12p)
141. Liu W, Su P, Chen S, Wang N, Ma Y, Liu Y, Wang J, Zhang Z, Li H, Webster TJ (2014) Synthesis of TiO_2 nanotubes with ZnO nanoparticles to achieve antibacterial properties and stem cell compatibility. Nanoscale 6:9050–9062
142. Huo K, Zhang X, Wang H, Zhao L, Liu X, Chu PK (2013) Osteogenic activity and antibacterial effects on titanium surfaces modified with Zn-incorporated nanotube arrays. Biomaterials 34:3467–3478
143. Jamuna-Thevi K, Bakar SA, Ibrahim S, Shahab N, Toff MRM (2011) Quantification of silver ion release, in vitro cytotoxicity and antibacterial properties of nanostuctured Ag doped TiO_2 coatings on stainless steel deposited by RF magnetron sputtering. Vacuum 86:235–241
144. Khan MM, Ansari SA, Lee J, Cho MH (2013) Novel Ag@TiO_2 nanocomposite synthesized by electrochemically active biofilm for nonenzymatic hydrogen peroxide sensor. Mater Sci Eng C 33:4692–4699
145. Colon G, Ward BC, Webster TJ (2006) Increased osteoblast and decreased Staphylococcus epidermidis functions on nanophase ZnO and TiO_2. J Biomed Mater Res A 78:595–604

Chapter 2
Contribution to the Recent Advances in Electrochemical Analysis of Pharmaceuticals

Milka L. Avramov Ivić, Slobodan D. Petrović, and Dušan Ž. Mijin

2.1 Introduction

Electrochemistry is rapidly growing area with a number of possible applications in the pharmaceutical analysis. Modern electrochemical methods are selective, sensitive, rapid, and provide easy techniques applicable to analyses in the pharmaceutical field. It is evident that the electroanalytical techniques at varying levels of sensitivity are required to solve analytical–pharmaceutical problems. The advantages of electrochemical methods are the simple procedures of the sample preparation and in most cases lack of interferences from excipients in the pharmaceutical dosage forms.

M.L.A. Ivić (✉)
ICTM-Institute of Electrochemistry, University of Belgrade, Njegoševa 12, P.O. Box 473, 11000 Belgrade, Serbia
e-mail: milka@tmf.bg.ac.rs

S.D. Petrović • D.Ž. Mijin
Faculty of Technology and Metallurgy, University of Belgrade, Karnegijeva 4, P.O. Box 3503, 11001 Belgrade, Serbia
e-mail: sloba@tmf.bg.ac.rs; kavur@tmf.bg.ac.rs

S. Djokić (ed.), *Biomedical and Pharmaceutical Applications of Electrochemistry*, Modern Aspects of Electrochemistry 60,
DOI 10.1007/978-3-319-31849-3_2

The electroanalysis of pharmaceutically active compounds is actively involved in new research areas of different techniques due to the progress in electronics and computer sciences [1]. Many new electroanalytical techniques that have been successfully applied for trace measurements of important pharmaceutically active compounds due to the high sensitivity and selectivity that they provide.

This review concerns on recent advances in the application of various modern electrochemical techniques to the analysis of pharmaceuticals and biological samples. It is known that different highly sensitive electrochemical techniques are well established in the analysis of selected drugs. The application and choice of the most preferred electrochemical techniques applied to the analysis is closely related on physicochemical properties of the organic functional groups that comprise any given drug structure, especially on redox properties of the pharmaceuticals and biomolecules in real samples.

Cyclic voltammetry (CV) is often the first experiment performed in an electrochemical study of pharmaceutical compound. It is effectively used in the fields of organic chemistry, biochemistry, and environmental electrochemistry. The effectiveness of CV is in capability for rapidly observing the redox behavior over a wide potential range and for the initial information about electrode/pharmaceutical compound interface. CV has become a popular tool for more than 40 years for studying electrochemical reaction. CV is the most versatile electroanalytical technique in pharmaceutical analysis [2].

A pulse technique was proposed by Barker and Gardner in order to increase the sensitivity of the technique and to lower the detection limits for electroactive species. Differential pulse voltammetry (DPV) is very useful for the determination of trace amounts of electroactive compound in pharmaceuticals and biological fluids. There are numerous studies related to the electrochemical aspects of antimicrobial drugs. Generally, these are focused on the electroanalytical determination of antimicrobial drugs of importance in medicine [2]. The used electroanalytical methods were rapid, requiring less than 5 min to perform. It showed the possibility of monitoring this drug compound, making

the method useful for pharmacokinetic and pharmacodynamic purposes. It requires no complex pretreatment of the active principle to be determined. Easy applicability and availability of low-cost instruments are the important advantages of DPV. DPV/DPP (Differential Pulse Polarography) is often the method of choice for therapeutic dose analysis because of the low limit of detection of approximately 10^{-8} M. Square wave voltammetry (SWV) is a large amplitude differential technique in which a waveform is composed of symmetrical square waves. Excellent sensitivity in SWV is gained from the fact that net current is large compared to either forward or backward current, coupled with effective discrimination against the charging current. The peak currents obtained are about four times higher than the differential pulse response. The major advantage of SWV is its speed. The effective scan rate is of the order of 500 mVs^{-1}. As a result, the analysis time is drastically reduced. A complete voltammogram can be recorded within a few seconds, compared to 2–3 min in differential pulse voltammetry. So, the entire voltammogram can be recorded with a single mercury drop. In addition, SWV is also more sensitive than DPV, because both forward and reverse currents are measured in the former, but only the forward currents are measured in the latter. Frequencies of 1–100 square-wave cycles per second permit the use of extremely fast potential scan rates. The analysis time is reduced; a complete voltammogram can be recorded within a few seconds, compared to about 3 min time required for DPV [2].

Electroanalytical techniques, especially modern stripping voltammetry, have been used for the sensitive determination of a wide range of pharmaceuticals. Such techniques enjoy the advantages that there is no need for derivatization and that these methods are less sensitive to matrix effects than other analytical techniques.

It is well known that anodic stripping voltammetry (ASV) is the most widely used form of stripping analysis. In this case, the metals are preconcentrated by electrodeposition onto a small-volume mercury electrode (thin mercury film or a hanging mercury drop).

Cathodic stripping voltammetry (CSV) is the “mirror image” of ASV. It involves anodic deposition of the analyte followed by stripping in a negative potential scan (cathodic scan). The method is generally applied to organic compounds and anions that are

capable of forming insoluble salts with mercury. During the stripping step, as the potential attains a value equal to the reduction potential of the analyte, it is stripped out in the form of anion. The resulting reduction peak current provides the desired quantitative information. Other electrodes, like rotating silver disk electrodes, can be used for halides. The method has a large number of applications in the field of organic and medicinal chemistry [2].

Higher sensitivity and selectivity compared to other voltammetric techniques are the important features of Adsorptive stripping voltammetry (AdSV). The main advantages of the stripping voltammetric method are its speed and simplicity. Each voltammetric run takes a few seconds. It involves no clean-up procedures, and simple dilution of the biological fluid with suitable solvent nearly eliminates most of the published chromatographic and spectroscopic methods requiring lengthy and tedious extraction procedures, such as liquid–liquid and solid-phase extraction. The sensitivity is significantly enhanced by adsorption of the drug on the electrode surface and after careful choice of the operating parameters extremely low detection limits can be reached. Compared with other techniques the DPAdSV and SWAdSV methods are cheap and the measurements are not time consuming, leading to results for analytical purposes of certain drugs in pharmaceutical formulation and biological fluids [2].

Modern electrochemical instrumentation, especially voltammetric techniques, provides reliable and reproducible data for the quantification of analyte. Further, use of modified electrodes proved to have excellent electroanalytical properties, such as wide potential windows, low background current, and good biocompatibility.

The new electrode materials were characterized by broader potential window, higher signal-to-noise ratio, mechanical stability enabling their application in flowing systems, and resistance toward passivation. The last requirement is especially important because electrode fouling is probably the biggest obstacle to more frequent applications of electroanalytical methods in environmental analysis. Last but not least the scientific word search for nontoxic electrode material friendly toward the environment and thus compatible with the concept of so-called green analytical chemistry.

It is obvious that mercury is the best electrode material for voltammetric determinations based on cathodic reduction [3]. However, because of fears of mercury toxicity (although unsubstantiated according to our opinion), there is a tendency to substitute mercury with other nontoxic materials. For that reason, new types of metal solid amalgam electrodes (MeSAE) and dental amalgam electrodes were introduced.

Carbon paste electrodes (CPE) and their utilization in analytical electrochemistry of pharmaceuticals are documented in [2] and [4]. Their use is driven by low cost of the measurements, wide working potential window in both positive and negative direction, ease of working surface renewal, low background currents, and reasonable repeatability.

Nearly all sp^2 carbon electrodes are susceptible to strong adsorption of polar species mainly due to the presence of polar functionalities on the surface. Over the past 15 years, advanced sp^3 carbon materials, conductive diamond thin films, have been prepared and studied thoroughly [4]. During this time, it has become apparent that these films are in many ways ideal as electrode materials for electrochemistry and thus can be used for high-sensitivity analytical measurements of a wide variety of organic and inorganic species.

Solid composite electrodes belong to the group of composite electrodes with randomly distributed two or more compounds, which exhibit after their mixing solid consistency. They are composed of at least one conductor phase and at least one insulator phase, particles of which are mutually mixed.

Portability and nontoxicity of Me-SAE make them useful substitute of mercury electrodes for on spot electroanalytical monitoring of electrochemically reducible substances and their mechanical properties make them compatible with measurements in flowing systems. SCE can be useful because of low cost, easy fabrication, and easy electrochemical pretreatment. Further attention must be paid to electrode pretreatment and to other means minimizing the electrode passivation complicating practical environmental applications of electroanalytical methods [4].

In recent years, various chemically modified electrodes were used in electroanalysis of drugs. Electrode surfaces are modified

by coating them with different types of polymers mainly conducting polymer, ion exchange, and redox polymers. Often chemical groups are attached to these coatings in order to introduce particular electrochemical effects.

They are based on an ion selective membrane that separates the sample from the inner electrolyte. The nature of the membrane determines the selectivity of the electrode. A membrane is considered to be any material that separates two solutions.

In recent years, nanomaterials have become extremely popular theme in electrochemical sensing research due to their electrical conductivity, unique structural and catalytic properties, high loading of biocatalysts, good stability, and excellent penetrability. Carbon nanotubes (CNTs) are used as electrode materials with useful properties for various potential applications.

The electrocatalytic properties of the oxides of noble metals in the electrooxidation of numerous organic molecules are well known. For example, oxidation of malic acid on a gold electrode proceeds only in the region where the electrode is covered by gold oxide. On a glassy carbon electrode modified by silver, reactivation of the formaldehyde anodic oxidation is observed in the region where the electrode is covered by silver oxide. On the bulk silver electrode and on the glassy carbon electrode modified by silver, alcohols such as methanol, ethylene glycol, and glycerol are oxidized only in the region where the electrodes are covered by silver oxide [5]. The electrochemical behavior of biological compounds such as glucose, hormones, and therapeutic drugs is frequently investigated on noble metal electrodes (Au, Pt, Ag).

2.2 Recent Trends in Development of Electrochemical Methods for Analysis of Pharmaceutical

In the following, the application of various electrochemical methods for analyzing of pharmaceuticals will be discussed in more details. For this review (chapter), the pharmaceuticals are grouped to their pharmacological activity, in several groups: antibiotics,

cardiovascular, central nervous system, anticancer, anti-inflammatory, and miscellaneous. The papers are presented, as much as possible, in their chronological order of their publication.

2.2.1 Antibiotics

The outstanding application of antibiotics in the human and veterinary medicine, for successful treatment of different diseases, and in the other fields, has made them one of the most important products of pharmaceutical industry from 1942 to these days. Antibiotics are among the most frequently prescribed medications today, although is evident the growth of microbial resistance. This fact is a serious medical problem and affects on successful control of diseases caused by resistant strains of bacteria. In this part, the several important groups of antibiotics are presented (cephalosporins, macrolides, tetracyclines, quinolones, etc.) with great spectrum of activity.

Azithromycin is a 15-cyclic lactone antibiotic (Fig. 2.1) and a semisynthetic erythromycin derivative. It exhibits some advantages over erythromycin, including better oral bioavailability, higher tissue concentrations, and fewer side effects. Azithromycin is active against some gram-positive and gram-negative microorganisms and functions by binding to the 50S subunit of the bacterial ribosome.

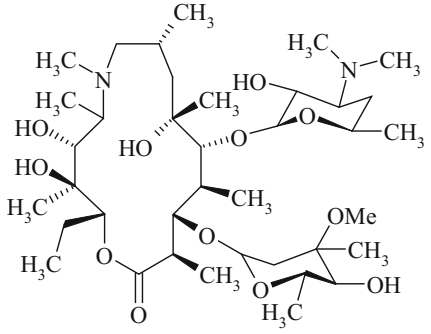

Fig. 2.1 Chemical structure of azithromycin

Azithromycin has been used to treat respiratory infections, skin and soft tissue infections, and some sexually transmitted diseases.

The oxidative properties and the assay of azithromycin and Hemomycin® at a gold electrode using cyclic linear sweep voltammetry were examined [6]. An aqueous solution of $NaHCO_3$ was used in one set of experiments, and methanol–aqueous $NaHCO_3$ mixture was used in the second one. Azithromycin (pure and as a content of capsules, Hemomycin®) was examined in both sets of experiments.

It is obvious from the cyclic voltammograms of pure azithromycin and of Hemomycin® in 0.05 M $NaHCO_3$ (Fig. 2.2) that the potential was cycled between −1.2 and 1.0 V vs. SCE in order to obtain the electrochemical reaction of antibiotic. In the first stage, after the addition of the antibiotic into the electrolyte, the potential was cycled between −0.6 and 1.0 V, but this was not sufficient for the electrochemical activation of azithromycin in 0.05 M $NaHCO_3$.

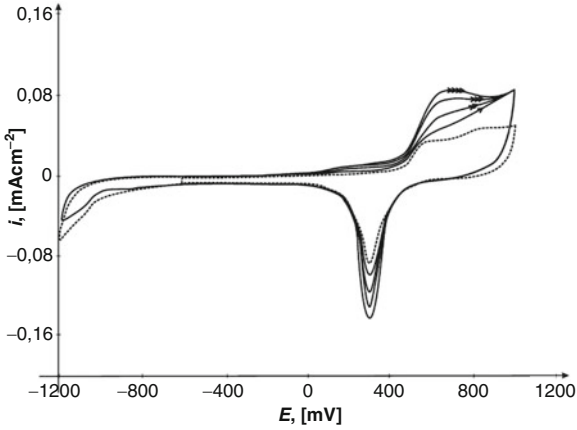

Fig. 2.2 Cyclic voltammogram of an Au electrode in 0.05 M $NaHCO_3$ (*dashed line*) and after the addition of 0.235, 0.353, 0.471, and 0.588 mg cm^{-3} pure azithromycin dihydrate (*full line*), the lowest concentration is indicated by *one arrow*, and the highest one with *four arrows*, sweep rate: 50 mVs^{-1}. Only the first sweep was recorded (Reproduced with a permission from Elsevier) [6]

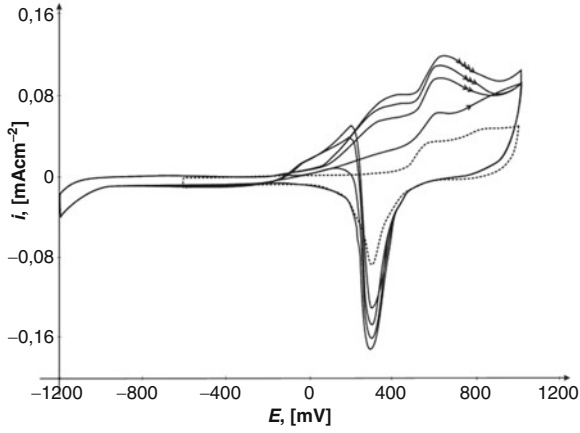

Fig. 2.3 Cyclic voltammogram of Au electrode in 0.05 M $NaHCO_3$ (*dashed line*) and after the addition of Hemomycin® from capsule of 0.235, 0.353, 0.471, and 0.588 mg cm^{-3} (*full line*), the lowest concentration is indicated by *one arrow*, and the highest one with *four arrows*, sweep rate: 50 mVs^{-1}. Only the first sweep was recorded (Reproduced with a permission from Elsevier) [6]

By extending the negative limit of the potential to −1.2 V vs. SCE, in the first (reverse) anodic sweep, the azithromycin was oxidized (both pure and Hemomycin®) and the observed anodic peak of the first cycle was described earlier for azithromycin dihydrate. On reaching the potential of −1.2 V vs. SCE, hydrogen evolution at the gold electrode occurred. The cyclic voltammograms of the pure gold electrode in the supporting electrolyte (Figs. 2.2 and 2.3) show that the hydrogen evolution was suppressed by azithromycin and Hemomycin® adsorption. Only the beginning of the electroactivity of azithromycin and Hemomycin® was affected by hydrogen evolution at a sweep rate of 50 mVs^{-1}. As will be presented later, the electrooxidation of azithromycin and Hemomycin® coincides with AuO formation but for this effect to occur, it seems that it is necessary to commence with azithromycin and Hemomycin® adsorption caused by hydrogen evolution. The suppressed hydrogen evolution resulting from the presence of both kinds of antibiotic in electrolyte supports this assumption. The purging of H_2 into the electrolyte had no effect. The experiment with $NaHCO_3$/

Na_2CO_3 buffer (pH 8) shows the activation of azithromycin did not occur on reaching a value of −1.2 V vs. SCE, because the buffer inhibited the production of electroactive hydrogen species. Measurements show that the pH value of the electrolyte (0.05 M $NaHCO_3$) was 8.48 at the beginning of all experiments but after 2 h it had increased to 8.72. It is interesting that the electrochemical oxidation of azithromycin and Hemomycin® was promoted by the electrochemical production of H species and that the anodic peak (in both cases) was quite stable during 2 h of cycling without a decrease in the peak current. It is quite possible that the solubility of azithromycin dihydrate and Hemomycin® in 0.05 M $NaHCO_3$ was improved by the evolution of hydrogen, which was probably the main cause for the initialization of azithromycin electrooxidation. A couple of patent applications concerning the improvement of the solubility of the azithromycin by ionization of the pure molecule in order to facilitate the application of this antibiotic in ophthalmology can be found in the literature [7, 8].

The assumption for the electrochemically improved solubility of azithromycin in 0.05 M $NaHCO_3$ is supported by the fact that the same reaction in an electrolyte containing methanol proceeded in the range of potentials from −0.6 to 1.0 V vs. SCE and did not require a potential of −1.2 V. This will be discussed later with the analysis of the role of CH_3OH:0.05 M $NaHCO_3$ electrolyte in the electrooxidation of azithromycin and Hemomycin®.

The quantitative electrochemical determination of azithromycin from capsules was successfully applied for the assay of the drug in the tested dosages with, as in the case of azithromycin dihydrate, the possibility for the development of the method for any dosage which may be needed to be detected, including biological samples.

Another set of experiments was performed with an electrolyte containing methanol in order to investigate the influence of methanol on oxidation of azithromycin dihydrate and Hemomycin® in 0.05 M $NaHCO_3$ at a gold electrode and to analyze possible differences in the electrochemical reactivity of the antibiotic in the two different electrolytes. The anodic oxidation of azithromycin dihydrate in the concentration range of 0.235–0.588 mg cm^{-3} is presented in Fig. 2.4. The consequences for the anodic oxidation of

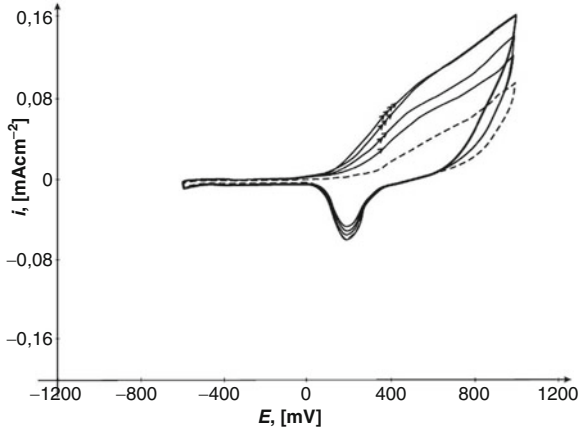

Fig. 2.4 Cyclic voltammogram of an Au electrode in 0.05 M $NaHCO_3$ (*dashed line*) and methanol in the ratio 50 %:50 % after the addition of 0.235, 0.353, 0.471, and 0.588 mg cm^{-3} of pure azithromycin dihydrate (*full line*), lowest concentration is indicated by *one arrow*, and the highest one by *four arrows*, sweep rate: 50 mVs^{-1}. Only the first sweep was recorded (Reproduced with a permission from Elsevier) [6]

azithromycin dihydrate in the presence of methanol are seen in the deformed anodic oxidation peak for each concentration, compared to the very well shaped peak in the absence of methanol, which appear at the same values of the potential for the same range of concentrations (Fig. 2.4).

This work showed that gold electrode can be successfully employed for the qualitative and quantitative electrochemical determination of azithromycin dihydrate and azithromycin from capsule (Hemomycin®) via its oxidation in the tested dosages. Also, there is a possibility for the application of this method for any dosage which is required to be analyzed, including biological samples.

Erythromycin is a natural compound metabolized by a strain of *Streptomyces erythreus*. It has proved invaluable for the treatment of bacterial infections in patients with β-lactam hypersensitivity. If the 6-hydroxy group is methylated, *clarithromycin* is obtained, which has an improved pharmacokinetic profile

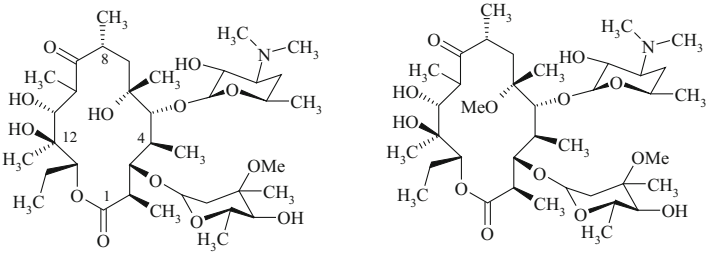

Fig. 2.5 Chemical structures of erythromycin (*left*) and clarithromycin (*right*)

compared to the parent molecule (Fig. 2.5). Azithromycin and clarithromycin present several clinical advantages over erythromycin, including enhanced spectrum activity, higher tissue concentrations, and improved tolerability. Clarithromycin is widely used for the eradication of *Helicobacter pylori* that causes gastritis and gastric ulcers.

The qualitative determination of the pure clarithromycin using its reactivity at a gold electrode in neutral electrolyte by cyclic linear sweep voltammetry was performed [9].

As in a case of azithromycin, for clarithromycin, our choice was 0.05 M $NaHCO_3$ as the supporting electrolyte. The solubility of clarithromycin in water is very poor, and it is slightly soluble in methanol. The methanol is avoided as the solvent (in a mixture with water) because of its activity on the oxides of gold and silver electrodes in different electrolytes.

In the first stage, after addition of the antibiotic into the electrolyte, the potential was cycled between −0.6 and 1.0 V. The electrochemical activation of clarithromycin is not observed as was the case with azithromycin. It was necessary to reach the negative potential value of −1.2 V vs. SCE with the hydrogen evolution occurrence at the gold electrode. The electrochemical activation of clarithromycin and the hydrogen evolution suppression is obvious from Fig. 2.6 and the same effects were already observed with azithromycin [6]. In Fig. 2.6 is also presented that starting from −1.2 V vs. SCE in anodic direction, the cyclic voltammogram first shows one small, wide, and reproducible anodic peak with a current maximum at −0.58 V vs. SCE. The two reproducible anodic

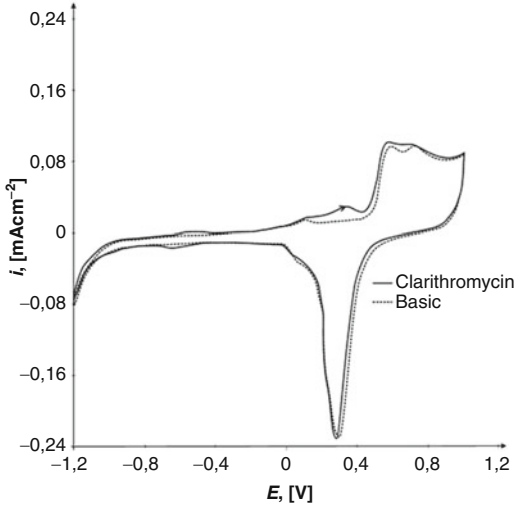

Fig. 2.6 Cyclic voltammogram of the Au electrode in 0.05 M $NaHCO_3$ (*dashed line*) and with the addition of 0.4 mg cm^{-3} of pure clarithromycin, third sweep (*full line*), sweep rate: 50 mVs^{-1} (Reproduced with a permission from Elsevier) [9]

peaks were also observed at +0.10 V vs. SCE and at +0.33 V vs. SCE. In the region of AuO formation, a minor increase of the oxide peaks of the gold electrode was observed. The reproducible cathodic peak is present in the reverse direction with a current maximum at –0.61 V vs. SCE.

It is shown for clarithromycin that observed peaks are not proportional to the concentration of antibiotic in the range of 0.235–0.588 mg cm^{-3}. In this range of concentrations, the four reproducible anodic and one cathodic peaks always qualitatively determine clarithromycin. In order to investigate the structural changes in clarithromycin molecule, electrochemical studies combined with the analysis of the bulk electrolyte after the electrochemical reactions by FTIR spectroscopy and HPLC were performed.

FTIR spectrum of pure clarithromycin and clarithromycin mixed with carbonates, both before the electrochemical experiment, served as reference for the further analysis. The observed changes in the molecule of clarithromycin were tracked with these data.

The potential was held at selected values corresponded to all observed current peaks for 4 h. The first sweep after holding the potential was recorded by cyclic voltammetry and two samples of the electrolyte were analyzed by FTIR and HPLC. The potential was held for 4 h at −0.58 V, at +0.10 V, at +0.33 V, and at −0.61 V vs. SCE.

The significant changes in clarithromycin molecular structure were observed when potential was held for 4 h at −0.61 V, at the cathodic peak, observed in Fig. 2.6. The first sweep after 4 h of holding the potential is presented in Fig. 2.7a and shows that, in addition to the current increase previously described in Fig. 2.6 (around 0.70 V vs. SCE) the anodic current rises by the end of the anodic scan.

A current increase at the potentials corresponding to OH^- adsorption/desorption was observed, not only during the first sweep, but also in the three subsequent sweeps at least. The FTIR spectrum reveals two obvious changes after potential holding (Fig. 2.7b): the disappearance of the 1730 cm^{-1} peak corresponding to the carbonyl group vibration of the lactone, and an intense reduction of the 1170 cm^{-1} peak, probably corresponding to the C–O vibration in the lactone, which implies changes in the ester bond of the lactone. The disappearance of the carbonyl band at 1690 cm^{-1} indicates a change in this group also. No absorptions were recorded in the 1000–1100 cm^{-1} range, which could be the result of changes in the ether and acetal bonds.

The FTIR analysis did not reveal clear changes in the molecule after 4 h of holding the potential at +0.10 V vs. SCE and at +0.33 V vs. SCE, except a minor reduction of the bands in the 1000–1100 cm^{-1} region.

HPLC analysis of the bulk electrolyte showed a significant decrease in the concentration of clarithromycin after the potential was held at selected values for 4 h. The qualitative determination of commercial clarithromycin (provided by Hemofarm and tested in tablets) at gold electrode, followed by FTIR analysis, is already successfully performed.

The reactivity of *erythromycin* [10] (pure) was investigated on a gold electrode in neutral electrolyte by cyclic voltammetry. The resulting structural changes were observed with HPLC and FTIR spectroscopy by analyzing the bulk electrolyte after the

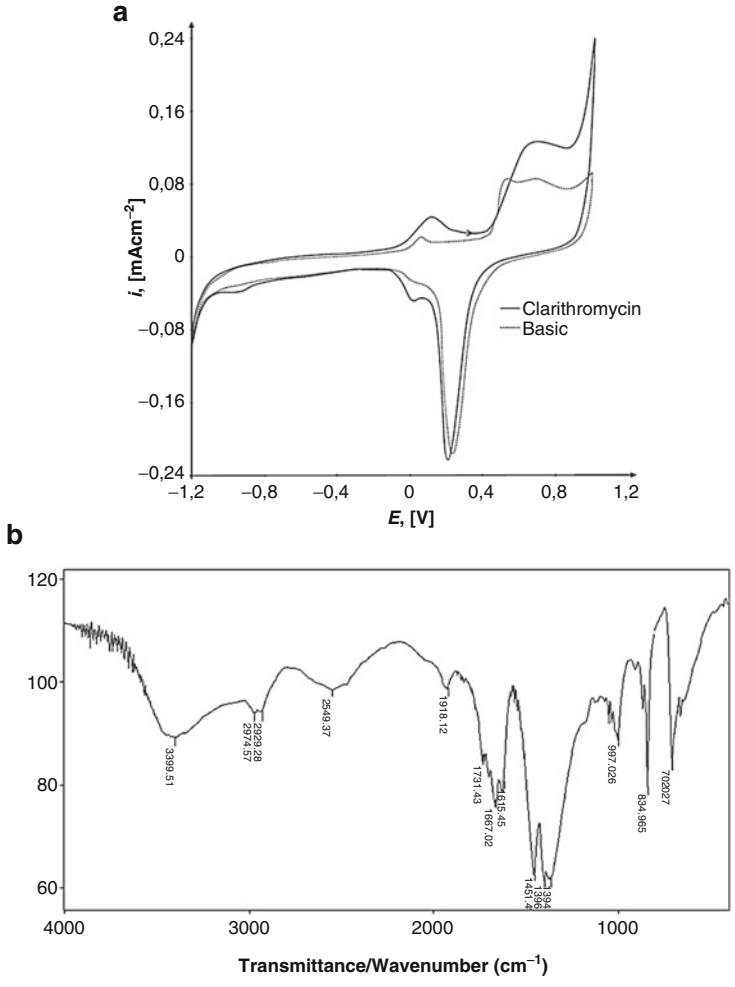

Fig. 2.7 (**a**) Cyclic voltammogram of the first sweep of the Au electrode in the presence of 0.4 mg cm^{-3} pure clarithromycin after the potential had been held for 4 h at –0.61 V vs. SCE in 0.05 M $NaHCO_3$ (*full line*). The voltammogram of the pure gold electrode is presented by the dashed line, sweep rate: 50 mVs^{-1}. (**b**) Infrared spectrum of 0.4 mg cm^{-3} pure clarithromycin in 0.05 M $NaHCO_3$ solution after 4 h electroreduction at –0.61 V vs. SCE under the conditions described in (**a**) (Reproduced with a permission from Elsevier) [9]

electrochemical reactions. The results were compared with those previously obtained for azithromycin and clarithromycin under the same experimental conditions. It was found that the electrochemical behavior of erythromycin A differs from that of azithromycin dihydrate. Comparison with the electrochemical activity of basic clarithromycin suggests that the electrochemical activity of erythromycin is similar but more pronounced than that of clarithromycin.

HPLC analysis confirmed these observations and showed that during the electrochemical oxidation of erythromycin A, the amount of starting macrolide decreased while the amount of starting impurities increased. Also some new products were observed. FTIR spectroscopy confirmed that erythromycin A is more reactive than clarithromycin, although similar changes in their molecular structures were observed.

Under the same experimental conditions, the cyclic voltammogram of erythromycin A exhibits three anodic and one cathodic reaction and one apparent anodic activity in the whole range of the formation of oxides (Fig. 2.8). From Fig. 2.8, it is clear that erythromycin A causes a suppression of the anodic and cathodic currents in the region from −0.35 to 0.0 V and a suppression of hydrogen evolution on a gold electrode. After the addition of antibiotic, pH of the electrolyte was 8.63 and did not change during the further electrochemical examination.

Beckmann rearrangement of erythromycin 9-oxime results in ring expansion to a 15-membered intermediate, the subsequent reduction, and N-methylation of which produce azithromycin with a quite different structure (Fig. 2.1). These structural differences cause the electrochemical behavior of erythromycin A to differ greatly from that of azithromycin dihydrate, which is active only in the oxide formation region and this activity is concentration dependent in the range 0.235–0.588 mg cm^{-3}. Comparing the voltammogram of basic clarithromycin with that of basic erythromycin A presented in Fig. 2.8, it is clear that the three anodic peaks appear at the same potentials. The cathodic reaction is shifted a little to more negative potentials in a case of erythromycin. The activity of clarithromycin is apparent only in the beginning of the region of oxide formation but that of erythromycin covers the

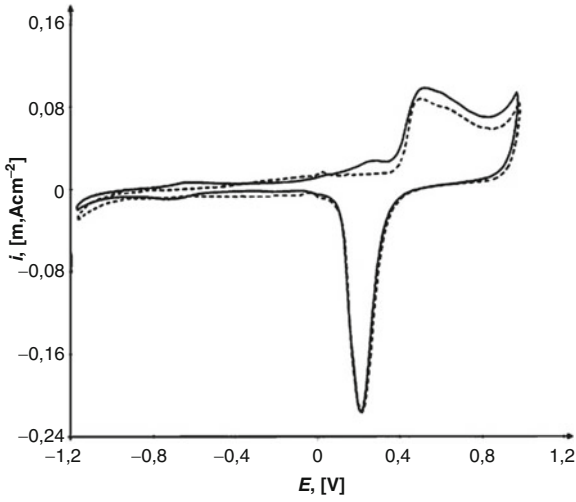

Fig. 2.8 Cyclic voltammogram of an Au electrode in 0.05 M $NaHCO_3$ (*dashed line*) and with the addition of 0.40 mg cm^{-3} erythromycin succinate (*full line*), sweep rate: 50 mVs^{-1}. Cathodic and anodic reaction was observed in the examined range of concentrations (from 0.235 to 0.588 mg cm^{-3}) (Reproduced with a permission from Elsevier) [10]

whole region. A suppression of the anodic and cathodic currents in the region from –0.35 to 0.0 V is more apparent in a case of erythromycin, as well as a suppression of hydrogen evolution. From the decrease of the capacitive currents and the absence of concentration dependence it was supposed that at the electrode surface exists an adsorbed layer of erythromycin/active intermediate species that undergoes transformation. The fouling of the currents after cyclic voltammetry is not observed during 4 h of cycling. Most probable explanation is that the electrode is cleaned in the region of the oxide reduction after each cycle and that erythromycin/active intermediates are not strongly adsorbed. The degradation ability of erythromycin A in different pH solutions suggested that it would be interesting to test its electrochemical behavior in the region of its low stability, acid solution: pH 2.17 and in the region of its high stability, neutral solution, pH 7.14. The second one is close to the pH value of the tested solution (pH 8.55) and is very important for

the possible analyses of biological samples with the same or similar pH values: human blood, urine, and plasma. Erythromycin A in electrolyte at pH 2.12 undergoes immediately to the spontaneous degradation and under the experimental conditions presented in Fig. 2.8. At pH 7.14, erythromycin A exhibited the same electrochemical activity as was observed at pH 8.55. In order to compare the activity of the entire tested macrolides, one can suggest continuing with using of 0.05 M $NaHCO_3$ in the further erythromycin A examination. The electrochemical behavior of commercial erythromycin, Erythromycin®, was studied in the concentration range 0.235–0.588 mg cm^{-3}. The obtained data are useful for the manufacturers of erythromycin A in a case that their commercial products in capsules and tablets contain the same or similar excipients. Due to the presence of excipients, the obtained electrochemical activity differed greatly from that of the basic erythromycin ethyl succinate. It is clear from Fig. 2.9 that the anodic activity at the beginning of the region of the formation of oxides is only small. The appearance of an additional cathodic peak at –0.25 V and an expanded cathodic activity in the region from –0.55 to –1.00 V was observed.

During the electrochemical oxidations of erythromycin A, the amount of starting macrolide decreased while the amount of starting impurities increased and some new products were observed. At the end of the electrochemical oxidations of erythromycin A (5 h), approximately 70 % of the starting compound was recovered. From the obtained results, it is obvious that erythromycin A underwent oxidative degradation. Probably, the first step in the oxidation process is the removal of the electron from one of the nitrogen atoms to form an aminium cation radical:

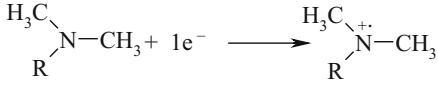

(2.1)

where R is a sugar moiety. Formed aminium radical cation is a very reactive species and rapidly reacts with the environment to form stable products. The formed radical cation can abstract hydrogen atom from the water resulting in salt formation (reaction 2.2) in an overall one-electron process. Hence, the formed cation inhibits further electrochemical oxidation.

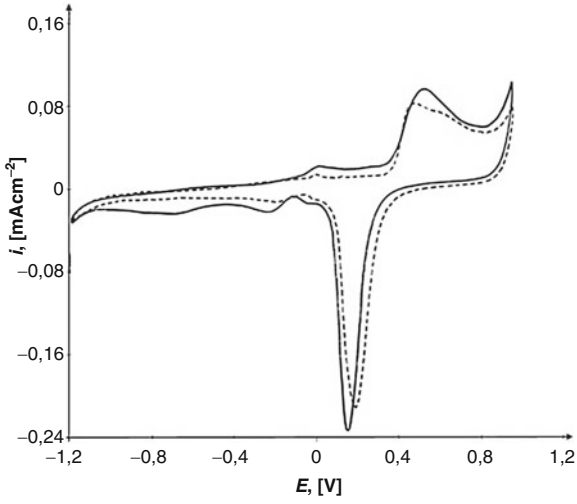

Fig. 2.9 Cyclic voltammogram of an Au electrode in 0.05 M $NaHCO_3$ (*dashed line*) and with the addition of 0.40 mg cm^{-3} Erythromycin® (*full line*) in a concentration of 0.40 mg cm^{-3}, sweep rate: 50 mVs^{-1} (Reproduced with a permission from Elsevier) [10]

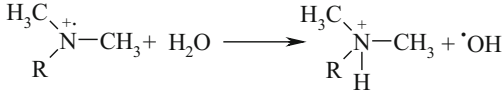

(2.2)

In addition to reaction 2.2, it is probable that the amine group underwent a demethylation reaction, resulting in the corresponding secondary amines. This reaction proceeds via an overall two-electron transfer step (ECE mechanism) (reactions 2.3–2.5). The rate determining steps in these mechanisms are the removal of the α-proton and the formation of an enamine as an intermediate (reactions 2.3 and 2.4).

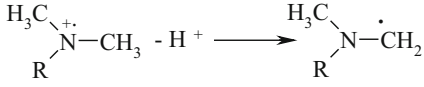

(2.3)

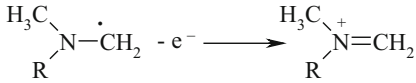

(2.4)

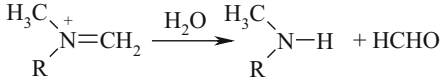

(2.5)

The electrochemical behavior of erythromycin A differs greatly from that of azithromycin dehydrate, which was caused by structural differences. Comparison of the electrochemical activity of basic erythromycin with that of clarithromycin showed that the electrochemical activity of erythromycin is more pronounced than that of clarithromycin. Taking into account that the 6-hydroxy group of erythromycin was methylated to obtain the clarithromycin, it can be assumed that the comparable but more pronounced electrochemical activity of erythromycin is caused by the free hydroxyl group.

Roxithromycin is a semisynthetic 14-membered-ring macrolide antibiotic (Fig. 2.10), in which the erythronolide A lactone ring has been modified by the replacement of the nine keto group with an etheroxime side chain, in order to prevent deactivation in the gastric milieu. The in vitro activity of roxithromycin is well known and is as effective as or more effective than

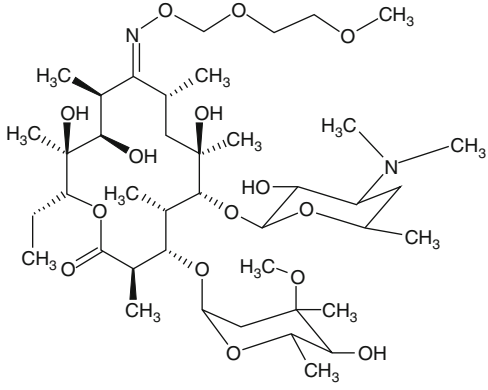

Fig. 2.10 Structure of the roxithromycin

other macrolide antibiotics against a wide range of infections. In vivo, roxithromycin has mostly been used to treat respiratory, urinary, and soft tissue infections. Gastrointestinal disturbances are the most frequent adverse effects but are less frequent than with erythromycin. Roxithromycin exhibits increased chemical stability and higher concentrations of antibiotic in the serum after oral administration compared to erythromycin.

The oxidative behavior of antibiotic roxithromycin standard [11] was studied at a gold electrode in 0.05 M $NaHCO_3$ using cyclic linear sweep voltammetry and differential pulse voltammetry. It was found that the value of the oxidative peak of pure roxithromycin at 0.81 V vs. SCE in 0.05 M $NaHCO_3$ at a scan rate of 50 mVs^{-1} is a linear function of the concentration in a range 0.10006–0.654 mg cm^{-3}.

The cyclic voltammogram of the clean electrode is presented with dashed line and the tested concentrations of roxithromycin standard, continuously added in the same experiment are presented in Fig. 2.11 (full lines). Only the first cycle was recorded. Cyclic voltammograms show two oxidative reactions with maximum current values at 0.5 and 0.8 V vs. SCE. In comparison to the clean electrode, the peak of the gold oxides reduction slightly decreases in the presence of roxithromycin with the increasing of the amount of antibiotic, but it is not a linear function of its concentration. The value of the oxidative peaks of pure roxithromycin at 0.81 V vs. SCE in 0.05 M $NaHCO_3$ at the scan rate of 50 mVs^{-1} is linear function of the concentration in a range of 0.10006–0.654 mg cm^{-3}.

Differential pulse voltammetry was employed in order to verify the results obtained by cyclic voltammetry. Differential pulse voltammograms were recorded at the gold electrode in 0.05 M $NaHCO_3$ solution containing different concentrations of roxithromycin. Potential was scanned from 0.6 to 1.0 V at a scan rate of 2 mVs^{-1}, pulse amplitude of 25 mV, and pulse time of 0.1 s. All voltammograms possess one anodic peak positioned at approximately 0.75 V, as presented in Fig. 2.12.

The deviation of the peak current density from the linear relationship at higher concentrations could be ascribed to the exhaustion of solution during the experiment. Taking into account that each DPV measurement lasted for 13.3 min (eight different

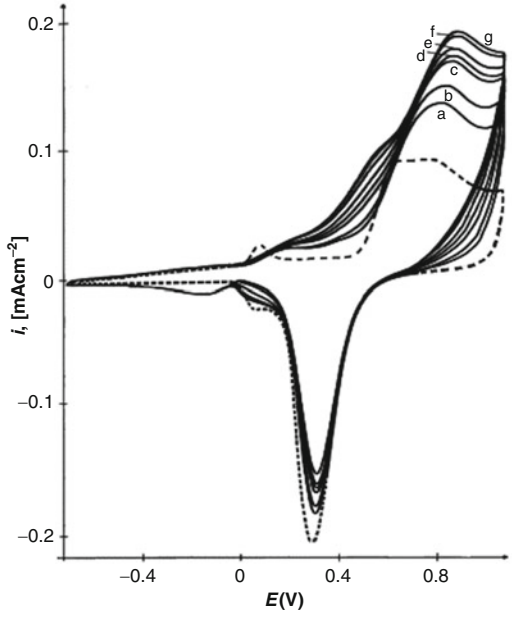

Fig. 2.11 Cyclic voltammogram of an Au electrode in 0.05 M $NaHCO_3$ (*dashed line*) and after the addition of roxithromycin (in the concentration range 0.10006–0.654 mg cm^{-3} (*full lines*, starting from 0.10006, then 0.196, 0.291, 0.385, 0.476, 0.566, and 0.654 mg cm^{-3}), sweep rate: 50 mVs^{-1}. Only the first sweep was recorded (Reproduced with a permission from Elsevier) [11]

concentrations were used) it is most likely that the actual concentration of roxithromycin became significantly lower than the calculated one, i.e., the amount of roxithromycin oxidized during the DPV procedure could not be neglected. Hence, it seems reasonable to assume that the linear range would have been extended to higher concentrations if larger scan rates had been used. It was already published that macrolide antibiotics like roxithromycin which contain a tertiary amino group are detectable.

HPLC analysis of Runac tablets confirmed the data obtained by the analysis of the current peak values vs. concentrations concerning the correlation of the obtained chromatographic peak areas with the investigated concentrations. For the determination of

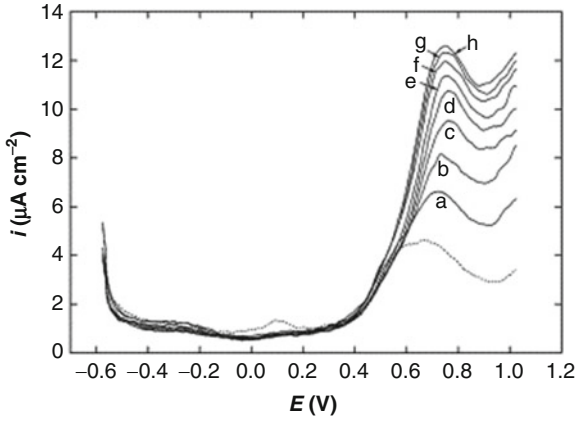

Fig. 2.12 Differential pulse anodic voltammograms obtained at the gold electrode in 0.05 M $NaHCO_3$ (*dashed line*) and in the presence of different concentrations of roxithromycin (*full lines*): (*a*) 0.1006, (*b*) 0.196, (*c*) 0.291, (*d*) 0.385, (*e*) 0.476, (*f*) 0.566, (*g*) 0.654, and (*h*) 0.741 mg cm^{-3}. Initial potential –0.6 V, final potential 1.0 V, scan rate 2 mVs^{-1}, pulse amplitude 25 mV, pulse time 0.1 s (Reproduced with a permission from Elsevier) [11]

roxithromycin in the spiked urine samples, the same values of roxithromycin concentrations (pharmacokinetic concentrations in the range 2.5–10 μg cm^{-3}) were used as in [9], where a sensitive chemiluminescence method was proposed for the determination of roxithromycin. Figure 2.13 represents cyclic voltammograms of the gold electrode in 0.05 M $NaHCO_3$ and after the addition of urine samples spiked with roxithromycin (in the concentration range 2.5–10 μg cm^{-3}). Cyclic voltammograms show that electrochemical oxidation of roxithromycin is represented by anodic peak between 0.60 and 0.90 V (with the current maximum at 0.85 V). This oxidative reaction is in direct correlation with the increasing of antibiotic concentration. It was found that the value of the oxidative peak of urine sample spiked with roxithromycin (at 0.85 V at the scan rate of 50 mVs^{-1}) is a linear function of the concentration in the range 2.5–10 μg cm^{-3}.

Anisomycin is a multifunctional antibiotic isolated from two different species of *Streptomyces* (Fig. 2.14). It is also an inhibitor

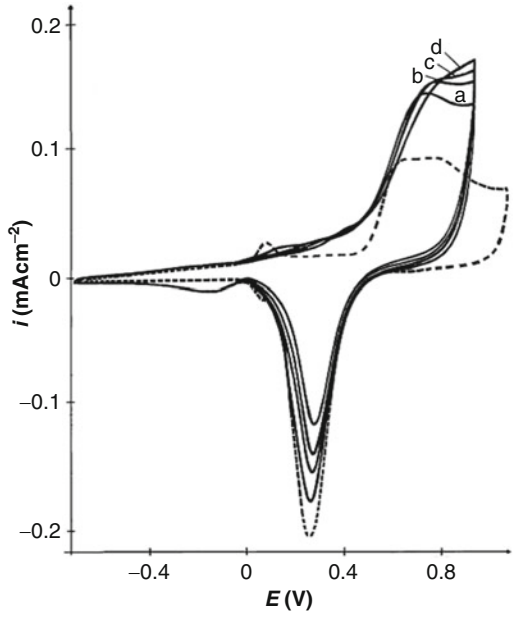

Fig. 2.13 Cyclic voltammogram of an Au electrode in 0.05 M $NaHCO_3$ (*dashed line*) and after the addition of urine samples spiked with roxithromycin (in the concentration range 2.5, 5, 7.5, 10 μg cm^{-3}) (*full lines*, assigned from *a* to *d*), sweep rate: 50 mVs^{-1}. Only the first sweep was recorded (Reproduced with a permission from Elsevier) [11]

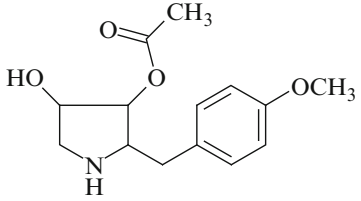

Fig. 2.14 Chemical structure of anisomycin

of protein synthesis and affects memory by inhibiting the consolidation of new memories and causing amnesia. Anisomycin is an immunosuppressant in low doses (<0.1 μM; M = mol dm^{-3}) indicating its possible application in treatment of some autoimmune diseases and in inhibition of the transplantation rejection. It suppresses malignant tumor cell growth and can be used as an antitumor agent. Anisomycin possesses herbicidal activity and selective activity against pathogenic protozoa and fungi.

The electrochemical activity of anisomycin was investigated on gold electrode using cyclic voltammetry in 0.05 M $NaHCO_3$ [12]. Square wave voltammetry was applied for quantitative determination of the drug and in spiked urine samples, followed by high performance liquid chromatography–tandem mass spectrometry (HPLC–MS/MS). The structural identification of anisomycin and its hydrolysis product in 0.05 M $NaHCO_3$ and under the potential cycling conditions in the absence and in the presence of biological sample (urine) was also performed by HPLC–MS/MS.

The CVs (subsequent scans, 1–20) of anisomycin on gold electrode in 0.05 M $NaHCO_3$ alongside the voltammetric response of Au electrode in blank solution (dot line) are presented in Fig. 2.15a. In the presence of anisomycin, the CV in the first cycle was changed so that an apparent current increase occurs in the whole region of the oxide formation and reduction. The changes induced by continuous cycling are expected to be correlated with the surface oxide formation. During the cycling between first and 20th cycles, the voltammograms show a slight decrease of anodic currents in the area of the oxide formation.

Figure 2.15b demonstrates the CVs of anisomycin-containing solution at different scan rates (v). The current density increases with the increased scan rate. In Fig. 2.15c the relationship between peak current and $v^{1/2}$ is displayed showing linearity, indicating that the anisomycin oxidation is diffusion-controlled process. Furthermore, the peak potential increases with increasing scan rate, and a straight line relationship is observed between peak potentials and ln of scan rates (Fig. 2.15d), suggesting that the anisomycin oxidation is an irreversible electrode process. According to the results presented in Fig. 2.15b, the kinetic parameters for the anisomycin oxidation are estimated from Laviron's

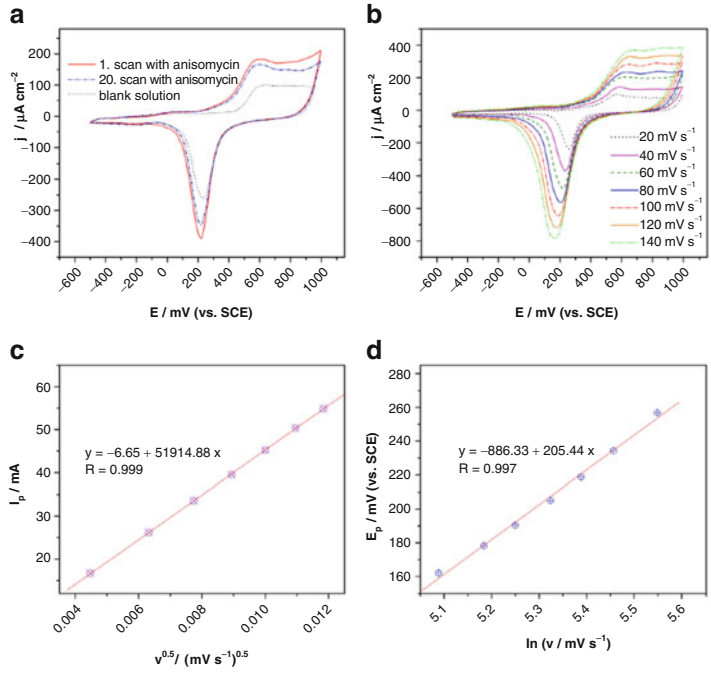

Fig. 2.15 Cyclic voltammogram of Au electrode using 0.05 M $NaHCO_3$ (*dashed line*) and with 0.037 nM anisomycin, (**a**) 1. and 20. scan, scan rate: 50 mV s^{-1}, (**b**) for scan rates: 20, 40, 60, 80, 100, 120, and 140 mV s^{-1}, (**c**) plot of peak current vs. $v^{1/2}$, (**d**) plot of peak potential shift vs. ln of scan rates (Reproduced with a permission from Elsevier) [12]

theory [13]. The value of αn is calculated from the slope of Ep vs. log v. The number of electrons transferred in the electrooxidation of anisomycin was calculated to be 1.1 (approximately equal to 1) assuming that the first electron transfer is rate determining so the transfer coefficient is equal to the symmetry factor which is 0.5. The value of ko (heterogeneous electron-transfer rate constant) is determined from the intercept of the previous plot if the value of Eo is known. The value of Eo is obtained from the intercept of Ep vs. v curve and the value is 267.2 mV. From this, ko was calculated as 0.23 s^{-1}. The HPLC–MS/MS method, used for confirmation of SWV results, exhibited good linearity in the observed concentration range in the absence (R=0.999) and in the presence of biological sample (R=0.978) (Fig. 2.16).

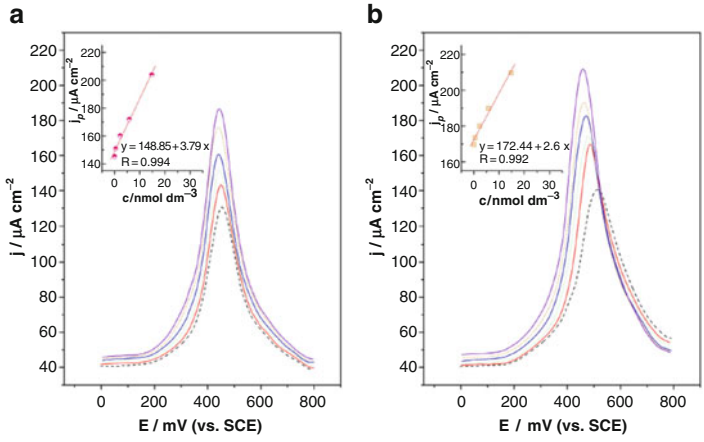

Fig. 2.16 Square wave voltammograms on Au electrode (*dashed line*) using 0.05 M $NaHCO_3$ and with anisomycin (0.037, 0.4, 2.23, 5.84, 14.77 nM) in the absence of biological sample (**a**) and in the presence of biological sample (**b**). Step size 5 mV, pulse size 100 mV, frequency 2 Hz and scan rate 10 mV s^{-1}, accumulation time 200 ms at 0.0 V. *Inset*: linear dependency of anodic peak currents vs. concentration of anisomycin (Reproduced with a permission from Elsevier) [12]

CV during 4 h of anisomycin oxidation (Fig. 2.17a) shows the appearance of the new anodic reactions with the increasing currents compared to Fig. 2.15a, suggesting simultaneous oxidation of anisomycin and the products of its oxidation. SWV (Fig. 2.17b) confirms that effect showing the increasing currents of the anodic peak.

During the cycling, samples of electrolyte were collected and analyzed by HPLC–MS/MS. It was determined that anisomycin hydrolysis occurs, and deacetylanisomycin (*m*/*z* 224) was identified as the hydrolysis product chromatographically separated from anisomycin. Figure 2.18 shows SRM chromatograms and MS/MS spectra of anisomycin (Fig. 2.18a) and its hydrolysis product (Fig. 2.18b) in 0.05 M $NaHCO_3$. Anisomycin hydrolysis under the CV conditions (Fig. 2.17a) is presented in Fig. 2.18c. In the first 2 h, the amount of anisomycin decreases while the amount of hydrolysis product increases. After that, the amounts of both anisomycin and the hydrolysis product decrease and by the end of

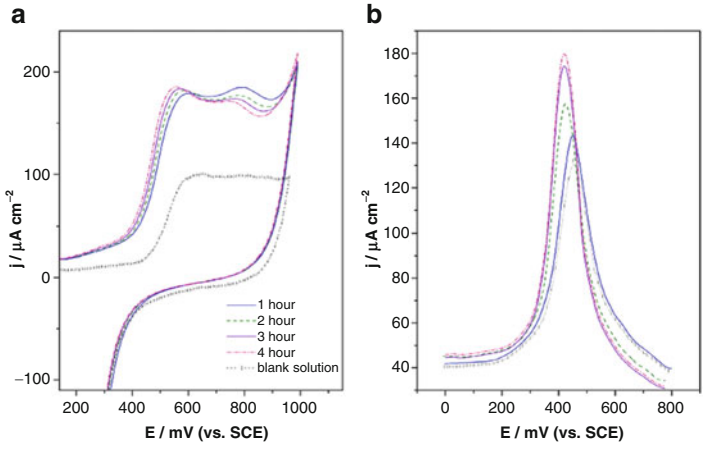

Fig. 2.17 Cyclic voltammograms (**a**) and square wave voltammograms (**b**) of Au electrode in 0.05 M $NaHCO_3$ (*dashed line*) and with 0.037 nM anisomycin, after 1, 2, 3, and 4 h of cycling, scan rate 50 mV s^{-1}. Square wave parameters: step size 5 mV, pulse size 100 mV, frequency 2 Hz and scan rate 10 mV s^{-1}, accumulation time 200 ms at 0.0 V (Reproduced with a permission from Elsevier) [12]

the experiment (4 h) their presence was neglectable. This confirms that after 2 h the electrooxidation products cause the apparent increase of anodic currents in Fig. 2.17. It was also determined that the hydrolysis of anisomycin proceeds in 0.05 M $NaHCO_3$ without electrochemical conditions (Fig. 2.18d). Within the first 30 min, only 3 % of anisomycin is hydrolyzed enabling the correct electroanalytical measurements for at least 30 min. Unlike the electrochemical experiment, the amount of hydrolysis product constantly increases and in 4 h only 69.5 % of anisomycin is hydrolyzed.

2.2.2 Cardiovascular Drugs

Cardiovascular drugs belong also to the most prescribed medications nowadays since various cardiovascular diseases are predominant in developed countries worldwide. In this group the most

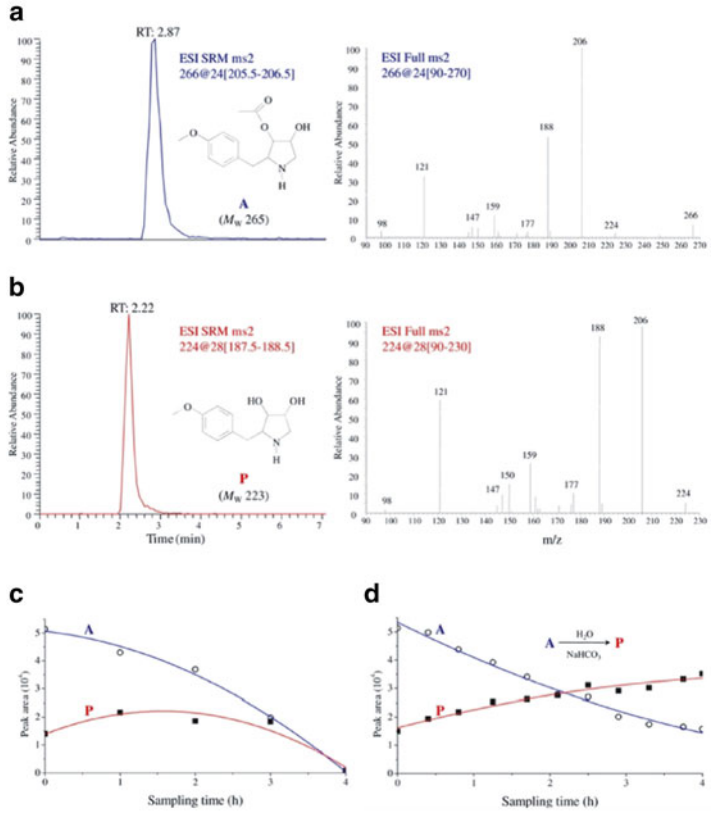

Fig. 2.18 SRM chromatogram and MS/MS spectrum of: (**a**) anisomycin, A, (**b**) the hydrolysis product, *P*. The degradation rate of *A* (*open circle*) and the formation of *P* (*filled square*) in the electrochemical experiment (**c**) and in 0.05 M $NaHCO_3$ (**d**) (Reproduced with a permission from Elsevier) [12]

important drugs are antihypertensives, cardiotonics, antiarrhythmics, anticoagulants, coronary vasodilators, and hypolipemics.

Amlodipine, chemically, 2-[(2-aminoethoxy)methyl]-4-(2-chlorophenyl)-1,4-dihydro-6-methyl-3,5-pyridinedicarboxylic acid, 3-ethyl,5-methylester, besylate (Fig. 2.19), is a dihydropyridine calcium channel blocker, which acts only on the L-type channel to produce their pharmacological effect. Like most of the

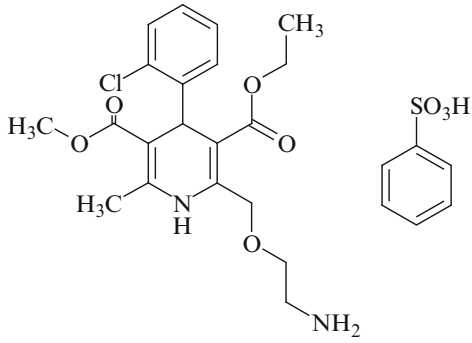

Fig. 2.19 Structure of amlodipine besylate

second-generation dihydropyridine derivatives, it has greater selectivity for the vascular smooth muscle than myocardial tissue and therefore their main effect is vasodilatation. Amlodipine is used alone or in combination with other medicines for the treatment of chronic stable angina, certain types of vasospastic angina, and in the management of mild-to-moderate essential hypertension.

The electrochemical behavior and determination of amlodipine besylate was performed on gold electrode in 0.05 M $NaHCO_3$ [14].

Before voltammetric experiments the electrode surfaces were characterized by AFM. AFM studies were conducted to give insight into the surface topography of the amlodipine/gold and amlodipine/o-MWCNT.

Figures 2.20 and 2.21 show typical two-dimensional (2D) and three-dimensional (3D) AFM images of amlodipine besylate obtained by dropping the water suspension of amlodipine on the gold surface.

The sample of amlodipine besylate/gold is made up of small agglomerates which are compact and uniformly cover the entire substrate (Fig. 2.20), with average diameter of 200 nm (Fig. 2.21).

Gold electrode modified by oxidized multiwall carbon nanotubes was prepared by placing a drop of the water suspension of the nanotubes on the gold surface. As shown in Fig. 2.22, it was clearly seen that randomly oriented MWCNT covered the entire surface of the substrate homogeneously, with average diameter of 100 nm (Fig. 2.23a).

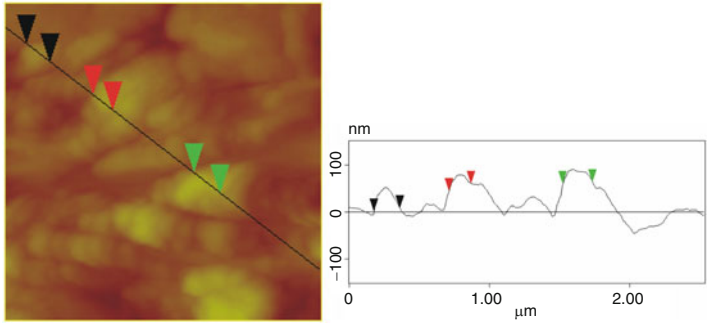

Fig. 2.20 2D AFM image and height profile (3×3×0.3 µm) of amlodipine besylate/Au (Reproduced with a permission from International Journal of Electrochemical Science) [14]

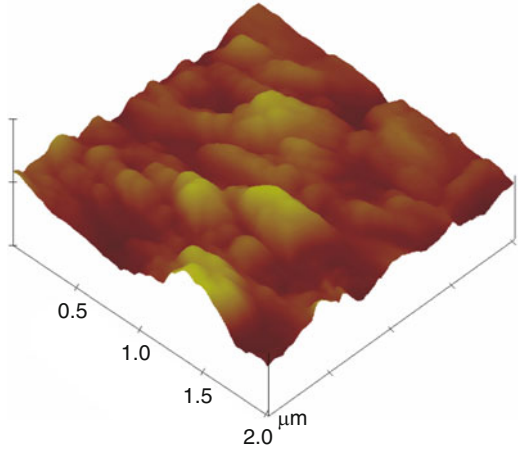

Fig. 2.21 3D image (2×2×0.3 µm) of amlodipine besylate/Au (Reproduced with a permission from International Journal of Electrochemical Science) [14]

The acid treatment of raw MWCNT, using strong oxidizing agent nitric acid, caused severe etching of the graphitic surface of the material, leading to tubes with a population of disordered sites and shortened nanotubes. Shortened o-MWCNT assembles on the

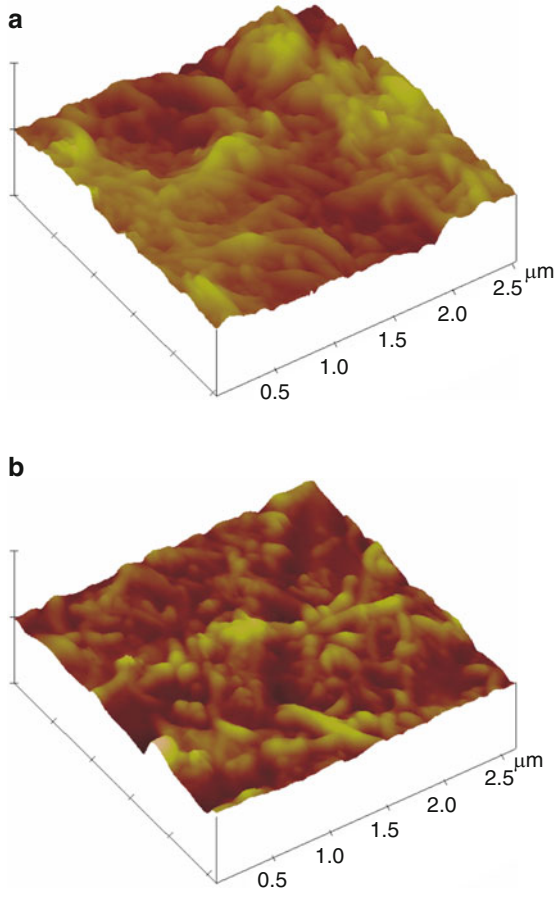

Fig. 2.22 3D AFM images of (**a**) o-MWCNT/Au (2.5 × 2.5 × 0.4 μm) and (**b**) amlodipine besylate/o-MWCNT/Au (2.5 × 2.5 × 0.5 μm) (Reproduced with a permission from International Journal of Electrochemical Science) [14]

gold electrode more easily because of their decreased rigidity and present oxygen functionality contributes better adherence to the gold electrode surface.

However, after adsorbing amlodipine, the diameter of o-MWCNT coated by amlodipine besylate became "wide" as

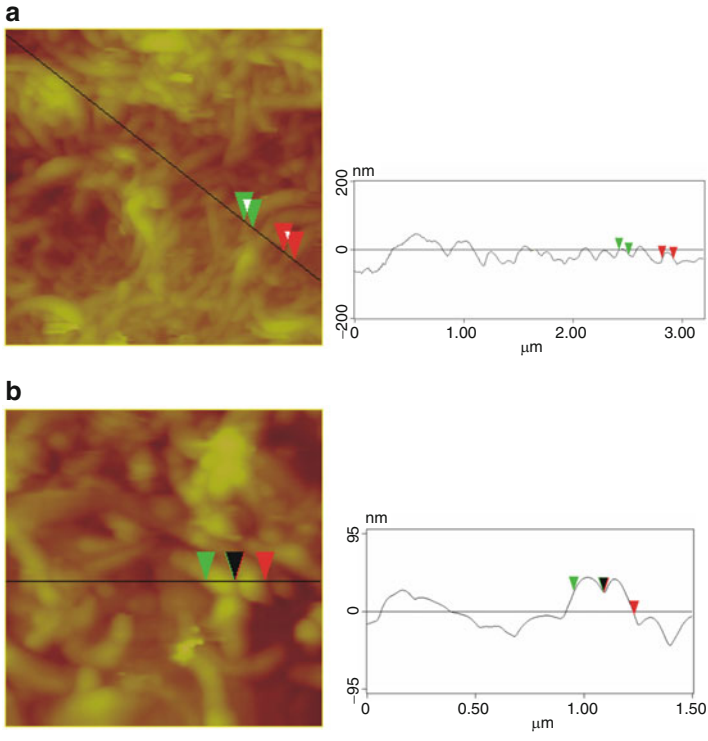

Fig. 2.23 2D images and height profiles of (**a**) o-MWCNT (3×3×0.4 µm) and (**b**) amlodipine besylate/o-MWCNT/Au (1.5×1.5×0.2 µm) (Reproduced with a permission from International Journal of Electrochemical Science) [14]

compared with the o-MWCNT with average diameter of 140 nm (Fig. 2.23b). The sample of amlodipine/o-MWCNT was also well dispersed, implying that the o-MWCNT would connect well the amlodipine on the surface.

Figure 2.24 presents the cyclic voltammograms of amlodipine besylate standard in 0.05 M $NaHCO_3$ obtained without accumulation. The small agglomerates of amlodipine besylate on gold seen by AFM (Fig. 2.20) cover the electrode surface and during the first cycle stay adsorbed on it causing the significantly lower currents in second and consecutive sweeps. In Fig. 2.24 and the following

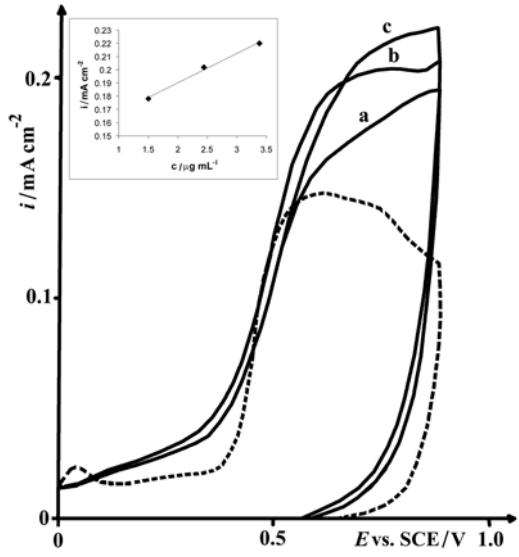

Fig. 2.24 Cyclic voltammogram of gold electrode in 0.05 M $NaHCO_3$ (*dashed line*) and in a presence of amlodipine besylate (*full line*) (*a*) 1.5 μg cm^{-3}, (*b*) 2.439 μg cm^{-3}, (*c*) 3.38 μg cm^{-3}, sweep: 50 mVs^{-1} (Reproduced with a permission from International Journal of Electrochemical Science) [14]

figures, only the first sweep is presented and the electrode surface was prepared for the each presented concentration as is described in experimental part.

The apparent anodic reaction, with wide plateau is observed between 0.5 and 0.85 V for all presented concentrations. In the inset of Fig. 2.24 is presented the linear dependency of the anodic currents vs. concentration in the investigated range (1.50–3.38 μg cm^{-3}), obtained at 0.75 V.

Figure 2.25 presents the cyclic voltammograms of Alopres in 0.05 M $NaHCO_3$ obtained without accumulation. All presented excipients, as was previously published, have no electrochemical activity under the same experimental conditions and amlodipine besylate as a content of Alopres exhibits in their presence also the linear dependency of the anodic current vs. concentration, but for

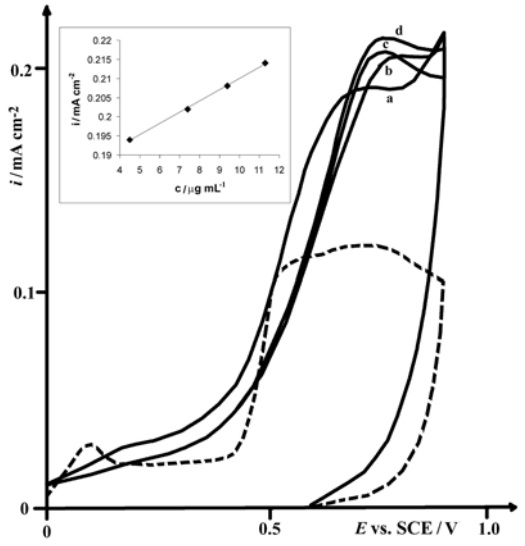

Fig. 2.25 Cyclic voltammogram of gold electrode in 0.05 M $NaHCO_3$ (*dashed line*) and in a presence of amlodipine in Alopres tablet (*full line*) (*a*) 5 μg cm^{-3}, (*b*) 6.5 μg cm^{-3}, (*c*) 9 μg cm^{-3}, (*d*) 12 μg cm^{-3} sweep: 50 mV s^{-1} (Reproduced with a permission from International Journal of Electrochemical Science) [14]

the higher values (4.0–11.5 μg cm^{-3}) obtained at 0.75 V (as is presented in the left corner of Fig. 2.25). Comparing Figs. 2.24 and 2.25 it can be supposed that excipients could cover the electrode surface and in some way prevent the formation of strongly adsorbed agglomerates of amlodipine besylate, causing its anodic reaction to occur at higher concentrations. For higher concentrations in Fig. 2.25 the shape of voltammograms stabilizes, which can be attributed to the reached equilibrium concerning the competitive adsorption between amlodipine besylate and some or all present excipients.

Square wave voltammetry analysis was applied in order to further examine the electrochemical determination of amlodipine in Alopres tablet on a gold electrode in a pH 11 phosphate buffer solution (Fig. 2.26). Voltammograms were recorded in the range of

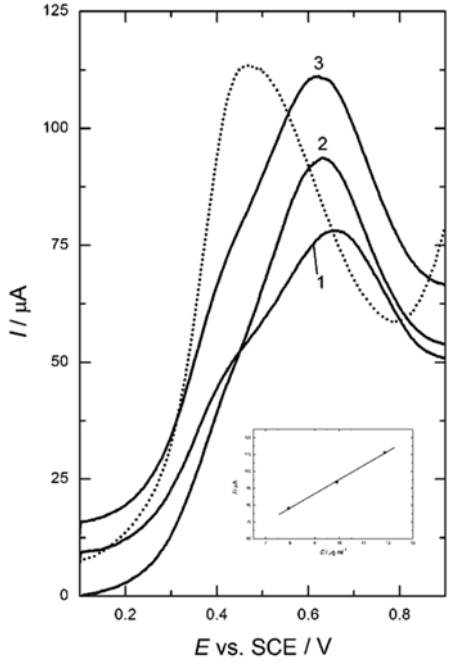

Fig. 2.26 Square-wave anodic stripping voltammograms recorded on a polycrystalline gold electrode for (1) 7.94, (2) 9.90 and (3) 11.86 μg cm^{-3} of amlodipine in Alopres tablet in a phosphate buffer solution pH 11 (the *dotted line* represents a blank solution). Accumulation time: 220 s at $E = +0.1$ V; step size: 2 mV; pulse size: 25 mV; frequency: 50 Hz; scan rate: 100 mVs^{-1} (Reproduced with a permission from International Journal of Electrochemical Science) [14]

potential between +0.1 and +0.9 V for different concentrations of amlodipine in Alopres tablet and before each scan a preconcentration step was performed at the potential of +0.1 V for 220 s in order to accumulate amlodipine besylate on the electrode surface.

In Fig. 2.27 is presented the oxidation of amlodipine in Alopres tablet on Au/o-MWCNT in a pH 11 phosphate buffer solution (7.94 μg cm^{-3}), with accumulation at 0.1 V during 220 s. The anodic activity of amlodipine in Alopres tablet is much lower on Au/o-MWCNT than on a gold electrode.

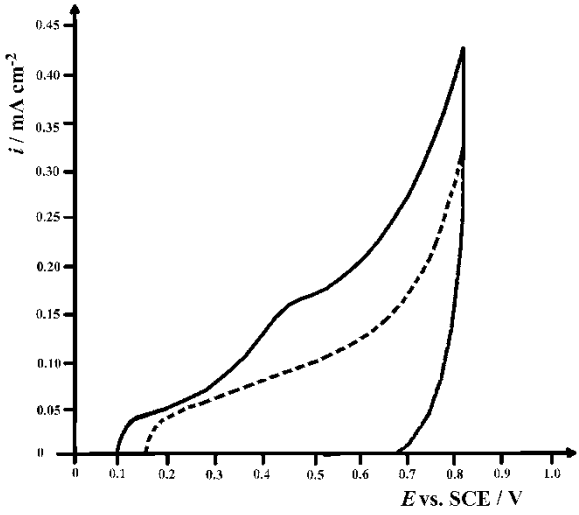

Fig. 2.27 Cyclic voltammograms of Au/o-MWCNT in phosphate buffer (pH = 11) (*dashed line*) and in a presence of amlodipine in Alopres tablet (*full line*), with accumulation at 0.1 V after 220 s, 7.94 μg cm^{-3}, sweep rate; 50 mV s^{-1} (Reproduced with a permission from International Journal of Electrochemical Science) [14]

Figure 2.22 clearly shows that randomly oriented o-MWCNT covered the entire surface of the substrate homogeneously, with the average diameter of 100 nm (Fig. 2.23a). The sample of amlodipine besylate/o-MWCNT was also well dispersed, implying that the o-MWCNT would connect well the amlodipine on the surface and inhibit its oxidation. This explains the better electrocatalytic activity of the gold surface which is covered with small agglomerates. Square wave voltammetry analysis was applied and on Au/o-MWCNT under the same experimental conditions and very low anodic activity of amlodipine in Alopres tablet is obtained, as is presented for cyclic voltammetry in Fig. 2.27. In [15] was published significant anodic oxidation of amlodipine besylate on a glassy carbon electrode modified by o-MWCNT in physiological solution. The results clearly show that glassy carbon electrode

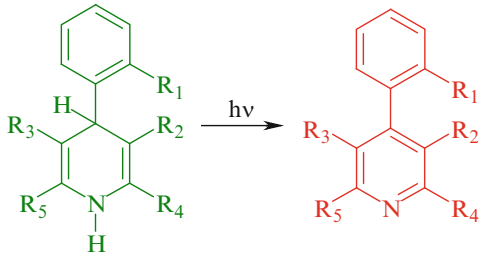

Fig. 2.28 1,4-Dihydropyridine oxidative degradation to pyridine derivative under the influence of light—amlodipine (R_1=Cl; R_2=COOMe; R_3=COOEt; R_4=$CH_2OCH_2CH_2NH_2$; R_5=Me), nifedipine (R_1=NO_2; R_2,R_3=COOMe; R_4,R_5=Me) (Reproduced with a permission from International Journal of Electrochemical Science) [16]

modified by o-MWCNT is better catalyst than gold modified by o-MWCNT for the oxidation of amlodipine besylate and in pharmaceutical preparation.

The electrochemical behavior of inclusion complexes of *nifedipine* (Nif) and *amlodipine* (Aml), a long-acting calcium channel blockers dihydropyridine (DHP) class, with β-cyclodextrin (βCD) and (2-hydroxypropyl)-β-cyclodextrin (HPβCD) (Fig. 2.28), is examined using cyclic and square wave voltammetry in 0.05 M $NaHCO_3$ and phosphate buffer (pH = 11) on a gold electrode [16]. The voltammograms show a single irreversible anodic wave with the current controlled by adsorption. It was found that phosphate buffer favors the electrochemical activity of both complexes of Nif with the linear dependency of the oxidative currents on their concentrations. In phosphate buffer, only HPβCD–Aml complex showed linear dependency of the oxidative currents on the concentration. In 0.05 M $NaHCO_3$ as electrolyte only HPβCD–Nif exhibited apparent activity. The initial potential of the anodic reaction as well as the value of the potential for anodic currents maximum of all the examined complexes in both electrolytes was shifted to the positive direction compared to their standards. In addition, the value of anodic currents decreased.

Nifedipine, dimethyl 1,4-dihydro-2,6-dimethyl-4-(2-nitrophenyl)pyridine-3,5-dicarboxylate, is a dihydropyridine calcium channel blocker. It is a peripheral and coronary vasodilator,

but it has little or no effect on cardiac conduction and negative inotropic activity is rarely seen in therapeutic doses. After oral administration of nifedipine, arterial dilation increases peripheral blood flow, but venous tone does not change. Nifedipine is used in the management of hypertension, angina pectoris, particularly when a vasospastic element is present, as in Prinzmetal's angina, but is not suitable for relief of an acute attack and in the treatment of Raynaud's syndrome.

1,4-Dihydropyridine calcium channel antagonist drugs are characterized by a high tendency to degradation when exposed to light. Oxidative aromatization of dihydropyridine fragment to the pyridine moiety is one of the main degradation pathways of amlodipine and related molecules of 1,4-dihydropyridine family (such as nifedipine) and occurs both in solution and in solid state and is promoted by light. These drugs absorb intensively in the UV-A (some derivates also in the visible) and are known to be photolabile. When amlodipine and corresponding besylate were irradiated in a solution, both in the presence and in the absence of air, it was found to give the aromatized pyridine as the main product. Under exposition of nifedipine to daylight or to certain wavelengths of artificial light it is converted to a nitrosophenylpyridine derivative, while expose to ultraviolet light leads to formation of nitrophenylpyridine derivative.

The inclusion complexes (Fig. 2.29) of nifedipine with β-cyclodextrin (βCD–Nif) or (2-hydroxypropyl)-β-cyclodextrin (HPβCD–Nif) and amlodipine besylate with β-cyclodextrin (βCD–Aml) or (2-hydroxypropyl)-β-cyclodextrin (HPβCD–Aml) were prepared in solid state by coprecipitation with 1:1 mol ratio and characterized by the application of spectroscopic methods FTIR, ^{1}H-NMR, and XRD. Formation of inclusion complexes with cyclodextrin alters the physical properties of the included components such as solubility, dissolution rate, photosensitivity, and stability.

Cyclic voltammograms of βCD–Nif [16] are presented in Fig. 2.30 in phosphate buffer (pH = 11) showing that in anodic direction its electrooxidation begins at 0.25 V with the increasing tendency until the current maximum appearing at the beginning of the oxide formation on gold electrode. This maximum current

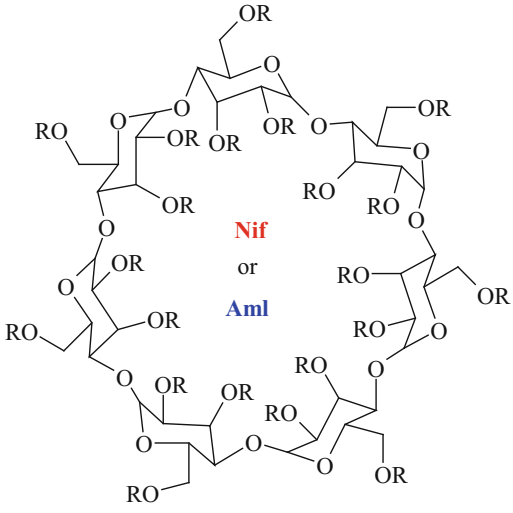

Fig. 2.29 Structure of β-cyclodextrin (βCD) (R=H) and (2-Hydroxypropyl)-β-cyclodextrin (HPβCD) (R=$CH_2CH_2(OH)CH_3$); *Nif* nifedipine, *Aml* amlodipine (Reproduced with a permission from International Journal of Electrochemical Science) [16]

value appears in the whole range of the oxide formation with slightly increasing from 0.9 to 1.0 V. In cathodic direction the presence of βCD–Nif leads to the smaller currents of the oxide reduction which is attributed to the reduction of the species oxidized in anodic direction.

The linear dependency of anodic currents vs. concentration of nifedipine in βCD–Nif in a range: 2.24–5.53 μg cm^{-3} was obtained at 0.77 V from the data in Fig. 2.30. The mentioned linear relationship corresponds to Eq. 1 given in Table 2.1.

Square wave voltammetry, as a fast, sensitive technique with low detection limit, was used for quantitative determination of nifedipine in βCD–Nif on the gold electrode. The square wave anodic stripping voltammograms for different concentrations of nifedipine in βCD–Nif recorded in phosphate buffer in the potential range from 0 to 1.0 V at the scan rate of 15 mV s^{-1} are presented in Fig. 2.31. Before each scan, the compound was

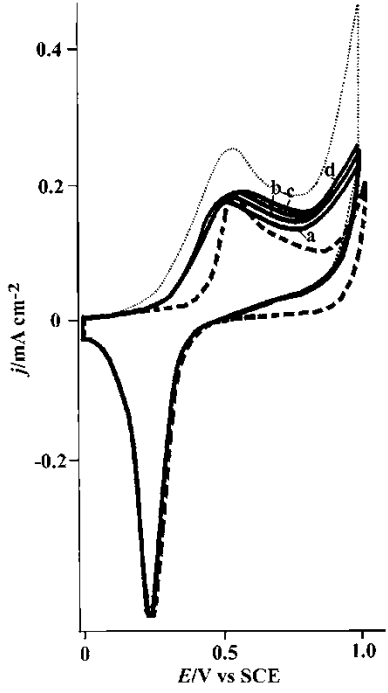

Fig. 2.30 Cyclic voltammogram of gold electrode in phosphate buffer (pH = 11) (*dashed line*) and in a presence of βCD–Nif. Nifedipine concentration: (*a*) 2.24 μg cm^{-3}, (*b*) 3.35 μg cm^{-3}, (*c*) 4.44 μg cm^{-3}, (*d*) 5.53 μg cm^{-3}, sweep: 50 mVs^{-1}; nifedipine standard 2.7 μg cm^{-3} (*dotted line*) (Reproduced with a permission from International Journal of Electrochemical Science) [16]

accumulated at the electrode surface at 0.1 V during 180 s. Each voltammogram is characterized by the well-defined peak at approximately 0.45 V and it is attributed to the oxidation of adsorbed inclusion complex. The current of anodic stripping peak exhibits linear dependence on the βCD–Nif concentration.

The linear dependency of anodic peak currents vs. concentration of nifedipine in βCD–Nif in a range: 4.44–8.72 μg cm^{-3} was obtained from the data in Fig. 2.31. The linear relationship is given by Eq. 2 given in Table 2.1.

Table 2.1 The linear dependency of anodic currents vs. concentration of nifedipine and amlodipine in studied complexes

No.	Complex	Buffer	Method	Equation, j (mA cm^{-2}) = $f(C/\mu$g cm$^{-3})$	R
1	βN[a]	Ph[b]	CV	j = 0.1226 (±0.0025) + 0.0098 (±0.0006) C	0.9962
2	βN	Ph	SWV	j_{pa} = 0.0876 (±0.0003) + 0.0019 (±0.00004) C	0.9998
3	HN[c]	Ph	CV	j = 0.1453 (±0.0018) + 0.0258 (±0.0006) C	0.9996
4	HN	Ph	SWV	j_{pa} = 0. 0727 (±0.0039) + 0.0069 (±0.0014) C	0.9802
5	HN	SBC[d]	CV	j = 0.0782 (±0.0021) + 0.0333 (±0.0011) C	0.9995
6	HN	SBC	SWV	j_{pa} = 0.0706 (±0.0004) + 0.0021 (±0.0001) C	0.9986
7	HA[e]	Ph	CV	j = 0.0679 (±0.0030) + 0.0132 (±0.0004) C	0.9994
8	HA	Ph	SWV	j = 0.0353 (±0.0008) + 0.0006 (±0.00006) C	0.9885

Reproduced with a permission from International Journal of Electrochemical Science [16]

[a]βCD–Nif

[b]Phosphate buffer

[c]HPβCD–Nif

[d]0.05 M $NaHCO_3$

[e]HPβCD–Aml

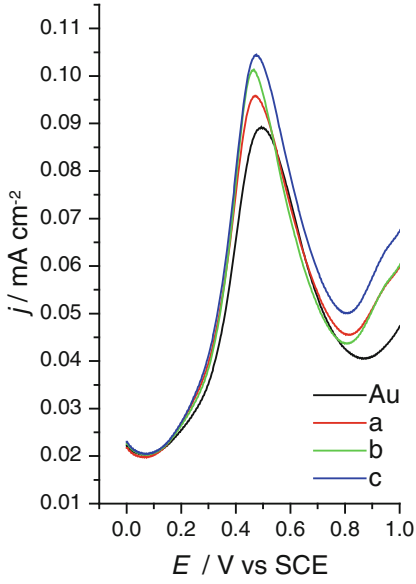

Fig. 2.31 Square wave anodic stripping voltammograms at gold electrode in phosphate buffer (pH = 11) and in a presence of βCD–Nif. Nifedipine concentration: (*a*) 4.44 μg cm^{-3}, (*b*) 6.66 μg cm^{-3}, (*c*) 8.72 μg cm^{-3}. Accumulation time: 220 s at $E = 0.1$ V; step size 2 mV, pulse size 20 mV, frequency 8 Hz, scan rate 15 mV s^{-1} (Reproduced with a permission from International Journal of Electrochemical Science) [16]

Cyclic voltammograms of HPβCD–Nif presented in Fig. 2.32 in phosphate buffer (pH = 11) show the same electrochemical behavior as was observed for βCD–Nif (Fig. 2.30). The linear dependency of anodic currents vs. concentration of nifedipine in HPβCD–Nif in a range: 1.82–3.60 μg cm^{-3} was obtained at 0.65 V from the data given in Fig. 2.32. The linear relationship corresponds to Eq. 3 (Table 2.1).

Although, it was showed earlier that the phosphate buffer is more suitable for the anodic oxidation of dihydropyridine class drugs, so we tested 0.05 M $NaHCO_3$ as electrolyte as well. All the examined inclusion complexes exhibited apparently lower electrochemical activity than in phosphate buffer. The lower activity but good linearity of the currents vs. concentrations was

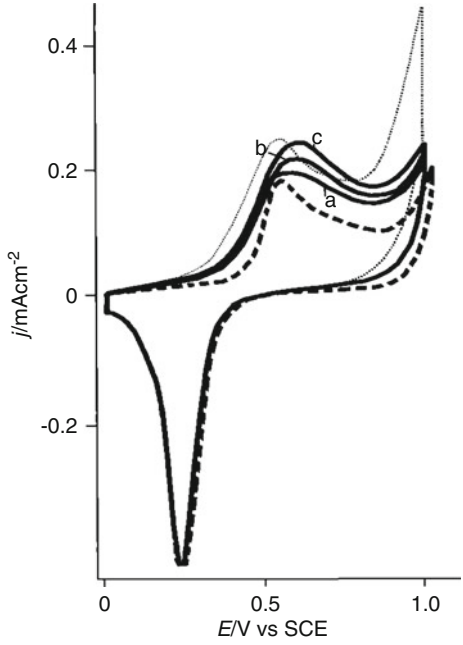

Fig. 2.32 Cyclic voltammogram of gold electrode in phosphate buffer (pH = 11) (*dashed line*) and in a presence of HPβCD–Nif. Nifedipine concentration: (*a*) 1.82 μg cm^{-3}, (*b*) 2.71 μg cm^{-3}, (*c*) 3.60 μg cm^{-3}, sweep: 50 mV s^{-1}; nifedipine standard 2.7 μg cm^{-3} (*dotted line*) (Reproduced with a permission from International Journal of Electrochemical Science) [16]

observed only in the case of the HPβCD–Nif. The linear dependency of anodic currents vs. its concentrations appears at 300 mV more positive potential than was the case in phosphate buffer (Figs. 2.32 and 2.33). The linear dependency in a range: 0.91–2.71 μg cm^{-3} obtained at 0.95 V from the data in Fig. 2.32 is given in Table 2.1 by Eq. 5.

Square wave voltammetry showed also the lower electrochemical activity of nifedipine in HPβCD–Nif in 0.05 M $NaHCO_3$ (lower anodic currents) (Fig. 2.34) than in phosphate buffer (Fig. 2.35). Each voltammogram is characterized by the well-defined peak at approximately 0.6 V which is more than 100 mV shifted to the

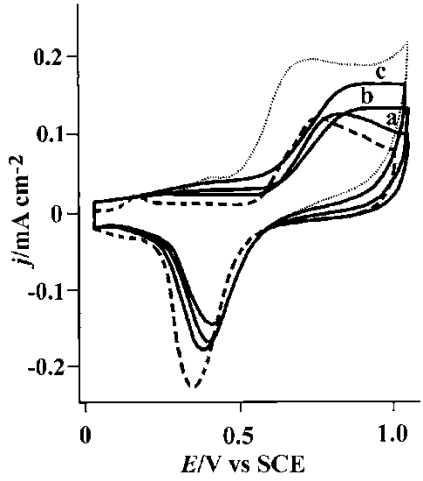

Fig. 2.33 Cyclic voltammogram of gold electrode in 0.05 M $NaHCO_3$ (*dashed line*) and in a presence of HPβCD–Nif (*full line*). Nifedipine concentration: (*a*) 0.91 μg cm^{-3}, (*b*) 1.82 μg cm^{-3}, (*c*) 2.71 μg cm^{-3}, sweep: 50 mVs^{-1}; nifedipine standard 2.7 μg cm^{-3} (*dotted line*) (Reproduced with a permission from International Journal of Electrochemical Science) [16]

positive potential comparing to phosphate buffer. The linear dependency of peak currents vs. concentration of nifedipine in HPβCD–Nif in a range: 0.91–2.71 μg cm^{-3} is presented by Eq. 6 (Table 2.1).

In the form of inclusion complexes, amlodipine exhibited much lower electrochemical activity in both electrolytes compared to nifedipine complexes. Only HPβCD–Aml in phosphate buffer exhibited one apparent electrochemical activity as is presented in Fig. 2.36 and square wave anodic stripping voltammograms are presented in Fig. 2.37. Cyclic voltammograms show an increase in anodic activity in the whole area of the oxide formation on gold electrode with the linear dependency on the concentrations at 0.85 V. The linear dependency of peak currents vs. concentration of amlodipine in HPβCD–Aml in a range: 3.26–9.58 μg cm^{-3} is presented by Eq. 7 (Table 2.1).

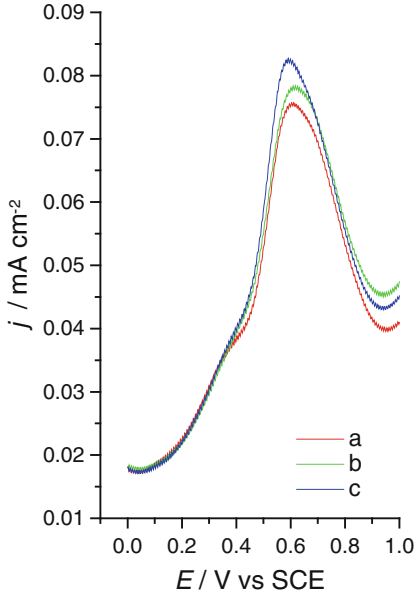

Fig. 2.34 Square wave anodic stripping voltammograms at gold electrode in 0.05 M $NaHCO_3$ and in a presence of HPβCD–Nif. Nifedipine concentration: (*a*) 0.91 μg cm^{-3}, (*b*) 1.82 μg cm^{-3}, (*c*) 2.71 μg cm^{-3}. Accumulation time: 180 s at $E=0.1$ V; step size 2 mV, pulse size 20 mV, frequency 8 Hz, scan rate 15 mV s^{-1} (Reproduced with a permission from International Journal of Electrochemical Science) [16]

By comparing the chemical structures of amlodipine and nifedipine, it is evident that presence of NO_2 group with a strong hydrophobic effect (coefficient hydrophobic substituent, $\pi=-0.85$) significantly decreases the total hydrophobic characteristics of nifedipine. On the other hand, the presence of Cl group as substituent ($\pi=+0.36$) increases the hydrophobic properties of amlodipine. It is important to note that the contribution of the hydrophobic effect to drug/CD complex stability is evident and significant but varies with the structure of drug species. These facts are in good agreements with our experimental data that HPβCD–Aml complex is more subjected to electrochemical adsorption and accumulation.

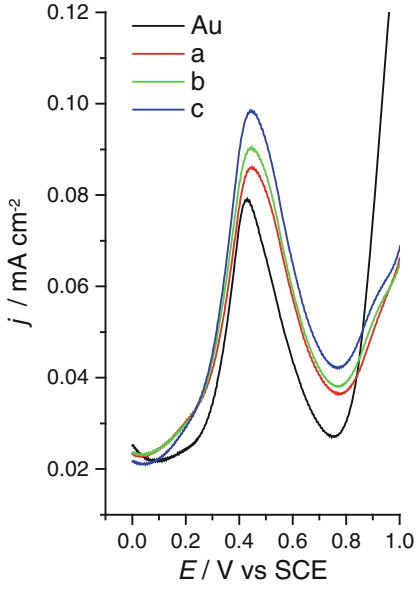

Fig. 2.35 Square wave anodic stripping voltammograms at gold electrode in phosphate buffer (pH = 11) and in a presence of HPβCD–Nif. Nifedipine concentration: (*a*) 1.82 μg cm^{-3}, (*b*) 2.71 μg cm^{-3}, (*c*) 3.60 μg cm^{-3}. Accumulation time: 180 s at $E = 0.1$ V; step size 2 mV, pulse size 20 mV, frequency 8 Hz, scan rate 15 mVs^{-1} (Reproduced with a permission from International Journal of Electrochemical Science) [16]

2.2.3 Central Nervous System Drugs

In modern civilization it is also evident the great demand for different medications related on treatment of various psychoactive states. The drug classes included in this section are depressants and stimulants of central nervous system, various local anesthetics, and also adrenergic and cholinergic agents.

The anodic behavior of *carbamazepine* (CBZ), an anticonvulsant drug (Fig. 2.38), has been studied on gold electrode in 0.1 mol dm^{-3} phosphate buffer of pH 7.0 by using cyclic voltammetry [17]. It has been found that the value of the oxidative current

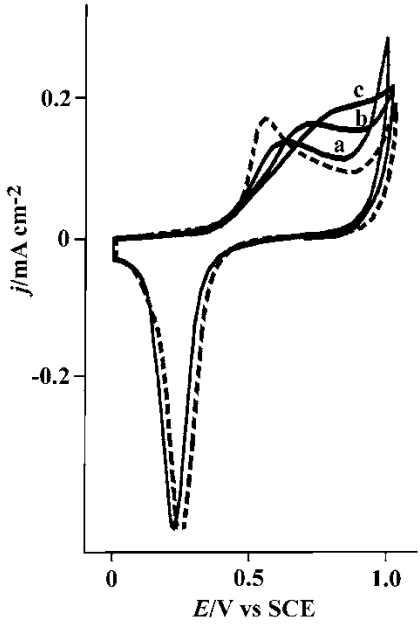

Fig. 2.36 Cyclic voltammogram of gold electrode in phosphate buffer (pH = 11) (*dashed line*) and in a presence of HPβCD–Aml. Amlodipine concentration: (*a*) 3.26 μg cm^{-3}, (*b*) 6.45 μg cm^{-3}, (*c*) 9.58 μg cm^{-3}, sweep: 50 mV s^{-1} (Reproduced with a permission from International Journal of Electrochemical Science) [16]

of pure CBZ at 0.90 V vs. SCE is a linear function of the concentration in a range from 1.0×10^{-7} to 1.0×10^{-4} mol dm^{-3}. The detection of CBZ in the concentration of 1.0×10^{-8} mol dm^{-3} is among the lowest that have been reported for this drug using voltammetric techniques. CBZ as a content of tablet Galepsine® has been quantitatively determined. It has also been demonstrated that the modification of gold electrode with bovine serum albumin (BSA) results in a decrease of the oxidative peak current due to the binding of the drug to BSA.

In the presence of the CBZ standard (at the concentration of 1.0×10^{-8} mol dm^{-3}), the reaction of the oxidation occurs in the area of the oxide formation with the apparent anodic activity from

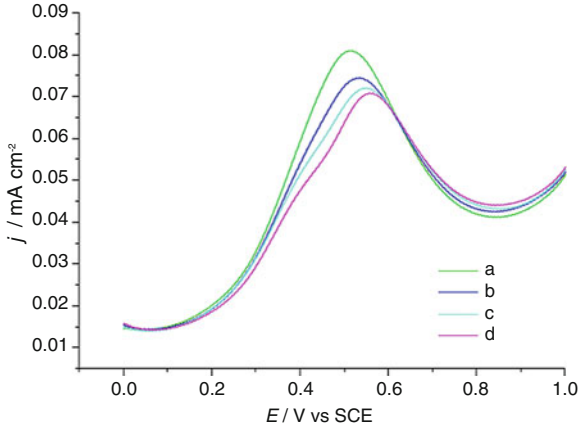

Fig. 2.37 Square wave anodic stripping voltammograms at gold electrode in phosphate buffer (pH = 11) and in a presence of HPβCD–Aml. Amlodipine concentration: (*a*) 9.58 μg cm^{-3}, (*b*) 11.13 μg cm^{-3}, (*c*) 12.65 μg cm^{-3}, (*d*) 14.17 μg cm^{-3}. Accumulation time: 180 s at $E = 0.1$ V; step size 2 mV, pulse size 20 mV, frequency 8 Hz, scan rate 15 mVs^{-1} (Reproduced with a permission from International Journal of Electrochemical Science) [16]

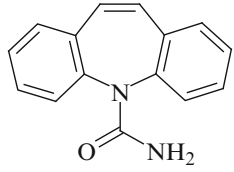

Fig. 2.38 Chemical structure of carbamazepine (5H-dibenzo-[b,f] azepine-5-carboxamide)

0.90 to 1.10 V, as it is presented in Fig. 2.39. The small lowering of the first gold oxide peak at 0.75 V is also apparent only for the concentration of 1.0×10^{-8} mol dm^{-3}. In the reverse sweep, the reaction of the oxide reduction has been decreased in the presence of CBZ at 0.44 V, which may be attributed to the reduction of products formed in the described anodic reactions, as it is the case with macrolide antibiotics [6, 11]. Furthermore, for all of the

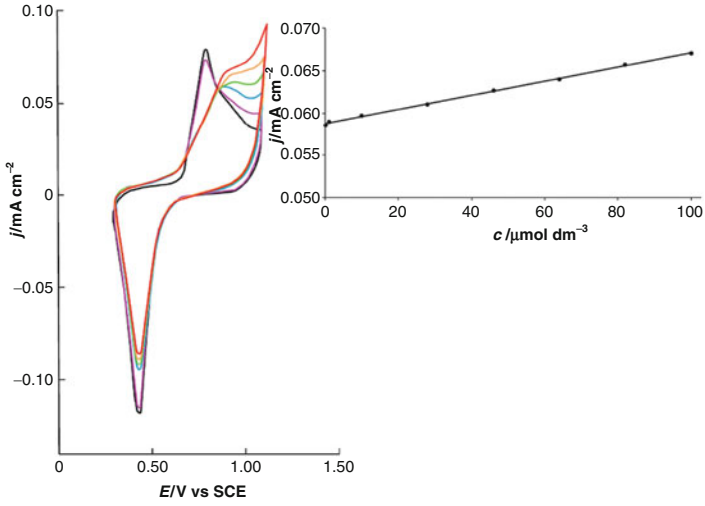

Fig. 2.39 The cyclic voltammograms of bare gold electrode (*black line*) and in the presence of the carbamazepine (CBZ) standard in the concentration from 1.0×10^{-8} to 1.0×10^{-4} mol dm^{-3} (1.0×10^{-8} mol dm^{-3} *pink line*, 1.0×10^{-7} mol dm^{-3} *blue line*, 1.0×10^{-6} mol dm^{-3} *green line*, 1.0×10^{-5} mol dm^{-3} *orange line*, 1.0×10^{-4} mol dm^{-3} *red line*) in 0.1 mol dm^{-3} phosphate buffer (pH 7.0), sweep rate 50 mVs^{-1} (only the first sweep is recorded). *Inset*: The dependency of the value of the oxidative currents of CBZ at 0.90 V on the concentration in the range 1.0×10^{-7}–1.0×10^{-4} mol dm^{-3} (Reproduced with a permission from Association of Chemical Engineers of Serbia) [17]

investigated concentrations of CBZ from 1.0×10^{-7} to 1.0×10^{-4} mol dm^{-3}, in anodic direction, cyclic voltammograms exhibited the changed shape compared to the cyclic voltammograms in the presence of 1.0×10^{-8} mol dm^{-3} of CBZ, as well as in its absence. The increasing anodic current values from 0.30 to 1.10 V due to the increased CBZ concentrations lead to the formation of the current shoulder with the maximum value at 0.95 V. The first gold oxide peak at 0.75 V completely diminished as shown in Fig. 2.39. Because it has tendency to undergo poisoning after the first sweep, gold electrode has been polished between successive additions of suitable aliquots of the working solution of CBZ in phosphate buffer solution to obtain good reproducible results, improved sensitivity, and resolution of voltammetric peaks.

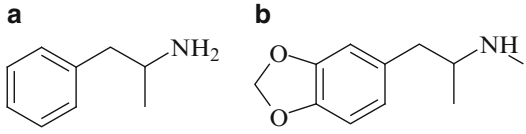

Fig. 2.40 Chemical structures of (**a**) amphetamine and (**b**) 3,4-methylenedio xy-*N*-methylamphetamine

The simple, fast, and cheap voltammetric procedure using gold electrode for the CBZ determination can be further developed as an additional method offering useful combinations with HPLC and with already investigated electrodes, such as glassy carbon electrode.

The abuse of *amphetamine type stimulants* (ATS) is on the rise worldwide. According to UNODC data, the number of ATS users is larger than the number of heroin and cocaine users combined. Amphetamine (A, Fig. 2.40a) and methamphetamine belong to the β-phenyl ethylamine structure sympathomimetic drugs that were utilized as psychostimulants, antidepressants, and appetite suppressants. 3,4-Methylenedioxy-*N*-methylamphetamine (MDMA, Fig. 2.40b) can induce euphoria and diminished anxiety.

There is an increasing interest in the development of rapid, selective, and sensitive methods for the identification and quantification of A and MDMA in illegal market samples. This has been realized using a variety of methodologies: chromatographic techniques, such as HPLC and gas chromatography, capillary electrophoresis, and infrared spectroscopy. Electroanalytical techniques have become powerful tools in modern analytical chemistry for the determination of amphetamine-type drugs. The electrochemical oxidation mechanism of amphetamine-like compounds has not been clarified.

Cyclic voltammetry of some ATS on gold electrode is at the first time performed as is presented in Fig. 2.41 [17].

The value of the oxidative current of the amphetamine standard at 0.80 V vs. SCE in 0.05 M $NaHCO_3$ at the scan rate of 50 mVs^{-1} was a linear function of the concentration in a range of 110.9–258.9 μM.

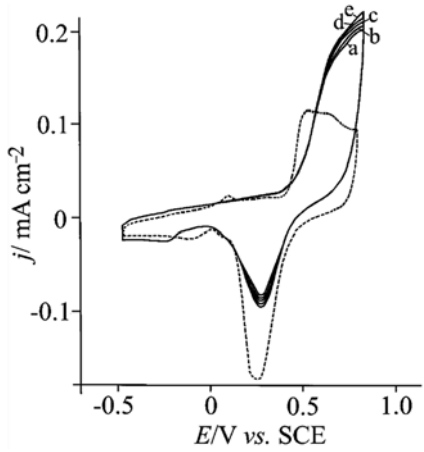

Fig. 2.41 Cyclic voltammogram of the gold electrode in 0.05 M $NaHCO_3$ (*dashed line*) and in a presence of amphetamine standard (*full line*) (*a*) 110.9, (*b*) 147.9 μM, (*c*) 184.9, (*d*) 221.9, and (*e*) 258.9 μM. Sweep rate: 50 mVs^{-1} (Reproduced with a permission from Serbian Chemical Society) [18]

The tested concentrations of the MDMA standard, continuously added in the same experiment, are presented in Fig. 2.42 (full lines). The cyclic voltammograms show an apparent oxidative reaction, with a sharp maximum at the end of the examined oxide region and maximum current values at 0.80 V. Contrary to amphetamine, the oxidation of MDMA began at 0.1 V at the gold electrode surface, 350 mV before oxide formation. This suggests that for MDMA, the gold electrode acted as a catalyst and its molecules were not strongly adsorbed, as in the case of amphetamine.

The urine samples spiked with amphetamine tablets (in the concentration range 110.9–258.9 μM) were analyzed in a same manner as was presented for A. The determination of A in the spiked urine samples was also realized by the standard addition method at two different concentration levels (110.9 and 184.9 μM). Four determinations were performed at each concentration level (Table 2.2). The mean recoveries for the two concentrations were 98.85 % and 97.36 % with relative standard deviations of 0.141 and 1.226, respectively.

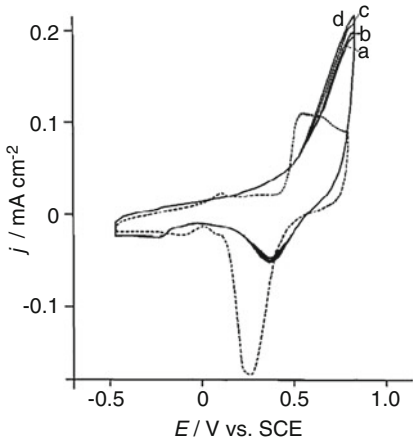

Fig. 2.42 Cyclic voltammogram of the gold electrode in 0.05 M $NaHCO_3$ (*dashed line*) and in a presence of MDMA standard (*full line*) (*a*) 38.7, (*b*) 77.1, (*c*) 153.7, and (*d*) 229.2 μM. Sweep rate: 50 mVs^{-1} (Reproduced with a permission from Serbian Chemical Society) [18]

Table 2.2 Determination of amphetamine in spiked urine samples using the CV method

Taken concentration (μM)	Recovery (%)		SD		RSD	
	CV	HPLC	CV	HPLC	CV	HPLC
110.9	98.25	99.85	0.138	0.100	0.141	0.110
184.9	97.36	99.87	1.201	0.750	1.226	0.805

Reproduced with a permission from Serbian Chemical Society [18]

The urine samples spiked with MDMA standard were analyzed as well and square wave anodic stripping voltammograms of spiked urine samples for the set of concentrations of MDMA presented in Fig. 2.43 are the same as those observed in the absence of urine. The voltammogram for the highest tested concentration of MDMA, 91.6 μM, in Fig. 2.43 shows that a small shoulder that appeared at 0.35 V, attributed to the presence of the urine of healthy volunteers, did not disturb the oxidation of MDMA and had no influence on the value of the oxidation peak. The peak could be slightly shifted to positive potential values (as is presented in Fig. 2.43)

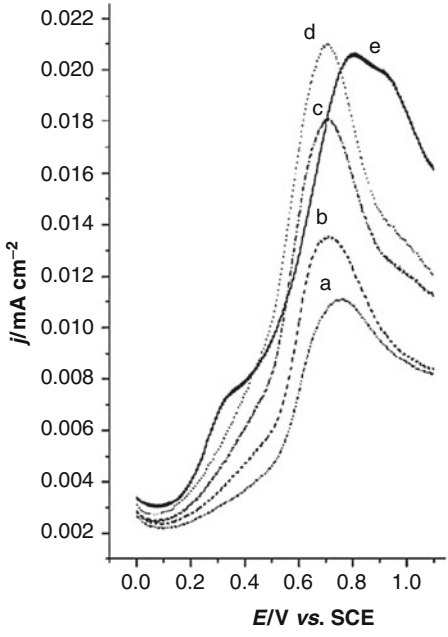

Fig. 2.43 Square wave anodic stripping voltammograms at the gold electrode in 0.05 M $NaHCO_3$ in a presence of MDMA standard, (*a*) 30.9, (*b*) 46.4, (*c*) 76.5, (*d*) 91.6, and (*e*) 91.6 μM spiked with urine. Accumulation time: 220 s at E=0.1 V; step size 2 mV, pulse size 25 mV, frequency 8 Hz, and scan rate 15 mVs^{-1} (Reproduced with a permission from Serbian Chemical Society) [18]

but it did not occur with all spiked urine samples and depended on the urine content, which is common in clinical praxis. The results obtained revealed that SWV could be successfully applied for the quantitative determination of MDMA in urine.

The oxidative ability of *donepezil* (Fig. 2.44), a frequently prescribed drug for the treatment of Alzheimer's disease is reported for the first time at a gold electrode [19]. It was oxidized by cyclic voltammetry and determined by square wave voltammetry in phosphate buffer electrolyte. Electrochemical degradation of donepezil was carried out by long-term potential cycling. The identification and characterization of the major product, isolated by preparative high performance liquid chromatography, was per-

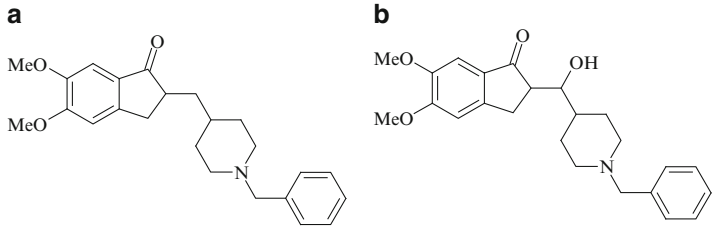

Fig. 2.44 The structures of donepezil (**a**) and the major degradation product (**b**)

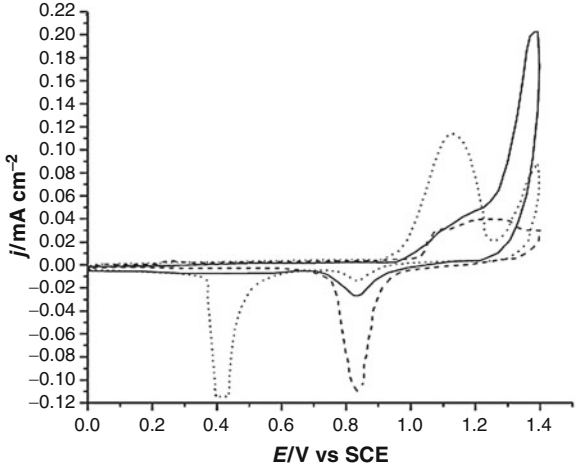

Fig. 2.45 Cyclic voltammogram of gold electrode (*dashed line*) and in a presence of donepezil (50 mg/100 cm^{-3}) in pH 3 phosphate buffer solution before (*dotted line*) and after continuous potential cycling (*full line*). Sweep rate 50 mVs^{-1} (Reproduced with a permission from John Wiley & Sons) [19]

formed by high resolution mass spectrometry and 1D and 2D nuclear magnetic resonance spectroscopy. Donepezil hydroxyl derivative was identified as the major electrochemical oxidation product from donepezil.

The donepezil electroactivity is examined by cyclic voltammetry as is presented in Fig. 2.45 showing in the first sweep an electrooxidation reaction from 0.9 to 1.25 V with the apparent current

maximum at 1.15 V and much smaller, second one at 1.4 V. The first anodic reaction appears before the oxide formation at gold electrode with the current maximum in the area of oxide formation suggesting that gold oxide favors the donepezil oxidation. In the reverse sweep, the apparent cathodic reaction appears at 0.4 V (dotted line). During the long-term potential cycling, the first anodic reaction decreases, the new one appears at 1.25 V, with high currents maximum at 1.4 V. The overlapping with the second anodic reaction cannot be excluded. The cathodic reaction apparently diminishes indicating independency of anodic processes (dotted line). Cyclic voltammetry allows the fast breaking of sites labile toward the oxidation in a donepezil. The linear dependence of the peak currents vs. square roots of sweep rates (25, 50, 100 and 200) mVs^{-1} suggests the diffusion control of the reaction. Electrochemical studies combined with the analysis of the bulk electrolyte after the electrochemical reactions by HPLC were performed. The HPLC method confirmed the existence of several degradation products. The targeted degradation product under study is marked as significant degradation product eluted at retention time of about 11.187 min. Analytical HPLC chromatograms of sample of donepezil bulk drug and sample of donepezil bulk drug electrochemically degraded are obtained by using the HPLC method and are shown in Fig. 2.46. To increase the amount of unknown degradation product of donepezil in the bulk electrolyte, the sample was exposed to 96 h of continuous potential cycling in electrochemical cell. A simple reverse phase semi-preparative chromatographic system was used for isolation of the degradation product from bulk electrolyte. In this chromatographic system, the degradation product eluted at about 14.0 min. The degradation product fraction was collected and then concentrated at room temperature under high vacuum. Purity of the isolated product was tested and found to be 99.0 %, before carrying out spectroscopic and spectrometric experiments. For structure elucidation of the degradation product high resolution mass spectrometry (HRMS) and 1D and 2D NMR experiments were used. Acquisition of HRMS data allowed a determination of the molecular formula. Using high resolution HPLCESI-TOF/MS, the MS spectra of the major degradation product from electro-

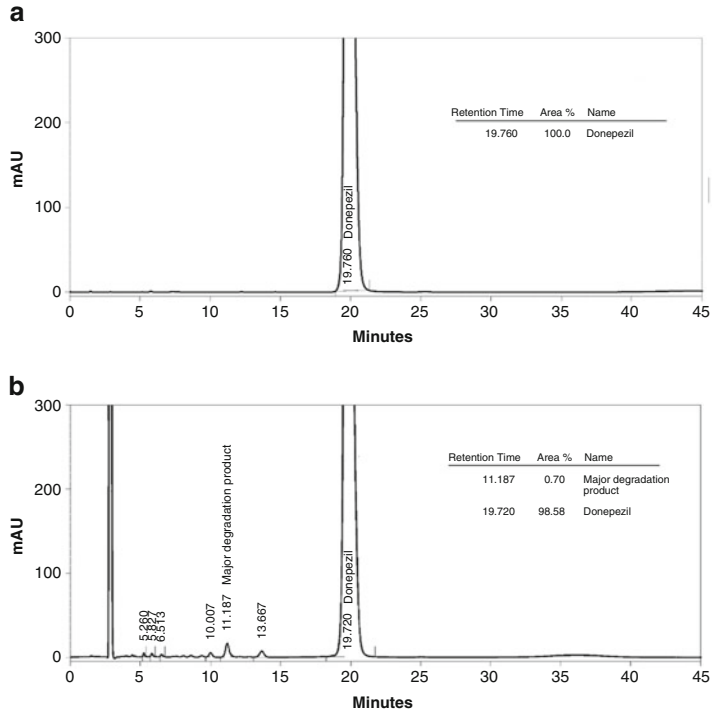

Fig. 2.46 HPLC chromatogram of donepezil bulk in phosphate buffer solution (pH 3) after 14 h of continuous potential cycling in electrochemical cell (**b**) and pure donepezil (**a**) (Reproduced with a permission from John Wiley & Sons) [19]

chemical degradation of donepezil drug substance were recorded in positive and negative mode. MS spectra show precursor ion peak at *m*/*z* 396.2169$[M+H]^+$ in positive mode, and at *m*/*z* 430.1791 $[M+Cl]^-$ and 440.2079 $[M+HCOO]^-$ in negative mode, indicating the molecular formula $C_{24}H_{29}NO_4$. The structure of donepezil degradation product was determined by 1D and 2D NMR spectroscopy.

The ^1H NMR and ^{13}C NMR spectra of the major degradation product are similar to that of donepezil, showing that they have the same basic structure. The corresponding structure of the major

degradation product was characterized as 2-[(1-benzylpiperidin-4-yl)(hydroxy)methyl]-5,6-dimethoxyindan-1-one. This compound has been reported as intermediate in various processes for the synthesis of donepezil and has been investigated for acetylcholine esterase inhibitory activity [20].

Golcu and Ozkan [21] suggested that at glassy carbon electrode the first main anodic reaction could be attributed to the oxidation of the nitrogen atom on the piperidinyl moiety in donepezil. The second anodic oxidation step of donepezil was assigned to the oxidation of alkoxybenzene.

In our study also two anodic reactions were observed. The first main reaction with the current maximum at 1.15 V could be assigned to the oxidation of the nitrogen atom while the second, much smaller anodic reaction (at 1.4 V) could be assigned to the oxidation of alkoxybenzene. This is in agreement with the results presented in [21]. It was suggested that oxidation of alkane to alcohol at Pt electrode [22] proceeds to the formation of secondary carbonium ion in the presence of an acid. Further, carbonium ion reacts with solvent, water, to form an alcohol. We believe that under the applied reaction conditions (acid, water) similar reaction mechanism proceeds at Au electrode during the oxidation of donepezil which leads to the formation of the major oxidation product (Fig. 2.44b). In SWV experiments, deposition times of 120 and 180 s and deposition potentials 0 and 0.2 V were tested but better sensitivity was obtained under conditions presented in Fig. 2.47. SW voltammograms recorded for increasing amount of donepezil (Fig. 2.4a) showed linear increase of peak currents with concentration in the range from 29.1 to 65.4 mg cm^{-3} (Fig. 2.47b).

Phenytoin (5,5-diphenylhydantoin—Fig. 2.48), one of the most frequently used anticonvulsant and antiarrhythmic drug, was examined and determined at bare gold electrode in 0.05 M $NaHCO_3$ using its anodic activity by cyclic voltammetry and square wave voltammetry [23]. Gold electrode is highly sensitive to the phenytoin concentration (the investigated level of concentrations is usually found in human serum of patients treated with phenytoin), providing linear relationships for a set of lower concentrations (0.5, 0.6, 0.8, 1.0 mmol dm^{-3}) and for a set of higher concentrations (10, 20, 30, 40, 50 mmol dm^{-3}). The effects of the substituent

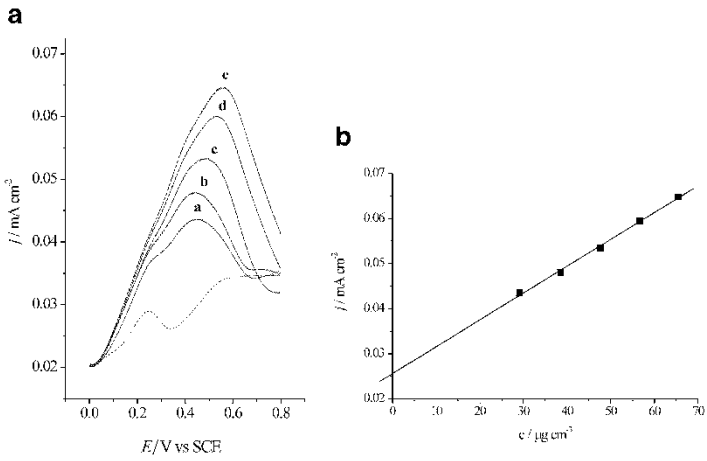

Fig. 2.47 (**a**) Square wave anodic stripping voltammograms of donepezil in concentration range from 29.1 to 65.4 mg cm^{-3} at gold electrode in pH 3 buffer solution (gold electrode: *dashed line*, donepezil concentration: (*a*) 29.1 mg cm^{-3}, (*b*) 38.5 mg cm^{-3}, (*c*) 47.6 mg cm^{-3}, (*d*) 56.6 mg cm^{-3}, (*e*) 65.4 mg cm^{-3}). Accumulation time: 120 s at $E = 0.0$ V; step size 2 mV, pulse size 25 mV, frequency 8 Hz, scan rate 15 mVs^{-1}. (**b**) The linear dependency of anodic peak currents vs. concentration of donepezil (Reproduced with a permission from John Wiley & Sons) [19]

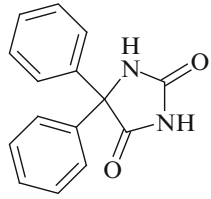

Fig. 2.48 Chemical structure of phenytoin

on the phenyl rings on the electrochemical behavior of two derivatives, 5,5-di(4-chlorophenyl) hydantoin and 5,5-di (4-methylphenyl)hydantoin, were examined by CV. A computational study in correlation with the experimental voltammetric results enabled to propose the oxidation mechanisms: the investigated compounds undergo oxidation involving transfer of $1e^-$ and 1 proton by irreversible, diffusion-controlled process.

Derivatives of hydantoin (imidazolidine-2,4-dione) are important anticonvulsant drugs in the treatment of epilepsy. Depending on the substituents attached to the heterocyclic ring, they can also act as antibacterial and antifungal agents, free radical scavengers, serotonin and fibrinogen receptor antagonists, antiproliferative agents, as well as skeletal muscle relaxants. Phenytoin (5,5-diphenylhydantoin or Dilantin) is a well-known anticonvulsant and antiarrhythmic agent in the treatment of grand mal and psychomotor epilepsy, but its versatile biological effects still attract considerable attention.

Cyclic voltammetry revealed electrochemical activity and concentration dependency of phenytoin in pH 8.4 using 0.05 M $NaHCO_3$ solution and thus possibility for its quantitative determination by square wave voltammetry. In SWV experiments, deposition times of 120 and 25 s and deposition potentials of 0.1 and 0.2 V as well as pulse amplitude of 50 mV were tested but better results were obtained under conditions presented in Figs. 2.49, 2.50, and 2.51.

SW voltammograms recorded for increasing amount of phenytoin for the set of lower concentrations showed linear increase of anodic peak currents to the concentration (insert in Fig. 2.49) with an excellent correlation coefficient ($R=0.995$). Square wave voltammetry also shows that all the lower concentrations of phenytoin start to oxidate at lower potentials than the oxide formation on gold electrode begins to develop as was observed with the cyclic voltammetry (Fig. 2.49). The concentration-dependent anodic peak obtained by SWV appears at the very beginning of the gold oxide formation.

By SWV the linear dependency of the current value of anodic peak on the analyte concentration is obtained with the 20 μM dm^{-3} phenytoin as the highest one. It could be explained by effect of the accumulation time which is long enough to accumulate higher amount of the phenytoin molecules at the gold electrode surface and at the interface with the electrolyte. When concentrations higher than 20 μM dm^{-3} of phenytoin are tested, the peak height observed by SWV increases slowly and it is not concentration dependent.

To investigate the influence of substituent on phenytoin, derivatives with electroaccepting and electron-donating functional

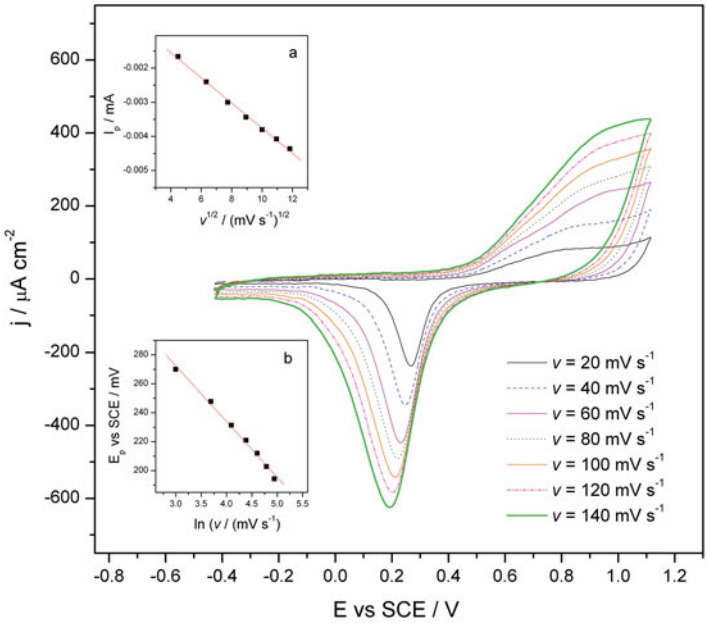

Fig. 2.49 CVs of 20 mmol dm^{-3} of phenytoin on gold electrode using 0.05 M $NaHCO_3$ for scan rates: 20, 40, 60, 80,100, 120, and 140 mVs^{-1}. Insets: plots of current vs. $v^{1/2}$ (*a*) and peak potential shift vs. ln of scan rates (*b*) (Reproduced with a permission from Elsevier) [23]

groups in the phenyl rings were synthesized. The synthesized derivatives of phenytoin (**1**), 5,5-di(4-chlorophenyl) hydantoin (**2**) and 5,5-di(4-methylphenyl) hydantoin (**3**), were investigated by cyclic voltammetry and compared with phenytoin (Fig. 2.52). The chloro derivative exhibits the quite similar voltammetric behavior as was observed with phenytoin (Figs. 2.49 and 2.52) with the little bit lower anodic currents and with the neglectable lowering of the currents of gold oxide reduction. The methyl derivative shows two anodic waves in the area of the gold oxide formation with the little bit higher currents than was observed with phenytoin and with the increased currents of gold oxide reduction. Both derivatives exhibit the higher currents at 1.1 V than phenytoin.

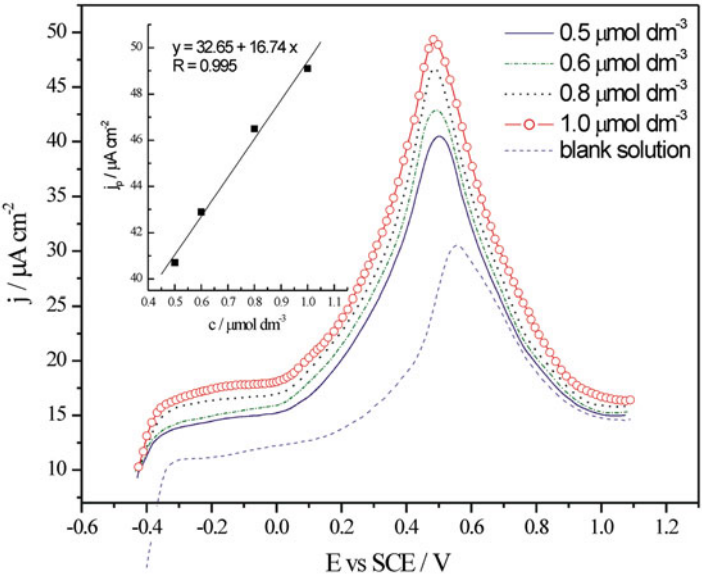

Fig. 2.50 Square wave anodic stripping voltammograms of phenytoin (5, 10, 15, 20) μM dm^{-3} obtained with the Au electrode (*dashed line*) at pH 8.4 using 0.05 M $NaHCO_3$. Accumulation time: 0.2 s at $E = 0.0$ V; step size 5 mV, pulse size 25 mV, frequency 10 Hz, scan rate 50 mVs^{-1}. *Insert*: The linear dependency of anodic peak currents vs. concentration of phenytoin (Reproduced with a permission from Elsevier) [23]

To compare the energy differences between systems involved into the oxidation mechanism, DFT M06-2X calculations with 6-311++G(d,p) basis set are carried out. To keep systems on the same level, the energy of H_2O molecule was added to the energy of hydantoin molecule (G) and corresponding radical cation (R^+) and the energy of H_3O^+ ion was added to the energy of radical and anionic species.

From the M06-2X results can be seen that the formation of radical in position N1 (RN1) is thermodynamically favored instead of the formation of radical in position N3 (RN3). The differences of the energy for formation of RN1 and RN3 radicals are 13.1 and

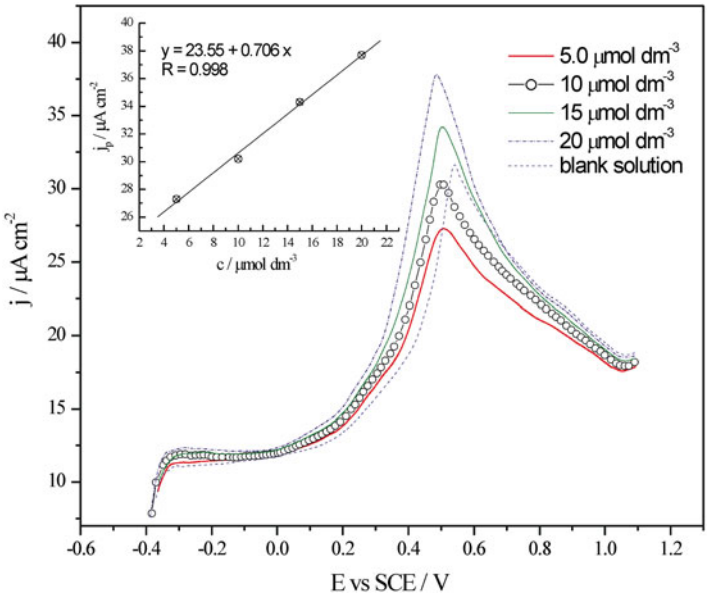

Fig. 2.51 Square wave anodic stripping voltammograms of phenytoin (5, 10, 15, 20 mmol dm^{-3}) obtained with the Au electrode using 0.05 M $NaHCO_3$. Accumulation time: 0.2 s at $E = 0.0$ V; step size 5 mV, pulse size 25 mV, frequency 10 Hz, scan rate 50 mVs^{-1}. Inset: the linear dependency of anodic peak currents vs. concentration of phenytoin (Reproduced with a permission from Elsevier) [23]

13.0 kcal mol^{-1} in vacuum and water for phenytoin. The mechanism of electrolytic oxidation can be divided in two steps: electrochemical abstraction of electron and abstraction of proton. The order of these steps can kinetically favor formation of the corresponding radical. The first route which consisted of abstraction of electron followed by abstraction of proton, from main molecule (G) via intermediate radical cation (R^+) leads to thermodynamically more stable radical RN1.

From the other side, second route considers the abstraction of proton in the first step and formation of anion on N1 (AN1) or N3 (AN3) as intermediates. The formation of AN3 is thermodynamically favored. Differences of the energy for formation of AN1 and

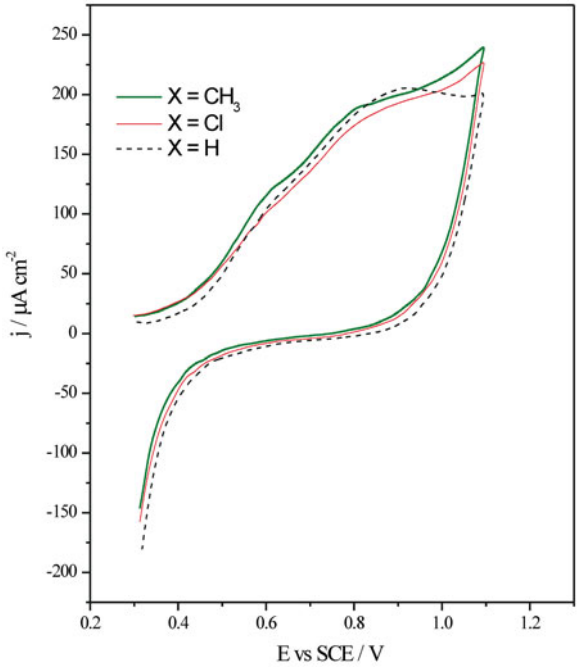

Fig. 2.52 CVs (first scan) of 20 mmol dm^{-3} phenytoin and its derivatives on gold electrode using 0.05 M $NaHCO_3$, scan rate: 50 mVs^{-1} (Reproduced with a permission from Elsevier) [23].

AN3 from phenytoin are −4.6 and −7.3 kcal mol^{-1} in vacuum and water and correspond with acidity of N1–H and N3–H bonds of hydantoins. Second step, electrochemical abstraction of electron needs 82.3 and 126.4 kcal mol^{-1} energy for formation of radical RN1 and 82.3 or 126.4 kcal mol^{-1} energy for formation of radical RN3 in vacuum and water for phenytoin.

The energy for abstraction of electron is dependent on the mechanistic path involved in. As both the paths are feasible, the ratio of the paths is in direct correlation to concentration of hydantoin and its anionic forms. The second mechanistic path slightly favors formation of RN3 radical.

These findings are in good correlation with experimental findings which show that voltammetric response depends on pH of solution of hydantoins. Voltammetric response of solution on

lower pH is on the bigger values and increase of pH leads to decrease of value of voltammetric response.

The energies of the frontier molecular orbital, HOMO and LUMO, are important parameters of the molecular electronic structure, because both are taking part in the chemical reaction. The molecule that has the lower HOMO energy has the weakest donating electron ability; otherwise, a higher HOMO energy implies that the molecule is a good electron donor. Energy of HOMO is a useful diagnostic criterion for oxidation. It has been reported that negative value of HOMO energy (equal to ionization potential) is directly proportional to oxidation potential. As well the energy difference between LUMO and HOMO orbital energies determines the chemical reactivity.

The HOMO orbital of all investigated molecules is π-like orbital and they are mainly localized on the phenyl groups and just partly distributed over the hydantoin ring. The HOMO and LUMO orbitals of investigated hydantoins are shown pictorially in Fig. 2.53.

An examination of HOMO energy values, from B3LYP/6-311++G(d.p) calculations, listed in Table 2.3 reflects that the hydantoin oxidation follows the same order as obtained from voltammetric results. Modulation of HOMO energy with changing functional group suggests that incorporation of substituent on phenyl rings can affect the oxidation potential.

The comparatively easier oxidation of 5,5′-(4,4′-dimethyl-diphenyl) hydantoin is evident from its lower negative HOMO energy (−6.75 eV) than phenytoin (−7.06 eV) due to the electron-donating effect of methyl groups.

Energy of HOMO in 5,5′-(4,4′-dichloro-diphenyl) hydantoin (**3**) is under the influence of two opposing effects (positive mesomeric and negative inductive) resulting in slightly higher negative value in vacuum (−7.11 eV) and lower in water (−7.02 eV) than phenytoin (**1**). This can be explained by the influence of solvation sphere of water which lower inductive effect as a result of electrostatic interaction with Cl groups of hydantoin **3**. As the COSMO model does not include electronic contribution for the creation of the hydrogen bonds, the overall effect is considerably smaller then expected. Nevertheless, predicted effect of electron-donating ability of Cl group in water has the same direction as the experimental results and supports the experimental findings.

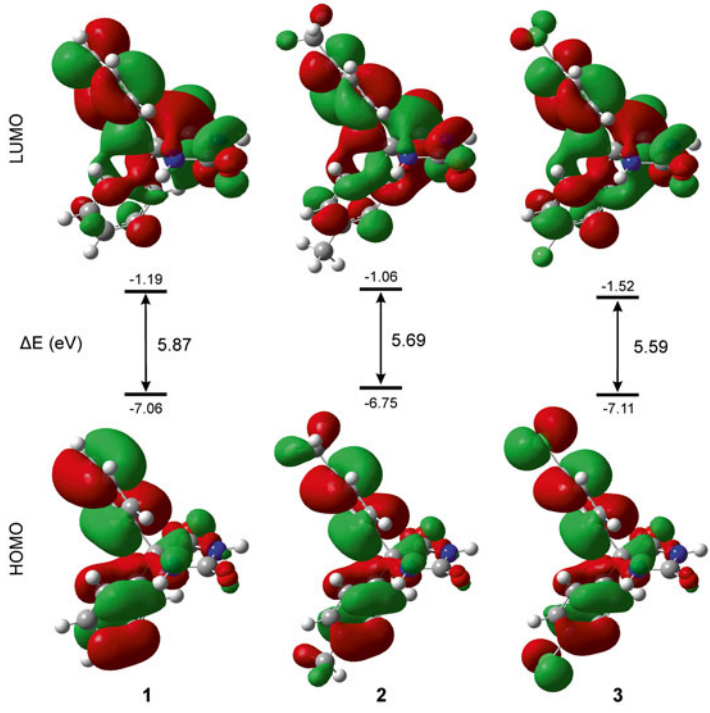

Fig. 2.53 The HOMO and LUMO molecular orbitals, their energies, and energy gaps for investigated hydantoins (Reproduced with a permission from Elsevier) [23]

The spin density distribution is an important quantum property of the radical species. SD maps can show the delocalization of the electron spin which determines stability of radicals and indicates its reactive sites. It can be seen from Fig. 2.54 that the SD of radical cation is delocalized over both phenyl group indicating on that way big influence of substituent to its stability. Energy difference of R^+ from UM06-2X/6-311++G(d,p) calculation for **1**, **2** and **3** is around 10 and 7 kcal/mol for vacuum and water. On the other side, the SD of radical RN1 and RN2 is mostly distributed between corresponding nitrogen atom and atoms of nearby carbonyl groups. Stability of RN1 and RN2 shows very small influence of substituent

Table 2.3 Energy values for HOMO, LUMO orbitals and their energy gap [eV], ionization potential (IP) [kcal mol^{-1}], and NBO charges [e^-] for the investigated hydantoins obtained from B3LYP/6311++G(d,p) calculations

	Energy				NBO charge						
Compd.	HOMO	LUMO	Gap	IP	N1	C2	O2	N3	C4	O4	C5
1	−7.06	−1.19	5.87	194.83	−0.658	0.815	−0.605	−0.658	0.711	−0.572	0.044
2	−6.75	−1.06	5.69	185.44	−0.661	0.814	−0.608	−0.659	0.712	−0.575	0.033
3	−7.11	−1.52	5.59	194.93	−0.661	0.815	−0.599	−0.657	0.710	−0.570	0.044

Reproduced with a permission from Elsevier [23]

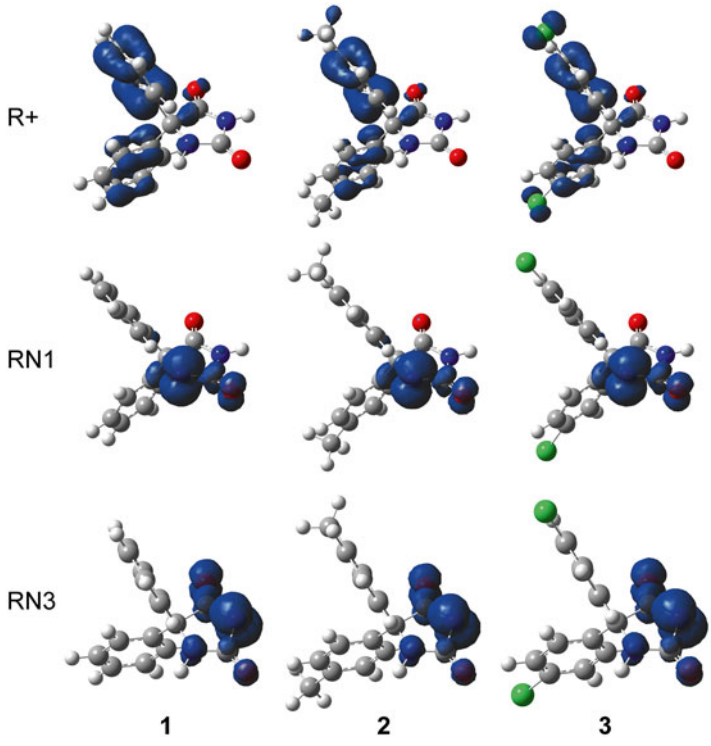

Fig. 2.54 Distribution maps of spin density (squared) for radical species for studied hydantoins (R^+—radical cation; RN1—radical in position N1; RN3—radical in position N3) (Reproduced with a permission from Elsevier) [23]

for correspondent radical, less than 0.7 kcal mol^{-1}, in all cases. As the SD maps for RN1 and RN2 show lot of similarity with HOMO orbital plots for AN1 and AN3 anions, the same conclusion can be derived for the electrochemical abstraction of electron from corresponding anions (second route in mechanism of electrolytic oxidation) especially for water as solvent. Energy difference for abstraction of electron from corresponding anion in water for **1**, **2,** and **3** is less than 2.5 kcal mol^{-1}.

The proposed mechanism for the oxidation of hydantoin derivatives is given at the following scheme (Fig. 2.55).

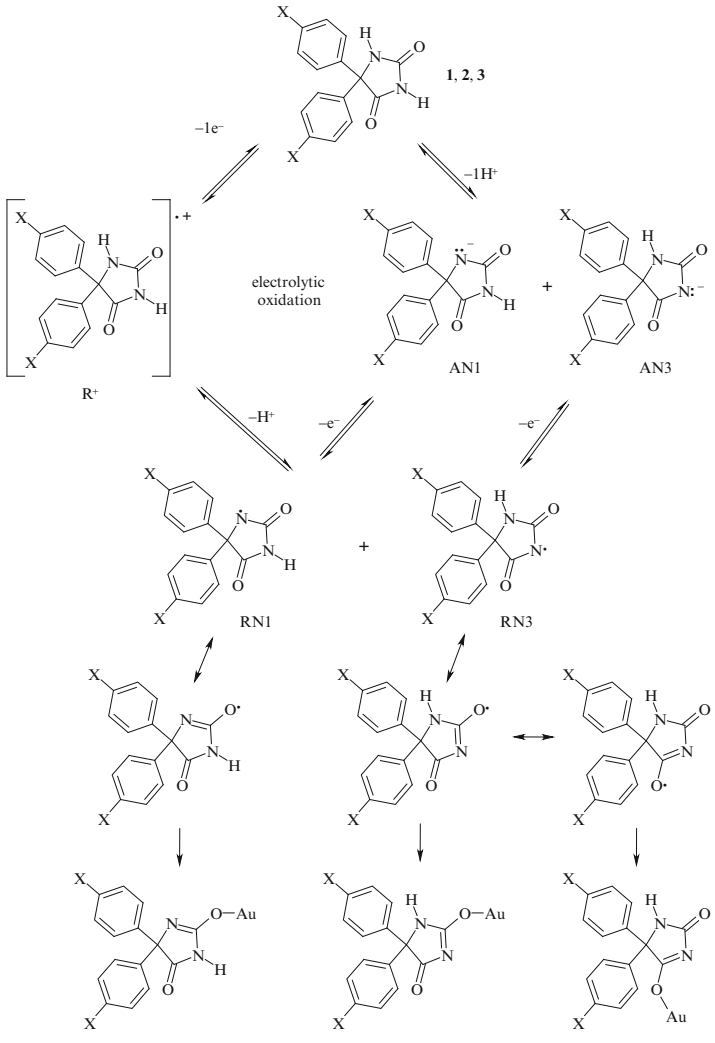

Fig. 2.55 Proposed mechanism for the oxidation of hydantoin derivatives (Reproduced with a permission from Elsevier) [23]

Many requests for the determination of the anticonvulsant drugs arise as a result of problems in the therapy of neurological disorders. Phenobarbital has a narrow therapeutic range, so its concentration needs to be monitored in order to adjust the dose to the optimal level for effective therapeutic control but with minimal side effects such as neurological toxicity [24]. The drug is frequently used in combination with paracetamol since its presence reduces the recurrence risk of simple febrile seizures [25]. DPV has been successfully applied for the determination of phenobarbital and paracetamol in pharmaceuticals [26]. Raoof et al. [27] have prepared a modified electrode by incorporation of multiwalled carbon nanotube and Pt-nanoparticles into a paste matrix. The DPV response of a drug mixture reveals two well-distinguished oxidation peaks, corresponding to the oxidation of phenobarbital and paracetamol, which allow their individual determination.

2.2.4 Anticancer Drugs

The chemotherapy of cancer and neoplastic disease has become very important in recent years. Most antineoplastic drugs are highly toxic to the patient and must be administered with extreme cautions. In this section, are noted several representative drugs with different structures and significant antitumor activity.

Idarubicin is an antracycline drug (Fig. 2.56) which exerts significant antitumor activity. The effect of surface modifications on the electrochemical behavior of the anticancer drug idarubicin was studied at multiwalled carbon nanotubes modified glassy carbon and edge plane pyrolytic graphite electrodes. The surface morphology of the modified electrodes was characterized by scanning electron microscopy [28]. The modified electrodes were constructed for the determination of idarubicin using adsorptive stripping differential pulse voltammetry. The experimental parameters such as supporting electrolyte, pH, accumulation time and potential, and amount of carbon nanotubes for the sensitive assay of idarubicin were studied as details.

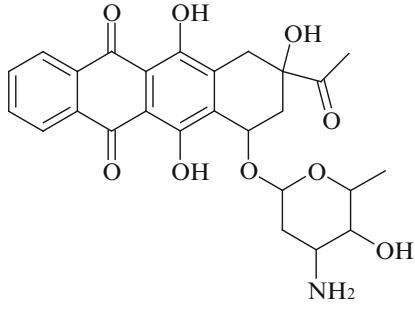

Fig. 2.56 Molecular structure of idarubicin

The results revealed that the modified electrodes showed an obvious electrocatalytic activity toward the oxidation of idarubicin by a remarkable enhancement in the current response compared with bare electrodes.

Under the optimized conditions, idarubicin gave a linear response in the range 9.36×10^{-8} to 1.87×10^{-6} M for modified glassy carbon and 9.36×10^{-8} to 9.36×10^{-7} M for modified edge plane pyrolytic graphite electrodes. The detection limits were found as 1.87×10^{-8} and 3.75×10^{-8} M based on modified glassy carbon and edge plane pyrolytic graphite electrodes, respectively. Interfering species such as ascorbic acid, dopamine, and aspirin showed no interference with the selective determination of idarubicin. The analyzing method was fully validated and successfully applied for the determination of idarubicin in its pharmaceutical dosage form. The possible oxidation mechanism of idarubicin was also discussed. The results revealed that the modified electrodes showed an obvious electrocatalytic activity toward the oxidation of idarubicin by a remarkable enhancement in the current response compared with bare electrodes.

Anthracyclines were originally isolated from a pigment producing *Streptomyces* and are among the most widely used anticancer agents. Idarubicin (IDA) is an anthracycline, which exerts antitumor activity in several solid tumors and hematological malignancies. Because the molecule is more lipophilic than the other anthracyclines it can be administered orally. IDA (Fig. 2.57), a

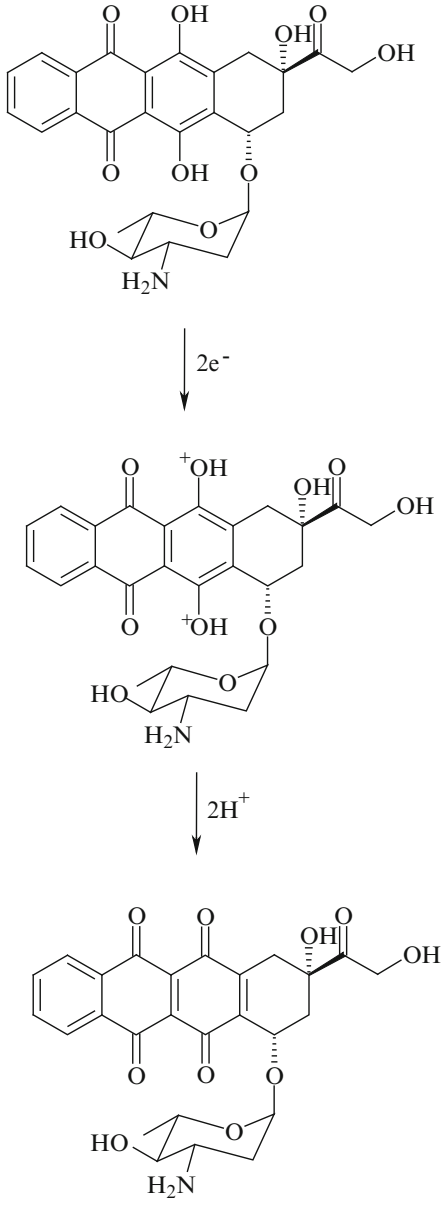

Fig. 2.57 The possible electrooxidation pathway of idarubicin on solid electrodes (Reproduced with a permission from John Wiley & Sons) [28]

synthetic analog of daunorubicin, acts by intercalating between DNA base pairs and inhibiting topoisomerase II. Additionally, it induces free oxygen radicals leading to destruction of DNA and cell membrane.

Idarubicin contains anthracycline and phenol moieties to exclude the possibility of the oxidation part of IDA. Moreover, IDA contains highly electroactive hydroxyl groups on the benzene rings. In general, the oxidation of phenol in a solution at high pH values will generate the phenoxy radical giving an additional oxidation and reduction process similar to anthracyclines such as epirubicin, doxorubicin, and daunorubicin. Therefore, voltammetric techniques are most suitable for investigating the redox properties of drug active compounds. This can give insight into the metabolic fate or in vivo redox process of pharmaceutical activity. The interest in developing electrochemical sensing devices for use in clinical assays is growing rapidly. Electrochemical sensors based on nanomaterial can cope for real samples, which did not have a complex composition and time-consuming preparation steps. The adsorptive stripping differential pulse voltammetric (AdSDPV) technique has been reemergent among electroanalytical techniques through the use of carbon nanotube-modified electrodes where a thin porous layer of nanotubes is in electrical contact with a suitable electrode.

Tamoxifen, [Z]-2-[4-(1,2-diphenyl-1-butenyl)-phenoxy]-*N*,*N*-dimethylethylamine (Tam), a nonsteroidal antiestrogen, has been the most important hormonal agent for treatment of breast cancer for more than two decades, and recently has been approved as a long-term chemopreventive agent for breast cancer in healthy women at high risk for developing breast cancer (Fig. 2.58). Tam undergoes chemical transformation to its phase I metabolites in vivo, resulting in a series of modified species, predominately through methylation or hydroxylation of the benzene rings on the tamoxifen structure, to structures such as 4-hydroxytamoxifen.

The electrochemical investigation of Tam at the glassy carbon electrode and ruthenium oxide (RuO_2) doped on Ebonex electrode in phosphate buffered solution has been studied, based on the adsorption behavior of Tam at the glassy carbon electrode surface [29]. The cyclic voltammetric behavior shows well-defined

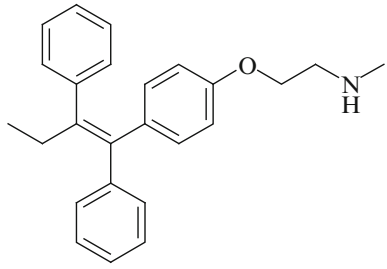

Fig. 2.58 Chemical structure of tamoxifen

irreversible anodic peak at 1.12 V, so to the cyclization reaction to form the corresponding phenanthrene derivative. A fully validated, simple, sensitive, selective, fast, and low-cost differential pulse and square wave adsorptive anodic stripping voltammetric methods were developed for determination of Tam in bulk form, and in spiked human urine and serum. The described methods could be recommended for use in trace analysis, quality control, and clinical laboratories. The phase I metabolite TamOH was shown to be significantly separated from Tamoxifen, being oxidized at a lower potential, but its lower adsorptive character and interfering species at its stripping potential limits our ability to validate a method for its determination.

The electrooxidative behavior of tamoxifen and 4-hydroxytamoxifen (TamOH) was investigated by cyclic, differential-pulse adsorptive anodic stripping (DPAdAS) and square-wave adsorptive anodic stripping (SWAdAS) voltammetric techniques. [29] The anodic oxidation peak of tamoxifen was attributed to the cyclization reaction to form the corresponding phenanthrene derivative and the mechanism of oxidation was postulated on the basis of controlled potential electrolysis and isolation of the oxidative product. Oxidative stripping analysis was successfully applied to the determination of tamoxifen in a bulk pharmaceutical formulation, and sensitivity in human urine and serum was validated. The achieved limits of detection (LOD) of bulk tamoxifen were 1.8×10^{-6} and 2.4×10^{-6} mol dm^{-3} for DPAdAS and SWAdAS, respectively. The LOD values for tamox-

ifen in human urine and serum sample analysis were 4.75×10^{-7} and 2.63×10^{-7} and 1.98×10^{-7} and 3.28×10^{-7} mol dm^{-3} for DPAdAS and SWAdAS, respectively. 4-hydroxytamoxifen is oxidized at more positive potentials than Tamoxifen, separated from the Tamoxifen stripping peak, and its adsorption to the glassy carbon electrode is less pronounced. This affects the ability to determine this important phase I metabolite in serum and urine samples.

2.2.5 Anti-inflammatory Drugs

Anti-inflammatory, especially nonsteroidal drugs continue to be of the more widely used groups of therapeutic drugs. The medicinal drugs covered in this section represent a major market in both prescription and nonprescription drugs.

As the very first electrochemical investigation of *oxaprozin*, nonsteroidal anti-inflammatory drug, using cyclic voltammetry on gold electrode in 0.05 mol dm^{-3} $NaHCO_3$, the synthesized drug, its analytical standard, and its content in Duraprox® tablets were characterized with one oxidation reaction and the three reduction reactions [30]. All they exhibited the linear concentration dependency of anodic currents at 0.83 V for the analytical standard and 0.85 V for Duraprox® tablets in the range of concentrations 8.44–32.78×10^{-6} mol dm^{-3}. The strong adsorption of bovine serum albumin (BSA) on gold electrode in 0.1 mol dm^{-3} phosphate buffer solution (pH 7.4) is shown and concentration dependency of anodic currents of oxaprozin standard on BSA/Au is studied. Following the Langmuir adsorption thermodynamic equation, the binding constants of oxaprozin on BSA/Au electrode was calculated with the results 1.23×10^5 dm^3 mol^{-1}.

Oxaprozin, 3-(4,5-diphenyl-1,3-oxazol-2-yl)propanoic acid (Fig. 2.59), is one of the leading nonsteroidal anti-inflammatory drugs (NSAIDs) in the US market, which is used in the treatment of a number of inflammatory musculoskeletal diseases, including rheumatoid arthritis, osteoarthritis, ankylosing spondylitis, tendinitis, and bursitis. It exhibits several advantages over other NSAIDs (e.g., aspirin, diclofenac, ibuprofen) including a low incidence of

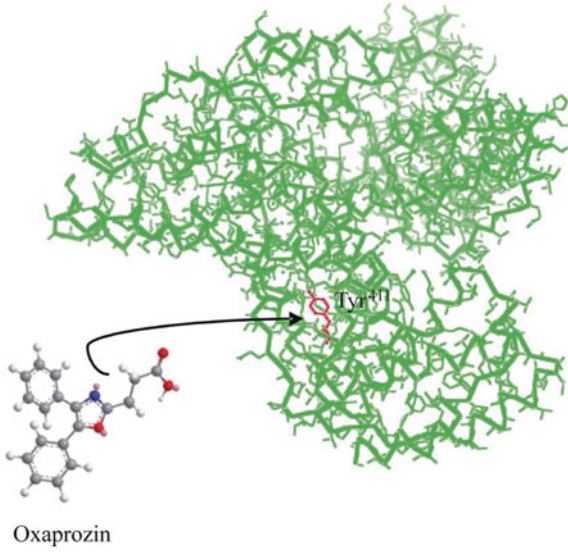

Fig. 2.59 Interaction of oxaprozin with serum albumin. The 3D structure was obtained using Pymol vs. 0.99 and data obtained from Protein Data Bank (PDB). PDB code of serum albumin: 2BXM (Reproduced with a permission from International Journal of Electrochemical Science) [30]

gastrointestinal side effects, a long half-life with long duration of action, and good patient compliance with a once-daily oral regimen. Several chromatographic methods have been presented in the literature for the determination of oxaprozin and its impurities in the bulk drug as well as in biological fluids.

As is presented in Fig. 2.60a, the cyclic voltammogram shows that on gold electrode in the presence of oxaprozin standard, the apparent reaction of the oxidation occurred in the area of the oxide formation with big anodic current plateau between +0.6 and +0.9 V. In the reverse sweep, the reaction of the oxide reduction was decreased in the presence of oxaprozin which can be attributed to the reduction of products formed in described anodic reaction. In the cathodic direction in reverse sweep, the two additional reduction reactions occurred: the first with the cathodic peak at −0.2 V and second one, with cathodic peak at −0.55 V. By cyclic

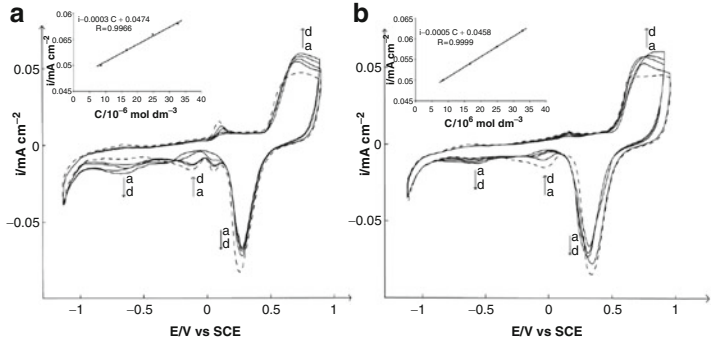

Fig. 2.60 The cyclic voltammograms on bare gold electrode (*dashed line*) as well as in the presence of oxaprozin standard (**a**) and oxaprozin tablets (Duraprox®) (**b**) (*full lines*) in the range of concentrations: $a = 8.44$ mol dm^{-3}; $b = 16.71$ mol dm^{-3}; $c = 24.83$ mol dm^{-3}; $d = 32.78$ mol dm^{-3} in 0.05 mol dm^{-3} $NaHCO_3$, sweep rate 50 mVs^{-1} (only the first sweep is recorded) (Reproduced with a permission from International Journal of Electrochemical Science) [30]

voltammetry on gold electrode, the synthesized oxaprozin as well as its analytical standard was characterized with one oxidation reaction and the three reduction reactions. The synthesized oxaprozin and analytical standard exhibited the identical electrochemical behavior and the concentration dependency of anodic currents at 0.83 V in the range of concentrations 8.44–32.78×10^{-6} mol dm^{-3}. This linearity is presented in the left corner of Fig. 2.60a. In Fig. 2.60b is shown the voltammetric characterization of the content of oxaprozin tablets (Duraprox®). Cyclic voltammograms of oxaprozin standard and as a content of Duraprox® tablets show an identical electrochemical activity of examined drugs and clearly indicate that the present excipients in tablets have no any influence on oxaprozin activity. Excipients were examined separately and did not exhibit any electrochemical activity under the experimental conditions presented in Fig. 2.2b and in [6, 11]. The concentration dependency of anodic currents of content of oxaprozin tablets (Duraprox®) at 0.85 V in the range of concentrations 8.44–32.78×10^{-6} mol dm^{-3} is linear. This linearity is shown in the left corner of Fig. 2.60b.

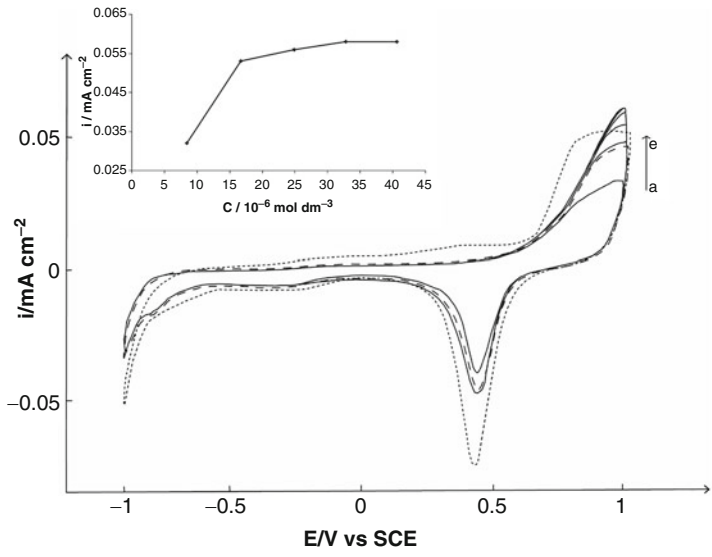

Fig. 2.61 The cyclic voltammogram of bare gold electrode (*d*) (*dotted line*) nd modified with BSA (*dashed line*) as well as in the presence of oxaprozin standard (full lines) in the range of concentrations: $a = 8.44$ mol dm^{-3}; $b = 16.71$ mol dm^{-3}; $c = 24.83$ mol dm^{-3}; $d = 32.78$ mol dm^{-3} in 0.1 mol dm^{-3} phosphate buffer solution (pH 7.4), sweep rate 50 mVs^{-1} (only the first sweep is recorded) (Reproduced with a permission from International Journal of Electrochemical Science) [30]

In Fig. 2.61 is presented the cyclic voltammogram of bare gold electrode (dotted line) and modified with BSA (dashed line) as well as in the presence of different concentrations of oxaprozin standard (full lines) in 0.1 mol dm^{-3} phosphate buffer solution (pH 7.4). It is clear that gold modified by BSA exhibited two times lower currents in the whole region of the applied potential which shows the strong adsorption of BSA on gold. As is shown in Fig. 2.61, the oxidative peak current increased gradually with the concentrations 8.44–24.83 mol dm^{-3} and then reached its saturation value at the concentration of oxaprozin more than 32.78×10^{-6} mol dm^{-3}, which indicated that the binding of oxaprozin with BSA had reached its equilibrium.

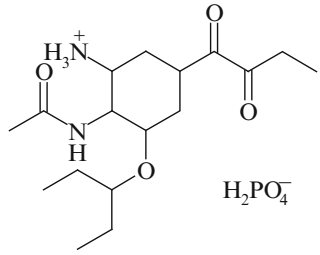

Fig. 2.62 Structural formula of oseltamivir phosphate

A gold electrode was also used in the voltammetric determination of *oseltamivir phosphate* (Fig. 2.62) standard in 0.05 M $NaHCO_3$ [31]. Oseltamivir phosphate as a standard and as a component of Tamiflu® capsule exhibited the identical cyclic voltammogram. The peaks originating from excipients in the capsule did not appear under the applied electrochemical conditions. An electrochemical method for the qualitative determination of oseltamivir phosphate in Tamiflu® capsules by cyclic voltammetry was developed. The presence of oseltamivir phosphate as standard and as a content of Tamiflu® capsule in electrolyte as well as their concentrations was simultaneously checked by HPLC. The lack of the current/concentration dependency was established. The non-pretreated glassy carbon electrode cannot be used for the determination of oseltamivir phosphate under identical experimental conditions presented for the gold electrode.

It is known that antivirals are valuable supplementation to vaccines for the control and prevention of influenza and are likely to be active against a new pandemic variant. Oseltamivir phosphate is the best known orally active neuraminidase inhibitor antiviral drug that slows the spread of influenza virus between cells in the body by stopping the virus from chemically cutting ties with its host cell median time to symptom alleviation is reduced by 0.5–1 days. The neuraminidase inhibitors are effective against both influenza A and B and are considered less toxic and less likely to promote development of drug-resistant influenza than adamantanes.

In our study of electrochemical behavior of oseltamivir phosphate and development of the appropriate method, a solution of oseltamivir phosphate standard was prepared and used in the cyclic voltammetry measurements. In the first part of the work, the gold electrode was used. The cyclic voltammogram of the clean gold electrode of oseltamivir phosphate (0.025 mg cm^{-3}) is presented in Fig. 2.63. Simultaneous HPLC analysis of the bulk of electrolyte confirmed that 0.025 mg cm^{-3} oseltamivir phosphate is presented in the electrolyte. Starting from −1.2 V one can observe an apparent reversible oxidative/reductive reaction between −0.5 and −0.7 V. In the anodic direction, the anodic current increases from 0.4 V and reaches the maximum starting from the area of the oxides formation. In the entire region of oxides formation at the gold electrode, the oxidative activity of oseltamivir phosphate is obvious. The lowering of the oxides reduction currents can also be noticed from the cyclic voltammogram. Starting from −0.8 V the exact same reactions were observed as it was obtained starting from −1.2 V, and as it is presented in Fig. 2.3. The potential was cycled continuously for 2 h and the cyclic voltammogram was quite stable in both cases. Holding the potential for 10 min at the peak potentials and in the area of oxide formation did not affect the voltammogram even in the first sweep. The cyclic voltammogram of oseltamivir phosphate at the gold electrode in 0.05 M $NaHCO_3$ (Figs. 2.63 and 2.64) is quite reproducible. With the addition of the next two aliquots of stock solution of oseltamivir phosphate containing 2.5 mg cm^{-3}, the linearity of the current–concentration dependency was not observed, and even the voltammogram remained the same. With the simultaneous HPLC analysis of the bulk of electrolyte, the presence of the added concentrations was confirmed.

The simple and fast voltammetric method for the qualitative determination of oseltamivir phosphate was developed and applied for the qualitative determination of oseltamivir phosphate in Tamiflu® capsules. Starting from −1.2 V as well as from −0.8 V, an apparent reversible oxidative/reductive reaction between −0.5 and −0.7 V occurs. In the anodic direction, the anodic current increases from 0.4 V and reaches a maximum starting from the area of the oxides formation. In the entire region of the oxides

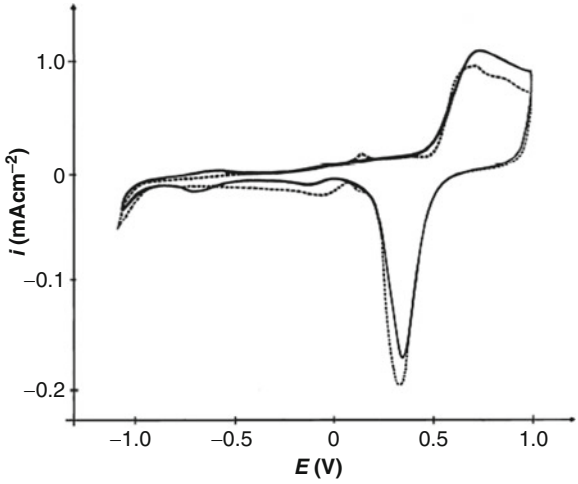

Fig. 2.63 Cyclic voltammogram of the clean gold electrode in 0.05 M $NaHCO_3$ (*dashed line*) and in the presence of 0.025 mg cm^{-3} oseltamivir phosphate (*full line*) in the area of the potential from −1.2 to 1.0 V, sweep rate 50 mVs^{-1} (Reproduced with a permission from Association of Chemical Engineers of Serbia) [31]

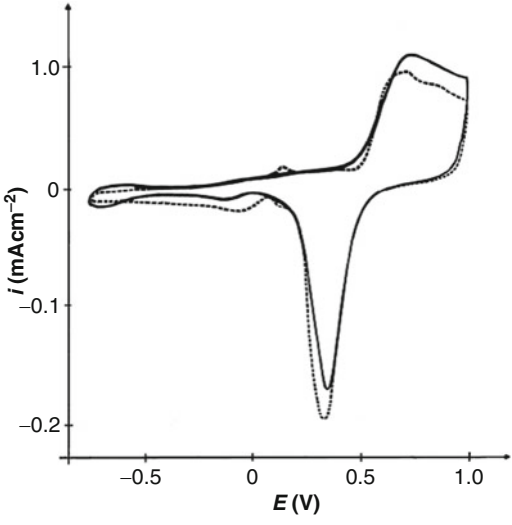

Fig. 2.64 Cyclic voltammogram of the clean gold electrode in 0.05 M $NaHCO_3$ (*dashed line*) and in a presence of 0.025 mg cm^{-3} oseltamivir phosphate (*full line*) in the area of the potential from –0.8 to 1.0 V, sweep rate 50 mVs^{-1} (Reproduced with a permission from Association of Chemical Engineers of Serbia) [31]

formation at the gold electrode, this maximum oxidative current of oseltamivir phosphate remains unchanged. The lowering of the oxides reduction currents is also noticed. The identical cyclic voltammograms of oseltamivir phosphate standard and of Tamiflu® capsule content showed that oseltamivir phosphate is qualitatively determined in Tamiflu® capsule content at the gold electrode in 0.05 M $NaHCO_3$. The glassy carbon electrode cannot be used as working electrode and did not exhibit any affinity to the oxidative/reductive reactions of oseltamivir phosphate starting from −1.2 V as well as from −0.8 V.

2.2.6 *Miscellaneous Drugs*

In this part, selected miscellaneous drugs with different pharmacological action are presented.

Clopidogrel methyl (+)-(*S*)-*α*-(*o*-chlorophenyl)-6,7-dihydrothieno-[3,2-*c*]pyridine-5(4*H*)-acetate (Fig. 2.65), is an antiplatelet agent widely used in the prevention of ischemic stroke, myocardial infarction, and stroke. It inhibits platelet aggregation by selectively preventing the binding of adenosine diphosphate (ADP) to its platelet receptor. This drug reduces thrombotic events in a wide range of patients (e.g., recent myocardial infarction, established peripheral arterial disease, and acute coronary syndrome). Clopidogrel is an inactive prodrug, and a biotransformation by the liver is necessary to induce expression of its antiaggregating activity. It is rapidly absorbed and undergoes extensive metabolism after oral administration and its plasma concentration goes down considerably rapidly.

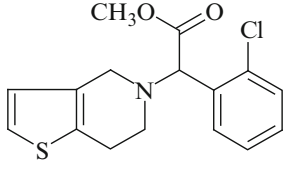

Fig. 2.65 Structure of clopidogrel

The determination of clopidogrel, an antiplatelet agent, was performed at a gold electrode in pH 3.7 acetate buffer using cyclic voltammetry and square wave voltammetry [32]. Each voltammogram was characterized by the well-defined peak at approximately 1.0 V. The current of anodic stripping peak exhibited a linear dependence on the clopidogrel concentration in the range from 317.89 to 935.16 μg cm^{-3}. The obtained linearity was applied to determine clopidogrel in the tablet form of the pharmaceutical preparation (Plavix®). The results were compared to the UV spectrophotometric and HPLC methods.

The electrochemical behavior of the pure standard of clopidogrel on gold electrode was first studied by cyclic voltammetry in pH 3.7 acetate buffer. As is presented in Fig. 2.66, clopidogrel exhibited an apparent oxidative ability in this electrolyte on a gold electrode. The cyclic voltammogram shows the beginning of anodic activity of clopidogrel in double layer region from 0.2 to 0.6 V. An apparent anodic current maximum appears at 1.0 V before oxide formation on the gold electrode and second one at 1.17 V in the area of oxide formation. The rapid increase of anodic current on gold oxide at 1.30 V in the presence of clopidogrel was observed as well as its shift by 0.1 V to a more negative potential, compared to a clean gold electrode (dashed line in Fig. 2.66).

The application of square wave voltammetry for the quantitative determination of clopidogrel on the gold electrode is presented in Fig. 2.67. The SW voltammograms for different concentrations of clopidogrel were recorded in pH 3.7 acetate buffer in the potential range from 0 to 1.5 V at a scan rate of 15 mVs^{-1}. Before each scan, the compound was accumulated at the electrode surface at 0 V for 180 s. Under these conditions, the oxidation of clopidogrel proceeded before oxide formation on Au and reached maximum currents at the onset potential of Au oxide formation. Each voltammogram was characterized by a well-defined peak at approximately 1.0 V. The currents of anodic stripping peak exhibited a linear dependence on the clopidogrel concentration, as shown in the inset of Fig. 2.67.

The voltammetric behavior of clopidogrel as the content of commercial tablets Plavix® was also in a first stage investigated by cyclic voltammetry. Its voltammetric behavior even in the pres-

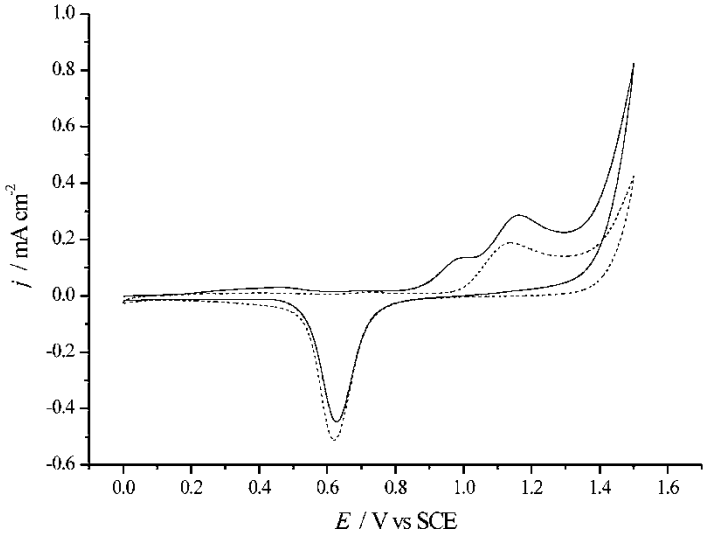

Fig. 2.66 Cyclic voltammogram of an Au electrode in pH 3.7 acetate buffer, *dashed line*, and after the addition of clopidogrel (concentration 32.0 μg cm^{-3}), *full line*; sweep rate: 50 mVs^{-1}. Only the first sweep is presented (Reproduced with a permission from Serbian Chemical Society) [32]

ence of the excipients present in Plavix® showed the same anodic activity as the standard substance, presented in Fig. 2.66, with a negligible reduction in the values of the current maximums.

Similarly as for clopidogrel, the oxidation of Plavix® at a gold electrode using square wave voltammetry proceeded at potentials before the formation of oxide on the Au. The square wave voltammogram was characterized by a well-defined peak at approximately 1.0 V.

The obtained linear relationship between current and concentration of clopidogrel in acetate buffer (pH 3.7) by SW voltammetry within the concentration range 0.317–0.935 mg cm^{-3} (Table 2.4) was used for the determination of clopidogrel in tablet form (Plavix®) and the results were compared with those obtained by the UV and HPLC methods. The validation of the SW procedure was carried out by evaluation of the limit of detection (*LOD*), limit

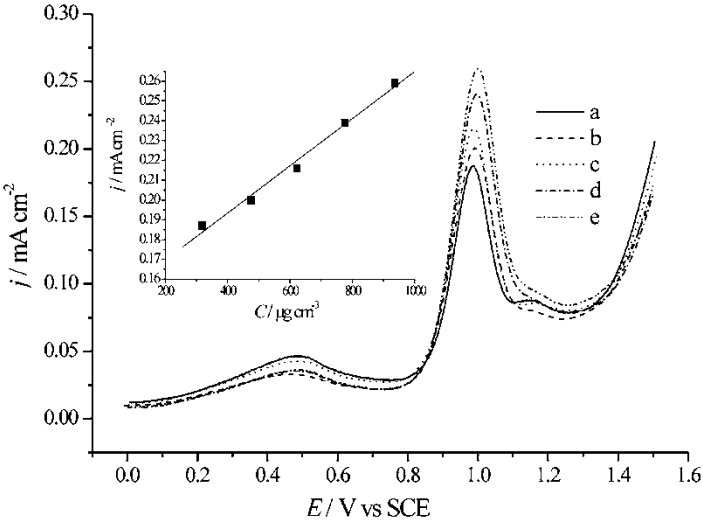

Fig. 2.67 Square wave anodic stripping voltammograms of clopidogrel at a gold electrode in acetate buffer (pH 3.7). Clopidogrel concentration: (*a*) 317.89, (*b*) 474.49, (*c*) 622.03, (*d*) 775.63, and (*e*) 935.16 μg cm^{-3}. Accumulation time: 180 s at $E = 0.0$ V; step size 2 mV, pulse size 20 mV, frequency 8 Hz, scan rate 15 mVs^{-1}. *Inset*: The linear dependency of the anodic peak current vs. concentration of clopidogrel (Reproduced with a permission from Serbian Chemical Society) [32]

of quantification (*LOQ*), and recovery. The *LOD* and *LOQ* were calculated from the calibration curves as kSD/b where $k = 3$ for *LOD* and 10 for *LOQ*, *SD* is the standard deviation of the intercept and b is the slope of the calibration curve. The *LOD* and *LOQ* values for the SW voltammetry method were 117.50 and 391.66 μg cm^{-3}, respectively.

Recovery studies were also performed to judge the accuracy of the SW voltammetry method by performing six measurements at low, intermediate, and high CLP concentrations (317.89, 622.03 and 935.16 μg cm^{-3}). Mean percentage recoveries of 99.6 % with relative standard deviation of 1.11 % were found and are presented in Table 2.4.

Table 2.4 Determination of clopidogrel by SWV, UV-spectrophotometry, and HPLC

Parameter	SWV	UV	HPLC
Range (mg cm^{-3})	0.317–0.935	0.030–0.747	0.032–0.962
Regression equation[a]			
Slope	0.00012	1.8104	233358783.00
S.D. of slope	7.09×10^{-6}	0.0003	0.0026
Intercept	0.1457	0.0076	36117.71
S.D. of intercept	0.0047	0.0001	0.0030
Regression coefficient	0.9947	0.9999	0.9999
Recovery (%)	99.6	99.94	99.57
S.D. (%)	1.11	1.65	1.38
LOD (μg cm^{-3})	117.50	8.56	8.24
LOQ (μg cm^{-3})	391.66	30.46	29.28

Reproduced with a permission from Serbian Chemical Society [32]

[a] $Y = a + bC$ where C is concentration of clopidogrel in mg cm^{-3}; Y is current per area unit (mA cm^{-2}), absorbance (A) and peak area unit (mAu), for SWV, UV, and HPLC methods, respectively. S.D.: standard deviation

Some selected examples of various applications of electrochemical methods in pharmaceutical analysis are given in following Table 2.5.

2.3 Conclusion

Recent trends in development of electrochemical methods for analysis of pharmaceuticals are listed with the highlights of electrochemical methods of analysis of antibiotics, cardiovascular drugs, central nervous system drugs, anticancer drugs, anti-inflammatory drugs, and miscellaneous drugs on gold electrode in neutral electrolytes. A polycrystalline gold electrode was selected as the optimal working electrode for the examination of the pharmaceutical compounds because it is defined with a completely reproducible cyclic voltammograms and, consequently, all the electrochemical reactions at this electrode can be attributed only to

Table 2.5 Selected papers of electrochemical methods for analysis of pharmaceuticals (2006–2015)

No	Analytes/drugs	Electrochemical methods	Electrode type	Medium	application	Reference
2.1. Antibiotics						
1	Ciprofloxacin (norfloxacin)	CV	GC	Aqueous solution 0.14 Phosphate buffer (pH 7.0)	Biological fluids	[33]
2	Netilmicin	LSASV	HMDE	BR buffer (pH=8.7)	Spiked humane urine, serum injectable formulations	[34]
3	Azithromycin	CV	Au	0.05 $NaHCO_3$ 0.05 $NaHCO_3$/CH_3OH 50/50	Standard capsules	[6]
4	Cephalosporins (cephalexin, cephalothin)	CV, DPV	CPE CPE/CoSal	Buffered solution (pH 3.0)	Human serum	[35]
5	Tetracyclines	CV	MWCNT-GCE	Phosphate buffer (pH 2.5)	Standards Water samples	[36]
6	Tetracyclines	CV	Au modified	Strong acidic electrolyte	Wastewater residues	[37]
7	Clarithromycin	CV	Au	0.05 M $NaHCO_3$	Standard tablets	[9]
8	Perfloxacin	CV, DPV, SWV	GC, BDDE	0.05 M $H2SO_4$ Acetate buffer pH 4 Acetate buffer pH 6	Tablet, ampule human serum	[38]

(continued)

Table 2.5 (continued)

No	Analytes/drugs	Electrochemical methods	Electrode type	Medium	application	Reference
9	Erythromycin A	CV	Au	0,05 $NaHCO_3$	Tablets	[10]
10	Ciprofloxacin	CV	MWCNT/GCE	Phosphate buffer (pH 7.0)	Urine/serum	[39]
11	Roxythromycin	CV, DPV	Au	0.05 M NaHCO3	Solid dosage form	[11]
12	Macrolide antibiotics	CV	Au	0.05 M $NaHCO_3$	Capsule, tablet	[40]
13	Macrolide antibiotics	CV	Au	0.05 M $NaHCO_3$	Solid dosage forms	[41]
14	Midecamycin	CV	Au	0.05 M $NaHCO_3$	Standard solid dosage forms	[42]
15	Rifampicin	Ads SV, SWV	GC, Pb-film electrode	Acetate buffer (pH 5.0)	Pharmaceutical formulations	[43]
16	Cefdinir	CV, SW adsv	HMDE	Phosphate buffer	Urine	[44]
17	Doxycycline	DPV, CV	MIP, NIP	BR buffer (pH 2.0–4.0)	Pharmaceutical samples	[45]
18	Cefixime	DPV, SWV, CV	GC	Acetate buffer (pH 3.5–5.5)	Serum, urine, breast milk	[46]
				BR buffer (pH 2.32–8.0)		
2.2. Cardiovascular drugs						
19	Atenolol	DPV	Graphite-polyurethane (60 %, w/w) composite	Universal buffer pH 10.0 phosphate buffer pH 7.4	Pharmaceutical formulations (tablets)	[47]

20	Antihypertensive drugs	CV	GC	BR buffer pH 2–11	Effect of surfactant Urine, tablets	[48]
21	Verapamil	DPV, OSWV	GC	Sulfuric acid (0.1, 0.5 M) acetate buffer (0.2 M, pH 3.51–5.71), phosphate buffer (0.2 M pH 2.5–12.01)	Ampule, tablets	[49]
22	Bisoprolol	DPV	GC, SWNT	BR buffer (0.04 M, pH 2.20–11.04), phosphate buffer pH 3.4–10	Urine	[50]
23	Cinnarizine	CV, ADSV	GC	BR buffer (pH 2.5–11.5)	Commercial formulations Spiked serum	[51]
24	Cinnarazine	CV, DPV	MWCNT	BR buffer pH 2.5	Pharmaceutical formulations, urine	[52]
25	Amlodipine	CV, SWV	MWCNT-modified	pH 7.2	Tablets, urine	[53]
26	Atorvastatin	CV, Ads DPV Ads SWV	GC	BR buffer pH 2.5	Dosage forms urine, serum	[54]

(continued)

Table 2.5 (continued)

No	Analytes/drugs	Electrochemical methods	Electrode type	Medium	application	Reference
27	Amlodipine	SWV, CV	Au	Phosphate buffer (pH 11)	Tablet	[14]
			Au-/o-MWCNT	0.05 M $NaHCO_3$	Standards	
28	Metoprolol	CV, SWV, DDP	HMDE, GCE	BR buffer pH 10.5, 3.0	Tablets, human serum	[55]
29	Amlodipin, Nifedipin	CV, SWV	Au	Phosphate buffer (pH 11)	Cyclodextrin, inclusion complexes	[16]
				0.05 M $NaHCO_3$		
30	Atorvastatin	CV, DPAdsv	VACNT-GO	Phosphate buffer (pH 2.0)	Tablet	[56]
31	Atorvastatin Amlodipine	DPV, SWV	GC	0.5 M H_2SO_4 pH 5.0	Binary mixtures	[57]
				BR buffer 3.0–9.0		
32	Verapamil	SWAdasv	MWCNT-PAH	0.25 M H_2SO_4	Tablets	[58]
	Propranolol	DPAdasv	GCE			
33	Valsartan	CV, DPP	HMDE	BR buffer (pH 6.0)	Tablets	[59]
34	Carvedilol	CV, LSW	Pt-electrode	Acetonitrile/0.1 M	Pharmaceutical preparations	[60]
				Tetrabutylammonium perchlorate		
2.3. Central nervous system drugs						
35	Carbidopa, Levodopa	DPV, CV	GC	0.1 M $HClO_4$	Pharmaceutical products	[61]

36	Lorazepam	DPV	HMDE	BR buffer (pH = 2.0)	Pharmaceutical preparations, tablets, urine, plasma	[62]
37	Paroxetine	SWAdsv, FIA-SWAdsv	HMDE	pH 8.8/borate buffer, 0.2 mol/L	Pharmaceutical products	[63]
38	Flavoxate	DPV, CV	HMDE	pH 4 acetate buffer	Tablets	[64]
39	Promethazine	CV, DPV	DNA/GCE (ox)	0,1 M acetate buffer pH = 5.0	Human blood samples	[65]
40	1,4-Benzodiazepines	CV	CPE-modified	Br buffer (pH 2.5/10.0)	Plasma, urine, standards	[62]
41	Fluoxetine	SWAdsSV	HMDE	phosphate buffer (pH 12.0)	Standards, human plasma	[66]
42	Clozapine	CV, DPV	Au-modified	0.05 M tris–HCl (pH 8.1)	Tablets	[67]
43	Domperidone	DPV, CV	GC	BR buffer (pH 2.6–10.3)	Tablets/waste water	[68]
44	Tetrazepam	DPP, ADSCV, DPV, SWV	HMDE	pH 11, pH 7	Tablet, bulk form, human serum	[69]
45	Trazodone	CV, DPV	MWCNT-modified GCE	Phosphate buffer 0.2 M, pH 7.0	Tablets, urine	[70]
46	Gabapentin	CV, DPV	Au	pH 12.0, 0.2 M buffer	Standards, urine	[71]

(continued)

Table 2.5 (continued)

No	Analytes/drugs	Electrochemical methods	Electrode type	Medium	application	Reference
47	Sertindole	CV	GC, BDDE	0.1 M H_2SO_4	Tablets	[72]
				BR buffer (pH = 3; 5), phosphate buffer		
48	Amphetamine drugs	DPV	GC	phosphate buffer pH 7.3	Tablets, standards, human serum	[73]
49	Pyridostigmine-bromide	SWCADSV DPCADSV, ADSV	Hg	BR buffer (pH 3.8)	Pharmaceutical dosage forms	[74]
50	Naratriptan	DPV	GC	BR buffer 0.1 M	Tablets	[75]
51	Ziprasidone	CV, DPV, SWV	BDDE, GCE	0.1 M H_2SO_4	Capsule, spiked serum	[76]
				Acetone buffer pH 4.75		
52	1,4-benzodiazepine	SWV	GCE-modified	0.15 M acetate buffer, pH 4.75	Pharmaceutical formulations	[77]
53	Methyldopa	SWV	MWCNT modified	0.1 M phosphate buffer	Tablets, urine	[78]
54	Carbamazepine	CV	Au	phosphate buffer (pH 7.0)	Tablets	[17]
55	Amphetamine	CV, SWV	Au	0.5 M $NaHCO_3$	Tablets, spiked urine	[18]

56	Donepezil	CV, SWV	Au	pH 3 phosphate buffer	Tablets	[19]
57	Levodopa, Cabergoline	CV, SWV	CPE-modified graphene nanosheets	pH 7.0	Human serum, urine, pharmaceutical formulations	[79]
58	Haloperidol	DPV, SWV	CPE-modified, MWCNT	BR buffer (pH 4.5–8.5)	Pharmaceutical samples, biological fluids	[80]
59	Amphetamine/ecstasy	SWV	GC	BR buffer (pH 1.2–12.2)	Spiked human serum	[16]
2.4. Anticancer drugs						
60	Rutin	CV, CASV	HMDE	BR buffer (pH 2–12), phosphate buffer (pH acetate buffer 2–8)	Tablets, human urine, blood serum	[81]
61	Acetylspiramycin	CV, DPV	GCE/MWNT/DHP	pH 4.0–8.0 phosphate buffer	Tablets	[82]
62	Gemcitabine	CV, DPV	GCE	Phosphate buffer (pH 7.4), BR buffer (pH 2–11)	Bulk/pharmaceutical formulations, injections	[83]
63	Gemcitabine	CV, DPV	Au	Phosphate buffer (pH 3.0–12.0)	Pharmaceutical formulations	[84]
64	Danusertib	CV, DPV, SWV	Au	0.1 M phosphate buffer (pH 7.0)	Pharmaceutical formulation	[85]
65	Picoplatin	CV, DPV	MWNT/GCE	0.05 mol/L KCl (pH 7.4)	Injection	[86]

(continued)

Table 2.5 (continued)

No	Analytes/drugs	Electrochemical methods	Electrode type	Medium	application	Reference
66	Idarubicin	CV, DPV, Ads DPV	GCE, MWCNT/GC	Phosphate buffer (pH 3.0)	Injection	[28]
67	Zanosar	DPP, CV	HMDE	pH 4.0	Urine samples, pharmaceutical preparations	[87]
68	Tamoxifen	DPADASV SWADASV, CV	GCE	BR buffer (pH 2–10)	Tablets, human blood	[29]
69	Temozolomide	DPV	GC	0.1 M phosphate buffer pH 7.0	Biosensor	[88]
2.5. Anti-inflammatory drugs						
70	Nimesulide	CV, DPV	GCE, CNT/GCE	0,05 M H_2SO_4	Human serum, tablets	[89]
71	Lidocaine	SWV, CV	BDDE	BR buffer (0.1 M) + 2 M NaOH	Pharmaceutical preparation	[90]
72	Meloxicam	CV, ASV	GC	Phosphate buffer (pH 6.0), BR buffer (pH 2–8)	Tablets, urine, plasma	[91]
73	Meloxicam	CV	GCE	Phosphate buffer	Standard	[92]
74	Sumatriptan	CV	PGE/MWCNT	BR buffer (pH 7,4)	Tablets	[93]

75	Ketoprofen	CV	DDDE, Pt	pH 6.0	Standard	[94]
76	Mefenamic acid, indomethacin, diclofenac	CV, DPV	GC	Phosphate buffer	Standards	[95]
77	NSAID-s	CV	ANMGC, Pt	0.1 M $LiClO_4$	Standards	[94]
				MeOH, EtOH, CH_3CN, mixture/H_2O		
78	Ibuprofen	CV, DPV	BDDE	BR buffer (pH 2–10)	Standards	[96]
79	Oxaprozin	CV	Pt, BSA-modified	0.05 M $NaHCO_3$	Standards	[30]
80	Paracetamol	DPV, CV	CILE, TCPE	pH = 4.6	Tablets, urine samples	[97]
2.6. Miscellaneous drugs						
81	Abacavir	DPAdsV, CV	MWCNT/EPPGE	BR buffer (pH 2.5), (0.04 M, pH 2–9), 0.1 M H_2SO_4	Tablets, human serum	[98]
82	Spironolactone drugs (aldactone)	CV, DPPAdsV	HMDE	BR buffer (pH 2.5)	Tablets, spiked urine, serum	[99]
83	Chloroquine	CV, DPV	DNA-modified CP	0.1 M phosphate buffer (pH 5.5)	Tablets	[100]
	Primaquine		CPE-modified (Cu-Nw-CPE)			

(continued)

Table 2.5 (continued)

No	Analytes/drugs	Electrochemical methods	Electrode type	Medium	application	Reference
84	Fosamprenavir	CV	GC, BDDE	0.1 M H_2SO_4	Tablets, urine samples	[101]
				Phosphate buffer pH 2.0		
85	Metformin	SWV, LSP, DPV	Pt	Acetate buffer pH 4.7	Urine, tablets	[102]
				MOPS buffer (pH 3.8–8.0)		
86	Nandrolone	SWV, CV, DPV	Fullerene-C60 modified electrode	0.1 M phosphate buffer (pH 2.0–10.0)	Blood and urine samples injection	[103]
87	Fluvastatin	CV, DPV, SWV	BDDE	BR buffer (pH 10.0)	Tablets, human serum	[104]
88	Valacyclovir	CV, DPV, SWV	GC	0.2 M Na_2SO_4	Tablets, gastric fluid, serum	[105]
				BR buffer pH 10.0		
				Phosphate buffer, pH 4.2		
89	Epinephrone/ascorbic acid	CV, SWASV, SLSV	SAM/Au	Sodium borate buffer (pH 4.4)	Simultaneous determination	[106]
					Standards/mixture	
90	Simvastatin	CV, SWV	Graphite electrode Hg	0.1 M $Na_2B_4O_7$-KH_2PO_4, pH 7.0, (buffer)	Pharmaceutical dosage formulations	[107]

91	Lamivudine	CV	HMDE	pH 3.4 (phosphate buffer)	Pharmaceutical formulations	[108]
92	Abacivir	LSV	HMDE	0.1 M sulfuric acid, acetate buffer, phosphate buffer, borate buffer	Tablets	[98]
93	Glipizide	CV, SWV-AdSV	HMDE	BR buffer (pH 6.0)	Tablets	[109]
94	Prednisolone	CV, OSWV	GC	0.4 M H_2SO_4 (pH 0,56)	Tablets, human serum	[110]
95	Danazol	SWV, CV, Sw-AdSv	HMDE	BR buffer (pH 2)	Capsules	[111]
96	Tinidazole	CV	poly (carmine) film modified GCE	Phosphate buffer (pH 5.7)	Tablets, ampule	[112]
97	Acyclovir	CV, LSV	MWNT-DHP film, GCE	Citrate–sodium hydrogen phosphate buffer (pH 7.36)	Tablets	[113]
98	Estrogens	CV, LSV, SWV	MWNT/GCE Pt/ MWNT/GCE	Phosphate buffer solution (pH 7.0)	Sensor	[114]
99	Oseltamivir	CV	Au	0.05 M $NaHCO_3$	Capsule	[31]
100	Omeprazol	DPP, CV	SMDE	Buffered solution 0,05 M pH 8	Standard acid decomposition	[115]

(continued)

Table 2.5 (continued)

No	Analytes/drugs	Electrochemical methods	Electrode type	Medium	application	Reference
101	Omeprazol	DPP, CV	GC	Acetic acid/sodium acetate buffer pH 5.10	Enteric-coated tablets	[116]
102	Prednisone/Prenisolone	OSWV	GC	Phosphate buffer (pH 7.2)	Pharmaceutical formulations, serum	[117]
103	Clopidogrel	CV, SWASV	Au	Acetate buffer (pH 3.7)	Solid dosage forms	[32]

BR buffer-Britton Robinson buffer, *CV* cyclic voltammetry, *GC* glassy carbon, *Au* gold, *LSASV* linear sweep adsorptive stripping voltammetry, *CPE/Cosal* carbon paste electrode modified with Co salophen, *HMDE* hanging mercury drop electrode, *MWCNT-GCE* multiwalled carbon nanotube modified electrode, *Ni-DIA* diamond thin film electrode modified with nickel, *BDDE* boron doped diamond electrode, *UME* ultramicroelectrode, *SMDE* static mercury drop electrode, *DPP* differential pulse polarography, *DPV* differential pulse voltammetry, *GC* glassy carbon, *OSW* osteryoung square wave voltammetry, *ADSSWV* adsorptive square wave voltammetry, *VACNT-GO* vertically aligned carbon nanotube/graphene oxide, *DPADSV* differential pulse adsorptive stripping voltammetry, *MWCNT-PAH/GCE* glassy carbon electrode modified with functionalized multiwalled, *SWADSV* square wave adsorptive stripping voltammetry, *FIA* flow injection analysis, *DPP* differential pulse polarography, *DNA/GCE(ox)-ds* DNA-modified electrode/pretreated glassy carbon, *Si-TipH* silica gel modified with titanium phosphate, *ADSCV* adsorptive cathodic stripping electrode, *CASV* cathodic stripping voltammetry, *SWNT* single wall carbon nanotubes, *DHP* dihexadecyl hydrogen phosphate, *DPAdSV* differential pulse adsorptive anodic stripping voltammetry, *CNT/GCE* carbon nanotubes modified GCE, *CILE* carbon ionic liquid electrode, *ANMGC* alumina nanoparticle modified glassy carbon, *EPPGE* edge plane pyrolitic graphite electrode, DNA-modified CP, *Cu-Nw-CPE* CPE modified by $Cu(OH)_2$ nanowire, *LSV* linear sweep voltammetry, *SAM/Au* self-assembled monolayer, *OSWV* osteryoung square wave voltammetry modified, *MWNT/GCE* multiwalled carbon nanotubes modified glassy carbon electrode

the studied molecule in the analysis of these drugs. CV, SWV, and DPV were used in combination with HPLC, AFM, FTIR, and MS–MS in the investigations of aforementioned drugs. The presented data show that different electrochemical methods with the use of gold as working electrode combined with spectroscopic, spectrometric, and chromatographic techniques gave a fast quantitative and qualitative response of the investigated standards as well as of the commercial drugs. With the drugs analysis in biological samples the very important data were collected for the further clinical investigations.

Acknowledgments The work was supported by the Ministry of Education, Science and Technological Development of the Republic of Serbia (Grant No. ON172013).

References

1. Ozkan SA (2012) Electroanalytical methods in pharmaceutical analysis and their validation. HNB, New York
2. Gupta V, Jain R, Radhapyari K, Jadon N, Agarwal S (2011) Voltammetric techniques for the assay of pharmaceuticals—a review. Anal Biochem 408:179–196
3. Barek J, Fischer J, Navratil T, Peckova K, Yosypchuk B, Zima J (2007) Nontraditional electrode materials in environmental analysis of biologically active organic compounds. Electroanalysis 19:2003–2014
4. Gupta AK, Dubey RS, Malik JK (2013) Application of modern electroanalytical techniques: recent trend in pharmaceutical and drug analysis. Int J Pharm Sci Res 4:2450–2458
5. Avramov-Ivić M, Jovanović V, Vlajnić G, Popić J (1997) The electrocatalytic properties of the oxides on noble metals in electrooxidation of some organic molecules. J Electroanal Chem 423:119–124
6. Avramov Ivic ML, Petrovic SD, Mijin DZ, Zivkovic PM, Kosovic IM, Drljevic KM, Jovanovic MB (2006) Studies on electrochemical oxidation of azithromycin and Hemomycin® at gold electrode in neutral electrolyte. Electrochim Acta 51:2407–2416
7. Antonio A, Mazzone MG, Moschetti V, Blanco AR (2001) Process for the preparation of aqueous formulations for ophthalmic use. US patent 6,277,829
8. Dawson CR, Bowman LM (2003) Topical treatment or prevention of ocular infections. US patent 6,569,443

9. Avramov Ivic ML, Petrovic SD, Vonmoos F, Mijin DZ, Zivkovic PM, Drljevic KM (2007) The qualitative electrochemical determination of clarithromycin and spectroscopic detection of its structural changes at gold electrode. Electrochem Commun 9:1643–1647
10. Avramov Ivic ML, Petrovic SD, Mijin DZ, Vanmoos F, Orlovic DZ, Marjanovic DZ, Radovic VV (2008) The electrochemical behavior of erythromycin A on a gold electrode. Electrochim Acta 54:649–654
11. Drljevic-Djuric KM, Jovic VD, Lacnjevac UC, Avramov Ivic ML, Petrovic SD, Mijin DZ, Djordjevic SB (2010) Voltammetric and differential pulse determination of roxithromycin. Electrochim Acta 56:47–52
12. Tolić LJ, Lović J, Petrović S, Mijin D, Grujić S, Laušević M, Avramov Ivić M (2015) Investigation of electrochemical behavior of anisomycin on gold electrode followed by HPLC–MS/MS analysis. Electrochem Commun 58:20–24
13. Laviron E (1979) The use of linear potential sweep voltammetry and of a.c. voltammetry for the study of the surface electrochemical reaction of strongly adsorbed systems and of redox modified electrodes. J Electroanal Chem 100:263–270
14. Stoiljković ZŽ, Avramov Ivić ML, Petrović SD, Mijin DŽ, Stevanović SI, Lačnjevac UČ, Marinković AD (2012) Voltammetric and square-wave anodic stripping determination of amlodipine besylate on gold electrode. Int J Electrochem Sci 7:2288–2303
15. Goyal RN, Bishnoi S (2010) A novel multi-walled carbon nanotube modified sensor for the selective determination of epinephrine in smokers. Bioelectrochemistry 79:234–240
16. Stoiljković ZZ, Jovanović VM, Mijin DŽ, Nikolić V, Nikolić LJ, Petrović SD, Avramov Ivić ML (2013) The electrochemical investigation of inclusion complexes of nifedipine and amlodipine with β-cyclodextrin and (2-hydroxypropyl)-β-cyclodextrin. Int J Electrochem Sci 8:9543–9557
17. Trišović NP, Božić BĐ, Petrović SD, Tadić SJ, Avramov Ivić ML (2014) Electrochemical characterization and determination of carbamazepine as pharmaceutical standard and tablet content on gold electrode. Hem Ind 68:207–212
18. Nevešćanin MM, Avramov Ivić ML, Petrović SD, Mijin DŽ, Banović Stević SN, Jovanović VM (2013) The use of a gold electrode for the determination of amphetamine derivatives and application to their analysis in human urine. J Serb Chem Soc 78:1373–1385
19. Mladenovic AR, Mijin DZ, Drmanic SZ, Vajs VE, Jovanovic VM, Petrovic SD, Avramov Ivic ML (2014) Electrochemical oxidation of donepezil and its voltammetric determination at gold electrode. Electroanalysis 26:893–897
20. Iimura Y, Naito T, Senaga M, Yamanishi Y (1997) Aralkylpiperidine derivative. JP Patent 09268176, CAN127:293137
21. Golcu A, Ozkan SA (2008) Electroanalytical determination of donepezil HCl in tablets and human serum by differential pulse and osteryoung square wave voltammetry at a glassy carbon electrode. Pharmazie 61:760–765

22. Grimshaw J (2000) Electrochemical reactions and mechanisms in organic chemistry. Elsevier, Amsterdam
23. Trišović NP, Božić BDJ, Lović JD, Vitnik VD, Vitnik ŽJ, Petrović SD, Avramov Ivić ML (2015) Electrochemical characterization of phenytoin and its derivatives on bare gold electrode. Electrochim Acta 161:378–387
24. Zhang J, Heineman WR, Halsall HB (1999) Capillary electrochemical enzyme immunoassay (CEEI) for phenobarbital in serum. J Pharm Biomed Anal 19:145–152
25. Clinical Practice Guidelines (2008) Febrile seizures: clinical practice guideline for the long-term management of the child with simple febrile seizures. Pediatrics 121:1281–1286
26. Ni Y, Wang Y, Kokot S (2004) Differential pulse stripping voltammetric determination of paracetamol and phenobarbital in pharmaceuticals assisted by chemometrics. Anal Lett 37:3219–3235
27. Raoof JB, Baghayeri M, Ojani R (2012) A high sensitive voltammetric sensor for qualitative and quantitative determination of phenobarbital as an antiepileptic drug in presence of acetaminophen. Colloids Surf B Biointerfaces 95:121–128
28. Kurbanoglu S, Dogan-Topal B, Uslu B, Can A, Ozkan SA (2013) Electrochemical investigations of the anticancer drug idarubicinusing multiwalled carbon nanotubes modified glassy carbonand pyrolytic graphite electrodes. Electroanalysis 25:1473–1482
29. Sharma DK, Mourya GL, Jhankal KK, Jones LA, Bhargava SK (2012) Electrochemical behaviour and validated determination of the anticancer drug tamoxifen. Der Pharm Lett 4:1599–1606
30. Bozic BDJ, Avramov Ivic ML, Trisovic NP, Petrovic SD, Uscumlic GS (2012) Electrochemical characterization of oxaprozin on bare gold electrode and electrode modified with bovine serum albumin. Int J Electrochem Sci 7:11609–11616
31. Avramov Ivić ML, Petrović SD, Mijin DŽ, Drljević-Đurić KM (2011) The qualitative determination of oseltamivir phosphate in Tamiflu® capsule by cyclic voltametry. Hem Ind 65:87–91
32. Mladenović AR, Jovanović VM, Petrović SD, Mijin DŽ, Drmanić SŽ, Avramov Ivić ML (2013) Determination of clopidogrel using square wave voltammetry at a gold electrode. J Serb Chem Soc 78:2131–2140
33. Torriero AAJ, Salinas E, Raba J, Silber JJ (2006) Sensitive determination of ciprofloxacin and norfloxacin in biological fluids using an enzymatic rotating biosensor. Biosens Bioelectron 22:109–115
34. Sun N, Mo W, Hu B, Shen Z (2006) Adsorptive stripping voltammetric determination of netilmicin in the presence of formaldehyde. Anal Bioanal Chem 385:161–167
35. Jamasbi ES, Rouhollahi A, Shahrokhian S, Haghgooc S, Aghajani S (2007) The electrocatalytic examination of cephalosporins at carbon paste electrode modified with CoSalophen. Talanta 71:1669–1674
36. Vega D, Agüí L, González-Cortés A, Yáñez-Sedeño P, Pingarrón JM (2007) Voltammetry and amperometric detection of tetracyclines at

multi-wall carbon nanotube modified electrodes. Anal Bioanal Chem 389:951–958
37. Wang H, Zhao H, Quan X (2012) Gold modified microelectrode for direct tetracycline detection. Front Environ Sci Eng 6:313–319
38. Uslu B, Topal BD, Ozkan SA (2008) Electroanalytical investigation and determination of perfloxacin in pharmaceuticals and serum at boron-doped diamond and glassy carbon electrodes. Talanta 74:1191–1200
39. Fotouhi L, Alahyari M (2010) Electrochemical behavior and analytical application of ciprofloxacin using a multi-walled nanotube composite film-glassy carbon electrode. Colloid Surf B 81:110–114
40. Avramov Ivić ML, Petrović SD, Mijin DŽ (2007) A study of the electrochemical activity of some macrolide antibiotics on a gold electrode in a neutral electrolyte. J Serb Chem Soc 72:1427–1436
41. Avramov Ivić ML, Petrović SD, Živković PM, Mijin DŽ, Drljević KM (2010) A study of the catalytic role of a gold electrode in the electrochemical activation of four macrolide antibiotics in sodium bicarbonate solution. Chem Ind Chem Eng Q 16:111–116
42. Drljevic Djuric KM, Avramov Ivic ML, Petrovic SD, Mijin DZ, Jadranin MB (2011) A voltammetric method for the quantitative determination of midecamycin compared to its simultaneous HPLC determination. Russ J Electrochem 47:781–786
43. Tyszczuk K, Korolczuk M (2009) New protocol for determination of rifampicine by adsorptive stripping voltammetry. Electroanalysis 21:101–106
44. Jain R, Radhapyari K, Jadon N (2007) Electrochemical evaluation and determination of cefdinir in dosage form and biological fluid at mercury electrode. J Electrochem Soc 154:F199–F204
45. Gurler B, Ozkorucuklu SP, Kir E (2013) Voltammetric behavior and determination of doxycycline in pharmaceuticals at molecularly imprinted and non-imprinted overoxidized polypyrrole electrodes. J Pharm Biomed Anal 84:263–268
46. Golcu A, Dogan B, Ozkan SA (2005) Anodic voltammetric behavior and determination of cefixime in pharmaceutical dosage forms and biological fluids. Talanta 67:703–712
47. Cervini P, Ramos LA, Cavalheiro ETG (2007) Determination of atenolol at a graphite–polyurethane composite electrode. Talanta 72:206–209
48. Atta NF, Darwish SA, Khalil SE, Galal A (2007) Effect of surfactants on the voltammetric response and determination of an antihypertensive drug. Talanta 72:1438–1445
49. Demircan Ş, Kır S, Ozkan SA (2007) Electroanalytical characterization of verapamil and its voltammetric determination in pharmaceuticals and human serum. Anal Lett 40:1177–1195
50. Goyal RN, Tyagi A, Bachheti N, Bishnoi S (2008) Voltammetric determination of bisoprolol fumarate in pharmaceutical formulations and urine using single-wall carbon nanotubes modified glassy carbon electrode. Electrochim Acta 53:2802–2808

51. Hegde RN, Hosamani RR, Nandibewoor ST (2009) Voltammetric oxidation and determination of cinnarizine at glassy carbon electrode modified with multi-walled carbon nanotubes. Colloid Surf B 72:259–265
52. El-Sayed GO, Yasin SA, El Badawy AA (2008) Voltammetric behavior and determination of cinnarizine in pharmaceutical formulations and serum. Anal Lett 41:3021–3033
53. Goyal RN, Bishnoi S (2010) Voltammetric determination of amlodipine besylate in human urine and pharmaceuticals. Bioelectrochemistry 79:234–240
54. Eskikoy D, Durmus Z, Kilic E (2011) Electrochemical oxidation of atorvastatin and its adsorptive stripping determination in pharmaceutical dosage forms and biological fluids. Collect Czech Chem Commun 76:1633–1649
55. Zorluoglu SL, Tasdemir IH, Ece A, Kiliç E (2013) A cooperative computational and experimental investigation on electrochemical behavior of metoprolol and its voltammetric determination. Can J Chem 91:951–959
56. Silva TA, Zanin H, Vicentini FC, Corat EJ, Fatibello-Filho O (2014) Differential pulse adsorptive stripping voltammetric determination of nanomolar levels of atorvastatin calcium in pharmaceutical and biological samples using a vertically aligned carbon nanotube/graphene oxide electrode. Analyst 139:2832–2841
57. Dogan-Topal B, Bozal B, Demircigil T, Uslu B, Ozkan S (2009) Electroanalytical studies and simultaneous determination of amlodipine besylate and atorvastatine calcium in binary mixtures using derivative of the ratio-voltammetric methods. Electroanalysis 21:2427–2439
58. Oliveira GS, Azzi DC, Vicentini FC, Sartori ER, Fatibello-Filho O (2013) Voltammetric determination of verapamil and propranolol using a glassy carbon electrode modified with functionalized multiwalled carbon nanotubes within a poly (allylamine hydrochloride) film. J Electroanal Chem 708:73–79
59. Habib IHI, Weshay SA, Toubar SS, El-Alamin MM (2008) Stripping voltammetric determination of valstartan in bulk and pharmaceutical products. Pharmazie 63:337–341
60. Yilmaz B, Ekinci D (2010) Voltammetric behavior of carvedilol in nonaqueous media and its analytical determination in pharmaceutical preparations. Rev Anal Chem 30:187–193
61. Socorro M, Quintino M, Yamashita M, Angnes L (2006) Voltammetric studies and determination of levodopa and carbidopa in pharmaceutical products. Electroanalysis 18:655–661
62. Ghasemi J, Niazi A, Ghorbani R (2006) Determination of trace amounts of lorazepam by adsorptive cathodic differential pulse stripping method in pharmaceutical formulations and biological fluids. Anal Lett 39:1159–1169
63. Nouws HPA, Delerue-Matos C, Barros AA, Rodrigues JA (2006) Electroanalytical determination of paroxetine in pharmaceuticals. J Pharm Biomed Anal 42:341–346

64. Ghoneim MM, El-Attar MA, Razeq SA (2006) Voltammetric quantitation at the mercury electrode of the anticholinergic drug flavoxate hydrochloride in bulk and in pharmaceutical formulation. Cent Eur J Chem 5:496–507
65. Yang ZS, Zhao J, Zhang DP, Liu YC (2007) Electrochemical determination of trace promethazine hydrochloride by a pretreated glassy carbon electrode modified with DNA. Anal Sci 23:569–572
66. Nouws HPA, Delerue-Matos C, Barros AA, Rodrigues JA, Santos-Silva A, Borges F (2007) Square-wave adsorptive-stripping voltammetric detection in the quality control of fluoxetine. Anal Lett 40:1131–1146
67. Huang F, Qu S, Zhang S, Liu B, Kong J (2007) Sensitive detection of clozapine using a gold electrode modified with 16-mercaptohexadecanoic acid self-assembled monolayer. Talanta 72:457–462
68. El-Shahawi MS, Bahaffi SO, El-Mogy T (2007) Analysis of domperidone in pharmaceutical formulations and wastewater by differential pulse voltammetry at a glassy-carbon electrode. Anal Bioanal Chem 387:719–725
69. Ghoneim M, El-Desoky HS, El-Ries MA, Abd-Elaziz AM (2008) Electrochemical determination of muscle relaxant drug tetrazepam in bulk form, pharmaceutical formulation, and human serum. Chem Pap 62:127–134
70. Hegde RN, Shetti NP, Nandibewoor ST (2009) Electro-oxidation and determination of trazodone at multi-walled carbon nanotube-modified glassy carbon electrode. Talanta 79:361–368
71. Hegde RN, Kumara Swamy BE, Shetti NP, Nandibewoor ST (2009) Electro-oxidation and determination of gabapentin at gold electrode. J Electroanal Chem 635:51–57
72. Altun Y, Dogan-Topal B, Ozkan SB (2009) Anodic behavior of sertindole and its voltammetric determination in pharmaceuticals and human using glassy carbon and boron-doped diamond electrodes. Electrochim Acta 54:1893–1903
73. Garrido EMPJ, Garrido JMPJ, Milhazes N, Borges F, Oliveira-Brett AM (2010) Electrochemical oxidation of amphetamine-like drugs and application to electroanalysis of ecstasy in human serum. Bioelectrochemistry 79:77–83
74. Jain R, Gupta VK, Jadon N, Radhapyari K (2010) Adsorptive stripping voltammetric determination of pyrodistigmine bromide in bulk, pharmaceutical formulations and biological fluid. J Electroanal Chem 648:20–27
75. Velasco-Aguirre C, Álvarez-Lueje A (2010) Voltammetric behavior of naratriptan and its determination in tablets. Talanta 82:796–802
76. Kul D, Gumustas M, Uslu B, Ozkan SA (2010) Electroanalytical characteristics of antipsychotic drug ziprasidone and its determination in pharmaceuticals and serum samples on solid electrodes. Talanta 82:286–295
77. Lozano-Chaves ME, Palacios-Santander JM, Cubillana-Aguilera LM, Naranjo-Rodrıguez I, Hidalgo-Hidalgo-de-Cisneros JL (2006) Modified carbon-paste electrodes as sensors for the determination of 1,4-benzodi-

azepines: Application to the determination of diazepam and oxazepam in biological fluids. Sens Actuator B Chem 115:575–583
78. Fouladgar M, Karimi-Maleh H (2013) Ionic liquid/multiwall carbon nanotubes paste electrode for square wave voltammetric determination of methyldopa. Ionics 19:1163–1170
79. Tajik S, Taher MA, Beitollahi H (2014) First report for electrochemical determination of levodopa and cabergoline: application for determination of levodopa and cabergoline in human serum, urine and pharmaceutical formulations. Electroanalysis 26:796–806
80. Bagheri H, Afkhami A, Panahi Y, Khoshsafar H, Shirzadmehr A (2014) Facile stripping voltammetric determination of haloperidol using a high performance magnetite/carbon nanotube paste electrode in pharmaceutical and biological samples. Mater Sci Eng C 37:264–270
81. Temerk YM, Ibrahim HSM, Schuhmann W (2006) Cathodic adsorptive stripping voltammetric determination of the antitumor drug rutin in pharmaceuticals, human urine, and blood serum. Microchim Acta 153:7–13
82. Peng Y, Lu C, Hu B, Wang Z, Hu S (2007) Development of an acetylspiramycin sensor based on a single-walled carbon nanotubes film electrode. Microchim Acta 158:79–84
83. Kalanur SS, Katrahalli U, Seetharamappa J (2009) Electrochemical studies and spectroscopic investigations on the interaction of an anticancer drug with DNA and their analytical applications. J Electroanal Chem 636:93–100
84. Naik K, Nandibewoor ST (2013) Electro-oxidation and determination of gemcitabine hydrochloride, and anticancer drug at gold electrode. J Ind Eng Chem 19:1933–1938
85. Popa OM, Diculescu VC (2013) Electrochemical and spectrophotometric characterisation of proteinkinase inhibitor and anticancer drug danusertib. Electrochim Acta 112:486–492
86. Ye L, Xiang M, Zhang Y, Luo L, Gao Y, Yu J, Cha J (2013) A novel electrochemical method for sensitive detection of anticancer drug picoplatin with graphene multi-walled carbon nanotubes modified glassy carbon electrode. Int J Electrochem Sci 8:12726–12734
87. Reddy CN, Prasad PR, Sreedhar NY (2013) Electrochemical analysis of antichemotherapeutic drug zanosar in pharmaceutical and biological samples by differential pulse polarography. J Anal Methods Chem 2013:Article ID 420761
88. Lopes IC, Oliveira SCB, Oliveira-Brett AM (2012) In situ electrochemical evaluation of anticancer drug temozolomid and its metabolits-DNA interaction. Anal Bioanal Chem 405:3783–3790
89. Wang C, Shao X, Liu Q, Qu Q, Yang G, Hu X (2006) Differential pulse voltammetric determination of nimesulide in pharmaceutical formulation and human serum at glassy carbon electrode modified by cysteic acid/CNTs based on electrochemical oxidation of l-cysteine. J Pharm Biomed 42:237–244

90. Oliveira RTS, Salazar-Banda GR, Ferreira VS, Oliveira SC, Avaca LA (2007) Electroanalytical determination of lidocaine in pharmaceutical preparations using boron-doped diamond electrodes. Electroanalysis 19:1189–1194
91. Farhadi K, Karimpour A (2007) Electrochemical determination of meloxicam in pharmaceutical preparation and biological fluids using oxidized glassy carbon electrodes. Chem Pharm Bull 55:638–642
92. Cristian A, Iorgulescu EE, Mihailciuc C (2010) Electrochemical studies using activated glassy carbon I. meloxicam. Rev Roum Chim 55:329–334
93. Ghalkhani M, Shahrokhian S, Ghorbani-Bidkorbeh F (2009) Voltammetric studies of sumatriptan on the surface of pyrolytic graphite electrode modified with multi-walled carbon nanotubes decorated with silver nanoparticles. Talanta 80:31–38
94. Tsopelas F, Ochsenkühn-Petropoulou M, Zikos N, Spyropoulou E, Andreadou I, Tsantili-Kakoulidou A (2011) Electrochemical study of some non-steroidal anti-inflammatory drugs: solvent effect and antioxidant activity. J Solid State Electrochem 15:1099–1108
95. Tabeshnia M, Heli H, Jabbari A, Moosavi-Movahedi AA (2010) Electrooxidation of some non-steroidal anti-inflammatory drugs on an alumina nanoparticle-modified glassy carbon electrode. Turk J Chem 34:35–45
96. Lima AB, Faria EO, Montes RHO, Cunha RR, Richter EM, Munoz RAA, dos Santos WTP (2013) Electrochemical oxidation of ibuprofen and its voltammetric determination at a boron-doped diamond electrode. Electroanalysis 25:1585–1588
97. Messina GA, De Vito IE, Raba J (2006) On-line microfluidic sensor integrated with an enzyme-modified pre-cell for the monitoring of paracetamol in pharmaceutical samples. Anal Chim Acta 559:152–158
98. Dogan B, Uslu B, Ozkan SA, Zuman P (2008) Electrochemical determination of HIV drug abacavir based on its reduction. Anal Chem 80:209–216
99. Al-Ghamdi AH, Al-Ghamdi AF, Al-Omar MA (2008) Electrochemical studies and square-wave adsorptive stripping voltammetry of spironolactone drug. Anal Lett 41:90–103
100. Mashhadizadeh MH, Akbarian M (2009) Voltammetric determination of some anti-malarial drugs using a carbon paste electrode modified with Cu(OH)2 nano-wire. Talanta 78:1440–1445
101. Gumustas M, Ozkan SA (2010) Electrochemical evaluation and determination of antiretroviral drug fosamprenavir using boron-doped diamond and glassy carbon electrodes. Anal Bioanal Chem 397:189–203
102. Skrzypek S, Mirceski V, Ciesielski W, Sokołowski A, Zakrzewski R (2007) Direct determination of metformin in urine by adsorptive catalytic square-wave voltammetry. J Pharm Biomed 45:275–281
103. Goyal RN, Gupta VK, Bachheti N (2007) Fullerene-C60-modified electrode as a sensitive voltammetric sensor for detection of nandrolone—an anabolic steroid used in doping. Anal Chim Acta 597:82–89

104. Dogan B, Tuncel S, Uslu B, Özkan SA (2007) Selective electrochemical behavior of highly conductive boron-doped diamond electrodes for fluvastatin sodium oxidation. Diam Relat Mater 16:1695–1704
105. Uslu B, Ozkan SA, Senturk Z (2006) Electrooxidation of the antiviral drug valacyclovir and its square-wave and differential pulse voltammetric determination in pharmaceuticals and human biological fluids. Anal Chim Acta 555:341–347
106. Sun YX, Wang SHF, Zhang XH, Huang YF (2006) Simultaneous determination of epinephrine and ascorbic acid at the electrochemical sensor of triazole SAM modified gold electrode. Sens Actuator B Chem 113:156–161
107. Komorsky-Lovric S, Nigovic B (2006) Electrochemical characterization of simvastatin by abrasive stripping and square-wave voltammetry. J Electroanal Chem 593:125–130
108. Jain R, Jadon N, Radhapyari K (2007) Cathodic adsorptive stripping voltammetric studies on lamivudine: an antiretroviral drug. J Colloid Interface Sci 313:254–260
109. Ghoneim EM, El-Attar MA, Hammam E, Khashaba PY (2007) Stripping voltammetric quantification of the anti-diabetic drug glipizide in bulk form and pharmaceutical formulation. J Pharm Biomed 43:1465–1469
110. Yilmaza S, Skrzypek S, Dilgin Y, Yagmura S, Coskun M (2007) Electrochemical oxidation of prednisolone at glassy carbon electrode and its quantitative determination in human serum and tablets by Osteryoung square wave voltammetry. Curr Anal Chem 3:41–46
111. Alghamdi AH, Belal FF, Al-Omar MA (2006) Square-wave adsorptive stripping voltammetric determination of danazol in capsules. J Pharm Biomed 41:989–993
112. Wang C, Wang F, Li C, Xu X, Li T, Wang C (2007) Voltammetric sensor for tinidazole based on poly(carmine) film modified electrode and its application. Dyes Pigments 75:213–217
113. Wang F, Chen L, Chen X, Hu S (2006) Studies on electrochemical behaviors of acyclovir and its voltammetric determination with nanostructured film electrode. Anal Chim Acta 576:17–22
114. Lin X, Li Y (2006) A sensitive determination of estrogens with a Pt nano-clusters/multi-walled carbon nanotubes modified glassy carbon electrode. Biosens Bioelectron 22:253–259
115. Qaisi AM, Tutunji MF, Tutunji LF (2006) Acid decomposition of omeprazole in the absence of thiol: a differential pulse polarographic study at the static mercury drop electrode (SMDE). J Pharm Sci 95:384–391
116. Yan JL (2006) Electrochemical behavior and the determination of omeprazole using glassy carbon electrode. J Appl Sci 6:1625–1627
117. Goyal RN, Bishnoi S (2009) Simultaneous voltammetric determination of prednisone and prednisolone in human body fluids. Talanta 79:768–774

Chapter 3
Anodisation and Sol–Gel Coatings as Surface Modification to Promote Osseointegration in Metallic Prosthesis

Silvia Cere, Andrea Gomez Sanchez, and Josefina Ballarre

3.1 Introduction

In situ degradation of metallic implants is a complex and undesirable phenomena. The clinic consequences of the liberation of potentially harmful ions or metallic particles to the body environment are related to prosthesis failure, pain and inflammation that end in the retrieving of the prosthetic device [1, 2].

Most of the materials used in permanent implants rely on the formation of a spontaneously formed passive layer on the surface to prevent oxidation of the metal. The passive film formed on the surface should be chemically stable in the body fluid, limit the migration of ions and electrons across the oxide–solution interface and tolerate the mechanical stress and abrasion. It has been reported [3, 4] that most of the metals that are used in prosthesis alloys (Al, Cr, Co, Fe, Mn, Ni, Ti, V with the possible exception of Ti) have biological roles in the human body. Some of them are essential in the normal process (such as Cr in sugar metabolism)

S. Cere (✉) • A.G. Sanchez • J. Ballarre
Electrochemistry and Corrosion Division, INTEMA (CONICET-University of Mar del Plata), Juan B. Justo 4302, B7608FDQ Mar del Plata, Argentina
e-mail: smcere@fi.mdp.edu.ar; aaguar@gmail.com; jballarre@fi.mdp.edu.ar

S. Djokić (ed.), *Biomedical and Pharmaceutical Applications of Electrochemistry*, Modern Aspects of Electrochemistry 60,
DOI 10.1007/978-3-319-31849-3_3

and others are toxic (such as Al for the peripheral neural system) while others can display both characteristics depending on the concentration. However, the benefits of implants in the orthopaedic surgery are clear despite the risk that the exposure of patients to metal contact can have.

As Prof. Black stated [3]: "Corrosion does matter", since all metallic implants corrode and their corrosion products are biologically active. So, the main challenge in metallic implants research is to *minimise the release of corrosion products* to the body environment when it is implanted in the body host. Since corrosion is a superficial phenomenon, the implant surface and the engineering of the surface play a key role in the performance in service of the implant. Cemented and cementless prosthesis are used in orthopaedic surgery and vast discussion about advantages and drawbacks of one procedure over the other are claimed based on their relative cost, surgery procedure and post-operative quality of life among others [5]. Cementless prosthesis is generally preferred for young active patients since there is more bone conservation and the less probability of loosening and also, for patients who are allergic to methylmethacrylate. A study presented on cementless primary total hip arthroplasty shows that in contrast with results obtained for cemented prosthesis, the results are satisfactory in the short time and tend to improve in time, being promising in the case of a revision surgery [6]. In this context, a second challenge that can be associated to the main one in this field of research appears: to modify the surface implant to improve the osseointegration process when cementless implants are used to improve bone fixation and stabilisation. Many researches have been developed in order to improve the bone implant interface to accelerate bone healing and improve bone anchorage [7, 8]. In this chapter, two strategies of surface modification are presented, both with the same general purpose: to create or enhance a barrier in order to minimise the corrosion of the metallic implant (and the consequent release of metallic ions to the body fluid) together with the functionalisation of the surface film to promote the osseointegration of the implant without using cement: the surface modification of valve metals by anodisation and the sol–gel coatings applied on metallic implants.

3.2 Surface Modification of Valve Metals by Anodisation for Permanent Implants

3.2.1 Valve Metals

Aluminium, titanium, vanadium, yttrium, zirconium, hafnium, niobium, tungsten and tantalum are a group of transition metals [9] with a very strong tendency to form on its surface coherent oxides, thermodynamically stable and with different degree of semiconductivity, which do not dissolve once formed (except in some cases in concentrated HF) [10]. Due to the extremely high affinity of these metals for oxygen they readily react with water or oxygen to form a dense, protecting passive layer [11] of a few nanometers that protects the underlying metal from corrosive processes, while re-form at high speed when it is destroyed [12]. The presence of these protective surface oxides confers to the underlying metals an excellent corrosion resistance in various media [11]. As a result, valve metals are used in various applications where corrosion resistance becomes important. Furthermore, oxides of metals of this family have interesting electronic properties resulting from their insulating or semiconducting nature [9, 13, 14].

Valve metals are receiving increasing attention both as alloying components of titanium and as base materials for biomedical applications. Aluminium and vanadium are being substituted by niobium, zirconium and tantalum in biomedical titanium alloys because of their apparent relation with certain severe affections [15, 16]. Numerous valve metals alloys with three, four or even five components were evaluated as candidates for permanent implants [17–20]. Alloy design is performed with two main objectives: obtain Young's Modulus closer to human alveolar bone, and thus avoid severe stress shielding caused by significant differences between implant and the surrounding bone [21–23] and increase biocompatibility and corrosion resistance.

Cytotoxicity of metal ions is an interesting parameter for first selection of an alloying element, and valve metals present promising results compared to other metals in cell culturing tests [24]. Hanawa analysed in detail the possible interactions of released metallic ions

in the human body and concluded that not only the toxicity of metals must be considered to discuss the safety of metallic materials but also the properties and changes of the oxide films in vivo and the quantification and behaviour of the released ions [25].

Titanium is, by far, the most used valve metal in biomedical applications, followed by zirconium. With this in mind this chapter section is focused on the effect of surface modification of titanium and zirconium and some of their alloys to be used as permanent implants.

The reduced ion release and excellent biocompatibility of pure titanium is largely attributed to the spontaneous formation of an inert surface passive film of non-stoichiometric TiO_2, typically 4–10 nm thick, poorly crystallised [26–28]. Big efforts are being conducted to perform modifications in the chemistry or the topography of the surface of titanium to induce the in vivo deposition of bioactive materials (apatite) or to promote cell adhesion or other specific responses of the tissue/material interactions. Surface modification methods include alkaline treatments [29–32], peroxide immersion [33–35], acid immersion [36, 37], mechanical treatments to induce controlled roughness [38, 39], thermal treatments [40] and anodisation [40–50]. Oxidation and electrochemical methods can modify surface oxide properties of implants, such as oxide thickness, chemical composition, crystal structure, porosity or pore structure, density and roughness [51].

Zirconium is a valve metal with excellent corrosion resistance in a wide range of conditions including aggressive organic solutions, different acids and alkalis [52]. The main application of zirconium is in the nuclear industry, because of its low neutron absorption coefficient [53]. In addition, its electrochemical resistance, together with its mechanical properties states it as a potential biomaterial [54]. Promising results have been obtained in some in vitro and in vivo studies of pure zirconium, pointing out this metal as a potential material for permanent implants [55–58]. Biocompatibility of zirconium was evaluated in vitro with cell adhesion tests and cell culture, with results comparable to those of pure titanium [59]. Zirconium and its alloys promote the osseointegration and its cytotoxicity is very low and, in some cases, lower than the reported for titanium alloys [24, 25]. Okazaki and Gotoh

determined by inductively coupled plasma–mass spectrometry the ions released to different solutions after static immersion. In their study, they determined less metallic ions released for the Ti–15Zr–4Nb–4Ta alloy than for classic Ti–6Al–4V alloy or the V free Ti–6Al–7Nb alloy. The amount of (Zr +Nb + Ta) was considerably less than (Al–Nb) or (Al +V) of the respective alloys. Moreover, in the Ti alloys containing Zr as alloying element, the quantity of Ti ions released to the solutions was smaller than in the other Ti alloys [60]. Besides, Ti–Nb–Zr alloys present adequate mechanical properties and also cytocompatibility.

The good performance of zirconium has been mainly attributed to its surface oxide film. Native ZrO_2 oxide film has a thickness between 2 and 5 nm [61–63]. The presence on a native ZrO_2 oxide (zirconia) on zirconium surface determines the low corrosion rate of the material, and therefore the low metal ion release to the biological media [64–67]. Moreover, zirconia, as a bulk ceramic material is widely used in dental applications due to its excellent biocompatibility and proven capability to facilitate the osseointegration process [68–72].

Zirconium alloy (Zr2.5Nb) coxofemoral permanent implants are currently being used due to its good wear resistance, osseointegration ability and low ion release rate in biological media [73–76]. Oxinium®™ is the commercial name of Zr–2,5Nb hip implants and femoral [77–80] with surface hydrothermal treatment to obtain 5 μm zirconia layer. Oxidised zirconium components combine the mechanical strength of zirconium metal with the wear resistance of a ceramic material (zirconia). Clinical studies evidence a performance equivalent to Cr–Co alloys [81–84]. Innocenti et al. performed clinical studies after 5 years of surgery, reporting the survival rate and clinical results of anodised zirconium femoral implants between years 2001 and 2003. The results indicate a survival rate of 98.7 % to 7 years. No referral cases are reported, and only missed septic component loss is reported. Although these implants' surface treatment is not intended to promote osseointegration, these results reinforce why is appealing the study of zirconium/zirconium oxide system as biomaterial for permanent implants [85]. It has been demonstrated that an artificial increase of the thickness and changes in the topography of the native oxide

will result in very strong reinforcement of the bone response [86, 87]. Further thickening of the surface oxide layer may be performed by different routes, including thermal treatments in air immersion in peroxide [88] or anodisation [63, 89].

3.2.2 *Anodising Process of Valve Metals*

Anodising process is a non-expensive surface modification process capable to be used even in complex geometries [42]. It was developed and used for more than 100 years at industrial scale to protect first aluminium and later other metals and alloys. This is a simple technique that can be performed on an industrial scale at low cost with good reproducibility and giving rise to homogeneous coatings regardless of the geometry of the part. Anodisation consists in the thickening of the surface oxide film of a valve metal by means of the anodic polarisation of the working electrode in a two or three electrode electrochemical cell immersed in an electrolyte. Both acid and alkaline electrolytes may be used, and the potential range of anodisation is wide. Anodic oxide films thickness varies from 10 nm to 50 μm depending on the anodisation parameters applied. The electrochemical oxide growth is greatly dependent upon the electrochemical parameters as well as the electrolytes employed [42, 43]. Anodising methods have strong effect on the structure, the crystallisation kinetics and the composition of the surface oxide films formed [90–93]. This electrochemical one-step method was extensively used to induce controlled chemical, topological and also electronic modifications.

The growing of anodic films on valve metals occurs irreversibly assisted by a field-assisted migration of ions through the film [94, 95]. The O^{2-} ions migrate to the interface metal/oxide (M/O) and react with the metal ions to form the oxide in contact with the metal substrate, while metal ions migrate to the interface oxide/electrolyte (O/E) and react with oxygen ions and other anions forming the outer layer of the film [96]. A linear relation between the applied potential and the thickness of the anodic film characterises the anodisation process, and anodising ratios between 1.5 and 3 nm/V are commonly reported [97].

There are currently two mechanisms proposed for the anodic oxide film formation on valve metals: The high-field law and the low-field approach. Both models are supported for numerous papers, including some of recent publication:

The high field law (HFL) [98, 99]: Describes the growth of non-porous oxide films as a field supported thermally activated hopping of metal ions [95, 100–102]. The main statement is that the electric field strength is very high (>1 MV cm^{-1}) during oxide growth. In order to have such ions to migrate, very large electric fields must be sustained in the oxide layer, typically in the order of 10^8–10^9 V/m [103]. The rate-determining step is located within the oxide. Both anions and cations are mobile, and the oxide grows at both interfaces. Under potentiostatic conditions, the anodic oxide film growth decreases with time due to an increase of layer thickness and a corresponding decrease of field strength.

Low-field approach [104]—The point defect model (PDM) [105–109]: from the assumptions of an oxide layer as a point defective phase containing cation vacancies and oxygen vacancies, with a concentration of point defect much greater than in the isolated bulk oxides. Considering that defects are generated and annihilated at the metal/film and film/solution interfaces. The model proposes that the electric field strength is independent of the voltage and distance through the film, that field strength is constant within the anodic film and the potential drop occurs in the metal/oxide interface [108–113].

Since the anodic growth occurs in the electrolytic media together with reduction reactions in the counter electrode, the Faraday law parameters often cannot be extracted from coulometric data, and therefore "indirect" measurements have to be used. Capacitance methods are the most used to evaluate the growing rate [99]. However, strong assumptions, like crystallinity of the anodic oxide, homogeneity and density have to be stated [114].

The thickness of anodic oxides on valve metals has a practical limit when the breakdown potential occurs [98, 115]. Electric breakdown potential is the potential when the linearity between the thickness of the anodic film and the applied potential is loosened [116, 117]. The electric breakdown phenomenon is characterised with the presence of sparks and small holes in the film surface

[14, 118–120]. A separated phenomenon occurs after the electric breakdown, named mechanical breakdown, characterised by the sudden drop of the potential and the appearance of fissures and areas with large fractures on anodised surfaces [119], and internal stress on the growing anodic layer is proposed as the origin of the occurrence of the breakdown phenomena [103, 121, 122]. Current density during anodising determines the potential of mechanical breakdown of the films [123].

Above the breakdown potential, the film obtained presents more porosity, less adherence [120] and fractures [124–126]. The quality of these anodic films as a barrier layer against corrosion diminishes, and passivity may be lost [46, 127, 128]. It is a well-documented fact that the thickening of anodic or thermally growth oxide films on valve metals *solely* does not necessarily lead to better corrosion resistance [129].

The anodic breakdown potential is reached at different anodic potentials for different electrolytes, pH, temperatures on each valve metal [116, 130]. For example, for zirconium, anodised in phosphoric acid at ambient temperature, breakdown potential is reached at 450 V [131].

The first evident modification of the surface of valve metals by anodic oxide growth is the change in colour of the metal samples. In aluminium, this fact leads to an entire industry of surface finishing [102, 132] and colouring of products [133]. In titanium and its alloys, the colour obtained by anodisation is often used to identify implants and tools of different sizes [42, 134].

The colours of anodic oxide films are the result of interference phenomenon of incident light on surface films. The coloration of thin films may be described by the multiple beam interference theory. When white light makes contact with the film, the reflected beam, which is formed by the interfering beams will be coloured [135, 136]. While anodic oxide colours are principally related to the thickness of the films, there are several factors that influence the resulting colour observed at each anodising condition, and that may alter the sequence of colours respect to the theoretical succession (yellow, brown, dark blue, sky blue, green, yellow). The main of them are substrate roughness, non-uniform film thickness over the entire sample, the surface oxide stoichiometry, defects or

impurities incorporated into the anodic oxide. For this reason, the colours reported differ for different authors, even when the same potential (and therefore the same thickness) is expected. The variation in colours is notorious when different electrolytes are used, or even when different concentrations of the same electrolyte vary. These differences are evident in studies of anodic oxides of titanium, when the reported colours differ from one author to the other [42, 137]. However, when starting conditions are maintained (i.e. substrate characteristics and electrolyte), the colours of oxide films can be used for a quick identification purpose of the resultant oxide thickness in association with the anodic-forming voltage [138, 139] since the colours obtained for each condition are highly reproducible and can be related to the thickness of the films (Fig. 3.1). The RGB values of digital images of the anodic films taken with controlled conditions (incident light, time of exposure among others) proved to be a useful tool to characterise and check the reproducibility of the anodising route [138].

The surface chemistry and topography of the oxide-generated layer has been thought to influence bone response [87, 140]. The implant performance was related to the oxide thickness, differences in surface oxide morphology, the difference between crystal structure of amorphous oxide in native oxides and a mixture of amorphous, anatase and rutile phases, and differences in

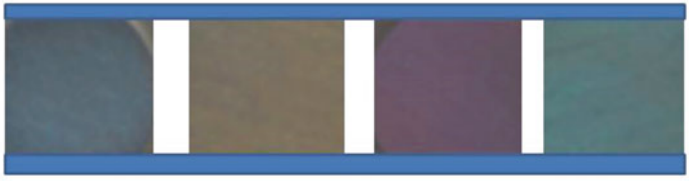

	30 V	60 V	90V	120V
R	124	123	114	120
G	136	121	125	130
B	140	111	140	131

Fig. 3.1 Colours obtained after anodisation at different potentials with the corresponding red–green–blue (RGB) values

surface roughness. The characterisation of the oxides present in the surface and its quantification are key issues for the future calcium phosphate deposition (being apatite formation the first insight of bone formation) in order to provide bioactivity and further mechanical fixation. However, the relationship between the anodisation process parameters and the surface characteristics of the oxide layer is still not fully understood, and therefore, an increasing number of articles are being published in this area. The characteristics of the films obtained strongly depend on the applied potential, and therefore, may be followed by classifying them by applied potential ranges. Surprisingly, the entire potential range was investigated to modify the surface of titanium implants, and also for other valve metals and alloys. Despite the numerous data available related to anodic film characteristics and in vitro and in vivo response, the strong influence of the anodisation parameters on the final surface condition gives a somehow contradictory state of the modified surfaces performance, due to the spread of the results presented. In this work, a detailed analysis of the surface modifications induced by anodisation in well-defined anodic potential ranges is described, in order to present a general picture of the influence of this widely used electrochemical process on the in vitro and in vivo performance of valve metals.

3.2.2.1 Low Potential Anodising (up to 10 V)

Films obtained by anodising at potentials below 10 V in both in pure valve metals and alloys present dielectric or semiconducting electronic characteristics, thickness between 2 and 20 nm and the characteristic interference colours. Anodisation at low potentials is mostly performed with the aim of increasing bioactivity of the surface with the modification of the composition or structure of the surface oxide layer [141] of valve metals. Chemical species from the electrolyte may be incorporated as impurities into the anodic film altering the electronic properties of the oxide formed with a similar effect of those reported for mechanical or chemical treatments [142].

Native oxide films on titanium and alloys are amorphous, inhomogeneous in composition and very thin (1.5–3 nm) [143]. They act as n-type semiconductors with a bandgap of 3.5 eV. On titanium alloys, an influence of the alloy composition on the electronic properties, composition of the anodic oxides and capacitive behaviour was reported by many authors [144]. Further immersion in simulated biological solutions does not alter electronic characteristics on titanium alloys, indicating that the nature of the interaction is adsorption [144]. However, common species in contact with implant materials as peroxide [88] or fluorides [142] may alter the surface layer electronic properties and therefore the in vivo performance. By electrochemical impedance spectroscopy (EIS), capacitive behaviour of the film was verified, and an increase in corrosion resistance in simulated body fluid (SBF) was often obtained compared to native oxides. Native oxide films present high corrosion resistance and stability in solutions with ions present in body fluids, as was extensively studied by several authors [33, 144–146]. As follows, films with the same thickness or anodised at the same potential may present differences in semiconductive properties when altering the alloy composition.

Bozzini et al. [147] anodised titanium in sulphuric acid at 2 V. They tested the material in SBF by electrochemical tests at different immersion time and found an apparent thickening of the surface film with immersion time and an increase in corrosion potential. However, they found a decrease in corrosion resistance when increasing the time of immersion. Schmidth et al. [148] studied the effect on the electronic properties of the surface film formed on titanium in a buffer solution of citric acid and sodium phosphate by applying potentials between 1 and 5 V. They found a decrease in donor density and a dielectric behaviour of the films thus formed at different pH. The anodic oxides behave also as an n-type semiconductor, according to the results reported by Ibris et al. [146].

Modification of the roughness, topology or anodic oxide characterisation presents many challenges in this anodisation potential range since the small thickness of the anodic films limits the techniques with suitable range of detection to be used.

3.2.2.2 Intermediate Potential Anodising (10–60 V)

Anodisation of titanium and other valve metals and alloys in acidic media at potentials between 10 and 60 V occurs in the linear portion of the potential vs. thickness curve, far from the breakdown potential.

In order to present an accurate comprehension of the surface modification performed with the anodisation process at these relative low potentials, adequate techniques have to be selected and critical comparison among them is desirable, since most of the thin film characterisation techniques used to evaluate changes in topography, surface chemistry, crystallographic phases present or even corrosion resistance of the modified implant surfaces often implies strong assumptions of film properties that are difficult to assure from experimental evidence. This is clearly evidenced in the determination of the anodic film thickness, which ranges from 10 to 150 nm according to numerous but sometimes contradictory reports obtained from results of different measurement techniques including X-ray Spectroscopy or Auger depth profiling [87], Ellipsometry [149], Atomic Force Microscopy (AFM) [49], Rutherford backscattering spectroscopy [150] or electrochemical impedance spectroscopy [114, 139]. Figure 3.2 shows the results

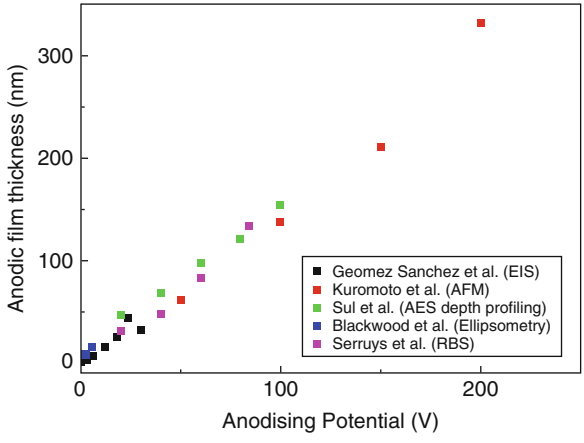

Fig. 3.2 Anodic film thickness obtained by various authors and different techniques. Reproduced from ref. [139] by permission of John Wiley & Sons Ltd

of films thickness vs. anodising potential for pure titanium according to different authors, to illustrate the variety of results.

The anodic oxides grow in this potential range in inhomogeneous framework with two characteristic shapes often found: as isolated islands (in zirconium [138], CP grade 2 titanium [139, 141]) in acidic media characterised by protrusions regularly present on the entire surface of the metal increasing the surface coverage when increasing the anodising potential, or as flower-like structures, of variable size and spacing for different applied potentials (niobium [151], CP titanium [152]). Figure 3.3 shows the two distinctive morphologies. Mogoda et al. determined that the rate of growing of anodic oxide filmson zirconium in phosphoric acid increases with increasing current densities and H_3PO_4 concentration. The oxide formed presented a duplex structure that they characterised by two dissolution rate laws [153].

Topological changes may be easily evaluated with contact mode AFM. An adequate scaling in AFM measurements is required in order to compare the results in literature. Related to the application as biomaterials, large scales (larger than 10 * 10 μm, up to 50 × 50 μm) are specially interesting [154], because they are related to biological features (size of the cells can be attached and protein adsorption among others). Different topographic characteristics have been evaluated by different authors, including roughness by mean of Ra, Rmn, fractal dimension and others [155]. The need to analyse surface features with complementary techniques resulted evident on titanium anodised in phosphoric acid at 30 V.

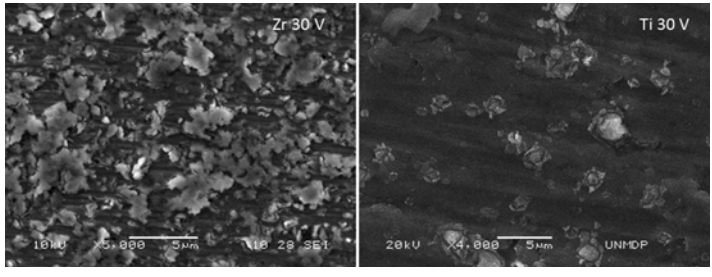

Fig. 3.3 Different morphologies obtained for Ti and Zr anodised both at 30 V in 1 mol/L phosphoric acid for 1 h

In this case, the changes produced in the surface morphology can not be observed by SEM, whereas the changes produced in the topography in the nanometrical range are evidenced by AFM. An increase in roughness parameters was detected, which may be beneficial for the implant fixation [139]. In zirconium anodised in the same conditions, AFM results indicate that although the amplitude of the surface features increases with anodising potential, the overall surface geometry does not alter significantly. Thus, simple surface roughness parameters can serve to establish the surface quality and the influence of the substrate on the structure of the oxide formed [156].

The crystallinity of the films and crystallographic phases present are a main topic in this type of anodic oxides and may be evaluated with Raman spectroscopy or grazing angle X ray diffraction (DRX). This inhomogeneous film formation presents also partially crystalline domains (in titanium, anatase phase) [157]. The influence of the crystalline phase on in vivo results was extensively evaluated, mainly in titanium and its alloys, where there is a general agreement in the better performance of the implants with anatase in their surface compared to amorphous titanium dioxide or rutile. The main routes to promote the presence of anatase are the careful selection of anodisation parameters (specially, electrolyte used, long periods at a constant potential, low current densities during anodisation) or the thermal treatments of the anodised implants. On zirconium, oxide films are mainly monoclinic ZrO_2, while the same crystallographic structure was detected in Zr2.5Nb anodised in the same conditions [158].

During the process of anodisation occurs the incorporation of ion species from the electrolyte and represents an important topic to be studied in permanent implant application [139]. Several authors agree in the beneficial effect of the incorporation of phosphates to anodic surface oxides on titanium and some of its alloys to the in vitro capability of precipitation of bioactive Ca–P compounds during immersion in simulated body fluids [159–162]. Hanawa postulated that phosphate ions incorporation into the anodic film stimulates the in vitro growing of hydroxyapatite (HA) biocompatible [159]. de Sena et al. also attributed bioactivity to the presence of phosphates present in anodic titanium oxides according to the results of SBF immersion tests [160]. Sul determined that the

incorporation of P during anodisation of titanium in phosphoric acid outcomes in an increase in biocompatibility compared to samples anodised in sulphuric acid [161], while Lee et al. found that the addition of phosphoric acid to sulphuric acid solution used as anodising electrolyte increases the nucleation capability of Ca–P bioactive compounds on titanium during immersion in SBF [162]. The inclusion of phosphorous as a zirconium phosphate in oxides grown in phosphoric acid has been demonstrated by both Raman spectroscopy and XPS [138].

Anodisation in phosphate-containing media is then an alternative to other electrochemical surface modification processes to promote Ca–P-rich compounds precipitation during immersion in SBF.

Alkaline immersion was studied also for pure zirconium [58] and titanium alloys containing zirconium [163], whereas cathodic polarisation treatments in Hanks solution to obtain Ca–P compounds on the metal surface were performed on commercially pure titanium [164, 165]. Compared to those surface modification processes, anodisation in H_3PO_4 proved to increase the apatite formation capability of zirconium in a single step, without any further chemical treatment or cathodic polarisation required to induce the precipitation of Ca–P compounds [166].

The electrical properties of oxide films in medical implants are an important property for establishing the level of defects in the oxide films formed [114]. The slopes of the Mott–Schottky plots give a quantitative estimate of the carrier number density. The decrease in this quantity when increasing the applied growth potential is in agreement with the behaviour found for anodic oxide films of other pure valve metals and can be related to the changes in film defects when increasing film thickness [114]. Carrier number in the range of potential under study was studied for titanium showing a decrease of the carrier number when increasing anodising potential. From the circuital fitting of EIS results and according to the Brug model, film thickness can be estimated, and the values obtained were in good agreement with those available from independent techniques, thus validating the estimation (see Fig. 3.2). The native oxide is present in the as-received condition, increasing thickness with anodising potential. The barrier effect is also enhanced with the increase of the thickness [139].

Electrochemical studies in SBF solution for as-received titanium and titanium anodised in phosphoric acid at potentials up to 30 V were performed to determine the best corrosion resistance condition [139]. The results indicate that the anodic films obtained at a constant potential of 30 V have higher barrier effect, and the protective layer remains effective against the aggressive anions present in SBF even after 30 days of immersion. In the same study, potentiodynamic assays show the decrease in the current density corresponding to anodised titanium evidencing an increase in the barrier effect of the anodic film compared with the native titanium oxide. The prolonged immersion in SBF leads to a slight increase in the passivity current density in both the as-received and anodised condition. Although the results evidence that the SBF exposition produces minor effects on titanium surfaces, the barrier layer remains effective against corrosion in SBF solution, since neither rupture of the film nor localised corrosion occurs. When comparing the performance of as-received with the titanium anodised at 30 V, corrosion resistance increases. The stability of the anodic film presents the anodised surface as the best candidate for a permanent implant [40, 167].

Due to the promising corrosion performance in SBF together with the biocompatible surface characteristics, anodic films on titanium obtained at 30 V were implanted on Wistar Rats to compare the osseointegration results of this modified surface with that corresponding to as-received titanium. After 8 weeks of implantation the bone percentage does not greatly differ for anodised and control specimens, however, there is a marked difference between their topologies: while the bone in the samples anodised at 30 V looks uniform and completely covers the implant surface, as-received samples present uncovered portions of the implant surface.

Gomez Sanchez et al. presented a study for Zr anodised in phosphoric acid at potentials up to 30 V. The rapid increase in thickness of the passive film and the absence of any significant dissolution in the passive state when increasing the anodising potential corroborates the excellent corrosion barrier properties of this material. Importantly, the incorporation of phosphate in the film does not lead to an impairment of its barrier properties. The oxide formed on the surface is mainly monoclinic ZrO_2 with the incorporation of phosphates from the electrolyte. The impedance results demonstrate the increase in thickness

of the anodic film with anodising potential and changes in thickness can be followed from impedance analysis. These results correlate with the XPS data in demonstrating clearly that without an oxidative treatment, the presence of low oxidation states of Zr on the surface or indeed, of some free metal, is observed. Thus, the electrochemical oxidation and the surface controls investigated can provide a simple route for improving the long-term stability of the anodically grown oxides [114]. It was found that Zr presents a low passive current density for all the anodising conditions studied after 24 h of immersion in SBF, although shows susceptibility to localised corrosion during anodic polarisation. The rupture potential increases when increasing thickness of the anodic surface film. The increase in the barrier effect when increasing anodising potential is also verified by EIS (Fig. 3.4). After 30 days of immersion in SBF solution, the electrochemical tests demonstrated certain degree of deterioration of the surface protective film on zirconium, in both the as-received and the anodised at 30 V samples. Conversely, the impedance modulus remains showing a

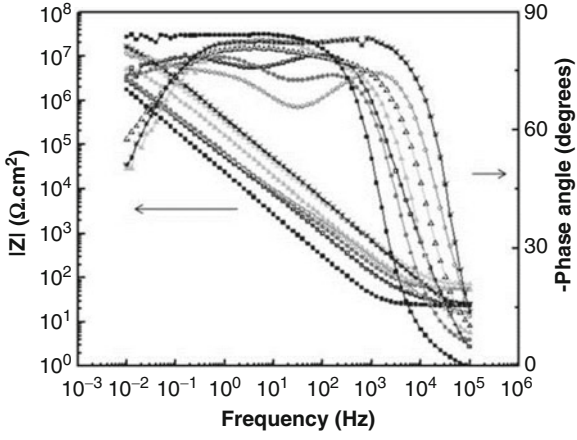

Fig. 3.4 Bode plots after 24 h in SBF solution of (*filled square*) Zr as-received, and anodised at (*open square*) 3 V, (*filled circle*) 6 V, (*open circle*) 9 V, (*filled triangle*) 18 V, (*open triangle*) 24 V, (*Asterisk*) 30 V. Solid line shows the equivalent circuit fitting. Reprinted from ref. [166]. with kind permission from Springer Science+Business Media

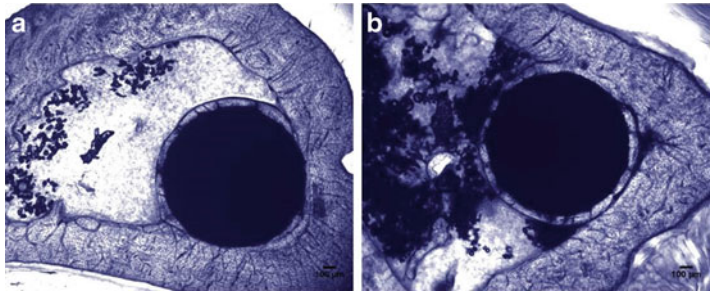

Fig. 3.5 Histology showing bone–implant interface in rat tibia cross section, 63 days after the implantation. (**a**) New bone formation around control implant. (**b**) New bone formation around anodised implant (staining: toluidine blue, original magnification ×4). Reprinted from ref. [89]. with kind permission from Springer Science+Business Media

higher corrosion resistance for the anodised condition with respect to the as-received zirconium. Surface modification of zirconium by anodisation has proved to be a treatment that can keep corrosion parameters in low values while is able to promote Ca–P compounds precipitation on the surface endorsing the bioactivity of the material and promoting bone regeneration.

In vivo experiments evidence bone generation and growth in contact with zirconium implants both in the as-received and anodised conditions. Although osseointegration is observed in anodised and as-received materials, the bone quality of the generated bone has to be analysed in terms of bone maturity and cell proliferation (Fig. 3.5). After 8 weeks, the bone for the modified surface has already reached a high level of organisation in both the mineral and the organic part and the maturity is comparable to the normal cortical bone [89, 138, 166, 168, 169].

3.2.2.3 Anodic Films Obtained at High Applied Potentials (60–200 V)

Yang et al. studied Ti anodised in sulphuric acid at potentials between 90 and 180 V and described a porous structure with cracks in the obtained surface [44]. Also Sul et al. and Lausma et al.

described the obtention of rough surfaces in a complete work about Ti anodised in acidic media at potential above 60–100 V [42, 43, 170, 171]. Rough porous bioactive Ti anodic layers were also obtained by galvanostatic anodisation in Ca–P-rich electrolytes by de Souza et al. [172]. The final potential reached during anodisation must be near the breakdown potential, according to the morphology of the surface obtained and thickness of the anodic layer. The anodic layers presented brittleness under normal and tangential loading and detachment at low loads.

The morphology of the surface layer on titanium is characterised by a continuous oxide layer with micrometrical pores (Fig. 3.6l). Anatase and rutile mixtures were the main compounds found in oxides growth in sulphuric acid [173].

Flower-like structure was found on niobium anodised at 100 V in phosphoric acid, and the formation mechanism of the flowers is attributed to tensile stresses formed in the anodic film [151]. Films grown at high potential present, in general, good adherence to substrate but a high degree of imperfections and pores, which present a drawback with respect to their corrosion-resistant requirement [174].

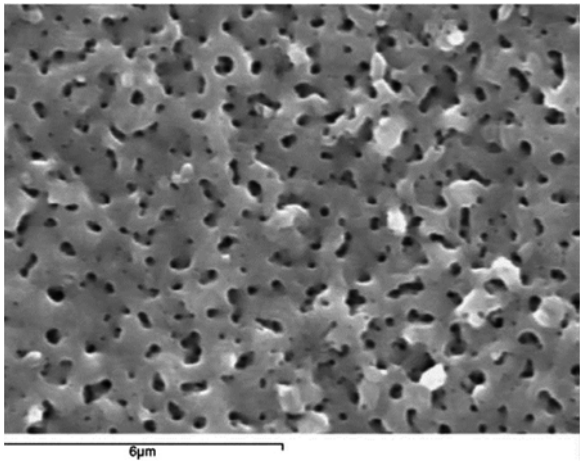

Fig. 3.6 SEM image of sample anodised in 0.5 M H_2SO_4 with current density 1080 A/m^2 and cell potential 140 V. Reprinted from ref [173] Copyright 2006, with permission from Elsevier

3.2.2.4 Anodic Oxides Obtained Above Electrolytic Breakdown Potential. Micro Arc Oxidation and Plasma Electrolytic Oxidation Treatments

Plasma electrolytic oxidation (PEO), micro arc oxidation (MAO), spark anodising or microplasma oxidation are different names [175] for an anodising process above the electrolytic breakdown potential of a metal substrate in a given electrolyte. The anodic oxides may reach thickness of tens and even hundreds of microns [176] and therefore the ceramic characteristics of the coatings obtained as wear resistance, high hardness and corrosion resistance may be exploited. These give a wide variety of technological applications [177], including biomaterials.

Micro arcs appear as lighting flashes (sparks) inside the anodising cell (electrical discharges), caused by localised electrical breakdown of the growing coating [175]. The electric discharges create plasma emission of high amounts of energy that produce local melting of the anode [178] and rapid cooling events [175]. The microdischarges rapidly develop and extinguish within 10^{-4} to 10^{-5} s on the vicinity of the anode and heat the metal substrate to less than 373–423 K. Simultaneously the local temperature and pressure inside the discharge channels formed by the electrical sparks reach 10^{3}–10^{4} K and 102–103 MPa. The coating is formed on the anode by chemical reactions governed by thermal and plasma conditions at the discharge zone [179]. These temperature and pressure are enough to give rise to plasma thermochemical interactions between the substrate and the electrolyte. These interactions result in the formation of melt-quenched high-temperature oxides and complex compounds on the surface, composed of both the substrate material and the electrolyte [180]. Whereas below the electrolytic breakdown the thickness of the anodic films growth with a linear relationship with the applied potential, the structure of the films changes completely when anodising at potentials above the linear region. The main surface characteristic is the formation of craters, holes in the micrometrical range [43] that substantially alter the roughness of the surface. Moreover, plasma electrolytic oxidation (PEO) coatings contain a fine, interconnected porosity network, which appears to extend throughout the entire thickness

of the coating [175]. The anodic film formed in acidic media was described with a duplex structure with an outer porous layer (10–15 μm) and an inner compact film of less than 100 nm. The coating thickness increases with the applied potential [181].

The rough surface generated by this process and the incorporation to the coating of chemical species from the electrolyte lead to an entire field of investigation of these modified surfaces of metallic valve metal implant materials [182], including selection of the anodising electrolyte, time, applied potential, current density, frequency and selection and post-anodising treatments.

In contrast to the classical anodising treatments performed below the electrolytic breakdown, which are commonly done in acidic inorganic media, MAO is often performed in electrolytes containing Ca and P that are incorporated in the oxide coating structure with the aim of improving biocompatibility and osseointegration rate in vivo. Using glycerolphosphate and calcium acetate Abbasi et al. identified hydroxyapatite, anatase and calcium titanate in the surface coating of pure titanium [180, 183]. In Ti alloy containing Nb, Ta and Zr, anodised in calcium glycerolphosphate and magnesium acetate, Tsutsumi et al. only found calcium phosphate after immersion in Hanks solution whereas the MAO coating consisted mainly of anatase and rutile [184]. Alkaline electrolytes were used to anodise pure zirconium with the aim of incorporating silicates during MAO treatment [185]. Post-anodisation treatments are often performed. Hydrothermal treatment using high pressure steam was used to crystallise hydroxyapatite [186]. Alkali treatment, consisting in the immersion of the anodised material in a concentrated NaOH solution at temperatures from 50 to 80 °C for some hours to several days is often used to promote titanate formation and also to alter the topography of the anodised surfaces [176]. By using electrophoresis, Samanipour et al. incorporated particles of ZrO_2 on MAO-treated titanium [187]. Ca-P-rich compounds were detected after immersion in Hank solution of pure zirconium specimens coated by MAO and further immersed in acid or alkaline solutions [188].

Electrochemical tests in SBF solution show similar results of those obtained in other anodisation condition for titanium, a diminish of the current density for the coated specimens compared with unanodised titanium, along with an increase in OCP potential [178]

In vitro tests results show an increase in osteoblast adhesion on the MAO-coated titanium samples compared to bare titanium [189].

All the above named treatments were able to induce Ca–P-rich compounds on the metal surface. However, the corrosion stability of those thick and porous films has not been completely studied [166].

3.2.2.5 Anodic Oxides on Valve Metals with Auto Ordered Structures: Nanopores and Nanotubes

The anodisation of valve metals in acidic inorganic media or containing ethylene glycol in the presence of fluoride ions (F^-) dramatically changes the anodic oxide structures obtained. As is clearly evidenced in Fig. 3.7, the addition of small amounts of HF to H_3PO_4 results in a totally new surface morphology of the anodic oxide, even when other anodisation parameters, such as anodising potential and time remain the same. Instead of the isolated islands in the nanometrical range, a fully covered surface of an anodic film with a periodic and ordered structure of parallel tubes on the surface is formed.

These interesting structures, with multiscale well-defined topological characteristics (roughness in the microescale, pore

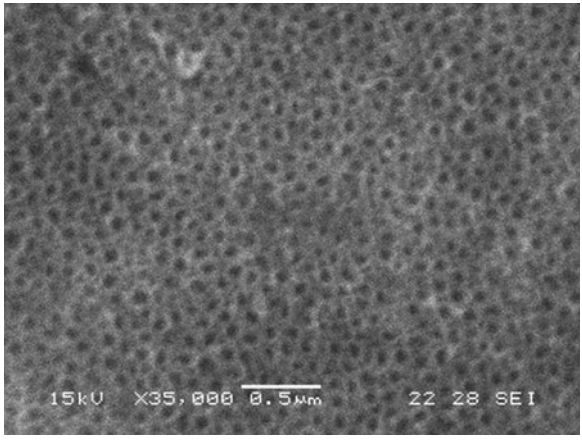

Fig. 3.7 SEM image of Ti showing a periodic and ordered structure of parallel tubes on the surface after anodising in HF + H_3PO_4

diameter in the nanoscale) have been studied for several research groups as potential surface design for osseointegrable implants on titanium [190], some of its alloys [191, 192] and other biocompatible valve metals as zirconium [50, 193, 194], tantalum or niobium [195]. The nanotubes are expected to promote bonding to bone due to their high surface area and the ability for cell interlocking [22].

Acidic mixtures with small amounts of HF are the most used electrolytes for nanotube formation of anodic oxides on titanium [196, 197] and its alloys, although organic electrolytes including glycerol [198, 199], diethylene glycol [200]. In zirconium, however, acidic water electrolytes with HF lead to an intense dissolution of the metal, and nanotubes are obtained mainly in organic electrolytes with F ion, with the exception of few reports of self-organised porous structure obtained on zirconium $Na_2SO_4 + NH_4F$ aqueous solution [201] and in H_2SO_4/NH_4F electrolyte [202]. The influence of small water contents on glycerol solutions with NH_4F can change the zirconium oxides structure from nanotubes to nanopores [203]. Other valve metals were in comparison less studied, but the growth of nanotubular structures is reported on Hf- [204] and Nb-containing titanium alloys [195].

The applied potential and time under constant anodic potential have a strong influence on the morphology of the anodic layers formed [197, 205]. Relative low potentials, from 3 to 60 V are often applied under potentiostatic regime for periods of time from a few minutes to more than 24 h. Tube diameter increases with the applied potential [190, 203, 206, 207]. However, change from nanotubular to flat anodic oxides occurs when increasing the anodic potential in some electrolytes, with an important influence of stirring regime [208]. A linear relationship between anodic potential and pore diameter was found for pure titanium anodised in NaF/glycerol electrolyte [209]. For pure titanium in glycerol–water solution with fluorides, Manole et al. found a change in the structure of the anodic films formed from nanotubes at low potentials (20–40 V) to nanopores at 60–80 V [210, 211]. Short time of applied potentials leads to nanopore structures, whereas longer periods (higher than 1 h) favour the formation of nanotubes. Once formed, nanotubes grow in length with anodising time at constant potential.

Topologies of the anodised surfaces change remarkably along with the changing of applied voltages, electrolyte concentration and time under anodic potential, as was reported by Zhao et al. for pure titanium [197]. The structure is highly sensitive also on temperature (in some cases it rises during anodisation) and stirring regimen [212]. The tubes are well aligned and often organised into high-density uniform arrays, with a barrier dense layer on their bottom [196].

A wide range of film thickness, from 100 to 1200 nm are reported with pore or tube diameters between 20 and 90 nm on pure titanium and some of its alloys. The incorporation of F– in the oxide structure was evidenced with XPS [196, 202, 213].

Thermal treatments are often performed to increase anatase crystalline structure on pure titanium or titanium alloys, but even after long thermal cycles, partial crystallinity is a main characteristic of these layers. In these post-anodisation treatments, different temperatures, time of treatment and even atmosphere were varied dramatically from high vacuum to air [214], or even dry oxygen [215]. Sealing boiling water treatments similar to those used in aluminium anodic oxides were also reported [216]. However, in zirconium, crystalline anodic oxides are often obtained with no need of further thermal treatments. Cubic and tetragonal phase mixtures are found [201].

According to recent studies [217], the anodisation of Ta, Nb and Zr in the presence of F– proceeds in three steps:

– Formation of a compact and protective metal oxide with a decay of current density (as in acidic media with no F–)
– Chemical dissolution of the oxide in the presence of fluoride anion and formation of metal oxide simultaneously with a rise of current density
– Reaching the equilibrium between oxidation and dissolution with a steady state of current density.

Biomimetic apatite growth after immersion in SBF solutions for different periods of time were the first in vitro tests performed to evaluate nanotubular structures as candidates for permanent implants. The presence of anatase, induced after thermal treatments in air post-anodisation, was indicated as the main factor

favouring the apatite formation on pure titanium [214]. After bioactivation by synthetic hydroxyapatite coating, nanotubular TiO_2 structures present higher apatite amount after SBF immersion than compact anodic oxides [190]. Similar results were found with bioactivation with hydrothermal immersion in Ca–P-rich solutions [218]. In zirconium, higher amount of apatite was found on nanotubular ZrO_2 than on compact ZrO_2 after 30 days of immersion in SBF [219]. Bioactivity of modified Ti surface by nanotubes is a subject of study with preliminary favourable results in vivo [200] and in vitro [220]. Electrochemical measurements in phosphate saline solution evidences on Ti13Nb13Zr alloy a similar corrosion resistance of native oxide compared to nanotubes grown in acidic media [23]. In SBF, anodic potentiodynamic experiments show smaller current densities on heat-treated nanotubular TiO_2 compared to polished titanium surfaces [218] whereas nanotubular ZrO_2 presents better corrosion resistance than non-anodised Zr only after thermal treatment [168].

Cell adhesion and antibacterial experiments results present promissory results for pure titanium with anodic nanotubes growth in acidic media [215, 221], whereas in Ti50Zr alloy, cell adhesion percentage dependence with nanotube diameter was determined [222]. The results of the cell proliferation assays indicated that the nanotubes with inner diameter (Di) ≈40 nm exhibited the highest percentage of cell adhesion of 41.0 %, compared to 25.9 % cell adhesion at Di ≈ 59 nm, 33.1 % at Di ≈ 64 nm and 33.5 % at Di ≈ 82 nm. The nanotubes with Di ≈ 59 nm exhibited the greatest roughness parameter of Sa (mean roughness), leading to the lowest ability to interlock with $SaOS_2$ cells.

It was observed increased blood serum protein adsorption, platelet adhesion and activation on titania nanotube arrays compared to smooth titanium [200]. Desirable effects of TiO_2 structures on titanium were found on vascular cells regarding to a potential use in vascular devices [223].

Even though nanotube structures have promising characteristics regarding a further use in permanent implants, including a periodic ordered structure in the micro and nanoscale formed with proven bioactive oxides (TiO_2, ZrO_2 in different crystallographic structures), the growth on substrates of high corrosion resistance

in biological media metals and alloys, of low cytotoxicity, the nanotubular structure often does not cover the entire implant surface, but nanotube islands and or clusters are separated by other less ordered oxide shapes, more like those obtained in F free electrolytes. The area of visible pores increases with anodising time but the precipitation of a layer of intermediate reaction products was always present in a detailed work of anodisation of pure Zr and Ti presented by Tsuchiya [224]. The consequence of this mixture of structures leads to a careful study and control of the actual capability of cover complex surfaces with the desired surface topography. However, big efforts are currently being done to understand the relation between anodisation parameters and different aspects of the nanotubular structures, in order to achieve certain rules to design the anodic process according to the desired surfaces requirements.

As a summary, anodisation, as a general process, is the electrochemical route that conducts to the formation of an oxide grown by an anodic process. Surface properties such as topography, roughness, oxide thickness and microstructure and oxide chemistry can be varied controlling anodising variables as electrolyte solution, current density, potential, temperature among others. It is a very well spread technique used in many industries, with a big potential in the field of implants devices since it can be adjusted to complex geometries, low cost comparative to other techniques and possibility of adapting to induce desirable changes in surface properties.

3.3 Sol–Gel Coatings on Metallic Implants

Surface modification by the sol–gel coatings applied on metallic implants can be applied with the objective of minimising the corrosion of the metallic implant together with the functionalisation of the surface film to promote the osseointegration of the cementless implants. This strategy of surface modification is more used for those materials that cannot develop a thick oxide by anodisation (stainless steel, CrCo alloys, Mg alloys) and/or to

functionalise the materials to include in the coating some features as bioactive particles (hydroxyapatite, glass particles), bacterise agents, corrosion inhibitors among others.

3.3.1 General Aspects About Sol–Gel Science and Synthesis

A colloid is a suspension in which the dispersed phase is so small (1–1000 nm) that gravitational forces are negligible and interactions are dominated by short-range forces. A sol is a colloidal suspension of solid particles in a liquid that can be used to generate polymers or particles from which ceramic materials can be made. A ceramic is a non-metallic and inorganic compound, which includes metal oxides, nitrides and carbides, both crystalline and no crystalline. In the sol–gel process, the precursors (starting compounds) for preparation of a colloid consist of a metal or metalloid element surrounded by various ligands (appendages not including another metal or metalloid atom). The alkoxides are members of the family of metalorganic compounds, which have an organic ligand attached to a metal or metalloid atom. The most thoroughly studied example is silicon tetraethoxide (or tetraethoxysilane, or tetraethyl orthosilicate, TEOS), $Si(OC_2H_5)_4$ [225].

Silica and doped silica materials obtained via sol–gel inorganic polymerisation process are functional materials with an impressive range of applications, including the two pillars of the chemistry practice, synthesis and analysis, but also, protective coatings, controlled release, adsorption, chromatography, separation, biotechnology, energy conservation, cultural heritage restoration, environmental remediation and many other fields of contemporary technology [226].

Functional sol–gel materials are generally synthesised via the hydrolytic polycondensation, at room temperature, of liquid precursors under controlled conditions. The synthesis is generally carried out in an organic co-solvent (since alkoxysilanes are not water soluble) [227] through simultaneous or sequential reactions of hydrolysis (Eq. 3.1) and polycondensation, releasing water (Eq. 3.2) and/or alcohol (Eq. 3.3).

$$\equiv \mathrm{Si} - \mathrm{OR} + \mathrm{H_2O} \leftrightarrow \equiv \mathrm{Si} - \mathrm{OH} + \mathrm{R} - \mathrm{OH} \tag{3.1}$$

$$\equiv \mathrm{Si} - \mathrm{OH} + \mathrm{HO} - \mathrm{Si} \equiv \leftrightarrow \equiv \mathrm{Si} - \mathrm{O} - \mathrm{Si} \equiv + \mathrm{H_2O} \tag{3.2}$$

$$\equiv \mathrm{Si} - \mathrm{OR} + \mathrm{HO} - \mathrm{Si} \equiv \leftrightarrow \equiv \mathrm{Si} - \mathrm{O} - \mathrm{Si} \equiv + \mathrm{R} - \mathrm{OH} \tag{3.3}$$

The overall gelation process is slow due to the low polarity of the Si–O bond in silicon alkoxides (the Si atoms bear a $\delta+ = 0.32$ low positive charge in TEOS). Therefore, catalysis is essential. This is a key advantage because, in practice, the relative hydrolysis and condensation rates are very sensitive to the medium, which allows a relatively independent control through acid or base catalysis. One- or two-step processes can be used. The structure of a sol–gel material indeed evolves sequentially as the product of successive and/or simultaneous hydrolysis, condensation and their reverse reactions (esterification and depolymerisation, respectively).

Overall, silica gels with a texture closer to that of polymeric gels derived from organic chemistry are obtained if the hydrolysis rate is larger than that of condensation. This is usually the case under acidic catalysis. On the other hand, bases accelerate the condensation above the hydrolysis reactions, which then favours the formation of denser colloidal silica particles and colloidal gels. The fundamental structural units of silica gel are similar to those of vitreous silica (long accepted as a continuous random network of nearly perfect SiO_4 tetrahedral units). It was proposed that the tetrahedral units are mostly arranged in cyclic siloxane structures, 4-rings $[(SiO)_4]$, which are thermodynamically favoured, plus less tensioned 6-rings $[(SiO)_6]$, which are kinetically favoured. Broken siloxane bridges and rings of different dimensions were considered structural defects [228]. Thus, by chemical control of the mechanisms and kinetics of the sol–gel reactions, by thoughtful choice of the sol–gel process parameters (such as the nature of the precursors, the use of surfactants, acid or base catalysis, temperature [229], water/precursor and co-solvent/precursor ratios, ageing, washing and drying conditions), it is possible to tailor the structure of the resulting gels over a wide range, affording materials with the desired functional properties. The same hydrolysis and polycondensation reactions take place with other precursors different than TEOS, like methyltriethoxysilane (MTES), replac-

ing an ethyl ligand a non-hydrolysable one like a methyl group in MTES [230]. This precursor's mix gives to the generated material a hybrid character and a potential versatility to the synthesis, generating new functional variables [231, 232].

3.3.2 Sol–Gel Thin Films

One of the key areas of application for sol–gel processing is in coatings, where many advantages over conventional methods include the ability to coat large, curved substrates in a cost-effective method using simple deposition equipment, the ability to obtain coatings with high and tailored homogeneity, low sintering temperatures and the capability to prepare materials which cannot be prepared by other methods (organic–inorganic hybrid materials) [233]. Due to the improvement in technology and techniques based on thin films by sol–gel processing methods, special attention has been focused in thin films formation based on sol–gel processing. Chemical and physical variables that influence coating formation by different methods (dip coating, spin coating, centrifuge methods, spray, etc.) are being studied to optimise the process and quality of the final product [234].

In the sol–gel film-forming process, solution precursors are deposited on a substrate by dipping or spinning. Figure 3.8 schematically represents the dipping process. During sol-gel thin film formation via dipping, inorganic or metal organic sols are deposited on the substrate surface by a complex steady-state process combining gravitational draining, solvent evaporation and continued condensation reactions (Fig. 3.9) [225]. Unlike conventional bulk gel formation, the drying stage overlaps the aggregation/gelation and ageing stages, establishing only a brief time span for condensation reactions to occur [228]. In addition, the entrainment of the inorganic species in the draining fluid layer establishes a shear field that increases with substrate withdrawal speed U_0. When the receding drying line velocity equals the withdrawal speed, U_0, the process is steady state with respect to the liquid bath surface. The structure of the final deposited film depends on the competition between such phenomena as evaporation (which compact the film), condensation reactions (which strengthen the film, increasing its resistance to compaction) and

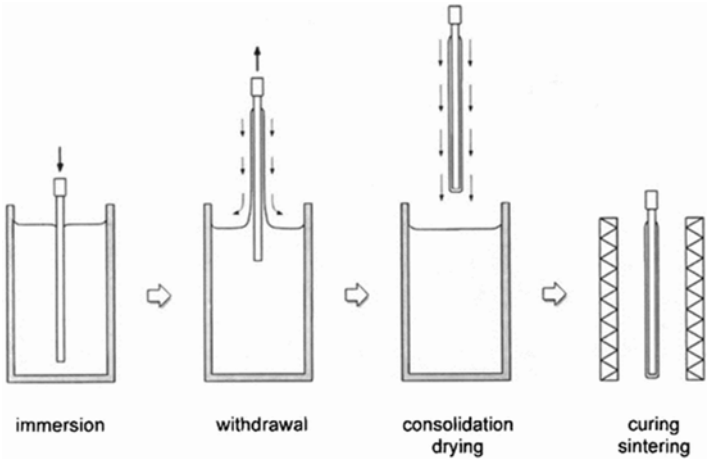

Fig. 3.8 Fundamental stages of sol–gel dip coating process. Reproduced with permission of Springer [235]

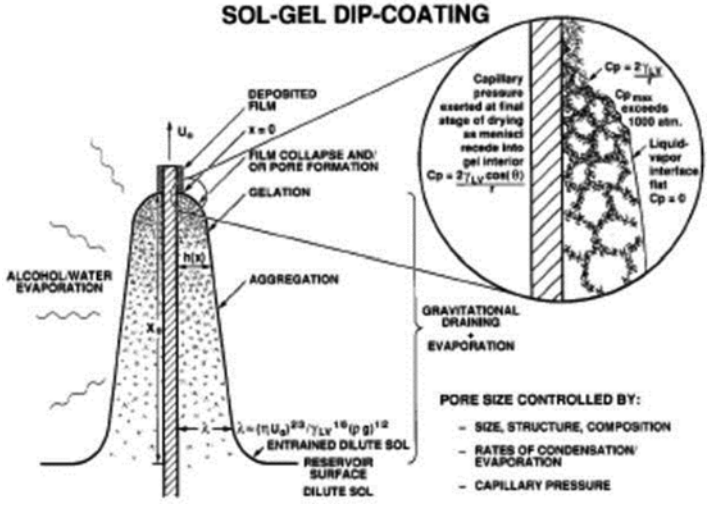

Fig. 3.9 Steady-state dip-coating process showing the sequent steps for film formation. Reprinted from ref. [228], Copyright 1992, with permission from Elsevier B.V.

shear-induced ordering. Often, compared with bulk gels, the brief time span of the deposition process causes the film structure to remain more compliant, allowing it to collapse at the final stage of drying as the liquid–vapour menisci recede into the film interior [234]. For alcohol-rich fluids common to sol-gel dip coating, steady-state conditions are attained in several seconds [228].

The formed film turns to solid state on the substrate by direct reaction with air between 200 and 500 °C [236]. One of the fundamental concerns in the thin film formation by dipping with sol–gel made materials is the limit or "critical thickness" of the film, which is the maximum thickness for a set system composition, preserving the homogeneity, constant thickness and flawless of the surface [230]. The phenomenon is rule by the sol composition, the degree of reaction reached (hydrolysis), solvent amount, second phases and the withdrawal speed.

Sol–gel coatings have already been used to good advantage in a wide variety of applications. These include transparent conductive coatings (based on oxides of Sb, In and Sn and ITO) [237, 238], passivation coatings (SiO_2, SiO_2–TiO_2, SiO_2–ZrO_2, Si–O–N coatings, coatings based on Al_2O_3–P_2O_5, etc.) [239–241], optical control coatings (TiO_2 films and some colour, SiO_2 coatings) [242], antireflection coatings (Si alkoxides with interconnected pores) [243, 244], porous coatings (Na, Ni, Mo and Pd hydrous titanate) [245], adhesion promoting coatings (organic complexes of Si, Ti, Al and Cr) [246], coatings in mechanical applications (SiO_2, porous Al_2O_3 coatings derived from $Al(OC_4H_9)_3$, SiO_2–TiO_2 coatings) [247–250], coatings in electrical–electronic applications [251], coatings applied onto metals to promote corrosion protection and bioactivity [226, 252–257].

3.3.3 *Metallic Implants: Substrates To Be Protected*

Metallic materials are most commonly used for load-bearing implants and internal fixation devices. They generally find applications in the fabrication of implant such as hip joint prosthesis, knee joint prosthesis, dental implants, cardiovascular devices, etc. (Fig. 3.10). The most commonly used metals and alloys for

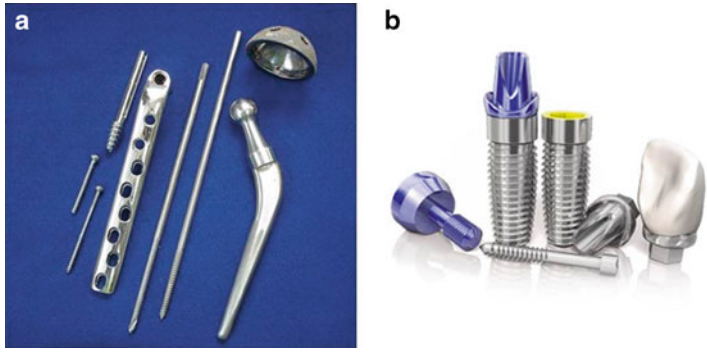

Fig. 3.10 Different types of permanent and transitory metallic implants for orthopaedic and dentistry (From http://www.1888implant.com/)

medical device applications include stainless steels, commercially pure titanium and its alloys, cobalt-based alloys and recently zirconium and magnesium alloys. Processing method and purity of the metal determines its mechanical and chemical properties. Some featured properties of a metallic material are its high tensile strength, high yield strength, resistance to cyclic loading (fatigue), resistance to time-dependent deformation (creep) and its corrosion resistance. Among the candidate materials to be used in dentistry and orthopaedic surgery, stainless steels, titanium and its alloys, cobalt-based alloys and magnesium are the most studied alloys to be functionalised with sol–gel coatings either to control their corrosion rate in body fluid and/or to promote bone formation.

Stainless steels are iron-base alloys with a minimum of 10.5 % Cr as an alloying element, needed to prevent the formation of rust. Stainless steel (18Cr–8Ni) was first used in orthopaedic surgery in 1926. For implant applications they must have the resistance to pitting and crevice corrosion from the body plasma. Special production techniques such as vacuum melting, vacuum arc melting and electro slag refining are required to produce high-quality stainless steels with minimum non-metal inclusions for implant applications [258]. Apart from implant applications commercial-grade stainless steels are also widely used for the manufacture of surgical and dental instruments. Although there are several types of stainless steels in use for medical applications, 316L (18Cr–14Ni–

2.5Mo) single phase austenitic (FCC) stainless steel is the most popular one for implant applications [259–262]. The "L" in the designation denotes its low carbon content and as a result it has high corrosion resistance in in vivo conditions [263]. Shih and co-workers studied the effect of surface treatment on the in vitro corrosion resistance and in vivo biocompatibility of 316L stainless steel [260, 264].

Co–Cr-based alloys are the most commonly used representative Co alloys for biomedical applications. The presence of Cr imparts the corrosion resistance and the addition of small amounts of other elements such as iron, molybdenum or tungsten can give very good high temperature properties and abrasion resistance [25]. The various types of Co–Cr alloys used for implant applications include Co–Cr–Mo (ASTM F75), Co–Cr–Mo (ASTM F799), Co–Cr–W–Ni (ASTM F90) and Co–Ni–Cr–Mo–Ti (ASTM F562).

The development of biodegradable implants is nowadays one of the more important areas in medical science [265]. A biodegradable material can be gradually dissolved after implanting. Compared with a traditional permanent implant, a biodegradable material will not cause permanent physical irritation or chronic inflammatory discomfort [266], and also it is thought to induce bone healing [267]. Magnesium is potentially a good temporary implant material for its non-toxicity to the human body. Mg^{2+} is present in large amount in the human body and involved in many metabolic reactions and biological mechanisms. The human body usually contains approximately 35 g per 70 kg body weight and the human body's daily demand for Mg is about 375 mg/day. Due to the excellent biocompatibility, magnesium alloys used to be introduced as implants into orthopaedic and trauma surgery in the first half of the last century. However, it was found that magnesium alloys corroded too rapidly, resulting in subcutaneous hydrogen gas release and consequently the approach of using magnesium alloys as permanent biomaterials was abandoned. Since rapid corrosion is almost an intrinsic response of magnesium to a chloride-containing solution [268] like the human body fluid or plasma, the application of coatings onto the surface could turn magnesium into a biodegradable implant material controlling dissolution rate or delaying corrosion process. In fact, with recent developments of

magnesium alloys and understandings of corrosion and prevention of magnesium alloys, controlling the corrosion performance of a magnesium alloy should be possible now [269, 270].

3.3.4 *Bioactivation of Permanent Metallic Implants*

Bioactive coatings are important for metallic implants such as hip prostheses and periodontal implants because some metals alone (as stainless steel or CrCo alloys) are bioinert, which means they are encapsulated with fibrous tissue after implantation [271]. Bioactive coatings have the potential to improve the stability of implants by bonding them to the host bone, where the hydroxyapatite (HA) layer forms on bioactive glass as a result of dissolution. Bioactive glasses are by nature biodegradable, and therefore a highly bioactive coating may degrade over time, causing instability of the metallic implant in the long term [272].

Glass can be made using two processing methods: the traditional melt-quenching route and the sol–gel route (Fig. 3.11). Bioglass® 45S5 and other commercial bioactive glasses are made by melt quenching, where oxides are melted together at high temperatures (above 1300 °C) in a platinum crucible and quenched in a graphite mould (for rods or monoliths) or in water (frit). The sol–gel route essentially forms and assembles nanoparticles of silica at room temperature. It is a chemistry-based synthesis route where a solution containing the compositional precursors undergoes polymer-type reactions at room temperature to form a gel [225]. The gel is a wet inorganic network of covalently bonded silica, which can then be dried and heated, e.g. to 600 °C, to become a glass. Typical bioactive compositions are in the ternary system [273], e.g. 58S (60 mol% SiO_2, 36 mol% CaO, 4 mol% P_2O_5) and 77S (80 mol% SiO_2, 16 mol% CaO, 4 mol% P_2O_5), or binary system s like 70S30C (70 mol% SiO_2, 30 mol% CaO). The physical differences in melt- and sol–gel-derived glasses are that sol–gel glasses tend to have an inherent nanoporosity (*a*) whereas melt-quenched glasses are dense [274]. The nanoporosity can

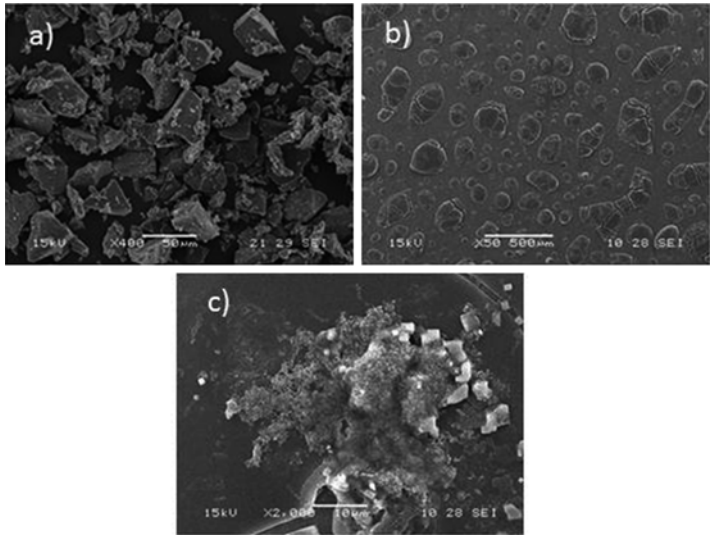

Fig. 3.11 (**a**) Melt-quenched and (**b**) sol–gel 45S5 bioactive glasses. (**c**) Dissolution and redeposition of Ca-P related compounds on sol–gel-derived glass

result in improved cellular response due to the nanotopography and a specific surface area two orders of magnitude higher than for similar compositions of melt-derived glass. The high surface area of sol–gel glasses results in high dissolution rates and, as there is no melting involved, sodium is not required in the composition. Nonetheless, sol–gel glasses have been produced close to the 45S5 composition, e.g. 49.15 mol% SiO_2, 25.80 mol% CaO, 23.33 mol% Na_2O, 1.72 mol% P_2O_5 [275], although the gels must not be heated above 600 °C if the glasses are to remain amorphous. Common precursors for introducing calcium and phosphate into the sol–gel are calcium nitrate tetrahydrate and triethylphosphate, respectively. The thermal process also removes by-products of the non-alkoxide precursors, such as nitrates from calcium nitrate. Among the different solutions which have been proposed, hydroxyapatite [HA, $Ca_{10}(PO_4)_6(OH)_2$] coatings on Ti have attracted much attention over the last two decades [271, 276]. The excellent biocompatibility of HA is closely related to its chemical and biological similarities with human hard tissues [277]. The problem resides in

the deposition method of the HA and related coatings: typically done by plasma spray [278, 279]. However, there are some problems associated with the plasma-spraying process, such as poor adherence to the substrate, chemical inhomogeneity and high porosity. Most of these problems are associated with the excessively high fabrication temperature. In vivo studies of HA coatings on Ti implants have revealed good fixation to the host bones and an increased amount of bone ingrowth into the implants [280, 281]. Along with HA, fluorapatite [FA, $Ca_{10}(PO_4)_6F_2$] coatings on metallic substrates have also attracted considerable attention in areas that require long-term chemical and mechanical stability of the coating layer [282, 283]. Pure FA has a lower bioresorption rate than HA, and has a level of biocompatibility comparable to that of HA, demonstrating good properties in fixation to bone and bone ingrowth [283]. F^- promotes the mineralisation and crystallisation of calcium phosphate in the bone forming process. In comparison with plasma spray, the sol–gel technique offers certain advantages, because of the high chemical homogeneity, fine grain structure and low crystallisation temperature of the resultant coating, as well as its being both an economical and technically simple procedure to perform [284].

Thus, one way to improve biocompatibility of metals is to apply a sol–gel coating of hydroxyapatite (HA) and fluor-hydroxyapatite (FHA) [285]. The surface morphology for coated Ti is shown in Fig. 3.12. The coating layers were phase pure, dense and uniform, and had a thickness of around 5 μm after heat treatment at 500 °C. The FHA layer showed much lower dissolution rate than pure HA, suggesting the tailoring of solubility with F^- incorporation within the apatite structure. The osteoblast-like MG63 and HOS cells grew and proliferated favourably on all the HA and FHA coatings and pure Ti. Especially, the HA- and FHA-coated Ti exhibited higher ALP expression levels as compared to pure Ti, confirming the improved activity and functionality of cells on the substrate via the coatings [285].

Inorganic–organic hybrid sol–gel materials are interpenetrating networks of inorganic and organic components that interact at the nanoscale [286]. The two components are indistinguishable above the nanoscale. This is different from nanocomposites,

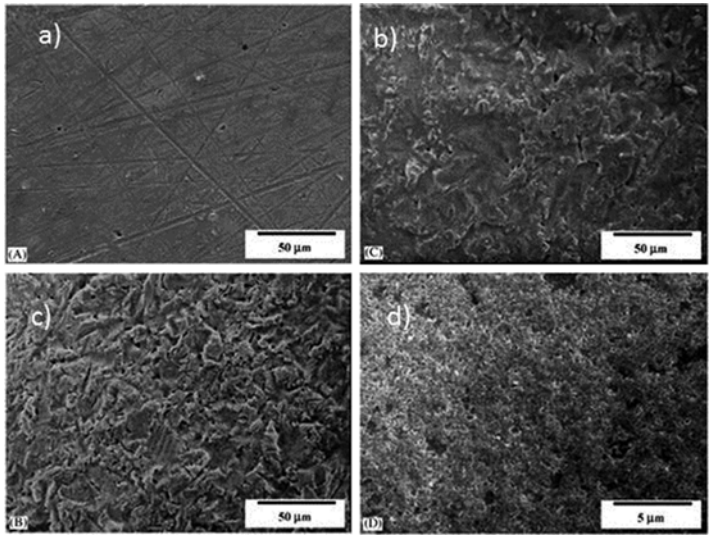

Fig. 3.12 SEM surface morphologies of the pure Ti and apatite-coated Ti after heat treatment at 500 °C for 1 h: (**a**) pure Ti, (**b**) HA coating, (**c**) 50FHA coating and (**d**) 50FHA coating at higher magnification. Reprinted from ref. [285], Copyright 2003, with permission from Elsevier Ltd.

which have distinguishable components. However, synthesis of hybrids is sometimes complex and there are several chemistry challenges that must be overcome before hybrids will be successful and used in tissue regeneration. Hybrids are synthesised introducing the polymer early in the sol–gel process, e.g. after hydrolysis of the TEOS, so that the inorganic (silica) network forms around the polymer molecules, resulting in molecular-level interactions [225]. The hypothesis is that the fine-scale interactions between the organic and inorganic chains lead to the material behaving as a single phase, resulting in controlled congruent degradation and the potential for tailoring the mechanical properties [286] (Fig. 3.13). The fine-scale dispersion of the two components means that cells are likely to attach to the hybrid surface as though it is one material, rather than bioactive particles dispersed in a polymer matrix. The aim is that a bioactive hybrid would have bioactivity similar to that of a bioactive glass, but have toughness and controlled congruent degradation [272].

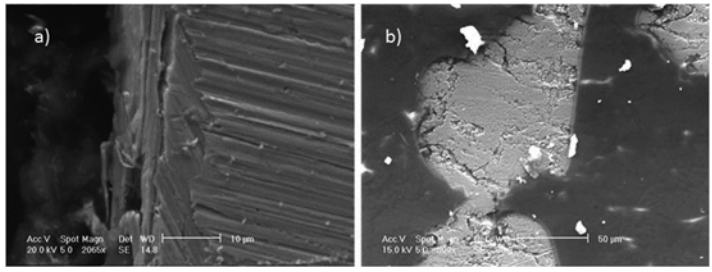

Fig. 3.13 Hybrid organic–inorganic silica-based sol–gel coating on surgical grade stainless steel. (**a**) Cross section showing the adaptability of the film to the substrate and (**b**) broken detached sample showing the smooth surface features of the coating

Methacrylate–silica-based sol–gel films [287, 288] could also be an option to simulate the open structure of collagen fibres in new uncalcified bone, for being the polymer structureless dense and more open than other hybrid coatings, and for having a biomimetic behaviour if they are correctly functionalised [289, 290]. The silica xerogel system is an attractive material to apply to metallic substrates, because sol–gel-derived silica xerogels are known to have excellent bioactivity and exhibit chemical bonding to the surrounding tissues, particularly bone [291, 292]. However, silica xerogels have one serious problem in that they undergo severe cracking during processing. In order to overcome this intrinsic weakness, silica xerogels have in recent years been combined with organic materials. Chitosan, a kind of polysaccharide, is a deacetylated derivative of chitin and has been widely applied in biomedical applications because of its cell compatibility, biodegradability and non-toxic characteristics. It is also flexible and easily formable as compared with inorganic materials. These properties of chitosan make it a suitable material for hybridisation with silica xerogels and as a room temperature-coating layer on metallic implants [293].

One way to minimise the release of corrosion products from the implant to the surrounding tissue is to apply protective hybrid organic–inorganic coatings [256, 287, 294–296]. Such films should also be functional with bioactive material for inducing the

formation of a semicrystalline hydroxyapatite (HA) rich layer onto the material surface, generating a natural bond to living tissues. HA can be detected after in vitro tests performed by soaking the material in simulated body solutions (SBF), Hank's balanced salt solution (HBSS) and other solutions that simulate body fluids [297–300]. This behaviour is considered an indication of in vitro bioactivity [301, 302].

Galliano and co-workers demonstrated that inorganic and hybrid SiO_2 coatings obtained from tetraethylorthosilicate (TEOS) and/or methyltriethoxysilane (MTES) as SiO_2 precursors using acid catalysts improve the corrosion behaviour of AISI 316L stainless steel in biological environments (Fig. 3.14) [303, 304]. Coatings were applied as mono and multilayers by a multistep method. XPS analysis of inorganic and hybrid SiO_2 coatings on steel substrates showed that using TEOS as the only precursor results in some extent of Fe diffusion, but the hybrid coatings prepared from MTES/TEOS limited the diffusion of iron to surface during thermal treatment, with much lower iron contents than those reported for bioactivity inhibition [256, 289, 305].

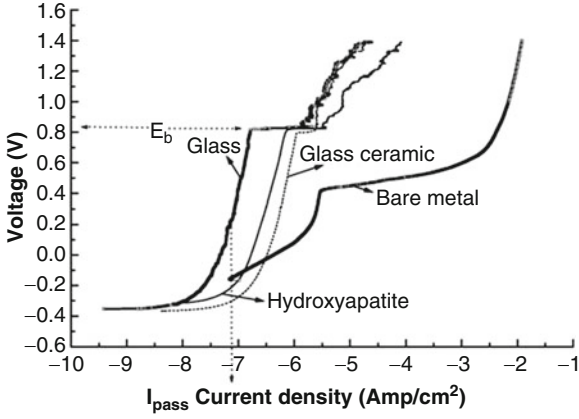

Fig. 3.14 Anodic polarisation curve for double-layer coatings on SS 316L containing glass, glass–ceramic and hydroxyapatite, compared with the uncoated substrate after 24 h immersion in SBF. Reprinted from ref. [303], Copyright 1998, with permission from Kluwer Academic Publishers.

Continuous and defect-free hybrid sol–gel coatings were also obtained on surgery alloys (Ti alloys, Co–Cr–Mo F75 alloy) [256]. The incorporation of bioactive glass or glass–ceramic particles on the surface promoted bioactivity. Electrochemical characterisation of samples coated with mono- and double-layer coatings showed a dramatic reduction of the passive current densities compared with the bare alloys. The coatings improved the protection potential of the base materials in the tested electrolytes. EIS results for immersion times of up to 6 months demonstrated the stability of the coatings and the prevention of electrolyte penetration. In vitro response was fast and dependent on the concentration and size of particles but not on the thickness of the coating. HA deposits of low crystallinity were observed for all the coated alloys after 3–7 days of immersion in SBF or HBSS. Sol–gel coatings act as diffusion barriers, strongly impeding ion release and avoiding biotoxicity (Fig. 3.15a, b) [256, 295, 304].

Pourhashem et al. have used a SiO_2–CaO–P_2O_5 bioglass coating via sol–gel method and silica–bioglass coatings prepared by suspensions containing bioglass particles to bioactivate and protect stainless steel [306]. In this research, double-layer coatings containing silica (SiO_2) intermediate layer and 45S5 bioglass (SiO_2–CaO–Na_2O–P_2O_5) top layer were prepared by sol–gel procedure on 316L stainless steel substrates.

The corrosion behaviour is essentially related to the morphology and defects of coated surface. The electrolyte can infiltrate into the inner portion of the coating through the structural imperfections such as pores, cracks and pinholes existing in the coating and comes into contact with the deeper portion of the coating. The barrier effect of coatings is increased by the first SiO_2 coating that prevents the contact of electrolyte with the substrate after the dissolution of bioactive particles [295]. After 7 days of exposure to SBF solution, the alkali and alkaline earth ions from the bioactive glass surface start to diffuse into the surrounding medium faster than ion precipitation on glass surface, leaving behind a corroded surface with increased surface area [307]; thus, the corrosion rate increases in the first days of immersion. Further, leaching of ions leads to an exposition of Si–OH networked surface. This active surface stimulates deposition of a thin film consisting of hydroxyapatite on the bioactive glass surface which slowly reduces the

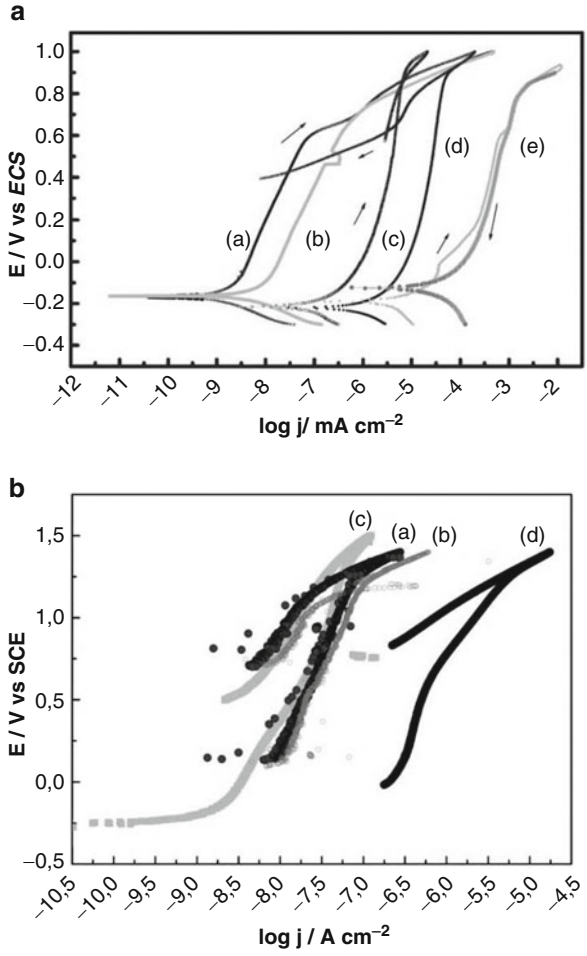

Fig. 3.15 (**a**) Potentiodynamic polarisation curve for the coated and uncoated CrCoMo alloy (F75) in neutral SBF solution. (*a*) Double-layer coating with 5 wt% glass–ceramic; (*b*) single layer with 5 wt% glass–ceramic; (*c*) double-layer coating with 10 wt% glass–ceramic; (*d*) single layer with 10 wt% glass–ceramic; (*e*) uncoated CrCoMo alloy. Reproduced from Ref [256] (2004) by permission of The Royal Society of Chemistry (RSC). (**b**) Potentiodynamic polarisation curves for the coated and uncoated Ti–6Al–4V alloy in neutral SBF solution. (*a*) Double-layer coating with 10 wt% glass; (*b*) double-layer coating with 10 wt% glass–ceramic; (*c*) single layer with 10 wt% glass; (*d*) uncoated Ti–6Al–4V alloy. Reproduced from Ref. [256] (2004) by permission of The Royal Society of Chemistry (RSC)

area of exposed surface and pores and defects presented in the coatings could be blocked by corrosion products of the metal or by the degradation of the particles present in the coating [295]. This blocking could cause a higher resistance to the diffusion of the electroactive species to reach the metallic substrate increasing the apparent resistance of the system with time and decreasing the rate of dissolution (Fig. 3.16) [306].

Metikoš-Hukovic' et al. [308] have done in vitro and in situ investigations in order to determine the dielectric and electric properties of CaP coatings obtained by the sol–gel method and their influence on corrosion stability of titanium and titanium alloys (Ti6Al4V and Ti6Al6Nb) in simulated Hank's Balanced Salt Solution (HBSS). The results were compared with those obtained for spontaneously formed surface films on the same electrode material in HBSS. In order to investigate the corrosion stability of implant materials covered with CaP coatings, the samples were exposed to physiological solution for 3 months and the measurements repeated.

Generally, it can be said that there is no discernible difference in the crystallisation pathway among the CaP powder and CaP coatings

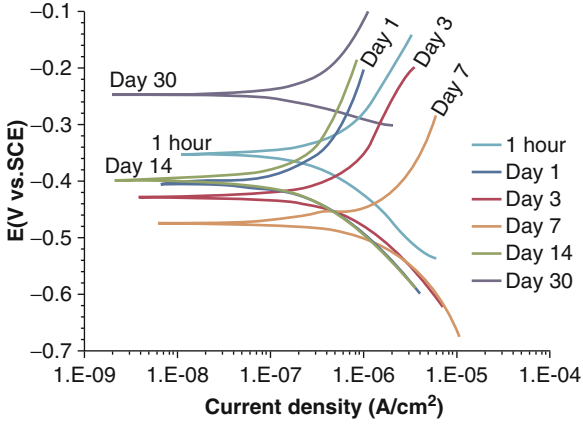

Fig. 3.16 Potentiodynamic polarisation curves of bioglass–silica-coated samples after soaking in SBF at 37 °C for different immersion times. Reprinted from ref. [306], Copyright 2013, with permission from Elsevier Ltd and Techna Group S.r.l

on Ti-alloy substrates. By studying the thermal behaviour of the same sol–gel-derived CaP coatings on Ti5Al2.5Fe (TAF) substrate, the formation of rutile at the substrate-coating interface was observed at approximately 700 °C and sintering at 600 °C for 10 min was found to be the optimum for CaP coatings on Ti-alloy substrates [309]. The impedance spectroscopy data, recorded under open-circuit conditions in HBSS, represent the response of the sol–gel CaP-coated titanium and titanium alloys, over a period of 90 min and 3 months (Fig. 3.17). The interpretation of the results is based upon a two-layer model of the surface film consisting of an inner barrier layer and a thicker porous outer layer. The inner barrier layer dominates the impedance spectra at higher frequencies while the outer layer dominates at low frequencies. The impedance data vary with immersion time, the main variable being an increase in the capacitance and a decrease in the resistance of the inner layer. Since the pores are filled with electrolyte, the contribution from this

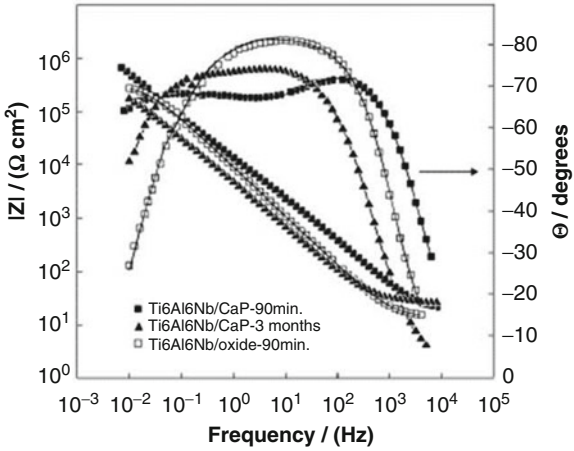

Fig. 3.17 Bode plot (impedance module/*Z*/ vs. log*f* and phase angle Θ vs. log*f*) of impedance spectra for the Ti6Al6Nb electrode, recorded in physiological HBSS at the open circuit potential: (*open square*) with a spontaneously nucleated passive film after 90 min of immersion in HBSS, (*filled square*) CaP coated after 90 min of immersion in HBSS and (*filled triangle*) CaP coated after 3 months of immersion in HBSS. Reprinted from ref. [308], Copyright 2002, with permission from Elsevier Science B.V.

porous layer to the electrochemical properties is rather small, and the impedance response is dominated by the inner layer which behaves as a non-ideal dielectric with high electronic resistance. The nature of both layers was found to depend on the nature of the electrode substrate material and the presence of phosphate anions [308]. The chemical composition of the substrate as well as the composition and crystallinity of the CaP coating has a direct influence on electrochemical–corrosion properties of the implant materials under in vitro conditions.

The total impedance was only determined by the impedance of the barrier layer and was equal to the impedance of the sample coated with a spontaneous oxide film. In contrast, the coating on the Ti6Al4V substrate with better crystallised HAP and b-TCP phases and with a smaller amount of carbonate incorporated in the structure of HAP exhibits a beneficial corrosion protection effect. Upon prolonged exposure to physiological solution, it retards the diffusion [33] of vanadyl ions via pore closure due to hydrolysis or precipitation of HAP from the solution [308, 310]. The influence of composition, stoichiometry and structure of the CaP coating on the electrochemical behaviour of the Ti6Al6Nb and Ti6Al4V alloys became significant only after 3 months of exposure to HBSS. Well-crystallised HAP and beta-TCP exhibited a beneficial corrosion protection effect on the substrate during prolonged exposure to HBSS. The incompletely crystallised and inhomogeneous coating containing hydroxyapatite with a larger amount of carbonate incorporated in the structure of HAP and b-TCP on the Ti6Al6Nb substrate completely dissolves after prolonged exposure to HBSS.

3.3.5 Bioactivation of Transitory Metallic Implants

The sol–gel coating technique has been widely investigated in regard to coating Mg and its alloys for both corrosion protection and increased bone adhesion (Fig. 3.18) [311]. Most of research involved in coating of Mg alloys is related to the use of calcium

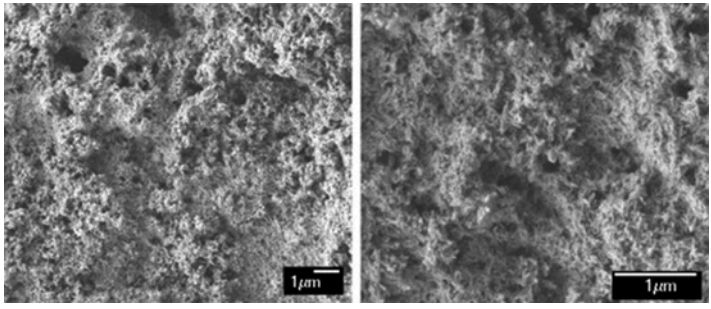

Fig. 3.18 Scanning electron micrographs of calcium phosphates created using a sol–gel technique (two magnifications). Reprinted from ref. [311], Copyright 2011, with permission from Elsevier Ltd.

and phosphorus elements included in the precursors, and water and ethanol often used as solvent. The phosphorus precursor, regularly phosphorus pentoxide or triethyl phosphite, is dissolved in ethanol and added to the solution to achieve hydrolysis of the sol [312–314]. The selected calcium precursor, most often calcium nitrate, is also dissolved in ethanol and then added to the hydrolysed phosphorus sol in a dropwise way. Special care has to be taken to the pH of the obtained sol since there is a spontaneous oxidation of the Mg alloys with acidic media (pH below 5). Samples to be coated are then dipped into the sol–gel to acquire a CaP coating, which is then cured at high temperatures (in the range of 350–600 °C) to increase the coating–substrate adhesion and to achieve the apatite structure within the applied coatings [315]. Curing temperatures for Mg substrates cannot exceed the melting point of pure Mg (650 °C) or the relevant alloy to avoid affecting the substrate.

Inorganic–organic hybrid sol–gel coatings are favourable for Mg since they require far lower curing temperatures (as mentioned earlier) and have the ability to incorporate factors that may further improve the adhesion or corrosion resistance of the Mg substrate [268, 316]. Papers have reported the formation of organic–inorganic hybrid films consisting of silane-based alkyls and phosphates to be effective in reducing corrosion rates of Mg AZ31B as determined via electrochemical methods [317].

Rojaee et al. probed that it was possible to prepare a bioceramic coating (HA coating) on AZ91 magnesium alloy by sol–gel in order to control the Mg biodegradability with the aim of improving the healthiness of the severely hurt tissues [318]. The author's objective was pointed out to establish a desired harmony between the need of patient body to Mg^{2+} ions and the degradation rate of the Mg-based implants as a new class of biodegradable/bioresorbable materials. This idea was followed by providing a sol–gel derived nanostructurarted hydroxyl-apatite (n-HAP) coating on AZ91 alloy using dip coating technique.

The electrochemical polarisation curves of the bare and n-HAp coated specimens are shown in Fig. 3.19. The intercept of the cathodic and anodic polarisation curves showed that the n-Hap-coated AZ91 alloys shifted the corrosion current density to more noble value. The corrosion potential concerning the n-Hap-coated AZ91 alloy shifted to a more positive potential. This could be a good indication of the coating stability, which is more likely due to the establishment of oxide inter-layer during heat treatment of the coated specimens [319]. An increase in anodic Tafel slope (βa)

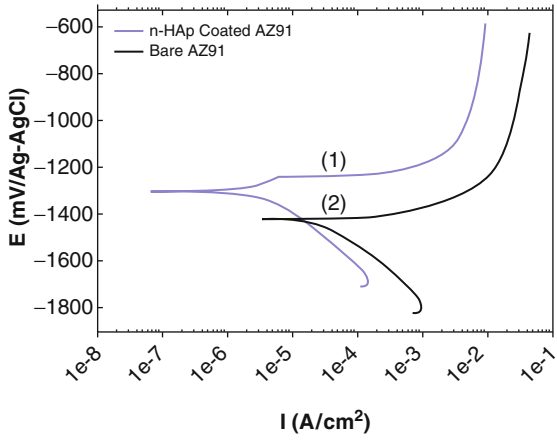

Fig. 3.19 Potentiodynamic polarisation curves of sol–gel-derived HA-coated AZ91 specimen (curve 1) and bare AZ91 specimen (curve 2) in SBF at 37 ± 1 °C. Reprinted from ref. [318], Copyright 2013, with permission from Elsevier B.V.

was observed in the n-Hap-coated specimen. That could be a response of the higher activation energy in releasing Mg^{2+} ions, causing lower corrosion rates.

In the EIS results of this kind of coatings is often observed an induction loop in the Nyquist plot at low frequencies (figure not shown). Low-frequency inductive loops in the impedance response can be ascribed to Faradaic reactions that involve adsorbed intermediate species in the reduction of hydrogen gas, rearrangement of surface charge at the coating/oxide/metal interface, releasing the oxidation products such as Mg^{2+} or $Mg(OH)_2$ and pitting corrosion mechanism [319, 320]. The whole corrosion process can be reflected by weight loss measurement and the optical degradation behaviour evaluation [321]. It was observed that degradation rate decreased as immersion time increased. Moreover, it shows that the HA-coated specimens were degraded more gradually than the bare AZ91 specimens. This indication merges with the results in electrochemical experiments. In addition, it is proven that surface conditions and physiological environments play important roles in Mg degradation [265, 268]. It seems that both bare and HA-coated AZ91 specimens were covered with partially protective corrosion products and apatite-like precipitations on the surface [322]. This event would help to reduce the rate of degradation [318]. To fully exploit the good biocompatibility of CaP glass protective coating for magnesium substrate, the integrity and longevity of such CaP protective coating still needs to be improved. Ren et al. [323] have proposed one possible approach to improve the corrosion resistance of CaP glass coating by employing a pretreatment interlayer to enhance the corrosion protection. Besides, fluoride conversion treatments are considered to be one of the promising techniques for the pretreatment of biodegradable magnesium alloys used as orthopaedic implants. Fluorine is a natural component of the human skeleton and teeth. As one of the essential trace elements required by the human body, fluorine is thought to stimulate osteoblast proliferation and could increase the mineral deposition rate in cancellous bones [323–325].

Some authors [317, 326] have reported the anticorrosion resistance and or a self-healing effect of sol–gel thin films on magnesium alloys. As alkoxides or inorganic salts precursors for the sols

such as Ce own a relatively low pH, and magnesium alloys would be degraded by the sol, it is important to find out a way to deal with the poor coating adhesion and subsequent corrosion of the coated magnesium alloys. Zhang et al. developed a novel approach to prepare sol–gel films, where appropriate additives were used to stabilise and disperse uniformly the inorganic salts, and to reach to sols with a certain pH that could be applied directly on magnesium alloys. In this work, novel Ce/Mg (CM) composite films were successfully prepared on AZ91D Mg alloy substrate via sol–gel process. Compared with the traditional method, this novel process using inorganic salts as precursors was lower cost, more environment friendly and simpler application procedures easily adaptable within industry [327]. The composite films represented a good alternative to existing ones to protect Mg alloy substrate against corrosion in 3.5 wt% NaCl solution basing on the cross-linking of Ce and Mg films. The Ce and Mg films are cross-linking through the pores, so the CM composite films act as an effective geometric layer against exposure to the corrosive media, as can be analysed by potentiodynamic tests (Fig. 3.20). The improvement with the conversion layer is displayed by both a anodic shift of *Ecorr* by 200 mV and a by a significant decrease of two orders of magnitude of the *Icorr* compared to the uncoated substrate, the passive range

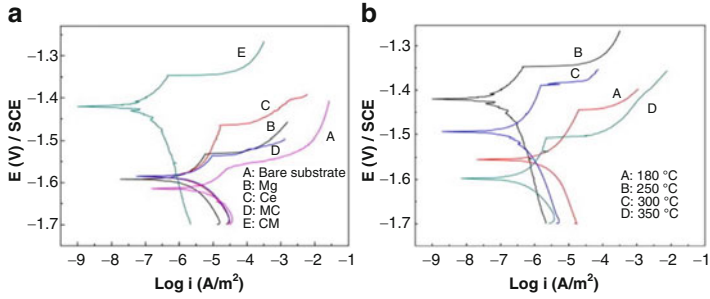

Fig. 3.20 Potentiodynamic polarisation curves of samples in 3.5 wt% NaCl solution: (**a**) different coated samples sintered at 250 °C compared with bare AZ91D magnesium alloy substrate at 25 °C; (**b**) CM samples with different sintering temperatures. Reprinted from ref. [327], Copyright 2009, with permission from Elsevier B.V.

indicates that the CM composite films passive a very active alloy, decrease the corrosion rate and the pitting susceptibility of the AZ91D Mg alloy.

The sol–gel process has been demonstrated to be an effective and tailor, environment-friendly route to prepare films on metallic substrates at low cost [319, 328, 329], with proven potential to be used in the formulation of protective [253, 294, 303, 330, 331] and bioactive coatings [305, 332].

3.4 Conclusions

The use of surface modification techniques as anodising process or sol–gel thin films coatings is two of many ways to prevent deterioration of metallic implants by generating a barrier and a bioactive surface to promote bone regeneration and a reaction with the surrounding media in a constructive way.

Corrosion of orthopaedics implants is a subject of concern, and many efforts are done in research to prevent the clinical issues that can be overcome as a result of undesirable corrosion rate. Either for permanent or temporary implants, surface treatments represent the best alternative to control the corrosion rate in body fluid and the possibility of modifying the surface to increase the osseointegration, minimising the harmful effect of by-products of electrochemical reactions and enhancing the bone healing.

References

1. Virtanen S (2008) Corrosion of biomedical implant materials. Corros Rev 26(2–3):147–172
2. Virtanen S, Milosev I, Gomez-Barrena E et al (2008) Special modes of corrosion under physiological and simulated physiological conditions. Acta Biomater 4(3):468–476
3. Black J (1988) Does corrosion matter? J Bone Joint Surg (Br) 70-B(4):517–520
4. Jacobs JJ, Gilbert JL, Urban RM (1998) Corrosion of metal orthopaedic implants. J Bone Joint Surg (Br) 80-A(2):268–282

5. Pennington M, Grieve R, Sekhon JS et al (2013) Cemented, cementless, and hybrid prostheses for total hip replacement: cost effectiveness analysis. BMJ 346:f1026
6. Rothman RH, Cohn JC (1990) Cemented versus cementless total hip arthroplasty: a critical review. Clin Orthop Relat Res 254:153–169
7. Albrektsson T, Branemark PI, Hansson HA et al (1981) Osseointegrated titanium implants. Requirements for ensuring a long-lasting, direct bone-to-implant anchorage in man. Acta Orthop Scand 52(2):155–170
8. Ehrenfest DMD, Coelho PG, Byung-Soo K et al (2009) Classification of osseointegrated implant surfaces: materials, chemistry and topography. Trends Biotechnol 28(4):198–206
9. Metikos-Hukovic M, Grubac Z (2003) The growth kinetics of thin anodic WO_3 films investigated by electrochemical impedance spectroscopy. J Electroanal Chem 556:167–178
10. Chappell MJ, Leach JSL (1980) Passivity and breakdown of passivity on valve metals. In: Frankenthal RP, Kruger J (eds) Passivity of metals. The Electrochemical Society, Pennington, pp 1003–1034
11. Michaelis A (2008) Valve metal, si and ceramic oxides as dielectric films for passive and active electronic devices. In: Electrochemical surface modification. Wiley, New York, pp 1–106
12. Hurlen T, Gulbrandsen E (1994) Growth of anodic films on valve metals. Electrochim Acta 39(14):2169–2172
13. Habazaki H, Ogasawara T, Konno H et al (2005) Growth of anodic oxide films on oxygen-containing niobium. Electrochim Acta 50:5334–5339
14. Habazaki H, Shimizu K, Nagata S et al (2005) Inter-relationship between structure and dielectric properties of crystelline anodic zirconia. Thin Solid Films 479:144–151
15. López MF, Gutiérrez A, Jiménez JA (2001) Surface characterization of new non-toxic titanium alloys for use as biomaterials. Surf Sci 482–485:300–305
16. Nag S, Banerjee R, Fraser HL (2005) Microstructural evolution and strengthening mechanisms in Ti–Nb–Zr–Ta, Ti–Mo–Zr–Fe and Ti–15Mo biocompatible alloys. Mater Sci Eng C 25(3):357–362
17. Li SJ, Yang R, Li S et al (2004) Wear characteristics of Ti–Nb–Ta–Zr and Ti–6Al–4V alloys for biomedical applications. Wear 257(9–10):869–876
18. Li SJ, Yang R, Niinomi M et al (2004) Formation and growth of calcium phosphate on the surface of oxidized Ti–29Nb–13Ta–4.6Zr alloy. Biomaterials 25(13):2525–2532
19. Taddei EB, Henriques VAR, Silva CRM et al (2004) Production of new titanium alloy for orthopedic implants. Mater Sci Eng C 24:683–687
20. Navarro M, Michiardi A, Castano C et al (2008) Biomaterials in orthopaedics. J R Soc Interface 5:1137–1158
21. Han X, Liu H, Wang D et al (2011) In vitro biological effects of Ti2448 alloy modified by micro-arc oxidation and alkali heatment. J Mater Sci Technol 27(4):317–324

22. Minagar S, Berndt CC, Wang J et al (2012) A review of the application of anodization for the fabrication of nanotubes on metal implant surfaces. Acta Biomater 8(8):2875–2888
23. Hernández-López JM, Conde A, de Damborenea J et al (2015) Correlation of the nanostructure of the anodic layers fabricated on Ti13Nb13Zr with the electrochemical impedance response. Corros Sci 94:61–69
24. Hanawa T (2002) Evaluation techniques of metallic biomaterials in vitro. Sci Technol Adv Mater 3:289–295
25. Hanawa T (2004) Metal ion release from metal implants. Mater Sci Eng C 24:745–752
26. Tengvall P, Lundström I (1992) Physico-chemical considerations of titanium as a biomaterial. Clin Mater 9:115–134
27. Liu X, Chu PK, Ding C (2004) Surface modification of titanium, titanium alloys, and related materials for biomedical applications. Mater Sci Eng R Rep 47(3-4):49–121
28. Milosev I, Kosec T, Strehblow H-H (2008) XPS and EIS study of the passive film formed on orthopedic Ti-6Al-7Nb alloy in Hank's physiological solution. Electrochim Acta 53:3547–3558
29. Kim H-M, Miyaji F, Kokubo T et al (1996) Preparation of bioactive Ti and its alloys via simple chemical surface treatment. J Biomed Mater Res 32:409–417
30. Wang CX, Wang M, Zhou X (2003) Nucleation and growth of apatite on chemically treated titanium alloy: an electrochemical impedance spectroscopy study. Biomaterials 24:3069–3077
31. Wang XJ, Li YC, Lin JG et al (2008) In vitro bioactivity evaluation of titanium and niobium metals with different surface morphologies. Acta Biomater 4(5):1530–1535
32. Faure J, Balamurugan A, Benhayoune H et al (2009) Morphological and chemical characterisation of biomimetic bone like apatite formation on alkali treated Ti6Al4V titanium alloy. Mater Sci Eng C 29(4):1252–1257
33. Aziz-Kerrzo M, Conroy KG, Fenelon AM et al (2001) Electrochemical studies on the stability and corrosion resistance of titanium-based implant materials. Biomaterials 22(12):1531–1539
34. Karthega M, Nagarajan S, Rajendran N (2010) In vitro studies of hydrogen peroxide treated titanium for biomedical applications. Electrochim Acta 55(6):2201–2209
35. Karthega M, Rajendran N (2010) Hydrogen peroxide treatment on Ti–6Al–4V alloy: a promising surface modification technique for orthopaedic application. Appl Surf Sci 256(7):2176–2183
36. Lu X, Zhao Z, Leng Y (2007) Biomimetic calcium phosphate coatings on nitric-acid-treated titanium surfaces. Mater Sci Eng C 27(4):700–708
37. Park J-W, Kim Y-J, Jang J-H et al (2010) Effects of phosphoric acid treatment of titanium surfaces on surface properties, osteoblast response and removal of torque forces. Acta Biomater 6(4):1661–1670

38. Browne M, Gregson PJ (2000) Effect of mechanical surface pretreatment on metal ion release. Biomaterials 21:385–392
39. Barranco V, Onofre E, Escudero ML et al (2010) Characterization of roughness and pitting corrosion of surfaces modified by blasting and thermal oxidation. Surf Coat Technol 204(23):3783–3793
40. Kumar S, Narayanan TSNS, Ganesh Sundara Raman S et al (2010) Surface modification of CP-Ti to improve the fretting-corrosion resistance: thermal oxidation vs. anodizing. Mater Sci Eng C 30(6):921–927
41. Hall J, Lausmaa J (2000) Properties of a new porous oxide surface on titanium implants. Appl Osseointegration Res 1(1):5–9
42. Sul Y-T, Johansson CB, Jeong Y et al (2001) The electrochemical oxide growth behaviour on titanium in acid and alkaline electrolytes. Med Eng Phys 23:329–346
43. Sul Y-T, Johansson CB, Petronis S et al (2002) Characteristics of the surface oxides on turned and electrochemically oxidized pure titanium implants up to dielectric breakdown: the oxide thickness, micropore configurations, surface roughness, crystal structure and chemical composition. Biomaterials 23(2):491–501
44. Yang B, Uchida M, Kim H-M et al (2004) Preparation of bioactive titanium metal via anodic oxidation treatment. Biomaterials 25(6):1003–1010
45. Chrzanowski W, Szewczenko J, Tyrlik-Held J et al (2005) Influence of the anodic oxidation on the physicochemical properties of the Ti6Al4V ELI alloy. J Mater Process Technol 162–163:163–168
46. Jaeggi C, Kern P, Michler J et al (2005) Anodic thin films on titanium used as masks for surface micropatterning of biomedical devices. Surf Coat Technol 200:1913–1919
47. Ng BS, Annergren I, Soutar AM et al (2005) Characterisation of a duplex TiO2/CaP coating on Ti6Al4V for hard tissue replacement. Biomaterials 26(10):1087–1095
48. Oh H-J, Lee J-H, Jeong Y et al (2005) Microstructural characterization of biomedical titanium oxide film fabricated by electrochemical method. Surf Coat Technol 198(1-3):247–252
49. Kuromoto N, Simao RA, Soares GA (2007) Titanium oxide films produced on commercially pure titanium by anodic oxidation with different voltages. Mater Charact 58:114–121
50. Cui X, Kim H-M, Kawashita M et al (2009) Preparation of bioactive titania films on titanium metal via anodic oxidation. Dent Mater 25:80–86
51. Sul Y-T, Johansson C, Byon E et al (2005) The bone response of oxidized bioactive and non-bioactive titanium implants. Biomaterials 26:6720–6730
52. Yau TL, Webster RT (1987) Corrosion of zirconium and hafnium. In: ASM International Handbook Committee (ed) Metals handbook, vol 13. ASM, Materials Park, pp 707–721
53. Cox B (2005) Some thoughts on the mechanisms of in-reactor corrosion of zirconium alloys. J Nucl Mater 336(2–3):331–368

54. Zander D, Köster U (2004) Corrosion of amorphous and nanocrystalline Zr-based alloys. Mater Sci Eng A 375–377:53–59
55. Cabrini RL, Guglielmotti MB, Almagro JC (1993) Histomorphometry of initial bone healing around zirconium implants in rats. Implant Dent 2:264–267
56. Costa OR, Guglielmotti MB, Rimoli E et al (1994) Use of zircalloy to induce bone regeneration. A 2-year follow-up study. Acta Odontol Latinoam 8(1):17–26
57. Guglielmotti MB, Guerrero C, Cabrini RL (1997) Chronodynamic evaluation of the stages of osseointegration in zirconium laminar implants. Acta Odontol Latinoam 10(1):11–23
58. Saldaña L, Mendez-Vilas A, Jiang L et al (2007) In vitro biocompatibility of an ultrafine grained zirconium. Biomaterials 28(30):4343–4354
59. Gallardo-Moreno AM, Pacha-Olivenza MA, Saldaña L et al (2009) In vitro biocompatibility and bacterial adhesion of physico-chemically modified Ti6Al4V surface by means of UV irradiation. Acta Biomater 5(1):181–192
60. Okazaki Y, Gotoh E (2005) Comparison of metal release from various metallic biomaterials in vitro. Biomaterials 26:11–21
61. Meisterjahn P, Hoppe HW, Shultze JW (1987) Electrochemical and XPS measurements on thin oxide films on zirconium. J Electroanal Chem 217:159–185
62. Bardwell JA, McKubre MCH (1991) AC Impedance spectroscopy of the anodic film on zirconium in neutral solution. Electrochim Acta 36(3/4):647–653
63. Preusser S, Stimming U, Wippermann K (1994) An optical and electrochemical investigation of ZrO2 thin films (from nm Ti mm thickness). Electrochim Acta 39(8/9):1273–1280
64. Patel AM, Spector M (1997) Tribological evaluation of oxidized zirconium using an articular cartilage counterface: a novel material for potential use in hemiarthroplasty. Biomaterials 18:441–447
65. Kohn DH (1998) Metals in medical applications. Curr Opin Solid State Mater Sci 3:309–316
66. Hanawa T (1999) In vivo metallic biomaterials and surface modification. Materials Sci Eng A A267:260–266
67. Hiromoto S, Hanawa T (2002) Re-passivation current of amorphous Zr65Al7.5Ni10Cu17.5 in a Hank's balanced solution. Electrochim Acta 47:1343–1349
68. Adolfsson E, Hermansson L (1999) Zirconia–fluorapatite materials produced by HIP. Biomaterials 20(14):1263–1267
69. Piconi C, Maccauro G (1999) Zirconia as a ceramic biomaterial. Biomaterials 20(1):1–25
70. Deville S, Chevalier J, Fantozzi G et al (2003) Low-temperature ageing of zirconia-toughened alumina ceramics and its implication in biomedical implants. J Eur Ceram Soc 23(15):2975–2982

71. Carinci F, Pezzetti F, Volinia S et al (2004) Zirconium oxide: analysis of MG63 osteoblast-like cell response by means of a microarray technology. Biomaterials 25(2):215–228
72. Chevalier J (2006) What future for zirconia as a biomaterial? Biomaterials 27:535–543
73. Blumenthal W (1976) Zirconium—behaviour in biological systems. J Sci Ind Res 35(7):485–490
74. Met C, Vandenbulcke L, Sainte Catherine MC (2003) Friction and wear characteristics of various prosthetic materials sliding against smooth diamond-coated titanium alloy. Wear 255(7–12):1022–1029
75. Sherepo KM, Red'ko IA (2004) Use of zirconium-based and zirconium-coated implants in traumatology and orthopedics. Biomed Eng 38(2):77–79
76. Lee JKL, Maruthainar K, Wardle N et al (2009) Increased force simulator wear testing of a zirconium oxide total knee arthroplasty. Knee 16:269–274
77. Ji R, Li XY, Dong H (2010) Ceramic conversion treatment of zirconium alloys to combat corrosion wear. Surf Eng 26:30–36
78. Richardson K (2001) Medical device innovator rebuilds lives with zirconium knee implant. Outlook 22:1–4
79. Stojilovic N, Bender ET, Ramsier RD (2005) Surface chemistry of zirconium. Prog Surf Sci 78(3-4):101–184
80. Gioe TJ, Sharma A, Tatman P et al (2011) Do "premium" joint implants add value? Analysis of high cost joint implants in a Community Registry. Clin Orthop Relat Res 469:48–54
81. Hunter G, Jones WM, Spector M (2005) Oxidized zirconium. In: Reis MD, Bellemans J, Victor J (eds) Total knee arthroplasty: a guide to get better performance. Springer, Heidelberg, pp 370–380
82. Good V, Widding K, Hunter G et al (2005) Oxidized zirconium: a potentially longer lasting hip implant. Mater Des 26:618–622
83. Hernigou P, Mathieu G, Poignard A, Manicom O, Filippini P, Demoura A (2007) Oxinium, a new alternative femoral bearing surface option for hip replacement. Eur J Orthop Surg Traumatol 17:243–246
84. Kim Y-HKJ-S, Huh W, Lee K-H (2010) Weight of polyethylene wear particles is similar in TKAS with oxidized zirconium and cobalt-chrome prostheses. Clin Orthop Relat Res 468:1296–1304
85. Innocenti M, Matassi F, Carulli C et al (2014) Oxidized zirconium femoral component for TKA: a follow-up note of a previous report at a minimum of 10 years. Knee 21(4):858–861
86. Albrektsson T, Johansson C, Lundgren AK et al (2000) A histomorphometrical and biomechanical analysis. Appl Osseointegration Res 1:21–24
87. Sul YT, Johansson CB, Kang Y et al (2002) Bone reactions to oxidized titanium implants with electrochemical anion sulphuric acid and phosphoric acid incorporation. Clin Implant Dent Relat Res 4(2):78–87

88. Pan J, Thierry D, Leygraf C (1994) Electrochemical and XPS studies of titanium for biomaterial applications with respect to the effect of hydrogen peroxide. J Biomed Mater Res 28:113–122
89. Katunar MR, Sanchez AG, Ballarre J et al (2014) Can anodised zirconium implant stimulate bone formation? Preliminary study in rat model. Prog Biomater 3:1–10
90. Aladjem A (1973) Review—anodic oxidation of titanium and its alloys. J Mater Sci 8:688–704
91. Blackwood DJ, Peter LM (1989) The influence of growth rate on the properties of anodic oxide films on titanium. Electrochim Acta 34(11):1505–1511
92. Delplancke J-L, Garnier A, Massiani Y et al (1994) Influence of the anodizing procedure on the structure and the properties of titanium oxide films and its effects on copper nucleation. Electrochim Acta 39(8/9): 1281–1289
93. Ohtsuka T, Otsuki T (1998) The influence of the growth rate on the semiconductive properties of titanium anodic oxide films. Corros Sci 40(6):951–958
94. Shibata T, Zhu Y-C (1995) The effect of film formation conditions on the structure and composition of anodic oxide films on titanium. Corros Sci 37(2):253–270
95. Linarez Pérez OE, Fuertes VC, Pérez MA et al (2008) Characterization of the anodic growth and dissolution of oxide films on valve metals. Electrochem Commun 10(3):433–437
96. Sato N (1990) An overview on the passivity of metals. Corros Sci 31:1–19
97. Macdonald DD (1999) Passivity—the key to our metals-based civilization. Pure Appl Chem 71(6):951–978
98. Lohrengel MM (1993) Thin anodic oxide layers on aluminium and other valve metals: high field regime. Mater Sci Eng R Rep 11(6):243–294
99. Lohrengel MM (1994) Formation of ionic space charge layers in oxide films on valve metals. Electrochim Acta 39(8/9):1265–1271
100. Olsson C-OA, Landolt D (2003) Anodisation of a Nb-Zr alloy. Electrochim Acta 48:3999–4011
101. Hodgson AWE, Kurz S, Virtanen S et al (2004) Passive and transpassive behaviour of CoCrMo in simulated biological solutions. Electrochim Acta 49:2167–2178
102. Schneider M, Lämmel C, Heubner C et al (2013) Anomalies in high-field growth of aluminium oxide using pulse anodizing. Surf Interface Anal 45(10):1497–1502
103. Van Overmeere Q, Proost J (2011) Stress-affected and stress-affecting instabilities during the growth of anodic oxide films. Electrochim Acta 56(28):10507–10515
104. Vanhumbeeck JF, Proost J (2009) Current understanding of Ti anodisation: functional, morphological, chemical and mechanical aspects. Corros Rev 27(3):117–204

105. Macdonald DD (1992) Point defect model for the passive state. J Electrochem Soc 139(12):3434–3449
106. Zhang L, Macdonald DD, Sikora E et al (1998) On the kinetics of growth of anodic oxide films. J Electrochem Soc 145(3):898–905
107. Macdonald DD (2011) The history of the Point Defect Model for the passive state: a brief review of film growth aspects. Electrochim Acta 56(4):1761–1772
108. Sloppy JD, Lu Z, Dickey EC et al (2013) Growth mechanism of anodic tantalum pentoxide formed in phosphoric acid. Electrochim Acta 87:82–91
109. Ellerbrock D, MacDonald DD (2014) Passivity of titanium, part 1: film growth model diagnostics. J Solid State Electrochem 18(5):1485–1493
110. Goossens A, Vazquez M, Macdonald DD (1996) The nature of electronic states in anodic zirconium oxide films part 1: the potential distribution. Electrochim Acta 41(1):35–45
111. Goossens A, Vazquez M, Macdonald DD (1996) The nature of electronic states in anodic zirconium oxide films part 2: photoelectrochemical characterization. Electrochim Acta 41(1):47–55
112. Bojinov M, Fabricius J, Kinnunen P et al (2001) Electrochemical study of the passive behavior of Ni-Cr alloys in a borate solution. A mixed-conduction model approach. J Electroanal Chem 504:29–44
113. Cabrera-Sierra R, Hallen JM, Vazquez-Arenas J et al (2010) EIS characterization of tantalum and niobium oxide films based on a modification of the point defect model. J Electroanal Chem 638(1):51–58
114. Gomez Sanchez A, Katunar M, Schreiner W et al (2014) Structure and dielectric properties of electrochemically grown ZrO2 films. Acta Chim Slov 61:316–327
115. Girginov A, Bojinov M (2008) Conduction mechanisms in the valve metal/oxide film/electrolyte system. J Univ Chem Technol Metall 43:29–36
116. Dyer CK, Leach JSL (1978) Breakdown and efficiency of anodic oxide growth on titanium. J Electrochem Soc 125(7):1032–1038
117. Nishimura R, Kudo K (1982) Anodic oxidation and kinetics of titanium in 1 M chloride solutions. Corros Sci 22(7):637–645
118. Habazaki H, Uozumi M, Konno H et al (2003) Influences of structure and composition on growth of anodic oxide films on Ti-Zr alloys. Electrochim Acta 48(20–22):3257–3266
119. Freitas MBJG, Eiras C, Bulhões LOS (2004) Breakdown of the niobium oxide film under galvanostatic polarisation and in acid solutions. Corros Sci 46(5):1051–1060
120. Park YJ, Shin K-H, Song H-J (2007) Effects of anodizing conditions on bond strength of anodically oxidized film on titanium substrate. Appl Surf Sci 253:6013–6018
121. Di Quarto F, Piazza S, Sunseri C (1983) Space charge effects on the growth of anodic oxide films on zirconium metal. J Electrochem Soc 130(5):1014–1021

122. Di Quarto F, Piazza S, Sunseri C (1984) Breakdown phenomena during the growth of anodic oxide films on zirconium metal: influence of experimental parameters on electrical and mechanical breakdown. J Electrochem Soc 131(12):2901–2906
123. Di Quarto F, Piazza S, Sunseri C (1986) A phenomenological approach to the mechanical breakdown of anodic oxide films on zirconium. Corros Sci 26(3):213–221
124. Badekas H, Panagopoulos C (1987) Titanium anodization under constant voltage conditions. Surf Coat Technol 31(4):381–388
125. Pauporté T, Finne J, Kahn-Harari A et al (2005) Growth by plasma electrolysis of zirconium oxide films in the micrometer range. Surf Coat Technol 199:213–219
126. Proost J, Vanhumbeeck JF, Van Overmeere Q (2009) Instability of anodically formed TiO2 layers (revisited). Electrochim Acta 55(2):350–357
127. Narayanan R, Seshadri SK (2007) Phosphoric acid anodization of Ti–6Al–4V—structural and corrosion aspects. Corros Sci 49(2):542–558
128. Song H-J, Kim M-K, Jung G-C et al (2007) The effects of spark anodizing treatment of pure titanium metals and titanium alloys on corrosion characteristics. Surf Coat Technol 201(21):8738–8745
129. Blackwood DJ, Chooi SKM (2002) Stability of protective oxide films formed on a porous titanium. Corros Sci 44:395–405
130. Yahalom J, Zahavi J (1970) Electrolytic breakdown crystallization of anodic oxide films on Al, Ta and Ti. Electrochim Acta 15:1429–1435
131. Trivinho-Strixino F, Guimarães FEG, Pereira EC (2008) Zirconium oxide anodic films: optical and structural properties. Chem Phys Lett 461(1–3):82–86
132. Schneider M, Kremmer K (2014) The effect of bath aging on the microstructure of anodic oxide layers on AA1050. Surf Coat Technol 246:64–70
133. Aggerbeck M, Canulescu S, Dirscherl K et al (2014) Appearance of anodised aluminium: effect of alloy composition and prior surface finish. Surf Coat Technol 254:28–41
134. Sul YT, Jeong Y, Johansson C et al (2006) Oxidized, bioactive implants are rapidly and strongly integrated in bone. Part 1—experimental implants. Clin Oral Implants Res 17(5):521–526
135. Delplancke JL, Degrez M, Fontana A et al (1982) Self-colour anodizing of titanium. Surf Technol 16(2):153–162
136. Van Gils S, Mast P, Stijns E et al (2004) Colour properties of barrier anodic oxide films on aluminium and titanium studied with total reflectance and spectroscopic ellipsometry. Surf Coat Technol 185(2–3):303–310
137. Pérez del Pino A, Fernández-Pradas JM, Serra P et al (2004) Coloring of titanium through laser oxidation: comparative study with anodizing. Surf Coat Technol 187(1):106–112
138. Gomez Sanchez A, Schreiner W, Duffó G et al (2011) Surface characterization of anodized zirconium for biomedical applications. Appl Surf Sci 257(15):6397–6405

139. Gomez Sanchez A, Schreiner W, Duffó G et al (2013) Surface modification of titanium by anodic oxidation in phosphoric acid at low potentials. Part 1. Structure, electronic properties and thickness of the anodic films. Surf Interface Anal 45(6):1037–1046
140. Sul YT, Johansson C, Wennerberg A et al (2005) Optimum surface properties of oxidized implants for reinforcement of osseointegration: surface chemistry, oxide thickness, porosity, roughness, and crystal structure. Int J Oral Maxillofac Implants 20(3):349–359
141. Löberg J, Gretzer C, Mattisson I et al (2014) Electronic properties of anodized TiO2 electrodes and the effect on in vitro response. J Biomed Mater Res B Appl Biomater 102(4):826–839
142. Petersson IU, Löberg JEL, Fredriksson AS et al (2009) Semi-conducting properties of titanium dioxide surfaces on titanium implants. Biomaterials 30(27):4471–4479
143. Birch JR, Burleigh TD (2000) Oxides formed on titanium by polishing, etching, anodizing or thermal oxidizing. Corros NACE 56(12):1233–1241
144. Hodgson AWE, Mueller Y, Forster D et al (2002) Electrochemical characterization of passive films on Ti alloys under simulated biological conditions. Electrochim Acta 47:1913–1923
145. Pan J, Thierry D, Leygraf C (1996) Electrochemical impedance spectroscopy study of the passive oxide film on titanium for implant application. Electrochim Acta 41(7/8):1143–1153
146. Ibris N, Mirza-Rosca JC (2002) EIS study of Ti and its alloys in biological media. J Electroanal Chem 526:53–62
147. Bozzini B, Carlino P, D'Urzo L et al (2008) An electrochemical impedance investigation of the behaviour of anodically oxidised titanium in human plasma and cognate fluids, relevant to dental applications. J Mater Sci Mater Med 19(11):3443–3453
148. Schmidt AM, Azambuja DS, Martini EMA (2006) Semiconductive properties of titanium anodic oxide films in McIlvine buffer solution. Corros Sci 48:2901–2912
149. Blackwood DJ, Greef R, Peter LM (1989) An ellipsometric study of the growth and open-circuit dissolution of the anodic oxide film on titanium. Electrochim Acta 34(6):875–880
150. Serruys Y, Sakout T, Gorse D (1993) Anodic oxidation of titanium in 1M H2SO4 studied by Rutherford backscattering. Surf Sci 282:279–287
151. Nagahara K, Sakairi M, Takahashi H et al (2007) Mechanism of formation and growth of sunflower-shaped imperfections in anodic oxide films on niobium. Electrochim Acta 52(5):2134–2145
152. Aloia Games L, Gomez Sanchez A, Jimenez-Pique E et al (2012) Chemical and mechanical properties of anodized cp-titanium in NH 4 H 2PO 4/NH 4F media for biomedical applications. Surf Coat Technol 206(23):4791–4798
153. Mogoda AS, El-Taib Heakal F, Ghoneim AA (1992) Formation and dissolution behaviour of ZrO2 film in H3PO4 acid solutions. Thin Solid Films 219(1–2):146–152

154. Shibata Y, Tanimoto Y (2015) A review of improved fixation methods for dental implants. Part I: surface optimization for rapid osseointegration. J Prosthodont Res 59(1):20–33
155. McRae GA, Maguire MA, Jeffrey CA et al (2002) A comparison of fractal dimensions determined from atomic force microscopy and impedance spectroscopy of anodic oxides on Zr–2.5Nb. Appl Surf Sci 191(1–4):94–105
156. Sanchez AG, Katunar M, Schreiner W et al (2014) Structure and dielectric properties of electrochemically grown ZrO2 films. Acta Chim Slov 61(2):316–327
157. Xing J, Xia Z, Hu J et al (2013) Time dependence of growth and crystallization of anodic titanium oxide films in potentiostatic mode. Corros Sci 75:212–219
158. Farina SB, Sanchez AG, Ceré S (2015) Effect of surface modification on the corrosion resistance of Zr-2.5Nb as material for permanent implants. Proc Mater Sci 8:1166–1173
159. Hanawa T, Ota M (1992) Characterization of surface film formed on titanium in electrolyte using XPS. Appl Surf Sci 55:269–276
160. de Sena LA, Rocha NCC, Andrade MC et al (2003) Bioactivity assessment of titanium sheets electrochemically coated with thick oxide films. Surf Coat Technol 166:254–258
161. Sul Y-T (2003) The significance of the surface properties of oxidized titanium to the bone response: special emphasis on potential biochemical bonding of oxidized titanium implant. Biomaterials 24:3893–3907
162. Lee J-H, Kim S-E, Kim Y-J et al (2006) Effects of microstructure of anodic titania on the formation of bioactive compounds. Mater Chem Phys 98:39–43
163. Müller FA, Bottino MC, Müller L et al (2008) In vitro apatite formation on chemically treated (P/M) Ti–13Nb–13Zr. Dent Mater 24(1):50–56
164. Tsutsumi Y, Nishimura D, Doi H et al (2009) Difference in surface reactions between titanium and zirconium in Hank's solution to elucidate mechanism of calcium phosphate formation on titanium using XPS and cathodic polarization. Mater Sci Eng C 29:1702–1708
165. Tsutsumi Y, Nishimura D, Doi H et al (2010) Cathodic alkaline treatment of zirconium to give the ability to form calcium phosphate. Acta Biomater 6(10):4161–4166
166. Gomez Sanchez A, Ballarre J, Orellano JC et al (2013) Surface modification of zirconium by anodisation as material for permanent implants: in vitro and in vivo study. J Mater Sci Mater Med 24(1):161–169
167. Mammeri F, Rozes L, Le Bourhis E et al (2006) Elaboration and mechanical characterization of nanocomposites thin films. Part II: correlation between structure and mechanical properties of SiO_2-PMMA hybrid materials. J Eur Ceram Soc 26:267–272
168. Wang L-N, Luo J-L (2012) Electrochemical behaviour of anodic zirconium oxide nanotubes in simulated body fluid. Appl Surf Sci 258(10):4830–4833

169. Hoerth RM, Katunar MR, Gomez Sanchez A et al (2014) A comparative study of zirconium and titanium implants in rat: osseointegration and bone material quality. J Mater Sci Mater Med 25(2):411–422
170. Lausmaa J, Kasemo B, Mattsson H (1990) Surface spectroscopic characterization of titanium implants materials. Appl Surf Sci 44:133–146
171. Lausmaa J, Kasemo B, Mattsson H et al (1990) Multi-technique surface characterization of oxide films on electropolished and anodically oxidized titanium. Appl Surf Sci 45:189–200
172. de Souza GB, de Lima GG, Kuromoto NK et al (2011) Tribo-mechanical characterization of rough, porous and bioactive Ti anodic layers. J Mech Behav Biomed Mater 4(5):796–806
173. Diamanti MV, Pedeferri MP (2007) Effect of anodic oxidation parameters on the titanium oxides formation. Corros Sci 49(2):939–948
174. El-Mahdy GA, Mahmoud SS, El-Dahan HA (1996) Effect of halide ions on the formation and dissolution behaviour of zirconium oxide. Thin Solid Films 286(1–2):289–294
175. Dunleavy CS, Golosnoy IO, Curran JA et al (2009) Characterisation of discharge events during plasma electrolytic oxidation. Surf Coat Technol 203(22):3410–3419
176. Sah SP, Tatsuno Y, Aoki Y et al (2011) Dielectric breakdown and healing of anodic oxide films on aluminium under single pulse anodizing. Corros Sci 53(5):1838–1844
177. Lukiyanchuk IV, Rudnev VS, Tyrina LM et al (2014) Plasma electrolytic oxide coatings on valve metals and their activity in CO oxidation. Appl Surf Sci 315:481–489
178. Oliveira FG, Ribeiro AR, Perez G et al (2015) Understanding growth mechanisms and tribocorrosion behaviour of porous TiO2 anodic films containing calcium, phosphorous and magnesium. Appl Surf Sci 341:1–12
179. Liu X, Li G, Xia Y (2012) Investigation of the discharge mechanism of plasma electrolytic oxidation using Ti tracer. Surf Coat Technol 206(21):4462–4465
180. Abbasi S, Bayati MR, Golestani-Fard F et al (2011) Micro arc oxidized HAp–TiO2 nanostructured hybrid layers-part I: effect of voltage and growth time. Appl Surf Sci 257(14):5944–5949
181. Quintero D, Galvis O, Calderón JA et al (2014) Effect of electrochemical parameters on the formation of anodic films on commercially pure titanium by plasma electrolytic oxidation. Surf Coat Technol 258:1223–1231
182. Wang Y, Yu H, Chen C et al (2015) Review of the biocompatibility of micro-arc oxidation coated titanium alloys. Mater Des 85:640–652
183. Abbasi S, Golestani-Fard F, Rezaie HR et al (2012) MAO-derived hydroxyapatite/TiO2 nanostructured multi-layer coatings on titanium substrate. Appl Surf Sci 261:37–42
184. Tsutsumi Y, Niinomi M, Nakai M et al (2012) Micro-arc oxidation treatment to improve the hard-tissue compatibility of Ti–29Nb–13Ta–4.6Zr alloy. Appl Surf Sci 262:34–38

185. Sowa M, Dercz G, Suchanek K et al (2015) Investigation of anodic oxide coatings on zirconium after heat treatment. Appl Surf Sci 346:534–542
186. Takebe J, Ito S, Miura S et al (2012) Physicochemical state of the nanotopographic surface of commercially pure titanium following anodization-hydrothermal treatment reveals significantly improved hydrophilicity and surface energy profiles. Mater Sci Eng C 32(1):55–60
187. Samanipour F, Bayati MR, Zargar HR et al (2011) Electrophoretic enhanced micro arc oxidation of ZrO2–HAp–TiO2 nanostructured porous layers. J Alloys Compd 509(38):9351–9355
188. Ha J-Y, Tsutsumi Y, Doi H et al (2011) Enhancement of calcium phosphate formation on zirconium by micro-arc oxidation and chemical treatments. Surf Coat Technol 205(21–22):4948–4955
189. Ribeiro AR, Oliveira F, Boldrini LC et al (2015) Micro-arc oxidation as a tool to develop multifunctional calcium-rich surfaces for dental implant applications. Mater Sci Eng C 54:196–206
190. Kodama A, Bauer S, Komatsu A et al (2009) Bioactivation of titanium surfaces using coatings of TiO2 nanotubes rapidly pre-loaded with synthetic hydroxyapatite. Acta Biomater 5(6):2322–2330
191. Kim W-G, Choe H-C, Ko Y-M et al (2009) Nanotube morphology changes for Ti–Zr alloys as Zr content increases. Thin Solid Films 517(17):5033–5037
192. Tsuchiya H, Akaki T, Nakata J et al (2009) Metallurgical aspects on the formation of self-organized anodic oxide nanotube layers. Electrochim Acta 54:5155–5162
193. Muratore F, Baron-Wiechéc A, Hashimoto T et al (2011) Growth of nanotubes on zirconium in glycerol/fluoride electrolytes. Electrochim Acta 56(28):10500–10506
194. Whitman SR, Raja KS (2014) Formation and electrochemical characterization of anodic ZrO2–WO3 mixed oxide nanotubular arrays. Appl Surf Sci 303:406–418
195. Feng XJ, Macak JM, Albu SP et al (2008) Electrochemical formation of self-organized anodic nanotube coating on Ti–28Zr–8Nb biomedical alloy surface. Acta Biomater 4(2):318–323
196. Gong D, Grimes CA, Varghese OK et al (2001) Tiranium oxide nanotube arrays prepared by anodic oxidation. J Mater Res 16(12):3331–3334
197. Zhao J, Wang X, Chen R et al (2005) Fabrication of titanium oxide nanotube arrays by anodic oxidation. Solid State Commun 134(10):705–710
198. Paulose M, Peng L, Popat KC et al (2008) Fabrication of mechanically robust, large area, polycrystalline nanotubular/porous TiO2 membranes. J Membr Sci 319(1–2):199–205
199. Zhao J, Wang X, Xu R et al (2008) Fabrication of high aspect ratio zirconia nanotube arrays by anodization of zirconium foils. Mater Lett 62(29):4428–4430
200. Smith BS, Yoriya S, Grissom L et al (2010) Hemocompatibility of titania nanotube arrays. J Biomed Mater Res A 95A(2):350–360

201. Ismail S, Ahmad ZA, Berenov A et al (2011) Effect of applied voltage and fluoride ion content on the formation of zirconia nanotube arrays by anodic oxidation of zirconium. Corros Sci 53(4):1156–1164
202. Tsuchiya H, Schmuki P (2004) Thick self-organized porous zirconium oxide formed in H2SO4/NH4F electrolytes. Electrochem Commun 6(11):1131–1134
203. Berger S, Jakubka F, Schmuki P (2008) Formation of hexagonally ordered nanoporous anodic zirconia. Electrochem Commun 10(12):1916–1919
204. Tsuchiya H, Macak J, Sieber I et al (2006) Self-organized nanoporous valve metal oxide layers. In: Marcus P, Maurice V (eds) Passivation of metals and semiconductors, and properties of thin oxide layers. Elsevier, Amsterdam, pp 187–192
205. Aïnouche L, Hamadou L, Kadri A et al (2014) Interfacial barrier layer properties of three generations of TiO2 nanotube arrays. Electrochim Acta 133:597–609
206. Bauer S, Kleber S, Schmuki P (2006) TiO2 nanotubes: tailoring the geometry in H3PO4/HF electrolytes. Electrochem Commun 8(8):1321–1325
207. Bauer S, Pittrof A, Tsuchiya H et al (2011) Size-effects in TiO2 nanotubes: diameter dependent anatase/rutile stabilization. Electrochem Commun 13(6):538–541
208. Narayanan R, Kwon T-Y, Kim K-H (2009) Anodic TiO2 from stirred Na2SO4/NaF electrolytes: effect of applied voltage and stirring. Mater Lett 63(23):2003–2006
209. Regonini D, Satka A, Jaroenworaluck A et al (2012) Factors influencing surface morphology of anodized TiO2 nanotubes. Electrochim Acta 74:244–253
210. Manole CC, Pirvu C, Demetrescu I (2009) TiO2: from nanotubes to nanopores by changing the anodizing voltage in floride-glycerol electrolyte. Key Engineering Materials 415:5–8
211. Manole CC, Pirvu C, Demetrescu I (2010) Evaluation of TiO2 nanotubes changes after ultrasonication treatment. Mol Cryst Liq Cryst 521(1):84–92
212. Yasuda K, Schmuki P (2007) Control of morphology and composition of self-organized zirconium titanate nanotubes formed in (NH4)2SO4/NH4F electrolytes. Electrochim Acta 52(12):4053–4061
213. Zhao J, Xu R, Wang X et al (2008) In situ synthesis of zirconia nanotube crystallines by direct anodization. Corros Sci 50(6):1593–1597
214. Kunze J, Müller L, Macak JM et al (2008) Time-dependent growth of biomimetic apatite on anodic TiO2 nanotubes. Electrochim Acta 53(23):6995–7003
215. Popat KC, Leoni L, Grimes CA et al (2007) Influence of engineered titania nanotubular surfaces on bone cells. Biomaterials 28(21):3188–3197
216. Souza MEP, Ballester M, Freire CMA (2007) EIS characterisation of Ti anodic oxide porous films formed using modulated potential. Surf Coat Technol 201(18):7775–7780
217. Minagar S, Berndt C, Wen C (2015) Fabrication and characterization of nanoporous niobia, and nanotubular tantala, titania and zirconia via anodization. J Funct Biomater 6(2):153

218. Park HH, Park IS, Kim KS et al (2010) Bioactive and electrochemical characterization of TiO_2 nanotubes on titanium via anodic oxidation. Electrochim Acta 55:6109–6114
219. Guo L, Zhao J, Wang X et al (2009) Bioactivity of zirconia nanotube arrays fabricated by electrochemical anodization. Mater Sci Eng C 29(4):1174–1177
220. Pittrof A, Bauer S, Schmuki P (2011) Micropatterned TiO2 nanotube surfaces for site-selective nucleation of hydroxyapatite from simulated body fluid. Acta Biomater 7(1):424–431
221. Lewandowska Ż, Piszczek P, Radtke A et al (2015) The evaluation of the impact of titania nanotube covers morphology and crystal phase on their biological properties. J Mater Sci Mater Med 26(4):1–12
222. Minagar S, Li Y, Berndt CC et al (2015) The influence of titania–zirconia–zirconium titanate nanotube characteristics on osteoblast cell adhesion. Acta Biomater 12:281–289
223. Peng L, Eltgroth ML, LaTempa TJ et al (2009) The effect of TiO2 nanotubes on endothelial function and smooth muscle proliferation. Biomaterials 30(7):1268–1272
224. Tsuchiya H, Macak JM, Ghicov A et al (2005) Self-organized porous TiO2 and ZrO2 produced by anodization. Corros Sci 47(12):3324–3335
225. Brinker CJ, Scherer GW (1990) Sol-gel science—the physics and chemistry of sol-gel processing. Academic/Elsevier, San Diego
226. Guglielmi M (1997) Sol-gel coatings on metals. J Sol-Gel Sci Technol 8(1):443–449
227. Sanchez C, In M (1992) Molecular design of alkoxide precursors for the synthesis of hybrid organic-inorganic gels. J Non-Cryst Solids 147–148:1–12
228. Brinker CJ, Hurd AJ, Schunk PR et al (1992) Review of sol-gel thin film formation. J Non-Cryst Solids 147–148:424–436
229. Izumi K, Tanaka H, Uchida Y et al (1992) Influence of firing conditions on adhesion of methyltrialoxysilane-derived coatings on steel sheets. J Non-Cryst Solids 147–148:483–487
230. Di Giampaolo Conde AR, Puerta M, Ruiz H et al (1992) Thick aluminosilicate coatings on carbon steel via sol gel. J Non-Cryst Solids 147–148:467–473
231. Babonneau F, Toutou C, Gavériaux S (1997) O NMR investigation of chemical homogeneity in hybrid systems. J Sol-Gel Sci Technol 8:553–556
232. Hoebbel D, Nacken M, Schmidt H (1998) A NMR study on the hydrolysis, condensation and epoxide ring-opening reaction in sols and gels of the system glycodoxypropyltrimethoxysilane-water-titaniumtetraethoxide. J Sol-Gel Sci Technol 12:169–179
233. Uhlmann D, Suratwala T, Davidson K et al (1997) Sol-gel derived coatings on glass. J Non-Cryst Solids 218:113–122
234. Brinker CJ, Hurd AJ, Frye GC et al (1990) Sol-gel thin film formation. J Non-Cryst Solids 121(1–3):294–302

235. Puetz J, Aegerter MA (2004) Dip coating technique. In: Aegerter M, Mennig M (eds) Sol-gel technologies for glass producers and users. Springer, New York, pp 37–48
236. Dislich H, Hussmann E (1981) Amorphous and crystalline dip coatings obtained from organometallic solutions: procedures, chemical processes and products. Thin Solid Films 77(1-3):129–140
237. Terrier C, Chatelon JP, Roger JA (1997) Electrical and optical properties of Sb:SnO2 thin films obtained by the sol-gel method. Thin Solid Films 295(1–2):95–100
238. Lee JH, Ko KH, Park BO (2003) Electrical and optical properties of ZnO transparent conducting films by the sol-gel method. J Cryst Growth 247(1–2):119–125
239. Metroke TL, Parkhill RL, Knobbe ET (2001) Passivation of metal alloys using sol-gel-derived materials—a review. Prog Org Coat 41(4):233–238
240. Pepe A, Galliano P, Aparicio M et al (2006) Sol-gel coatings on carbon steel: electrochemical evaluation. Surf Coat Technol 200(11):3486–3491
241. Vasiliu I, Gartner M, Anastasescu M et al (2007) Structural and optical properties of the SiO2-P2O5 films obtained by sol-gel method. Thin Solid Films 515(16):6601–6605
242. Han C, Pelaez M, Likodimos V et al (2011) Innovative visible light-activated sulfur doped TiO2 films for water treatment. Appl Catal B Environ 107(1–2):77–87
243. Chen D (2001) Anti-reflection (AR) coatings made by sol-gel processes: a review. Sol Energy Mater Sol Cells 68(3–4):313–336
244. Lien SY, Wuu DS, Yeh WC et al (2006) Tri-layer antireflection coatings (SiO2/SiO2-TiO2/TiO2) for silicon solar cells using a sol-gel technique. Sol Energy Mater Sol Cells 90(16):2710–2719
245. Boissiere C, Grosso D, Chaumonnot A et al (2011) Aerosol route to functional nanostructured inorganic and hybrid porous materials. Adv Mater 23(5):599–623
246. Fedrizzi L, Rodriguez FJ, Rossi S et al (2001) The use of electrochemical techniques to study the corrosion behaviour of organic coatings on steel pretreated with sol-gel zirconia films. Electrochim Acta 46(24–25):3715–3724
247. Aldrich-Smith G, Jennet N, Housden J (2004) Adhesion of thin coatings-the VAMAS (TWA 22-2) interlaboratory exercise. Surf Coat Technol 196(2–3):336–344
248. Zhang X, Hu L, Sun D (2006) Nanoindentation and nanoscratch profiles of hybrid films based on (methacrylopropyl)trimethoxysilane and tetraethoxysilane. Acta Mater 54:5469–5475
249. Ballarre J, Jimenez-Pique E, Anglada M et al (2009) Mechanical characterization of nano-reinforced silica based sol–gel hybrid coatings on AISI 316L stainless steel using nanoindentation techniques. Surf Coat Technol 203(20):3325–3331

250. Ballarre J, López DA, Cavalieri AL (2009) Frictional and adhesive behavior of organic-inorganic hybrid coatings on surgical grade stainless steel using nano-scratching technique. Wear 266(11–12):1165–1170
251. Natsume Y, Sakata H (2000) Zinc oxide films prepared by sol-gel spin-coating. Thin Solid Films 372(1):30–36
252. de Lima Neto P, Atik M, Avaca LA et al (1994) Sol-gel coatings for chemical protection of stainless steel. J Sol-Gel Sci Technol 2:529–534
253. de Damborenea JJ, Pellegri N, de Sanctis O et al (1995) Electrochemical behavior of SiO2 sol-gel coatings on stainless steels. J Sol-Gel Sci Technol 4:239–244
254. Habibovic P, Barrere F, van Blitterswijk CA et al (2002) Biomimetic hydroxyapatite coatings on metal implants. J Am Ceram Soc 85(3):517–522
255. Chou T, Chandrasekaran C, Cao GZ (2003) Sol-gel derived hybrid coatings for corrosion protection. J Sol-Gel Sci Technol 26:321–327
256. Duran A, Conde A, Gómez Coedo A et al (2004) Sol-gel coatings for protection and bioactivation of metals used in orthopaedic devices. J Mater Chem 14:2282–2290
257. Im K-H, Lee S-B, Kim K-M et al (2007) Improvement of bonding strength to titanium surface by sol-gel derived hybrid coating of hydroxyapatite and titania by sol-gel process. Surf Coat Technol 202(4-7):1135–1138
258. Biehl V, Breme J (2001) Metallic biomaterials. Mat-wiss, u Werkstofftech 32:137–144
259. Bastidas JM, Polo JL, Torres CL et al (2001) A study of the stability of AISI 316L stainless steel pitting corrosion through its transfer function. Corros Sci 43:269–281
260. Shih C-C, Shih C-M, Su Y-Y et al (2004) Effect of surface oxide properties on corrosion resistance of 316L stainless steel for biomedical applications. Corros Sci 46:427–441
261. Balamurugan A, Balossier G, Kannan S et al (2006) Elaboration of sol-gel derived apatite films on surgical grade stainless steel for biomedical applications. Mater Lett 60(17–18):2288–2293
262. López DA, Duran A, Ceré S (2008) Electrochemical characterization of AISI 316L stainless steel in contact with simulated body fluid under infection conditions. J Mater Sci Mater Med 19(5):2137–2144
263. Walczak J, Shahgaldi F, Heatley F (1998) In vivo corrosion of 316L stainless steel hip implants: morphology and elemental composition of corrosion products. Biomaterials 19:229–237
264. Shih C-C, Shih C-M, Su Y-Y et al (2005) Galvanic current induced by heterogeneous structures on stainless steel wire. Corros Sci 47:2199–2212
265. Staiger MP, Pietak AM, Huadmai J et al (2006) Magnesium and its alloys as orthopedic biomaterials: a review. Biomaterials 27(9):1728–1734
266. Black J (2006) Biological performance of biomaterials: fundamentals of biocompatibility, 4th edn. CRC Press/Taylor & Francis Group, Florida
267. Kraus T, Fischerauer SF, Hänzi AC et al (2012) Magnesium alloys for temporary implants in osteosynthesis: in vivo studies of their degradation and interaction with bone. Acta Biomater 8(3):1230–1238

268. Song G, Atrens A (2003) Understanding magnesium corrosion. A framework for improved alloy performance. Adv Eng Mater 5(12):837–858
269. Song G (2005) Recent progress in corrosion and protection of magnesium alloys. Adv Eng Mater 7(7):563–586
270. Song G, Song S (2007) A possible biodegradable magnesium implant material. Adv Eng Mater 9(4):298–302
271. Hench LL, Wilson J (1993) An introduction to bioceramics. Advanced series in ceramics, vol 1. World Scientific Hench, Singapore
272. Jones JR (2013) Review of bioactive glass: from Hench to hybrids. Acta Biomater 9(1):4457–4486
273. Li R, Clark AE, Hench LL (1991) An investigation of bioactive glass powders by sol-gel processing. J Appl Biomater 2(4):231–239
274. Sepulveda P, Jones JR, Hench LL (2001) Characterization of melt-derived 45S5 and sol-gel-derived 58S bioactive glasses. J Biomed Mater Res 58(6):734–740
275. Siqueira RL, Peitl O, Zanotto ED (2011) Gel-derived SiO2-CaO-Na2O-P2O5 bioactive powders: synthesis and in vitro bioactivity. Mater Sci Eng C 31(5):983–991
276. Ducheyne P, Cuckler JM (1992) Bioactive ceramic prosthetic coatings. Clin Orthop Relat Res 276:102–114
277. Hench LL (1991) Bioceramics: from concept to clinic. J Am Ceram Soc 74(7):1487–1510
278. Chen CC, Huang TH, Kao CT et al (2004) Electrochemical study of the intro degradation of plasma-sprayed hydroxyapatite/bioactive glass composite coatings after heat treatment. Electrochim Acta 50:1023–1029
279. Brama M, Rhodes N, Hunt J et al (2007) Effect of titanium carbide coating on the osseointegration response in vitro and in vivo. Biomaterials 28:595–608
280. Vercaigne S, Wolke JGC, Naert I et al (1998) Historphometrical and mechanical evaluation of titanium plasma-spray-coated implants placed in the cortical bone of goats. J Biomed Mater Res 41:41–48
281. Inagaki M, Yokogawa Y, Kameyama T (2003) Bond strength improvement of hydroxyapatite/titanium composite coating by partial nitriding during RF-thermal plasma spraying. Surf Coat Technol 173(1):1–8
282. Bhadang KA, Gross KA (2004) Influence of fluorapatite on the properties of thermally sprayed hydroxyapatite coatings. Biomaterials 25:4935–4945
283. Arguedas R, Ledezma-Gairaud M, Sáenz A et al (2008) Synthesis and kinetic study of hydroxy/fluorapatite solid solution formation by decomposition of a Ca-EDTA complex. Z Anorg Allg Chem 634:1791–1794
284. Weng W, Baptista JL (1998) Sol-gel derived porous hydroxyapatite coatings. J Mater Sci Mater Med 9(3):159–163
285. Kim H-W, Kim H-E, Knowles JC (2004) Fluor-hydroxyapatite sol–gel coating on titanium substrate for hard tissue implants. Biomaterials 25(17):3351–3358
286. Novak BM (1993) Hybrid nanocomposite materials—between inorganic glasses and organic polymers. Adv Mater 5(6):422–433

287. Pellice S, Galliano P, Castro Y et al (2003) Hybrid sol-gel coatings produced from TEOS and γ-MPS. J Sol-Gel Sci Technol 28:81–86
288. Pellice SA, Williams RJJ, Sobrados I et al (2006) Solutions of hybrid silica microgels as precursors of sol–gel coatings. J Mater Chem 16:3318–3325
289. Ballarre J, López DA, Rosero NC et al (2008) Electrochemical evaluation of multilayer silica–metacrylate hybrid sol–gel coatings containing bioactive particles on surgical grade stainless steel. Surf Coat Technol 203(1–2):80–86
290. López DA, Rosero-Navarro NC, Ballarre J et al (2008) Multilayer silica-methacrylate hybrid coatings prepared by sol-gel on stainless steel 316L: electrochemical evaluation. Surf Coat Technol 202(10):2194–2201
291. Santos EM, Radin S, Shenker BJ et al (1998) Si-Ca-P xerogels and bone morphogenetic protein act synergistically on rat stromal marrow cell differentiation in vitro. J Biomed Mater Res 41(1):87–94
292. Avnir D, Lev O, Livage J (2006) Recent bio-applications of sol-gel materials. J Mater Chem 16(11):1013–1030
293. Jun S-H, Lee E-J, Yook S-W et al (2010) A bioactive coating of a silica xerogel/chitosan hybrid on titanium by a room temperature sol–gel process. Acta Biomater 6(1):302–307
294. de Sanctis O, Gomez L, Pellegri N et al (1990) Protective glass coatings on metallic substrates. J Non-Cryst Solids 121:338–343
295. Garcia C, Ceré SM, Durán A (2004) Bioactive coatings prepared by sol-gel on stainless steel 316L. J Non-Cryst Solids 348:218–224
296. García C, Ceré S, Durán A (2006) Bioactive coatings deposited on titanium alloys. J Non-Cryst Solids 352(32–35):3488–3495
297. Oyane A, Nakanishi K, Kim H-M et al (1999) Sol-gel modification of silicone to induce apatite-forming ability. Biomaterials 20:79–84
298. Kokubo T, Takadama H (2006) How useful is SBF in predicting in vivo bone bioactivity? Biomaterials 27:2907–2915
299. Balamurugan A, Balossier G, Kannan S et al (2007) In vitro biological, chemical and electrochemical evaluation of titania reinforced hydroxyapatite sol-gel coatings on surgical grade 316L SS. Mater Sci Eng C 27(1):162–171
300. Bohner M, Lemaitre J (2009) Can bioactivity be tested in vitro with SBF solution? Biomaterials 30:2175–2179
301. Kokubo T, Kushitani H, Sakka S et al (1990) Solutions able to produce in vivo surface-structure changes in bioactive glass-ceramic A. W. J Biomed Mater Res 24:721–734
302. de Aza AH, Velázquez P, Alemany MI et al (2007) In situ bone-like apatite formation from bioeutectic ceramic in SBF dynamic flow. J Am Ceram Soc 90(4):1200–1207
303. Galliano P, de Damborenea JJ, Pascual MJ et al (1998) Sol-gel coatings on 316L stainless steel for clinical applications. J Sol-Gel Sci Technol 13:723–727

304. Ballarre J, Orellano JC, Bordenave C et al (2002) In vivo and in vitro evaluation of vitreous coatings on cobalt based alloys for prothetics devices. J Non-Cryst Solids 304(5):278–285
305. Ballarre J, Liu Y, Mendoza E et al (2012) Enhancing low cost stainless steel implants: bioactive silica-based sol-gel coatings with wollastonite particles. Int J Nano Biomater 4(1):33–53
306. Pourhashem S, Afshar A (2014) Double layer bioglass-silica coatings on 316L stainless steel by sol–gel method. Ceram Int 40(1 pt A):993–1000
307. Ballarre J, Pellice SA, Schreiner WH et al (2009) Coatings containing silica nanoparticles and glass ceramic particles applied onto surgical grade stainless steel. Key Eng Mater 396–398:311–314
308. Metikoš-Huković M, Tkalčec E, Kwokal A et al (2003) An in vitro study of Ti and Ti-alloys coated with sol–gel derived hydroxyapatite coatings. Surf Coat Technol 165(1):40–50
309. Tkalcec E, Sauer M, Nonninger R et al (2001) Sol-gel-derived hydroxyapatite powders and coatings. J Mater Sci 36(21):5253–5263
310. Hanawa T, Ota M (1991) Calcium phosphate naturally formed on titanium in electrolyte solution. Biomaterials 12(8):767–774
311. Shadanbaz S, Dias GJ (2012) Calcium phosphate coatings on magnesium alloys for biomedical applications: a review. Acta Biomater 8(1):20–30
312. Rámila A, Balas F, Vallet-Regí M (2002) Synthesis routes for bioactive sol-gel glasses: alkoxides versus nitrates. Chem Mater 14(2):542–548
313. Rusu VM, Ng C-H, Wilke M et al (2005) Size-controlled hydroxyapatite nanoparticles as self-organized organic-inorganic composite materials. Biomaterials 26(26):5414–5426
314. Izquierdo-Barba I, Salinas AJ, Vallet-Regí M (2013) Bioactive glasses: from macro to nano. Int J Appl Glas Sci 4(2):149–161
315. Montenero A, Gnappi G, Ferrari F et al (2000) Sol-gel derived hydroxyapatite coatings on titanium substrate. J Mater Sci 35(11):2791–2797
316. King AD, Birbilis N, Scully JR (2014) Accurate electrochemical measurement of magnesium corrosion rates; a combined impedance, mass-loss and hydrogen collection study. Electrochim Acta 121:394–406
317. Lamaka SV, Montemor MF, Galio AF et al (2008) Novel hybrid sol-gel coatings for corrosion protection of AZ31B magnesium alloy. Electrochim Acta 53(14):4773–4783
318. Rojaee R, Fathi M, Raeissi K (2013) Controlling the degradation rate of AZ91 magnesium alloy via sol–gel derived nanostructured hydroxyapatite coating. Mater Sci Eng C 33(7):3817–3825
319. Barranco V, Carmona N, Galván JC et al (2010) Electrochemical study of tailored sol–gel thin films as pre-treatment prior to organic coating for AZ91 magnesium alloy. Prog Org Coat 68(4):347–355
320. Orazem ME, Tribollet B (2008) Equivalent circuits analogs. In: Electrochemical impedance spectroscopy. Wiley, Somerset, pp 157–158
321. Yang L, Zhang E (2009) Biocorrosion behavior of magnesium alloy in different simulated fluids for biomedical application. Mater Sci Eng C 29(5):1691–1696

322. Zomorodian A, Santos C, Carmezim MJ et al (2015) "In-vitro" corrosion behaviour of the magnesium alloy with Al and Zn (AZ31) protected with a biodegradable polycaprolactone coating loaded with hydroxyapatite and cephalexin. Electrochim Acta 179:431–440
323. Ren M, Cai S, Liu T et al (2014) Calcium phosphate glass/MgF2 double layered composite coating for improving the corrosion resistance of magnesium alloy. J Alloys Compd 591:34–40
324. Zheng Y, Wu J, Ng JC et al (2002) The absorption and excretion of fluoride and arsenic in humans. Toxicol Lett 133(1):77–82
325. Bakhsheshi-Rad HR, Idris MH, Abdul-Kadir MR (2013) Synthesis and in vitro degradation evaluation of the nano-HA/MgF2 and DCPD/MgF2 composite coating on biodegradable Mg-Ca-Zn alloy. Surf Coat Technol 222:79–89
326. Li Q, Zhong X, Hu J et al (2008) Preparation and corrosion resistance studies of zirconia coating on fluorinated AZ91D magnesium alloy. Prog Org Coat 63(2):222–227
327. Zhang S, Li Q, Fan J et al (2009) Novel composite films prepared by sol-gel technology for the corrosion protection of AZ91D magnesium alloy. Prog Org Coat 66(3):328–335
328. Trabelsi W, Triki E, Dhouibi L et al (2006) The use of pre-treatments based on doped silane solutions for improved corrosion resistance of galvanised steel substrates. Surf Coat Technol 200(14–15):4240–4250
329. Wang D, Bierwagen Gordon P (2009) Sol-gel coatings on metals for corrosion protection. Prog Org Coat 64(4):327–338
330. Balamurugan A, Sockalingum G, Michel J et al (2006) Synthesis and characterisation of sol gel derived bioactive glass for biomedical applications. Mater Lett 60(29–30):3752–3757
331. Ballarre J, López DA, Schreiner WH et al (2007) Protective hybrid sol-gel coatings containing bioactive particles on surgical grade stainless steel: surface characterization. Appl Surf Sci 253(17):7260–7264
332. Gallardo J, Galliano P, Duran A (2001) Bioactive and protective sol-gel coatings on metals for orthopaedic prostheses. J Sol-Gel Sci Technol 21:65–74

Chapter 4
Electrochemical Production of Polymer Hydrogels with Silver Nanoparticles for Medical Applications as Wound Dressings and Soft Tissue Implants

Vesna B. Mišković-Stanković

4.1 Introduction

This chapter explored the novel nanostructured biomaterials suitable for medical applications as wound dressings, soft tissue implants (maxillofacial implants, nucleus pulposus replacements in intervertebral discs), drug delivery devices, and carriers for cell cultivation. The Ag/alginate, Ag/poly(*N*-vinyl-2-pyrrolidone) (Ag/PVP), Ag/polyvinyl alcohol (Ag/PVA), and Ag/polyvinyl alcohol/graphene (Ag/PVA/Gr) nanocomposites synthesized according to original electrochemical procedures will be discussed in the chapter.

In recent decades, a constant increase in the number of microorganisms resistant to existing antibiotics revived the clinical use of silver. Variety of silver-containing products have been developed and utilized especially for treatments of infections in burns, open wounds, and chronic ulcers. The synthesis of silver nanoparticles (AgNPs) became very interesting for potential applications in many areas, including biomedicine, since nanocrystalline silver is proved to be the most efficient antimicrobial agent with a wide

V.B. Mišković-Stanković (✉)
Faculty of Technology and Metallurgy, University of Belgrade, Karnegijeva 4, P.O. Box 3503, 11120 Belgrade, Serbia
e-mail: vesna@tmf.bg.ac.rs

S. Djokić (ed.), *Biomedical and Pharmaceutical Applications of Electrochemistry*, Modern Aspects of Electrochemistry 60,
DOI 10.1007/978-3-319-31849-3_4

inhibiting spectrum toward different types of microorganisms. However, one of the key problems for application of AgNPs is strong tendency of these particles to agglomerate due to high specific surface area and surface energy. To overcome this problem, polymers are used as capping agents to prevent AgNPs agglomeration, but also as their carriers, in the hydrogel form. Hydrogel form is applicable as wound dressing or soft tissue implant. AgNPs embedded in hydrogel matrices are attractive for biomedical applications due to possibility for their controlled release resulting in antimicrobial activity. These gels are hydrophilic, biocompatible, biodegradable, easily processed into different shapes, and approved for medical use. Thus, combination of AgNPs with biocompatible hydrogels, like alginate, PVA, and PVP, provides potential for design of improved medical treatments and devices (antimicrobial wound dressings, soft tissue implants). Two electrochemical methods for material fabrication were used: (1) electrochemical synthesis of AgNPs in the polymer solution under galvanostatic conditions, followed by electrostatic extrusion or freezing–thawing, and (2) electrochemical reduction of Ag^+ ions into AgNPs inside the polymer hydrogel, with the variation of applied voltage and implementation time. The electrochemical procedures exhibit advantages over chemical methods for the synthesis of small metal particles: the high purity of the metal, particularly important for biomedical applications, and the possibility of a precise particle size control, which can be achieved by adjusting deposition current density, voltage, and potential.

Based on MTT test of cytotoxicity, antibacterial tests, and in vitro tests in bioreactor, the evidence presented here demonstrated that novel electrochemically produced polymer hydrogels with silver nanoparticles for wound dressing and soft tissue implants are excellent candidates for future biomedical applications.

4.2 Silver/Alginate Nanocomposites

Silver is a historically well-known metal for its broad antimicrobial activity while nanocrystalline silver was reported to be more potent than its cationic form [1]. The large specific surface area

and high fraction of surface atoms on silver nanoparticles (AgNPs) lead to enhanced antibacterial activity compared to bulk silver metal [2]. However, AgNPs in aqueous solutions tend to agglomerate and preparation of a stable dispersion using polymers as stabilizing agents is one of the directions to solve this problem [3]. Additional approaches involving polymers as nanoparticle stabilizers and/or carriers include in situ synthesis of AgNPs within polymer networks in hydrogels [4, 5] as well as polymer fiber or fabric coatings by AgNPs [1]. These three main approaches for synthesis and stabilization of AgNPs using polymers are schematically represented in Fig. 4.1.

Combinations of polymers and AgNPs provide advantages of both components such as biocompatibility and variety of forms and shapes of polymers, and optical, sensing, catalytic, and antimicrobial properties of nanoparticles, the last of which is especially attractive for biomedical applications. Additionally, depending on the polymer form and structure, as well as the nature of nanoparticle

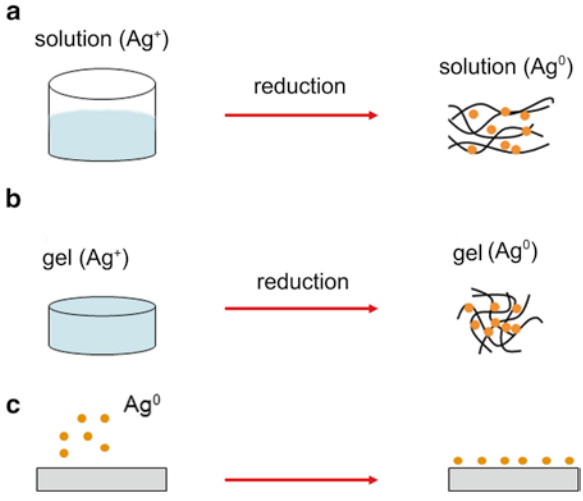

Fig. 4.1 Synthesis and stabilization of silver nanoparticles using polymers: (**a**) Ag^+ ions in polymer solutions and obtained nanoparticles Ag^0 stabilized by polymer chains; (**b**) polymer gels saturated with Ag^+ ions and obtained nanoparticles Ag^0 stabilized within the polymer network; (**c**) surfaces coated with nanoparticles Ag^0 (physical vapor deposition)

immobilization, these nanocomposites can provide immediate or controlled release of nanoparticles. Some of the widely studied polymers for biomedical applications in general as well as in combinations with AgNPs are alginate, chitosan, poly(vinyl alcohol) (PVA), and poly(*N*-vinyl-2-pyrrolidone) (PVP) [4, 6].

Alginate is especially attractive biomaterial since it is a naturally derived linear copolymer that easily forms biocompatible hydrogels, which are already in medical use. It is composed of 1,4-linked β-D-mannuronic acid (M-block) and α-L-guluronic acid (G-block) units (Fig. 4.2). Aqueous solutions of alginates are known to form hydrogels in the presence of divalent cations such as Ca^{2+} via ionic interactions between acid groups on G blocks and the gelating ions. As a result, calcium/alginate gels are physically cross-linked polymers with mechanical and structural properties that depend on alginate composition [7–9]. These gels are hydrophilic, biocompatible, biodegradable, and easily processed into different shapes, which made them attractive for variety of applications in biotechnology and biomedicine such as gelling agents in food products, substrates for immobilization of cells and bioactive molecules, tissue engineering scaffolds, carriers for drug delivery, as well as for wound dressings [10–13].

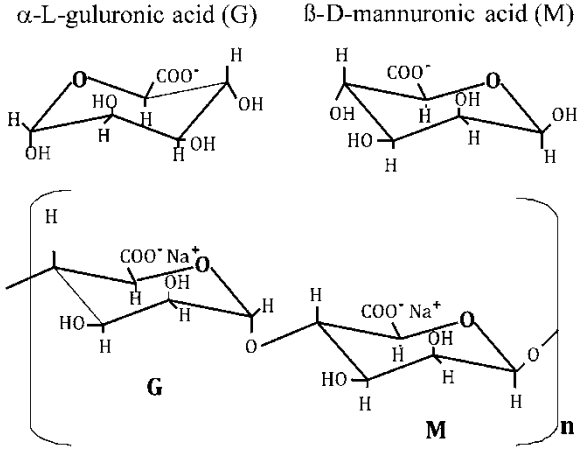

Fig. 4.2 Monomer units and molecular structure of Na-alginate (reprinted from [20] with permission from Elsevier)

Wound dressings based on alginate, mostly as Ca-alginate hydrogel, are already in commercial use, providing biocompatibility and high sorption capacity, and thus regulation of moisture levels that leads to rapid granulation and reepithelization of the damaged tissue. Supplementation of silver to alginate dressings offers the advantage of an additional feature of antimicrobial activity, so that a number of products based on alginate fibers with incorporated silver ions were produced [11]. These dressings are easily removed and replaced without causing much trauma due to the highly hydrophilic alginate gel nature. In addition, alginate hydrogels are widely investigated for regeneration and engineering of a number of tissues and organs, including skeletal muscle, blood vessels, nerve, pancreas, liver, and cartilage. High water content in these gels supports efficient transport of nutrients and gases and provides aqueous environment comparable to that in soft tissues. Also, alginate gels could be introduced into the body to fill irregularly shaped defects by a minimally invasive procedure. All of these properties make alginate hydrogels attractive and potentially applicable as soft tissue implants.

However, incorporation of AgNPs within alginate solutions and/or hydrogels provides possibilities for controlled and prolonged release of Ag nanoparticles and/or ions and production of variety of formulations with different compositions and forms. Alginate as an anionic polymer with high charge density can stabilize nanoparticles by a negative charge resulting in stability against agglomeration [2]. There are several recent approaches investigated for synthesis of AgNPs in combination with alginate, which will be overviewed in this chapter with the special attention to electrochemical synthesis of AgNPs.

4.2.1 Synthesis of AgNPs in Alginate Solutions

Chemical reduction is one of the most used methods for production of AgNPs as colloidal dispersions in water or organic solvents [4]. This method was also applied in alginate solutions supplemented with silver salts (e.g., nitrate, sulfate) using sodium borohydride as the reductant [2, 14, 15]. Alginate was shown to be a good capping

agent of AgNPs, which were in the size range 3–20 nm as determined in different studies, while the obtained colloid solutions were investigated for several potential applications. It was shown to be possible to form nanocomposite thin films by using a layer-by-layer dipping technique alternating between anionic colloid alginate solution and cationic poly(diallyldimethylammonium chloride) (PDADMAC) solution [14]. The obtained nanocomposite films displayed fast color change upon exposure to water or to a less polar solvent such as ethanol making them attractive for potential sensing applications or optical switches.

Another advantage of using alginate solutions is that they can be easily mixed with solutions of other polymers in order to obtain final products with improved properties as compared to using either polymer alone. Alginate colloid solution with chemically synthesized AgNPs was successfully mixed with sago starch and ethylene glycol and the obtained mixture was casted and dried so to produce nanocomposite films attractive for potential use as wound dressings [15]. The obtained films exhibited enhanced wound healing patterns as compared to untreated controls in in vivo studies in rats.

In another study, dialyzed alginate colloid solution with chemically synthesized AgNPs was freeze-dried for 3 days and cross-linking by dipping in 0.2 M $CaCl_2$ solution resulting in formation of a nanocomposite Ca/alginate sponge [2]. The obtained sponge exhibited antimicrobial activity against *E. coli* and *K. pneumonia*, but also cytotoxicity toward human fibroblasts. On the other hand, the amounts of proinflammatory cytokines released from macrophages treated with the nanocomposite Ca/alginate sponge were lower as compared to the control, indicating potential anti-inflammatory activity of this product if medically used [2].

In order to avoid addition of chemical reductants and the need for purification of the obtained colloid solution, radiation techniques can be used. Gamma irradiation of the alginate solution supplemented with silver nitrate and isopropanol resulted in formation of a colloid solution containing AgNPs in the size range 5–30 nm and stable for 6 months [16].

Finally, a simpler, novel method for production of AgNPs using alginate both as a reducing agent and a stabilizer was recently

developed based on just heating the solution of silver nitrate and alginate at 90° C for 1 h [17]. The obtained colloid solution contained AgNPs in the size range 5–21 nm and was further mixed with chitosan solution. The mixture was then casted and dried resulting in formation of nanocomposite films that exhibited antibacterial activity against both Gram-negative and Gram-positive bacteria, having stronger effects on the latter group [17].

4.2.2 Electrochemical Synthesis of AgNPs in Alginate Colloid Solutions and Production of Nanocomposite Hydrogels Based on Alginate Colloid Solutions with Electrochemically Synthesized AgNPs

Electrochemical synthesis of metal nanoparticles, as compared to conventional chemical methods, offers advantages especially attractive for biomedical applications, such as high purity of the particles and possibility for a precise particle size control achieved by adjusting current density or applied potential [18]. This method was recently applied and optimized for controlled production of AgNPs using Na/alginate as a capping agent [19, 20].

4.2.2.1 Electrochemical Synthesis of AgNPs in Alginate Colloid Solutions

Ag/alginate colloid solutions were obtained from 2 % w/v Na/alginate, 0.1 M KNO_3, and $AgNO_3$ in the concentration range between 0.5 and 3.9 mM [20] by electrochemical synthesis performed galvanostatically. Current density was varied between 5 and 50 mA cm^{-2}, while the time was varied between 0.5 and 10 min. Due to alginate gel deposited at the counter electrode, the concentration of alginate decreased from 2.0 to 1.9 w/v %. This could be expected, since the dissolved alginate consists of Na^+ ions and negatively charged alginate residues [20].

Ag/alginate colloid solutions obtained under various experimental conditions (i.e., variation of $AgNO_3$ concentration in the initial alginate solution, applied current density, and implementation time) were analyzed using transmission electron microscopy (Fig. 4.3). The nanoparticles obtained were all spherical in shape, approximately 10–30 nm in diameter, independently of applied current density. The nanoparticles synthesized at current density of 5 mA cm^{-2} seemed to be slightly smaller, but formed larger aggregates (Fig. 4.3a), so it can be considered that applied current density does not affect the size of Ag nanoparticles. It is known from the literature [21, 22] that nanoparticles of the dimensions obtained exhibit antimicrobial characteristics.

Regardless of the parameters of synthesis (i.e., $AgNO_3$ concentration in the initial alginate solution, applied current density, and implementation time), UV–Vis analysis has shown that Ag/alginate colloid solutions exhibited surface plasmon absorption band peaking in the wavelength range of 405–440 nm, corresponding to particles whose radii are smaller than ~30 nm [23, 24]. In addition, absorption spectra of Ag/alginate colloid solution corresponded to

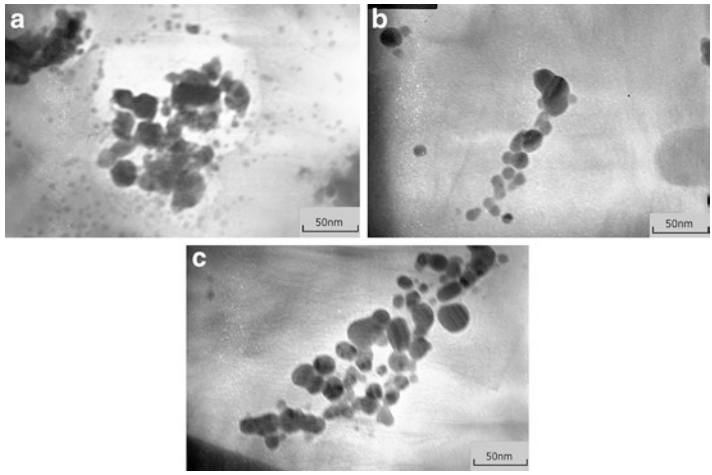

Fig. 4.3 TEM micrographs of electrochemically synthesized silver nanoparticles in Ag/alginate colloid solutions ($c = 3.9$ mM, $t = 10$ min) at different values of current density: (**a**) 5 mA cm^{-2}, (**b**) 15 mA cm^{-2}, and (**c**) 50 mA cm^{-2} (scale bar = 50 nm) (reprinted from [20] with permission from Elsevier)

Lorentzian fit implying monodispersity of the nanoparticles [25], which is consistent with TEM measurements. On the contrary, UV–Vis spectra of pure alginate solution and dissolved control alginate microbeads did not exhibit the absorbance peak in the examined range of wavelengths, as shown in Fig. 4.4. These results correspond to a plasmon resonance effect originating from the quantum size of AgNPs [26] and thus confirmed the presence of Ag nanoparticles in Ag/alginate colloid solutions, as well as in Ag/alginate microbeads.

UV–Vis spectra were used also to determine the effects in all of the parameters of synthesis ($AgNO_3$ concentration in the initial alginate solution, applied current density, and time) on the amount and relative size of silver nanoparticles formed, i.e., on the absorbance maximum, A_{max}, and the wavelength of the absorbance maximum, λ_{max}, in different Ag/alginate colloid solutions (Figs. 4.5 and 4.6, respectively). It was observed that the increase in $AgNO_3$ concentration in the initial

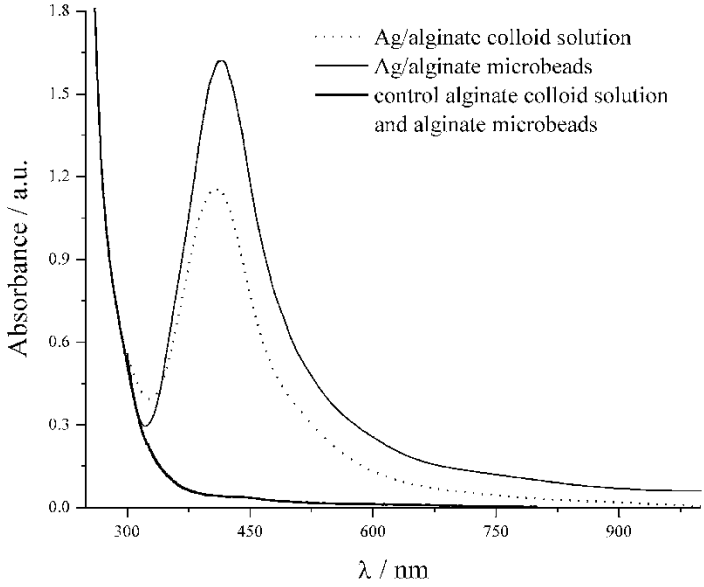

Fig. 4.4 Absorption spectra of control alginate solution and alginate microbeads, Ag/alginate colloid solution (c=3.9 mM, j=50 mA cm^{-2}, t=10 min) and Ag/alginate microbeads; absorbance corresponds to a 100 μL sample of either colloid solution or microbeads (reprinted from [20] with permission from Elsevier)

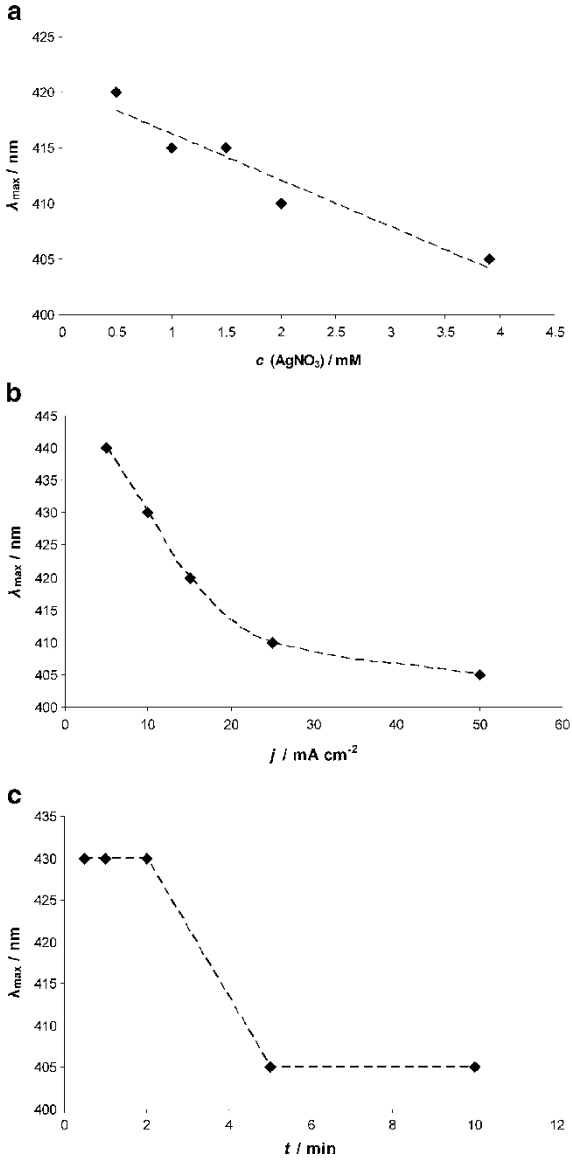

Fig. 4.5 Absorbance maximum wavelength, λ_{max}, of Ag/alginate colloid solutions as a function of: (**a**) $AgNO_3$ concentration in the initial alginate solution, (**b**) current density, and (**c**) time (reprinted from [20] with permission from Elsevier)

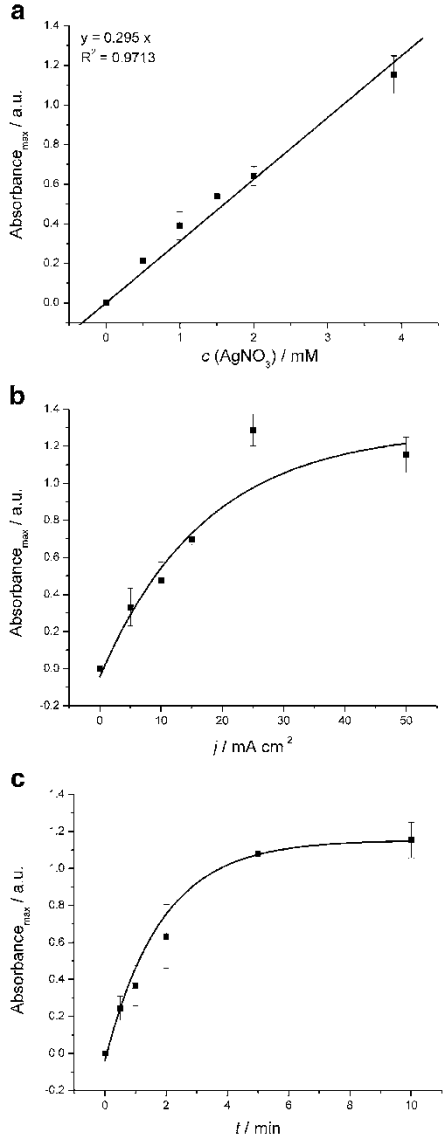

Fig. 4.6 Absorbance maxima, A_{max}, of Ag/alginate colloid solutions as a function of: (**a**) $AgNO_3$ concentration in the initial alginate solution, (**b**) current density, and (**c**) time (all data are average of at least $n=2$) (reprinted from [20] with permission from Elsevier)

alginate solution (Fig. 4.5a), applied current density (Fig. 4.5b), and time (Fig. 4.5c) decreases the λ_{max} arriving at the value of 405 nm in the solution synthesized at $c=3.9$ mM, $j=50$ mA cm^{-2}, $t=10$ min. Lower λ_{max} values were reported to correspond to smaller nanoparticles [27, 28].

Figure 4.6 shows the dependence of the absorbance maximum in Ag/alginate colloid solutions on the $AgNO_3$ concentration in the initial alginate solution (Fig. 4.6a), applied current density (Fig. 4.6b), and time (Fig. 4.6c). As it can be seen, the increase in all of these parameters of synthesis (i.e., $AgNO_3$ concentration in the initial alginate solution, applied current density, and time) led to the increase of the absorbance maximum.

Linear increase in absorbance maximum with the increase of $AgNO_3$ concentration in the initial alginate solution (Fig. 4.6a) is expected, since the absorbance is proportional to the concentration of silver nanoparticles formed [29–31]. The higher concentrations of Ag^+ ions in the initial alginate solution resulted in higher concentrations of nanoparticles. Similarly, it could be expected that higher values of current density and longer times will result in more intensive nanoparticle formation as observed up to the current density of 25 mA cm^{-2} and time of 6 min. However, further increases in these parameters had a little effect on AgNP concentration (Fig. 4.6b, c) although they induced shift of the absorbance maxima toward 405 nm, as already described (Fig. 4.5b, c). As a consequence, the Ag/alginate colloid solution, synthesized at 50 mA cm^{-2}, for 10 min, with $AgNO_3$ concentration in the initial alginate solution of 3.9 mM, was chosen for further investigations as well as for the production of Ag/alginate hydrogel microbeads, due to the higher concentration and smaller dimensions of Ag nanoparticles obtained.

The cyclic voltammetry analysis was performed for Pt electrode in 1.9 w/v % alginate solution and in Ag/alginate colloid solution (Fig. 4.7), as well as for Pt electrode in 1.9 w/v % alginate solution containing 0.1 M KNO_3 + 3.9 mM $AgNO_3$ (Figs. 4.8 and 4.9) in order to get better insight into the silver reduction process.

Cyclic voltammogram for Pt electrode in 1.9 w/v % alginate solution (Fig. 4.7) has shown the presence of the anodic peak at around 270 mV, and the cathodic peak at −40 mV. These peaks are

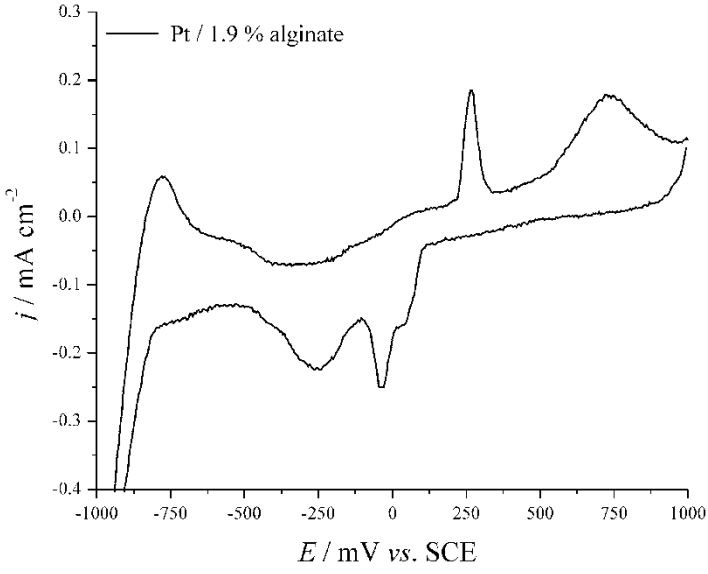

Fig. 4.7 Stationary cyclic voltammogram for Pt electrode in 1.9 w/v % alginate solution (reprinted from [20] with permission from Elsevier)

related to the redox reaction of alginate. Namely, –OH groups from pyranose rings originating from uronic acid residues in the alginate molecule (Fig. 4.2) can be oxidized to >C=O or –COOH groups. These peaks do not appear in cyclic voltammograms for Pt electrodes in silver-contained solutions (Figs. 4.8 and 4.9); they are either being overlapped by more intense current peaks originating from the Ag/Ag^+ oxidation/reduction process, or they disappeared because of the interaction of alginate hydroxyl groups with silver ions and/or silver nanoparticles.

Figure 4.8 shows stationary cyclic voltammograms for Pt electrode in 1.9 w/v % alginate solution containing 0.1 M KNO_3 + 3.9 mM $AgNO_3$ and in Ag/alginate colloid solution, which exhibited anodic peaks, appearing at around 450 and 465 mV, respectively. As the corresponding counterpart, one cathodic peak appeared at about 165 mV (in 1.9 w/v % alginate solution containing 0.1 M KNO_3 + 3.9 mM $AgNO_3$), and around 25 mV (in Ag/alginate colloid solution), which corresponded to the reduction of

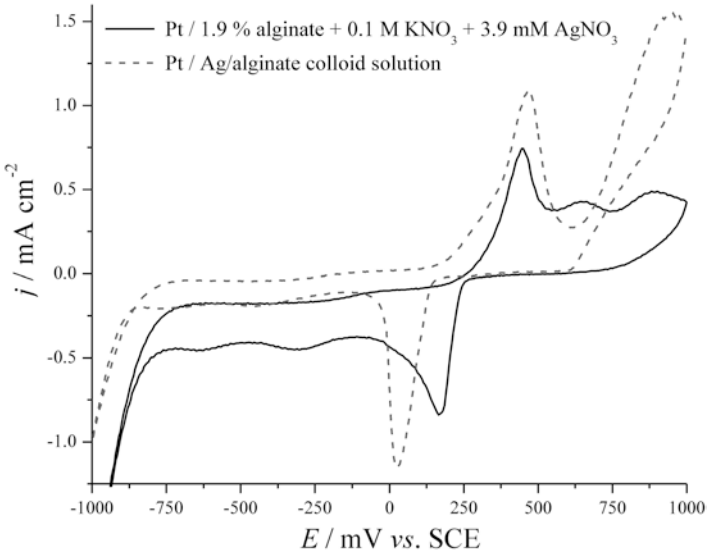

Fig. 4.8 Stationary cyclic voltammograms for Pt electrode in 1.9 w/v % alginate solution containing 0.1 M KNO_3 + 3.9 mM $AgNO_3$ and in Ag/alginate colloid solution (c = 3.9 mM, j = 50 mA cm^{-2}, t = 10 min) (reprinted from [20] with permission from Elsevier)

silver. The shift of this cathodic peak in Ag/alginate colloid solution toward more negative potential indicates differences in the reduction process. In 1.9 w/v % alginate solution containing 0.1 M KNO_3 + 3.9 mM $AgNO_3$, Ag^+ reduction appears as formation of silver nanoparticles. On the other hand, in Ag/alginate colloid solutions, the appearance of the cathodic peak can probably be explained due to the further growth of already formed silver nanoparticles (somewhat restricted by the presence of alginate molecules) and resynthesis of silver nanoparticles from eventually present residual silver ions.

In the stationary cyclic voltammogram for Pt electrode in 1.9 w/v % alginate solution containing 0.1 M KNO_3 + 3.9 mM $AgNO_3$, the second anodic peak is observed at around 645 mV (Fig. 4.8). Since this peak does not have a related counterpart, all sweeps of cyclic voltammetry analysis obtained for Pt electrode in this solution (Fig. 4.9) should be concerned.

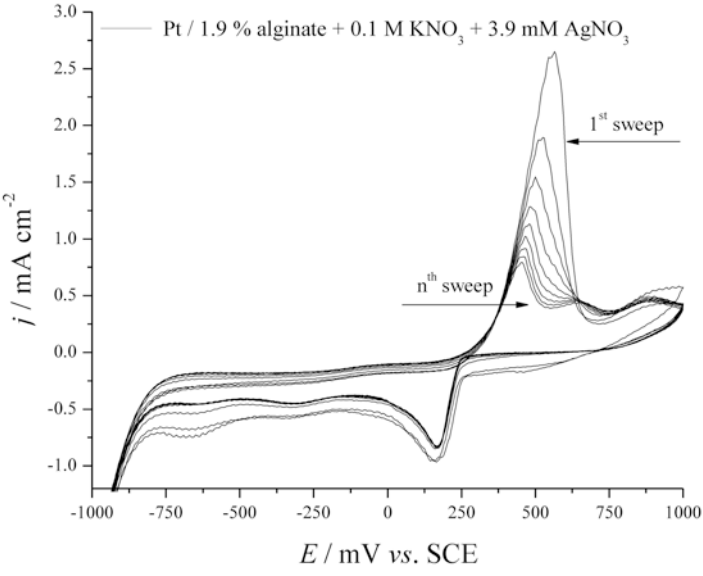

Fig. 4.9 Cyclic voltammograms for Pt electrode in 1.9 w/v % alginate solution containing 0.1 M KNO_3 + 3.9 mM $AgNO_3$ (reprinted from [20] with permission from Elsevier)

At Fig. 4.9, the anodic peak is observed at around 565 mV, which decreased with every following sweep, and also changed the peaking position toward more negative potentials, arriving at the value of 450 mV in the *n*th sweep, as it can be seen in Fig. 4.8. At some point between the sixth and seventh sweep, a new anodic peak appeared at around 645 mV as a result of the separation/disjunction of the corresponding peak (at 565 mV). The absence of the cathodic counterpart for this anodic peak appearing at 645 mV indicates that the reduction process is not affected by further influence of the applied current, and it continues due to the synthesis of silver nanoparticles from Ag^+ ions. On the other hand, the decrease in the current peak intensity at 565 mV indicates lowering of the content of silver available for oxidation due to the synthesis of silver nanoparticles. The appearance of the second anodic peak at a more positive potential value suggests that a certain amount of silver becomes even less susceptible for oxidation [28] probably as a consequence of the

entrapment of silver nanoparticles by alginate molecules during this process, suggesting that synthesized silver nanoparticles are very stable. This result points to the validity of alginate as a choice for the electrochemical synthesis of silver nanoparticles in the solution, considering that more stable nanoparticles are formed in solutions of capping agents that exhibit a certain level of bonding with silver ions and silver nanoparticles formed.

Interactions of alginate molecules with Ag nanoparticles were investigated using FT-IR spectroscopy, performed on alginate and Ag/alginate thin films (Fig. 4.10). The films were obtained by solvent evaporation from alginate solution and Ag/alginate colloid solution.

Pure alginate spectrum showed the following absorption bands: broad absorption band peaking in the region of 3250–3400 cm^{-1}

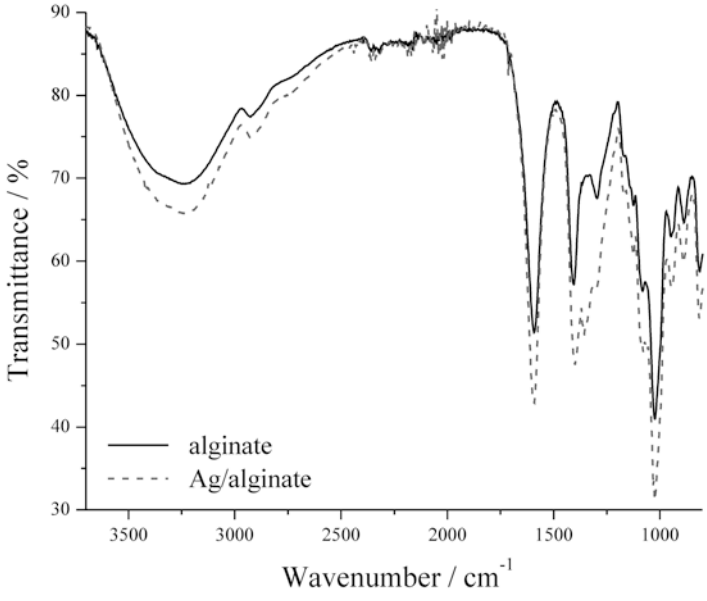

Fig. 4.10 IR spectra of alginate and Ag/alginate thin films obtained by solvent evaporation from alginate solution and Ag/alginate colloid solution ($c = 3.9$ mM, $j = 50$ mA cm^{-2}, $t = 10$ min) (reprint from [20] with permission from Elsevier)

(at 3257 cm^{-1}) indicating the weak H-bonding of hydroxyl groups, followed by a peak at 2927 cm^{-1}, which can be assigned to vibration of the CH group. The alginate spectrum also displayed absorption peaks at 1712, 1593, and 1406 cm^{-1} corresponding to the H–O–C=O stretching vibrations, asymmetric and symmetric stretching of carboxylate vibrations, respectively, followed by characteristic absorption bands of polysaccharide structure appearing at 1367 and 1296 cm^{-1} (C–C–H and O–C–H bending), 1124 cm^{-1} (C–O stretching), 1082 cm^{-1} (both C–O and C–C stretching of pyranose rings), and at 1024 cm^{-1} (C–O stretching). Also, the characteristic bands of uronic acid residues peak at 949 cm^{-1} (C–O stretching vibration), 887 cm^{-1} (C1–H deformation vibration of the β-mannuronic acid residues), and 814 cm^{-1} (C1–H deformation vibration of the α-guluronic acid residues). These results are in accordance with the results found in literature for pure alginate [27].

On the other hand, Ag/alginate spectrum exhibited several differences in peak positions compared to the pure alginate spectrum, suggesting possible bonding between alginate molecules and Ag nanoparticles. The most important differences observed are in two spectral ranges, i.e., between 1370 and 1205 cm^{-1} and between 1160 and 1015 cm^{-1}. Absorption bands of the pure alginate appearing in the first specified range at 1367 and 1296 cm^{-1} shift toward 1358 and 1298 cm^{-1}, respectively, in the Ag/alginate spectrum. This possibly indicates interactions of Ag nanoparticles with OH groups in uronic acid residues, observed as a shift of the C–OH bending vibration. In the second mentioned spectral range, the vibration frequency shifted from 1082 cm^{-1} recorded for pure alginate to 1078 cm^{-1} recorded in Ag/alginate spectrum as a result of the coordination of both OH and ether groups to Ag nanoparticles, which weakened the strength of C–O bond in these two functional groups. Moreover, the C–O frequency slightly shifted from 1024 cm^{-1} recorded for pure alginate to 1026 cm^{-1} recorded for Ag/alginate spectrum, pointing out to interactions of the ring C(5) oxygen atoms of both, guluronic and mannuronic acid residues with Ag nanoparticles. Overall, the comparison of peak positions in pure alginate and Ag/alginate thin film spectra indicates the bonding of hydroxyl and ether groups, as well as ring oxygen

atoms in uronic acid residues of alginate molecules, by coordination with Ag nanoparticles.

The findings obtained by FTIR spectroscopy are in accordance with cyclic voltammetry results and indicate the bonding of alginate molecules with Ag nanoparticles, which prove alginate to be a good choice for the electrochemical synthesis of silver nanoparticles. Namely, the synthesis process of metal nanoparticles is shown to be a competition between two different cathode surface processes, i.e., the particle formation, by reduction and stabilization of metal ions by the capping agent, and the metallic film deposition at the cathode surface [18]. The metal deposition on the cathode limits the yield of the particle synthesis, because when the electrode surface is totally covered by the metallic deposit, the only process that occurs is further deposition of metal coating. Therefore, deposition process must be minimized. So the role of the capping agent is to accelerate metal nanoparticle formation and lower the metal deposition on the cathode [32]. Furthermore, efficiency of the capping agent is in tight connection with its potential to bond to the metal nanoparticle surfaces. Thus, silver is successfully electrochemically synthesized in the solutions of PVP, PANI, PAMAM, PVA [32–36], and for the first time alginate [20].

4.2.2.2 Production of Alginate Microbeads with Incorporated Silver Nanoparticles

Alginate microbeads with incorporated AgNPs were obtained by electrostatic extrusion of Ag/alginate nanocomposite solutions [20] at a constant flow rate of 25.2 mL h^{-1} through a blunt edge, stainless steel needle using a 5 mL syringe, and a syringe pump as described previously [37]. The needle was connected to a positive electrode of a high voltage d.c. generator at applied electrostatic potential of 6 kV and positioned 2.5 cm above the gelling bath containing 1.5 % w/v $Ca(NO_3)_2 \cdot 2H_2O$, which was grounded. At the tip of the needle, a stream of droplets was formed and collected in the bath, which provided exchange of Na^+ and Ca^{2+} ions and alginate gelling. The obtained microbeads were left in the bath for additional 30 min in order to complete gelling [20].

Electrostatic extrusion of Ag/alginate colloid solutions resulted in formation of uniform hydrogel microbeads incorporated with AgNPs, which colored the beads in yellow (Fig. 4.11). At the experimental conditions applied ($c = 3.9$ mM, $j = 50$ mA cm^{-2}, $t = 10$ min), the microbead size was found to be 487.75 ± 16.5 μm. Presence of AgNPs was confirmed by UV–Vis spectroscopy of dissolved microbeads (Fig. 4.4). It can be observed that the absorption maximum wavelength remained at 405 nm verifying that nanoparticle aggregation did not occur during the production process. In addition, a somewhat higher magnitude of the absorption maximum was observed for microbeads as compared to Ag/alginate colloid solution due to further Ag^+ ions reduction during the electrostatic extrusion. Thus, it can be concluded that practically all AgNPs in alginate solution were preserved and incorporated in the microbeads.

Antibacterial activity of Ag/alginate microbeads, obtained from colloid solution having maximum of 1 mM of AgNPs, was estimated in suspension cultures of *Staphylococcus aureus* (*S. aureus*), since this concentration was reported to be limiting not inducing cytotoxic effects [38]. Briefly, aliquots of 24 h old *S. aureus* culture in saline solution (~10^8 CFU mL^{-1}) were

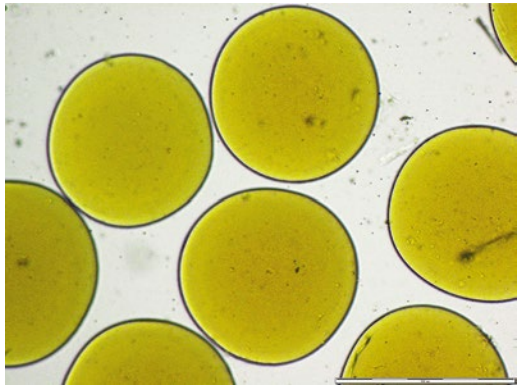

Fig. 4.11 Optical micrograph of Ag/alginate microbeads; *yellow* color in accordance with the presence of AgNPs (scale bar = 500 μm) (reprinted from [20] with permission from Elsevier)

transferred into flasks containing sterile Ag/alginate beads and sterile Luria-Bertani (LB) medium (1 w/v % NaCl, 1 w/v % tryptone, 0.5 w/v % yeast extract), while culture in pure LB medium served as a control, and incubated in a shaking water-bath at 37° C for 24 h. Medium samples after 1 h and at the end of the incubation period were spread on agar plates and incubated at 37 °C in an incubator for 24 h. Numbers of colonies formed were then counted. The maximal possible concentration of released Ag nanoparticles and ions in the bacterial suspension thus was ~0.3 mM. After 1 h of incubation, the concentration of *S. aureus* in microbead groups was significantly lower than the initial concentration, while it started to increase in the control (Table 4.1). After 24 h of incubation, the concentration of bacterial cells in microbead groups increased to 1.33×10^6 CFU mL^{-1}, but still it was significantly lower (almost three orders of magnitude) than the concentration of 9.9×10^8 CFU mL^{-1} measured in the control group [20].

These results have demonstrated that Ag/alginate microbeads efficiently released AgNPs and/or Ag^+ ions and induced bactericidal effects in suspensions of *S. aureus*. The maximal possible concentration of released silver from the beads was ~32 μg mL^{-1} (~0.3 mM), inducing the decrease in bacterial concentration of 95.8 % after 1 h of incubation. These results are in agreement with other studies of antimicrobial activity of different systems containing AgNPs against *S. aureus* where minimum inhibitory concentrations of AgNPs were reported to range from 0.34 to 259 μg mL^{-1}, depending on the size, shape, and surface modifications of nanoparticles [39–43].

Table 4.1 Colonies count of *Staphylococcus aureus* in control suspension and in suspension with 0.4 g mL^{-1} Ag/alginate beads with the maximum possible concentration of AgNPs and Ag^+ released of ~0.3 mM

	Initial	1 h	24 h
Control (CFU[a] mL^{-1})	5.0×10^5	7.95×10^5	9.9×10^8
Ag/alginate (CFU mL^{-1})	$(4.85 \pm 0.64) \times 10^5$	$(2.04 \pm 0.48) \times 10^5$	$(1.33 \pm 0.75) \times 10^6$

Reprinted from [20] with permission from Elsevier
[a]Colony-forming units

Furthermore, nanocomposite hydrogels in the form of microbeads (<1 mm in diameter) are suitable for controlled release of AgNPs and/or ions due to the large specific surface area and short internal diffusion distances. Alginate microbeads were shown to be suitable for immobilization of variety of cell types such as insect and mammalian cells [44] as well as brewing yeast cells [45]. It was shown previously that alginate microbeads could be also used for cartilage tissue engineering as supports for chondrogenic cells (e.g., bone marrow stromal cells [46] and bovine calf chondrocytes [47]) coupled with biomimetic bioreactors that imitate physiological conditions in articular cartilage. Supplementation of AgNPs within alginate microbeads could potentially provide an additional feature of prolonged sterility of the engineered implant.

As confirmed, one of the techniques for controlled production of uniform hydrogel microbeads is electrostatic droplet generation based on extrusion of alginate solution under the action of electrostatic forces that disrupt the liquid filament at the capillary/needle tip to form a charged stream of small droplets collected in a gelling bath [48, 49]. As Na^+ ions are exchanged with Ca^{2+} ions from the gelling solution, droplets solidify forming microbeads down to 50 μm in diameter [49, 50]. The process of electrostatic droplet formation is a complex function of a number of parameters [51, 52], while for a chosen electrode setup and the polymer, the applied electrostatic potential was shown to be the key determinant of the droplet and, consequently, also the microbead size [51]. For potential biomedical utilization of nanocomposite hydrogels, it is required that the production procedure is simple, precisely regulated, and scalable while the final products are pure, sterile, and with controlled properties. In specific, the possibilities for sterilization and manipulation of Ag/alginate colloid solutions with retention of AgNPs have been investigated [52] as well as production of nanocomposite microbeads regarding the effects of electrostatic extrusion parameters on the microbead size and AgNP concentration. In addition, the effects of AgNP incorporation in alginate hydrogels on biomechanical properties of packed beds of microbeads were studied in a biomimetic bioreactor with dynamic compression that imitates in vivo conditions in the native articular cartilage.

Sterilization of Alginate Colloid Solutions with AgNPs

Initially synthesized Ag/alginate colloid solution with 3.9 mM silver concentration was diluted with 1.9 % w/v Na/alginate yielding colloid solutions with different concentrations of AgNPs [52]. Sterilization by boiling for 30 min of the initial and a diluted colloid solution (silver concentration of 1 mM) was shown to even further stabilize the nanoparticles as indicated by the UV–Vis absorption spectra. Specifically, the absorption spectra of all corresponding samples were not significantly different exhibiting surface plasmon absorption band maxima at the wavelength of ~405 nm (Fig. 4.12). Maximal absorbance at this wavelength corresponds to AgNPs with the diameter of about 20 nm based on theoretical predictions of surface plasmon absorption bands for spherical AgNPs suspended in water [23]. Indeed, diameters of electrochemically synthesized AgNPs in alginate solutions were in the range 10–30 nm as determined previously by transmission electron microscopy [20]. Furthermore, the maximum absorbance value slightly increased for about 10 % upon sterilization implying slight further reduction of Ag^+ ions and/or nanoparticle stabilization (Fig. 4.12).

Furthermore, dilution of Ag/alginate colloid solution did not affect AgNPs as confirmed by UV–Vis spectra showing unchanged surface plasmon absorption band maxima at ~405 nm. In addition, a series of diluted colloid solutions was made for which absorbance values determined at the wavelength of 405 nm showed linear dependence on the concentration of silver nanoparticles/ions ($r^2 > 0.99$) indicating preservation of AgNPs (Fig. 4.13).

Effects of Electrostatic Extrusion Parameters

AgNPs were retained during the microbead production process as revealed by UV–Vis spectrometry as described earlier [20] (Fig. 4.14 inset). The value of absorbance maximum positioned at ~405 nm was even higher for nanocomposite microbeads as compared to that of the initial colloid solution implying higher concentration of AgNPs. Absorbance values at the wavelength of 405 nm

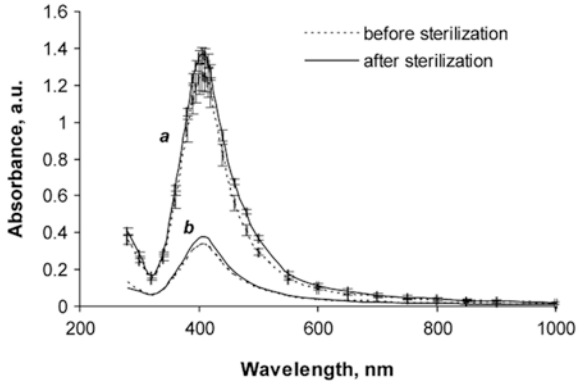

Fig. 4.12 Absorption spectra of (*a*) initial Ag/alginate colloid solution (3.9 mM silver concentration) and (*b*) 3.9-fold diluted Ag/alginate colloid solution (1 mM silver concentration) before and after sterilization by boiling for 30 min (data represent average of $n=3$; standard deviations (<10 %) are omitted in the graph for data (*b*) in order for spectra to be distinguishable) (reprinted from [52] with permission from Serbian Chemical Society)

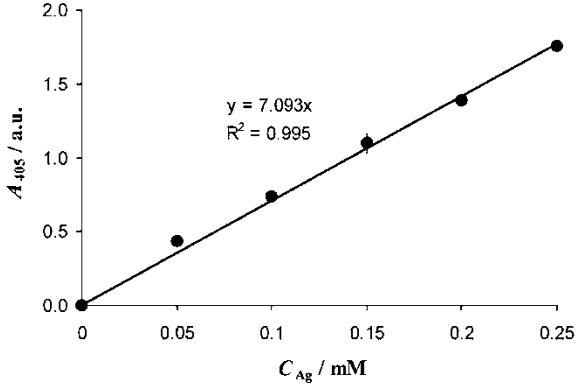

Fig. 4.13 UV–Vis spectrometry analysis of Ag/alginate colloid solutions diluted with 1.9 % w/v Na/alginate: absorbance at the wavelength of 405 nm, A_{405}, as a function of concentration of silver nanoparticles/ions in diluted solutions, C_{Ag} (data represent average of $n \geq 3$) (reprinted from [52] with permission from Serbian Chemical Society)

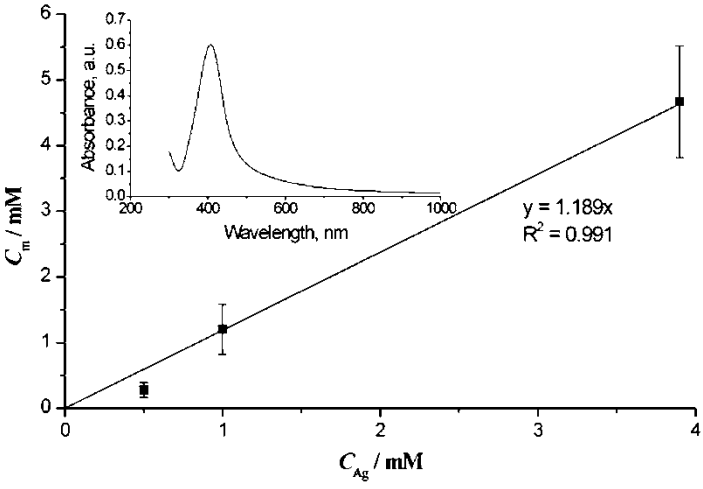

Fig. 4.14 Concentration of silver nanoparticles/ions in microbeads, C_m, as a function of the concentration in corresponding source Ag/alginate colloid solutions, C_{Ag}; *insert*: absorption spectrum of dissolved Ag/alginate microbeads showing absorbance maximum at the wavelength of ~405 nm (data represent average of $n \geq 3$) (reprinted from [52] with permission from Serbian Chemical Society)

determined for Ag/alginate colloid solution extruded at different electrostatic potentials up to 7.5 kV remained constant (1.0 ± 0.1). Moreover, addition of sodium citrate to Ag/alginate colloid solution was shown to induce negligible effects on absorbance measured at 405 nm (~2 %). However, measurements of the concentration of silver nanoparticles/ions in microbeads by AAS confirmed higher concentrations in microbeads as compared to the corresponding source Ag/alginate solutions (Fig. 4.14). It can be seen that concentration of silver nanoparticles/ions in Ag/alginate microbeads was in average ~20 % higher than that in the corresponding source colloid solution with the exception of the lowest initial concentration of 0.5 mM where the measured concentration in microbeads was significantly lower (0.3 ± 0.1 mM). These results can be explained by combined effects of mass losses during the extrusion, which were measured in this study to be up to 35 % as well as of contraction of the alginate gel during gelation as

reported in literature [53] inducing higher silver concentrations in microbeads as compared to the source colloid solutions.

In overall, these results convincingly demonstrate that practically all initial Ag^+ ions were reduced during the electrochemical synthesis of AgNPs, which were further retained during the electrostatic extrusion.

Investigation of the effects of electrostatic extrusion parameters on the size of the obtained Ag/alginate microbeads has shown strong effects of the electrostatic potential (Fig. 4.15). Model predictions [52] were in qualitative agreements with the experimental data predicting to some extent sharper decrease in microbead diameter in the region of the critical electrostatic potential (approximately in the range 4–5 kV). In the region of applied potentials lower than the critical value, the liquid surface tension decreases due to repulsion of charged molecules at the droplet surface causing the decrease in the droplet diameter as well.

It should be added that under the same electrostatic extrusion conditions used for production of microbeads for biomechanical characterization, the presence of AgNPs in Ag-alginate colloid solutions in the concentration range up to 3.9 mM did not influence the microbead diameter as compared to the control 1.9 % w/v Na/alginate solution amounting to ~600 μm (600 ± 40 μm).

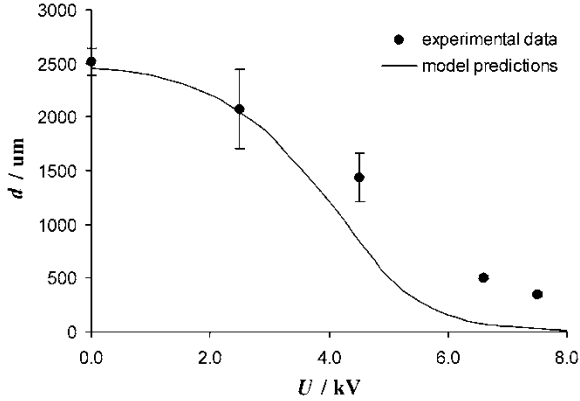

Fig. 4.15 Diameter of Ag/alginate microbeads as a function of the applied electrostatic potential: experimental data and model predictions (reprinted from [52] with permission from Serbian Chemical Society)

Biomechanical Characterization of Ag/Alginate Microbeads Under Bioreactor Conditions

Biomechanical properties of packed beds of nanocomposite microbeads with different concentrations of incorporated AgNPs (1, 1.5, and 3.9 mM concentrations in the source colloid solutions) were examined in a biomimetic bioreactor while packed bed of 1.9 % w/v Ca/alginate microbeads served as a control [52]. The experiments were performed under dynamic compression at 10 % strain in two regimes: at a loading rate of 337.5 μm s^{-1} and at sequential increments of 50 μm displacement every 30 min. All microbeads exhibited similar approximately linear responses to the dynamic loading although the values determined for the control microbeads were slightly lower than those of Ag/alginate microbeads (Fig. 4.16a). Values of compression moduli determined from the slopes of the best stress–strain linear fits were 141 ± 2 and 154 ± 4 kPa, for packed beds of the control and Ag/alginate microbeads, respectively. On the other hand, equilibrium stresses determined at sequential strains after 30 min pauses were significantly different for the control and Ag/alginate microbeads (Fig. 4.16b) yielding equilibrium unconfined compression moduli of 47 ± 0.5 and 34 ± 2 kPa, respectively.

Values of compression moduli determined for packed beds of control alginate microbeads (1.9 % w/v Ca-alginate) were slightly higher than those determined in our previous study for packed beds of 2 % w/v Ca-alginate microbeads (compression modulus of 141 ± 2 vs. 111 ± 8 kPa, respectively, and equilibrium unconfined compression modulus of 47 ± 0.5 vs. 32 ± 0.4 kPa, respectively) [47]. This result can be attributed to significantly smaller microbeads used in this study (600 ± 30 μm) as compared to those used in the previous study (780 ± 30 μm) consistent with the influence of the entrapped water within the packed bed, as reported previously [47]. It can be assumed that the packed bed of smaller microbeads retains water more efficiently in the smaller interstitial channels, which contributes to mechanical properties of the bed.

Slight effects of AgNP presence on mechanical properties of alginate microbeads are consistent with weak interactions of the nanoparticles with polymer chains, so that phase transition,

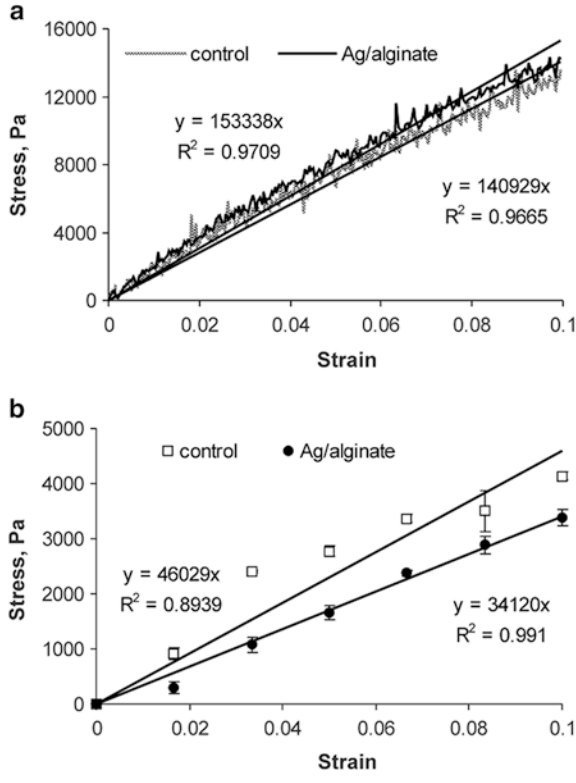

Fig. 4.16 Stress–strain relationships for packed beds of Ag/alginate and control alginate microbeads: (**a**) at a loading rate of 337.5 μm s^{-1}; (**b**) at sequential increments of 50 μm (data represent average of $n = 3$) (reprinted from [52] with permission from Serbian Chemical Society)

thermosensitivity, and viscoelasticity of the polymer gel were reported to remain unchanged [54]. Presence of AgNPs in alginate microbeads apparently induced a slight increase in dynamic compression modulus while the decrease in the equilibrium unconfined compression modulus (Fig. 4.16a). These results imply that under dynamic conditions AgNPs induced higher retention of water within the hydrogel matrix while when the hydrogels were provided with time to relax, negative effects of AgNPs on the hydrogel strength were revealed. In addition, although the influence of the

nanoparticle presence could be distinguished with respect to the control alginate hydrogel, the effects of AgNP concentration in the investigated range (1.5–3.9 mM) could not be perceived. These results are in agreement with reported effects of AgNPs at low concentrations (<1 wt%) incorporated within poly(vinyl alcohol) (PVA) hydrogels [55]. Specifically, addition of AgNPs was shown to induce an abrupt increase in the hydrogel elastic modulus, which then remained constant as the AgNP concentration was increased up to 0.8 wt%. On the contrary, during the stress relaxation, Ag/PVA nanocomposites exhibited reduced stability as compared to pure PVA hydrogels. These results were explained by interactions of nanoparticles with polymer chains inducing immobilization of interfacial regions and enhanced stiffness during loading. However, loading also induced debonding of nanoparticles, which allowed easier structural rearrangements of polymer chains during the stress relaxation [55] consistent with the lower equilibrium unconfined compression modulus determined in the present study for nanocomposite microbeads as compared to that of the controls.

4.2.2.3 Alginate-Based Nanocomposite Hydrogels with Incorporated Silver Nanoparticles

Alginate, poly(vinyl alcohol) (PVA), and poly(*N*-vinyl-2-pyrrolidone) (PVP) are among mostly studied polymers for biomedical applications in general, including also immobilization of AgNPs [4, 6]. All three polymers form biocompatible hydrogels, which differ in mechanical strength.

PVA and PVP are synthetic polymers that can form hydrogels by physical cross-linking such as ionizing radiation and, in the case of PVA, various other methods including repeated freezing and thawing cycles [56]. PVA/PVP blends are especially attractive for potential replacements of articular cartilage [57] and nucleus pulposus [58] due to improved mechanical and lubricative properties as compared to either hydrogel alone [59]. Implantation of hydrogels offers advantages of immediate and controlled biomechanical function of the implant [57–59], while incorporation of AgNPs could provide prolonged sterility at the implantation site. AgNPs were

produced in PVA by different methods including solvent evaporation, electron radiation, UV light, thermal annealing, in situ chemical reduction, and sonochemical method [4]. Similarly, AgNPs were produced in PVP using UV light, chemical and electrochemical reduction, microwave and γ-irradiation, and ultrasound. In addition, PVA/PVP hydrogels with incorporated AgNPs for potential antimicrobial wound dressings were produced by mixing of AgNPs suspension with a PVA/PVP aqueous solution and submitting the mixture to freezing–thawing cycles [32, 60–66].

A general mechanism of AgNP formation and growth was proposed recently and consists of consecutive steps of classical nucleation and growth, aggregative nucleation and growth, and Ostwald ripening [67]. The aggregative regime was described by Kolmogorov–Johnson–Mehl–Avrami (KJMA) model and was reported to dominate the nanoparticle growth. Thus, the growth kinetics was modeled by a modified KJMA expression so to include the onset of Ostwald ripening:

$$\frac{\bar{V}(t)}{\bar{V}_{\lim}} = 1 - \exp\left(-\left(k_g t\right)^n\right) + \left[\frac{t - \tau_O}{1 + \exp\left(-2w\left(t - \tau_O\right)\right)}\right] k_O \qquad (4.1)$$

where $\bar{V}(t)$ is the mean nanoparticle volume and $\bar{V}_{\lim}$ the limiting mean volume at the end of the active-growth period, k_g is the aggregation rate parameter, and n is the Avrami exponent. The onset of Ostwald ripening at the time τ_O is included in the model by the rate constant k_O multiplied by a logistic turn-on function with the arbitrarily chosen time width w. The model predictions qualitatively and quantitatively agreed well with the experimental data and the aggregative growth was considered as a potential contributing mechanism in all nanoparticle-forming reactions [67].

The possibilities for production of blends with PVA and PVP with incorporated AgNPs have been investigated [68]. Two particular hydrogel forms were of interest: microbeads ($\leq$1 mm in diameter) and discs (~1 cm in diameter). Microbeads are attractive as efficient donors of AgNPs and/or ions due to large specific surface area while macroscopic discs are attractive for potential applications as biomedical, antimicrobial implants. The utility of nanocomposite

beads for active AgNPs delivery was demonstrated on Ag/alginate/PVA by UV–Vis spectroscopy and in antimicrobial tests in *Escherichia coli* suspensions. On the other hand, possibilities for tuning compositions and mechanical properties of nanocomposite hydrogels as potential implants were studied by evaluation of mechanical properties of Ag/alginate/PVA and Ag/alginate/PVA/PVP discs in a biomimetic bioreactor providing dynamic compression in physiological regimes relevant for articular cartilage.

The obtained Ag/alginate colloid solutions exhibited surface plasmon absorption band peaking at the wavelength of ~405 nm with the peak intensity increasing over approximately 3 days after the electrochemical synthesis (Fig. 4.17a). After this initial period, the Ag/alginate colloid solution stabilized with the maximum absorbance intensity staying at the wavelength of ~405 nm and amounting to 1.112 ± 0.193 as determined in multiple colloid solutions produced at different times. The absorbance spectra were stable for 30–40 days with the maximum intensity varying less than 4 %. However, with further increase in the aging time, the absorption intensity decreased while the absorption spectra broadened (Fig. 4.17b) and the solution color turned from dark brown to pale yellow. UV–Vis spectroscopy showed the presence of AgNPs, which continued to grow in alginate solution after the end of the electrochemical synthesis. Modeling of the absorbance intensity over time indicated that the growth is governed by coalescence of primary nanocrystals, which is an interface and diffusion-controlled process as deduced from the Avrami exponent <1 [69, 70]. In the same time, small nanoparticles dissolve to provide growth of larger nanoparticles, presenting the much slower Ostwald ripening process. The latter process becomes dominating after the active growth has ceased, i.e., after approximately 3 days after synthesis. This mechanism is in agreement with the general AgNP growth model proposed by Richards et al. [67].

In order to get an insight in the process of Ag/alginate colloid solution stabilization after the electrochemical synthesis, the absorbance intensity at 405 nm over time was modeled [68] according to the procedure proposed by Richards et al. [67]. The nanoparticle diameter was assumed to be proportional to the absorbance intensity. Mean nanoparticle volumes, $\bar{V}(t)$, over time were then calculated based on the spherical particle shape.

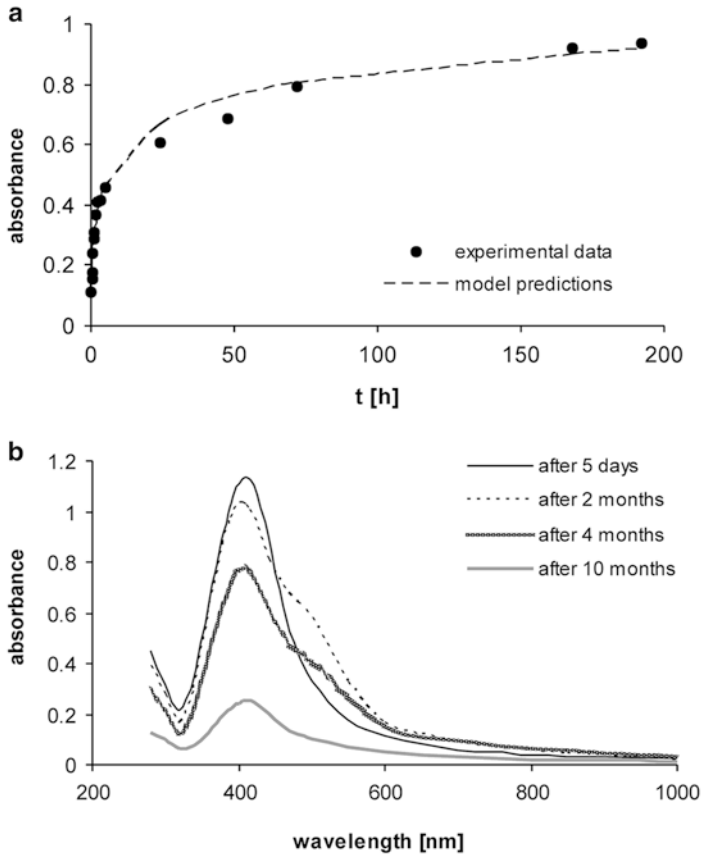

Fig. 4.17 UV–Vis spectroscopy studies of Ag/alginate colloid solutions: (**a**) absorbance intensity at 405 nm over time after electrochemical synthesis of AgNPs: experimental data (*symbols*) and model predictions (*line*); (**b**) absorption spectra after aging for 5 days, 2, 4, and 10 months (data represent average of $n=3$) (reprinted from [68] with permission from Springer)

According to the experimental observations of the absorbance intensity increase (Fig. 4.17a), it was assumed that the active nanoparticle growth lasted for approximately 3 days and the Eq. (4.1) has been applied to the experimental data with parameters $w=2$ min^{-1} and $\tau_0 \sim 60$ min that were proposed by Richards et al.

[67]. Fitted parameters, thus, were the aggregation rate constant, k_g; the Ostwald ripening rate constant, k_O; and the Avrami exponent n. Good agreement with experimental data was obtained for model predictions with parameters $k_g = 0.037\ h^{-1}$, $k_O = 2.7 \times 10^{-3}\ h^{-1}$, and $n = 0.68$ (Fig. 4.17a). It should be noted that prolonging the onset time for Ostwald ripening till after the active growth has ceased ($\tau_O = 72$ h) resulted in poor model predictions.

Stability studies of Ag/alginate solutions have indicated that the colloid solutions are certainly stable in the time frame from day 3 to 30 and these solutions were used in all further investigations. Ag/alginate colloid solutions were easily miscible with PVA and PVP solutions forming uniform mixtures with incorporated AgNPs.

Ag/Hydrogel Microbeads

Uniform, spherical alginate microbeads (720 ± 24 μm in diameter) with incorporated AgNPs were successfully produced using electrostatic extrusion of Ag/alginate colloid solution (Fig. 4.18a). However, under commonly employed extrusion parameters (7 kV applied potential, 2.5 cm electrode distance), Ag/alginate/PVA colloid solution formed elongated microbeads (935 ± 56 μm) with noticeable tails regardless of the increase in $Ca(NO_3)_2 \cdot 2H_2O$ concentration to 3% w/v (Fig. 4.18b). In order to obtain spherical microbeads, electrode distance was increased to 8 cm. At the applied electrostatic potential of 7 kV, uniform beads (1266 ± 141 μm) were obtained (Fig. 4.18c) while the increase to 8 kV produced bimodal microbead size distribution with mean microbead diameters of 521 ± 7 and 173 ± 6 μm (Fig 4.18d). Further increase in electrode distance resulted in formation of large non-uniform beads since electrostatic field was too low to induce a decrease in the droplet size. Thus, the Ag/alginate/PVA beads produced at the electrode distance of 8 cm and at 7 kV were further submitted to freezing–thawing cycles and used in further studies.

Presence of AgNPs in Ag/alginate/PVA solution and beads was confirmed by UV–Vis spectroscopy upon dissolution of the beads in Na-citrate showing the maximum absorbance in the wavelength range of 400–410 nm (Fig. 4.19).

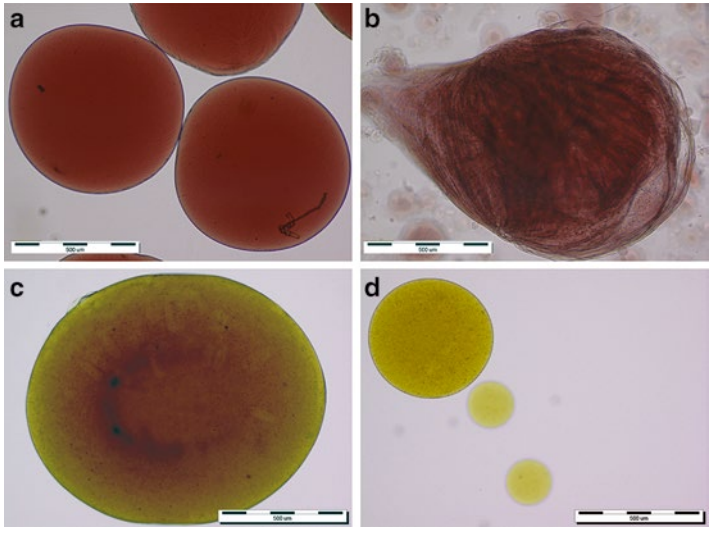

Fig. 4.18 Ag/hydrogel microbeads: (**a**) Ag/alginate; (**b–d**) Ag/alginate/PVA after electrostatic extrusion at: (**b**) 2.5 cm electrode distance, 7 kV, (**c**) 8 cm electrode distance, 7 kV, (**d**) 8 cm electrode distance, 8 kV (reprint from [68] with permission from Springer)

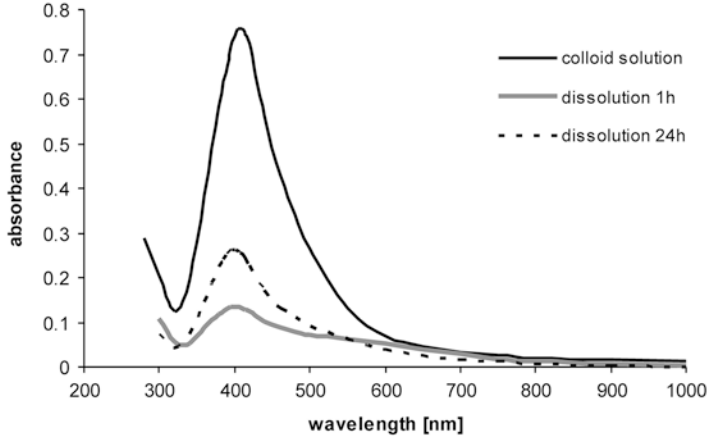

Fig. 4.19 UV–Vis absorption spectra of Ag/alginate/PVA colloid solution and beads upon dissolution for 1 h and for additional 24 h in fresh Na-citrate solutions (reprint from [68] with permission from Springer)

Table 4.2 Colonies count of *E. coli* ATCC-25922 in control suspension and in suspension with 0.4 g mL^{-1} Ag/alginate/PVA beads with the maximum possible concentration of AgNPs and Ag^+ released of 1 mM

	Initial	1 h	24 h
Control (CFU mL^{-1})	1.2×10^6	2.96×10^6	6.2×10^8
Ag/alginate/PVA (CFU mL^{-1})	$(1.45 \pm 0.18) \times 10^6$	$(3.61 \pm 2.13) \times 10^4$	$(1.58 \pm 0.67) \times 10^3$

Reprinted from [68] with permission from Springer

Ag/alginate/PVA beads were used in antibacterial tests against *E. coli* so that maximal concentration of released Ag nanoparticles and ions in the bacterial suspension could be 1 mM. The beads have shown strong antimicrobial activity inducing a decrease in the cell concentration after 1 h of incubation to less than 3 % of the initial value while after 24 h of incubation the average cell concentration dropped to ~1600 CFU mL^{-1} (Table 4.2).

Ag/Hydrogel Discs

Mixtures of Ag/alginate colloid solution and PVA as well as PVA/PVP solutions upon freezing and thawing cycles and alginate gelation formed flat hydrogel discs [68]. In order to evaluate possibilities for modification and control of biomechanical properties of potential nanocomposite implants, the obtained discs were tested in the biomimetic bioreactor, using the procedure that was described previously [47]. Compression was performed in two regimes: (1) at a loading rate of 337.5 μm s^{-1} and (2) at sequential increments of 50 μm displacement every 30 min.

In all cases, stress was a linear function of the applied strain as it can be observed in Figs. 4.20 and 4.21. Compression moduli determined from the slopes of stress–strain functions obtained at the loading rate of 337.5 m s^{-1} increased with the composition complexity starting from 64.9 kPa determined for pure PVA discs, 79.4 kPa for Ag/alginate/PVA discs, and reaching 115.2 kPa for Ag/alginate/PVA/PVP discs (Fig. 4.20). However, equilibrium stresses determined at sequential strains after 30 min pauses were

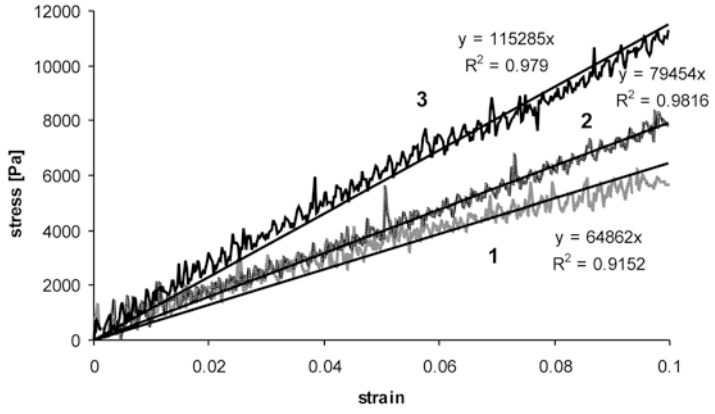

Fig. 4.20 Stress–strain relationships at a loading rate of 337.5 μm s^{-1} and best linear fits for discs of: PVA (*line 1*), Ag/alginate/PVA (*line 2*), and Ag/alginate/PVA/PVP (*line 3*); (data represent average of $n=3$) (reprinted from [68] with permission from Springer)

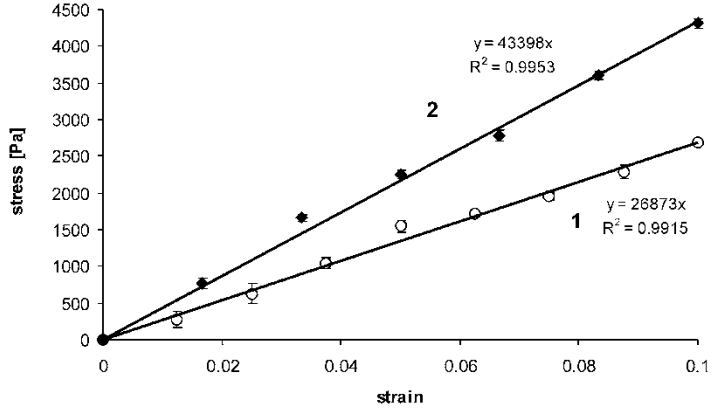

Fig. 4.21 Stress–strain relationships at sequential increments of 50 μm displacement every 30 min and best linear fits for discs of: PVA and Ag/alginate/PVA (data 1) and Ag/alginate/PVA/PVP (data 2); (data represent average of $n=3$) (reprinted from [68] with permission from Springer)

not statistically different for the pure PVA and Ag/alginate/PVA discs (Fig. 4.21). Therefore, a common equilibrium unconfined compression modulus value of 26.9 kPa was determined for both disc types. Yet, the equilibrium unconfined compression modulus for Ag/alginate/PVA/PVP discs was significantly higher (43.4 kPa) consistently with the higher compression modulus determined under dynamic compression.

Results of all biomechanical tests are summarized in Table 4.3.

Experimentally determined compression moduli were in the range of those reported in literature for PVA/PVP hydrogels obtained by freezing and thawing that varied from ~10 to ~230 kPa depending on the hydrogel composition, number of freezing–thawing cycles, applied strain, and compression rate [57, 58, 71, 72]. In addition, results obtained in the present study show influence of addition of Ag/alginate into PVA to form nanocomposite hydrogel with slightly modified mechanical properties. In specific, the nanocomposite hydrogel demonstrated ~20 % higher dynamic modulus as compared to the control PVA hydrogel while the equilibrium unconfined compression moduli were essentially the same for both hydrogels. It could be assumed that alginate and AgNPs interfere with PVA polymer network hampering the response to dynamic compression but when provided sufficient time for network relaxation, mechanical strengths of nanocomposite and pure PVA hydrogels insignificantly differed.

Table 4.3 Summary of biomechanical properties of Ag/hydrogel discs determined in the bioreactor with dynamic compression

Disc composition	Compression modulus, kPa	Equilibrium unconfined compression (Young's) modulus, kPa
5.6 % w/v PVA	64.9 ± 2.4	26.9 ± 0.7
5.6 % w/v PVA, 1.3 % w/v Ag/alginate	79.4 ± 1.4	
11 % w/v PVA, 5 % w/v PVP, 0.4 % w/v Ag/alginate	115.2 ± 4.4	43.4 ± 0.7

Reprinted from [68] with permission from Springer

4.2.2.4 A Comprehensive Approach to In Vitro Functional Evaluation of Ag/Alginate Nanocomposite Hydrogels

It has been previously shown that nanocomposite Ag/alginate microbeads could be easily produced by electrostatic extrusion of alginate colloid solutions containing electrochemically synthesized AgNPs [20, 68]. The microbead form is advantageous for controlled release of immobilized active substances due to the large surface-to-volume ratio [73]. In tissue engineering applications, particulate cell supports provide short diffusion distances enabling uniform cell distribution and tissue regeneration with structures allowing for development of vasculature between individual particles as well as possibilities for minimally invasive implantation by injection [74].

Recently, it was developed a comprehensive approach to investigate potentials for utilization of alginate microbeads with incorporated AgNPs in biomedical applications focusing on wound treatment and soft tissue implants [75]. The focus was on Ag/alginate microbeads as a suitable form for efficient release of silver nanoparticles and/or ions as well as for drying possibilities so to potentially produce antimicrobial powders. Next, an effort has made to couple studies of antibacterial activity and investigations of cytotoxicity of the obtained wet and dried Ag/alginate microbeads. In addition, cytotoxicity studies were performed in parallel in conventional monolayer cultures and in 3D bioreactor cultures of bovine calf chondrocytes in order to mimic the physiological environment upon biomaterial implantation.

Rehydration of Dry Ag/Alginate Microbeads

It is important to investigate possibilities for drying and reswelling of the Ag/alginate microbeads, since they are attractive for potential biomedical applications as antibacterial powders for wound treatments [75]. Briefly, in the first experimental series, Ag/alginate microbeads (760 ± 30 μm in diameter) with the AgNP concentration of 4.87 ± 0.05 mM were dried at room temperature until the constant

weight yielding approximately 5 % of the initial wet weight. Dried microbeads retained a relatively spherical shape (240 ± 30 μm in diameter) and preserved a greater part of AgNPs as verified by FE-SEM analysis (Fig. 4.22). FE-SEM micrographs have shown microbead interiors where individual spherical AgNPs could be distinguished approximately 10–30 nm in diameter as previously determined by transmission electron microscopy of Ag/alginate colloid solutions [20]. In addition, cross-sections of wet and dried Ag/alginate microbeads appeared similar showing only occasional aggregation of AgNPs in the latter case. Comparison of UV–Vis spectra of the initial wet and then dried microbeads with different AgNP concentrations, upon dissolution in Na-citrate, has shown an unchanged absorbance peak position at approximately 405 nm yielding a difference in the absorbance value of approximately 15–20 % with respect to the initial microbeads (Fig. 4.23). These losses could be attributed to nanoparticle aggregation during hydrogel network contraction over drying being slightly more pronounced at higher AgNP concentrations (Fig. 4.23). Thus, it could be assumed that dried microbeads retained ~80–85 % of AgNPs initially present before drying.

Possibilities for alginate gel rehydration and release of AgNPs from dried Ag/alginate microbeads were investigated in the physiological saline solution at room temperature in order to mimic contact with wound secretions. Rehydration of dried microbeads over 5 days is presented in Fig. 4.24. After 24 h in the saline

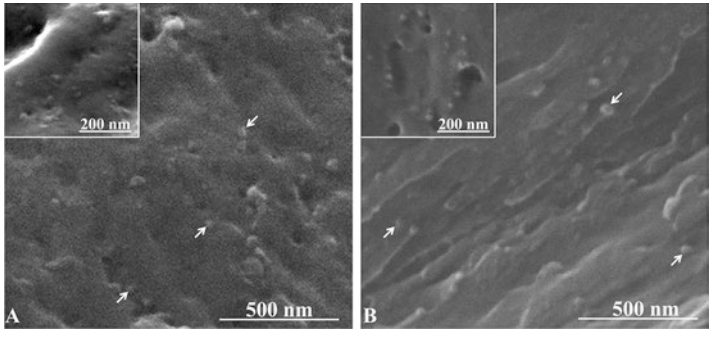

Fig. 4.22 FE-SEM micrographs of cross-sections of a wet (**a**) and dried (**b**) Ag/alginate microbead; *white arrows* designate individual silver nanoparticles (reprinted from [75] with permission from Elsevier)

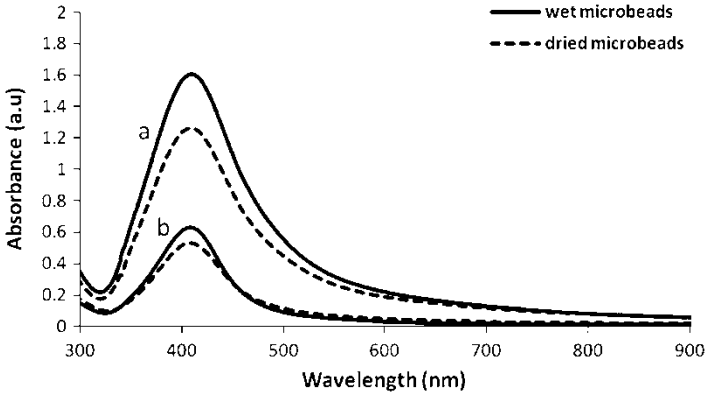

Fig. 4.23 Typical UV–Vis absorption spectra of wet and dried Ag/alginate microbeads based on the same sample wet weight with different silver concentrations in the initial wet microbeads: (**a**) 4.2±0.4 mM, (**b**) 1.2±0.05 mM (data represent average of $n \geq 2$; standard deviations ($\leq 10\,\%$) are omitted from the graph in order for the spectra to be distinguishable) (reprinted from [75] with permission from Elsevier)

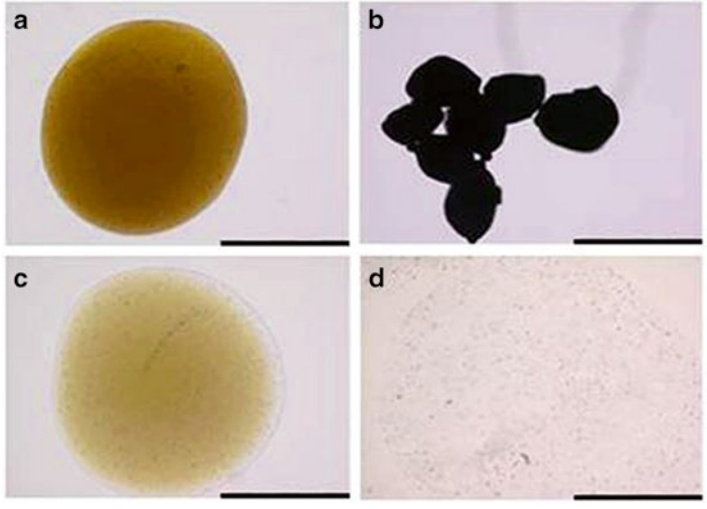

Fig. 4.24 Rehydration of dried Ag/alginate microbeads: (**a**) a representative wet microbead, (**b**) dried microbeads, (**c**) a representative dried microbead rehydrated for 24 h in the saline solution, (**d**) a representative dried microbead rehydrated for 5 days in the saline solution (scale bar: 500 μm) (reprinted from [75] with permission from Elsevier)

solution, both initially wet as well as dried microbeads increased in size reaching similar average diameters (1000 ± 40 and 1020 ± 40 μm, respectively) while in both cases approximately 95 % of the initially present AgNPs were lost as determined by the absorbance intensity at 405 nm. Furthermore, after 5 days in the saline solution all microbeads appeared fractured and devoid of AgNPs, as expected, due to diffusion of AgNPs/ions and Cl^- ions and formation of AgCl [75].

The obtained results indicate potentials for use of dry Ag/alginate microbeads, which successfully retained AgNPs while demonstrating similar swelling behavior in the physiological saline solution as wet microbeads.

Cytotoxicity Studies

In order to evaluate in vitro cytotoxicity of Ag/alginate microbeads, two types of experimental studies were carried out: monolayer cultures of bovine calf chondrocytes and 3D cultures of the same cell type immobilized in alginate microbeads in perfusion bioreactors [75].

Full thickness articular cartilage was harvested aseptically from the femoropatellar grooves of either 6- or 12-month-old bovine calves within 8 h of slaughter. Primary chondrocytes obtained from the cartilage of 6-month-old calves were used for cytotoxicity studies in monolayer cultures. Primary chondrocytes isolated from the cartilage of 12-month-old calves were directly immobilized in alginate microbeads and used for 3D cell cultures in perfusion bioreactors.

Cytotoxicity Studies in Monolayer Cell Cultures

Cytotoxicity of Ag/alginate microbeads with different concentrations of AgNPs was determined first in monolayer chondrocyte cultures using the standard MTT test [76]. Cultures with pure Ca/alginate microbeads without AgNPs were also established in order to verify alginate biocompatibility, while monolayer cultures alone served as a control.

Cell survival is defined as the ratio of the number of cells grown in the presence of the investigated agent and the number of cells in the control. Since the number of live cells is directly proportional to the absorbance, the cell survival, S, can be calculated as:

$$S(\%) = A_u / A_c \cdot 100 \tag{4.2}$$

where A_u is the absorbance of cells grown in the presence of alginate or Ag/alginate microbeads and A_c is the absorbance of control cells. Cytotoxicity was rated as following: noncytotoxic (>90 % cell survival), slightly cytotoxic (60–90 % cell survival), moderately cytotoxic (30–59 % cell survival), and severely cytotoxic (≤30 % cell survival) [77].

The cell viability was determined after 48 h and the effects of AgNP concentrations on the cell survival, S, in the presence of alginate and Ag/alginate microbeads is presented in Fig. 4.25. It could be seen that presence of alginate and Ag/alginate microbeads with released silver concentrations of up to 5 μg mL^{-1} induced negligible effects on bovine calf chondrocyte survival (S>90 %). However, when released silver concentration was

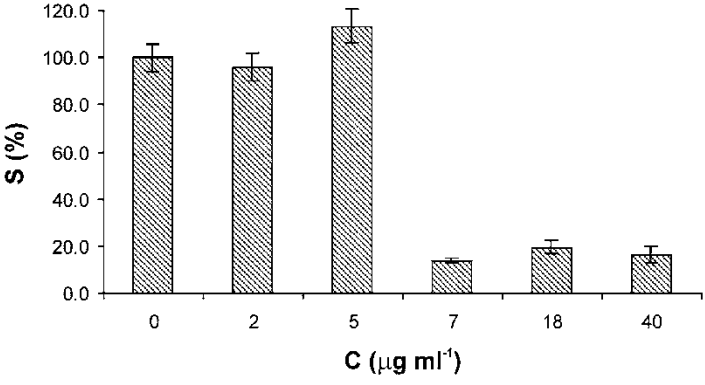

Fig. 4.25 Survival, S, of bovine calf chondrocytes cultured in the presence of alginate or Ag/alginate microbeads with different AgNP concentrations normalized to the control sample as a function of total released silver concentrations in the medium, C (reprinted from [75] with permission from Elsevier)

increased to about 7 μg mL^{-1} it induced severe cytotoxicity ($S = 13.9 \pm 0.8\,\%$).

The obtained results are in agreement with other studies of the effects of different systems containing AgNPs on various mammalian cell types, where cytotoxic concentrations of AgNPs were reported to range from 1.6 to 50 μg mL^{-1} [78, 79].

Overall, results of Ag/alginate microbead cytotoxicity studies in monolayer cell cultures have shown that Ag/alginate microbeads released approximately 40–50 % of the initial AgNP amount and that the released silver concentrations in the culture medium up to 5 μg mL^{-1} were not cytotoxic for chondrocytes [75].

Cytotoxicity Studies in 3D Cell Cultures in Perfusion Bioreactors

In order to examine cytotoxicity of Ag/alginate microbeads under conditions that imitate the physiological environment upon potential implantation in vivo, the 3D cultures of bovine calf chondrocytes immobilized in alginate microbeads were established in perfusion bioreactors [75] Alginate microbeads with immobilized chondrocytes were produced by electrostatic droplet generation using 6.3 kV electrostatic potential, 3 cm electrode distance, and 1.5 % w/v $CaCl_2$ gelling solution [52].

In order to investigate possible cytotoxic effects of the Ag/alginate microbeads under conditions imitating physiological environment in vascularized tissues in vivo, a 3D cell culture was established in perfusion bioreactors. Cell-loaded microbeads were mixed with Ag/alginate microbeads in the approximate ratio 3:1 and cultivated in perfusion bioreactors under continuous medium flow of 0.38 mL min^{-1}. The applied flowrate corresponded to the superficial medium velocity of ~100 μm s^{-1}, which is in the range of blood velocities in capillaries. After 2 weeks of bioreactor cultivation, microbeads slightly deformed, while the concentration of immobilized cells slightly but not significantly decreased with the viability preserved at 78 % implying slight cytotoxic effects. In order to determine the maximal concentration of the released AgNPs and/or ions in the medium to which the cells were exposed, corresponding to the first medium exchange (i.e., 72 h), a parallel experiment was performed using Ag/alginate microbeads

(5.5 ± 0.4 mM AgNPs concentration), pure alginate microbeads instead of cell loaded microbeads, and saline solution instead of the cultivation medium. The concentration of free Ag^+ ions in the saline solution was 0.9 ± 0.3 μg mL^{-1} not significantly different from measured Ag^+ concentrations in the monolayer studies due to low solubility of AgCl. Thus, the total amount of released AgNPs and/or ions from Ag/alginate microbeads was determined based on measured silver concentrations in initial microbeads and after the experiment (5.5 ± 0.4 mM and 102 ± 16 μM, respectively). Based on the mass of Ag/alginate microbeads and measured saline solution volumes the total silver concentration in the saline solution can be calculated as 9.3 ± 0.9 μg mL^{-1}. This concentration corresponds to strong cytotoxicity as determined in monolayer cultures (Fig. 4.25). However, under in vivo-like settings in perfusion bioreactors and 3D environment, this concentration had only a negligible effect on cell viability. Consequently, cells in monolayers could be regarded as more sensitive to AgNPs and Ag^+ than cells surrounded by the alginate matrix in a 3D environment. Thus, these results stress the importance of the comprehensive biomaterial assessment including different aspects and settings, and demonstrate the utility of biomimetic bioreactors for functional biomaterial evaluation under in vivo-like conditions.

Antibacterial Activity

Antibacterial activity of wet and dried Ag/alginate microbeads was estimated against *S. aureus* TL and *E. coli* ATCC 25922 [75]. Both microbead types demonstrated the release of AgNPs and/or ions inducing growth delay of both *S. aureus* and *E. coli* (Tables 4.4 and 4.5, respectively). After 1 h of incubation, bacterial concentrations in both microbead groups were lower than the initial concentrations (reduction of about 1 log 10-unit) and slowly increased over the next 23 h reaching the colonies count of the order of 106 CFU mL^{-1}. Still these values were significantly lower than those measured in the control groups (reduction of almost 3 log 10-units). It is interesting to note that both wet and dried microbeads exhibited similar antibacterial activity against both investigated bacterial strains with the exception of the slightly

Table 4.4 Colonies count of *Staphylococcus aureus* TL in the control suspension and suspensions with wet and dried Ag/alginate microbeads at the concentration of 0.4 g mL^{-1} based on the microbead wet weight

	Initial	1 h	24 h
Control (CFU mL^{-1})	3.8×10^5	6.6×10^5	2.7×10^9
Wet microbeads (CFU mL^{-1})	3.8×10^5	$(9.5 \pm 2.1) \times 10^4$	$(6.9 \pm 1.3) \times 10^6$
Dried microbeads (CFU mL^{-1})	$(3.7 \pm 0.3) \times 10^5$	$(9.5 \pm 4.9) \times 10^4$	$(5.3 \pm 2.8) \times 10^6$

Reprinted from [75] with permission from Elsevier

Table 4.5 Colonies count of *Escherichia coli* ATCC 25922 in the control suspension and in suspensions with wet and dried Ag/alginate microbeads at the concentration of 0.4 g mL^{-1} based on the microbead wet weight

	Initial	1 h	24 h
Control (CFU mL^{-1})	2.8×10^6	7.6×10^6	2.3×10^9
Wet microbeads (CFU mL^{-1})	$(1.7 \pm 0.2) \times 10^6$	$(8.3 \pm 0.3) \times 10^4$	$(3.1 \pm 1.5) \times 10^6$
Dried microbeads (CFU mL^{-1})	$(2.2 \pm 0.4) \times 10^6$	$(5.0 \pm 3.7) \times 10^5$	$(4.3 \pm 5.9) \times 10^3$

Reprinted from [75] with permission from Elsevier

stronger effect found in the *E. coli* culture after 24 h incubation with dried Ag/alginate microbeads (Table 4.5).

The obtained results are in agreement with other studies of different systems containing AgNPs against *S. aureus* and *E. coli*, where the minimum inhibitory concentrations of AgNPs were reported to range from 0.34 to 120 μg mL^{-1} for *S. aureus* and 0.26–180 μg mL^{-1} for *E.* coli [39, 42, 80–86], considering that antibacterial activity could be attributed mainly to the release of AgNPs and/or ions. If the results of antibacterial activity of Ag/alginate microbeads are compared to the results of cytotoxicity studies, it can be assumed that the release of silver nanoparticles and/or ions can be tuned so to induce antibacterial activity without causing cytotoxic effects. This assumption is supported by the finding that the total concentration of released silver present as AgNPs, Ag^+, and/or AgCl of about 9–10 μg mL^{-1} could induce bacteriostatic

effects (i.e., growth delay) without affecting viability of cells embedded in a tissue-like matrix in perfusion bioreactors.

Overall, it could be assumed that wet Ag/alginate microbeads could be attractive for tissue engineering applications in combinations with cell scaffolds, constructs, or soft tissue implants providing a sterile environment, either in vitro or in vivo. On the other hand, dried Ag/alginate microbeads could be applied as antibacterial powders in wound treatments providing moisture capture by rapid alginate matrix reswelling and antibacterial effects due to the release of AgNPs and/or ions.

4.2.2.5 In Vivo Studies

Deep, necrotic, infected, and heavily exuding wounds (e.g., burns, ulcers) present a serious clinical problem since conventional wound treatment methods do not promote healing. Dressings based on alginate effectively regulate moisture levels in wounds leading to rapid granulation and reepithelization of the damaged tissue [87, 88]. These dressings are also easily removed and replaced without causing much trauma due to the hydrophilic nature of the hydrogel. Various medical products containing silver were developed, such as antimicrobial wound dressings, ointments, and coatings [89, 90]. Furthermore, silver nanoparticles were reported to be even more potent than silver ions due to attachment and interactions with the bacterial cell membrane, release of silver ions and, possibly, penetration into the cell interior [4].

It was previously shown that AgNPs can be produced within aqueous alginate solutions by electrochemical synthesis while the obtained colloid solutions can be further manipulated to obtain nanocomposite Ag/alginate hydrogels [20, 68]. This method is particularly advantageous for potential use in biomedicine and pharmacy due to the precise control of particle size and high purity of the obtained nanocomposite hydrogels containing only gelling cations, alginate, and AgNPs. Furthermore, nanocomposite hydrogels could be produced in different forms such as films, sheets, microbeads [20, 52], and microfibers [91]. The latter two hydrogel forms were shown to effectively release AgNPs and/or ions owing to the large specific surface area and short internal diffusion dis-

tances, which induced antibacterial effects against *E. coli* and *S. aureus* [20, 68]. Thus, nanocomposite alginate solutions and hydrogels could be very attractive active agents for treatments of deep as well as superficial wounds due to biocompatibility, variety of product forms, and prolonged and controlled release of AgNPs resulting in potentially higher antimicrobial efficiency as compared to products utilizing silver ions.

Ag/Alginate colloid solutions containing 1 mM AgNPs, 1.73 % w/v alginate, and 0.1 g dm^{-3} ascorbic acid were obtained by dilution of the initially synthesized colloid solution as described previously [20] and used in wound treatment studies on rats. Ag/alginate microfibers were produced by extrusion of the colloid solution containing 1.4 mM AgNPs and 1.73 % w/v alginate [91]. Resulting microfibers had a mean diameter of 250 ± 40 μm and exhibited the absorption maximum at ~410 nm [92].

Male Wistar rats were used for studies of effectiveness of nanocomposite Ag/alginate solutions and microfibers for wound treatments in a rat burn model [92]. Thermal burn injuries were standardized as reported in literature [93] in order to obtain deep second-degree burns of the same size. The animals were divided randomly into three groups: control group (G1, $n = 9$), group treated with 1 mM Ag/alginate colloid solution (G2, $n = 9$), and group treated with Ag/alginate microfibers (G3, $n = 9$) [92].

Wound contraction is a parameter used for assessment of wound healing. After 1 day of thermal injuries, wound areas in all three groups were not significantly different and were ~2-fold higher as compared to the initial burns. Then the wounds started to continuously contract in all groups until complete restoration (Fig. 4.26). The wound contraction was consistently faster in treated groups, whereas significant differences as compared to the control were observed 11 days after the thermal injury induction and this trend was maintained until the end of experiment. The scabs fell off between 10 and 12 days after the injury induction in treated groups (G2 and G3) and between 15 and 16 days in the control. It is interesting to note that wound contraction appeared slightly slower in the group treated with microfibers (G3) as compared to the group treated with Ag/alginate solutions (G2) until the scabs fell off (Fig. 4.26). However, thereafter wounds in the group G3 rapidly contracted and completely healed at day 19 as compared to day 21 in the group G2. In the same time, wounds in the control group G1, on day 21 were still visible.

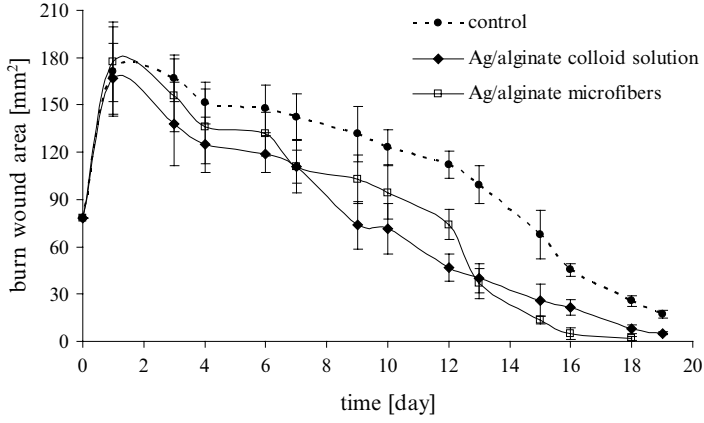

Fig. 4.26 Burn wound area as a function of time for the control group (G1), group treated with Ag/alginate colloid solution (G2), and the group treated with Ag/alginate microfibers (G3) (reprint from [92] with permission from Serbian Wound Healing Society)

In Fig. 4.27a, photographs of wounds in all three groups on day 11 are shown while Fig. 4.27b presents the wounds at the time of animal sacrifice. Macroscopic analysis of the wounds at day 11 has shown thin and dry crusts with detachment of edges in all three groups. In addition, the complete wound healing in treated groups (G2 and G3) was on days 21 and 19, respectively, while in the control group even after 21 days the wounds did not completely heal (Fig. 4.27b).

The obtained results indicated that both Ag/alginate solutions and microfibers significantly enhanced healing of second-degree burns in rats. These macroscopic findings were also supported by the results of histological analyses, which have shown enhanced granulation and reepithelization, reduced inflammation, and improved organization of the extracellular matrix in both treated groups (Fig. 4.28) [94].

It should be pointed out that silver concentrations were 0.011 % w/w for the Ag/alginate colloid solution and 0.016 % w/w for Ag/alginate microfibers, which are more than two orders of magnitude lower than those in commercial silver-containing alginate dressings [11].

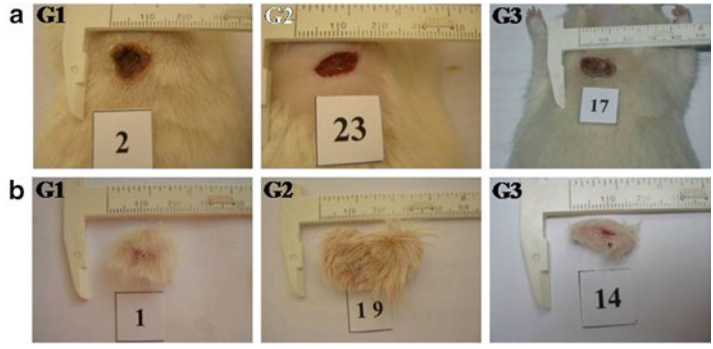

Fig. 4.27 Clinical evaluation of second-degree burn healing in Wistar male rats. (**a**) Thermal lesions 11 days after induction in the control (G1), the group treated with Ag/alginate colloid solution (G2), and the group treated with Ag/alginate microfibers (G3). (**b**) Thermal lesions at the time of sacrifice: 21 days after injury induction in the control (G1) and the group treated with Ag/alginate colloid solution (G2) and 19 days after injury induction in the group treated with Ag/alginate microfibers (G3) (reprinted from [92] with permission from Serbian Wound Healing Society)

4.3 Silver/Poly(*N*-Vinyl-2-Pyrrolidone) Nanocomposites

4.3.1 Electrochemical Synthesis of Silver Nanoparticles Inside PVP Hydrogel

Ag/PVP hydrogel nanocomposites were successfully obtained by electrochemical synthesis of silver nanoparticles inside a PVP hydrogel. The PVP hydrogels obtained by gamma irradiation, subsequently equilibrated in a solution containing 3.9×10^{-3} M $AgNO_3$. The electrochemical synthesis of Ag nanoparticles was performed by imposing a constant voltage, in the range of 15–300 V during different times [95].

The absorption spectra of the Ag/PVP nanocomposites exhibited a surface plasmon band with absorbance maxima at ≈416 nm, confirming the formation of AgNPs (Fig. 4.29). The absorbance intensity, which is related to the concentration of AgNPs, increased with increasing applied voltage and time, up to the values of 200 V

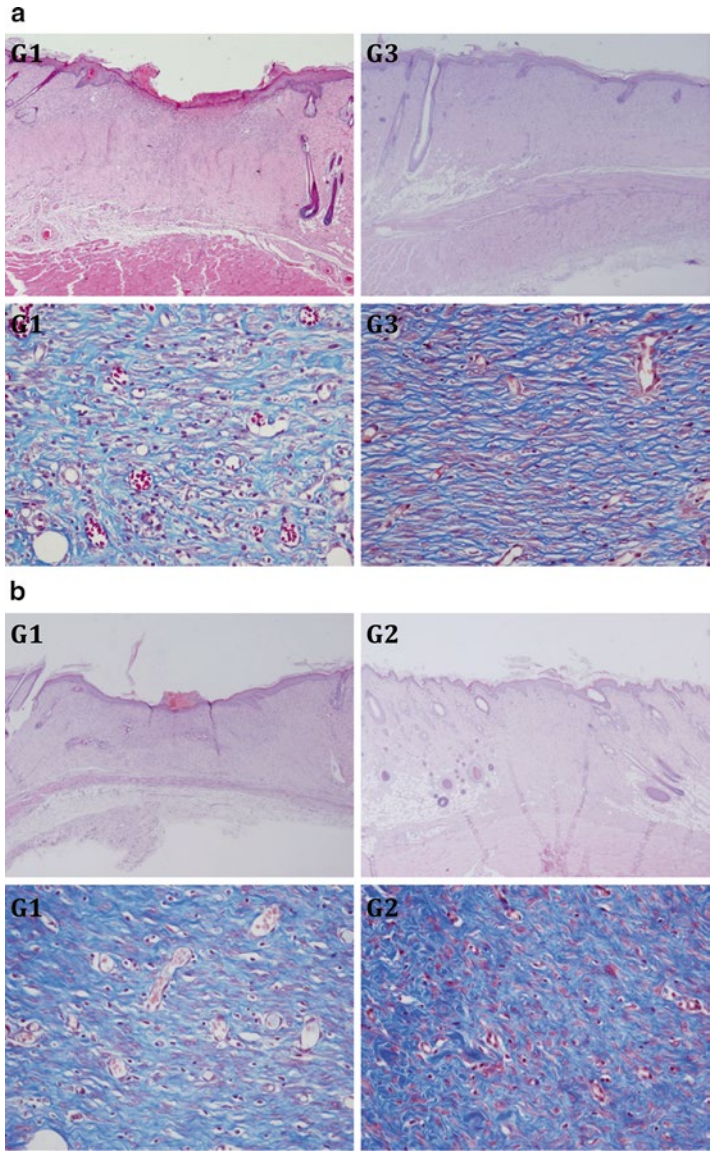

Fig. 4.28 Histological analyses of second-degree burn healing in Wistar male rats (**a**) treated with Ag/alginate microfibers 11 days, (**b**) treated with Ag/alginate colloid solution 21 days, in the control (G1), the group treated with Ag/alginate colloid solution (G2), and the group treated with Ag/alginate microfibers (G3)

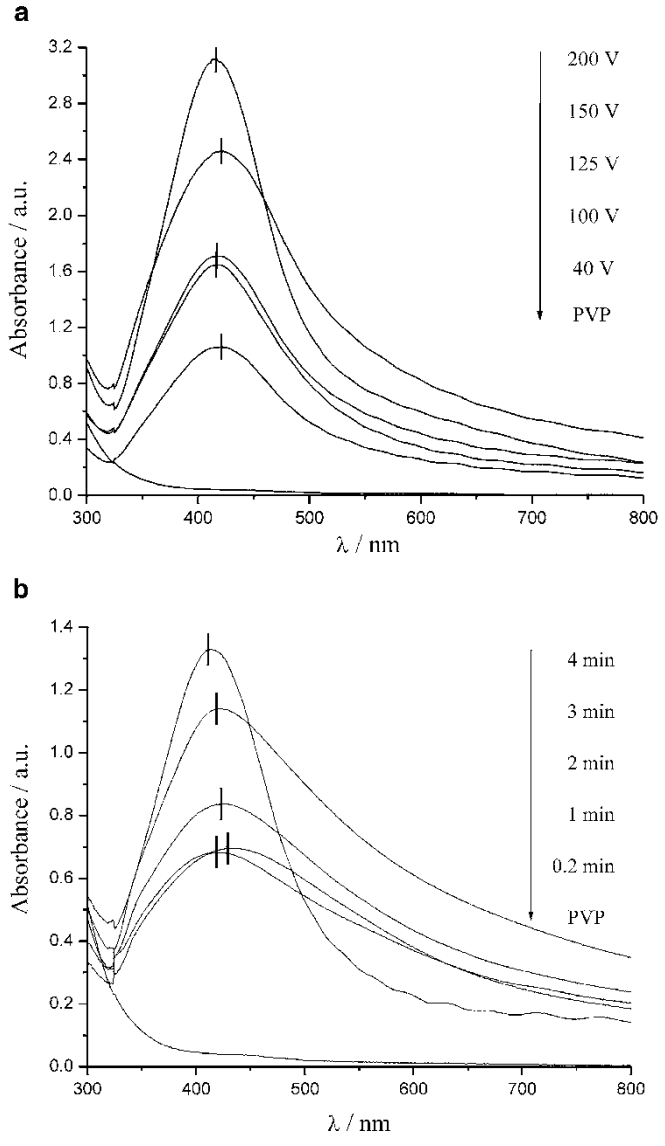

Fig. 4.29 Absorption spectra of the pure PVP and of Ag/PVP nanocomposites hydrogels obtained at (**a**) different values of the applied voltage during 4 min, and (**b**) different values of time at 30 V, 72 h after the synthesis (reprinted from [95] with permission from Wiley)

and 4 min, respectively (Fig. 4.29a, b), while further increases in both applied voltage and time did not follow this trend.

In order to evaluate the optimum conditions for the synthesis of the silver nanoparticles inside the PVP hydrogel network, the values of absorbance maximum wavelength, λ_{max}, and the full width at half-maximum absorbance, β, for the absorption spectra of Ag/PVP hydrogel nanocomposites obtained under different experimental conditions are summarized in Table 4.6.

Bearing in mind that lower values of the wavelength of the absorbance maximum and of the full width at half-maximum (fwhm) absorbance correspond to smaller silver nanoparticles [96, 97], an applied voltage of 200 V and time of 4 min were chosen as the optimal conditions for the synthesis of the AgNPs, and the further investigations were performed on Ag/PVP hydrogel nanocomposites obtained under these conditions. In addition, under these conditions, the highest value of the absorbance, corresponding to the highest concentration of embedded silver nanoparticles, was observed. The higher value of the applied voltage and prolonged times did not result in a higher concentration of silver nanoparticles.

Theoretical predictions of the UV–Vis spectra for monodisperse nanoparticles should follow a Lorentzian plasmon resonance band, while a Gaussian distribution should indicate polydispersity [25]. Here, the absorption spectrum of the Ag/PVP hydrogel nanocomposite was more in agreement with a Lorentzian than with a Gaussian fit (Fig. 4.30), which suggests monodispersity of the silver nanoparticles in the Ag/PVP hydrogel nanocomposite. The

Table 4.6 Absorption spectrum parameters: absorbance maximum wavelength, λ_{max}, and the full width at the half-maximum absorbance, β, for the absorption spectra of Ag/PVP hydrogel nanocomposites obtained under different experimental conditions

t = 4 min		
U (V)	λ_{max} (nm)	β (nm)
40	421	147
100	416	148
125	417	151
150	421	183
200	416	120

Reprinted from [95] with permission from Wiley

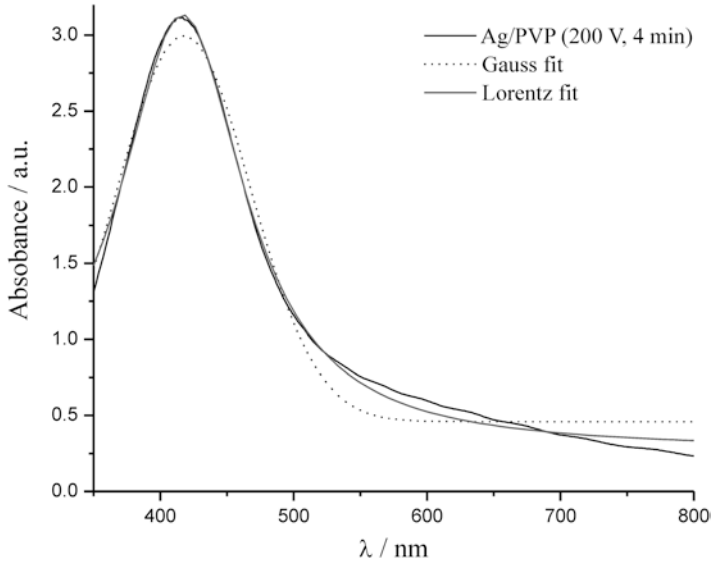

Fig. 4.30 Absorption spectra of Ag/PVP hydrogel nanocomposite ($U = 200$ V, $t = 4$ min), and appropriate Lorentzian and Gaussian fits of the absorption spectra curves (reprinted from [95] with permission from Wiley)

same result was obtained in a previous study in which an Ag/alginate colloid solution was investigated [20].

However, the existence of silver nanoparticles inside the PVP hydrogels was not evident during and immediately after synthesis; the complete yellow coloration of the Ag/PVP hydrogel nanocomposites occurred 24 h after the synthesis. This suggested the synthesis of silver nanoparticles was a gradual process. Namely, the first step of AgNPs synthesis would be the reduction of Ag^+ ions into Ag atoms inside the PVP network, which occurred as a cathodic reaction. The as-formed Ag atoms became seeds or nuclei for the further growth and the formation of AgNPs, which gave the yellow color to Ag/PVP hydrogel nanocomposites. It is reported in the literature that AgNPs formation, presuming nucleation and growth, is the result of classical nucleation and growth, aggregative nucleation and growth, and Ostwald ripening processes, which can occur either in consecutive or parallel regimes [67]. It is generally considered that

the nanoparticles obtained from molecular (atom) precursors grow by classical nucleation and growth, while nanoparticles originated from smaller nanocrystals grow by Ostwald ripening. There are also reports that aggregative growth contributes in both growing processes [67]. A previous study, concerning the synthesis of silver nanoparticles in alginate solutions, confirmed the growth of AgNPs for 3 days after the synthesis by aggregative mechanism and Ostwald ripening. After that period, Ag/alginate colloid solution remained stable for additional 30–40 days [20].

Figure 4.31 represents field-emission SEM microphotographs of pure PVP hydrogel (Fig. 4.31a) and PVP hydrogel incorporated with silver nanoparticles (Fig. 4.31b), and a histogram presenting particle size distribution of AgNPs (Fig. 4.31c).

It can be observed that pure PVP network consists of relatively uniform voids, 449 ± 72 nm in size (Fig. 4.31a). In Fig. 4.31b these voids are not evident. There are lots of clusters of small AgNPs along the cross-section of the Ag/PVP hydrogel nanocomposite. The size of AgNPs is measured to be 75 ± 19 nm, and the average cluster size was 209 ± 33 nm.

Comparing the UV–Vis spectroscopy results with FE-SEM imaging, it is observed that the spectroscopy "sees" the small particles, rather than clusters, suggesting that the absorption peak position of 416 nm corresponds to the 75 nm AgNPs. This is in agreement with the literature data, where the absorption peak positions of 416 and 418 nm correspond to AgNPs of 55 and 60 nm in size, respectively [98, 99].

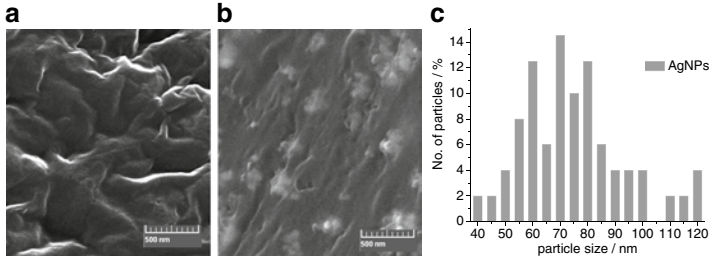

Fig. 4.31 FE-SEM microphotographs of PVP hydrogel (**a**) without and (**b**) with embedded silver nanoparticles, and (**c**) histogram of AgNPs particle size distribution (reprinted from [95] with permission from Wiley)

In order to obtain more information about the reduction of silver ions into AgNPs inside PVP hydrogel network, and to evaluate eventual side effects of the synthesis, Ag/PVP nanocomposites were investigated by cyclic voltammetry. First, the solutions containing 3.9 mM $AgNO_3$, 10 wt% PVP, and 0.1 M KNO_3 (either containing one single component, or all of them) were examined in order to monitor the oxidation/reduction processes occurring in aqueous solutions (Fig. 4.32). The solutions without silver ions exhibited a broad cathodic peak at −250 mV, originating from Pt oxide reduction formed during the anodic sweep (Fig. 4.32, Inset). The anodic counterpart of this peak is not clearly seen; however, a broad current increase in the potential range from 0.0 to 1.0 V is obvious.

The processes of reduction and oxidation on Pt in the silver-containing solutions (Fig. 4.4) were observed as the main cathodic peak at about 160 mV, corresponding to the silver deposition on

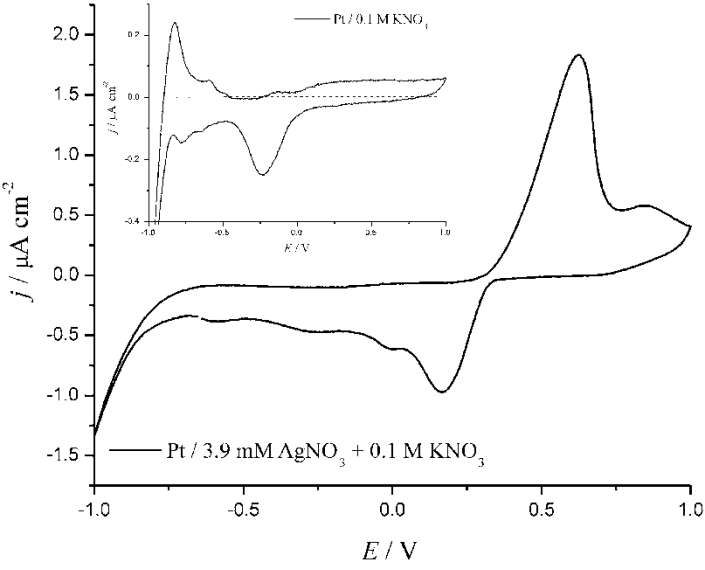

Fig. 4.32 Cyclic voltammogram of Pt electrode in 3.9 mM $AgNO_3$+0.1 M KNO_3. *Inset*: cyclic voltammogram of a Pt electrode in 0.1 M KNO_3 (reprinted from [95] with permission from Wiley)

the platinum electrode, and anodic peak around 600 mV related to the oxidation of silver, with a smaller broad peak at ≈850 mV, which can probably be attributed to the oxidation of Pt on the sites not covered by Ag. This could be confirmed by the small peaks in the cathodic branch after the Ag reduction peak.

Cyclic voltammograms of PVP hydrogel (curve a) and Ag/PVP hydrogel nanocomposite immediately after the synthesis (curve b) and after reswelling in 0.1 M KNO_3 (curve c), obtained at 200 V in 4 min, are shown in the inset of Fig. 4.33a. The monitoring was performed immediately after synthesis and after drying and reswelling in 0.1 M KNO_3 because of the visual observation that the freshly prepared Ag/PVP hydrogel nanocomposite was not colored, while the reswollen one was dark yellow. Actually, the freshly obtained, colorless Ag/PVP hydrogel nanocomposite becomes dark yellow only 24 h after the synthesis (Fig. 4.33b). Higher current intensity seen in curve b, corresponding to the greater mobility of the system components, indicates that the majority of the silver present in

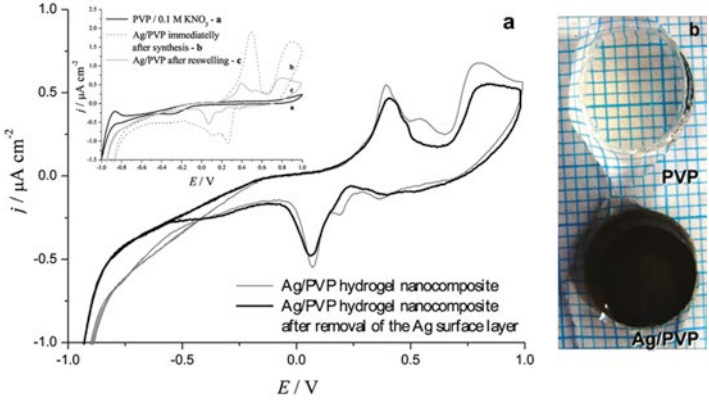

Fig. 4.33 (**a**) Cyclic voltammograms of Ag/PVP hydrogel nanocomposite after reswelling in 0.1 M KNO_3 solution and of the same Ag/PVP hydrogel nanocomposite after removal of the Ag surface layer. *Inset*: Cyclic voltammograms of (a) PVP hydrogel, (b) Ag/PVP hydrogel nanocomposite immediately after synthesis, and (c) Ag/PVP hydrogel nanocomposite after reswelling in 0.1 M KNO_3 solution. (**b**) Photographs of pure PVP hydrogel and Ag/PVP hydrogel nanocomposite after reswelling in 0.1 M KNO_3 solution (reprinted from [95] with permission from Wiley)

newly synthesized Ag/PVP hydrogel nanocomposite was still in the form of Ag atoms, and that the growth processes had not yet started. On the other hand, cyclic voltammograms of the reswollen Ag/PVP hydrogel nanocomposite (curve c) exhibited peaks with significantly lower current intensity, confirming the entrapment of AgNPs inside the PVP network.

The inset of the Fig. 4.33a shows that Ag/PVP hydrogel nanocomposite immediately after the synthesis (curve b) caused an anodic peak at around 490 mV and one (broad and unusually shaped) at 900 mV; both could originate from the oxidation of Ag particles and those trapped in PVP hydrogel. Their counterparts, two cathodic peaks at ≈115 and ≈265 mV, correspondingly suggest the reduction of silver ions, and those inside the PVP network.

In the case of the reswollen Ag/PVP hydrogel nanocomposite (curve c), all currents are considerably smaller, suggesting the entrapment of AgNPs inside the PVP network. There are now three anodic peaks at around 390, 545, and 800 mV that can be related to the different oxidation processes of silver nanoparticles in the Ag/PVP hydrogel nanocomposite. The corresponding cathodic peaks were observed at ≈70, ≈185, and ≈370 mV. Since there is an appearance of the third pair of peaks, it was checked if there was an influence of the side effect of the synthesis, meaning the Ag layer deposited at the surface of the hydrogel. The cyclic voltammetry of this Ag/PVP nanocomposite hydrogel, from which the outer layer is removed by cutting, was also monitored (Fig. 4.33a). This cyclic voltammogram exhibited neither the anodic peak at 545 mV, nor its counterpart at 185 mV. This suggests that those peaks could be attributed to the oxidation/reduction processes of the Ag surface layer deposited during the synthesis. This is also in accordance with the oxidation/reduction processes of silver in the solution (Fig. 4.32), since the appropriate pair of peaks is positioned at 600 and 160 mV, and the slight shifts toward 545 and 185 mV could be explained by the influence of the hydrogel network. Now the other two pairs of peaks could be commented. Similarly to the peaks observed for the Ag/PVP nanocomposite immediately after the synthesis, the pair of peaks 390 mV/70 mV can be attributed to the oxidation/reduction of AgNPs inside the hydrogel, and the pair of peaks 800 mV/370 mV can also suggest the oxidation/reduction of

AgNPs inside the hydrogel, but of those firmly entrapped inside, and coordinately bonded to PVP molecules.

The results suggest that there are two types of AgNPs inside the hydrogel, those that are relatively free, and susceptible to the oxidation, as well as those that are already bonded to PVP molecules, and hence less reactive. Since FE-SEM imaging shown the formation of clusters of small nanoparticles, the "free" nanoparticles could be those attached between themselves, only, and the less reactive ones those nanoparticles at the interface with the PVP hydrogel.

Evaluation of the potential biomedical use for Ag/PVP nanocomposites was performed in a novel bioreactor with mechanical stimulation and interstitial medium flow under physiological regimes simulating in vivo conditions in articular cartilage (dynamic compression at 10 % strain, 0.42 Hz, 1 h on/1 h off, medium flow rate 5×10^{-3} cm^3 s^{-1} corresponding to superficial medium velocity of 25 μm s^{-1}—these conditions were set to mimic walking, and blood velocities found in capillaries (superficial medium velocity ranges from 10 to 100 μm s^{-1})). The hydrogel discs of pure PVP and the Ag/PVP nanocomposites were tested at the 10 % strain in two regimes: (a) at a loading rate of 337.5 μm s^{-1} and (b) at sequential increments of 100 μm displacement at the same loading rate with pauses of 30 min. In all experiments, the stress was shown to be an almost linear function of the applied strain for both hydrogel types (Figs. 4.34 (regime a) and 4.35 (regime b)). Values of the compression module for pure PVP and Ag/PVP hydrogel nanocomposites were calculated from the slopes of the best linear fits of the experimental stress–strain curves (Fig. 4.34).

The value of compression module obtained at the loading rate of 337.5 μm s^{-1} for PVP discs was 37.6 kPa, and for Ag/PVP discs was about 22.3 % higher: 48.4 kPa (Fig. 4.34), indicating that the presence of AgNPs led to a slight decrease in hydrogel elasticity. One of the factors contributing to different biomechanical behavior of the Ag/PVP hydrogel nanocomposites compared to the pure PVP hydrogel could be the possibility of fluid retention. A slower SBF release from Ag/PVP hydrogel nanocomposites could be explained by the entrapment of ions originating from SBF in the hydrogel voids that are already occupied with AgNPs, making the

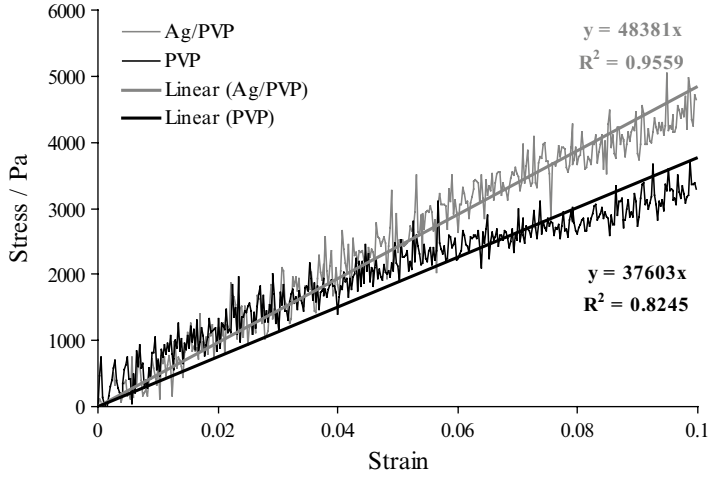

Fig. 4.34 Representative stress–strain relationships and best linear fits for PVP and Ag/PVP hydrogel discs at a loading rate of 337.5 μm s^{-1} (data represent the average of three measurements) (reprinted from [95] with permission from Wiley)

transit of these ions through the Ag/PVP hydrogel nanocomposites more difficult. In addition, the charging of the AgNPs over time, as a result of the interactions with the polyelectrolyte SBF solution, may change the swelling affinity of the nanocomposites and, consequently, the mechanical properties, by retaining a certain amount of liquid for a longer time than pure PVP, probably by solvation of the charged AgNPs. The sorption characteristics of the investigated samples are in accordance with these results and will be further discussed in the next section.

The second experiment in the bioreactor, performed at sequential increments of 100 μm displacements with pauses of 30 min, enabled the evaluation of the equilibrium unconfined compression (Young's) modules for the PVP and Ag/PVP nanocomposite hydrogels. The period of 30 min was provided for stress relaxation, i.e., to relax the PVP polymer network. The equilibrium stress–strain relationships, as well as those obtained at a loading rate of 337.5 μm s^{-1}, followed linear trends and the equilibrium unconfined compression modules were also calculated from the

slopes of the best linear fits of the experimental stress–strain curves (Fig. 4.35).

The values of equilibrium unconfined compression modules were found to be quite similar: 31.1 kPa for the PVP discs and 32.0 kPa for the Ag/PVP discs. The difference between these values for the pure PVP and the Ag/PVP nanocomposite hydrogels (2.8 %) was significantly lower than that obtained at a loading rate of 337.5 μm s^{-1} (22.3 %). This may suggest that the presence of AgNPs has no influence on the biomechanical properties of the PVP hydrogels, since the equilibrium unconfined compression module values are obtained after the period of polymer relaxation.

The possibility of measuring the mechanical properties of hydrogel samples using this bioreactor system was proven by the obtained values of the equilibrium unconfined compression modules. For both the PVP hydrogel and the Ag/PVP hydrogel nanocomposites, these values were in agreement with the values of the Young's module reported for chemically cross-linked PVP hydrogels [100], ranging from 19 to 504 kPa. In addition, the application

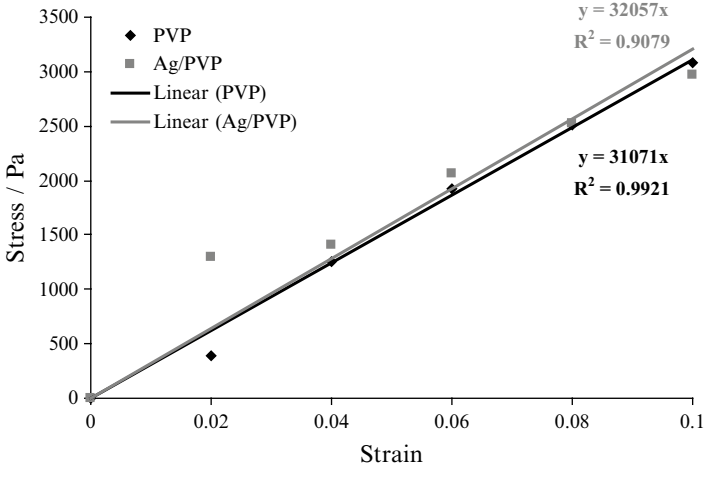

Fig. 4.35 Representative stress–strain relationships and best linear fits for PVP and Ag/PVP hydrogel discs at sequential increments of 100 μm displacement every 30 min (data represent the average of three measurements) (reprinted from [95] with permission from Wiley)

of PVP hydrogels and Ag/PVP hydrogel nanocomposites in medicine is rather promising, since the minimal values of the Young's modulus found in the literature required for the application of hydrogels as wound dressings were in the range of 1.5–150 kPa [101, 102]. This suggests that regarding the mechanical properties, both types of investigated hydrogels could potentially be applicable in medicine.

In order to determine the sorption characteristics of the pure PVP and Ag/PVP xerogels (dry gels), the intake of simulated body fluid was monitored gravimetrically for 72 h at 37 ± 1 °C (sorption curves, Fig. 4.36a). The reduced sorption curves (Fig. 4.36b) are plotted as a dependence m_t/m_∞ vs. $t^{1/2}/\delta$, following the second Fickian diffusion law given by Eq. (4.3), for a flat plane and short times: [103]

$$\frac{m_t}{m_\infty} = \frac{4}{\delta}\frac{D^{1/2}}{\pi^{1/2}}t^{1/2} \tag{4.3}$$

where m_t is the amount of SBF absorbed at time t, m_∞ is the amount of SBF absorbed at equilibrium, D is the diffusion coefficient of SBF through pure the PVP and Ag/PVP hydrogels, and δ is the thickness of the hydrogel sample.

As it can be observed in Fig. 4.36a, the initial sorption of SBF was linear until a steady state was reached. The linearity is in accordance with the assumption that the absorption was controlled by Fickian diffusion. The values of diffusion coefficient, D, of SBF through pure PVP and Ag/PVP hydrogels were calculated from the slopes of the initial linear region of the reduced sorption curves (Fig. 4.36b). The values obtained were $1.23 \cdot 10^{-4}$ cm^2 s^{-1} for pure PVP and $1.33 \cdot 10^{-4}$ cm^2 s^{-1} for Ag/PVP hydrogel nanocomposite. The diffusion coefficient of SBF in the Ag/PVP composite was slightly higher than in pure PVP, by about 8 %, indicating slightly facilitated absorption of SBF into the Ag/PVP hydrogel, compared to pure PVP. It could be presumed that the presence of AgNPs expands the PVP hydrogel network, enabling slightly faster SBF diffusion, and therefore promotes the sorption ability of the Ag/PVP hydrogel nanocomposites.

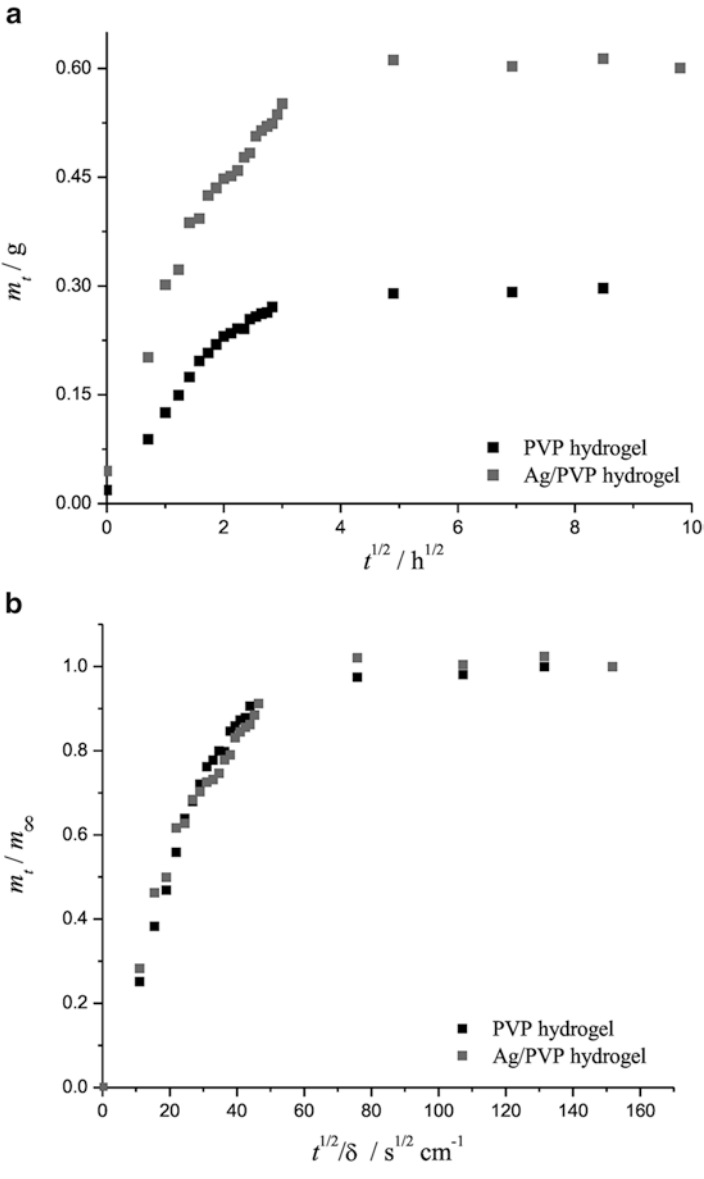

Fig. 4.36 Sorption curves (**a**) and reduced sorption curves (**b**) of PVP and Ag/PVP hydrogels in SBF at 37 °C (reprinted from [95] with permission from Wiley)

The obtained sorption curves are in accordance with slight differences in the biomechanical characteristics of PVP and Ag/PVP hydrogels, which could be supported with the results of the investigation of the mechanical properties under dynamic conditions. The higher value of the dynamic compression modulus, obtained for the Ag/PVP hydrogel nanocomposites could be due to the higher amount of SBF absorbed during the same time, as compared to pure PVP. This suggests that the increase in swelling ability, as well as a decrease in the hydrogel elasticity, was the consequence of the incorporation of the AgNPs. The reason could be found in the fact that the AgNPs, when embedded inside the PVP hydrogel network, expand the network, enabling faster SBF diffusion, and due to the retained solution, make the PVP hydrogel slightly stiffer by undermining the elastic behavior of the polymer network, but only under dynamic conditions.

The silver release kinetics from an Ag/PVP hydrogel nanocomposite during time of exposure to SBF at 37 °C is presented in Fig. 4.37. It is presented as the amount of silver remaining inside a sample as a function of time. The cumulative values of released silver were obtained as sums of the measured silver concentrations

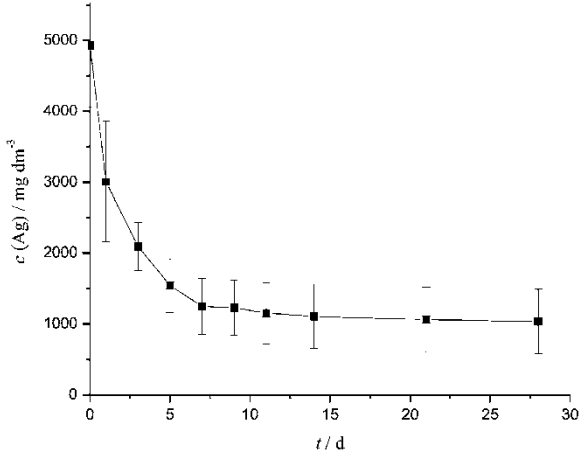

Fig. 4.37 Time dependence of the silver concentration inside an Ag/PVP nanocomposite hydrogel during release under static conditions (the data represent the average of three measurements) (reprinted from [95] with permission from Wiley)

at certain times, while the total content of silver inside the hydrogels was determined as a sum of all the amounts of the released silver, per measurement, and the amount of silver remaining after different release times.

It can be observed that the silver concentration inside Ag/PVP nanocomposite initially decreased sharply with time. After 7 days of silver release, a plateau was observed, indicating a significant lowering of the silver release rate. However, it can also be seen that even after 28 days, the Ag/PVP nanocomposite had still retained about 20 % of the initial silver content. This is very important since the remaining silver can preserve the sterility of the samples over time.

Furthermore, the potential application of Ag/PVP nanocomposites as antibacterial agents was demonstrated by their effect against *S. aureus*. The investigation of antimicrobial activity was performed by the agar diffusion test. After 24 h of incubation, an obvious clear zone of ≈1 mm appeared around the disc specimens (Fig. 4.38), indicating the absence of bacterial growth. This suggests the reaching of the

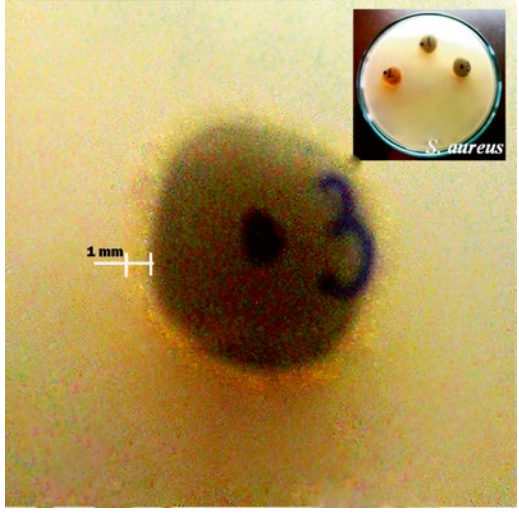

Fig. 4.38 An Ag/PVP nanocomposite hydrogel sample used in the investigation of the antimicrobial activity against *S. aureus* by the agar diffusion test (reprinted from [95] with permission from Wiley)

minimum inhibitory concentrations of released silver around the Ag/PVP hydrogel nanocomposite specimens. After removal of Ag/PVP hydrogel nanocomposite specimens from the Petri dishes, the zone of the bacterial growth inhibition was also observed on the agar surface, at the locations of previous specimen positions, suggesting acceleration of the top-down diffusion of silver [95]. These results demonstrated that the Ag/PVP nanocomposites efficiently released AgNPs and/or Ag^+ ions and induced bactericidal effects against *S. aureus*.

*4.3.2 Biocompatibility of Ag/Poly(*N*-Vinyl-2-Pyrrolidone) Hydrogel Nanocomposites*

Biomaterials aimed for applications in open wounds have to be characterized regarding hemocompatibility as well. Peripheral blood mononuclear cells (PBMC) mainly consist of lymphocytes and monocytes and represent a well-defined and described subpopulation of inflammatory cells [104]. Recently, the potentials of the synthesized Ag/PVP nanocomposites for biomedical applications were evaluated [105]. In specific, the biocompatibility of Ag/PVP nanocomposites containing different silver concentrations was studied by evaluating cytotoxic effects in monolayer cultures of two cell types—PBMC and human cervix carcinoma cells (HeLa).

4.3.2.1 Cytotoxicity

Survivals of target PBMC and HeLa cells grown in the presence of pure PVP and Ag/PVP nanocomposites obtained from PVP hydrogel swollen in 3.9 mmol dm^{-3} $AgNO_3$ solution were determined by MTT test [105]. The presence of pure PVP hydrogel caused only a slight decrease in the target cell survival, i.e., 84 ± 9 % for PBMC and 73 ± 9 % for HeLa cells as compared to controls. On the other hand, in the presence of Ag/PVP nanocomposites there was a notable decrease in cell survival, i.e., 60 ± 7 % for PBMC, and 56 ± 8 % for HeLa cells as compared to controls.

These results indicated that the sensitivity of normal PBMC and malignant HeLa cells to the presence of pure PVP hydrogels and Ag/PVP nanocomposites was not significantly different and the subsequent experiments were performed using PBMC only. After the preliminary experiments, cytotoxicity of pure PVP hydrogels and Ag/PVP nanocomposites in PBMC cultures was further studied as a function of AgNP concentration in nanocomposites and compared to cytotoxicity of Ag^+ ions originating from addition of $AgNO_3$ solutions [105].

Figure 4.39 presents survival, *S*, of nonstimulated and PHA-stimulated PBMC exposed to pure PVP hydrogel and Ag/PVP nanocomposites obtained from PVP hydrogels swollen in solutions of different $AgNO_3$ concentrations (1–16 mmol dm^{-3}), compared to the controls. In comparison, Fig. 4.40 presents survival, *S*, of nonstimulated and PHA-stimulated PBMC exposed to Ag^+ ions from $AgNO_3$ solutions, compared to the controls. It could be observed that the increase in silver concentration in both, Ag/PVP nanocomposites (Fig. 4.39) and $AgNO_3$ solutions (Fig. 4.40) induced decrease in target cell survival.

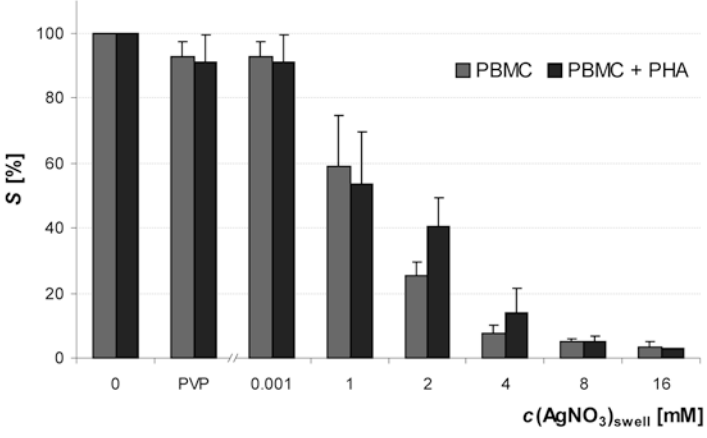

Fig. 4.39 Survival, *S*, of nonstimulated and PHA-stimulated PBMC cultured for 72 h in the presence of pure PVP hydrogel or Ag/PVP nanocomposites obtained from PVP hydrogels swollen in solutions of different $AgNO_3$ concentrations, $c(AgNO_3)_{swell}$, compared to the control (data represent the average of three measurements; *error bars* represent standard deviations) (reprinted from [105] with permission from Elsevier)

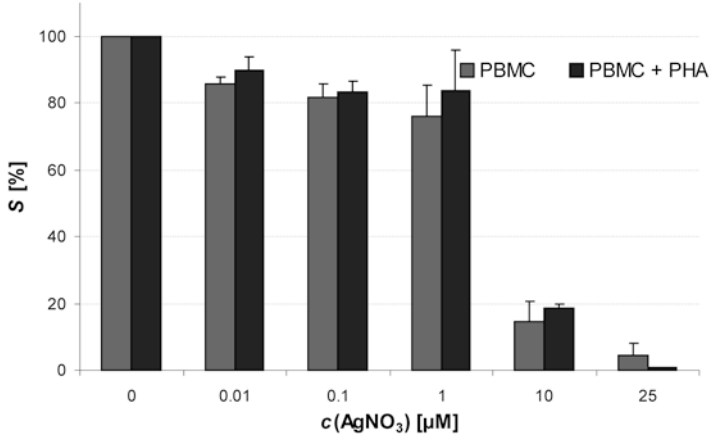

Fig. 4.40 Survival, *S*, of nonstimulated and PHA-stimulated PBMC cultured for 72 h as a function of the concentration of $AgNO_3$ solutions, $c(AgNO_3)$, compared to the control sample (data represent the average of two measurements; *error bars* represent standard deviations) (reprinted from [105] with permission from Elsevier)

It should be noted that the presence of pure PVP hydrogel leads only to a slight decrease in the survival of nonstimulated and PHA-stimulated PBMC, i.e., 92.6 ± 4.7 % and 91.0 ± 8.5 %, respectively, referring to the control sample (Fig. 4.39). On the other hand, survival of PBMC remarkably decreased in the presence of Ag/PVP nanocomposites. It can be deduced that the release of silver from Ag/PVP nanocomposites obtained from PVP hydrogels swollen in 1 mmol dm^{-3} $AgNO_3$ solutions exerted slight cytotoxicity in nonstimulated PBMC culture, while Ag/PVP nanocomposites obtained from PVP hydrogels swollen in more concentrated $AgNO_3$ solutions exerted pronounced cytotoxicity. It should be also noted that the presence of PHA had negligible effects on cell survival as cytotoxic effects were not significantly different in nonstimulated and PBMC cultures stimulated for proliferation.

Effects of direct exposure of investigated cell types to Ag^+ ions from $AgNO_3$ solutions of different concentrations are presented in Fig. 4.40.

It can be seen that the presence of Ag^+ ions in the concentrations up to 1 μmol dm^{-3} induced only a low decrease in PBMC

survival, corresponding to slight cytotoxicity. However, Ag^+ concentration of 10 μmol dm^{-3} produced significant decrease in PBMC survival, down to less than 20 %. Again, the presence of PHA had negligible effects on cell survival in all cultures.

IC_{50} values, defined as the concentration of an agent inhibiting cell survival by 50 % as compared to the control, determined from Fig. 4.40, for Ag^+ ions were 4.8 and 5.6 μmol dm^{-3}, for nonstimulated and PHA-stimulated PBMC, respectively. These results are comparable with the previous report of Hidalgo and Domínguez [106]. In their study, human dermal fibroblasts were exposed to $AgNO_3$ at concentrations of 4.12–82.4 μmol dm^{-3} for 8 and 24 h. After 24 h, Ag^+ ions at the concentration of 16.5 μmol dm^{-3} caused 50 % decrease in protein content, in the presence of 10 % of fetal calf serum (FCS). Yet, the authors did not examine prolonged times of cell exposure to silver ions. Slightly higher IC_{50} values obtained in this study after 72 h exposure of PBMC to Ag^+ ions confirm the fact that silver cytotoxicity to human cells is dependant not only on the ion concentration and exposure period, but on the cell type, too.

From the in vitro experiments here presented, it can be observed that AgNPs and Ag^+ ions exhibited dose-dependent cytotoxicity in PBMC cultures. In addition, there were no remarkable differences in cytotoxicity of the investigated agents in nonstimulated and PHA-stimulated PBMC cultures. The results suggest that the same slight cytotoxic effects are induced in 1 μmol dm^{-3} $AgNO_3$ solution as in the presence of Ag/PVP nanocomposite obtained from the PVP hydrogel swollen in the $AgNO_3$ solution of three orders of magnitude higher concentration (1 mmol dm^{-3}).

4.3.2.2 Silver Release

Figure 4.41 shows the decrease in silver concentrations within Ag/PVP nanocomposites under static conditions, in perfusion bioreactors and in the bioreactor with dynamic compression coupled with SBF perfusion, up to 42 days. The initial concentration of AgNPs in Ag/PVP nanocomposites obtained from PVP hydrogel swollen in 3.9 mmol dm^{-3} $AgNO_3$ solution was determined to be 206.2 ± 62.2 mg dm^{-3}. This value yields approximately 50 % of the

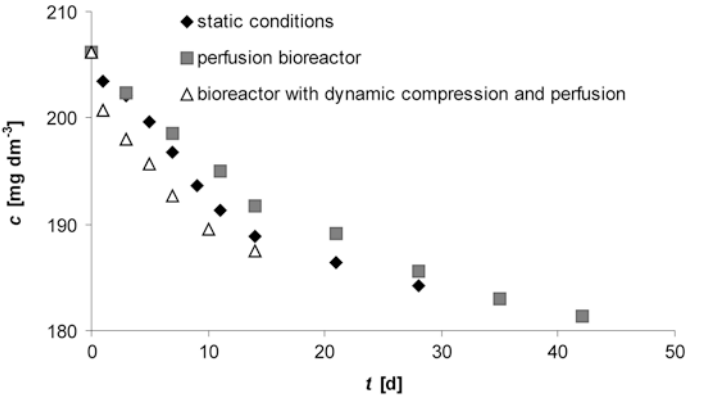

Fig. 4.41 Silver concentrations in Ag/PVP nanocomposites during release studies under static conditions, in perfusion bioreactors and in the bioreactor with dynamic compression coupled with SBF perfusion (data represent the average of three measurements; standard deviations are within 10 % but error bars are omitted for the figure clarity) (reprinted from [105] with permission from Elsevier)

value that would be expected if the reduction of all Ag^+ ions present in the swollen hydrogel were complete. The experimentally determined value was used in further calculations in the diffusion model that is later discussed.

Differences in the silver release profiles obtained in the three investigated systems were statistically insignificant (under 3 %), which implies that under all investigated conditions the governing mass transport phenomenon was internal diffusion. This finding suggests that the flow of SBF both in perfusion bioreactors as well as in the bioreactor with dynamic compression coupled with SBF perfusion is carried out mostly around and not through the samples, leaving diffusion as the sole silver release mechanism. Also, surface washout of silver in the bioreactors as compared to static conditions did not contribute to the amounts of silver released, suggesting that the Ag/PVP nanocomposite surfaces were not significant sources of silver, which was indeed the aim of the nanocomposite synthesizing procedure. It should be noted that a slightly lower release rate observed in perfusion bioreactors as compared to static conditions was probably due to the more frequent medium

exchange and, thus, the slightly increased diffusion driving force in the latter system.

On the other hand, silver concentrations in Ag/PVP nanocomposites in the bioreactor with dynamic compression coupled with SBF perfusion were consistently lower than those in the other two systems indicating a slightly higher silver release rate in the former system (Fig. 4.41), probably as a result of dynamic compression. Namely, dynamic compression was performed at the 10 % strain and a loading rate of 337.5 μm s^{-1} (yielding the frequency of 0.37 Hz) in 1 h on/1 h off regime, which enabled slight intensification of the silver release. The amount of released silver over the 14-day bioreactor study yielded ~9 % of the total initial content. It is also important to note that the effects of dynamic compression on the silver release rate are not highly pronounced as may be expected, due to the reverse medium flow inside the hydrogel during the decompression phase. Thus, the overall effect is insignificantly different as compared to pure diffusion observed under static conditions.

It is interesting to quantitatively describe decrease in silver concentrations in the Ag/PVP nanocomposites. Regardless of the experimental conditions, silver concentration decrease in Ag/PVP nanocomposites is rather low, up to 12 % that was determined after 42 days under static conditions (Fig. 4.41). Minor influences of hydrodynamic bioreactor conditions on the silver release rate are most likely the consequence of stability of silver nanoparticles inside the highly cross-linked PVP hydrogel network, since they coordinate with amide-carbonyl groups of PVP molecules [107]. As a result, these Ag/PVP nanocomposites could be used for a prolonged period of time, preserving the sterility of a soft tissue implant, for example.

The influence of different experimental conditions (static, SBF perfusion, dynamic compression coupled with SBF perfusion) on the silver release from Ag/PVP nanocomposites was quantified by application of the diffusion model. In order to distinguish the slight influence of dynamic compression, results obtained under these conditions were modeled separately from the results obtained in the other two systems.

Linear dependences of the reduced desorption curves (Fig. 4.42) confirmed the assumption that the diffusion mechanism obeys the

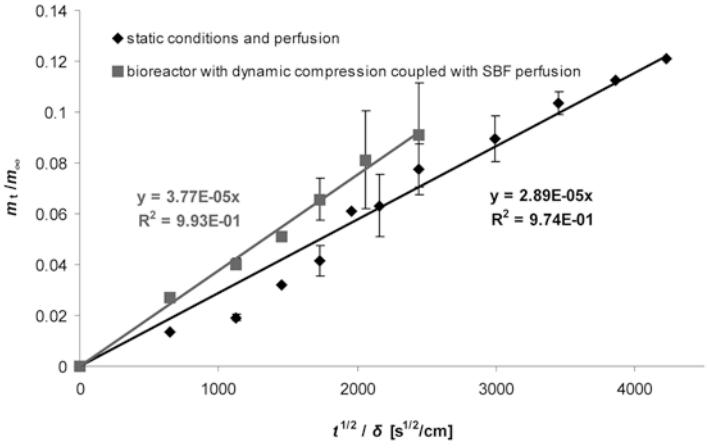

Fig. 4.42 Linear parts of the reduced desorption curves and best linear fits for silver release from Ag/PVP nanocomposites under static conditions and SBF perfusion, and in the bioreactor with dynamic compression coupled with SBF perfusion (data represent the average of three measurements; error bars represent standard deviations) (reprinted from [105] with permission from Elsevier)

second Fick's law of diffusion. Diffusion coefficient of AgNPs through Ag/PVP nanocomposite network of 1.64×10^{-10} cm^2 s^{-1} was calculated from the slope of the reduced desorption curve for static and SBF perfusion bioreactor conditions, while the apparent diffusion coefficient of 2.79×10^{-10} cm^2 s^{-1} was calculated for silver release in the bioreactor with dynamic compression coupled with SBF perfusion. As it can be observed, dynamic compression induced for ~40 % higher silver release rate compared to static conditions and SBF perfusion as determined by the value of the apparent diffusion coefficient.

The diffusion model can be used in conjunction with results of cytotoxicity studies to predict performance and the possible life time of Ag/PVP nanocomposites applied in different environments. Namely, it was shown [105] that the final concentration of released silver in medium after 72 h is calculated to be 0.4 μmol dm^{-3}. Considering that the slight cytotoxicity of this Ag/PVP nanocomposite is achieved after 72 h, this should be the time after which the wound dressing is to be removed/changed.

On the other hand, the system that simulates physiological conditions in articular cartilage (bioreactor with dynamic compression coupled with SBF perfusion) would correspond to a soft tissue implant in a synovial joint, e.g., knee. The volume of synovial fluid (SF) in normal human joints is approximately 0.5–2.0 cm^3 [108, 109]. However, since SF undergoes continuous turnover by trans-synovial flow into synovial lymph vessels, water and proteins in the SF are replaced within a period of 2 h or less [109]. Now, the diffusion model can be used to calculate the amount of silver released from the same Ag/PVP nanocomposite obtained from PVP hydrogel swollen in 1 mmol dm^{-3} $AgNO_3$ solution if potentially implanted in the knee, during 2 h needed for the complete replacement of SBF. By using the diffusion model (Eq. 4.3), the apparent diffusion coefficient of 2.79×10^{-10} cm^2 s^{-1} determined for the bioreactor with dynamic compression coupled with SBF perfusion, and the total amount of silver in this Ag/PVP nanocomposite, the amount of the released silver after 2 h was calculated to be 0.1 and 0.03 μmol dm^{-3}, for the volume of SF in normal human joints of 0.5 and 2 cm^3, respectively. These results mean that during the time needed for the complete replacement of SBF in the knee joint of 2 h, silver concentrations will be below the value that was determined in this study to induce only slight cytotoxicity (0.4 μmol dm^{-3}). The other benefit is that the implanted Ag/PVP nanocomposite would preserve its sterility for prolonged time.

Model predictions thus imply that Ag/PVP nanocomposites could be used both as wound dressings and cartilage implants without harming effects to the surrounding tissue.

4.4 Silver/Polyvinyl Alcohol Nanocomposites

4.4.1 Electrochemical Synthesis of Silver Nanoparticles in Poly(Vinyl Alcohol) Solution

Poly(vinyl alcohol) (PVA) is a widely used synthetic polymer. The benefits of its use lie in its properties: nontoxicity, water solubility, biocompatibility, biodegradability, and excellent mechanical

properties [110–115]. Also, its low price and wide availability makes PVA a polymer of choice in large number of applications. Hydrogels made of PVA have recently become attractive as matrices for repairing and regenerating several types of tissues and organs in the fields of tissue engineering and regenerative medicine [116–125]. The significant swelling capacity of PVA hydrogels, that enables the absorption of exudates generated during the process of wound healing, makes them adequate biomaterials for wound dressings [121, 126–129].

Recently, silver nanoparticles were electrochemically synthesized by reduction of silver ions, first time using PVA as a capping agent [130]. The effect of the PVA concentration on the amount and size of AgNPs was investigated, as well as the interaction between silver nanoparticles and PVA. The advantages of this procedure are especially attractive for biomedical applications: all steps of synthesis are clean, few chemicals are used, and the obtained Ag/PVA colloid solution is biocompatible and biodegradable. Ag/PVA colloid dispersions were obtained by electrochemical reduction of silver ions in PVA solutions containing 5 or 10 wt% PVA, 0.1 M KNO_3, and 3.9 mM $AgNO_3$. Applied current density was 25 mA cm^{-2} and synthesis time was 10 min.

UV–Vis spectroscopy was employed to monitor the silver nanoparticles formation. Figure 4.43 shows the absorption spectra of pure 10 wt% PVA solution and Ag/PVA colloid dispersions with 5 and 10 wt% of PVA in the initial solution. PVA spectrum did not exhibit the absorbance peak in the examined range of wavelengths. Both Ag/PVA colloid dispersions exhibited absorption spectra with two bands peaking at around 400 nm and around 650 nm.

The first absorption peak at ~400 nm confirms the formation of silver nanoparticles. The second absorption band peaking at nearly 650 nm can be explained by aggregation or agglomeration of silver nanoparticles present in the colloid dispersion [21, 28]. The only difference between the spectra of Ag/PVA colloid dispersions obtained from initial solutions containing 5 and 10 wt% PVA was in the absorbance intensity, where higher absorbance exhibited the solution with higher PVA concentration. This suggests that a higher concentration of silver nanoparticles was obtained with higher concentration of PVA in the initial solution, since the silver

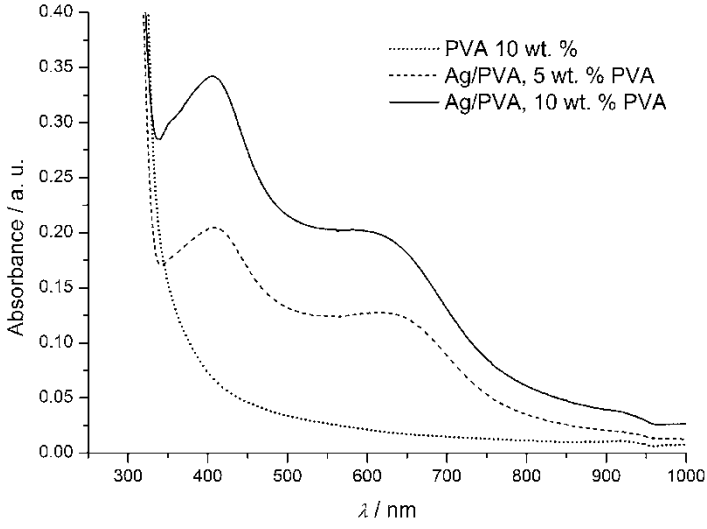

Fig. 4.43 Absorption spectra of 10 wt% PVA solution and Ag/PVA colloid dispersions with 5 and 10 wt% PVA (reprinted from [130] with permission from Serbian Chemical Society)

nanoparticles concentration is proportional to the absorbance intensity.

UV–Vis analysis was also used to determine the effect of PVA concentration on the amount and relative size of silver nanoparticles. The time dependences of the absorbance maximum, A_{max}, and the wavelength of the absorbance maximum, λ_{max}, are represented in Figs. 4.44 and 4.45, respectively. It can be seen in Fig. 4.44 that increase in PVA concentration increases the absorbance maximum indicating the greater amount of silver nanoparticles in Ag/PVA colloid dispersion. For both Ag/PVA colloid solutions A_{max} increases up to 20th day and remains almost constant up to 30th day, while further increase in A_{max} is a consequence of gelation. It can be said that the absorbance maximum is reached 20 days after the synthesis when the silver nanoparticles growth is terminated.

Figure 4.45 represents the time dependence of the wavelength of the absorbance maximum, λ_{max}. It can be noticed for both Ag/PVA dispersions that the λ_{max} increases up to 20th day, and then

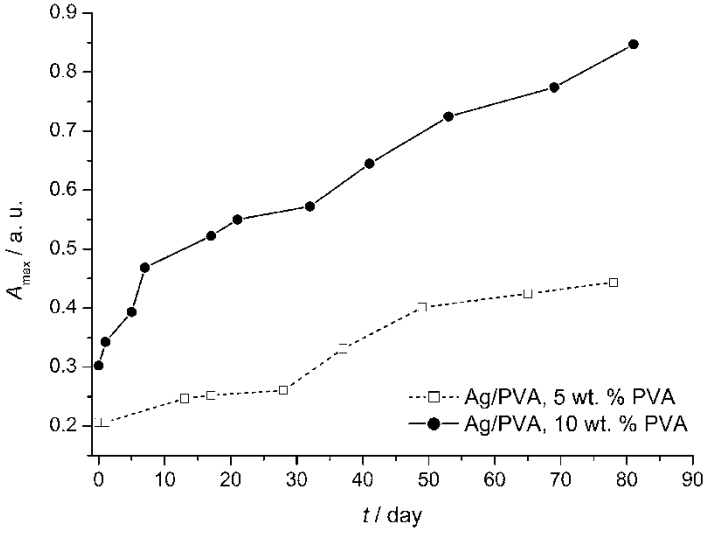

Fig. 4.44 Absorbance maximum, A_{max}, of Ag/PVA colloid dispersions with 5 and 10 wt% PVA as a function of time (reprinted from [130] with permission from Serbian Chemical Society)

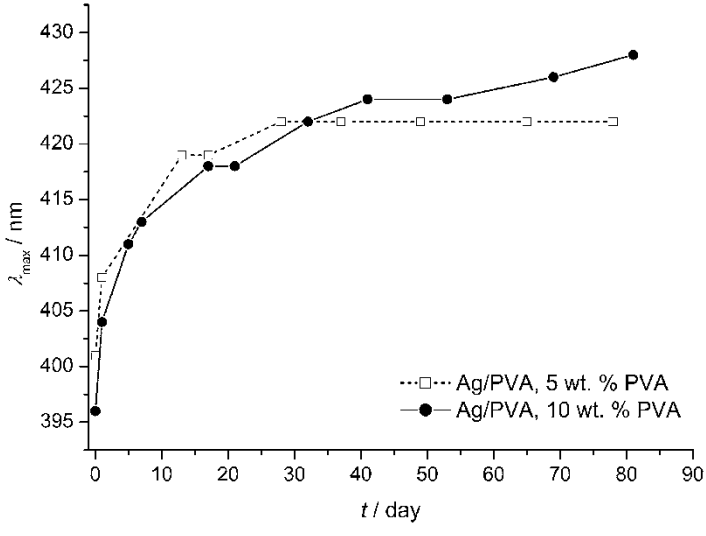

Fig. 4.45 Absorbance maximum wavelength, λ_{max}, of Ag/PVA colloid dispersions with 5 and 10 wt% PVA as a function of time (reprinted from [130] with permission from Serbian Chemical Society)

remains almost constant, as well as the concentration of PVA solution does not effect the size of synthesized silver nanoparticles. This is in accordance with the previous assumption that the growth of silver nanoparticles terminated around 20 days after the synthesis.

The cyclic voltammetry of Pt electrode analysis was performed in 10 % wt. PVA solution and in Ag/PVA colloid dispersion (Fig. 4.46) obtained from the initial solutions containing 5 and 10 wt% PVA. A better insight into the oxidation/reduction processes occurring in aqueous solutions of silver was obtained by the comparison with cyclic voltammograms of Pt electrode in solutions containing 3.9 mM $AgNO_3$ and 0.1 M KNO_3 [95].

Cyclic voltammogram of Pt electrode in 10 % wt. PVA solution (Fig. 4.46a) exhibited a broad cathodic peak at −100 mV, originating from Pt oxide reduction formed during the anodic sweep. The anodic counterpart of this peak is not seen due to the overlapping with the oxidation current at potentials more positive than 400 mV.

Figure 4.46b shows stationary cyclic voltammograms of Pt electrode in Ag/PVA colloid dispersions obtained from the initial solutions containing 5 and 10 wt% PVA. Ag/PVA colloid solution obtained from the initial solution containing 5 wt% PVA exhibited an anodic peak at around 611 mV which originates from the oxidation of Ag particles. This is connected with the oxidation/reduction processes of silver in the solution [95] where the appropriate pair of peaks appeared at 600 and 160 mV, respectively, and minimal shifts toward more positive potentials (611 and 165 mV) could be the effect of the influence of the polymer molecules present in the solution. A small broad anodic peak appeared at around 870 mV probably due to the oxidation of free Pt surface. The cathodic counterpart for the Pt oxide formation is not seen. However, considering the intensities of the cathodic currents in the potential region −200 to 200 mV, the cathodic counterpart for the Pt oxide formation could be overlapped with the Ag^+ reduction peak.

In the case of Ag/PVA colloid dispersion obtained from the initial solution containing 10 wt% PVA (Fig. 4.46b), three anodic peaks are obvious, at around 595, 667, and 871 mV. The first two can be related to the different oxidation processes of silver nanoparticles in the Ag/PVA colloid dispersion, while the peak at

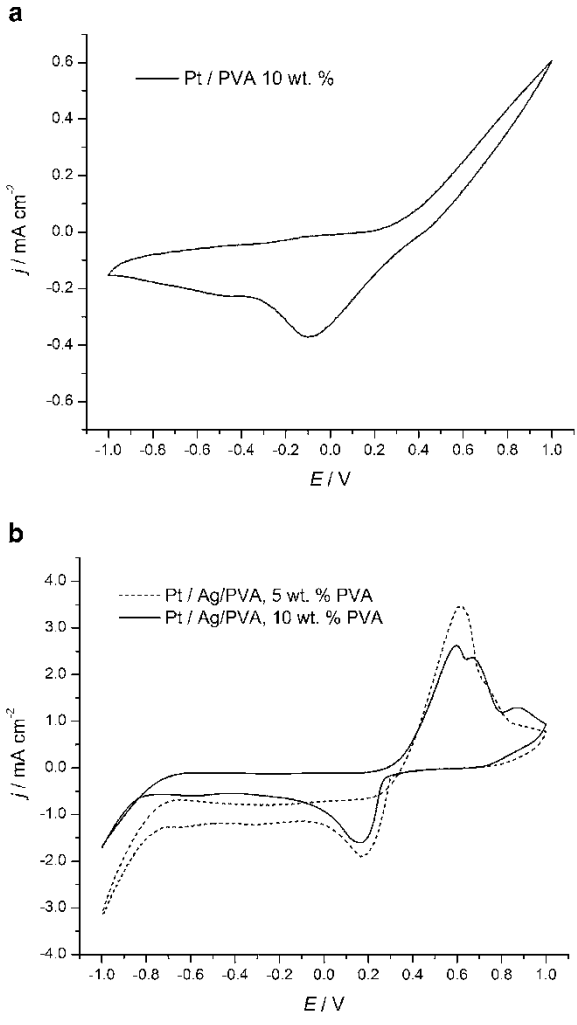

Fig. 4.46 Stationary cyclic voltammograms of Pt electrode in 10 wt% PVA solution (**a**), and Ag/PVA colloid dispersions with 5 and 10 wt% PVA (**b**) (Reprinted from [130] with permission from Serbian Chemical Society)

around 871 mV is related with the Pt oxide, as mentioned earlier. Only one cathodic peak at 160 mV was observed. Two anodic peaks suggest the difference between silver species; one is even less susceptible for oxidation [131]. This could be explained bearing in mind the entrapment of silver nanoparticles by PVA molecules, which implies the enhanced stability of silver nanoparticles obtained. Moreover, the coordination between Ag nanoparticles and hydroxyl groups of PVA was confirmed by FTIR and will be discussed in the next section. The results indicated two types of AgNPs in Ag/PVA colloid dispersion, the relatively free ones that are susceptible to the oxidation, and those already bonded to PVA molecules, and hence less reactive.

Since it was proved that the higher concentration of silver nanoparticles in Ag/PVP solution was synthesized from initial 10 wt% PVA solution (UV–Vis measurements) as well as more stable silver nanoparticles were formed (CV measurements), all further characterizations were performed on Ag/PVA solution synthesized from 10 wt% PVA.

Ag/PVA colloid dispersion obtained under the chosen experimental conditions (10 wt% PVA, $c(AgNO_3) = 3.9$ mM, $j = 25$ mA cm^{-2}, $t = 10$ min) was analyzed using transmission electron microscopy. TEM microphotograph confirms the spherical shape of the synthesized silver nanoparticles (Fig. 4.47a). Average diameter of silver nanoparticles obtained was found to be 15 ± 9 nm (Fig. 4.47b).

FT-IR measurements were performed on pure PVA and Ag/PVA thin films in order to determine the type of interactions between PVA molecules and silver nanoparticles. Thin PVA and Ag/PVA films were obtained by solvent evaporation from 10 wt% PVA solution and Ag/PVA colloid dispersion obtained from the initial solution containing 10 wt% of PVA, respectively (Fig. 4.48). The IR spectrum of Ag/PVA thin film exhibited few differences comparing to the spectrum of the pure PVA. Important change was observed for the bands peaking at 1377 and 1325 cm^{-1} (in PVA spectrum) and 1352 cm^{-1} (in Ag/PVA spectrum). A strong band peaking at 1377 cm^{-1} is the result of the coupling of –OH in-plane vibration with C–H wagging vibrations. The increase in the intensity of the band at 1377 cm^{-1}, along with the slight shift of the band

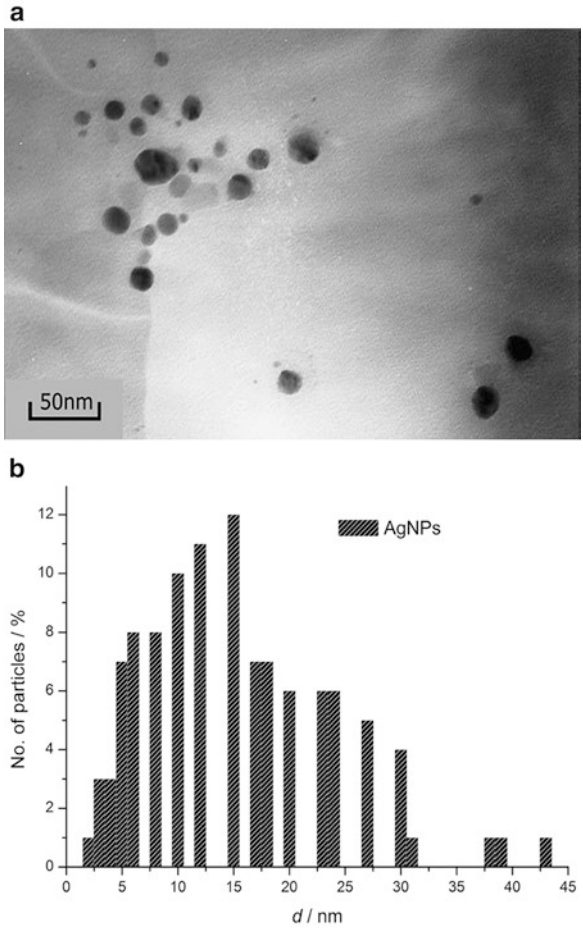

Fig. 4.47 (**a**) TEM microphotograph of electrochemically synthesized silver nanoparticles in Ag/PVA colloid dispersion with 10 wt% PVA, (**b**) histogram of AgNPs particle size distribution (reprinted from [130] with permission from Serbian Chemical Society)

position (toward 1352 cm^{-1} in Ag/PVA spectrum), and a disappearance of the band peaking at 1325 cm^{-1} upon incorporation of Ag nanoparticles, suggests interaction between AgNPs and –OH groups originating from PVA molecules through the decoupling

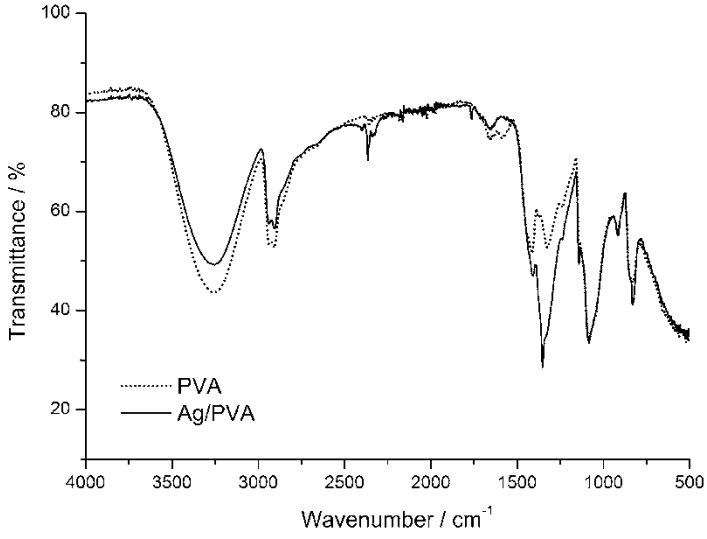

Fig. 4.48 IR spectra of PVA and Ag/PVA thin films (PVA content in the initial solutions 10 wt%) (reprinted from [130] with permission from Serbian Chemical Society)

between the corresponding vibrations. These results are in accordance with the results obtained from cyclic voltammetry, which indicated that PVA interacts with silver nanoparticles. As noted, there are two types of nanoparticles, one which is more reactive, peaking at more negative values of the potential, and the other one, peaking at more positive values of the potential and thus more stable, bonded with PVA molecules.

4.4.2 The Effect of Graphene on the Ag/PVA Nanocomposites

In order to study the effect of graphene on the characteristics of Ag/PVA nanocomposites, Ag/PVA and Ag/PVA/Gr (0.01 wt% Gr) nanocomposite colloid dispersions were obtained by electrochemical reduction of silver ions in PVA and PVA/Gr colloid

dispersions, respectively, containing 10 wt% PVA, 0.1 M KNO_3, 3.9 mM $AgNO_3$ and in the case of Ag/PVA/Gr 0.01 wt% Gr additionally. The applied current density was 40 mA cm^{-2} and the reaction time was 30 min [132].

The absorption spectra of pure PVA solution and Ag/PVA and Ag/PVA/Gr colloid dispersions are shown in Fig. 4.49. The PVA spectrum did not exhibit an absorbance peak in the examined range of wavelengths. Both Ag/PVA and Ag/PVA/Gr colloid dispersions exhibited absorption spectra with two bands peaking at around 400 and around 650 nm. The first absorption peak at ≈400 nm confirmed the formation of AgNPs, while the second absorption band peaking at nearly 650 nm indicated aggregation or agglomeration of the AgNPs. Because the concentration of AgNPs is proportional to the absorbance intensity, it was concluded that presence of graphene slightly decreased the amount of AgNPs in the Ag/PVA/Gr colloid dispersion.

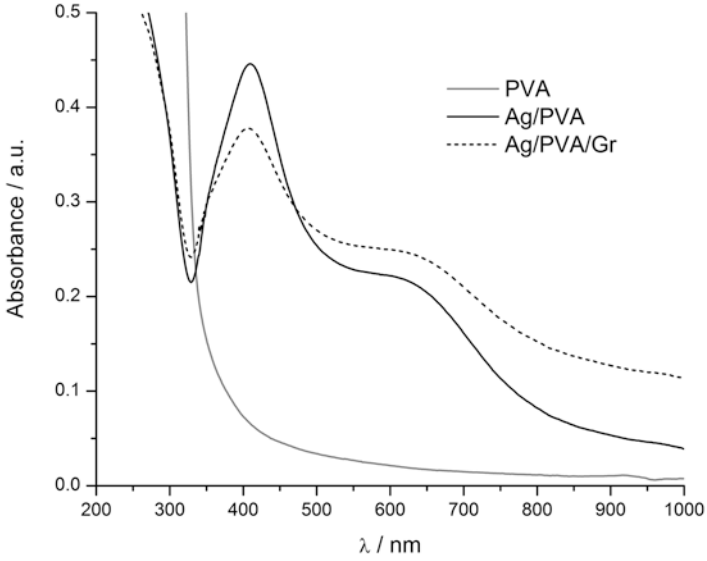

Fig. 4.49 UV–Vis spectra of 10 wt% PVA solution and Ag/PVA and Ag/PVA/Gr colloid dispersions at 14th day after synthesis (reprinted from [132] with permission from Elsevier)

UV–Vis analysis was also used to determine the effect of aging time on the amount and relative size of AgNPs in the colloid dispersions. The time dependences of the absorbance maximum, A_{max}, and the wavelength of the absorbance maximum, λ_{max}, are presented in Fig. 4.50a, b, respectively. The presence of graphene decreased A_{max}, indicating a smaller amount of AgNPs in the Ag/PVA/Gr colloid dispersion (Fig. 4.50a). For both Ag/PVA and Ag/PVA/Gr colloid dispersions, A_{max} increased up to the 15th day and then increased slowly up to the 20th day, while a further increase in A_{max} with time was the consequence of gelation. The absorbance maximum was attained 15 days after the synthesis, when the growth of the silver nanoparticles terminated.

For both Ag/PVA and Ag/PVA/Gr colloid dispersions, λ_{max} increased with time, reaching a value of 407 nm for Ag/PVA/Gr, and 410 nm for Ag/PVA on the 15th day (Fig. 4.50b). A lower λ_{max} value has been reported to correspond to smaller nanoparticles, results therefore suggested that AgNPs in the Ag/PVA/Gr colloid dispersions had smaller dimensions than those in the Ag/PVA colloid dispersions, suggesting that graphene sheets situated between the polymer chains prevented the further growth and aggregation or agglomeration of AgNPs.

From the TEM micrographs depicted in Fig. 4.51, it is obvious that the AgNPs had sphere-like morphologies at the nanoscale level. Diameter of AgNPs was approximately 10–40 nm for both Ag/PVA (Fig. 4.51a) and Ag/PVA/Gr (Fig. 4.51b) colloidal dispersions. It was assumed that the following three-step mechanism of particle assembly occurred: (1) silver ions interacted with the hydroxyl groups of PVA, (2) nearby silver atoms that had been reduced electrochemically aggregated at close range (primary nanoparticles), and (3) nearby primary nanoparticles coalesced with other primary nanoparticles or interacted with PVA molecules to form larger aggregates (secondary nanoparticles). As a consequence, entrapment of silver nanoparticles by PVA molecules occurred; this implied that the AgNPs had enhanced stability. The small dimensions and low aggregation of AgNPs in the Ag/PVA/Gr dispersion due to the presence of transparent graphene sheets situated between the PVA polymer chains prevented further growth and aggregation or agglomeration of AgNPs. This is in agreement with the results obtained from UV–Vis (Fig. 4.50b).

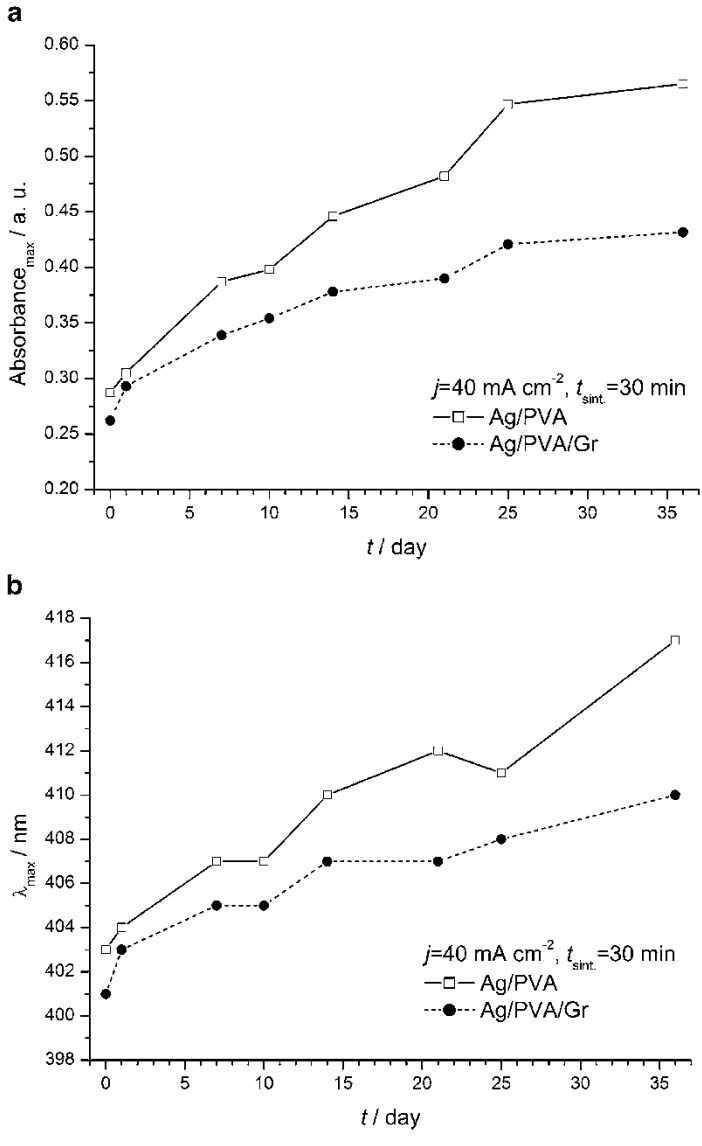

Fig. 4.50 Absorbance maximum, A_{max} (**a**) and absorbance maximum wavelength, λ_{max} (**b**) of Ag/PVA and Ag/PVA/Gr colloid dispersions as a function of time (reprinted from [132] with permission from Elsevier)

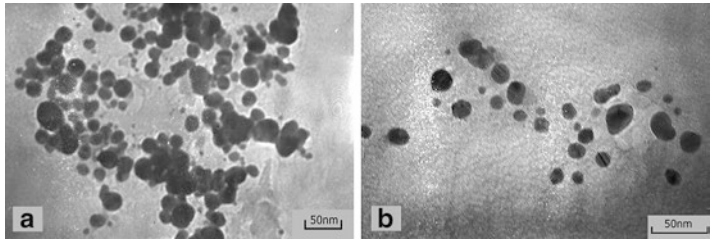

Fig. 4.51 TEM microphotographs of electrochemically synthesized silver nanoparticles in (**a**) Ag/PVA and (**b**) Ag/PVA/Gr colloid dispersions (reprinted from [132] with permission from Elsevier)

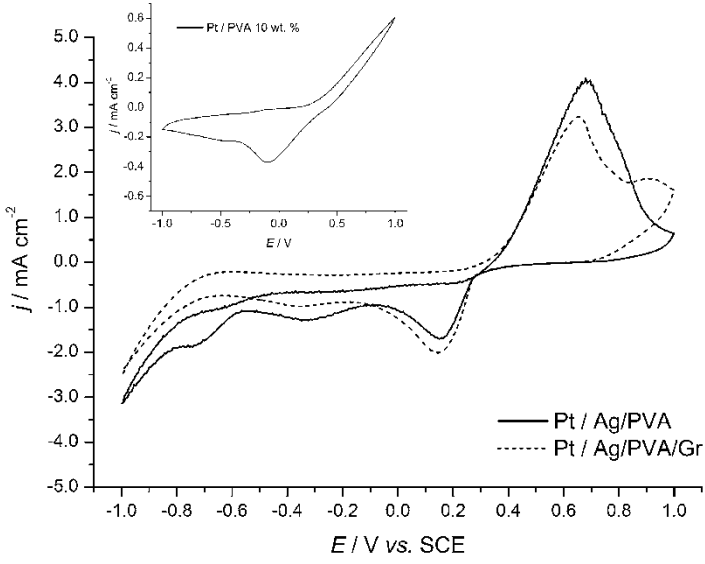

Fig. 4.52 Stationary cyclic voltammograms of Pt electrode in Ag/PVA and Ag/PVA/Gr colloid dispersions (*inset*: stationary cyclic voltammogram of Pt electrode in PVA 10 wt% solution) (reprinted from [132] with permission from Elsevier)

Cyclic voltammetry analysis of the Pt electrodes was performed in 10 wt% PVA solution and Ag/PVA and Ag/PVA/Gr colloid dispersions (Fig. 4.52).

Cyclic voltammogram of the Pt electrode in 10 wt% PVA solution (inset in Fig. 4.52) exhibited a broad cathodic peak at about −100 mV, originating from reduction of the Pt oxide formed during the anodic sweep. The anodic counterpart of this peak at about 850 mV, corresponding to Pt oxide formation, was slightly visible due to overlap with the oxidation current at potentials more positive than 400 mV. The shift of the cathodic peak from −250 to −100 mV, as well as the slightly visible anodic peak at about 850 mV with respect to the reference solution containing 3.9 mM $AgNO_3$ and 0.1 M KNO_3 [95] was attributed to the presence of PVA polymer chains that impeded oxidation/reduction processes on the Pt electrode.

Cyclic voltammogram of the Pt electrode in the Ag/PVA colloid dispersion (Fig. 4.52) exhibited two anodic peaks: a main peak at around 680 mV, which originated from the oxidation of AgNPs, and a small, slightly visible anodic peak at around 870 mV due to oxidation of free Pt surfaces and Pt oxide formation. Two cathodic counterparts were observed: a peak at around 180 mV corresponding to the reduction of AgNPs, and a peak at around 300 mV originating from reduction of Pt oxide. Shifts of the anodic peak due to AgNP oxidation and the cathodic peak due to AgNP reduction toward more positive potentials (680 and 180 mV, respectively) in comparison with reference solution containing 3.9 mM $AgNO_3$ and 0.1 M KNO_3 (600 and 160 mV, respectively) was a consequence of PVA polymer chains that impeded oxidation/reduction processes on the Pt electrodes.

In the cyclic voltammogram of the Pt electrode in Ag/PVA/Gr colloid dispersion (Fig. 4.52), two anodic peaks were obvious—one at around 650 mV due to AgNP oxidation, and the second at around 950 mV due to oxidation of free Pt surfaces and Pt oxide formation. Two cathodic counterparts were observed: a peak at around 130 mV corresponding to AgN reduction and a peak at around 370 mV due to reduction of the Pt oxide. The shift of the anodic peak of AgNP oxidation and the cathodic peak of AgNP reduction toward more negative potentials (650 and 130 mV, respectively) in comparison with Ag/PVA colloid dispersion (680 and 180 mV, respectively) indicated that the AgNPs in the Ag/PVA/Gr dispersion had smaller dimensions and/or lower aggrega-

tion due to graphene sheets situated between the polymer chains that prevented the further growth and aggregation or agglomeration of AgNPs. This is in agreement with the results obtained from UV–Vis (Fig. 4.50b) and TEM (Fig. 4.51).

Ag/PVA and Ag/PVA/Gr nanocomposite films were obtained from colloid dispersions by solvent evaporation at 60° C, and these films were characterized by FE-SEM, Raman spectroscopy, FT-IR, XRD, XPS, TGA, and tensile tests [132].

FE-SEM microphotographs showed that AgNPs in the Ag/PVA/Gr film (Fig. 4.53b) had smaller dimensions and/or lower aggregation than AgNPs in the Ag/PVA film (Fig. 4.53a) due to graphene sheets between the polymer chains that prevented the further growth and aggregation or agglomeration of AgNPs in the Ag/PVA/Gr film.

Raman analyses (Fig. 4.54) were performed to verify the incorporation of graphene in Ag/PVA/Gr composite film. Raman spectroscopy of graphene is generally characterized by two main features: the *G*-peak, which arises from first-order scattering of the E_{2g} phonon from sp^2 carbon atoms (in the range of 1500–1600 cm^{-1}), and the *D*-peak (in the range of 1200–1500 cm^{-1}), which arises from the breathing mode of *k*-point photons with A1g symmetry. In Fig. 4.54 the *D*-peak at 1379 cm^{-1} represents edges, other defects, disordered sp^3-bonded carbon atoms, and impurities, while the *G*-band at 1618 cm^{-1} corresponds to ordered sp^2-bonded carbon atoms. The low intensity of both *D* and *G* peaks was attributed to the low concentration of graphene in the Ag/PVA/Gr composite

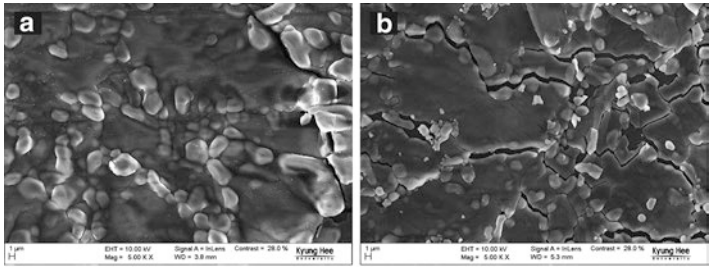

Fig. 4.53 FE-SEM microphotographs of (**a**) Ag/PVA and (**b**) Ag/PVA/Gr films (reprinted from [132] with permission from Elsevier)

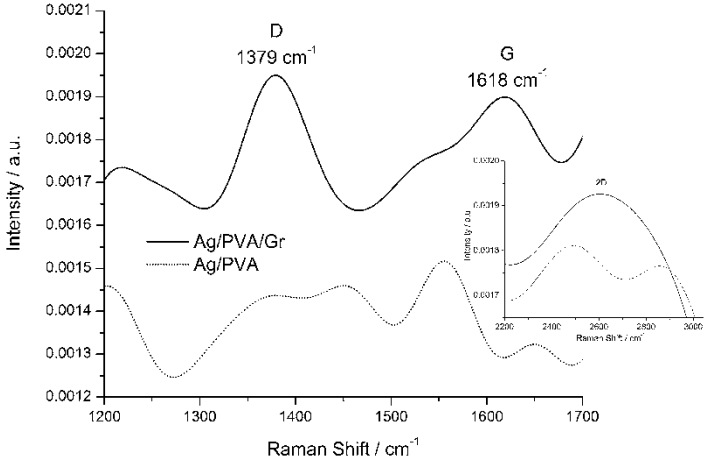

Fig. 4.54 Raman spectra of Ag/PVA and Ag/PVA/Gr films (reprinted from [132] with permission from Elsevier)

film. Raman analysis confirmed that graphene was in its pure form [133–135]. Raman spectrum uniquely reflects graphene's electronic structure. In a precise manner are easily distinguished fingerprints for single, bilayers, and multiples thus allowing high-throughput, nondestructive identification of graphene layers [136]. Inset in Fig. 4.54 measures a single 2D peak in graphene. As previously reported 2D band is a function of the number of layers for 514.5 and 633 nm excitations and bilayer has a much broader and upshifted 2D contrary to single-layer graphene [137]. These are also quite distinct in bulk graphite. Therefore, we can confidently report that Raman spectrum of Ag/PVA/Gr confirms the incorporation of single-layer graphene into the composite.

FT-IR measurements of Ag/PVA and Ag/PVA/Gr films were performed to characterize the interactions among PVA molecules, AgNPs, and graphene. The spectra of PVA (as reference), Ag/PVA, and Ag/PVA/Gr exhibited characteristic peaks associated with PVA (Fig. 4.55).

The IR spectra of the Ag/PVA and Ag/PVA/Gr films exhibited a few differences compared to that of pure PVA. Important changes were observed for bands peaking at 1418 and 1323 cm^{-1}

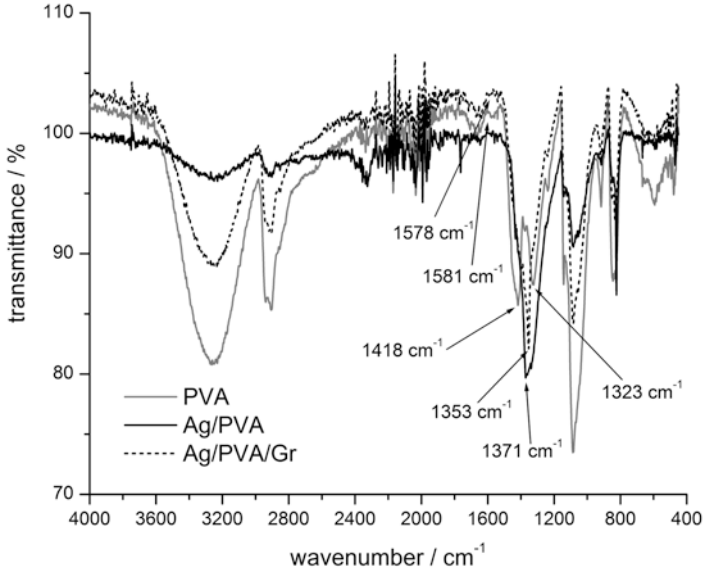

Fig. 4.55 FT-IR spectra of PVA, Ag/PVA and Ag/PVA/Gr films (reprinted from [132] with permission from Elsevier)

in the PVA spectrum corresponding to coupling of the –OH in-plane vibration with C–H wagging vibrations. The shift of the band peaking at 1418 cm^{-1} in PVA to 1371 cm^{-1} in Ag/PVA and 1353 cm^{-1} in Ag/PVA/Gr spectra, and the disappearance of the band peaking at 1323 cm^{-1} in Ag/PVA and Ag/PVA/Gr spectra upon incorporation of AgNPs, suggested in both cases an interaction between the AgNPs and the hydroxyl groups of the PVA molecules through decoupling between the corresponding vibrations. The greater shift of the band at 1418 cm^{-1} for PVA to 1353 cm^{-1} for Ag/PVA/Gr than for Ag/PVA (1371 cm^{-1}) indicated the occurrence of additional hydrogen bonding interactions between the OH^- groups present in PVA and oxygen-containing groups in graphene sheets situated between the polymer chains in the Ag/PVA/Gr film that prevented further growth and aggregation or agglomeration of AgNPs, as proven by the FE-SEM microphotographs (Fig. 4.53).

XRD patterns of Ag/PVA and Ag/PVA/Gr films are shown in Fig. 4.56. In both Ag/PVA and Ag/PVA/Gr diagrams, the broad peaks at $2\theta = 19.65°$ and 19.45°, respectively, corresponding to the (002) lattice plane, are related to the characteristic peak of PVA at $2\theta = 19.3°$ due to the semicrystalline structure of PVA [138]. It was clear that the five diffraction peaks for Ag/PVA and Ag/PVA/Gr films at 2θ of 38.2, 44.4, 64.6, 77.4, and 81.5 corresponded to Bragg's reflections from the (111), (200), (220), (311), and (222) crystal planes of Ag. A weak broad peak near 25° indicated that graphene was present in the Ag/PVA/Gr films [139–141].

The average crystallite domain size, D_p, was calculated from the half height width ($\beta_{1/2}$) of the XRD reflection of the (002) plane, using the Scherer equation:

$$D_p = \frac{K\lambda}{\beta_{1/2}\cos\theta} \tag{4.4}$$

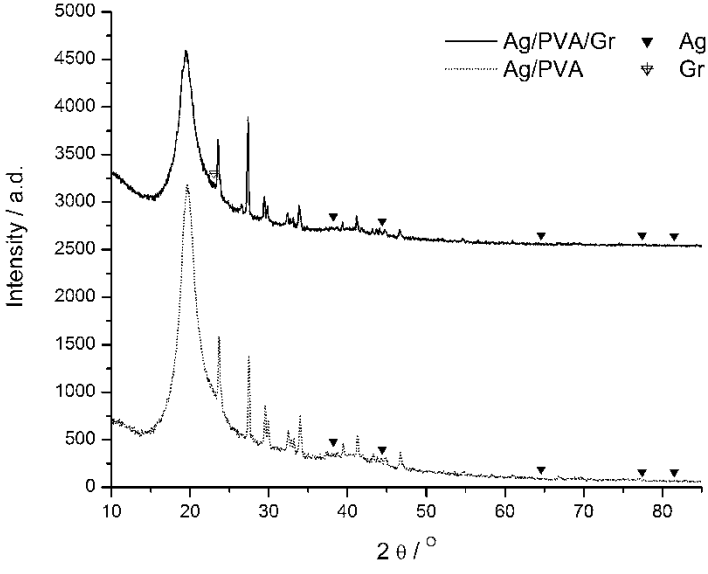

Fig. 4.56 XRD patterns of Ag/PVA and Ag/PVA/Gr films (reprinted from [132] with permission from Elsevier)

where λ is the wavelength of the X-ray radiation of 1.5418 Å, K is the shape coefficient equal to 0.9, and θ is the diffraction angle. The average crystallite domain size, D_p, of 0.2782 nm for PVA has been changed upon incorporation of AgNPs and graphene sheets to 0.2880 and 0.2602 nm, for Ag/PVA and Ag/PVA/Gr film, respectively, indicating in both cases an interaction between the AgNPs and the hydroxyl groups of PVA molecules, as well as additional interactions between PVA molecules and graphene sheets situated between the polymer chains in the Ag/PVA/Gr film. Single-layer graphene comprises carbon atoms arranged periodically in a hexagonal manner, and the nearest distance between two carbon atoms is 0.142 nm. Multilayer graphene sheets contain several graphene monolayers with an interwall distance of 0.340 nm [142]. However, the average crystallite domain size of the (002) lattice plane in Ag/PVA/Gr was calculated to be 0.2602 nm, indicating the occurrence of hydrogen bonding interactions between the OH^- groups present in PVA and oxygen-containing groups in graphene. This confirmed the hypothesis [132] that graphene sheets situated between the polymer chains prevented the further growth and aggregation or agglomeration of AgNPs as observed by FTIR and FE-SEM.

Elemental compositions of Ag/PVA as a reference and Ag/PVA/Gr films were investigated via surface analysis by XPS (Fig. 4.57a, b), respectively.

XPS survey spectra of both films revealed the presence of carbon (C1s), oxygen (O1s), and silver (Ag3d), as reported in Table 4.7. The C1s peak may have originated from the PVA itself (binding energy (BE) of 285.02 eV) or from added graphene with a BE of 284.95 eV, because the C1s peak corresponding to the BE of 285.0 eV could be attributed to aromatic hydrocarbons, actually C=C (sp^2 bond) in the graphitic network. The BE of the Ag3d peak (≈368 eV) agreed with that reported in the literature, indicating formation of a nanocomposite with silver [143]. The O1s peak may have originated from PVA itself with a BE of 533.0 eV or from added graphene with a binding energy of 532.9 eV due to C–O bonds, which are characteristics of C–O stretches of graphene sheets [144]. Survey spectra of the Ag/PVA/Gr film revealed indisputable evidence of graphene incorporation, namely, an

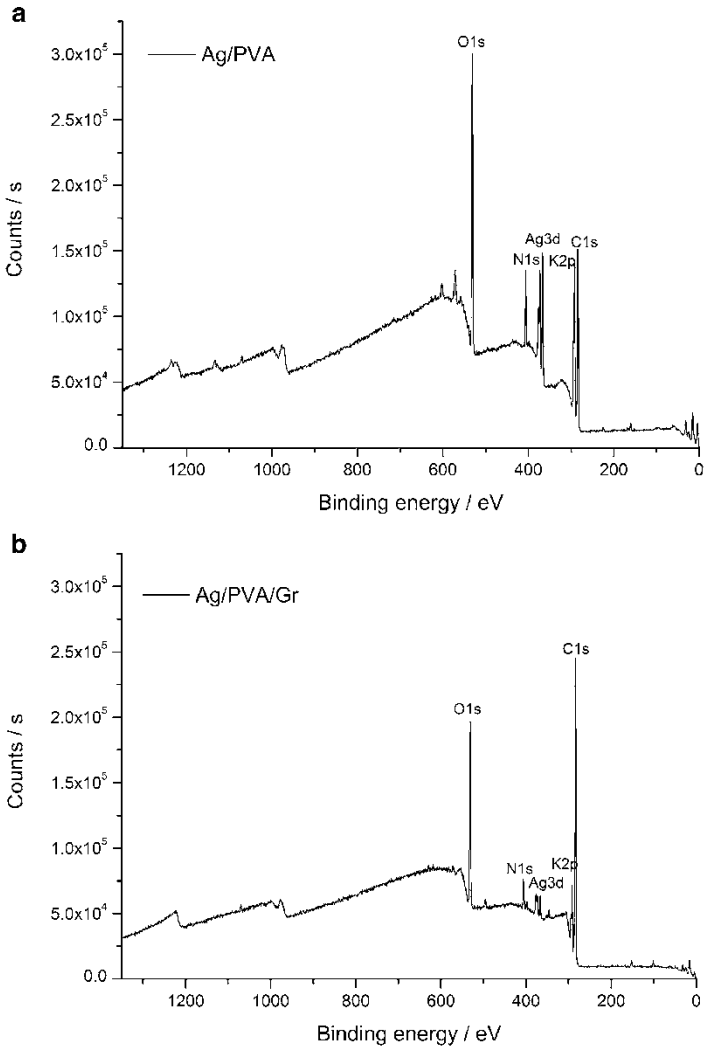

Fig. 4.57 XPS survey spectra of (**a**) Ag/PVA and (**b**) Ag/PVA/Gr films (reprinted from [132] with permission from Elsevier)

Table 4.7 Atomic percentages of elements at Ag/PVA and Ag/PVA/Gr films surface determined by XPS

Element content (at%)			
	C1s	O1s	Ag3d
Ag/PVA	56.54	41.36	2.10
Ag/PVA/Gr	77.38	22.30	0.32

Reprinted from [132] with permission from Elsevier

increased C1s content and decreased O1s content. The smaller atomic percentage of silver in Ag/PVA/Gr film than Ag/PVA film indicated smaller AgNPs, as was observed by FE-SEM (Fig. 4.53b).

Thermogravimetric analysis (TGA) and corresponding differential thermogravimetric analysis (DTG) were performed to investigate the effect of incorporation of graphene sheets on the thermal stability of the polymer matrix. As shown in Fig. 4.58a, both Ag/PVA and Ag/PVA/Gr films showed a three-step weight loss process. The small weight loss in the first step at about 70–120 °C was attributed to the loss of absorbed water. The weight loss at about 230–320 °C during the second step suggested the degradation of PVA (in Ag/PVA film) or PVA and graphene (in Ag/PVA/Gr film). The third weight loss step at about 350–600 °C was attributed to further decomposition of the remaining composites. DTG curves are shown in Fig. 4.58b; the peak temperature of the DTG curve represents the temperature at which the maximum weight loss rate was reached. The peak temperature of the Ag/PVA/Gr film was about 282 °C, 8 °C higher than that of the Ag/PVA film; this confirmed bonding between PVA molecules and graphene sheets [145, 146]. Similarly, the smaller weight loss at 450°C (Fig. 4.58a) for Ag/PVA/Gr (77.26 wt%) than for Ag/PVA (80.21 wt%) demonstrated that the Ag/PVA/Gr film was more stable than the Ag/PVA film due to stronger interactions between molecules in the former.

To evaluate the mechanical properties of Ag/PVA and Ag/PVA/Gr films, tensile tests were performed [132]. Typical stress–strain curves are shown in Fig. 4.59. The tensile strength of the Ag/PVA/Gr film relative to that of Ag/PVA film increased by 16.4 % from 121.2 to 141.1 MPa, and the Young's modulus increased by 126.9 % from 0.309 to 0.701 GPa. The elongation at break of the Ag/PVA film was the same as that of the Ag/PVA/Gr film. The

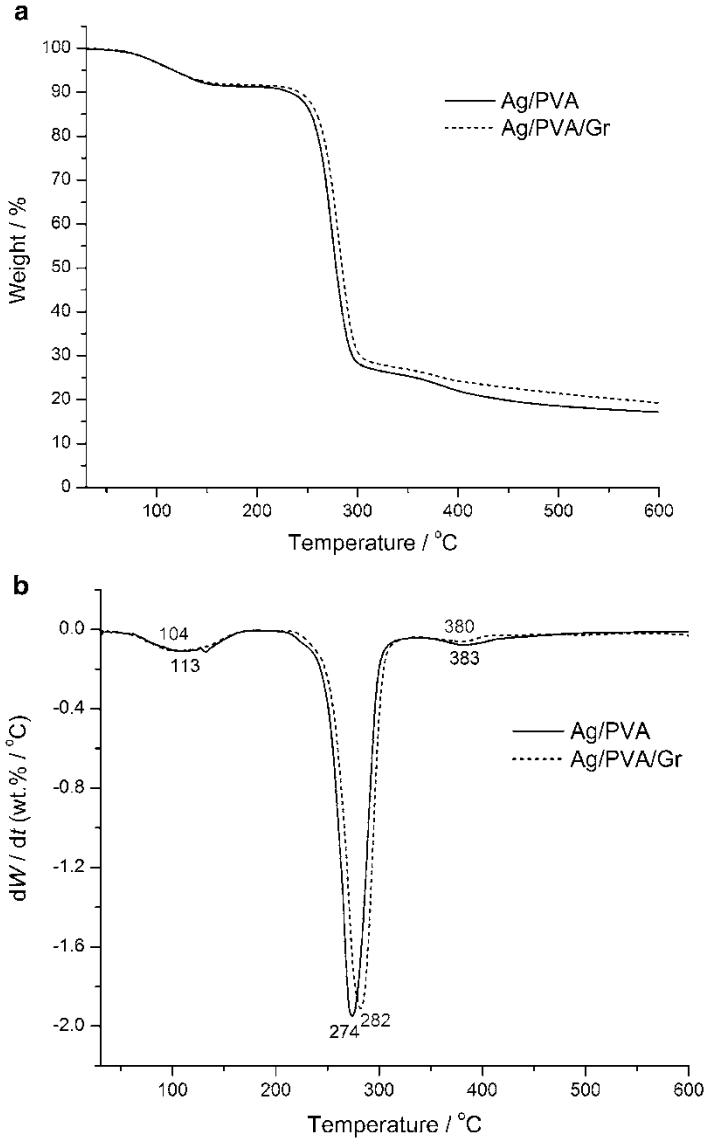

Fig. 4.58 (**a**) TGA and (**b**) DTG curves of Ag/PVA and Ag/PVA/Gr films (reprinted from [132] with permission from Elsevier)

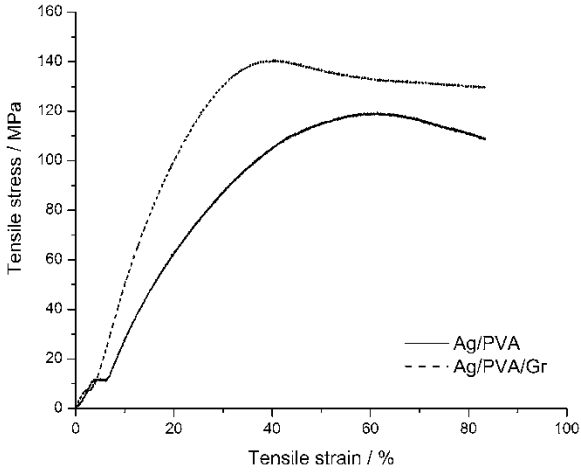

Fig. 4.59 Stress-strain curves of Ag/PVA and Ag/PVA/Gr films (reprinted from [132] with permission from Elsevier)

enhanced mechanical properties, i.e., greater values of tensile strength and Young's modulus, of the Ag/PVA/Gr film are the consequences of incorporation of Gr into the PVA matrix and bonding between PVA molecules and graphene sheets.

Ag/PVA and Ag/PVA/Gr nanocomposite hydrogel discs were obtained from colloid dispersions by the freeze–thaw method in five cycles of successive freezing and thawing (one cycle involved freezing for 16 h at −18 °C and thawing for 8 h at 4 °C) [132]. The discs were characterized by atomic absorption spectroscopy to monitor silver release and agar diffusion and spread plate tests to determine antibacterial activity.

Kinetics of silver release from Ag/PVA and Ag/PVA/Gr hydrogel nanocomposites as a function of time of exposure to SBF at 37 °C are depicted in Fig. 4.60 as the amount of silver remaining inside the sample as a function of time. Silver concentration inside Ag/PVA and Ag/PVA/Gr hydrogels initially decreased sharply with time, and after 3 days of silver release (16 % and 19 % of the initial silver content, respectively) a plateau was observed, indicating a significant lowering of the silver release rate. However, it can also be seen that even after 28 days, both Ag/PVA and Ag/PVA/Gr

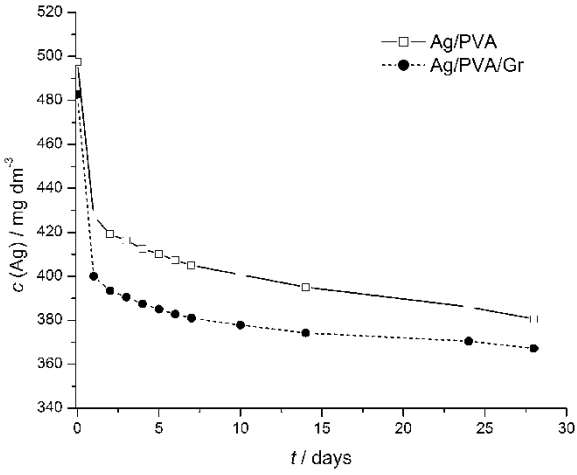

Fig. 4.60 Time dependence of the silver concentration inside Ag/PVA and Ag/PVA/Gr hydrogels during release under static conditions (reprinted from [132] with permission from Elsevier)

discs still retained 76% of the initial silver content as a consequence of the stability of AgNPs inside the highly cross-linked PVA hydrogel network. This is very important, because the remaining silver can preserve the sterility of the samples over time. For example, these hydrogels could be used to preserve the sterility of a soft tissue implant over time. In addition, both Ag/PVA and Ag/PVA/Gr hydrogel nanocomposites had antibacterial activity against *S. aureus* and *E. coli*.

Antibacterial activities of the samples toward *S. aureus* and *E. coli* were evaluated quantitatively by monitoring the changes in the number of viable bacterial cells in suspension. Figures 4.61 and 4.62 depict the antibacterial activity of Ag/PVA and Ag/PVA/Gr hydrogels against *S. aureus* TL and *E. coli* in PB, respectively.

Both Ag/PVA and Ag/PVA/Gr hydrogels significantly reduced bacterial cell viability after just 1 h of incubation when compared to the initial number of cells in suspension. Ag/PVA resulted in a three logarithmic unit reduction of *S. aureus* colonies and a two logarithmic unit reduction of *E. coli* colonies, while Ag/PVA/Gr resulted in complete reduction of *S. aureus* and a five logarithmic

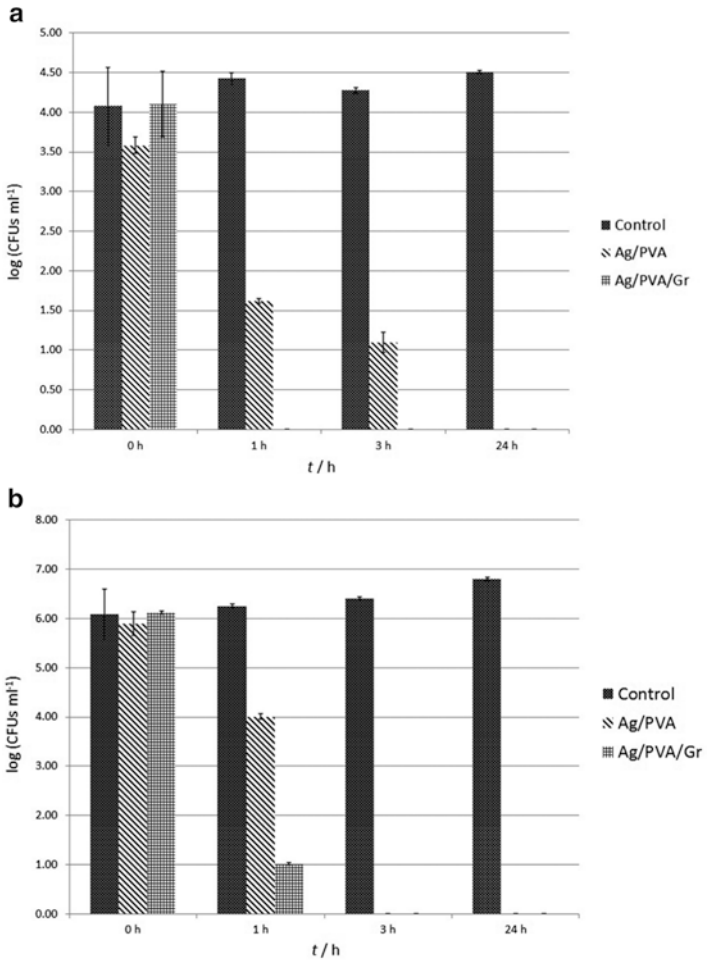

Fig. 4.61 Reduction of viable cell number of (**a**) *S. aureus* and (**b**) *E. coli* after contact with Ag/PVA and Ag/PVA/Gr hydrogels for 0, 1, 3, and 24 h in PB as compared to the control w/o samples (reprinted from [132] with permission from Elsevier)

unit reduction of *E. coli* colonies (Fig. 4.61). Ag/PVA killed all *S. aureus* colonies after 24 h and all *E. coli* colonies after 3 h (Fig. 4.62).

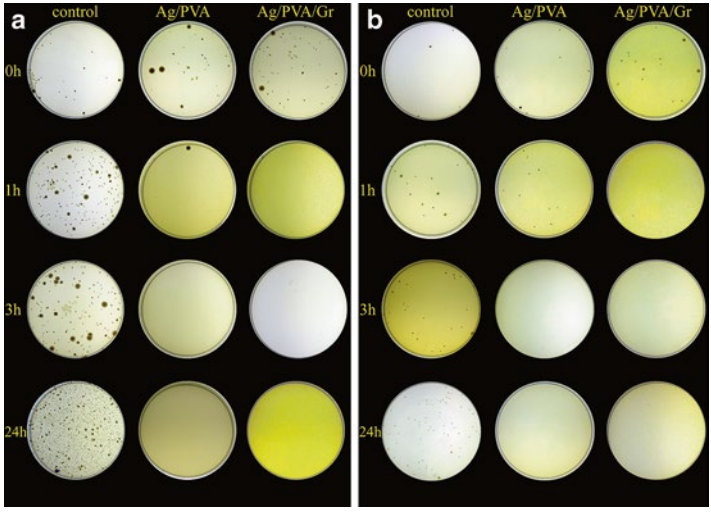

Fig. 4.62 Antibacterial activity of: control—×10,000 dilution, Ag/PVA—directly from the suspension and Ag/PVA/Gr—directly from the suspension, samples on LB agar plates after 0, 1, 3, and 24 h against (**a**) *S. aureus* and (**b**) against *E. coli* (reprinted from [132] with permission from Elsevier)

In contrast, Ag/PVA/Gr completely destroyed all *S. aureus* TL and *E. coli* colonies after 3 and 24 h, respectively (Fig. 4.62). The greater antibacterial activity of Ag/PVA/Gr than Ag/PVA could be a consequence of the smaller dimensions of the AgNPs embedded in the hydrogel network, as discussed earlier. Based on these results, the immediate release of silver ions results in a rapid drop in the number of CFU after 1 h of exposure, indicating that both Ag/PVA and Ag/PVA/Gr can prevent biofilm formation.

4.5 Conclusions

Silver nanoparticles (AgNPs) in combination with biocompatible polymer (alginate, PVP, and PVA) solutions and hydrogels provide possibilities for the design of a variety of antimicrobial products attractive for biomedical use, such as wound dressings and

potentially, soft tissue implants. Electrochemical synthesis of AgNPs in polymer solutions is especially attractive for biomedical applications, since it provides high purity of nanoparticles and precise control of the nanoparticle size.

It was found that increase in $AgNO_3$ concentration in the initial alginate solution, applied current density, and time increased the concentration and decreased the size of electrochemically synthesized Ag nanoparticles. Ag/alginate colloid solutions were successfully utilized for production of alginate hydrogel microbeads with incorporated Ag nanoparticles, which were demonstrated to efficiently release the AgNPs as antimicrobial agents against *S. aureus* cultures. The electrochemical synthesis coupled with electrostatic extrusion technique is shown to be a simple procedure that allows for easy production of alginate hydrogel microbeads with Ag nanoparticles and are attractive for potential applications as biocompatible carriers and/or efficient donors of AgNPs. Practically all Ag^+ ions added to the alginate solution are reduced during the electrochemical synthesis indicating high efficiency of this production method. Furthermore, AgNPs were preserved during manipulation and gelation of the Ag/alginate colloid solution yielding even higher concentrations in nanocomposite microbeads for about 20 % as compared to the source colloid solutions. Incorporation of AgNPs in alginate microbeads slightly affected biomechanical properties of the packed beds determined in a biomimetic bioreactor, strengthening the gel under dynamic compression but inducing easier polymer restructuring during relaxation and lowering the equilibrium unconfined compression modulus. In addition, the Ag/alginate colloid solutions can be mixed with solutions of other biocompatible polymers and submitted to different gelation procedures in order to form nanocomposite hydrogels with mechanical, antimicrobial and biodegradation properties that can be tuned according to specific utilization requirements. The use of 3D cultures and biomimetic bioreactors is valuable when developing novel biomaterials and predicting the biomaterial behavior upon implantation. In specific, bovine calf chondrocytes in monolayer cultures were shown to be more sensitive to released AgNPs and/or ions as compared to chondrocytes immobilized in alginate microbeads and cultured in perfusion bioreactors. In vivo

study on a rat burn model has demonstrated potentials of the novel nanocomposite materials based on alginate and AgNPs as wound dressing.

The Ag/PVP hydrogel nanocomposites with the highest concentration of AgNPs were obtained by silver ion reduction within the PVP matrix. The investigation of the mechanical properties under bioreactor conditions suggested that the Ag/PVP nanocomposites met the requirements required for wound dressing applications. The release of silver from the Ag/PVP nanocomposites was confirmed both by an investigation of silver release kinetics under static conditions and by the antimicrobial activity against *S. aureus*, indicating that even after 28 days, the nanocomposites had still retained about 20 % of the initial silver content. Biocompatibility of these Ag/PVP nanocomposites was investigated by cytotoxicity assays in PBMC and HeLa cell cultures. It was shown that the cytotoxicity of AgNPs released from Ag/PVP nanocomposites is dose dependant, so that slight cytotoxicity is induced by Ag/PVP nanocomposites synthesized from 1 mmol dm^{-3} $AgNO_3$ solution. Kinetics of silver release was examined under static conditions, continuous SBF perfusion (in perfusion bioreactors), and under dynamic compression coupled with SBF perfusion (in the biomimetic bioreactor simulating in vivo conditions in articular cartilage). Diffusion was the dominant mechanism of silver release in static conditions and under SBF perfusion, while a slight contribution of dynamic compression was observed in the biomimetic bioreactor. Silver release kinetics modeling provided estimation of the time allowed for PBMC to be safely exposed to Ag/PVP nanocomposites under static and perfusion conditions.

AgNPs were successfully incorporated into PVA and PVA/Gr matrices using electrochemical silver ion reduction to obtain stable colloid dispersions, films, and hydrogels. UV–Vis, TEM, CV, and FE-SEM demonstrated that AgNPs in Ag/PVA/Gr nanocomposites had smaller dimensions than those in Ag/PVA nanocomposites due to graphene sheets embedded between PVA chains. Ag/PVA/Gr nanocomposites exhibited greater thermal stability and better mechanical properties (tensile strength increased by 16.4 % and Young's modulus by 126.9 %) than Ag/PVA nanocomposites. Slow

silver release, as well as the high content of silver remaining (76 %) after 28 days in simulated body fluid confirmed that both Ag/PVA/Gr and Ag/PVA hydrogels can preserve sterility over time. This characteristic, together with their strong antibacterial activity, indicates that Ag/PVA/Gr and Ag/PVA hydrogels are excellent candidates for soft tissue implants and wound dressings.

Acknowledgments The author wishes to thank all coworkers who contributed with their work to obtain the experimental results presented in this chapter. Their names can be seen in our joint papers listed in the references.

This research was financed by the Ministry of Education, Science and Technological Development, Republic of Serbia, contract No. III 45019.

References

1. Bhattacharya R, Mukherjee P (2008) Biological properties of "naked" metal nanoparticles. Adv Drug Deliv Rev 60:1289–1306
2. Seo SY, Lee GH, Lee SG, Jung SY, Lim JO, Choi JH (2012) Alginate-based composite sponge containing silver nanoparticles synthesized in situ. Carbohydr Polym 90:109–115
3. Abou El-Nour KMM, Eftaiha A, Al-Warthan A, Ammar RAA (2010) Synthesis and applications of silver nanoparticles. Arab J Chem 3:135–140
4. Sharma VK, Yngard RA, Lin Y (2009) Silver nanoparticles: green synthesis and their antimicrobial activities. Adv Colloid Interface Sci 145:83–96
5. Obradovic B, Miskovic-Stankovic V (2013) Silver nanoparticles in alginate solutions and hydrogels aimed for biomedical applications. In: Armentano I, Kenny JM (eds) Silver nanoparticles: synthesis, uses and health concerns. Nova Science, Hauppauge, pp 247–260
6. Armentano I, Dottori M, Fortunati E, Mattioli S, Kenny JM (2010) Biodegradable polymer matrix nanocomposites for tissue engineering: a review. Polym Degrad Stab 95:2126–2146
7. Martinsen A, Skjak-Braek G, Smidsrod O (1989) Alginate as immobilization material. I. Correlation between chemical and physical properties of alginate gel beads. Biotechnol Bioeng 33:79–89
8. Gombotz WR, Wee SF (1998) Protein release from alginate matrices. Adv Drug Deliv Rev 31:267–285
9. Drury JL, Dennis RG, Mooney DJ (2004) The tensile properties of alginate hydrogels. Biomaterials 25:3187–3199
10. Melvik JE, Dornish M (2005) Alginate as a carrier for cell immobilisation. In: Nedovic V, Willaert RG (eds) Focus on biotechnology: fundamentals of

cell immobilisation biotechnology. Kluwer Academic, Dordrecht, pp 33–53
11. Qin Y (2005) Silver-containing alginate fibres and dressings. Int Wound J 2:172–176
12. Augst AD, Kong HJ, Mooney DJ (2006) Alginate hydrogels as biomaterials. Macromol Biosci 6:623–633
13. Wiegand C, Heinze T, Hipler U-C (2009) Comparative in vitro study on cytotoxicity, antimicrobial activity, and binding capacity for pathophysiological factors in chronic wounds of alginate and silver-containing alginate. Wound Repair Regen 17:511–521
14. Dubas ST, Pimpan V (2008) Optical switch from silver nanocomposite thin films. Mater Lett 62:3361–3363
15. Marie Arockianathan P, Sekara S, Sankara S, Kumaran B, Sastry TP (2012) Evaluation of biocomposite films containing alginate and sago starch impregnated with silver nano particles. Carbohydr Polym 90:717–724
16. Liu Y, Chen S, Zhong L, Wu G (2009) Preparation of high-stable silver nanoparticle dispersion by using sodium alginate as a stabilizer under gamma radiation. Radiat Phys Chem 78:251–255
17. Sharma S, Sanpui P, Chattopadhyay A, Ghosh SS (2012) Fabrication of antibacterial silver nanoparticle—sodium alginate–chitosan composite films. RSC Adv 2:5837–5843
18. Rodrigues-Sanchez L, Blanco MC, Lopez-Quintela MA (2000) Electrochemical synthesis of silver nanoparticles. J Phys Chem B 104:9683–9688
19. Obradovic B, Miskovic-Stankovic V, Jovanovic Z, Stojkovska J (2010) Production of alginate microbeads with incorporated silver nanoparticles. The Intellectual Property Office of the Republic of Serbia Patent No. 53508, Nov 2014
20. Jovanovic Z, Stojkovska J, Obradovic B, Miskovic-Stankovic V (2012) Alginate hydrogel microbeads incorporated with Ag nanoparticles obtained by electrochemical method. Mater Chem Phys 133:182–189
21. Mohan YM, Lee K, Premkumar T, Geckeler KE (2007) Hydrogel networks as nanoreactors: a novel approach to silver nanoparticles for antibacterial applications. Polymer 48:158–164
22. Sambhy V, MacBride MM, Peterson BR, Sen A (2006) Silver bromide nanoparticle/polymer composites: dual action tunable antimicrobial materials. J Am Chem Soc 128:9798–9808
23. Slistan-Grijalva A, Herrera-Urbina R, Rivas-Silva JF, Ávalos-Borja M, Castillón-Barraza FF, Posada-Amarillas A (2005) Classical theoretical characterization of the surface plasmon absorption band for silver spherical nanoparticles suspended in water and ethylene glycol. Phys E 27:104–112
24. Slistan-Grijalva A, Herrera-Urbina R, Rivas-Silva JF, Ávalos-Borja M, Castillón-Barraza FF, Posada-Amarillas A (2005) Assessment of growth of silver nanoparticles synthesized from an ethylene glycol–silver nitrate–polyvinylpyrrolidone solution. Phys E 25:438–448

25. Angelescu DG, Vasilesku M, Somoghi R, Teodoresku VS (2010) Kinetics and optical properties of the silver nanoparticles in aqueous L64 block copolymer solutions. Colloids Surf A 366:155–162
26. Mulvaney P (1996) Surface plasmon spectroscopy of nanosized metal particles. Langmuir 12:788–800
27. Šileikaitė A, Prosyčevas I, Puišo J, Juraitis A, Guobienė A (2006) Analysis of silver nanoparticles produced by chemical reduction of silver salt solution. Mater Sci Medzg 12:287–291
28. Li X, Xu A, Xie H, Yu W, Xie W, Ma X (2010) Preparation of low molecular weight alginate by hydrogen peroxide depolymerization for tissue engineering. Carbohydr Polym 79:660–664
29. Krklješ AN, Marinović-Cincović MT, Kačarević-Popović ZM, Nedeljković JM (2007) Radiolytic synthesis and characterization of Ag-PVA nanocomposites. Eur Polym J 43:2171–2176
30. Krklješ A, Nedeljković JM, Kačarević-Popović Z (2007) Fabrication of Ag-PVA hydrogel nanocomposite by γ-irradiation. Polym Bull 58:271–279
31. Li M-G, Shang Y-J, Gao Y-C, Wang G-F, Fang B (2005) Preparation of novel mercury-doped silver nanoparticles film glassy carbon electrode and its application for electrochemical biosensor. Anal Biochem 341:52–57
32. Yin B, Ma H, Wang S, Chen S (2003) Electrochemical synthesis of silver nanoparticles under protection of poly(N-vinylpyrrolidone). J Phys Chem B 107:8898–8904
33. Lim PY, Liu RS, She PL, Hung CF, Shih HC (2006) Synthesis of Ag nanospheres particles in ethylene glycol by electrochemical-assisted polyol process. Chem Phys Lett 420:304–308
34. Bouazza S, Alonzo V, Hauchard D (2009) Synthesis and characterization of Ag nanoparticles–polyaniline composite powder material. Synth Met 159:1612–1619
35. Štofik M, Strýhal Z, Malý J (2009) Dendrimer-encapsulated silver nanoparticles as a novel electrochemical label for sensitive immunosensors. Biosens Bioelectron 24:1918–1923
36. Jin W-J, Jeon HJ, Kim JH, Youk JH (2007) A study on the preparation of poly(vinyl alcohol) nanofibers containing silver nanoparticles. Synth Met 157:454–459
37. Nedović VA, Obradović B, Leskošek CI, Trifunović O, Pešić R, Bugarski B (2001) Electrostatic generation of alginate microbeads loaded with brewing yeast. Process Biochem 37:17–22
38. Obradović B, Stojkovska J, Jovanović Ž, Mišković-Stanković V (2011) Novel hydrogel nanocomposites based on alginate and silver nanoparticles. In: Book of abstracts of the 24th European conference on biomaterials, Dublin, September 2011, poster/rapid fire presentation VII—324
39. Valodkar M, Modi S, Pal A, Thakore S (2011) Synthesis and anti-bacterial activity of Cu, Ag and Cu–Ag alloy nanoparticles: a green approach. Mater Res Bull 46:384–389

40. Mirzajani F, Ghassempour A, Aliahmadi A, Esmaeili MA (2011) Antibacterial effect of silver nanoparticles on *Staphylococcus aureu*. Res Microbiol 162:542–549
41. Fayaz AM, Balaji K, Girilal M, Yadav R, Kalaichelvan PT, Venketesan R (2010) Biogenic synthesis of silver nanoparticles and their synergistic effect with antibiotics: a study against gram-positive and gram-negative bacteria. Nanomed Nanotechnol 6:103–109
42. Ruparelia JP, Chatterjee AK, Duttagupta SP, Mukherji S (2008) Strain specificity in antimicrobial activity of silver and copper nanoparticles. Acta Biomater 4:707–716
43. Guzman M, Dille J, Godet S (2012) Synthesis and antibacterial activity of silver nanoparticles against gram-positive and gram-negative bacteria. Nanomed Nanotechnol 8:37–45
44. Goosen MFA, Mahmud ESC, M-Ghafi AS, M-Hajri HA, Al-Sinani YS, Bugarski B (1997) Immobilization of cells using electrostatic droplet generation. In: Bickerstaff GF (ed) Immobilization of enzymes and cells. Humana, Totowa, pp 16–174
45. Nedovic VA, Obradovic B, Leskosek-Cukalovic I, Vunjak-Novakovic G (2001) Immobilized yeast bioreactor systems for brewing. In: Thonart P, Hofman M (eds) Focus on biotechnology, vol IV, Engineering and manufacturing for biotechnology. Kluwer Academic, Dordrecht, pp 277–292
46. Osmokrovic A, Obradovic B, Bugarski D, Bugarski B, Vunjak-Novakovic G (2006) Development of a packed bed bioreactor for cartilage tissue engineering. FME Trans 34:65–70
47. Stojkovska J, Bugarski B, Obradovic B (2010) Evaluation of alginate hydrogels under in vivo–like bioreactor conditions for cartilage tissue engineering. J Mater Sci Mater Med 21:2869–2879
48. Keshavartz T, Ramsden G, Phillips P, Mussenden P, Bucke C (1992) Application of electric field for production of immobilized biocatalysts. Biotechnol Tech 6:445–450
49. Bugarski B, Li Q, Goosen MFA, Poncelet D, Neufeld RJ, Vunjak G (1994) Electrostatic droplet generation: mechanism of polymer droplet formation. AIChE J 40:1026–1031
50. Manojlovic V, Djonlagic J, Obradovic B, Nedovic V, Bugarski B (2006) Investigations of cell immobilization in alginate: rheological and electrostatic extrusion studies. J Chem Technol Biotechnol 81:505–510
51. Poncelet D, Babak VG, Neufeld RJ, Goosen M, Bugarski B (1999) Theory of electrostatic dispersion of polymer solutions in the production of microgel beads containing biocatalyst. Adv Colloid Interface Sci 79:213–228
52. Stojkovska J, Zvicer J, Jovanović Ž, Mišković-Stanković V, Obradović B (2012) Controlled production of alginate nanocomposites with incorporated silver nanoparticles aimed for biomedical applications. J Serb Chem Soc 77:1709–1722
53. Velings NM, Mestdagh MM (1995) Physico-chemical properties of alginate gel beads. Polym Gels Networks 3:311–330

54. Schexnailder P, Schmidt G (2009) Nanocomposite polymer hydrogels. Colloid Polym Sci 287:1–11
55. Mbhele ZH, Salemane MG, van Sittert CGCE, Nedeljkovic JM, Djokovic V, Luyt AS (2003) Fabrication and characterization of silver–polyvinyl alcohol nanocomposites. Chem Mater 15:5019–5024
56. Thomas BH, Fryman JC, Liu K, Mason J (2009) Hydrophilic-hydrophobic hydrogels for cartilage replacement. J Mech Behav Biomed Mater 2:588–595
57. Ma R, Xiong D, Miao F, Zhang J, Peng Y (2009) Novel PVP/PVA hydrogels for articular cartilage replacement. Mater Sci Eng C 29:1979–1983
58. Joshi A, Fussell G, Thomas J, Hsuan A, Lowman A, Karduna A, Vresilovic E, Marcolongo M (2006) Functional compressive mechanics of PVA/PVP nucleus pulposus replacement. Biomaterials 27:176–184
59. Zheng Y, Huang X, Wang Y, Xu H, Chen X (2009) Performance and characterization of irradiated poly(vinyl alcohol)/polyvinylpyrrolidone composite hydrogels used as cartilage replacement. J Appl Polym Sci 113:736–741
60. Carotenuto G, Pepe GP, Nicolais L (2000) Preparation and characterization of nano-sized Ag/PVP composites for optical applications. Eur Phys J B 16:11–17
61. Pastoriza-Santos I, Liz-Marzán LM (2002) Formation of PVP-protected metal nanoparticles in DMF. Langmuir 18:2888–2894
62. Eid M, El-Arnaouty MB, Salah M, Soliman E-S, Hegazy E-S A (2012) Radiation synthesis and characterization of poly(vinyl alcohol)/poly(N-vinyl-2-pyrrolidone) based hydrogels containing silver nanoparticles. J Polym Res 19:1–10
63. Shin HS, Yang HJ, Kim SB, Lee MS (2004) Mechanism of growth of colloidal silver nanoparticles stabilized by polyvinyl pyrrolidone in γ-irradiated silver nitrate solution. J Colloid Interface Sci 274:89–94
64. Wang H, Xueliang Qiao X, Chen J, Wang X, Ding S (2005) Mechanisms of PVP in the preparation of silver nanoparticles. Mater Chem Phys 94:449–453
65. Lee WF, Tsao KT (2010) Effect of silver nanoparticles content on the various properties of nanocomposite hydrogels by in situ polymerization. J Mater Sci 45:89–97
66. Yu H, Xu X, Chen X, Lu T, Zhang P, Jing X (2007) Preparation and antibacterial effects of PVA-PVP hydrogels containing silver nanoparticles. J Appl Polym Sci 103:125–133
67. Richards VN, Rath NP, Buhro WE (2010) Pathway from a molecular precursor to silver nanoparticles: the prominent role of aggregative growth. Chem Mater 22:3556–3567
68. Obradovic B, Stojkovska J, Jovanovic Z, Miskovic-Stankovic V (2012) Novel alginate based nanocomposite hydrogels with incorporated silver nanoparticles. J Mater Sci Mater Med 23:99–107
69. Sung J-M (2001) Nonisothermal phase formation kinetics in sol-gel-derived strontium bismuth tantalate. J Mater Res 16:2039–2044

70. Chraska T, Hostomsky J, Klementova M, Dubsky J (2009) Crystallization kinetics of amorphous alumina–zirconia–silica ceramics. J Eur Ceram Soc 29:3159–3165
71. Spiller KL, Laurencin SJ, Charlton D, Maher SA, Lowman AM (2008) Superporous hydrogels for cartilage repair: evaluation of the morphological and mechanical properties. Acta Biomater 4:17–25
72. Thomas J, Gomes K, Lowman A, Marcolongo M (2004) The effect of dehydration history on PVA/PVP hydrogels for nucleus pulposus replacement. J Biomed Mater Res Part B Appl Biomater 69B:135–140
73. De Vos P, Faas MM, Strand B, Calafiore R (2006) Alginate-based microcapsules for immunoisolation of pancreatic islets. Biomaterials 27:5603–5617
74. Orr DE, Burg KJL (2008) Design of a modular bioreactor to incorporate both perfusion flow and hydrostatic compression for tissue engineering applications. Ann Biomed Eng 36:1228–1241
75. Stojkovska J, Kostic D, Jovanovic Z, Vukasinovic-Sekulic M, Miskovic-Stankovic V, Obradovic B (2014) A comprehensive approach to *in vitro* functional evaluation of Ag/alginate nanocomposite hydrogels. Carbohydr Polym 111:305–314
76. Mosmann T (1983) Rapid colorimetric assay for cellular growth and survival: application to proliferation and cytotoxicity assays. J Immunol Methods 65:55–63
77. Meriç G, Dahl JE, Eystein Ruyter I (2008) Cytotoxicity of silica–glass fiber reinforced composites. Dent Mater 24:1201–1206
78. Hussain SM, Hess KL, Gearhart JM, Geiss KT, Schlager JJ (2005) In vitro toxicity of nanoparticles in BRL 3A rat liver cells. Toxicol In Vitro 19:975–983
79. Park EJ, Yi J, Kim Y, Choi K, Park K (2010) Silver nanoparticles induce cytotoxicity by a Trojan-horse type mechanism. Toxicol In Vitro 24:872–878
80. Panáček A, Kvítek L, Prucek R, Kolář M, Večeřová R, Pizúrová N, Sharma VK, Nevěčná T, Zbořil R (2006) Silver colloid nanoparticles: synthesis, characterization, and their antibacterial activity. J Phys Chem B 110:16248–16253
81. Kong H, Jang J (2008) Antibacterial properties of novel poly(methyl methacrylate) nanofiber containing silver nanoparticles. Langmuir 24:2051–2056
82. Sanpui P, Murugadoss A, Durga Prasad PV, Ghosh SS, Chattopadhyay A (2008) The antibacterial properties of a novel chitosan–Ag-nanoparticle composite. Int J Food Microbiol 124:142–146
83. Marius S, Lucian H, Marius M, Daniela P, Irina G, Romeo-Iulian O, Simona D, Viorel M (2011) Enhanced antibacterial effect of silver nanoparticles obtained by electrochemical synthesis in poly(-amide-hydroxyurethane) media. J Mater Sci Mater Med 22:789–796
84. Morones JR, Elechiguerra JL, Camacho A, Holt K, Kouri JB, Ramírez JT, Yacaman MJ (2005) The bactericidal effect of silver nanoparticles. Nanotechnology 16:2346–2353

85. Pal S, Tak KY, Song MJ (2007) Does the antibacterial activity of silver nanoparticles depend on the shape of the nanoparticle? A study of the Gram-negative bacterium Escherichia coli. Appl Environ Microbiol 73:1712–1720
86. Sondi I, Salopek-Sondi B (2004) Silver nanoparticles as antimicrobial agent: a case study on *E. coli* as a model for Gram-negative bacteria. J Colloid Interface Sci 275:177–182
87. Paul W, Sharma CP (2004) Chitosan and alginate wound dressings: a short review. Trends Biomater Artif Organs 18:18–23
88. Queen D, Orsted H, Sanada H, Sussman G (2004) A dressing history. Int Wound J 1:59–77
89. Travan A, Pelillo C, Donati I, Marsich E, Benincasa M, Scarpa T et al (2009) Non-cytotoxic silver nanoparticle-polysaccharide nanocomposites with antimicrobial activity. Biomacromolecules 10:1429–1435
90. Dubas ST, Wacharanad S, Potiyaraj P (2011) Tunning of the antimicrobial activity of surgical sutures coated with silver nanoparticles. Colloids Surf A 380:25–28
91. Vidovic S, Zvicer J, Stojkovska J, Miskovic-Stankovic V, Obradovic B (2012) Nanocomposite microfibers based on alginate and PVA hydrogels with incorporated silver nanoparticles. In: Abstract of the 3rd TERMIS world congress, Vienna, Austria, 29.P18. J Tiss Eng Reg Med 6(suppl 1):189
92. Stojkovska J, Jovanović Ž, Jančić I, Bufan B, Milenković M, Mišković-Stanković V, Obradović B (2013) Novel Ag/alginate nanocomposites for wound treatments: animal studies. Wounds 4(1–2):17–22
93. dos Santos Tavares Pereira D, Madruga Lima-Ribeiro MH, de Pontes-Filho NT, dos Anjos Carneiro-Leão AM, dos Santos Correia MT (2012) Development of animal model for studying deep second-degree thermal burns. J Biomed Biotechnol Article ID 460841, 7 pp
94. Mišković-Stanković V, Stojkovska J, Jovanović Ž, Jančić I, Bufan B, Milenković M, Obradović B (2014) Novel Ag/alginate nanocomposites for wound ttreatments. In: Abstract book of the VI Serbian Congress of Pharmacy with international participations, Belgrade, Serbia, p 122
95. Jovanović Ž, Radosavljević A, Stojkovska J, Nikolić B, Obradović B, Kačarević-Popović Z, Mišković-Stanković V (2014) Silver/poly(*N*-vinyl-2-pyrrolidone) hydrogel nanocomposites obtained by electrochemical synthesis of silver nanoparticles inside the polymer hydrogel aimed for biomedical applications. Polym Compos 35(2):217–226
96. Hovel H, Fritz S, Hilger A, Kreibig V, Vollmer M (1993) Width of cluster plasmon resonances: bulk dielectric functions and chemical interface damping. Phys Rev B 48:18178–18188
97. He R, Qian X, Yin J, Zhu Z (2002) Preparation of polychrome silver nanoparticles in different solvents. J Mater Chem 12:3783–3786
98. Kora AJ, Sashidhar RB, Arunachalam J (2010) Gum kondagogu (Cochlospermum gossypium): a template for the green synthesis and stabilization of silver nanoparticles with antibacterial application. Carbohydr Polym 82:670–679

99. Kora AJ, Sashidhar RB, Arunachalam J (2012) Aqueous extract of gum olibanum (Boswellia serrata): a reductant and stabilizer for the biosynthesis of antibacterial silver nanoparticles. Process Biochem 47:1516–1520
100. Davis TP, Huglin MB, Yip DCF (1988) Properties of poly (N-vinyl-2-pyrrolidone) hydrogels crosslinked with ethyleneglycol dimethacrylate. Polymer 29:701–706
101. Nickerson MT, Paulson AT, Wagar E, Farnworth R, Hodge SM, Rousseau D (2006) Some physical properties of crosslinked gelatin–maltodextrin hydrogels. Food Hydrocoll 20:1072–1079
102. Rattanaruengsrikul V, Pimpha N, Supaphol P (2009) Development of gelatin hydrogel pads as antibacterial wound dressings. Macromol Biosci 9:1004–1015
103. Crank J (1970) The mathematics of diffusion. Clarendon Press, Oxford
104. Schmal H, Niemeyer P, Roesslein M, Hartl D, Loop T, Südkamp NP, Stark GB, Mehlhorn AT (2007) Comparison of cellular functionality of human mesenchymal stromal cells and PBMC. Cytotherapy 9:69–79
105. Jovanović Ž, Radosavljević A, Kačarević-Popović Z, Stojkovska J, Perić-Grujić A, Ristić M, Matić IZ, Juranić ZD, Obradović B, Mišković-Stanković V (2013) Bioreactor validation and biocompatibility of Ag/poly(*N*-vinyl-2-pyrrolidone) hydrogel nanocomposites. Colloids Surf B 105:230–235
106. Hidalgo E, Domínguez C (1998) Study of cytotoxicity mechanisms of silver nitrate in human dermal fibroblasts. Toxicol Lett 98:169–179
107. Jovanović Ž, Krklješ A, Stojkovska J, Tomić S, Obradović B, Mišković-Stanković V, Kačarević-Popović Z (2011) Synthesis and characterization of silver/poly(*N*-vinyl-2-pyrrolidone) hydrogel nanocomposite obtained by *in situ* radiolytic method. Radiat Phys Chem 80:1208–1215
108. Dewire P, Einhorn TA (2001) Diagnosis and Medical/Surgical Management. In: Moskowitz RW, Howell DS, Altman RD, Buckwalter JA, Goldberg VM (eds) Osteoarthritis. W.B. Saunders, Philadelphia, pp 49–68
109. Levick JR, Mason RM, Coleman PJ, Scott D (1999) Physiology of synovial fluid and trans-synovial flow. In: Archer CW, Benjamin M, Caterson B, Ralphs JR (eds) Biology of the synovial joint. Harwood Academic, Amsterdam, pp 235–252
110. Han M, Yun J, Kim H, Lee Y (2012) Effect of surface modification of graphene oxide on photochemical stability of poly(vinyl alcohol)/graphene oxide composites. J Ind Eng Chem 18:752–756
111. Yang L, Li Y, Hu H, Jin X, Ye Z, Ma Y, Zhang S (2011) Preparation of novel spherical PVA/ATP composites with macroreticular structure and their adsorption behavior for methylene blue and lead in aqueous solution. Chem Eng J 173:446–455
112. Alcântara MTS, Brant AJC, Giannini DR, Pessoa JOCP, Andrade AB, Riella HG, Lugão AB (2012) Influence of dissolution processing of PVA blends on the characteristics of their hydrogels synthesized by radiation—part I: gel fraction, swelling, and mechanical properties. Radiat Phys Chem 81:1465–1470

113. Gaume J, Rivaton A, Thérias S, Gardette J-L (2012) Influence of nanoclays on the photochemical behaviour of poly(vinyl alcohol). Polym Degrad Stab 97:488–495
114. Jipa IM, Stroescu M, Stoica-Guzun A, Dobre T, Jinga S, Zaharescu T (2012) Effect of gamma irradiation on biopolymer composite films of poly(vinyl alcohol) and bacterial cellulose. Nucl Instrum Methods B 278:82–87
115. Constantina M, Fundueanua G, Bortolotti F, Cortesi R, Ascenzi P, Menegatti E (2004) Preparation and characterisation of poly(vinyl alcohol)/cyclodextrin microspheres as matrix for inclusion and separation of drugs. Int J Pharm 285:87–96
116. Georgieva N, Bryaskova R, Tzoneva R (2012) New polyvinyl alcohol-based hybrid materials for biomedical application. Mater Lett 88:19–22
117. Islam A, Yasin T (2012) Controlled delivery of drug from pH sensitive chitosan/poly (vinyl alcohol) blend. Carbohydr Polym 88:1055–1060
118. Gonzalez JS, Maiolo AS, Hoppe CE, Alvarez VA (2012) Composite gels based on poly (vinyl alcohol) for biomedical uses. Proc Mater Sci 1:483–490
119. Maiolo AS, Amado MN, Gonzalez JS, Alvarez VA (2012) Development and characterization of poly (vinyl alcohol) based hydrogels for potential use as an articular cartilage replacement. Mater Sci Eng C 32:1490–1495
120. Killeen D, Frydrych M, Chen B (2012) Porous poly (vinyl alcohol)/sepiolite bone scaffolds: preparation, structure and mechanical properties. Mater Sci Eng C 32:749–757
121. Jiang S, Liu S, Feng W (2011) PVA hydrogel properties for biomedical application. J Mech Behav Biomed Mater 4:1228–1233
122. Zaina NAM, Suhaimi MS, Idris A (2011) Development and modification of PVA–alginate as a suitable immobilization matrix. Process Biochem 46:2122–2129
123. Khodja AN, Mahlous M, Tahtat D, Benamer S, Youcef SL, Chader H, Mouhoub L, Sedgelmaci M, Ammi N, Mansouri MB, Mameri S (2013) Evaluation of healing activity of PVA/chitosan hydrogels on deep second degree burn: pharmacological and toxicological tests. Burns 39:98–104
124. Singh B, Pal L (2011) Radiation crosslinking polymerization of sterculia polysaccharide–PVA–PVP for making hydrogel wound dressings. Int J Biol Macromol 48:501–510
125. Huang M-H, Yang M-C (2008) Evaluation of glucan/poly(vinyl alcohol) blend wound dressing using rat models. Int J Pharm 346:38–46
126. Singh B, Pal L (2012) Sterculia crosslinked PVA and PVA-poly(AAm) hydrogel wound dressings for slow drug delivery: mechanical, mucoadhesive, biocompatible and permeability properties. J Mech Behav Biomed Mater 9:9–21
127. Păduraru OM, Ciolacu D, Darie RN, Vasile C (2012) Synthesis and characterization of polyvinyl alcohol/cellulose cryogels and their testing as carriers for a bioactive component. Mater Sci Eng C 32:2508–2515

128. Salarizadeh P, Javanbakht M, Abdollahi M, Naji L (2013) Preparation, characterization and properties of proton exchange nanocomposite membranes based on poly(vinyl alcohol) and poly(sulfonic acid)-grafted silica nanoparticles. Int J Hydrogen Energy 38:5473–5479
129. Ahmad AL, Yusuf NM, Ooi BS (2012) Preparation and modification of poly (vinyl) alcohol membrane: effect of crosslinking time towards its morphology. Desalination 287:35–40
130. Surudžić R, Jovanović Ž, Bibić N, Nikolić B, Mišković-Stanković V (2013) Electrochemical synthesis of silver nanoparticles in poly(vinyl alcohol) solution. J Serb Chem Soc 78:2087–2098
131. Buraidah MH, Arof AK (2011) Characterization of chitosan/PVA blended electrolyte doped with NH_4I. J Non-Cryst Solids 357:3261–3266
132. Surudzić R, Janković A, Bibić N, Vukašinović-Sekulić M, Perić-Grujić A, Mišković-Stanković V, Park SJ, Rhee KY (2016) Physico-chemical and mechanical properties and antibacterial activity of silver/poly(vinyl alcohol)/graphene nanocomposites obtained by electrochemical method. Compos Part B 85:102–112
133. Van Hoa N, Byung-Keuk K, Youl-Lae J, Jae-Jin S (2012) Preparation and antibacterial activity of silver nanoparticles-decorated graphene composites. J Supercrit Fluids 72:28–35
134. Li J, Liu C (2010) Ag/graphene heterostructures: synthesis, characterization and optical properties. Eur J Inorg Chem 2010:1244–1248
135. Baby TT, Ramaprabhu S (2011) Synthesis and nanofluid application of silver nanoparticles decorated graphene. J Mater Chem 21:9702–9709
136. Ferrari AC, Meyer JC, Scardaci V, Casiraghi C, Lazzeri M, Mauri F, Piscanec S, Jiang D, Novoselov KS, Roth S, Geim AK (2006) Raman spectrum of graphene and graphene layers. Phys Rev Lett 97:187401–187404
137. Ferrari AC (2007) Raman spectroscopy of graphene and graphite: disorder, electron-phonon coupling, doping, and nonadiabatic effects. Solid State Commun 143:47–57
138. Bryaskova R, Pencheva D, Kale GM, Lad U, Kantardjiev T (2010) Synthesis, characterisation and antibacterial activity of PVA/TEOS/Ag-Np hybrid thin films. J Colloid Interface Sci 349:77–85
139. Tang Z, Lei Y, Guo B, Zhang L, Jia D (2012) The use of rhodamine B-decorated graphene as a reinforcement in polyvinyl alcohol composites. Polymer 53:673–680
140. Wang S, Zhang Y, Abidi N, Cabrales L (2009) Wettability and surface free energy of graphene films. Langmuir 25:11078–11081
141. Ouyang Y, Chen L (2011) Surface-enhanced Raman scattering studies of few-layer graphene on silver substrate with 514 nm excitation. J Mol Struct 992:48–51
142. Liu Y, Huang J, Li H (2013) Synthesis of hydroxyapatite–reduced graphite oxide nanocomposites for biomedical applications: oriented nucleation and epitaxial growth of hydroxyapatite. J Mater Chem B 1:1826–1834

143. Josh AC, Markad GB, Haram SK (2015) Rudimentary simple method for the decoration of graphene oxide with silver nanoparticles: their application for the amperometric detection of glucose in the human blood samples. Electrochim Acta 161:108–114
144. Bon SB, Valentini L, Verdejo R, Fierro JLG, Peponi L, Lopez-Manchado MA, Kenny JM (2009) Plasma fluorination of chemically derived graphene sheets and subsequent modification with butylamine. Chem Mater 21:3433–3438
145. Yuan X (2011) Enhanced interfacial interaction for effective reinforcement of poly(vinyl alcohol) nanocomposites at low loading of graphene. Polym Bull 67:1785–1797
146. Gong L, Yin B, L-p L, Yang M-b (2015) Nylon-6/Graphene composites modified through polymeric modification of graphene. Compos Part B Eng 73:49–56

Chapter 5
Biocompatible Hydroxyapatite-Based Composite Coatings Obtained by Electrophoretic Deposition for Medical Applications as Hard Tissue Implants

Vesna B. Mišković-Stanković

5.1 Introduction

Synthetic hydroxyapatite (HAP) as the most promising ceramic material used for biomedical applications has excellent bioactivity, biocompatibility, and the chemical composition similar to that of the bone. The development of synthetic materials with close resemblance to the biological and mechanical properties of natural bone tissue is required to overcome load-bearing problem. Titanium has found wide application as basic metal material due to its attributes of strength, stiffness, toughness, impact resistance, and corrosion resistance for manufacturing bioceramic coatings such as hydroxyapatite. However, HAP is very brittle, and for this reason, a great attention has been focused on the development of composite HAP coatings. Natural biodegradable polymer lignin (Lig) is considered as alternative for the development of the new biocomposite coating. On the other hand, the general idea of using graphene (Gr) as

V.B. Mišković-Stanković (✉)
Faculty of Technology and Metallurgy, University of Belgrade, Karnegijeva 4, P.O. Box 3503, 11120 Belgrade, Serbia
e-mail: vesna@tmf.bg.ac.rs

S. Djokić (ed.), *Biomedical and Pharmaceutical Applications of Electrochemistry*, Modern Aspects of Electrochemistry 60,
DOI 10.1007/978-3-319-31849-3_5

nanofiller is to minimize the brittleness of HAP and gain improved mechanical properties of biocomposite coating. However, in recent years problems regarding bacterial infection of bone implants have been resulting in body rejection. In order to stop bacterial infection, it is crucial to inhibit bacterial adhesion since biofilm can be very resistant to immune response and antibiotics. The antimicrobial activity of silver has been known for a very long time. Additionally, silver cation does not develop bacterial resistance and at the same time shows low toxicity to human cells. Hence, the possibility to prevent the implant infections using the antimicrobial properties of Ag has generated great interest in the development of silver-doped hydroxyapatite coatings.

This chapter explored the novel nanostructured biomaterials suitable for medical applications as for hard tissue implants (hips, knees, ankle, shoulder, elbow joints), drug delivery devices, and in dentistry as dental restorations, implants, orthodontics, synthesized according to original electrochemical procedures. It refers to lignin- and graphene-based nanocomposite coatings doped with silver and deposited on titanium substrate using electrophoretic deposition (EPD) method. EPD has allowed the formation of thin films of controlled thickness and morphology, by changing the deposition parameters (voltage, time). Based on MTT test of cytotoxicity, antibacterial tests and in vitro bioactivity test the evidence presented here demonstrated that novel electrophoretically produced coatings for hard tissue implants are an excellent candidates for future biomedical applications.

5.2 Hydroxyapatite Coatings for Hard Tissue Implants

Traditional metallic implants are irreplaceable in repairing damaged bone tissue, but the greatest concern is their gradual electrochemical degradation [1]. Bone fractures are one of the most common forms of injury along with bone diseases and that is why metallic implants with bioactive and biocompatible-coated material are often used in order to enhance the bone healing process [2].

Synthetic hydroxyapatite (HAP, $Ca_{10}(PO_4)_6(OH)_2$) has long been known as one of the best coating materials for metallic implants due to its biocompatible, osteoconductive, and osteoinductive properties [3]. Besides controlling the stoichiometry of synthetic HAP, the control of crystallinity, porosity, particle shape, surface area, and agglomeration characteristics are of great interest [4, 5].

Materials implanted in the human body face an environment that is extremely delicate, but at the same time hostile. The implants face a severe corrosive environment that includes blood and body fluid composed of several constituents (water, sodium, chlorine, proteins, plasma, and amino acids) along with mucin in the case of saliva. The noncompatible metal ions released by the implants into the body are found to cause allergic and toxic reactions. In order to minimize direct contact between metal and body fluids, and to limit the release of undesired metallic ions in the body, biocompatible and bioactive coatings on the metallic substrate, such as HAP, are suggested by many researchers [6–8].

Titanium and its alloys have become the material of choice for long-term implant application for their favorable corrosion resistance as well as their low toxicity, biocompatibility, and good mechanical properties, such as high strength, durability, and light weight [9–12]. Hence, a good combination of the biocompatibility of hydroxyapatite and the excellent mechanical properties of titanium are considered a promising approach to fabricate more suitable bone implants. The concept of coating titanium implant surfaces with HAP combines the mechanical benefits of metal alloys with the biocompatibility of HAP [13].

Postoperative infections are the result of bacterial adhesion to the implant surface and subsequent biofilm formation at the implantation site [14]. In order to stop bacterial infection, it is crucial to inhibit bacterial adhesion since biofilm can be very resistant to immune response and antibiotics [15]. The antimicrobial activity of silver and silver ions has been known for a very long time; additionally, silver cation does not develop bacterial resistance and at the same time shows low toxicity to human cells [16, 17]. Therefore, the possibility to prevent the bone implant infections by using antimicrobial properties of Ag has generated great interest in the development of silver-doped HAP coatings [18].

There are various methods to deposit ceramic coatings on metal surfaces, plasma spraying, sputtering, pulsed laser deposition, sol–gel, electrophoresis, and electrodeposition [19]. Among these, electrophoretic deposition (EPD) emerges as a method of choice due to its simple setup and formation of uniform coatings, even on substrates of complex shape [5, 20–23]. Other advantages are that EPD represents an inexpensive electrochemical technique that can be carried out at room temperature with the possibility of coating thickness and morphology controlled by adjusting deposition parameters. The necessary condition that enables successful EPD is a stable suspension/sol, where the particles have a high zeta potential while the ionic conductivity of the suspension is kept at a low value [5, 24].

In recent years, research has been focused to improve the biocomposite HAP/polymer coatings and other functional properties of the implant, such as good adhesion properties, chemical stability, bioactivity, biocompatibility, and antimicrobial properties [25]. Biodegradable natural or synthetic polymers are used to develop new biocomposite coatings. Use of the polymer dictates that thermal treatment of the composite material to be performed at lower sintering temperatures [26]. Development of HAP/biopolymer coatings is especially important for applications in medicine, specifically transplantational surgery, because their mechanical properties are most similar to natural bone tissue [27]. Other characteristics of biocomposite coating that make it biocompatible are nontoxicity, corrosion stability, and controlled biodegradibility, as well as elastic modulus, therefore suitable for specific biomedical applications. The use of natural biopolymers, such as polysaccharides—alginate, chitosan/chitin and hyaluronic acid, proteins—collagen and silk, as well as different biofibers—lignin and cellulose, offers the advantage of improving the adhesion of bioceramic coating by decreasing its brittleness [27]. Significant interest and investigations were focused on the fabrication of composite coatings: HAP/chitosan [18, 20, 28–32], HAP/chitosan/carbon nanotubes [33], aluminosilicate nanotubes/HAP/hyaluronic acid [34], HAP/alginate [35], Bioglass®/HAP/chitosan and Bioglass®/HAP/alginate coatings [36], HAP/glucose [37], Y_2O_3/HAP [38], HAP/lignin [39–47], and HAP/graphene [48, 49].

5.3 Hydroxyapatite/Lignin Coatings for Hard Tissue Implants

5.3.1 Hydroxyapatite/Lignin Coatings Electrodeposited on Titanium Substrate

Based on recent research organosolv lignin emerged as a suitable candidate for composite hydroxyapatite/natural polymer coatings. Lignin (Lig) is a complex natural polyphenolic polymer connected with a variety of chemical bonds [50]. Lignin possesses antioxidant and antimicrobial properties; therefore, its incorporation in different materials is interesting in medical applications due to its biocompatibility, hydrophilicity, and thermal stability [39, 41, 42]. As complex natural polymer networks composed primarily of phenolic moieties, lignins have a wide variety of chemical bonds [43, 50]. Among the functional groups present in lignin, the most reactive chemical sites are phenolic hydroxyl groups [51]. Other major chemical functional groups in lignins include methoxyl, carbonyl, and carboxyl groups, varying on the plant origin and the applied pulping processes [51]. Organosolv lignins are being examined because they show significantly improved solubility and thermal properties compared to sulfite or kraft lignins [40]. Biocomposite hydroxyapatite/lignin as a 3D scaffold was first studied by Mansur et al. [41] where organosolv lignin polymer was used. Pan et al. [52] examined the solubility and physicochemical properties of extracted organosolv lignin. Excellent solubility of lignin, more than 90 %, is obtained from the solution which contained more than 65 % of ethanol. For the same reason, the HAP/Lig coatings on titanium precipitated from ethanol suspensions.

Recently, hydroxyapatite/lignin (HAP/Lig) and silver/hydroxyapatite/lignin (Ag/HAP/Lig) biocomposite coatings on titanium were developed by EPD technique, mimicking the structure and properties of natural bone [43–47] with the aim to improve porosity structure to prompt osteogenesis. Organosolv Alcell lignin was extracted from a mixture of North American hardwoods (maple, birch, and poplar) by an organosolv process using a mixture of ethanol–water. A nanosized HAP powder was obtained using a

modified chemical precipitation method, by the reaction of calcium oxide with phosphoric acid described elsewhere [53, 54]. A modified chemical precipitation method was also employed for preparing the Ag/HAP powder ($Ca_{9.95}Ag_{0.05}(PO_4)_6(OH)_2$) using calcium oxide and $AgNO_3$ solution, yielding a final concentration of silver ion of 0.4 ± 0.1 wt% [43, 45].

The particle size distribution (PSD) measurement of HAP/Lig and Ag/HAP/Lig with 1 wt% Lig suspensions was made by using dynamic light scattering technique. The obtained average particle size is around 363.0 nm, for HAP/Lig suspension, and 207.3 nm, for Ag/HAP/Lig suspension [43, 45]. It was assumed for both suspensions that bigger particles are agglomerates of smaller ones, since transmission electron microscopy images of the HAP powder demonstrated that HAP particles are nanosized in the range of 50–100 nm [53]. Also, it was noticed that pure HAP suspension had much higher average particle size value (1500 nm) compared to HAP/Lig suspension [43]. Therefore, it can be concluded that lignin decreases agglomeration of HAP nanoparticles.

The ζ-potential is a measure of the strength of interactions between colloid particles, and hence it relates to colloid solution stability. A biomaterial's ζ-potential indicates its electric surface properties; bioceramic particles must be electrically charged for electrophoretic deposition on metal substrates. High positive ζ-potential values of HAP/Lig and Ag/HAP/Lig suspensions of 28 and 29 mV, respectively, indicate positively charged particle surfaces of HAP/Lig and Ag/HAP/Lig particles, thus enabling the attraction of particles by negatively charged cathode and successful electrophoretic deposition of coatings on titanium substrate [44, 45].

Electrophoretic deposition of HAP/Lig and Ag/HAP/Lig coatings on titanium was performed from ethanol suspensions [43–46]. The deposition parameters, applied voltage, and deposition time significantly influence the coating morphology and thickness. The process was optimized by varying EPD voltage from 50 to 100 V at different deposition times of 30 s to 5 min [43]. Increase in deposition time up to 5 min at constant voltage of 60 V enhances the mass of HAP/Lig and Ag/HAP/Lig coatings since more particles are reaching the cathode. On the other hand, the obtained coatings are more porous since greater amounts of hydrogen evolved

from the cathode leaving more vacancies in the deposited coatings. Therefore, the optimal ratio of coating mass and porosity in both composite coatings was achieved at constant voltage of 60 V for 45 s [43].

The influence of the lignin concentration in the range of 0.5–10 wt% Lig on the microstructure, morphology (Fig. 5.1), phase composition, thermal behavior, antimicrobial activity, and cytotoxicity of composite HAP/Lig coatings electrodeposited on titanium was investigated in order to find the optimal lignin concentration for producing HAP/Lig composite coatings [43, 44, 47]. SEM micrograph of sintered HAP/Lig coating with 1 wt% Lig (Fig. 5.1b) shows homogeneous fracture-free surface. Comparing SEM micrographs of the sintered HAP coatings with different amount of incorporated lignin, HAP/Lig coating with 1 wt% Lig indicated that

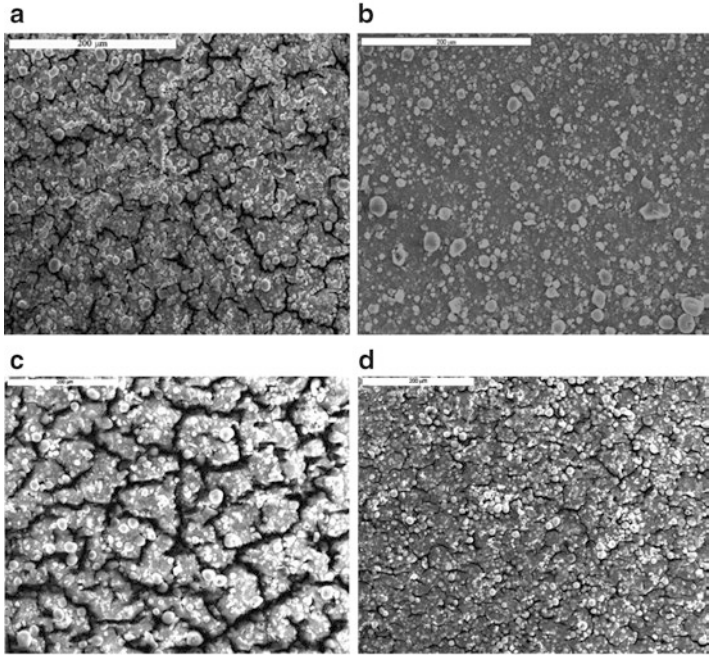

Fig. 5.1 SEM micrographs of sintered HAP/Lig coatings with (**a**) 0.5, (**b**) 1, (**c**) 3, and (**d**) 10 wt% Lig (reprinted from [44] with permission from Elsevier)

lignin strengthens the bonding between HAP particles and the substrate surface. Based on these results the optimal lignin concentration to obtain coatings with a smooth surfaces without fractures was 1 wt%. Four types of hydrogen bonding were proposed as possible interactions between HAP and lignin [43]: between phenolic hydroxyl –OH from lignin and –OH from HAP, between α-carbonyl from lignin side chain –C=O and –OH from HAP, between –OH from lignin and PO_4^{3-} from HAP, and between an ether bond oxygen from lignin C–O–C and –OH from HAP.

The phase composition and structure of HAP and HAP/Lig coatings were investigated by XRD analysis [43, 44]. All the peaks in XRD patterns of the nonsintered HAP/Lig coatings (0.5–10 wt% Lig) corresponded to the hydroxyapatite. After sintering, the diffraction peaks of all HAP/Lig coatings become sharper and of higher intensity with a decrease in peak width, indicating that sintered coatings had a better crystallinity [44]. A higher degree of crystallinity would make coatings less prone to dissolution in body fluids [55]. The sintering depends on the characteristics of the initial HAP powder, and the smaller particles have a tendency to aggregate in order to minimize their high free surface energy, resulting in densification and an increase in the grain size [56, 57]. Therefore, the initial nanosized HAP powder was successfully sintered at temperature of 900 °C and the same temperature was applied as thermal treatment of all composite HAP/Lig coatings, although the usually applied sintering temperature is in the range between 1000 and 1300 °C [58].

By comparing the XRD patterns of sintered HAP and HAP/Lig coatings, the partial HAP decomposition during thermal treatment at 900 °C was confirmed only for pure HAP coating and HAP/Lig coating with 0.5 wt% Lig, while HAP/Lig coatings containing 1, 3, and 10 wt% Lig did not show any new crystalline phase [43, 44]. As an example, the differences between XRD patterns of pure HAP coating and HAP/Lig coating with 1 wt% Lig are presented in Fig. 5.2. In the case of pure HAP coating, beside the main peaks corresponding to HAP, the observed new diffraction peaks for CaO, $Ca(OH)_2$, and $CaCO_3$ crystalline phases indicated the HAP coating decomposition that were not observed for HAP/Lig coating with 1 wt% Lig. It can be explained by reaction

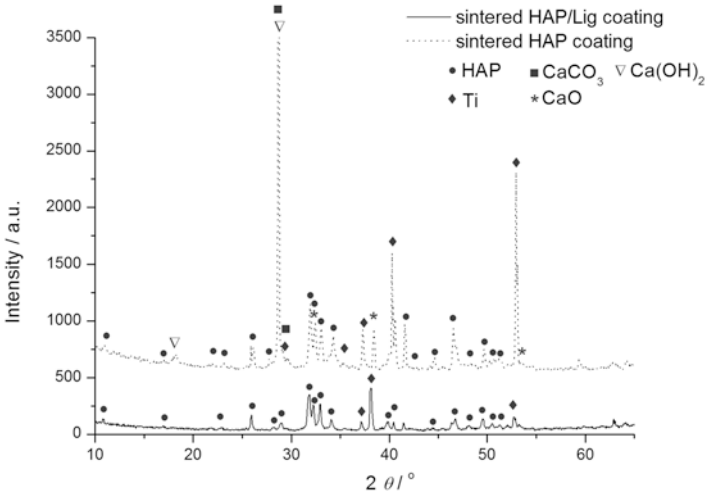

Fig. 5.2 XRD patterns of sintered HAP and HAP/Lig (1 wt% Lig) coatings (reprinted from [47] with permission from MDPI)

of CaO, generated during HAP decomposition at sintering temperature, with traces of atmospheric water and CO_2, yielding $Ca(OH)_2$ and $CaCO_3$, respectively [59]. In the case of sintered HAP/Lig coating with 0.5 wt% Lig, beside these peaks a new phase TiP appeared [44] that could be explained by the diffusion of phosphorous ions into the Ti surface as a result of HAP decomposition. It was reported that during the thermal treatments, the diffusion of calcium (limited diffusion) and phosphorus (profuse diffusion) ions into the Ti substrate occurs, resulting in the HAP decomposition [44, 60].

Comparing the diffraction patterns of all sintered HAP/Lig coatings, it can be concluded that degradation of hydroxyapatite did not occur for lignin concentrations of 1 wt% and higher, meaning that higher lignin concentrations protect the HAP lattice from decomposition during sintering.

The mean crystallite domain size, D_p, of the HAP/Lig coatings was calculated using the Scherrer equation (5.1), from the half height width, $\beta_{1/2}$, of XRD reflection of (002) plane at $2\theta \approx 26°$:

$$D_p = \frac{K\lambda}{\beta_{1/2}\cos\theta} \tag{5.1}$$

where λ is the wavelength of the X-ray radiation, K is the shape coefficient equal to 0.9, and θ is the diffraction angle. No microstrain corrections were taken into account. The values of mean crystallite domain size were calculated to be between 35 and 39 nm for HAP/Lig coatings with 0.5, 1, 3, and 10 wt% Lig, indicating that mean crystallite domain size does not depend on the lignin concentration.

The qualitative analysis of the XPS spectra of pure HAP and HAP/Lig coatings revealed certain differences between nonsintered and sintered coatings. The quantitative analysis data of the XPS spectra obtained from high-resolution measurements are presented in Table 5.1 [43, 44].

The carbon content of nonsintered HAP/Lig coating with 1 wt% Lig is higher than that of nonsintered HAP coating, which confirms the presence of lignin. On the other hand, the carbon content of the nonsintered HAP/Lig coatings increased with increasing lignin concentration, proving that lignin was bonded to the

Table 5.1 Quantitative XPS analysis data for HAP and HAP/Lig coatings

HAP/Lig (wt% Lig)		Ca	P	C	Ca/P
0 (Pure HAP)	Nonsintered	19.4	11.3	7.2	1.72
	Sintered	16.5	5.5	21.7	3.00
0.5	Nonsintered	19.1	11.3	8.2	1.69
	Sintered	18.4	7.9	15.9	2.33
1	Nonsintered	19.3	10.8	10.5	1.79
	Sintered	18.7	8.9	11.3	2.10
3	Nonsintered	18.4	12.0	11.7	1.53
	Sintered	18.8	10.8	12.9	1.74
10	Nonsintered	15,8	10,3	21,3	1.53
	Sintered	17,1	9,6	18,9	1.78

Reprinted from [44] with permission from Elsevier

HAP lattice. However, the highest increase in the carbon content after sintering was evidenced for pure HAP and HAP/Lig coating with 0.5 wt% Lig, which could be explained by $CaCO_3$ formation by reaction between CaO with atmospheric CO_2. XRD analysis also confirmed the decomposition of HAP and HAP/Lig coating with 0.5 wt% Lig (Fig. 5.2). A small increase in the carbon content for sintered HAP/Lig coatings with 1 and 3 wt% Lig, and decrease in carbon content for sintered HAP/Lig coatings with 10 wt% Lig compared to nonsintered coatings, indicated the absence of HAP decomposition during sintering. This means that lignin limited the formation of $CaCO_3$. XPS results are in accordance with the XRD results obtained for HAP/Lig coatings with lignin concentration higher than 0.5 wt% pointing to the absence of HAP lattice decomposition during sintering.

The calculated Ca/P ratio varied in the range of 1.53–1.69 for the nonsintered HAP and HAP/Lig coatings, which is similar to the Ca/P ratio for stoichiometric HAP (1.67). According to the literature [61], stable HAP phases correspond to Ca/P ratio within a range of 1.3–1.8. It could be observed that the Ca/P ratios of the sintered HAP/Lig coatings were higher than those of the nonsintered (Table 5.1). The highest increase in Ca/P ratio to 3.00 for sintered HAP coating and 2.33 for sintered HAP/Lig coating with 0.5 wt% Lig can be explained by diffusion of phosphorus ions, resulting in the partial HAP decomposition and also the presence of a new TiP peak in XRD pattern [44]. It could be concluded that lignin limited the decomposition of the HAP lattice of sintered HAP/Lig coatings with 1–10 wt% Lig as indicated by the smaller increase in carbon content and smaller Ca/P ratio, compared to pure HAP coating and HAP/Lig coating with 0.5 wt% Lig that was also observed from XRD results.

ATR-FTIR measurements were used to identify and verify the presence of specific functional groups on the surfaces of nonsintered and sintered HAP and HAP/Lig coatings [43, 44]. The spectra of nonsintered HAP and HAP/Lig coatings with different lignin concentration exhibit characteristic $\nu_1PO_4^{3-}$, $\nu_3PO_4^{3-}$, and $\nu_4PO_4^{3-}$ bands typical for the PO_4^{3-} group. In addition, the characteristic band at 630 cm^{-1} corresponds to the vibration of structural OH^- groups [23]. The ATR-FTIR spectra of HAP/Lig coatings before

sintering are very similar to the ATR-FTIR spectrum of pure HAP coating with respect to the functional groups, which indicates that the lignin in HAP/Lig coatings does not significantly alter the structure of the hydroxyapatite lattice [43, 44]. However, in the ATR-FTIR spectrum of HAP/Lig coatings, the appearance of C–H deformation vibration corresponds to C–H bonds in the aromatic rings [44, 62], as well as to bands for the methoxy group of lignin [44, 63]. This implies that lignin in the HAP/Lig coating did not change the formation and structure of the HAP lattice.

Most of the lignin hydroxyl groups are phenolic hydroxyl groups, which have a strong ability to form hydrogen bonds with the carbonyl groups and would induce an obvious shift of the band position to lower wavenumbers. The appearance of ν(O–H) vibrations in OH^- groups from HAP, occurred at a lower wavelength than expected, confirmed the intermolecular hydrogen bonds (P–O···OH) between OH^- groups from lignin and PO_4^{3-} groups from hydroxyapatite [44, 64]. Comparing the ATR-FTIR spectra for sintered HAP/Lig coatings, it was observed that HAP decomposition during sintering does not occur for coatings with lignin concentration 1, 3, and 10 wt% Lig [43, 44]. In other words, lignin concentrations of 1 wt% and higher prevent HAP decomposition and/or diffusion of phosphorus ions into the Ti surface due to the established hydrogen bonds.

5.3.1.1 Mechanical Properties

Nanoindentation technique has become a method of choice for studies of mechanical characteristics of bicomposite coatings due to its many advantages: test depth can be less than coating thickness, the nanomechanical response of the coated system can be measured on the substrate in situ, and test can be performed at variable displacements. The technique thus represents a unique way of ascertaining elastic, plastic, and fracture responses of surfaces [65].

The elastic modulus and hardness of sintered HAP coating and HAP/Lig coating with 1 wt% lignin were analyzed by nanoindentation test [47]. The mean hardness, H, was measured to be 7.40 GPa

for the HAP coating, while the mean reduced elastic modulus, E_r, was found to be 132 GPa. These values are in good agreement with published data [65] for bulk hydroxyapatite (H = 6.19–6.76 GPa and E_r = 122–125 GPa), as well as for thin film coatings. The HAP/Lig (1 wt% Lig) coating showed mean hardness of 6.90 GPa and mean reduced elastic modulus of 134 GPa, which were comparable to those of the pure HAP coating. In general, for biomedical metallic implants aimed for total hip and knee replacements, the bonding strength (or interlaminar shear strength) between implant and coating layer is the most important issue for lifespan of replaced implant [66, 67]. Therefore, the obtained E_r and H results for HAP/Lig coating lead to the conclusion that lignin does not significantly affect the mechanical properties of the composite, probably due to small concentrations of incorporated lignin.

5.3.1.2 Cytotoxicity and Antibacterial Activity

Cell survival was determined using the 3-(4,5-dimethylthiazol-2-yl) -2,5-diphenyltetrazolium bromide (MTT) test [47] according to the method of Mosmann [68] that was modified by Ohno and Abe [69]. The MTT test is based on 3-(4,5-dimethylthiazol-2-yl)-2,5-diphenyltetrazolium bromide to assess the activity of living cells by their mitochondrial dehydrogenase activity. The nutrient medium was RPM1 1640 medium supplemented with 10 % heat-inactivated bovine serum, penicillin (100 IU mL^{-1}), streptomycin (100 μg mL^{-1}), L-glutamine (3 mM), and 25 mM Hepes. In order to analyze the biological effects of HAP and HAP/Lig coatings on human cells, cytotoxicity experiments were conducted on human peripheral blood mononuclear cells (PBMC) after stimulation to proliferation with mitogen phytohemagglutinin (PHA). The survival of PHA-stimulated PBMC in control sample and in the presence of pure HAP and HAP/Lig coatings (1 and 10 wt% Lig) were investigated 72 h after seeding.

Cell survival (S, %) is defined as the ratio of the number of cells grown in nutrient medium with coating and the number of cells grown in control wells containing nutrient medium without coating, multiplied by 100. As the number of live cells is directly propor-

tional to the absorbance of live metabolically active MTT-treated cells, for the calculation of cell survival, absorbance of the newly formed formazan was used instead of the number of live cells:

$$S(\%) = A_u / A_c \cdot 100 \tag{5.2}$$

where A_u is the absorbance of the cells grown in the presence of a coating and A_c is the absorbance of the cells of the control sample. The absorbance of the blank was always subtracted from the absorbance of the corresponding cell sample. The results are reported as the average value ± standard deviation (SD) from three independent experiments.

The survival of PBMC stimulated to proliferate with mitogen phytohemagglutinin (PHA) in control sample and in the presence of sintered HAP and HAP/Lig coatings with 1 and 10 wt% Lig (Table 5.2) show that the survival of the PHA-stimulated PBMC did not decrease significantly with increasing lignin concentration [44]. MTT results indicate that HAP and both HAP/Lig coatings could induce a mild decrease in survival of healthy immunocompetent PHA-stimulated PBMC but that all the results were similar to that of the control sample ($S = 100\,\%$). According to literature [70], HAP coating and HAP/Lig coating with 1 wt% Lig can be classified as nontoxic, while HAP/Lig coating with 10 wt% Lig as slightly cytotoxic.

The reason for the slight lignin cytotoxicity could be due to its known absorption capability, i.e., it could slightly nonspecifically absorb some of the micronutrient constituents needed for sustain-

Table 5.2 Cell survival of PBMC cells stimulated to proliferation in the presence of sintered HAP and HAP/Lig coatings

Cell type	PHA-stimulated peripheral blood mononuclear cells (PBMC)		
Material	HAP coating	HAP/Lig coating, 1 wt% Lig	HAP/Lig coating, 10 wt% Lig
Cell survival (S), %	93.4 ± 4.0	90.4 ± 8.2	83.7 ± 5.8
Classification	Noncytotoxic	Noncytotoxic	Slightly cytotoxic

Reprinted from [44] with permission from Elsevier

ing tested PBMC proliferation, but also could be due to lignin antioxidant activity, as shown in tests on human keratinocytes and mouse fibroblasts [71]. On the other hand, one can speculate that lignin structures became more condensed upon sintering, which could have led to formation of highly condensed aromatic structures, known for their toxicity.

Postsurgical infections of the implantation site are the major problem and inevitably lead to revision surgeries. Antibacterial activities of the samples were tested for microorganisms that are responsible for most of the interhospital infections. Gram-positive bacterium *Staphylococcus aureus* (*S. aureus*) and Gram-negative bacterium *Escherichia coli* (*E. coli*) can cause serious infections. The antibacterial activity of sintered HAP and HAP/Lig (1 wt% Lig) coatings on titanium was tested on two bacteria types, bacterial strains *E. coli* (ATCC-25922) and *S. aureus* TL by using agar diffusion method [47]. The results of antimicrobial activity were estimated by measuring the inhibition zone of bacterial growth formed around the samples (mm). There was no light zone around HAP coating and HAP/Lig coating (1 wt% Lig) after 24 h of incubation in the case of both bacterial strains, meaning that both pure HAP and HAP/Lig coating with 1 wt% Lig did not exhibit antimicrobial activity. Therefore, the subsequent course of research aimed to obtain biocomposite coating doped with silver ions, a major antimicrobial agent.

5.3.2 Silver-Doped Hydroxyapatite/Lignin Coatings Electrodeposited on Titanium Substrate

5.3.2.1 Sintered Silver-Doped Hydroxyapatite/Lignin Coatings

In Vitro Bioactivity

The in vitro bioactivity of silver-doped hydroxyapatite/lignin (Ag/HAP/Lig) coating electrodeposited on Ti was tested by immersion in simulated body fluid (SBF) solution. The influence of silver on the microstructure, morphology, phase composition, thermal behavior,

antimicrobial activity, and cytotoxicity, as well as on corrosion stability and bioactivity of Ag/HAP/Lig coating with 1 wt% Lig in SBF was investigated [45]. After 7 days in SBF the samples were characterized by SEM, XRD, and attenuated total reflection Fourier transform infrared spectroscopy (ATR-FTIR) analysis.

Surface morphology of the sintered Ag/HAP/Lig coating before and after 7 days of immersion in SBF at 37 °C is shown in Fig. 5.3. The SEM micrograph (Fig. 5.3a) revealed smooth and uniform surface of Ag/HAP/Lig coating with no fractures before soaking in SBF, while Fig. 5.3b represents coating surface after immersion in SBF. Newly formed plate-shaped apatite crystals are evident after immersion in SBF solution. A relatively high porosity of implant surface along with improved mechanical stability provides better cell adhesion that facilitates osteointegration. The key point is that high interconnected porosity structures enable the penetration of osteoblasts leading to better connection between the implant and the bone [10].

Obvious bioactivity was confirmed by forming a bone-like apatite layer on the coating surface after 7 days of immersion in SBF. The composition of new plate-shaped crystals was revealed by ATR-FTIR and XRD spectrum analysis [45], while the formation of apatite has been previously explained by Sun et al. [72]. The negatively charged hydroxyapatite surface interacts with Ca^{2+} ions from SBF forming an amorphous positive Ca-rich surface. Subsequently, thus formed surfaces interact with the negative

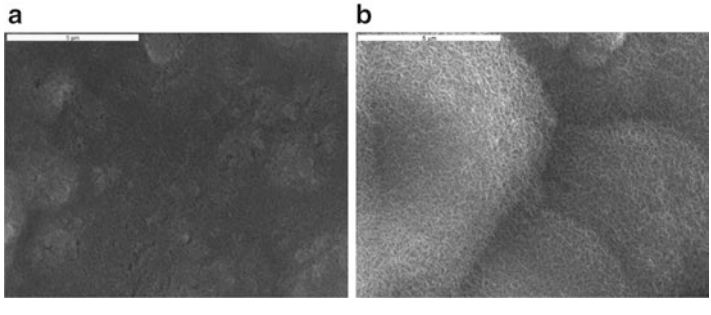

Fig. 5.3 SEM micrographs of sintered Ag/HAP/Lig (1 wt% Lig) coating (**a**) before and (**b**) after immersion in SBF solution at 37 °C. Scale bar: 5 μm (reprinted with permission from [45]. Copyright 2013 American Chemical Society)

PO_4^{3-} ions in the SBF to form Ca-poor apatite, which gradually crystallizes into bone-like apatite. Once formed in SBF, the apatite grows spontaneously, consuming the calcium and phosphate ions, incorporating minor ions, such as sodium, magnesium, and carbonate, and thereby developing a bone mineral-like compositional and structural feature [73].

XRD analysis was performed to determine the phase composition and structure of Ag/HAP/Lig coatings before and after immersion in SBF (Fig. 5.4a). XRD diffractogram of Ag/HAP/Lig coating before immersion in SBF showed only characteristic hydroxyapatite peaks without any additional crystalline phases even after sintering, meaning that lignin protected Ag/HAP lattice during sintering [45].

Labeled XRD peaks match very well hydroxyapatite, but incorporation of Ag in the hydroxyapatite crystal lattice causes a shift of specific HAP peaks toward smaller 2θ values, confirming the silver substitution for calcium [45]. The evidence of Ag presence was verified through the shift of characteristic HAP peaks (crystal planes (002), (211), (112), and (300)) toward smaller angles for the Ag/HAP coating before immersion in SBF solution compared to the pure HAP coating. The additional peaks that originate from the Ti substrate indicate the suboxide of titanium, Ti_3O, as seen in Fig. 5.4a, which is classified as a nonstoichiometric oxide deficient in oxygen. The complex valence status of Ti appears to be due to the oxygen diffusion from the exterior surface to the inside during sintering. According to Ye et al. [74], Ti metal and Ti suboxides on the composite surfaces are believed to be more active than TiO_2 in the physiological environment and can activate chemical bonding between the implant surface and adjacent biomolecules. After 7 days of immersion in SBF solution, a new phase was detected by observing the shift in characteristic hydroxyapatite peaks toward higher angles (Fig. 5.4a). These findings were attributed to carbonate ions in the lattice and confirmed, therefore, the growth of carbonated hydroxyapatite onto the surface of Ag/HAP/Lig coating. Therefore, the shifting of XRD diffraction peaks is typical for weak crystalline, carbonated HAP, as it is found in bone.

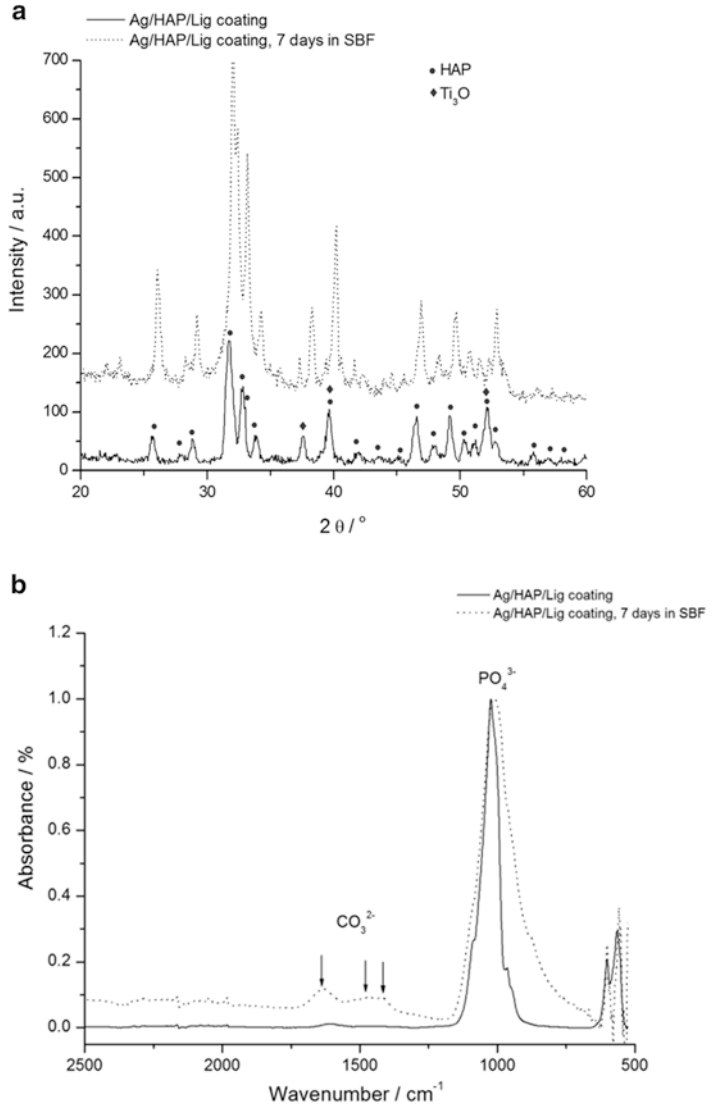

Fig. 5.4 (**a**) XRD patterns and (**b**) attenuated total reflection Fourier transform infrared spectroscopy (ATR-FTIR) spectra of sintered Ag/HAP/Lig (1 wt% Lig) coating, before and after 7 days immersion in SBF at 37 °C (reprinted with permission from [45]. Copyright 2013 American Chemical Society)

The mean crystallite domain size, D_p, was calculated at $2\theta \approx 26°$ by Eq. (5.1). The crystallite domain size of Ag/HAP/Lig coatings before and after soaking in SBF solution was calculated to be almost the same, 20.8 and 22.0 nm, respectively, indicating the homogeneous surface. Small difference between the crystallite size before and after immersion is probably due to the incorporation of CO_3^{2-} ions into the apatite lattice by occupying the OH^- sites or the PO_4^{3-} positions [75].

In general, the bioactivity of implanted apatite coated materials can be evaluated by the formation of bone-like apatite on their surface. The presence of CO_3^{2-} bands in ATR-FTIR spectrum is clear evidence of its incorporation in the HAP layer since it is well known that the biological hydroxyapatite also contains carbonate groups [76]. Thus, Ag/HAP/Lig coating was investigated by the ATR-FTIR method before and after immersion in SBF solution as shown in Fig. 5.4b. As it can be seen before immersion in SBF, the ATR-FTIR spectrum exhibited characteristic hydroxyapatite bands as found in the literature [77, 78]. Namely, the presence of phosphate groups was confirmed by vibrational bands at 960, 1016, and 1089 cm^{-1} in the FTIR spectrum. Also, the weak characteristic bands at around 3573 and 627 cm^{-1} corresponding to the vibration of structural OH– groups have been found in the hydroxyapatite lattice. The absence of a low-intensity wide band at wavenumbers between 1400 and 1585 cm^{-1} in the ATR-FTIR spectrum of Ag/HAP/Lig before immersion in SBF solution confirmed that there was no decomposition of hydroxyapatite, as also detected by XRD diffractogram (Fig. 5.4a).

ATR-FTIR analysis, as an efficient and sensitive method for detection of small amounts of carbonates [79], was also used to investigate Ag/HAP/Lig coating surface after 7 days of soaking in SBF solution. During 7 days of immersion in SBF at 37 °C carbonated apatite was formed (Fig. 5.4b) which can be seen from three peaks at 1640, 1476, and 1420 cm^{-1}, attributed to the vibrational bands of CO_3^{2-} groups. According to the literature, B-type carbonated apatite appears on the surface after soaking in SBF solution [74, 80, 81]. The spectrum of bone-like apatite showed a high concentration of OH^- and PO_4^{3-} groups compared to the peaks appearing in the spectrum of Ag/HAP/Lig coating before immersion in

SBF, which allows the coating surface to exhibit the negative surface potentials required for apatite nucleation. Therefore, the formation of carbonated HAP is very beneficial due to its weak crystalline form that resembles human bone, a property that facilities osteointegration [79].

The chemical composition of the outermost coating surface level is important because it would be in direct contact with the bone tissue and dissolve first at the initial stage of implantation. It has been shown that the optimum Ca/P ratio is 1.67–1.76 [82]. From semiquantitative XPS analysis of Ag/HAP/Lig coating, Ca/P ratio was calculated to be 1.62 [45], which is close in value to the Ca/P ratio in stoichiometric hydroxyapatite (1.67). Thus, Ca/P ratio for the Ag/HAP/Lig coating after sintering remained constant (1.62) confirming the lignin protection of Ag/HAP lattice during sintering [82].

EIS measurements were employed to investigate the corrosion stability of Ag/HAP/Lig coating in the physiological environment. The Nyquist plots for the impedance of Ag/HAP/Lig coating deposited on titanium after a prolonged exposure time in SBF solution at 37 °C were obtained, where the high-frequency range is attributed to the coating, while the low-frequency range describes the characteristics of the passive oxide layer on titanium [45]. Fitting of experimental data obtained from Nyquist plots for 14 days in SBF was accomplished by using the equivalent electrical circuit (EEC) shown in Fig. 5.5, consisting of the electrolyte resistance, R_s, the coating pore resistance, R_c, and constant phase elements, CPE_c and CPE_{ox}, which represent all the frequency-dependent electrochemical phenomena, such as the coating capacitance, C_c,

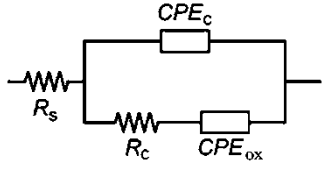

Fig. 5.5 Equivalent electrical circuit for sintered Ag/HAP/Lig (1 wt% Lig) coating on titanium during the time of SBF exposure at 37 °C (reprinted with permission from [45]. Copyright 2013 American Chemical Society)

and passive oxide film capacitance, C_{ox}. CPE is used in these models to compensate nonhomogeneity in the system and is defined by two parameters, Y_0 and n. The impedance of CPE is represented by the following equation [83–85]:

$$Z_{CPE} = Y_0^{-1} \cdot (j\omega)^{-n} \tag{5.3}$$

where $j=(-1)^{1/2}$, $\omega=2\pi f$ is frequency in rad s^{-1} and f is the frequency in Hz. If n values range from 0.8 to 1, the impedance of CPE can be considered to be the one of the pure capacitor:

$$Z_{CPE} = (j\omega C)^{-n} \tag{5.4}$$

In this case Y_0 gives a pure capacitance (C). The impedance data in the complex plane were well fitted by the proposed EEC and three basic criteria were used to evaluate the general accuracy of the fit: visual fit to Nyquist plots, low goodness of fit, and low relative standard errors for every circuit element [85]. The obtained fitting results are listed in Table 5.3.

As seen in Table 5.3, n_c and n_{ox} values for Ag/HAP/Lig coating are close to 0.8, therefore CPE_c can be considered as coating capacitance, C_c, while CPE_{ox} can be considered as capacitance of oxide film on the titanium surface beneath Ag/HAP/Lig coating, C_{ox}. The time dependence of coating pore resistance, R_c, and the coating capacitance, C_c, of the Ag/HAP/Lig coating during 14 days in SBF are presented in Table 5.3. It can be noticed that the pore resistance, R_c, increased and coating capacitance, C_c, decreased during the exposure to SBF, which is related to the growth of the newly formed apatite layer on the coating surface. The continuous increase in R_c up to 6.3 kΩ cm^2 and decrease in C_c up to 547.1 μF cm^{-2} reflect the process of the apatite nucleation after prolonged time in SBF, which was clearly seen in SEM images (Fig. 5.3), as well as from XRD and ATR-FTIR (Fig. 5.4a, b, respectively). This suggests that Ag/HAP/Lig coating surface represented the site of nucleation and growth of new apatite layer. According to the literature, transformation of hydroxyapatite with a bone-like crystallinity apatite layer in the human body certainly induces stable bonding to bone [86].

Table 5.3 The fitting values of equivalent electrical circuits parameters for sintered Ag/HAP/Lig (1 wt% Lig) coating

Sample	t (h)	R_s (Ω cm^2)	CPE$_{ox}$ (C_{ox}) (μF cm^{-2})	n_{ox}	CPE$_c$ (C_c) (μF cm^{-2})	n_c	R_c (kΩ cm^2)
Ag/HAP/Lig	1	43.3	1030.0	0.76	745.2	0.88	4.3
	3	44.5	1046.0	0.80	697.6	0.88	5.2
	6	44.5	1010.0	0.81	667.9	0.88	5.9
	8	44.1	880.1	0.77	655.8	0.88	6.1
	24	29.2	620.8	0.70	627.2	0.88	5.6
	72	23.1	821.3	0.76	588.2	0.88	6.4
	120	31.5	610.4	0.74	560.6	0.89	5.9
	168	18.8	782.4	0.77	559.3	0.88	5.8
	240	21.8	522.0	0.74	543.5	0.88	6.3
	288	21.3	475.8	0.70	529.0	0.88	6.9
	336	17.7	403.2	0.71	547.1	0.87	6.3

Mechanical Properties

Ag/HAP coating had reduced elastic modulus, E_r, and mean hardness, H, of 172 and 14.5 GPa, respectively, while Ag/HAP/Lig coating with 1 wt% lignin had slightly higher H and lower E_r values of 173 and 13.3 GPa, respectively [47]. Comparing HAP and HAP/Lig coating and their counterparts with silver, it was observed that addition of Ag contributed to the increase of both E_r (172 vs. 132 GPa) and H (14.5 vs. 7.40 GPa) of the composites.

An evaluation of E/H value is a prerequisite for the evaluation of fracture toughness [87]. In the case of pure HAP and Ag/HAP coatings, E_r/H ratios were 17.86 and 11.87, respectively, while in the case of HAP/Lig and Ag/HAP/Lig coatings E_r/H ratios were 19.34 and 13.00, respectively, indicating that Ag reinforcement caused decrements in the value of E_r/H, implying that toughness values

may be affected with Ag addition. On the other hand, calculated E_r/H ratios for HAP and HAP/Lig coatings were 17.86 vs. 19.34, respectively, for Ag/HAP and Ag/HAP/Lig the same comparison in E_r/H ratio was noticed 11.87 vs. 13.00, respectively. Therefore, it can be concluded that the change in E_r/H ratio was not significant for pure coatings vs. coatings with incorporated lignin. Therefore, small concentration of 1 wt% lignin does not affect mechanical properties of composite.

The relationship between material surface properties and biological response to it is a major issue in biomedical materials research. The Ag/HAP/Lig composite can serve as a potential biomaterial because silver addition improves its bactericidal property, since it was shown that HAP/Lig does not prevent bacterial growth.

Cytotoxicity and Antibacterial Activity

Cytotoxicity of Ag/HAP/Lig (1 wt% Lig) coating was determined by MTT test against PBMC and PHA-stimulated PBMC cells [45, 47] since it is important to produce the biomaterials that will not exert toxic effects against cells of the surrounding tissue as well as against healthy immunocompetent PBMC, components of the immune response. Examination of cytotoxic effects of the investigated Ag/HAP/Lig coating with 1 wt% Lig (Table 5.4) showed mild decrease in survival of healthy immunocompetent PBMC,

Table 5.4 Cell survival of peripheral blood mononuclear cells (PBMC) and PHA-stimulated peripheral blood mononuclear cells (PBMC + PHA) in the presence of sintered Ag/HAP/Lig (1 wt% Lig) coating

Cell type	
Peripheral blood mononuclear cells (*PBMC*)	
Cell survival (*S*), %	89.4 ± 3.5
Classification	Noncytotoxic
PHA-stimulated peripheral blood mononuclear cells (*PBMC*)	
Cell survival (*S*), %	83.8 ± 6.3
Classification	Noncytotoxic

Reprinted from [47] with permission from MDPI

unstimulated (89.4 %), and PHA stimulated (83.8 %) compared to the control cell sample ($S = 100$ %), while cell survival of PHA-stimulated PBMC in the presence of Ag/HAP coating was 90.4 %. According to the literature [70], both Ag/HAP and Ag/HAP/Lig coating with 1 wt% Lig were displayed as noncytotoxic against target PBMC cells.

Recently, research in orthopedic surgery has focused on the development of surface-modified devices that are capable of releasing drugs adapted to the clinical situation (antibiotics, antimicrobial agents, etc.) in a controlled and predictable manner, according to established kinetic laws. Silver, as Ag ions and Ag nanoparticles, are well known as primary inorganic antimicrobial agents that have been widely used in different fields of medicine. Although not completely revealed, it is assumed that Ag ion disrupts the bacterial cell integrity by binding to the enzymes and proteins within the bacteria, thus accelerating their death.

The antibacterial activity of sintered Ag/HAP/Lig (1 wt% Lig) coatings was tested against pathogenic Gram-positive bacteria strain *S. aureus* TL [47]. Test bacteria were activated by two successive precultures in LB broth (composition yeast extract 5 gL^{-1}, tryptone 10 gL^{-1}, NaCl 5 gL^{-1}) and incubated at 37 °C during the night. Prior to antibacterial test, an overnight culture, not older than 18 h, was diluted in physiological solution (10^{-1}) and 2 % (*v*/*v*) of culture was used to inoculate a test tube with 7 mL of sterile modified phosphate-buffered (PB) solution (pH = 7.4) with 15 mg titanium-coated samples. The initial number of bacteria in each suspension was between 10^4 and 10^5 CFU mL^{-1} and concentration of coating material was approximately 2 mg mL^{-1}. Thus, prepared samples were incubated for 24 h at 37 °C, without shaking. Blank with no titanium-coated samples (bacteria in PB solution) was used as control. The number of bacteria in a sample was monitored at the beginning of the experiment and after 1 and 24 h of incubation. After 24 h incubation at 37 °C, the number of colonies on agar plates containing 25–250 colonies was enumerated using a colony counter and expressed as CFU mL^{-1} to obtain the number of viable *S. aureus*. Antibacterial activity of the Ag/HAP/Lig coating (Table 5.5) could be noticed immediately after inoculation of samples and further reduction of cell viability for two logarithmic units is achieved after

Table 5.5 Reduction of viable cell number of *S. aureus* TL after incubation with sintered Ag/HAP/Lig (1 wt% Lig) coating for 0, 1, and 24 h

	S. aureus TL		
Bacteria strain type	Initial	1 h	24 h
Control (CFU mL^{-1})	1.0×10^5	3.0×10^4	9.9×10^4
Ag/HAP/Lig (CFU mL^{-1})	2.5×10^4	2.0×10^3	No bacteria

Reprinted from [47] with permission from MDPI

just 1 h of incubation when compared to the initial number of cells in suspensions (percentage of cell reduction 97.67 %). Based on silver ion release results, the concentration of silver ions after 1 h was 0.4493 ppm [46], which is a sufficiently small concentration to achieve antibacterial effect without causing cytotoxicity (Table 5.4).

In comparison to the reported results of Stanic et al. [88], the antimicrobial efficiency of Ag/HAP/Lig coating exhibited higher reduction of bacteria strain *S. aureus* TL, since after 24 h analyzed samples did not contain any viable cells. The total reduction in the bacterial numbers after 24 h indicated antimicrobial activity of 0.5 wt% Ag in Ag/HAP/Lig coating, providing good protection against infection. Moreover, an immediate silver ion release provided for the imminent drop in CFU numbers even after 1 h of exposure, which is the bactericidal effect needed for prevention of biofilm formation [89].

5.3.2.2 Nonsintered Silver-Doped Hydroxyapatite/Lignin Coatings

In Vitro Bioactivity

SEM microphotograph (Fig. 5.6a) revealed the surface homogenicity of nonsintered Ag/HAP/Lig (1 wt% Lig) coating before immersion in SBF, while Fig. 5.6b represents coating surface after immersion in SBF. This crystalline surface is much more pronounced and visible in FE-SEM microphotograph of Ag/HAP/Lig coating after soaking in SBF (Fig. 5.6c). Newly formed plate-shaped apatite crystals are evident in Fig. 5.6b and c after soaking in SBF solution. The

composition of new apatite crystals was revealed by ATR-FTIR and XRD analysis [46]. It can be seen (Fig. 5.7) that before immersion in SBF the FTIR spectrum exhibited characteristic hydroxyapatite bands [77, 78], while PO_4^{3-} groups were confirmed by vibrational bands at 963, 1021, and 1086 cm^{-1} in FTIR spectrum.

The appearance of small peak around 3600 cm^{-1} along with broad band at 1600 cm^{-1} corresponds to the OH^- stretching in the hydroxyapatite lattice. Two peaks at 1420 and 1448 cm^{-1} characteristic for methoxy groups revealed the presence of biopolymer lignin in Ag/HAP/Lig coating [63]. Polymer can be traced through the appearance of the slight shoulder at 875 cm^{-1} from the C–H vibration in the aromatic rings [62]. The band at 635 cm^{-1} for OH^- vibrations from HAP lattice indicates the intermolecular hydrogen bonds between HAP and Lig [64]. Also, the appearance of absorption peak

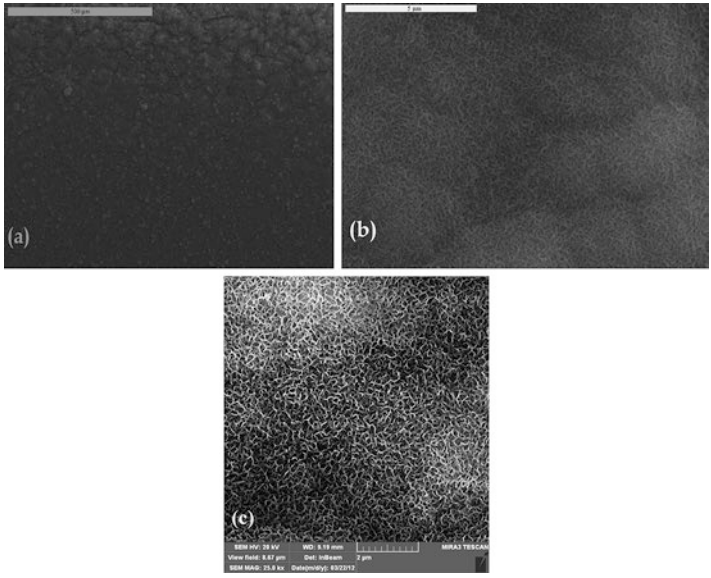

Fig. 5.6 SEM microphotographs of nonsintered Ag/HAP/Lig (1 wt% Lig) coating: (**a**) before and (**b**) after 7 days of immersion in SBF at 37 °C and (**c**) FE-SEM microstructure of Ag/HAP/Lig coating after 7 days of immersion in SBF at 37 °C (reprinted from [46] with permission from Elsevier)

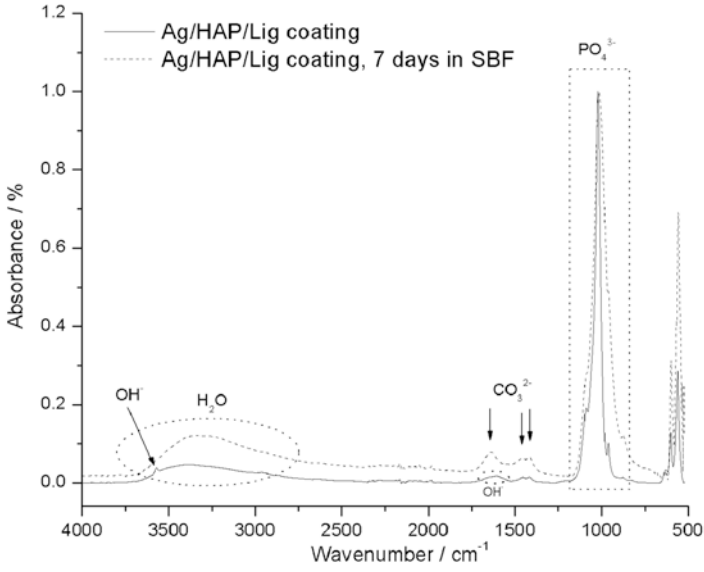

Fig. 5.7 ATR-FTIR spectra of nonsintered Ag/HAP/Lig (1 wt% Lig) coating before and after 7 days of immersion in SBF at 37 °C (reprinted from [46] with permission from Elsevier)

at 1101 cm^{-1} due to (P–O) stretching of the phosphorous group proposed that intermolecular hydrogen bonds between OH^- groups from lignin and PO_4^{3-} groups from HAP were established [90].

The spectrum of the nonsintered Ag/HAP/Lig coating after 7 days immersion in SBF solution (Fig. 5.7) exhibited the broad absorbance band at 3380 cm^{-1} attributed to the OH^- stretching with higher intensity than the intensity before immersion revealing the formation of new bone-like apatite layer on the coating surface [72]. Also, another confirmation of presence of biological apatite was observation of three peaks at 1642, 1460, and 1424 cm^{-1} attributed to the vibrational bands of CO_3^{2-} groups. According to literature the B-type carbonated apatite appears on the surface after soaking in SBF solution [77, 80]. Therefore, the bioactivity of Ag/HAP/Lig coating is proved by these results and its surface represents favorable substrate for apatite nucleation, which was also confirmed by SEM and FE-SEM images (Fig. 5.6).

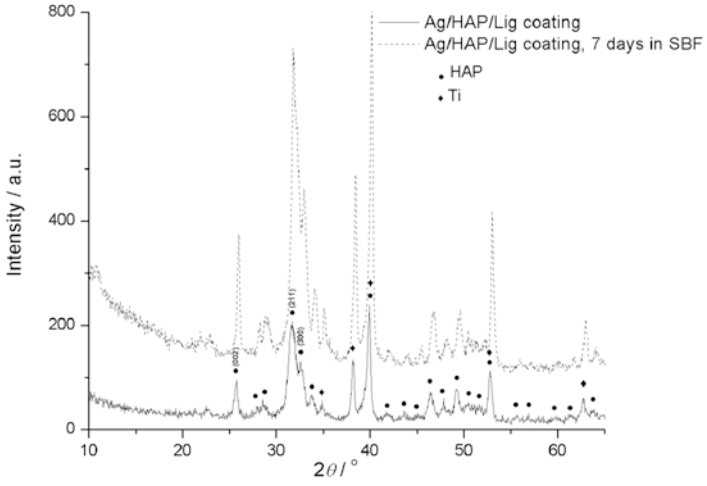

Fig. 5.8 XRD patterns of nonsintered Ag/HAP/Lig (1 wt% Lig) coating before and after 7 days of immersion in SBF at 37 °C (reprinted from [46] with permission from Elsevier)

The XRD patterns of nonsintered Ag/HAP/Lig coating before and after immersion in SBF are shown in Fig. 5.8. Characteristic hydroxyapatite peaks at (002), (211), and (300) crystal planes at $2\theta = 25.74°$, 31.56° and 32.47°, respectively, are well observed on Ag/HAP/Lig diffractogram before immersion in SBF.

After 7 days of immersion in SBF the new carbonated HAP phase was detected by observing the shift in characteristic HAP peaks at (002), (211), and (300) crystal planes toward higher angles, which is beneficial due to its weak crystalline form that resembles human bone, a property that facilities osteointegration [79].

Surface analysis performed by XPS measurements on nonsintered Ag/HAP/Lig coating before soaking in SBF is illustrated in Fig. 5.9, by deconvoluted spectra corresponding to characteristic elements for hydroxyapatite (Ca and P). The measured binding energy (BE) values were calibrated by the C1s (hydrocarbon C–C, C–H) of 285 eV. The Ca 2p spectrum of the Ag/HAP/Lig coating has doublet Ca 2p 3/2 (BE of 347.1 eV) and Ca 2p 1/2 (BE of 350.6 eV) peaks and the P 2p spectrum has single P 2p 3/2 peak at

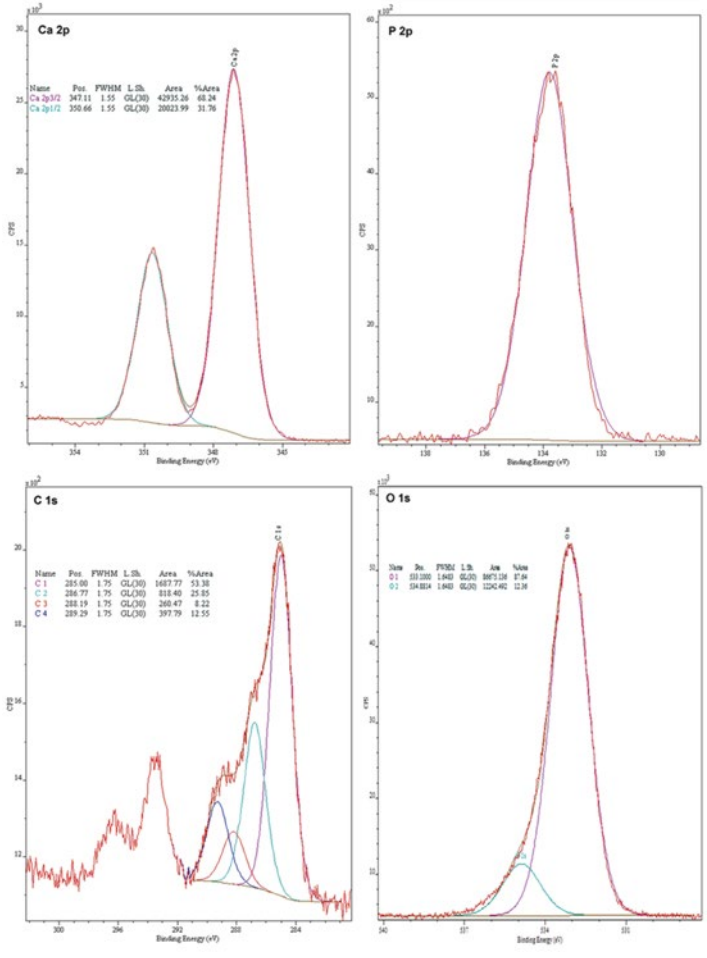

Fig. 5.9 Deconvoluted XPS lines of component elements Ca, P, C, and O for the nonsintered Ag/HAP/Lig (1 wt% Lig) coating (reprinted from [46] with permission from Elsevier)

BE position of 133.6 eV, indicating the presence of hydroxyapatite [91, 92]. The deconvoluted elements of the C 1s had four components with peak positions at 285, 286.7, 288.2, and 289.3 eV which correspond to aromatic hydrocarbons, alkoxy, and $RCOO^-$ groups,

respectively [93]. Concerning the C 1s line, the new peak occurred at 289.3 eV (C=O bonds) suggesting the presence of the polymer lignin [94]. It is known that the interaction mechanism of hydrogen bonding can be detected by XPS. The hydrogen bonding between C=O and −OH groups represented that the O 1s BE of the C=O groups increases, while at the same time the O 1s BE of the −OH groups decreases. The O 1s signal at 533.1 eV may be attributed to PO_4^{3-} groups, while at 532.4 eV corresponds to −OH groups by hydroxyapatite [94, 95]. Therefore, the O 1s lines are at higher BE than it is for O 1s for PO_4^{3-} groups indicating hydrogen bonding between lignin and HAP lattice.

From semiquantitative XPS analysis Ca/P ratio was calculated to be 1.62 (Table 5.6), similar to the value of Ca/P ratio in stoichiometric hydroxyapatite (1.67). The stable hydroxyapatite has to be within a range of 1.3–1.8 for Ca/P ratio [82].

EIS measurements were performed in order to study the corrosion stability of nonsintered Ag/HAP/Lig coating during exposure to SBF solution at 37 °C. The Nyquist plots for the impedance of Ag/HAP/Lig coatings on titanium and bare titanium, used as reference, after 3, 5, and 7 days in SBF are presented in Fig. 5.10a, b, respectively. Inset in Fig. 5.10a provides Nyquist plots for the impedance of Ag/HAP/Lig coatings on titanium in the high-frequency range. High-frequency range is attributed to the Ag/HAP/Lig coating, while the low-frequency range represents the characteristics of the passive titanium oxide film beneath the coating.

The Nyquist plots were fitted with the equivalent electrical circuits shown in Fig. 5.11. The equivalent circuit used for the fitting of impedance data for Ag/HAP/Lig coating during initial time of exposure (Fig. 5.11a) consists of the electrolyte resistance, R_s; the coating pore resistance, R_p; the constant phase elements CPE_c and CPE_{ox}, which include all the frequency-dependent electrochemical phenomena, namely, coating capacitance, C_c, and capacitance of passive oxide film beneath Ag/HAP/Lig coating, C_{ox}, respectively, and diffusion processes. The equivalent circuit used for the fitting of impedance data for Ag/HAP/Lig coating during prolonged time of exposure (Fig. 5.11b) consists of the electrolyte resistance, R_s; the coating pore resistance, R_p; and constant phase element, CPE_c. For impedance analysis of bare titanium, the equivalent circuit

Table 5.6 Atomic percentages and Ca/P ratio at sample surface of nonsintered Ag/HAP/Lig (1 wt% Lig) coating determined by XPS

	Element				
	C 1s (%)	O 1s (%)	Ca $2p_{3/2}$ (%)	P 2p (%)	Ca/P
Sample					
Ag/HAP/Lig	5.5	63.9	18.3	11.3	1.62

Reprinted from [46] with permission from Elsevier

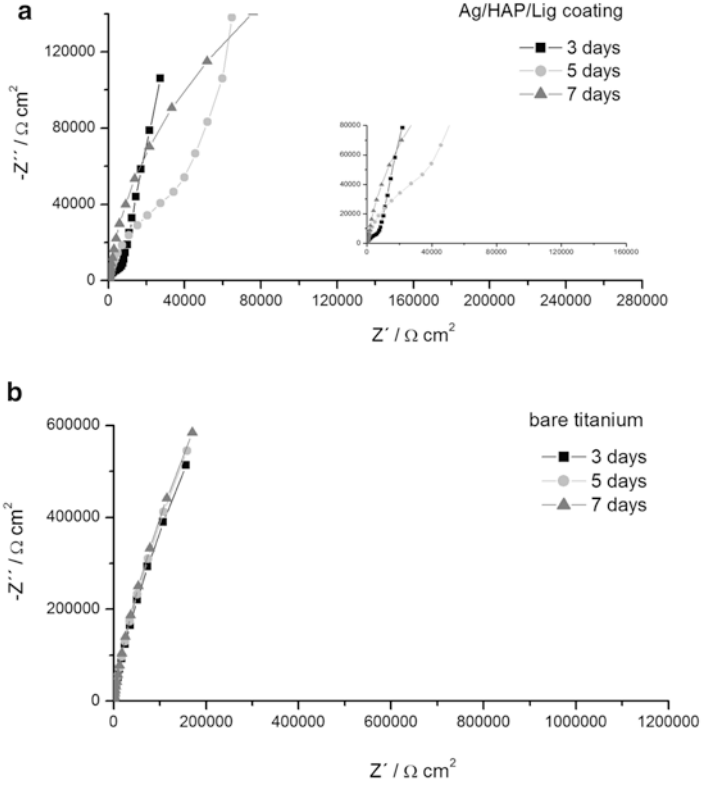

Fig. 5.10 The Nyquist plots of (**a**) nonsintered Ag/HAP/Lig (1 wt% Lig) coating on titanium and (**b**) bare titanium, after different times of exposure to SBF at 37 °C (reprinted from [46] with permission from Elsevier)

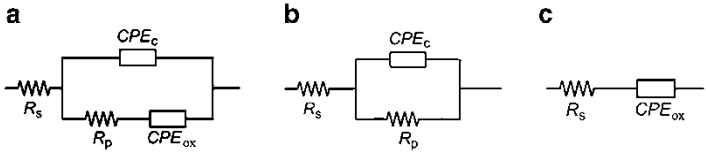

Fig. 5.11 Equivalent electrical circuits for (**a**) nonsintered Ag/HAP/Lig (1 wt% Lig) coating on titanium during initial time of exposure to SBF, (**b**) nonsintered Ag/HAP/Lig (1 wt% Lig) coating on titanium during prolonged time of exposure to SBF, and (**c**) bare titanium (reprinted from [46] with permission from Elsevier)

Table 5.7 The fitting values of equivalent electrical circuit parameters for nonsintered Ag/HAP/Lig (1 wt% Lig) coating

Sample	t (h)	R_s (Ω cm^2)	CPE_{ox} (C_{ox}) (μF cm^{-2})	n_{ox}	CPE_c (C_c) (μF cm^{-2})	n_C	R_p (kΩ cm^2)
Ag/HAP/Lig	1	29.4	118.0	0.91	33.3	0.88	10.4
	72	50.6	101.9	0.91	34.4	0.88	13.0
	120	87.8	75.8	1.00	36.4	0.87	110.3
	168	82.0	–	–	35.4	0.86	634.7
Bare titanium	1	21.1	33.2	0.88	–	–	–
	72	72.9	26.8	0.89	–	–	–
	120	13.9	25.7	0.90	–	–	–
	168	29.7	24.1	0.90	–	–	–

Reprinted from [46] with permission from Elsevier

represented in Fig. 5.11c was used, where R_s is the electrolyte resistance and CPE_{ox} is constant phase element for passive oxide film on titanium surface. The fitting results are listed in Table 5.7.

It can be seen from Table 5.7, that n_c and n_{ox} values for Ag/HAP/Lig coating and bare titanium are higher than 0.8, therefore CPE_c can be considered as coating capacitance, C_c, while CPE_{ox} can be considered as capacitance of oxide film on titanium surface beneath Ag/HAP/Lig coating, C_{ox}. Equivalent electrical circuit shown in Fig. 5.11a was used for fitting of Nyquist plots of Ag/HAP/Lig

coating during 5 days of exposure to SBF solution. According to these results, R_p and C_c remain almost constant during first 3 days of exposure to SBF solution, indicating the corrosion stability of the coating. However, after fifth day R_p value was ten times higher indicating the beginning of the formation of new apatite layer. After seventh day the impedance Nyquist plot could not be fitted more with equivalent circuit shown in Fig. 5.11a and instead the equivalent circuit in Fig. 5.11b was used. After 7 days in SBF solution the calculated value of R_p was 634.7 kΩ cm^2, indicating the deposit of newly formed carbonated HAP on the coating surface. This was confirmed by SEM and FE-SEM images (Fig. 5.6) as well as ATR-FTIR and XRD results (Figs. 5.7 and 5.8, respectively).

EIS spectra of bare titanium (Fig. 5.10b) exposed to SBF solution are related to the equivalent electrical circuit shown in Fig. 5.11c. Its impedance plot exhibits behavior typical of a thin passive oxide film on titanium surface. Furthermore, the slight decrease in C_{ox} during immersion time (Table 5.7) corresponded to a slow growth of the titanium oxide film, indicating a long-term stability of the thin oxide film in SBF solution.

Cytotoxicity and Antibacterial Activity

The coatings doped with silver ions provided high initial concentration of antimicrobial agent in surrounding tissue. This property is especially important in early critical postimplantation period since it prevents initial adhesion of bacteria [89]. However, continuous silver ion release after this critical period is also desirable to prevent bacteria biofilm formation. Concentration of silver ion released from the nonsintered Ag/HAP/Lig coating during 10 days in SBF solution at 37 °C is shown in Fig. 5.12.

The cumulative silver ion release from the Ag/HAP/Lig with 1 wt% Lig coating after 10 days was measured to be 1.704 ppm. Jamuna-Thevi et al. [89] previously reported that minimum silver ion concentration is 0.1 ppb and the maximum cytotoxic concentration toward human cells is 10 ppm, therefore the measured concentrations were within this range. The silver release from nonsintered Ag/HAP/Lig coating was within the initial antibacterial concentration of silver, which is found to be 56 ppb [89].

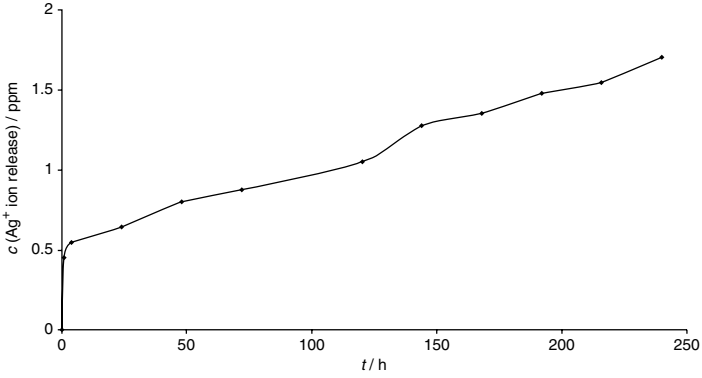

Fig. 5.12 Time dependence of silver ion release from nonsintered Ag/HAP/Lig (1 wt% Lig) coating during 10 days of immersion in SBF at 37 °C (reprinted from [46] with permission from Elsevier)

Cytotoxicity of Ag/HAP/Lig (1 wt% Lig) coating, as well as of nonsintered Ag/HAP and Ag/HAP/Lig (10 wt% Lig) coatings, was determined by MTT test against PBMC and PHA-simulated PBMC cells (Table 5.8).

Examination of cytotoxic effects of the investigated Ag/HAP and Ag/HAP/Lig coatings showed mild decrease in survival of healthy immunocompetent PBMC, unstimulated, and PHA stimulated compared to the control cell sample ($S = 100\,\%$). According to classification found in literature [70], Ag/HAP coating and Ag/HAP/Lig coating with 1 wt% Lig displayed as noncytotoxic against target PBMC, while Ag/HAP/Lig coating with 10 wt% Lig is classified as slightly cytotoxic. The survival of PBMC was higher in the presence of Ag/HAP/Lig coating with 1 wt% Lig than in the presence of Ag/HAP/Lig coating with 10 wt% Lig, therefore the optimum nontoxic lignin concentration is 1 wt%.

Antibacterial effect of nonsintered Ag/HAP/Lig (1 wt% Lig) coatings was investigated against pathogenic Gram-positive bacteria strain *S. aureus* [46]. The titanium-coated samples without silver (HAP and HAP/Lig coatings) were used as a

Table 5.8 Survival of PBMC cells and stimulated PBMC with addition of mitogen phytohaemagglutinin (PHA) in the presence of nonsintered Ag/HAP and Ag/HAP/Lig coatings

Cell type			
Peripheral blood mononuclear cells (*PBMC*)			
Material	Ag/HAP coating	Ag/HAP/Lig coating, 1 wt% Lig	Ag/HAP/Lig coating, 10 wt% Lig
Cell survival (*S*), %	94.6 ± 4.2	89.4 ± 3.5	76.0 ± 7.6
Classification	Noncytotoxic	Noncytotoxic	Slightly cytotoxic
PHA-stimulated peripheral blood mononuclear cells (*PBMC*)			
Cell survival (*S*), %	92.1 ± 5.0	83.8 ± 6.3	79.6 ± 6.3
Classification	Noncytotoxic	Noncytotoxic	Slightly cytotoxic

Reprinted from [46] with permission from Elsevier

control when comparing the antibacterial effect of Ag/HAP and Ag/HAP/Lig coatings. Figures 5.13 and 5.14 depict the antibacterial activity of titanium-coated samples against strain *S. aureus* TL in PB solution. Pure HAP and HAP/Lig coatings did not show any antibacterial effect and inhibition was not observed even after 24 h. A slight decrease in the total number of cells after 1 h of incubation with samples HAP and HAP/Lig probably occurs as a result of adhesion of cells to the particles of HAP. Antibacterial activity of the Ag/HAP and Ag/HAP/Lig coatings could be noticed immediately after inoculation of samples and further reduction of cells viability for two logarithm units is achieved after just 1 h of incubation when compared to the initial number of cells in suspensions (percentage of cell reduction was 98.17 % and 97.67 %, respectively). Based on the silver ion released results, concentration of silver ion after 1 h was 0.4493 ppm (Fig. 5.12), which is sufficiently small

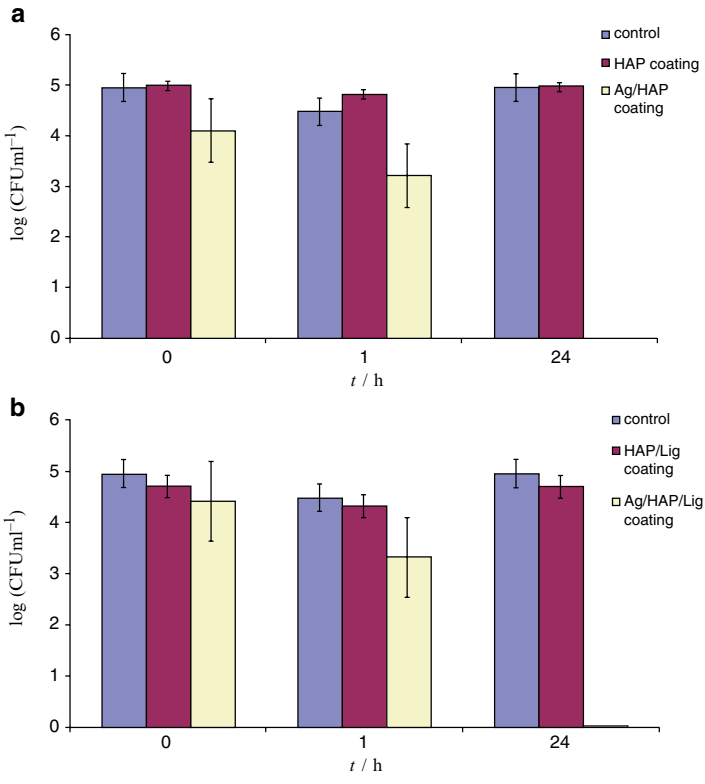

Fig. 5.13 Reduction of viable cell number of *S. aureus* TL after contact with nonsintered (**a**) HAP and Ag/HAP coatings and (**b**) HAP/Lig and Ag/HAP/Lig coatings, for 0, 1, and 24 h in PB as compared to the control w/o samples (reprinted from [46] with permission from Elsevier)

concentration to achieve antibacterial effect without causing cytotoxicity (Table 5.8). The antibacterial efficiency of nonsintered Ag/HAP and Ag/HAP/Lig coatings exhibited high reduction of bacteria strain *S. aureus* TL, since after 24 h, analyzed samples did not contain any viable cell and visible colony were not detected in a samples directly taken from suspension (Fig. 5.14), providing good protection against infection. An immediate silver ion release provides for the imminent drop in CFU numbers even after 1 h of exposure, which is bactericidal effect needed for prevention of biofilm formation [89].

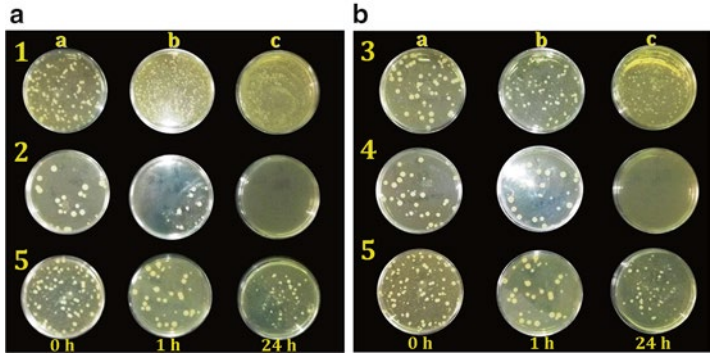

Fig. 5.14 Antibacterial activity of nonsintered *1*—HAP, *2*—Ag/HAP, *3*—HAP/Lig, and *4*—Ag/HAP/Lig coatings on LB agar plates, after 0, 1, and 24 h, columns: *a*—dilution 100×, *b*—directly from the suspension, *c*—directly from the suspension, respectively, and *5*—control (reprinted from [46] with permission from Elsevier)

5.4 Hydroxyapatite/Graphene Coatings for Hard Tissue Implants

5.4.1 Hydroxyapatite/Graphene Coatings Electrodeposited on Titanium Substrate

Carbon nanomaterials with two-dimensional (2D) morphologies as a single layer of sp^2-hybridized carbon atoms packed in a honeycomb form, known as graphene (Gr), have been reported recently. The extraordinary electrical, thermal, and mechanical properties (tensile strength 130 GPa and Young's modulus 0.5–1 TPa) and high specific surface area (up to 2630 m^2g^{-1}) have drawn great attention as a reinforcement in the composite field of material science [96–98]. Graphene materials possess physical properties identical to those of carbon nanotubes (CNTs) but have a larger surface area. It has been reported that inclusion of Gr into polymer or ceramic matrices leads to remarkable improvements in the properties of the host materials [96]. Furthermore, graphene nanosheets (GNSs), formed by several layers of Gr with a thickness of up to 100 nm [99], are much easier to produce than other graphene materials and successfully use as nanofillers for

polymers [100], metals [101], and ceramics [98, 102] to produce composites with exceptional mechanical properties.

Biomaterials used in orthopedic surgery usually encounter complex service environments and therefore require versatile performances from the materials [1, 103, 104]. HAP provides bioactivity, biocompatibility, and an ability to initiate osteogenesis, but on the other side it lacks good mechanical properties. Because of its poor mechanical properties, such as an intrinsic brittleness, low fracture toughness (0.8–1.2 MP), low flexural strength (<140 MPa), and wear resistance [105], the main focus of HAP research has been to improve its mechanical performance by combining it with various reinforcements.

The focus of the latest published research has been the fabrication of Gr or its derivatives to create reinforced HAP biocomposites because of the exciting findings regarding the biological performance of Gr [103]. Nonetheless, the mechanical properties of hydroxyapatite limit its use in the regeneration of various parts of the bone systems, especially those under significant mechanical tension. The incorporation of Gr or its derivatives as reinforcing materials in HAP composites has been studied and reported using in situ synthesis [106, 107], spark plasma sintering (SPS) [108], biomimetic mineralization [78, 109, 110], chemical vapor deposition [111], and electrospinning [112]. The general idea of using Gr as nanofiller is to minimize the brittleness of HAP and gain an improved composite. Any reinforcement material for HAP should not only significantly improve the mechanical properties but also retain HAP's original biocompatibility. Latest published reports on graphene materials aimed to demonstrate that crack deflection is more effective for sheet-like reinforcement than for tubular-like reinforcement, suggesting that Gr exhibits a more pronounced toughening effect on brittle materials than do carbon nanotubes (CNTs) [113]. Also, reports on CNTs cytotoxicity in organic environments are disconcerting [114]. Unlike CNTs, Gr is synthesized in relatively pure ways and is therefore expected to show little cytotoxicity, since few metallic catalyst particles are associated with its production [115]. Also, recent reports have discussed the qualities of Gr and Gr-based composites, including low toxicity toward human osteoblasts [116], excellent antibacterial properties [117],

and its potential to initialize apatite mineralization [78]. Therefore, our aim was to explore the potential of implementing Grs as HAP reinforcement for load-bearing orthopedic applications.

In the recent study [48], the hydroxyapatite/graphene (HAP/Gr) composite was electrodeposited on Ti using the EPD to obtain uniform bioactive coating with improved mechanical strength and favorable corrosion stability in SBF solution. Electrophoretic deposition was performed from ethanol suspension containing 1 wt% of nanosized HAP and 0.01 wt% of Gr. The HAP/Gr composites were deposited using the constant voltage method at 60 V and a deposition time of 2 min.

The surface morphology of the HAP/Gr composite coating after air drying is shown in Fig. 5.15a. Compared to the pure HAP coating (Fig. 5.15b), the HAP/Gr composite coating had fewer cracks and no peeling off the Ti surface in the macroscopic observation. That is a solid indication that Gr effectively acts as a nanoreinforcement filler and prevents the creation and propagation of cracks by frictional pull out, crack deflection, and crack bridging as the major toughening mechanism that resists crack propagation [98]. Namely, the high specific surface area of graphene nanosheets is capable of forming an increased contact area with matrix. As a result, the bonding strength between graphene and HAP grain could be significantly enhanced, and more energy would be required to make the nanofiller pull-out from HAP matrix. As previously reported by Zhang et al. [98], rough and wrinkled surface texture of the GNSs

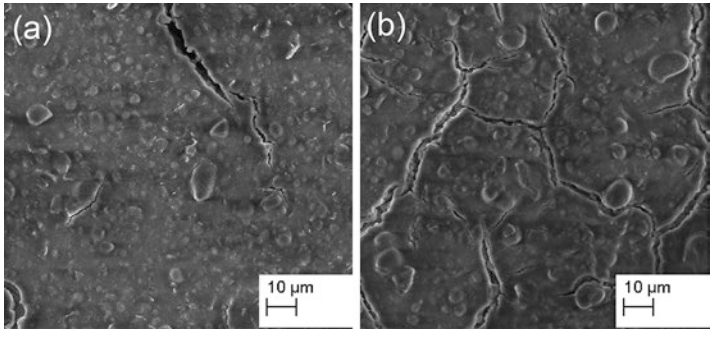

Fig. 5.15 FE-SEM micrographs of the HAP/Gr (**a**) and pure HAP (**b**) coatings (reprinted from [48] with permission from Elsevier)

also plays an important role in enhancing mechanical interlocking, leading to an increased load transfer efficiency between HAP matrix and GNSs. In addition, it was shown that the two ends of the GNS are well bonded to the adjacent HAP grains with GNS plane nearly parallel to the fracture surface. For ceramics, it is well known that the toughness of grain boundaries is lower than the grains. Thus, as grain-boundary toughening mechanism, it is hypothesized that the grain bridging by GNSs has a fundamental role in inhibiting crack propagation along grain boundary.

Further evidence of bonding between Gr and HAP is characterized by the FT-IR spectrum of HAP/Gr composite coating shown in Fig. 5.16. Three absorption bands were clearly distinguished at 1089, 1024, and 962 cm^{-1} in the ν_3 and ν_1 phosphate mode region. The FT-IR spectra have distinct intensity vibrational bands at 601 and 560 cm^{-1}, corresponding to the ν_4 vibrational mode, as well as

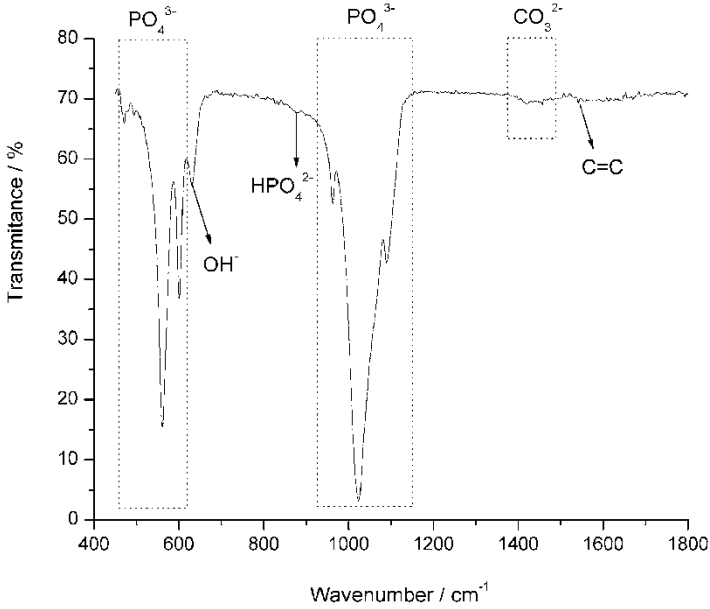

Fig. 5.16 FT-IR spectrum in the wavenumber range of 400–1800 cm^{-1} of the HAP/Gr coating (reprinted from [48] with permission from Elsevier)

a weak intensity band at 470 cm^{-1} as a component of the ν_2 mode that corresponds to P–O bending [105]. The characteristic band at 630 cm^{-1} can be attributed to structural OH^- groups in the HAP lattice [118]. The low intensity band at 875 cm^{-1} indicates the acidic phosphate group HPO_4^{2-} due to the P-(OH) stretching vibration [105, 119]. The absorbance bands in the range of 1500–1400 cm^{-1} correspond to ν_3 asymmetrical stretching vibrations of the CO_3^{2-} ions. The position of the carbonate bands indicates predominately B-type HAP, which is the preferential substitution in human bones, known for its excellent bioactivity and osteoinductivity [120]. Very small bands at ~1540 cm^{-1} correspond to the skeletal vibration of Gr [121, 122] due to sp^2 hybridized C=C vibration stretching, confirming its presence in the composite coating.

The surface elements of the HAP/Gr composite coating and the pure HAP coating were characterized by XPS [48]. In the XPS spectra, the Ca2p spectrum reveals a doublet with $Ca2p_{3/2}$ (BE = 347.29 eV) and $Ca2p_{1/2}$ (BE = 350.82 eV), and the P2p spectrum reveals a single P2p peak at BE = 133.33 eV, indicating the presence of HAP [92, 123]. The main O1s peak component at BE = 531.27 eV for the HAP/Gr coating is attributed to PO_4^{3-} groups [91]. Incorporation of Gr and the formation of the new composite are clearly evidenced by the presence of C1s in the HAP/Gr coating, whereas no trace of carbon is detected in the pure HAP coating (Table 5.9). According to the literature, the C1s peak with BE = 285.0 eV is attributed to aromatic hydrocarbons [124], which is in excellent compliance with the single-sheet Gr structure of honeycomb six-membered rings. Even though the ideal Ca/P ratio for stoichiometric HAP is known to be 1.67, stable HAP phases have been found to exist over a range of Ca/P ratios from 1.3 to 1.8 [61]. Therefore, HAP/Gr composite represents a true hybrid coating with a Ca/P ratio of 1.58, which is greater than that of the pure HAP coating, 1.50 (Table 5.9), and closer to the stoichiometric value (Ca/P = 1.67). The XPS results confirm the presence of Gr and stand in good agreement with the FT-IR analysis result.

Table 5.9 Atomic percentage of carbon and Ca/P ratio at HAP/Gr and HAP coatings surface

Coating	C1s (at.%)	Ca/P
HAP/Gr	11.90	1.58
HAP	–	1.50

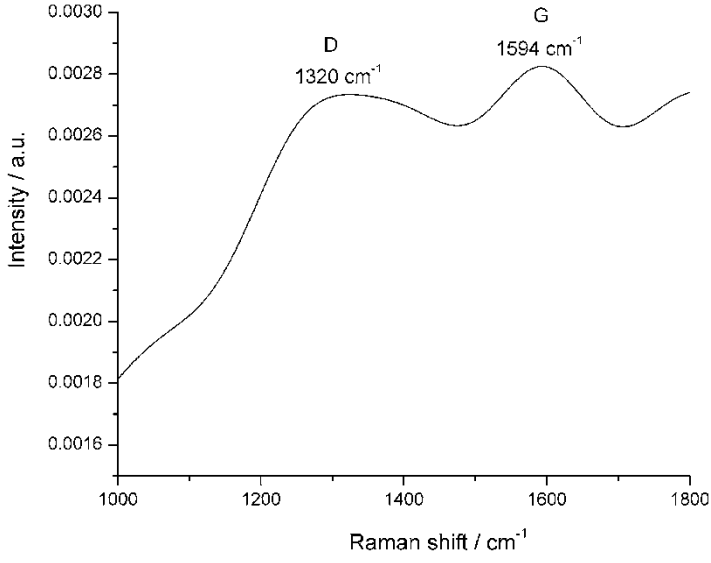

Fig. 5.17 *D* and *G* band region in Raman spectrum of the HAP/Gr coating (reprinted from [48] with permission from Elsevier)

Raman spectroscopy has proved to be the most useful and precise tool to characterize Gr. Therefore, measurements were performed to verify the Gr presence in the HAP/Gr composite coating. The spectrum in Fig. 5.17 reveals a distinct pattern of single-layer Gr. The first main feature is the *G*-peak, visible at 1594 cm^{-1}, which arises due to the in-plane vibration of sp^2 carbon atoms [125]. The *G*-band corresponds to ordered sp^2-bonded carbon atoms. The second pronounced band is the *D*-peak, at 1320 cm^{-1}. The *D*-band represents defects originating from the disordered aromatic structure on the Gr edges [126]. The low intensity of both the *D* and *G* peaks can be attributed to a low concentration of Gr in the HAP/Gr coating.

The EPD-assembled HAP/Gr composite coating was subjected to thermogravimetric analysis to explore their thermal stability in detail. The thermogravimetric (TG) and differential TG (DTG) curves in Fig. 5.18 reveal the weight loss of the HAP/Gr

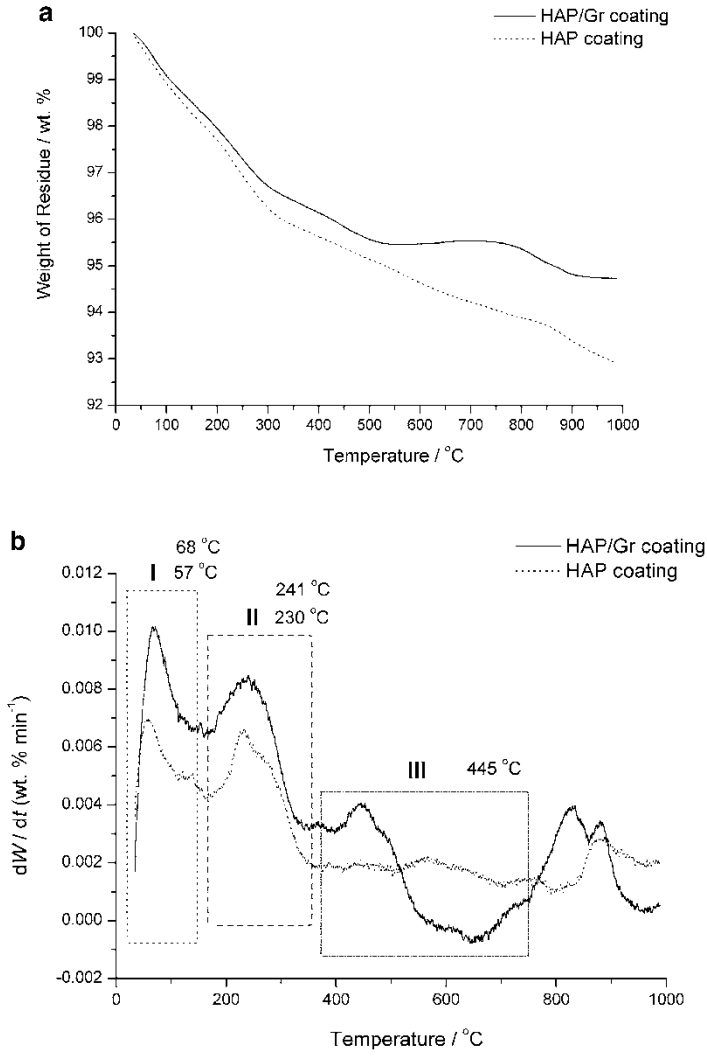

Fig. 5.18 (**a**) TG curves of the HAP/Gr and HAP coatings; (**b**) DTG curves of the HAP/Gr and HAP coatings (reprinted from [48] with permission from Elsevier)

coating in the observed temperature range (25–1000 °C). Interestingly, even the low loading of Gr changed the thermal pattern of the HAP/Gr coating (Fig. 5.18a). The total weight loss for the HAP/Gr coating in the temperature range of 25–1000 °C was 5.28 wt%, confirming the greater thermal stability of graphene-based HAP coating compared to pure HAP coating, which lost 7.16 wt%. The HAP/Gr coating decomposed in a three-step weight loss process, as is clearly seen in Fig. 5.18b. The first stage occurred up to 150 °C, as observed by the sharp peak in the DTG curve at 68 °C. This stage is usually assigned to desorption of adsorbed water molecules on the crystallite surface. In the second stage, corresponding to the temperature range from 150 to 350 °C, a peak in the DTG curve appears at 241 °C that is attributed to the release of crystalline water that represents the beginning of HAP dehydroxylation [44, 45] and unstable carbon in the Gr structure [127]. The third stage, observed between 350 and 750 °C, is revealed in a peak in the DTG curve at 445 °C that originates from decomposition of the remaining unstable carbon, shown in the literature for different Gr composites [127, 128]. The third stage can also be attributed to the dehydroxylation and early slow decomposition of HAP [44]. At temperatures between 750 and 1000 °C, HAP decomposition occurs.

The pure HAP coating decomposed in a manner similar to its HAP/Gr counterpart. The first stage, up to 150 °C with a sharp peak in the DTG curve at 57 °C, is assigned to desorption of water molecules adsorbed on the crystallite surface. The second stage, from 150 to 350 °C with a peak in the DTG curve at 230 °C, corresponds to the release of crystalline water, i.e., the onset of HAP dehydroxylation. The third stage, between 350 and 750 °C, could be attributed to the complete dehydroxylation of HAP followed by its initial decomposition. Above 750 °C, HAP decomposes. An important distinction in the thermal pattern is observed in the peak in the DTG curve for the HAP/Gr composite coating at 445 °C indicating the decomposition of the remaining Gr. That peak is not evident for the pure HAP coating, as expected.

All experimental results obtained from SEM, FT-IR, XPS, and TGA analyses confirm the mechanism of the formation of the com-

posite HAP/Gr coating, as follows. According to Liu et al. [129] there is no obvious evidence indicating the chemical reaction between HAP and graphene sheets at their interfaces. It is instead very likely that HAP and graphene sheets are connected by Van der Waals bonding. Nucleation of HAP crystals probably originates on either the graphene wall or the cross-section of graphene multisheets, followed by subsequent crystal growth along or perpendicular to the surface of the graphene sheet. They proved that the (300) plane of HAP crystals is very likely parallel to the surface of graphene walls. According to the atomic structure of HAP, its (300) plane contains Ca atoms at each corner of the rectangle and the distance between each pair of Ca atoms is 0.9418 and 0.6884 nm, whereas the distance between two neighboring Ca atoms in plane (100) is 0.9418 and 0.3442 nm, respectively. In addition, it was revealed that the distance between adjacent graphene sheets is 0.347 nm. In fact, single-layer graphene is constituted by carbon atoms arranged periodically in a hexagonal manner, and the nearest distance between two carbon atoms is 0.142 nm. Multilayer graphene sheets contain several graphene monolayers with the interwall distance of 0.34 nm. On the other hand, the lattice spacing of the (002) plane of HAP is 0.344 nm. Since (300) plane takes priority over the (100) plane to match with the surface of graphene sheets, and the open ends of graphene multisheets form relatively stronger interfaces with the (002) plane of HAP crystals than other planes like (211), it can be considered that the (300) plane of HA forms a naturally strong and coherent interfacial bond with the surface of the graphene wall and the cross-section of graphene builds with the (002) plane of HAP crystals a stronger interface due to the smaller lattice mismatch. As a consequence, the less cracked morphology and greater thermal stability of our HAP/Gr coating were noticed in comparison to pure HAP coating.

5.4.1.1 Mechanical Properties

The mechanical properties of the HAP/Gr and pure HAP coatings deposited on the Ti surface by EPD were examined using nanoindentation test and load-penetration depth curves

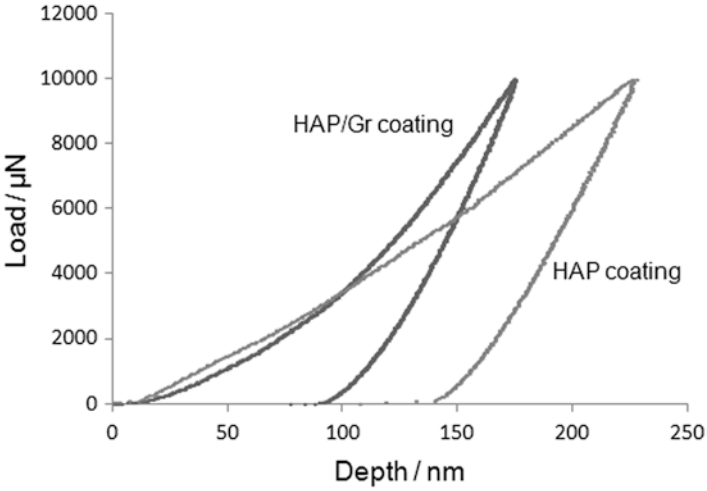

Fig. 5.19 Load-penetration depth curves for indents on HAP and HAP/Gr coatings (reprinted from [48] with permission from Elsevier)

Table 5.10 The values of mean hardness, H, mean reduced elastic modulus, E_r, and E_r/H ratio obtained from the nanoindentation testing of HAP and HAP/Gr coatings

Coating	$\boldsymbol{H}$ (GPa)	$\boldsymbol{E}_r$ (GPa)	$\boldsymbol{E}_r$ ($\boldsymbol{H}$)
HAP	7.4 ± 3.3	132.2 ± 25.5	17.86
HAP/Gr	14.8 ± 2.0	190.9 ± 18.0	12.90

(Fig. 5.19, Table 5.10). The HAP/Gr composite coating was more resistant to indentation and had a higher load than HAP at the same indentation depth. For the HAP/Gr composite, the mean hardness, H, was 14.8 ± 2.0 GPa, almost twice as high as the measured hardness values of pure HAP (7.4 ± 3.3 GPa). The mean reduced elastic modulus, E_r, of the HAP/Gr composite was 190.9 ± 18.0 GPa, an increase of almost 50 % (HAP E_r = 132.2 ± 25.5 GPa). The differences in the nanomechanical behaviors of these two coatings could also be revealed from Fig. 5.19. It can be clearly observed that the HAP/Gr composite coating with higher hardness has much lower penetration depth

than that of the HAP coating. Moreover, the higher reduced modulus of the HAP/Gr composite coating can be reflected from Fig. 5.19, since the slope of the initial portion of the unloading curve for the HAP/Gr composite coating is obviously higher than that for the HAP coating. These results are a definite demonstration that the introduction of graphene effectively improves the mechanical properties of HAP, even at a very low concentration. This can be attributed to the proposed toughening mechanism and grain bridging by graphene nanosheets that act by inhibiting crack propagation along the grain boundary. The E_r/H ratio indicates fracture toughness [47, 87]. For pure HAP and HAP/Gr coatings, the E_r/H ratios were 17.86 and 12.90, respectively, indicating that Gr reinforcement caused decrements in the value of E_r/H, implying that toughness increases with Gr addition as a result of crack bridging, deflection, and grain bridging by the Gr nanofiller.

Although it is well known that the mechanical properties of the metals and alloys used for implantation are not well matched with those of bone, resulting in stress-shielding effects, and stress shielding phenomenon can lead to severe clinical issues such as implant loosening and reduced stimulation of new bone growth [130, 131], there are few points that need to be considered especially for long-term implantation since the effect of biological compatibility has a greater bearing than the mechanical compatibility. The biological responses to implant materials strongly depend on the implant's surface properties since the interaction between the cells and biomaterials takes place at the tissue–implant interface. That is why the bioactivity of HAP/Gr composite coating was thoroughly tested by two standard different methods: by the immersion of the material in simulated body fluid (SBF) and by using a cell culture test for examining cell proliferation and differentiation. Moreover, the HAP/Gr composite coating can provide a Ti-based implant with not only the bioactivity and biocompatibility for facilitating chemical bonding with living bone tissues [67], but also a combination of high hardness and high modulus can enhance the wear resistance of the base material to prevent from formation of wear debris from the implant surface [132].

5.4.1.2 In Vitro Bioactivity

The bioactivity of the HAP/Gr composite coating was assessed by immersion in SBF solution, at 37 °C for 7 days. XRD patterns, taken before and after immersion in SBF, are shown in Fig. 5.20. High-intensity HAP peaks at crystal planes (002), (211), (112), and (300), $2\theta = 25.8$, 32.0, 32.9, and 34.1°, perfectly match the HAP pattern. As predicted, the Ti substrate is mainly present in its pure form on the coating interface. According to a report by Sharma et al. [133], thermally reduced Gr showed a broad (002) peak at $2\theta = 23$–26°. However, HAP diffraction peaks mostly shielded that peak. In addition, the specific broad peak at $2\theta = 22°$ observed for pure Gr is also overlapped by diffraction peaks originating from HAP. Finally, the carbon peak at $2\theta = 26.6°$, as it appears in diffractograms, is attributed to starting carbon material. The XRD results along with FT-IR (Fig. 5.16) and Raman (Fig. 5.17) verified the successful Gr transfer along with HAP by

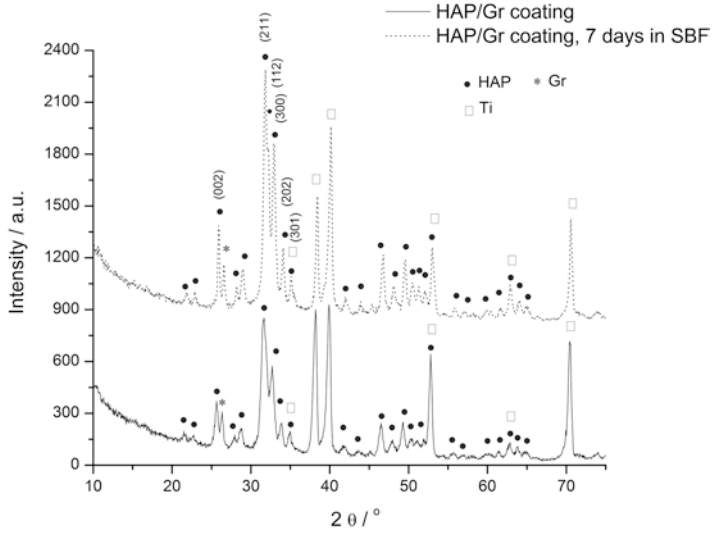

Fig. 5.20 XRD patterns of the HAP/Gr coating before and after immersion in SBF at 37 °C for 7 days (reprinted from [48] with permission from Elsevier)

EPD in the HAP/Gr coatings. The formation of a bone-like apatite layer on the surface of bioactive materials has been reported after soaking those materials in a biomimetic system such as SBF. The shift of characteristic HAP peaks at crystal planes (002), (211), and (300) toward higher angles is evident after immersing the HAP/Gr composite coating in SBF for 7 days (Fig. 5.20). Those findings were attributed to carbonate ions in the crystal lattice and confirmed the growth of carbonated HAP. Therefore, the shifting of diffraction peaks is typical for weak crystalline, carbonated HAP, as it is found in bone. Using the X-ray Line Profile Fitting Program (XFIT) with a fundamental parameters convolution approach for generating line profiles [134], the coherent domain sizes and microstrain of the HAP/Gr composite coating were calculated using the (002), (211), (112), (300), (202), and (301) crystal planes. The crystallite domain size is calculated to be 18.9 and 33.7 nm, before and after immersion in SBF, respectively. The difference between the crystallite size before and after immersion is probably due to the incorporation of CO_3^{2-} ions into the apatite lattice by occupying the OH^- sites or the PO_4^{3-} position [75].

The FE-SEM microphotograph in Fig. 5.21a displays the surface homogeneity of the HAP/Gr composite coating before immersion in SBF. Individual rod-like HAP grains, less than 50 nm in size, can be distinguished. In Fig. 5.21b, the FE-SEM image of the

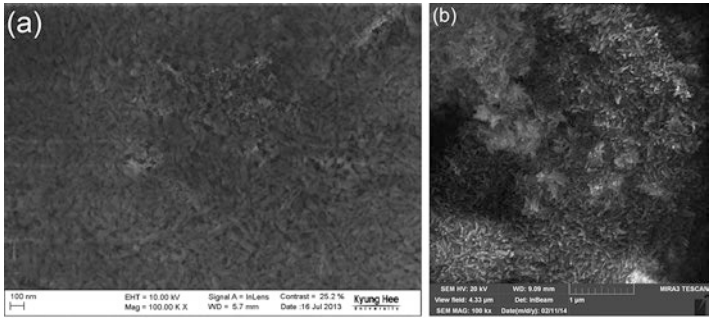

Fig. 5.21 FE-SEM micrographs of the HAP/Gr coating before (**a**) and after (**b**) immersion in SBF at 37 °C for 7 days (reprinted from [48] with permission from Elsevier)

HAP/Gr coating after soaking in SBF, the newly formed apatite layer containing plate-shaped HAP crystals is clearly visible under high magnification (×100,000). The mineralization area ultimately penetrates the whole surface of the HAP/Gr composite. The morphology of the mineralization product varies dramatically with incorporation of Gr into the HAP matrix. Easily distinct are curled, plate-shaped apatite forms on the HAP/Gr composite coating. Also, the observed highly porous surface structure after soaking is beneficial for better cell adhesion, as it enables better connection between the implant and the bone.

The high bioactivity of the HAP/Gr composite coating is confirmed by the formation of an apatite layer after just 7 days soaking in SBF, as proven by XRD and FE-SEM analysis. According to the mechanism proposed by Zhang et al. [98], the mineralization process proceeds in three stages: (1) dissolution-controlled stage, (2) precipitation-controlled stage, and (3) formation of bone-like apatite. In the first stage, dissolution of phosphate and calcium ions occurs. Calcium ion dissolution is governed by grain refinement and accelerates on the surface of the HAP/Gr coatings due to the suppression of HAP grain growth caused by adding Gr on the grain boundaries. As a result, the smaller grain size of the composite leads to increased specific area and improved interaction with SBF. In the second step, precipitation of an apatite layer occurs on the negative surface of the HAP/Gr coating as a consequence of the dissolution of calcium ions and subsequent emergence of nucleation sites. These events, elevated concentration of calcium ions in SBF, higher negative charge, and more available nucleation sites, allow the HAP/Gr composite coating to form a Ca-rich layer penetrating the whole sample surface. The third stage is the final formation of apatite as the Ca-rich layer attracts phosphate ions from the SBF and forms bone-like apatite clusters.

The corrosion stability of HAP/Gr and HAP coatings was evaluated in SBF solution by EIS measurements [48] to predict bone implant behavior after an implantation period in a human body and study corrosion caused by the hostile environment. To study corrosion stability and resistance of the biocomposite HAP/Gr coating, as well as a HAP coating as a reference, impedance spectra during different exposure times in SBF at 37 °C are presented in Fig. 5.22a, b.

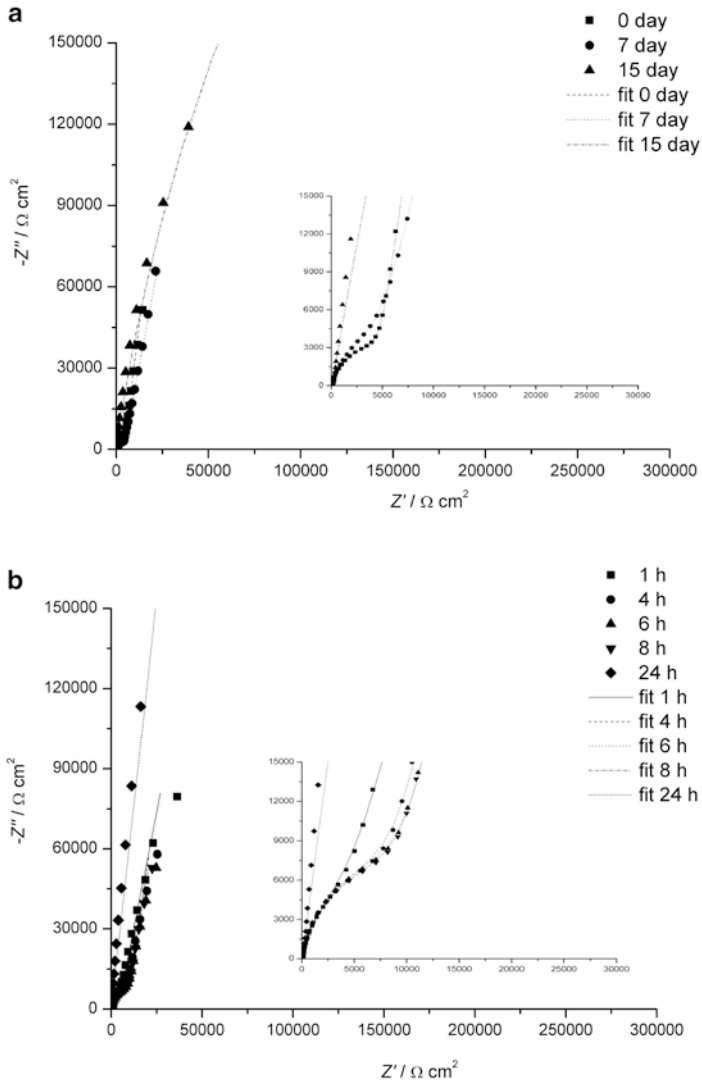

Fig. 5.22 The Nyquist plots of the HAP/Gr (**a**) and HAP coatings (**b**) after different immersion times in SBF at 37 °C (*dash line*—fitting) (reprinted from [48] with permission from Elsevier)

Fitting of the Nyquist plots was accomplished using the equivalent electrical circuits (EECs) shown in Fig. 5.11a, c. The fitted curves for different periods of immersion in SBF are shown in Fig. 5.22, and the obtained fitting values for each EEC parameter are presented in Table 5.11 for both the HAP/Gr and HAP coatings.

As clearly seen in Table 5.11, the n_c and n_{ox} values are higher than 0.80 for both coatings; therefore CPE_c can be considered the coating capacitance, C_c, and CPE_{ox} can be considered the capacitance of the oxide film on the Ti surface beneath the coating, C_{ox}. The EEC shown in Fig. 5.11a was used for fitting the Nyquist plots of the HAP/Gr composite coating over 14 days, and the EEC in Fig. 5.11c was used for fitting the Nyquist plot for the 15th day of SBF exposure, when coating adhesion loss had occurred. The R_c for the HAP/Gr composite coating decreased slightly during the first 2 days, indicating that the SBF solution diffused into the coating pores and filled it out during the initial 48 h. After the third day, increasing values of R_c indicate the beginning of the biomineralization process to form a new apatite layer onto the HAP/Gr surface. Finally, the calculated value of R_c was 34.2 kΩ cm^2 (Table 5.11) after 14 days of immersion in SBF solution. The high value of the coating pore resistance denotes improved bioactivity, which suggests that the HAP/Gr composite coating surface represented a site of nucleation and growth for a new apatite layer recognized as carbonated HAP, as confirmed by XRD (Fig. 5.20) and FE-SEM (Fig. 5.21). According to the literature, the transformation of HAP to a bone-like apatite in the human body certainly induces stable bonding to natural bone [86]. On the other hand, the pure HAP coating loses its corrosion stability after just 24 h, as evidenced by the diminishing semicircle in the Nyquist plot (Fig. 5.22), whereas the HAP/Gr composite retained its protective attributes. The obtained Nyquist plots for the pure HAP coating during the initial exposure of 8 h in SBF were fitted by the EEC in Fig. 5.11a. The values of R_c and C_c (Table 5.11) increased slightly during the initial 8 h period, indicating new apatite layer formation. However, after 24 h, fitting could only be done with the EEC in Fig. 5.11c that considers CPE_{ox}, indicating coating adhesion loss. Based on the EIS data, it is evident that the composite HAP/Gr composite coating exhib-

Table 5.11 Fitting values of equivalent electrical circuit parameters and goodness of fit (GOF) for the HAP/Gr and HAP coatings

t (h)	R_s (Ω cm^2)	R_c (kΩ cm^2)	CPE_c (μF cm^{-2})	n_c	CPE_{ox} (μF cm^{-2})	n_{ox}	Goodness of fit (GOF)
HAP/Gr							
1	20.6	12.5	60.4	0.80	131	0.87	1.57e^{-4}
3	21.7	11.5	58.4	0.81	209	0.93	1.38e^{-4}
5	21.7	9.3	56.0	0.81	213	0.91	6.52e^{-5}
7	22.7	7.6	53.2	0.82	215	0.90	6.27e^{-5}
24	36.1	3.9	47.8	0.85	227	0.90	2.37e^{-5}
48	38.2	3.7	48.7	0.84	194	0.90	3.65e^{-4}
72	21.6	5.0	49.8	0.84	180	0.86	1.75e^{-4}
120	42.2	6.5	53.8	0.83	146	0.85	2.09e^{-4}
168	45.8	9.3	58.2	0.82	117	0.84	2.66e^{-4}
216	66.6	15.1	58.1	0.82	96	0.85	2.33e^{-4}
264	18.9	27.5	57.9	0.81	65	0.87	3.16e^{-4}
312	48.9	34.2	57.7	0.82	58	0.85	5.10e^{-4}
360	81.6	–	–	–	49	0.86	7.37e^{-3}
HAP							
1	26.5	12.7	61.5	0.87	81	0.80	5.21e^{-4}
2	27.3	13.6	60.1	0.88	115	0.82	4.32e^{-4}
4	27.4	15.1	58.5	0.88	169	0.86	4.00e^{-4}
6	27.6	15.6	57.4	0.88	190	0.86	2.88e^{-4}
8	27.3	15.0	56.6	0.88	202	0.87	2.14e^{-4}
24	39.6	–	–	–	55.7	0.90	2.84e^{-3}

Reprinted from [48] with permission from Elsevier

ited biomimetic mineralization superior to its pure HAP counterpart. This is an additional confirmation of the proposed mechanism of enhanced precipitation of a newly formed apatite layer, evidenced also by FE-SEM.

5.4.1.3 Cytotoxicity and Antibacterial Activity

Cell survival in the presence of HAP/Gr composite coatings on Ti was determined using a standard MTT test [48]. Cell survival of PBMCs, calculated according to Eq. (5.2), was 72.3 ± 4.3 %. Examination of the cytotoxic effects showed a mild decrease in the survival of healthy immunocompetent PBMC compared to the control cell sample. According to a classification found in the literature [70], HAP/Gr composite coating can be considered noncytotoxic within the margin of error against target PBMC.

The antibacterial activity of HAP/Gr coating was tested against *S. aureus* TL and *E. coli* (ATCC 25922) in suspension using the spread-plate method [48]. Figure 5.23a, b depicts the antibacterial activity of Ti samples coated with HAP/Gr against strains of *S. aureus* TL and *E. coli* in PB, respectively. The antibacterial activity of Gr itself is controversial and demands further investigation. No antimicrobial activity of the HAP/Gr composite coating could be noticed immediately after inoculation of samples. Cell viability remained at the same level as observed up to 3 h postincubation when compared to the initial number of cells in suspension. After 24 h of exposure noticeable bacterial growth was evident in case of both bacteria. Based on the presented data, HAP/Gr coatings exhibited no reduction of *S. aureus* TL or *E. coli* after 24 h. The same behavior of *S. aureus* TL was reported for a pure HAP coating [46]. These results expand on the mixed opinions regarding an antibacterial effect of graphene.

Silver-Doped Hydroxyapatite/Graphene Coatings Electrodeposited on Titanium Substrate

Biocomposite Ag/HAP/Gr coatings were electrodeposited on titanium using EPD process, in order to obtain the bioactive coatings with antimicrobial activity aimed for hard tissue implants [49]. A nanosized Ag/HAP powder was prepared utilizing modified chemical precipitation method that involves reaction of calcium oxide, phosphoric acid, and silver nitrate [44, 45]. Silver ion concentration was kept at 0.4 ± 0.1 wt% in the final powder.

The microscopic view of the Ag/HAP/Gr coating surface morphology after air drying is shown in Fig. 5.24a. Compared to the Ag/HAP coating (Fig. 5.24b), the Ag/HAP/Gr composite coating had fewer cracks.

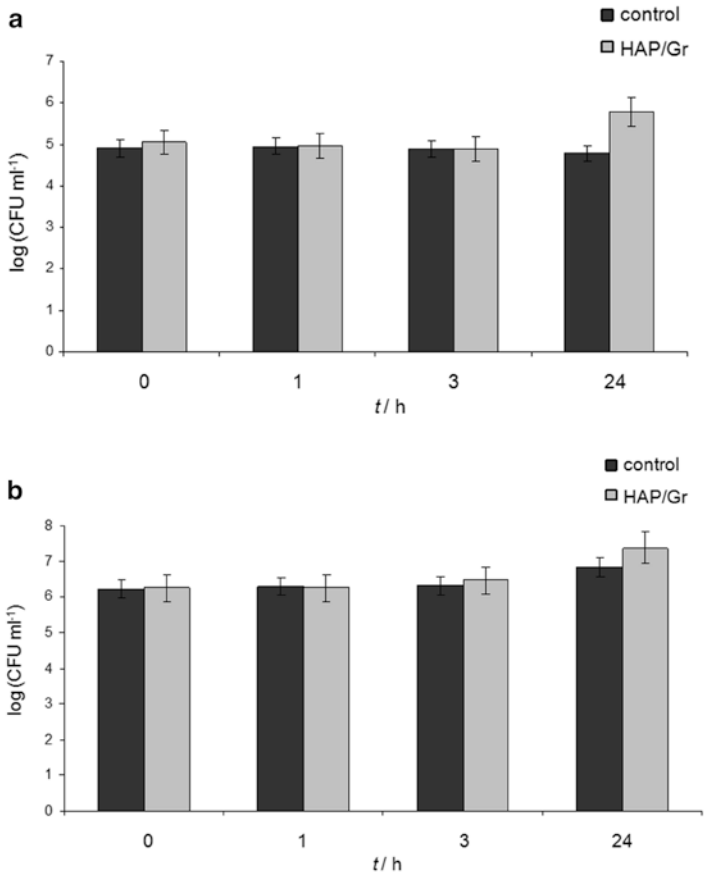

Fig. 5.23 Reduction of viable cell number of *S. aureus* (**a**) and *E. coli* (**b**) after contact with the HAP/Gr coating for 0, 1, 3 and 24 h in PB as compared to the control w/o samples (reprinted from [48] with permission from Elsevier)

Judging by FE-SEM analysis, addition of nanoreinforcement filler strongly prohibits resurfacing and crack propagation. Graphene nanosheets are shown to prevent crack propagation by frictional pull out, crack deflection, and crack bridging [98]. The less cracked morphology of graphene-based coating can be explained by the bonding mechanism between HAP lattice and graphene sheets, as was explained for HAP/Gr coating (Sect. 4.1).

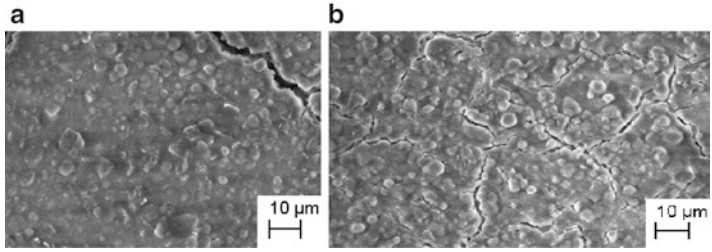

Fig. 5.24 FE-SEM micrographs of the Ag/HAP/Gr (**a**) and Ag/HAP (**b**) coatings, magnification ×1000 (reprinted from [49] with permission from Elsevier)

Raman spectroscopy was performed in order to confirm the incorporation of graphene in composite Ag/HAP/Gr coating. The *D* peak at 1260 cm^{-1} corresponding to edges, other defects, disordered sp^3-bonded carbon atoms and impurities, and *G*-peak at 1588 cm^{-1} corresponding to ordered sp^2-bonded carbon atoms (Fig. 5.25a) confirmed the graphene structure in its pure form.

FT-IR analysis was employed to shed light on the Gr presence in the composite coating and possible bonding within. In Fig. 5.25b the most prominent bands at the wave numbers 1089, 1024, 962, 601, 560, and 470 cm^{-1} are attributed to stretching and bending of phosphate groups in hydroxyapatite. The low intensity band at 875 cm^{-1} is assigned to acidic phosphate group, HPO_4^{2-} ions [119]. The band at 630 cm^{-1} corresponds to structural OH^- groups of HAP lattice [118]. The stretching vibrations of CO_3^{2-} ions in HAP are evidenced by the absorbance bands (1500–1200) cm^{-1} that correspond to $\nu_3CO_3^{2-}$. Analyzing this spectrum, the exact position of the CO_3^{2-} bands indicates prevalence of B-type hydroxyapatite advantageous in the human bone due to excellent bioactivity and osteoinductivity [120]. Absorption bands located at ~1540 cm^{-1} in the FT-IR spectrum of the composite correspond to the skeletal vibration of Gr [121, 122].

The thermogravimetric (TG) and differential TG (DTG) curves of Ag/HAP/Gr coating over temperature range of 25–1000 °C are shown in Fig. 5.26.

Similarly to HAP/Gr coating, from DTG curve can be clearly seen that thermal decomposition occurred in three steps. The first stage is evident from 25 to 150 °C, with 3.39 wt% mass loss and

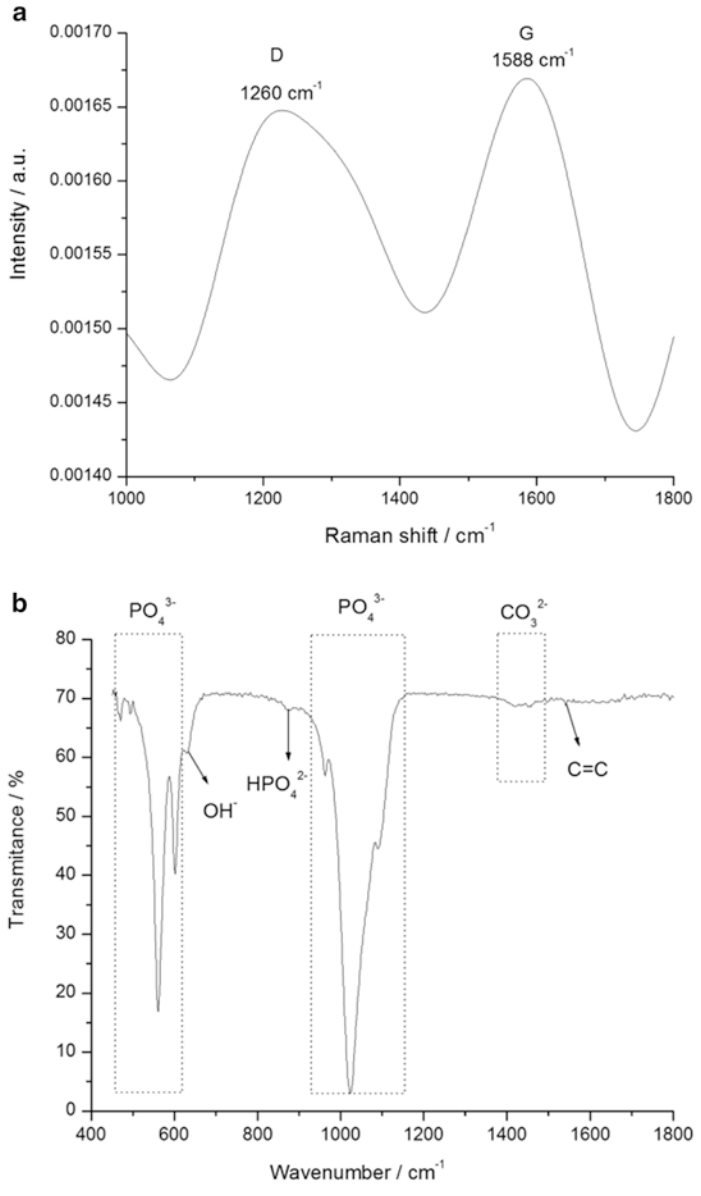

Fig. 5.25 *D* and *G* band region in Raman spectrum (**a**) and FT-IR spectrum in the wavenumber range of 400–1800 cm^{-1} (**b**) of the Ag/HAP/Gr coating (reprinted from [49] with permission from Elsevier)

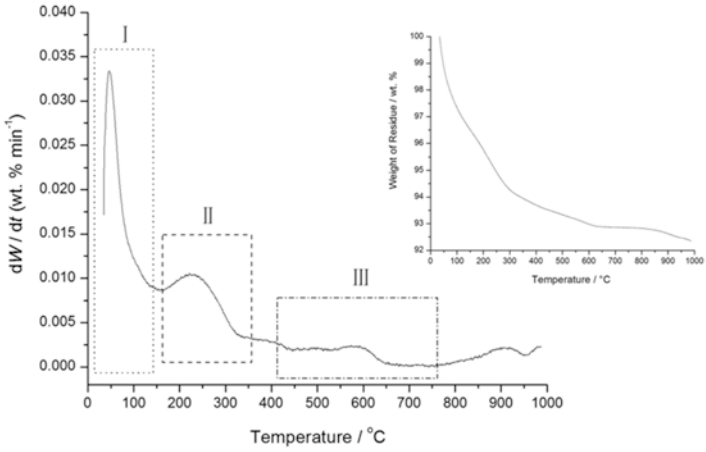

Fig. 5.26 TG (*inset*) and DTG curves of the Ag/HAP/Gr coating (reprinted from [49] with permission from Elsevier)

sharp peak in DTG curve at 46 °C. This stage is assigned to desorption of adsorbed water from the crystallite surface. Second stage (150–350 °C), with 2.62 wt% mass loss and peak in DTG curve at 239 °C, is attributed to the finalization of crystalline water release process and the beginning of HAP dehydroxylation [44, 45] and decomposing of unstable carbon in graphene structure [127]. Finally, the third stage (350–750 °C) with 1.11 wt% mass loss and peak in DTG curve at 584 °C, originated from decomposition of remaining unstable carbon, also evidenced in literature for different graphene composites [127, 128]. Also, this stage can be attributed to early slow decomposition of HAP that also continues above 750 °C. Total weight loss for the Ag/HAP/Gr coating in the temperature range of 25–1000 °C was 7.12 wt% (Fig. 5.26), confirming the greater thermal stability of graphene-based Ag/HAP compared to Ag/HAP as reference, 7.90 wt% [135]. The thermal stability of Ag/HAP/Gr composite was substantially improved as a consequence of bonding mechanism between graphene sheets and hydroxyapatite lattice.

The surface elements of Ag/HAP/Gr coating as well as Ag/HAP coating as reference were characterized by XPS [49]. Survey spectrum of Ag/HAP/Gr coating is shown in Fig. 5.27.

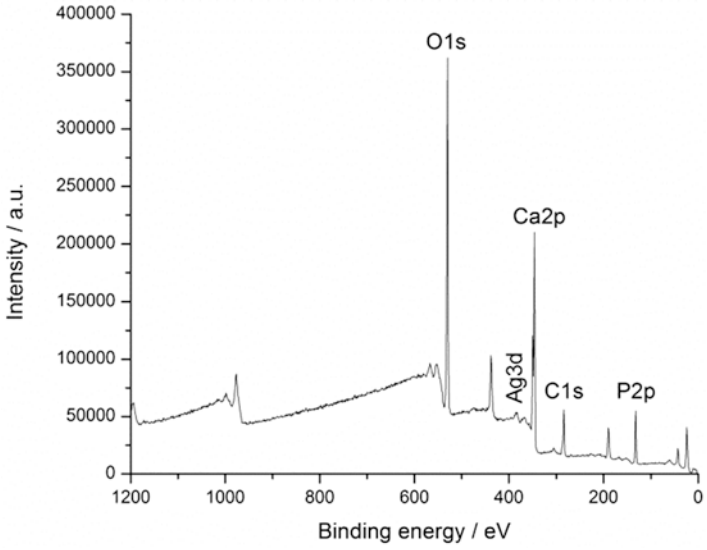

Fig. 5.27 XPS general spectrum of the Ag/HAP/Gr coating (reprinted from [49] with permission from Elsevier)

Table 5.12 Atomic percentage of carbon and Ca/P ratio at Ag/HAP/Gr and Ag/HAP coatings surface

Coating	C1s/at.%	Ca/P
Ag/HAP/Gr	12.05	1.52
Ag/HAP	–	1.50

The XPS narrow scan spectra of Ag element are present in both Ag/HAP and Ag/HAP/Gr coatings [49]. The peak for Ag3d peak (BE = 369.5 eV) agrees well with the literature data [136]. Observation of main peak O1s at binding energy of 531.3 eV for Ag/HAP/Gr coating is attributed to the presence of PO_4^{3-} groups incorporated within apatite lattice [91]. Survey spectra of the Ag/HAP/Gr coating revealed graphene incorporation, while no trace of C1s was detected for the Ag/HAP sample (Table 5.12). The C1s peak corresponding to the binding energy of 285.0 eV could be attributed to aromatic hydrocarbons [124], actually C=C sp^2 bonds in the graphitic network.

Based on the survey spectra Ca/P ratio for the Ag/HAP/Gr composite coating was calculated to be 1.52 (Table 5.12). Since stable HAP phases have been found to exist over a range 1.3–1.8 [61], graphene provided an optimal Ca/P ratio in the composite thus enabling successful bone integration with biomaterial.

5.4.1.4 Mechanical Properties

Nanoindentation testing was conducted to investigate the effect of added graphene to mechanical properties of the Ag/HAP/Gr coating (Table 5.13). For the Ag/HAP/Gr composite coating, the mean hardness, H, was 15.5 ± 3.3 GPa, which is approximately 10 % increase compared to measured hardness values of Ag/HAP (14.5 ± 5.8 GPa). The mean reduced elastic modulus, E_r, of the Ag/HAP/Gr composite was 183.0 ± 21.9 GPa, an increase of almost 10 % (Ag/HAP, E_r = 172.1 ± 36.9 GPa). Overall the mechanical properties of Ag/HAP/Gr are improved due to addition of Gr as nanofiller even at low concentration. The impact of Ag addition is revealed by comparing Ag/HAP and pure HAP coating, as observed Ag contributed to the increase of both E_r (172.1 vs. 132.2 GPa) and H (14.5 vs. 7.40 GPa) [47].

An evaluation of E_r/H value is a prerequisite for the evaluation of fracture toughness [47, 87]. In the case of pure HAP and Ag/HAP coatings, E_r/H ratios were 17.86 and 11.87, respectively, while in the case of HAP/Gr and Ag/HAP/Gr coatings E_r/H ratios were 12.90 and 11.81, respectively, indicating that Ag reinforcement caused decrements in the value of E_r/H, implying that toughness increases with Ag addition [47].

Table 5.13 The values of mean hardness, H, mean reduced elastic modulus, E_r, and E_r/H ratio obtained from the nanoindentation testing of Ag/HAP and Ag/HAP/Gr coatings

Coating	H/GPa	E_r/GPa	E_r/H
Ag/HAP	14.5 ± 5.8	172.1 ± 36.9	11.87
Ag/HAP/Gr	15.5 ± 3.3	183.0 ± 21.9	11.81

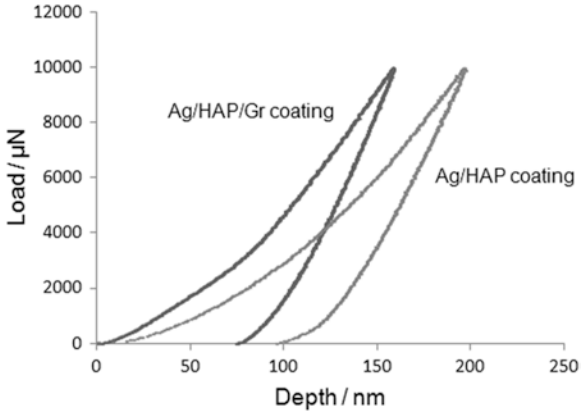

Fig. 5.28 Load-penetration depth curves for indents on Ag/HAP and Ag/HAP/Gr coatings (reprinted from [49] with permission from Elsevier)

Representative load–displacement curves of both Ag/HAP and Ag/HAP/Gr coatings obtained through nanoindentation are shown in Fig. 5.28. The Ag/HAP/Gr coating is more resistant to indentation, has higher hardness, and much lower penetration depth than the Ag/HAP coating. Also, the higher reduced modulus of the Ag/HAP/Gr coating indicates that the slope of the initial portion of the unloading curve for the Ag/HAP/Gr coating is obviously higher than that for the Ag/HAP coating. The impact of graphene reflects on increased contact area with the surrounding HAP matrix and as a result, the bonding strength between graphene and HAP grains is significantly enhanced. Improved mechanical properties stem from increased energy required to pull the nanofiller out from the HAP matrix. Graphene as a two-dimensional component reduces the crack formation within the composite by bridging effect between adjacent HAP grains and also HAP and nanofiller itself.

According to the proposed bonding mechanism between graphene sheets and hydroxyapatite lattice, graphene nanosheets are well bonded to the nearby HAP grains, thus increasing the toughness along grain boundaries and inhibiting crack propagation along

the grain boundary. Therefore, enhanced mechanical properties of the Ag/HAP/Gr composite coating are result of crack bridging, deflection, and grain bridging by the graphene nanofiller.

5.4.1.5 In Vitro Bioactivity

The bioactivity of Ag/HAP/Gr coating was tested by immersion in SBF solution at 37 °C for 7 days [49]. XRD patterns, before and after immersion in SBF, are shown in Fig. 5.29a. The diffractogram revealed HAP, but incorporation of Ag in the crystal HAP lattice causes a shift of specific peaks to the left, confirming the silver substitution for calcium. In addition, Ag was also recognized by appearance of characteristic peak at $2\theta = 43.9°$. High-intensity HAP peaks at (211), (112), and (300) crystal planes at $2\theta = 32.0$, 32.9, and 34.1° are easily distinguished, as well as presence of Ti substrate in its pure form on the coating interface. Thermally reduced graphene showed a broad (002) peak at $2\theta = 23–26°$ [133], but strong HAP diffraction peaks at crystal plane (002) mostly shield graphene peak. In addition, the specific broad peak at $2\theta = 22°$ observed for pure graphene is also overlapped by HAP diffraction peaks. Finally, the carbon peak at $2\theta = 26.6°$ is evidenced.

Upon soaking in a biomimetic system, bioactive materials form bone-like apatite layer on their surfaces. After immersion in SBF evident is the shift of characteristic peaks for Ag/HAP/Gr coating toward higher angles. Carbonated HAP as it appears in diffractogram (shift in HAP diffraction peaks), mimicking bone mineral, is especially advantageous. The crystallite domain size is calculated to be 17.6 and 22.3 nm, before and after immersion in SBF, respectively. Coherent domain sizes and microstrain of Ag/HAP/Gr coating were calculated by using (002), (211), (112), (300), (202), and (301) crystal planes. Difference between crystallite size before and after immersion is due to the CO_3^{2-} incorporation into the HAP lattice by occupying either the OH^- or the PO_4^{3-} sites [75].

Homogenous surface of Ag/HAP/Gr coating before immersion in SBF with rod-like HAP grains (≤50 nm in size) is observed in FE-SEM microphotographs (Fig. 5.29b). Inset in Fig. 5.29b shows the FE-SEM image after soaking in SBF, with a newly formed

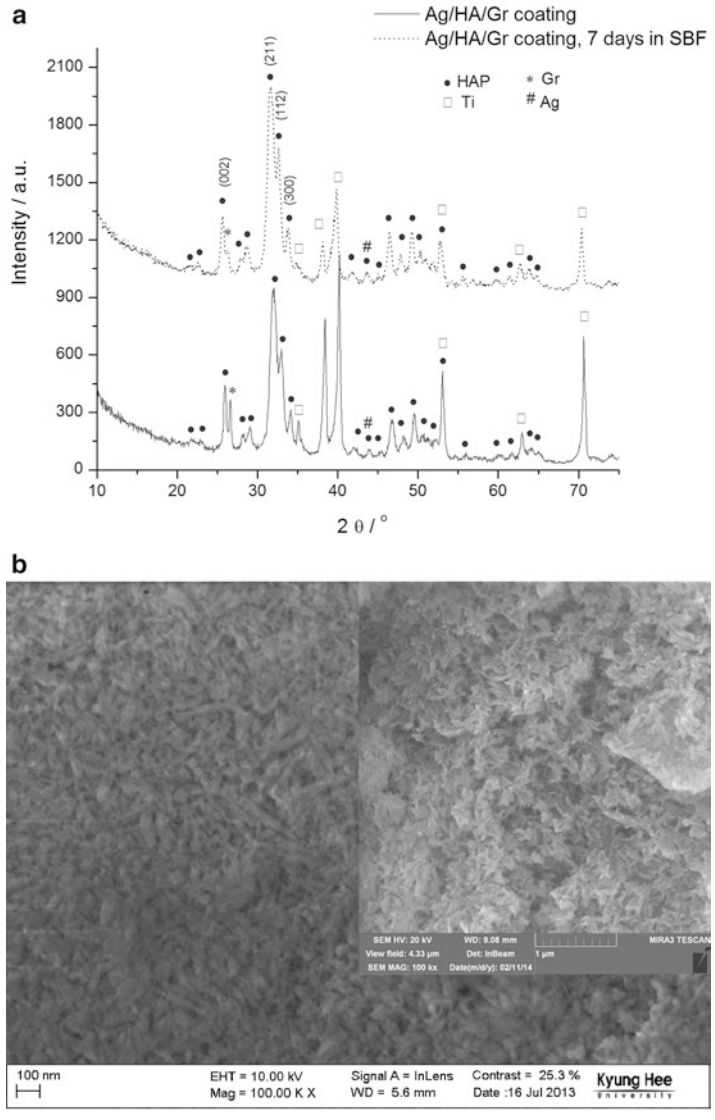

Fig. 5.29 XRD patterns (**a**) and FE-SEM microphotographs (**b**) of the Ag/HAP/Gr coating before and after immersion in SBF (*inset* in (**b**): Ag/HAP/Gr coating, 7 days in SBF, 37 °C) (reprinted from [49] with permission from Elsevier)

highly porous apatite layer containing plate-shaped HAP crystals beneficial for better cell adhesion. The high bioactivity of Ag/HAP/Gr coating is confirmed by forming an apatite film after just 7 days soaking in SBF. The apatite composition of newly formed crystals was confirmed by XRD results (Fig. 5.29a).

The corrosion stability of Ag/HAP/Gr coating was studied in SBF solution by EIS. The experimental impedance data of Ag/HAP/Gr coating and Ag/HAP coating, used as a reference, after different exposure times in SBF at 37 °C are presented as Nyquist plots (Fig. 5.30). Fitting of Nyquist plots was accomplished by using the equivalent electrical circuits (EEC) shown in Fig. 5.11a, c. The fitted curves at different times of immersion in SBF are shown in Fig. 5.30, while obtained fitting results are presented in Table 5.14.

In Table 5.14, n_c values are higher than 0.80, therefore CPE_c can be considered as coating capacitance C_c, while CPE_{ox} can be considered as capacitance of oxide film on titanium surface beneath Ag/HAP/Gr and Ag/HAP coatings, C_{ox}. EEC shown in Fig. 5.11a was used for fitting the Nyquist plots during 21 days of exposure to SBF. According to these results, R_c slightly decreased during first 3 days, indicating that coating pores were filled with SBF. However, after 7 days R_c values started to increase, indicating the beginning of new apatite layer formation. Furthermore, after 21 days, the calculated value of R_c was 73.9 kΩ cm^2, indicating the deposition of a newly formed carbonated HAP, which was confirmed also by XRD and FE-SEM (Fig. 5.29). The high value of coating pore resistance denotes improved bioactivity. This suggests that the Ag/HAP/Gr coating surface represented the site of nucleation and growth of new apatite layer—carbonated HAP. After 24 days, the Nyquist plots could not be fitted by the same EEC, instead EEC in Fig. 5.11c was used, when coating lost its adhesion property.

Correlating the behavior of Ag/HAP coating that looses its corrosion stability after 72 h as evidenced by semicircle diminishing in the Nyquist plot (Fig. 5.30b), Ag/HAP/Gr composite retained its protective attributes. The obtained Nyquist plots for Ag/HAP coating during exposure of 24 h in SBF were fitted by EEC in Fig. 5.11a. After initial 8 h period when R_c and C_c (Table 5.14) values were kept constant, substantial increase occurred at 24 h indicating the

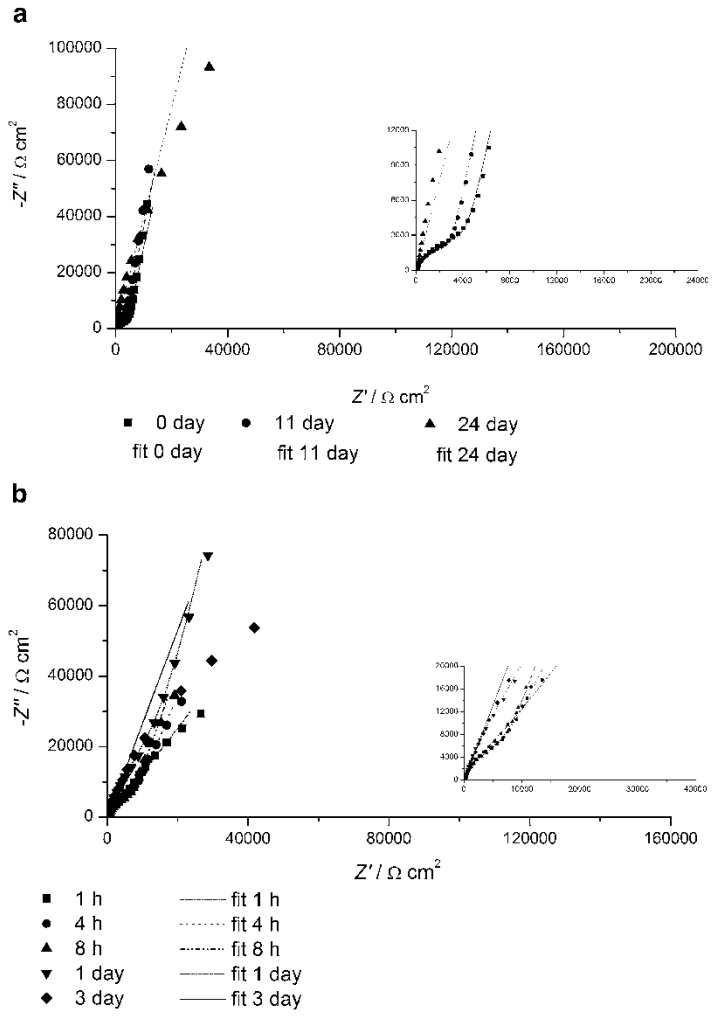

Fig. 5.30 The Nyquist plots of the Ag/HAP/Gr (**a**) and Ag/HAP coatings (**b**) after different immersion times in SBF at 37 °C (*dash line*—fitting) (reprinted from [49] with permission from Elsevier)

Table 5.14 Fitting values of equivalent electrical circuit parameters and goodness of fit (GOF) for the Ag/HAP/Gr and Ag/HAP coatings

t (h)	R_s (Ω cm^2)	R_c (kΩ cm^2)	CPE_c (μF cm^{-2})	n_c	CPE_{ox} (μF cm^{-2})	n_{ox}	Goodness of fit (GOF)
Ag/HAP/Gr							
1	38.83	6.12	55.1	0.804	241	0.882	$5.84e^{-4}$
2	38.87	5.95	53.2	0.808	255	0.887	$4.69e^{-4}$
4	39.13	5.83	57.7	0.813	264	0.888	$3.89e^{-4}$
6	39.46	5.84	50.4	0.816	264	0.892	$3.87e^{-4}$
8	39.63	5.69	49.3	0.819	271	0.898	$3.12e^{-4}$
24	31.45	3.51	44.6	0.849	299	0.917	$3.06e^{-5}$
72	15.30	2.48	38.6	0.871	303	0.879	$3.08e^{-5}$
168	31.08	3.05	35.5	0.883	248	0.913	$2.26e^{-5}$
264	25.88	4.17	43.6	0.850	197	0.884	$3.45e^{-4}$
360	68.65	9.42	52.1	0.824	135	0.854	$1.07e^{-4}$
504	133.2	73.9	51.1	0.816	82	0.823	$5.31e^{-4}$
576	74.38	–	–	–	45	0.851	$7.67e^{-3}$
Ag/HAP							
1	30.1	9.50	92.3	0.83	119	0.70	$3.90e^{-4}$
4	31.0	12.9	91.7	0.83	200	0.80	$1.63e^{-4}$
8	31.7	12.0	88.6	0.83	223	0.80	$1.38e^{-4}$
24	37.1	90.3	97.6	0.82	71	0.92	$2.43e^{-4}$
72	54.7	–	–	–	153	0.80	$3.84e^{-3}$

Reprinted from [49] with permission from Elsevier

new apatite layer formation. However, after 72 h, fitting could only be done by EEC in Fig. 5.11c that considers CPE_{ox}, indicating the coating adhesion loss. Based on the EIS data, it is evident that composite Ag/HAP/Gr coating exhibited superior biomimetic mineralization compared to its Ag/HAP counterpart. This is an additional

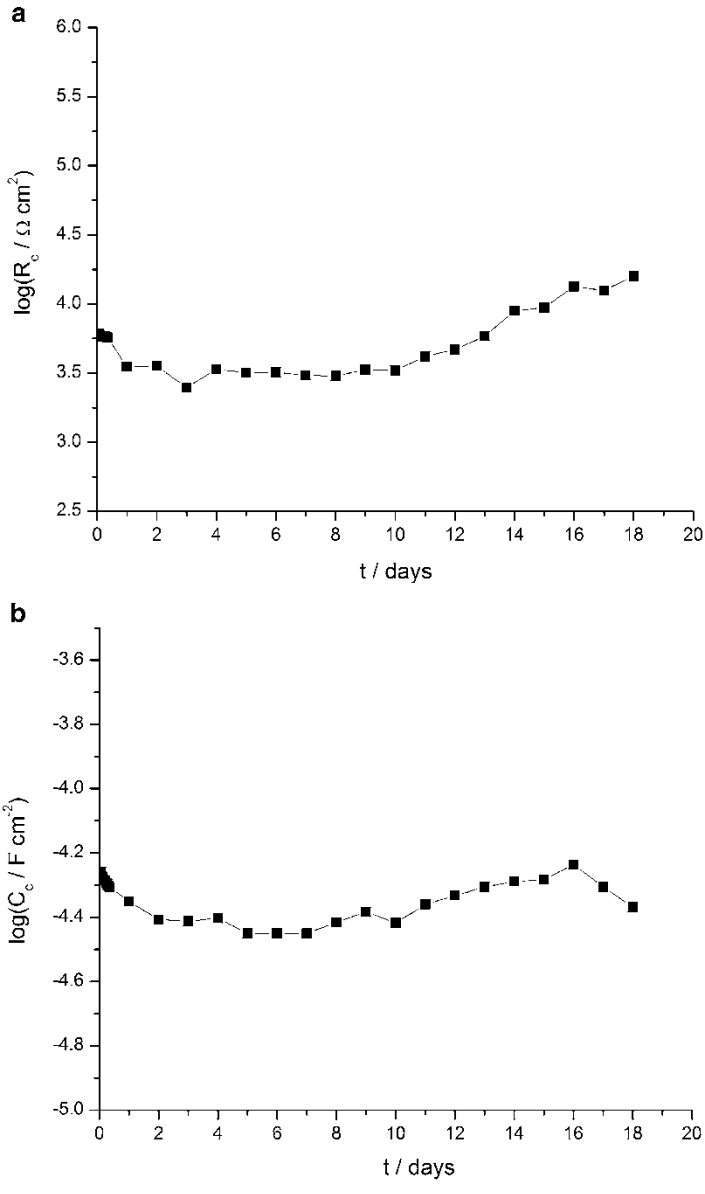

Fig. 5.31 Time dependence of coating pore resistance, R_c (**a**) and coating capacitance, C_c (**b**) of the Ag/HAP/Gr coating during exposure to SBF solution at 37 °C (reprinted from [49] with permission from Elsevier)

conformation of the proposed mechanism of enhanced precipitation of newly formed apatite layer, evidenced also by FE-SEM.

Long-term stability of Ag/HAP/Gr coating is best verified through time dependences of coating pore resistance, R_c and coating capacitance, C_c, as shown in Fig. 5.31a, b, respectively. These properties reflect electrochemical properties of graphene-based composite coating in SBF solution mimicking in vitro conditions. The Ag/HAP/Gr coating pore resistance (Fig. 5.31a) and coating capacitance (Fig. 5.31b) remain almost constant over 18 days of exposure to SBF solution, indicating the maintenance of good stability of the Ag/HAP/Gr coating in SBF solution.

5.4.1.6 Cytotoxicity and Antibacterial Activity

Cytotoxicity was determined by MTT test against healthy PBMC. Cell survival of PBMCs, calculated according to Eq. (5.2), was 79.6 ± 11.2 %. Examination of cytotoxic effects showed mild decrease in survival of healthy immunocompetent PBMC compared to the control cell sample. According to the classification found in literature [137] and presented in Table 5.15, Ag/HAP/Gr coatings displayed as noncytotoxic against target PBMC.

The antibacterial activity of Ag/HAP/Gr coating was tested against *S. aureus* TL and *E. coli* (ATCC 25922) by agar diffusion method and spread-plate test [49]. The results of qualitative antimicrobial agar diffusion tests showed that Ag/HAP/Gr affects both microorganisms. The average inhibition zone was 2.5 mm for *Staphylococcus aureus* TL. In the case of *Escherichia coli* the average inhibition zone is much less pronounced, only 0.5 mm. Antibacterial activity was also investigated quantitatively by monitoring changes in the viable number of bacterial cells in suspension. Figure 5.32a, b depicts the antibacterial activity of Ag/HAP/Gr coating against strain *Staphylococcus aureus* TL and *Escherichia coli* in PB.

Table 5.15 Cytotoxicity classification

Cell survival (%)	≥100	75–99	50–74	25–49	1–24	0
Classification	0	1	2	3	4	5

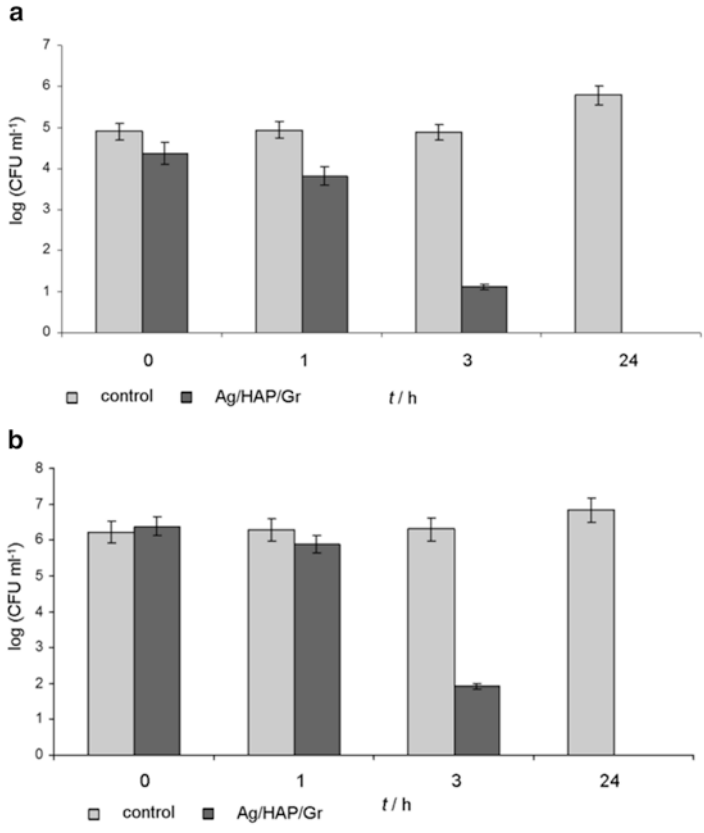

Fig. 5.32 Reduction of viable cell number of *S. aureus* (**a**) and *E. coli* (**b**) after contact with the Ag/HAP/Gr coating for 0, 1, 3, and 24 h in PB as compared to the control w/o samples (reprinted from [49] with permission from Elsevier)

As previously reported [46], antibacterial activity of the graphene-free Ag/HAP coating against *S. aureus* TL was noticed immediately after inoculation and the same trend was clearly evidenced throughout the 24 h duration of the experiment. Similar antimicrobial activity was noticed for the Ag/HAP/Gr coating. Namely, antimicrobial activity of the Ag/HAP/Gr coating (Fig. 5.32a, b) could be noticed immediately after inoculation of samples and subsequently one logarithmic unit

reduction of cell viability is achieved after only 1 h of incubation. Calculations based on initial number of cells in suspensions and 1 h postincubation revealed that Ag/HAP/Gr coating exhibited reduction of both bacteria, *S. aureus* TL (72.9% percentage of cell reduction) and *E. coli* (68.4% percentage of cell reduction). Graphene-based coating exhibited strong antibacterial activity also after 3 h of exposure, therefore suppressing harmful biofilm formation. Exactly as in the case of Ag/HAP coating, after 24 h, analyzed Ag/HAP/Gr samples did not contain any viable cell and visible colony even when samples were taken directly from the suspensions. An immediate silver ion release for both Ag/HAP and Ag/HAP/Gr coatings provided for the imminent drop in CFU numbers, which fits well with bactericidal properties necessary for prevention of biofilm formation [89].

5.5 Conclusions

Composite HAP/Lig and Ag/HAP/Lig coatings on titanium were obtained by electrophoretic deposition and sintered at a temperature of 900 °C, considerably lower than the usual sintering temperature due to nanosized particle dimension of HAP and Ag/HAP powders used for synthesis. The lignin allowed the formation of a compact, well adherent, and homogeneous coatings due to the establishment of different hydrogen bonds between the functional groups of hydroxyapatite and lignin. Based on XRD, ATR-FTIR, and XPS results, it was confirmed that lignin concentrations of 1 wt% and higher protect hydroxyapatite lattice from decomposition during sintering. Quantitative XPS measurements showed that the Ca/P ratio for both HAP/Lig and Ag/HAP/Lig coatings is similar to the stoichiometric Ca/P ratio.

The cytotoxicity determined by MTT assay indicates that HAP/Lig coating with 1 wt% Lig slightly reduced survival of healthy unstimulated PBMC and was classified as nontoxic. However, the absence of zones of inhibition of bacterial growth around the HAP/Lig coating with 1 wt% Lig was evident. Immediate and continuous release of Ag ions in Ag/HAP/Lig nonsintered coating indicated

the optimal inhibitory concentration of antibactericidal agents that diminish the growth of bacteria strain *S. aureus* TL. Cytotoxicity testing revealed that Ag/HAP/Lig coating with 1 wt% Lig was classified as nontoxic against PBMC cell lines. The newly formed bone-like plate-shaped apatite crystals observed on the surface of the Ag/HAP/Lig coating after soaking in SBF confirmed its bioactivity by FE-SEM, SEM, XRD, and ATR-FTIR results. Spontaneous growth on the surface of Ag/HAP/Lig coating of biologically active bone-like apatite layer can be tracked by impedance changes during soaking in SBF. However, this new apatite does not disturb the silver ion release from coating material and therefore the combination of the two results provides a strong platform for developing materials that are both bioactive and antimicrobial.

Composite HAP/Gr and Ag/HAP/Gr coatings were produced by EPD on titanium substrate using constant voltage method. Graphene incorporation was evidenced by FT-IR, Raman spectroscopy, and XPS spectra, and facilitated more uniform coating surface with less microcracks. The calculated Ca/P ratio for both HAP/Gr and Ag/HAP/Gr coatings is similar to the stoichiometric Ca/P ratio. The greater thermal stability of graphene-based coatings compared to the graphene-free coatings was confirmed by TGA, emphasizing improvements brought in by graphene addition. The nanoindentation results demonstrated that graphene nanosheets even at a very low concentration improved the mechanical properties of HAP effectively. EIS, XRD, and FE-SEM analyses clearly confirm the bioactivity of both HAP/Gr and Ag/HAP/Gr coatings in the formation of an apatite layer after soaking in SBF. Based on the EIS data, the graphene-based coatings exhibited superior biomimetic mineralization compared to the graphene-free coatings.

In vitro cytotoxicity evaluation indicated both graphene-based coatings as noncytotoxic against PBMC. No antibacterial effect of HAP/Gr coating could be observed against two common types of bacteria, *S. aureus* TL and *E. coli*, while Ag/HAP/Gr coatings exhibited strong antibacterial activity against *S. aureus* and *E. coli* after only 3 h of exposure, therefore suppressing harmful biofilm formation.

Therefore, the evidence presented here demonstrated that a nano-sized lignin-based and graphene-based HAP coatings produced by electrophoretic deposition on titanium substrate are excellent candidates for future biomedical hard tissue implants.

Acknowledgments The author wishes to thank all coworkers who contributed with their work to obtain the experimental results presented in this chapter. Their names can be seen in our joint papers listed in the references.

This research was financed by the Ministry of Education, Science and Technological Development, Republic of Serbia, contract No. III45019.

References

1. Manivasagam G, Dhinasekaran D, Rajamanickam A (2010) Biomedical implants: corrosion and its prevention—a review. Recent Pat Corros Sci 2:40–54
2. Eftekhari S, El Sawi I, Shaghayegh Bagheri Z, Turcotte G, Bougherara H (2014) Fabrication and characterization of novel biomimetic PLLA/cellulose/hydroxyapatite nanocomposite for bone repair applications. Mater Sci Eng C 39:120–125
3. Fidancevska E, Ruseska G, Bossert J, Lin Y-M, Boccaccini AR (2007) Fabrication and characterization of porous bioceramic composites based on hydroxyapatite and titania. Mater Chem Phys 103:95–100
4. Djošić MS, Mišković-Stanković VB, Milonjić S, Kačarević-Popović ZM, Bibić N, Stojanović J (2008) Electrochemical synthesis and characterization of hydroxyapatite powders. Mater Chem Phys 111:137–142
5. Mišković-Stanković VB (2014) Electrophoretic deposition of ceramic coatings on metal surfaces. In: Đokić S (ed) Electrodeposition and surface finishing, vol 57, Modern aspects of electrochemistry. Springer, New York, pp 133–216
6. Rath PC, Besra L, Singh BP, Bhattacharjee S (2012) Titania/hydroxyapatite bi-layer coating on Ti metal by electrophoretic deposition: characterization and corrosion studies. Ceram Int 38:3209–3216
7. Geetha M, Singh AK, Asokamani R, Gogi AK (2009) Ti based biomaterials, the ultimate choice for orthopaedic implants—a review. Prog Mater Sci 54:397–425
8. Swetha M, Sahithi K, Moorthi A, Srinivasan N, Ramasamy K, Selvamurugan N (2010) Biocomposites containing natural polymers and hydroxyapatite for bone tissue engineering. Int J Biol Macromol 47:1–4
9. Wang CX, Wang M, Zhou X (2002) Electrochemical impedance spectroscopy study of the nucleation and growth of apatite on chemically treated titanium. Langmuir 18:7641–7647

10. García C, Ceré S, Durán A (2006) Bioactive coatings deposited on titanium alloys. J Non Cryst Solids 352:3488–3495
11. Kung K-C, Lee T-M, Lui T-S (2010) Bioactivity and corrosion properties of novel coatings containing strontium by micro-arc oxidation. J Alloys Compd 508:384–390
12. Moseke C, Gbureck U, Elter P, Drechsler P, Zoll A, Thull R, Ewald A (2011) Hard implant coatings with antimicrobial properties. J Mater Sci Mater Med 22:2711–2720
13. Stoch A, Brozek A, Kmita G, Stoch J, Jastrzebski W, Rakowska A (2001) Electrophoretic coating of hydroxyapatite on titanium implants. J Mol Struct 596:191–200
14. Mourino V, Cattalini JP, Boccaccini AR (2012) Metallic ions as therapeutic agents in tissue engineering scaffolds: an overview of their biological applications and strategies for new developments. J R Soc Interface 9:401–419
15. Rameshbabu N, Sampath Kumat TS, Prabhakar TG, Sastry VS, Murty KVGK, Prasad Rao K (2007) Antibacterial nanosized silver substituted hydroxyapatite: synthesis and characterization. J Biomed Mater Res A 80A:581–591
16. Lee I-S, Whang C-N, Oh K-S, Park J-C, Lee K-Y, Lee G-H, Chung S-M, Sun X-D (2006) Formation of silver incorporated calcium phosphate film for medical applications. Nucl Instrum Methods B 242:45–47
17. Pang X, Zhitomirsky I (2008) Electrodeposition of hydroxyapatite–silver–chitosan nanocomposite coatings. Surf Coat Technol 202: 3815–3821
18. Simchi A, Tamjid E, Pishbin F, Boccaccini AR (2011) Recent progress in inorganic and composite coatings with bactericidal capability for orthopaedic applications. Nanomed Nanotechnol 7:22–39
19. Song YW, Shan DY, Han EH (2008) Electrodeposition of hydroxyapatite coating on AZ91D magnesium alloy for biomaterial application. Mater Lett 62:3276–3279
20. Boccaccini AR, Keim S, Ma R, Li Y, Zhitomirsky I (2010) Electrophoretic deposition of biomaterials. J R Soc Interface 7:S581–S613
21. Corni I, Ryan MP, Boccaccini AR (2008) Electrophoretic deposition: from traditional ceramics to nanotechnology. J Eur Ceram Soc 28:1353–1367
22. Boccaccini AR, Cho J, Subhani T, Kaya C, Kaya F (2010) Electrophoretic deposition of carbon nanotube–ceramic nanocomposites. J Eur Ceram Soc 30:1115–1129
23. Kaya C, Singh I, Boccaccini AR (2008) Multi-walled carbon nanotube-reinforced hydroxyapatite layers on Ti6Al4V medical implants by electrophoretic deposition (EPD). Adv Eng Mater 10:131–138
24. Van der Biest OO, Vandeperre LJ (1999) Electrophoretic deposition of materials. Annu Rev Mater Sci 9:327–352
25. Sun L, Berndt CC, Gross KA (2002) Hydroxyapatite/polymer composite flame-sprayed coatings for orthopedic applications. J Biomat Sci Polym Ed 13:977–990

26. Shuai C, Nie Y, Gao C, Lu H, Hu H, Wen X, Peng S (2012) Poly(l-lactide acid) improves complete nano-hydroxyapatite bone scaffolds through the microstructure rearrangement. Electron J Biotechnol 15:1–13
27. Alves Cardoso D, Jansen JA, Leeuwenburgh SCG (2012) Synthesis and application of nanostructured calcium phosphate ceramics for bone regeneration. J Biomed Mater Res Part B 100B:2316–2326
28. Wang J, de Boer J, de Groot K (2004) Preparation and characterization of electrodeposited calcium phosphate/chitosan coating on Ti6Al4V plates. J Dent Res 83:296–301
29. Martin H, Schulz KH, Bumgardner JD, Schneider JA (2008) Enhanced bonding of chitosan to implant quality titanium via four treatment combinations. Thin Solid Films 516:6277–6286
30. Xianmiao C, Yubao L, Yi Z, Li Z, Jidong L, Huanan W (2009) Properties and *in vitro* biological evaluation of nano-hydroxyapatite/chitosan membranes for bone guided regeneration. Mater Sci Eng C 29:29–35
31. Gebhardt F, Seuss S, Turhan MC, Hornberger H, Virtanen S, Boccaccini AR (2012) Characterization of electrophoretic chitosan coatings on stainless steel. Mater Lett 66:302–304
32. Mahmoodi S, Sorkhi L, Farrokhi-Rad M, Shahrabi T (2013) Electrophoretic deposition of hydroxyapatite–chitosan nanocomposite coatings in different alcohols. Surf Coat Technol 216:106–114
33. Batmanghelich F, Ghorbani M (2013) Effect of pH and carbon nanotube content on the corrosion behavior of electrophoretically deposited chitosan–hydroxyapatite–carbon nanotube composite coatings. Ceram Int 39:5393–5402
34. Deen I, Zhitomirsky I (2013) Electrophoretic deposition of composite halloysite nanotube–hydroxyapatite–hyaluronic acid films. J Alloys Compd 586:S531–S534
35. Cheong M, Zhitomirsky I (2008) Electrodeposition of alginic acid and composite films. Colloids Surf A 328:73–78
36. Zhitomirsky D, Roether JA, Boccaccini AR, Zhitomirsky I (2009) Electrophoretic deposition of bioactive glass/polymer composite coatings with and without HA nanoparticle inclusions for biomedical applications. J Mater Process Technol 209:1853–1860
37. Li P, Huang Z, Liu R, Xiao X (2009) Preparation of porous hydroxyapatite coating with glucose as pore producer. J Chin Ceram Soc 37:1864–1868
38. Parente P, Sanchez-Herencia AJ, Mesa-Galan MJ, Ferrari B (2013) Functionalizing Ti-surfaces through the EPD of hydroxyapatite/nanoY_2O_3. J Phys Chem B 117:1600–1607
39. Raschip IE, Vasile C, Ciolacu D, Cazacu G (2007) Semi-interpenetrating polymer networks containing polysaccharides. I Xanthan/Lignin networks. High Perform Polym 19:603–620
40. Park Y, Doherty WOS, Halley PJ (2008) Developing lignin-based resin coatings and composites. Ind Crop Prod 27:163–167

41. Mansur HS, Mansur AAP, Bicallho SMCM (2005) Lignin-hydroxyapatite/tricalcium phosphate biocomposites: SEM/EDX and FTIR characterization. Key Eng Mater 284–286:745–748
42. Martinez MM, Pacheco A, Vargas VM (2009) Histological evaluation of the biocompatibility and bioconduction of a hydroxyapatite-lignin compound inserted in rabbits shinbones. Rev MVZ Córdoba 14:1624–1632
43. Erakovic S, Veljovic DJ, Diouf PN, Stevanovic T, Mitric M, Milonjic S, Miskovic-Stankovic VB (2009) Electrophoretic deposition of biocomposite lignin/hydroxyapatite coatings on titanium. Int J Chem React Eng 7:A62
44. Eraković S, Veljović DJ, Diouf PN, Stevanović T, Mitrić M, Janaćković DJ, Matić IZ, Juranić ZD, Mišković-Stanković VB (2012) The effect of lignin on the structure and characteristics of composite coatings electrodeposited on titanium. Prog Org Coat 75:275–283
45. Eraković S, Janković A, Veljović DJ, Palcevskis E, Mitrić M, Stevanović T, Janaćković DJ, Mišković-Stanković V (2013) Corrosion stability and bioactivity in simulated body fluid of silver/hydroxyapatite and silver/hydroxyapatite/lignin coatings on titanium obtained by electrophoretic deposition. J Phys Chem B 117:1633–1643
46. Eraković S, Janković A, Matić IZ, Juranić ZD, Vukašinoć-Sekulić M, Stevanović T, Mišković-Stanković VB (2013) Investigation of silver impact on hydroxyapatite/lignin coatings electrodeposited on titanium. Mater Chem Phys 142:521–530
47. Erakovic S, Jankovic A, Tsui GCP, Tang CY, Miskovic-Stankovic V, Stevanovic T (2014) Novel bioactive antimicrobial lignin containing coatings on titanium obtained by electrophoretic depostion. Int J Mol Sci 15:12294–12322
48. Janković A, Eraković S, Mitrić M, Matić IZ, Juranić ZD, Tsui GCP, Tang CY, Mišković-Stanković V, Rhee KY, Park SJ (2015) Bioactive hydroxyapatite/graphene composite coating and its corrosion stability in simulated body fluid. J Alloys Compd 624:148–157
49. Janković A, Eraković S, Vukašinović-Sekulić M, Mišković-Stanković V, Park SJ, Rhee KY (2015) Graphene-based antibacterial composite coatings electrodeposited on titanium for biomedical applications. Prog Org Coat 83:1–10
50. Baurhoo B, Ruiz-Feria CA, Zhao X (2008) Purified lignin: nutritional and health impacts on farm animals—a review. Anim Feed Sci Technol 144:175–184
51. Gosselink RJA, Abächerli A, Semke H, Malherbe R, Käuper P, Nadif A, van Dam JEG (2004) Analytical protocols for characterisation of sulphur-free lignin. Ind Crop Prod 19:271–281
52. Pan X, Kadla JF, Ehara K, Gilkes N, Saddler JN (2006) Organosolv ethanol lignin from hybrid poplar as a radical scavenger: relationship between lignin structure, extraction conditions, and antioxidant activity. J Agric Food Chem 54:5806–5813

53. Palcevskis E, Dindune A, Kuznecova L, Lipe A, Kanepe Z (2005) Granulated composite powders on basis of hydroxyapatite and plasma-processed zirconia and alumina nanopowders. Latv J Chem 2:128–138
54. Veljovic DJ, Jokic B, Petrovic R, Palcevskis E, Dindune A, Mihailescu IN, Janackovic DJ (2009) Processing of dense nanostructured HAP ceramics by sintering and hot pressing. Ceram Int 35:1407–1413
55. Kwok CT, Wong PK, Cheng FT, Man HC (2009) Characterization and corrosion behavior of hydroxyapatite coatings on Ti6Al4V fabricated by electrophoretic deposition. Appl Surf Sci 255:6736–6744
56. Landi E, Tampieri A, Celotti G, Sprio S (2000) Densification behaviour and mechanisms of synthetic hydroxyapatites. J Eur Ceram Soc 20:2377–2387
57. Mostafa NY (2005) Characterization, thermal stability and sintering of hydroxyapatite powders prepared by different routes. Mater Chem Phys 94:333–341
58. Ma J, Liang CH, Kong LB, Wang C (2003) Colloidal characterization and electrophoretic deposition of hydroxyapatite on titanium substrate. J Mater Sci Mater Med 14:797–801
59. Ye HZ, Liu XY, Hong HP (2009) Characterization of sintered titanium/hydroxyapatite biocomposite using FTIR spectroscopy. J Mater Sci Mater Med 20:843–850
60. Filiaggi MJ, Pilliar RM, Coombs NA (1993) Post-plasma-spraying heat treatment of the HA coating/Ti-6A1-4V implant system. J Biomed Mater Res 27:191–198
61. Caroline Victoria E, Gnanam FD (2002) Synthesis and characterisation of biphasic calcium phosphate. Trends Biomater Artif Organs 16:12–14
62. Scholze B, Meier D (2001) Characterization of the water-insoluble fraction from pyrolysis oil (pyrolytic lignin). Part I. PY–GC/MS, FTIR, and functional groups. J Anal Appl Pyrolysis 60:41–54
63. Rodrigues PC, Cantao MP, Janissek P, Scarpa PCN, Mathias AL, Ramos LP, Gomes MAB (2002) Polyaniline/lignin blends: FTIR, MEV and electrochemical characterization. J Eur Polym 38:2213–2217
64. El-Hendawy A-NA (2006) Variation in the FTIR spectra of a biomass under impregnation, carbonization and oxidation conditions. J Anal Appl Pyrolysis 75:159–166
65. Roop Kumar R, Wang M (2002) Modulus and hardness evaluations of sintered bioceramic powders and functionally graded bioactive composites by nano-indentation technique. Mater Sci Eng A 338:230–236
66. Hahn B-D, Lee J-M, Park D-S, Choi J-J, Ryu J, Yoon W-H, Lee B-K, Shin D-S, Kim H-E (2009) Mechanical and *in vitro* biological performances of hydroxyapatite–carbon nanotube composite coatings deposited on Ti by aerosol deposition. Acta Biomater 5:3205–3214
67. Kaya C (2008) Electrophoretic deposition of carbon nanotube-reinforced hydroxyapatite bioactive layers on Ti–6Al–4V alloys for biomedical applications. Ceram Int 34:1843–1847

68. Mosmann T (1983) Rapid colorimetric assay for cellular growth and survival: application to proliferation and cytotoxicity assays. J Immunol Methods 65:55–63
69. Ohno M, Abe T (1991) Rapid colorimetric assay for the quantification of leukemia inhibitory factor (LIF) and interleukin-6 (IL-6). J Immunol Methods 145:199–203
70. Sjogren G, Sletten G, Dahl JE (2000) Cytotoxicity of dental alloys, metals, and ceramics assessed by Millipore filter, agar overlay, and MTT tests. J Prosthet Dent 84:229–236
71. Ugartondo V, Mitjans M, Pilar Vinardell M (2008) Comparative antioxidant and cytotoxic effects of lignins from different sources. Bioresour Technol 99:6683–6687
72. Sun R, Li M, Lu Y, Wang A (2006) Immersion behavior of hydroxyapatite (HA) powders before and after sintering. Mater Charact 56:250–254
73. Kim H-M, Himeno T, Kokubo T, Nakamura T (2005) Process and kinetics of bonelike apatite formation on sintered hydroxyapatite in a simulated body fluid. Biomaterials 26:4366–4373
74. Ye H, Liu XY, Hong H (2009) Cladding of titanium/hydroxyapatite composites onto Ti6Al4V for load-bearing implant applications. Mater Sci Eng C 29:2036–2044
75. Gu YW, Khor KA, Cheang P (2004) Bone-like apatite layer formation on hydroxyapatite prepared by spark plasma sintering (SPS). Biomaterials 25:4127–4134
76. Pecheva EV, Pramatarova LD, Maitz MF, Pham MT, Kondyuirin AV (2004) Kinetics of hydroxyapatite deposition on solid substrates modified by sequential implantation of Ca and P ions: part I. FTIR and Raman spectroscopy study. Appl Surf Sci 235:176–181
77. Mavropoulos E, Costa AM, Costa LT, Achete CA, Mello A, Granjeiro JM, Rossi AM (2011) Adsorption and bioactivity studies of albumin onto hydroxyapatite surface. Colloids Surf B 83:1–9
78. Liu H, Xi P, Xie G, Shi Y, Hou F, Huang L, Chen F, Zeng Z, Shao C, Wang J (2012) Simultaneous reduction and surface functionalization of graphene oxide for hydroxyapatite mineralization. J Phys Chem C 116:3334–3341
79. Stoch A, Jastrzebski W, Brozek A, Trybalska B, Cichocinska M, Szarawara E (1999) FTIR monitoring of the growth of the carbonate containing apatite layers from simulated and natural body fluids. J Mol Struct 511–512:287–294
80. Wang L-N, Luo J-L (2011) Fabrication and formation of bioactive anodic zirconium oxide nanotubes containing presynthesized hydroxyapatite via alternative immersion method. Mater Sci Eng C 31:748–754
81. Dong Z, Li Y, Zou Q (2009) Degradation and biocompatibility of porous nano-hydroxyapatite/polyurethane composite scaffold for bone tissue engineering. Appl Surf Sci 255:6087–6091

82. Bai X, Sandukas S, Appleford MR, Ong JL, Rabiei A (2009) Deposition and investigation of functionally graded calcium phosphate coatings on titanium. Acta Biomater 5:3563–3572
83. Popović MM, Grgur BN, Mišković-Stanković VB (2005) Corrosion studies on electrochemically deposited PANI and PANI/epoxy coatings on mild steel in acid sulfate solution. Prog Org Coat 52:359–365
84. Sluyters-Rehbach M (1994) Impedances of electrochemical systems: terminology, nomenclature and representation—part I: cells with metal electrodes and liquid solutions. Pure Appl Chem 66:1831–1891
85. Orazem ME, Tribollet B (2008) Electrochemical impedance spectroscopy. Wiley, Hoboken
86. Park J-H, Lee D-Y, Oh K-T, Lee Y-K, Kim K-M, Kim K-N (2006) Bioactivity of calcium phosphate coatings prepared by electrodeposition in a modified simulated body fluid. Mater Lett 60:2573–2577
87. Afzal MAF, Kalmodia S, Kesarwani P, Basu B, Balani K (2012) Bactericidal effect of silver-reinforced carbon nanotube and hydroxyapatite composites. J Biomater Appl 27:967–978
88. Stanic V, Janackovic DJ, Dimitrijevic S, Tanaskovic SB, Mitric M, Pavlovic MS, Krstic A, Jovanovic D, Raicevic S (2011) Synthesis of antimicrobial monophase silver-doped hydroxyapatite nanopowders for bone tissue engineering. Appl Surf Sci 257:4510–4518
89. Jamuna-Thevi K, Bakar SA, Ibrahim S, Shahab N, Toff MRM (2011) Quantification of silver ion release, *in vitro* cytotoxicity and antibacterial properties of nanostuctured Ag doped TiO_2 coatings on stainless steel deposited by RF magnetron sputtering. Vacuum 86:235–241
90. Mendes LC, Rodrigues RC, Silva EP (2010) Thermal, structural and morphological assessment of PVP/HA composites. J Therm Anal Calorim 101:899–905
91. Yao ZQ, Ivanisenko YU, Diemant T, Caron A, Chuvilin A, Jiang JZ, Valie RZ, Qi M, Fecht H-J (2010) Synthesis and properties of hydroxyapatite-containing porous titania coating on ultrafine-grained titanium by micro-arc oxidation. Acta Biomater 6:2816–2825
92. Roguska A, Pisarek M, Andrzejczuk M, Dolata M, Lewandowska M, Janik-Czachor M (2011) Characterization of a calcium phosphate–TiO2 nanotube composite layer for biomedical applications. Mater Sci Eng C 31:906–914
93. Battistoni C, Casaletto MP, Ingo GM, Kaciulis S, Mattogno G, Pandolfi L (2000) Surface characterization of biocompatible hydroxyapatite coatings. Surf Interface Anal 29:773–781
94. Dupraz A, Nguyen TP, Richard M, Daculsi G, Passuti N (1999) Influence of a cellulosic ether carrier on the structure of biphasic calcium phosphate ceramic particles in an injectable composite material. Biomaterials 20:663–673
95. Viornery C, Chevolot Y, Leonard D, Aronsson B-O, Pechy P, Mathieu HJ, Descouts P, Gratzel M (2002) Surface modification of titanium with

phosphonic acid to improve bone bonding: characterization by XPS and ToF-SIMS. Langmuir 18:2582–2589
96. Neelgund GM, Oki A, Luo Z (2013) *In situ* deposition of hydroxyapatite on graphene nanosheets. Mater Res Bull 48:175–179
97. Biris AR, Ardelean S, Lazar MD, Dervishi E, Watanabe F, Ghosh A, Biswas A, Biris AS (2012) Synthesis of few-layer graphene over gold nanoclusters supported on MgO. Carbon 50:2252–2263
98. Zhang L, Liu W, Yue C, Zhang T, Li P, Xing Z, Chen Y (2013) A tough graphene nanosheet/hydroxyapatite composite with improved *in vitro* biocompatibility. Carbon 61:105–115
99. Liu J, Yan H, Reece MJ, Jiang K (2012) Toughening of zirconia/alumina composites by the addition of graphene platelets. J Eur Ceram Soc 32:4185–4193
100. Kuilla T, Bhadra S, Yao D, Kim NH, Bose S, Lee JH (2010) Recent advances in graphene based polymer composites. Prog Polym Sci 35:1350–1375
101. Bartolucci SF, Paras J, Rafiee MA, Rafiee J, Lee S, Kapoor D, Koratkar N (2011) Graphene–aluminum nanocomposites. Mater Sci Eng A 528:7933–7937
102. Belmonte M, Ramírez C, González-Julián J, Schneider J, Miranzo P, Osendi MI (2013) The beneficial effect of graphene nanofillers on the tribological performance of ceramics. Carbon 61:431–435
103. Liu Y, Dang Z, Wang Y, Huang J, Li H (2014) Hydroxyapatite/graphene-nanosheet composite coatings deposited by vacuum cold spraying for biomedical applications: Inherited nanostructures and enhanced properties. Carbon 67:250–259
104. Witte F (2010) The history of biodegradable magnesium implants: a review. Acta Biomater 6:1680–1692
105. Baradaran S, Moghaddam E, Basirun WJ, Mehrali M, Sookhakian M, Hamdi M, Nakhaei Moghaddam MR, Alias Y (2014) Mechanical properties and biomedical applications of a nanotube hydroxyapatite-reduced graphene oxide composite. Carbon 69:32–45
106. Li M, Wang Y, Liu Q, Li Q, Cheng Y, Zheng Y, Xi T, Wei S (2013) *In situ* synthesis and biocompatibility of nano hydroxyapatite on pristine and chitosan functionalized graphene oxide. J Mater Chem B 1:475–484
107. Rodriguez-Lorenzo LM, Benito-Garzón L, Barroso-Bujans F, Fernández M (2008) Synthesis and biocompatibility of hydroxyapatite in a graphite oxide matrix. Key Eng Mater 396–398:477–480
108. Zhu J, Wong HM, Yeung KWK, Tjong SC (2011) Spark plasma sintered hydroxyapatite/graphite nanosheet and hydroxyapatite/multiwalled carbon nanotube composites: mechanical and in vitro cellular croperties. Adv Eng Mater 13:336–341
109. Kim S, Ku SH, Lim SY, Kim JH, Park CB (2011) Graphene–biomineral hybrid materials. Adv Mater 23:2009–2014

110. Bressan E, Ferroni L, Gardin C, Sbricoli C, Gobbato L, Ludovichetti FS, Tocco I, Carraro A, Piattelli A, Zavan B (2014) Graphene based scaffolds effects on stem cells commitment. J Transl Med 12:296 (p 1–15)
111. Biris AR, Mahmood M, Lazar M, Dervishi E, Watanabe F, Mustafa T, Baciut G, Baciut M, Bran S, Ali S, Biris AS (2011) Novel multicomponent and biocompatible nanocomposite materials based on few-layer graphenes synthesized on a gold/hydroxyapatite catalytic system with applications in bone regeneration. J Phys Chem C 115:18967–18976
112. Ma HB, Su WX, Tai ZX, Sun DF, Yan XB, Liu B, Xue QJ (2012) Preparation and cytocompatibility of polylactic acid/hydroxyapatite/graphene oxide nanocomposite fibrous membrane. Chin Sci Bull 57:3051–3058
113. Rafiee MA, Rafiee J, Srivastava I, Wang Z, Song HH, Yu ZZ et al (2010) Fracture and fatigue in graphene nanocomposites. Small 6(2):179–183
114. Lahiri D, Ghosh S, Agarwal A (2012) Carbon nanotube reinforced hydroxyapatite composite for orthopedic application: a review. Mater Sci Eng C 32(7):1727–1758
115. Park S, Ruoff RS (2009) Chemical methods for the production of graphenes. Nat Nanotechnol 4(4):217–224
116. Kalbacova M, Broz A, Kong J, Kalbac M (2010) Graphene substrates promote adherence of human osteoblasts and mesenchymal stromal cells. Carbon 48(15):4323–4329
117. Hu WB, Peng C, Luo WJ, Lv M, Li XM, Li D et al (2010) Graphene based antibacterial paper. ACS Nano 4(7):4317–4323
118. Kudin KN, Ozbas B, Schniepp HC, Prud'homme RK, Aksay IA, Car R (2008) Raman spectra of graphite oxide and functionalized graphene sheets. Nano Lett 8(1):36–41
119. Eraković S, Janković A, Ristoscu C, Duta L, Serban N, Visan A, Mihailescu IN et al (2014) Antifungal activity of Ag:hydroxyapatite thin films synthesized by pulsed laser deposition on Ti and Ti modified by TiO2 nanotubes substrates. Appl Surf Sci 293:37–45
120. Wu C-C, Huang S-T, Tseng T-W, Rao Q-L, Lin H-C (2010) FT-IR and XRD investigations on sintered fluoridated hydroxyapatite composites. J Mol Struct 979:72–76
121. Fan Z, Wang J, Wang Z, Ran H, Li Y, Niu L et al (2014) One-pot synthesis of graphene/hydroxyapatite nanorod composite for tissue engineering. Carbon 66:407–416
122. Lian P, Zhu X, Liang S, Li Z, Yang W, Wang H (2010) Large reversible capacity of high quality graphene sheets as an anode material for lithium-ion batteries. Electrochim Acta 55(12):3909–3914
123. Xie X, Hu K, Fang D, Shang L, Tran SD, Cerruti M (2015) Graphene and hydroxyapatite self-assemble into homogeneous, free standing nanocomposite hydrogels for bone tissue engineering. Nanoscale 7:7992–8002
124. Watling KM, Parr JF, Rintoul L, Brown CL, Sullivan LA (2011) Raman, infrared and XPS study of bamboo phytoliths after chemical digestion. Spectrochim Acta A 80(1):106–111

125. Li M, Liu Q, Jia Z, Xu X, Shi Y, Cheng Y et al (2013) Graphene oxide/hydroxyapatite composite coatings fabricated by electrophoretic nanotechnology for biological applications. Carbon 67:185–197
126. Nguyen VH, Kim BK, Jo Y-L, Shim J-J (2012) Preparation and antibacterial activity of silver nanoparticles-decorated graphene composites. J Supercrit Fluids 72:28–35
127. Loryuenyong V, Totepvimarn K, Eimburanapravat P, Boonchompoo W, Buasri A (2013) Preparation and characterization of reduced graphene oxide sheets via water-based exfoliation and reduction methods. Adv Mater Sci Eng 2013:Article ID 923403 (5 pages). doi:10.1155/2013/923403
128. Liang BJ, Huang Y, Zhang L, Wang Y, Ma Y, Guo T, Chen Y (2009) Molecular-level dispersion of graphene into poly(vinyl alcohol) and effective reinforcement of their nanocomposites. Adv Funct Mater 19(14):2297–2302
129. Liu Y, Huang J, Li H (2013) Synthesis of hydroxyapatite–reduced graphite oxide nanocomposites for biomedical applications: oriented nucleation and epitaxial growth of hydroxyapatite. J Mater Chem B 1:1826–1834
130. Niinomi M, Nakai M (2011) Titanium-based biomaterials for preventing stress shielding between implant devices and bone. Int J Biomaterials 2011:Article ID 836587 (10 pages). doi:10.1155/2011/836587
131. Niinomi M (2011) Low modulus titanium alloys for inhibiting bone atrophy. In: Pignatello R (ed) Biomaterials science and engineering. InTech, Shanghai, pp 249–268
132. Huang L-Y, Xu K-W, Lu J, Guelorget B, Chen H (2001) Nano-scratch and fretting wear study of DLC coatings for biomedical application. Diam Relat Mater 10:1448–1456
133. Sharma G, Gosavi SW (2014) Thermoluminescence properties of graphene–nano ZnS composite. J Lumin 145:557–562
134. Cheary RW, Coelho AA (1992) A fundamental parameters approach to X-ray line-profile fitting. J Appl Crystallogr 25(2):109–121
135. Janković A, Eraković S, Dindune A, Veljović DJ, Stevanović T, Janaćković DJ, Mišković-Stanković V (2012) Electrochemical impedance spectroscopy of a silver-doped hydroxyapatite coating in simulated body fluid used as a corrosive agent. J Serb Chem Soc 77:1609–1623
136. Ciobanu CS, Iconaru SL, Pasuk I, Vasile BS, Lupu AR, Hermenean A, Dinischiotu A, Predoi D (2013) Structural properties of silver doped hydroxyapatite and their biocompatibility. Mater Sci Eng C 33:1395–1402
137. Hu Y, Darcos V, Monge S, Li S, Zhou Y, Su F (2014) Tunable thermoresponsive P(NIPAAm-coDMAAm)-b-PLLA-b-P(NIPAAm-co-DMAAm) triblock copolymer micelles as drug carriers. J Mater Chem B 2:2738–2748

Index

S. Djokić (ed.), *Biomedical and Pharmaceutical Applications of Electrochemistry*, Modern Aspects of Electrochemistry 60,
DOI 10.1007/978-3-319-31849-3